

Lecture Notes in Mechanical Engineering

Dean Vučinić
Vidya Chandran
Alam Md. Mahbub
C. B. Sobhan *Editors*

Applications of Computation in Mechanical Engineering

Select Proceedings of 3rd International
Conference on Computing in Mechanical
Engineering (ICCME 2021)

 Springer

Lecture Notes in Mechanical Engineering


Series Editors

Fakher Chaari, National School of Engineers, University of Sfax, Sfax, Tunisia

Francesco Gherardini , Dipartimento di Ingegneria “Enzo Ferrari”, Università di Modena e Reggio Emilia, Modena, Italy

Vitalii Ivanov, Department of Manufacturing Engineering, Machines and Tools, Sumy State University, Sumy, Ukraine

Editorial Board

Francisco Cavas-Martínez , Departamento de Estructuras, Construcción y Expresión Gráfica Universidad Politécnica de Cartagena, Cartagena, Murcia, Spain

Francesca di Mare, Institute of Energy Technology, Ruhr-Universität Bochum, Bochum, Nordrhein-Westfalen, Germany

Mohamed Haddar, National School of Engineers of Sfax (ENIS), Sfax, Tunisia

Young W. Kwon, Department of Manufacturing Engineering and Aerospace Engineering, Graduate School of Engineering and Applied Science, Monterey, CA, USA

Justyna Trojanowska, Poznan University of Technology, Poznan, Poland

Lecture Notes in Mechanical Engineering (LNME) publishes the latest developments in Mechanical Engineering—quickly, informally and with high quality. Original research reported in proceedings and post-proceedings represents the core of LNME. Volumes published in LNME embrace all aspects, subfields and new challenges of mechanical engineering.

To submit a proposal or request further information, please contact the Springer Editor of your location:

Europe, USA, Africa: Leontina Di Cecco at Leontina.dicecco@springer.com

China: Ella Zhang at ella.zhang@springer.com

India: Priya Vyas at priya.vyas@springer.com

Rest of Asia, Australia, New Zealand: Swati Meherishi at swati.meherishi@springer.com

Topics in the series include:

- Engineering Design
- Mechanical Structures and Stress Analysis
- Engine Technology
- Nanotechnology and Microengineering
- Control, Robotics, Mechatronics
- MEMS
- Theoretical and Applied Mechanics
- Fluid Mechanics
- Engineering Thermodynamics, Heat and Mass Transfer
- Manufacturing
- Precision Engineering, Instrumentation, Measurement
- Tribology and Surface Technology

Indexed by SCOPUS and EI Compendex. All books published in the series are submitted for consideration in Web of Science.

To submit a proposal for a monograph, please check our Springer Tracts in Mechanical Engineering at <https://link.springer.com/bookseries/11693>

Dean Vučinić · Vidya Chandran ·
Alam Md. Mahbub · C. B. Sobhan
Editors

Applications of Computation in Mechanical Engineering

Select Proceedings of 3rd International
Conference on Computing in Mechanical
Engineering (ICCME 2021)

 Springer

Editors

Dean Vučinić
(Editor-in-Chief), The Brussels School
of Governance
Vrije Universiteit Brussel
Brussels, Belgium

Alam Md. Mahbub
Harbin Institute of Technology (Shenzhen)
University
Shenzhen, China

Vidya Chandran
Department of Mechanical Engineering
SCMS School of Engineering
and Technology
Ernakulam, India

C. B. Sobhan
School of Materials Science
and Engineering
National Institute of Technology Calicut
Calicut, Kerala, India

ISSN 2195-4356

ISSN 2195-4364 (electronic)

Lecture Notes in Mechanical Engineering

ISBN 978-981-19-6031-4

ISBN 978-981-19-6032-1 (eBook)

<https://doi.org/10.1007/978-981-19-6032-1>

© The Editor(s) (if applicable) and The Author(s), under exclusive license to Springer Nature Singapore Pte Ltd. 2023

This work is subject to copyright. All rights are solely and exclusively licensed by the Publisher, whether the whole or part of the material is concerned, specifically the rights of translation, reprinting, reuse of illustrations, recitation, broadcasting, reproduction on microfilms or in any other physical way, and transmission or information storage and retrieval, electronic adaptation, computer software, or by similar or dissimilar methodology now known or hereafter developed.

The use of general descriptive names, registered names, trademarks, service marks, etc. in this publication does not imply, even in the absence of a specific statement, that such names are exempt from the relevant protective laws and regulations and therefore free for general use.

The publisher, the authors, and the editors are safe to assume that the advice and information in this book are believed to be true and accurate at the date of publication. Neither the publisher nor the authors or the editors give a warranty, expressed or implied, with respect to the material contained herein or for any errors or omissions that may have been made. The publisher remains neutral with regard to jurisdictional claims in published maps and institutional affiliations.

This Springer imprint is published by the registered company Springer Nature Singapore Pte Ltd.

The registered company address is: 152 Beach Road, #21-01/04 Gateway East, Singapore 189721, Singapore

Preface I

Dear Authors and Esteemed Participants,

It is with immense satisfaction that we write the foreword to the proceedings of the Third International Conference on Computing in Mechanical Engineering, sponsored by the All India Council for Technical Education. The conference was hosted virtually by the SCMS School of Engineering and Technology, Cochin, and witnessed an extravagant display of computational techniques and their application in mechanical and related engineering.

ICCME was launched in 2015, with a vision to become a regular global platform for computing enthusiasts from academia and industry to interact, discuss, and disseminate their ideas and views on computational methods. After the second edition of ICCME in 2017, which was a grand success with participants from around the globe, it took a long four years to showcase the eminence of this prestigious event since the world was busy fighting the pandemic. ICCME, relaunched in 2021 under the sponsorship of the All India Council for Technical Education, partnering with Springer Publications, brought the best experience of computational analysis in mechanical engineering to its participants. Keynote lectures by the most eminent computational experts from academia discussed the theory of novel computing techniques, methods, and their applications, while a hands-on experience on computing tools was provided by the expert team from Cadence—Numecca, Belgium. We were fortunate enough to have Prof. Alam Md. Mahbub and Prof. Bale V. Reddy with us for ICCME from the very beginning of the conference in 2015.

We conclude with a positive note and hope to meet all our organizers, panelists, speakers, delegates, and sponsors in person during the next edition of ICCME.

Brussels, Belgium

Prof. Dr. Ir. Dean Vučinić
(Editor-in-Chief)

Ernakulam, India

Dr. Vidya Chandran

Preface II

This conference proceedings volume contains the selected contributions to computing in mechanical engineering presented at ICCME'21—The Third International Conference on Computing in Mechanical Engineering, a virtual event held during September 22–24, 2021, hosted by the SCMS School of Engineering and Technology, Ernakulam, India.

Computers manifest themselves as a tool for designing, analyzing, and experimenting the scientific processes with much ease and accuracy. The applications of computers in the field of mechanical engineering extended the horizons of research and development. Computational skills when used effectively with scientific experiments and sound theoretical knowledge can tremendously increase research output. Processes such as fluid flow, solidification and melting, combustion in the IC engines, and many other complex and fast physical phenomena can be visualized, and every minute aspect of these processes can be better comprehended through computational techniques.

The application of computing is not limited to computational fluid dynamics (CFD), but it is hard to find an area in mechanical engineering where computation is not used as a tool for enhancing productivity. While CFD can be used for visualizing and predicting flow characteristics, computer-aided designing is used in the design and installation phase, MATLAB for optimizing designs and processes, CNC programming for controlling machines and processes, and BIM in the decommissioning phase. High-performance computing employing cluster, blade, and cloud environments has indeed paved the way for the most convenient and state-of-the-art

applications of computing in mechanical and allied engineering fields turning tedious impossible calculations into possible.

Brussels, Belgium

Dean Vučinić
(Editor-in-Chief)

Ernakulam, India
Shenzhen, China
Calicut, India

Vidya Chandran
Alam Md. Mahbub
C. B. Sobhan

Acknowledgments

The organizing committee of ICCME'21 expresses our sincere gratitude to Dr. G. P. C. Nayar, Founder and Chairman of SCMS Group of Educational Institutions, whose visions lead us through the path of excellence. Guidance and support from Prof. Pramod P. Thevannoor, Vice-Chairman, SCMS Group, Dr. S. Gopakumar, Senior Group Director, SCMS Group, Dr. Praveensal C. J., Principal, SCMS School of Engineering and Technology, for the conduct of the conference is acknowledged thankfully. We acknowledge the contribution of Dr. Sheeja Janardhanan, organizing chair, ICCME'15 and ICCME'17, for elevating the conference to a global platform for disseminating knowledge in the computing domain.

About the Conference



Third International Conference on Computing in Mechanical Engineering 2021 (ICCME'21)

The International Conference on Computing in Mechanical Engineering (ICCME'21) focuses on the applications of computation and simulation techniques in mechanical engineering and related fields. The conference provides a platform for all computing enthusiasts from academia and industry to discuss and disseminate their ideas and findings.

ICCME'21 invited contributions in thirteen tracks, highlighting computing as a tool for analysis in core mechanical engineering research. From the one hundred and twenty-seven extended abstracts received, sixty-five papers were selected and presented at the conference. From the presented papers, twenty eight were selected and included in this conference proceedings. The proceedings also includes the written versions of the plenary talk delivered during the conference. The selected papers cover a wide range of computing aspects in mechanical engineering, especially in fluid flow and heat transfer, material science, manufacturing, and industrial engineering.

The conference was inaugurated by Prof. Dr. Gerardo Carbajal, Florida Polytechnic University, USA. Plenary talk by Prof. Dr. Ir. Dean Vučinić, Vrije Universiteit, Brussels, and his project consortium from the DIV group were greatly appreciated by the participants for the effort taken by the team to make the session lively and informative. Invited lectures by Prof. Dr. Alam Md. Mahbub, Harbin Institute of Technology, Shenzhen, China, Prof. Dr. B. V. Reddy, Ontario Tech University, Canada, Dr. Arul Prakash, Indian Institute of Technology Madras, India, and Dr. M. Sekar, AAA College of Engineering, India, added to the take away from the conference on diverse aspects of computing.

The third edition of ICCME, after the grand success of the previous two editions, ICCME'15 and ICCME'17, had the added advantage of hands-on training sessions on multiphysics engineering simulation software, Omnis 5.1, for the conference participants, offered by Cadence Numeca, Belgium. The conference also hosted a panel discussion on the pros and cons of experimental and computational methods among six computing experts.

The conference was supported financially under Grant for Organizing Conferences (GOC) by the All India Council for Technical Education (AICTE). It is our pleasant duty to acknowledge the support provided by the Board of Directors, SCMS Group of Educational Institutions, Cochin, for hosting the conference.

We thank all the participants for choosing ICCME as a platform to present and publish their research. This conference was a success in bringing all the engineers, scientists, academicians, and students to a common platform for discussing, interacting, exchanging, and disseminating the recent ideas, methods, trends, problems, and solutions of computational methods for solving problems in mechanical engineering through technical paper presentations on a conglomeration of diversified topics which apply computational techniques.

Editors

Dean Vučinić (Editor-in-Chief)

Vidya Chandran

Alam Md. Mahbub

C. B. Sobhan

Conference Organizers

Chief Patron

Dr. G. P. C. Nayar, Chairman, SCMS Group

Patrons

Prof. Pramod P. Thevannoor, Vice-Chairman, SCMS Group

Prof. S. Gopakumar, Senior Group Director, SCMS Group

Dr. Praveensal C. J., Principal, SCMS School of Engineering and Technology

Advisory/Technical Program Committee

Prof. Dr. Ir. Dean Vučinić, Professor, Brussels School of Governance, Vrije Universiteit Brussel, Belgium

Dr. Alam Md. Mahbub, Professor, Harbin Institute of Technology, University Town, Shenzhen, China

Dr. B. V. Reddy, Professor, Department of Mechanical Engineering, UOIT, Oshawa, ON, Canada

Dr. Tony Varghese, Research Scientist, Boise State University, Idaho, USA

Dr. Siby Thomas, Postdoctoral Research Associate, Colorado School of Mines, Golden, CO, USA

Dr. Sivasankara Rao Ede, Postdoctoral Research Fellow, Fayetteville State University, Fayetteville, USA

Dr. Alexander Sergeevich Pugachuk, Junior Researcher, Joint Institute for High Temperatures of the Russian Academy of Sciences, Moscow, Russia

Dr. K. Arul Prakash, Professor, Department of Applied Mechanics, IIT Madras, Tamil Nadu, India

Dr. C. B. Sobhan, Professor, School of Materials Science and Engineering, NIT Calicut, Kerala, India

Dr. C. P. Jawahar, Professor and Head, Department of Mechanical Engineering, Amity University, Gwalior, Madhya Pradesh

Dr. Tide P. S., Professor, Department of Mechanical Engineering, School of Engineering, CUSAT, Kochi, India

Dr. T. C. Bera, Assistant Professor, Department of Mechanical Engineering, BITS Pilani, Rajasthan, India

Dr. M. Sekar, Principal, AAA College of Engineering and Technology, Sivakasi, Tamil Nadu, India

Dr. Senthil Prakash M. N., Associate Professor, Department of Mechanical Engineering, Cochin University College of Engineering, Kuttanad, Alappuzha, India

Dr. Pradeep M. Kammath, Assistant Professor, Department of Mechanical Engineering, Government Engineering College, Thrissur, India

Dr. Rajesh P. Nair, Assistant Professor, Department of Ship Technology, CUSAT, Kochi, India

Dr. Gibin George, Assistant Professor, Department of Mechanical Engineering, SCMS School of Engineering and Technology, Karukutty, Ernakulam, India

Organizing Committee Members

Department of Mechanical Engineering, SCMS School of Engineering and Technology, Ernakulam, Kerala, India

Organizing Chair

Dr. Vidya Chandran, Associate Professor

Convener

Dr. Rag R. L., Professor and Head

Co-convener

Dr. Mahesh Rengaraj, Professor

Technical Program coordinators

Dr. Jenson Joseph, Associate Professor

Dr. Manikandan H., Assistant Professor

Publication Coordinators

Dr. Raghav G. R., Associate Professor

Dr. Gibin George, Assistant Professor

AICTE Auditors

Dr. Sam Joshy, Associate Professor

Mr. Sujith R., Assistant Professor

Organizing Secretary

Mr. Noel Joseph Gomez, Assistant Professor

Treasurers

Mr. Vishnu H., Assistant Professor

Mr. Jose Sheril D'Cotha, Assistant Professor

Media and Publicity In-charge

Mr. Ajith Kumar, Assistant Professor

Mr. Anup Kumar T. M., Assistant Professor

Session Organizers

Mr. Suraj R., Assistant Professor

Mr. Francis Thomas, Assistant Professor

Hospitality In-charge

Mr. Rakesh A., Assistant Professor

Mr. Manoj Jose Kalathil, Assistant Professor

Quality Controllers

Mr. Sanoj Varghese, Assistant Professor

Dr. Anjana Viswanath, Assistant Professor

Workshop Organizers

Mr. Nikhil Asok N., Assistant Professor

Mr. Sanju A. C., Assistant Professor

Coordinator—Panel Discussion

Mr. Dhanesh S., Assistant Professor

Student Coordinators

Mr. Fahad Bin Shahabudheen

Mr. Adarsh Chandran

Contents

Conceptual Design of Zero-Emission Sailing Ship Renewable Energy Challenges	1
Željko Hederić, Dean Vučinić, Mislav Brlić, Mislav Bezovnik, Ivan Rutnik, Marko Cuković, Mario Čačić, Antonio Hmura, Dina Jukić, Miljenko Švarcmajer, and Bojan Vučinić	
Modeling and Simulation in Materials and Manufacturing	
Simulation Analysis of Composite Materials for Divergence Elimination	21
Kalaivanan, Ganesh Karthic, Vyas Jatinkumar Manubhai, N. P. Pavai, V. Aravinth, S. Poornachandran, and Naveen Velmurugan	
Effect of Fiber Drawing on Tensile Strength of UHMWPE Single Fibers: Simulation via Von Mises Stress Criterion	35
Shubhanker Singh, Vishal Das, D. N. Tripathi, and N. Eswara Prasad	
Prediction of In-Process Forces and Tool Durability in Stationary Shoulder Friction Stir Welding: A Process Modeling Approach	49
Vikash Kumar and Buchibabu Vicharapu	
Wire Arc Additive Manufacturing of ATI 718PLUS®: A Process Modeling Approach	59
Mohammad Shabbar and Buchibabu Vicharapu	
A Review on Computational Techniques for Nanostructured Polymer Composite Materials	69
G. R. Raghav, Gibin George, R. Sujith, and Nikhil Ashok	
Design and Computational Analysis of DeusCell—A Piston Actuated Modular Reconfigurable Robot	79
Aaditya Radhakrishnan, Abel P. Johnson, Nikhil Roy, Ruben Geo Ribu, and B. Deepak	

Structural Design of Ultimate Terrain Electric Vehicle Suspension System 93
 Jerin Joseph, Justine Joseph, Karthik S. Rajendran, and M. S. Anoop

Modal Analysis of Motorcycle Handlebar 109
 T. G. Ajay Krishnan, R. Ajay Krishna, S. Akash, Akhildev K. Vasudevan, and B. Rajesh Menon

Computing in Medicine and Biology

CFD Analysis to Minimize the Spread of COVID-19 Virus in Air-Conditioned Classroom 121
 Adnan Memon and Balkrushna Shah

A Viable Approach to Medical Image Processing for CFD Simulations of the Upper Respiratory Tract 137
 Akash James, Joshua Mathew Jacob, Liza Mathew, and Ajith Kumar Arumugham-Achari

Evaluation of Hemodynamics Parameters in Carotid Bifurcation System using Numerical Simulation 149
 H. N. Abhilash, S. M. Abdul Khader, Raghuvir Pai, Nitesh Kumar, Mohammad Zuber, John Corda, and Masaaki Tamagawa

Comparison of Newtonian and Non-Newtonian Flow in Abdominal Aorta and Renal Artery Using Numerical Simulation 163
 B. Gowrava Shenoy, Nitesh Kumar, A. B. V. Barbouza, S. M. Abdul Khader, A. Ravindra Prabhu, Masaaki Tamagawa, and B. Raghuvir Pai

Analysis and Prediction of COVID-19 Spread in Ernakulam District, Kerala 173
 Serin Kuriakose, Zarin Pilakkadavath, C. Rohini, and S. Sreedevi

Optimization Techniques

Solar Water Pumping System Design and Analysis-A Numerical Study at Dum Dum, Kolkata 187
 A. Kr. Roy and S. Dutta

A Model for Prediction of Water Level and Pressure in an Industrial Boiler Using Multivariate Regression 201
 V. K. Haribhakta, R. S. Jha, A. K. Kelkar, A. N. Khairnar, and H. S. Khade

Optimisation of Parameters in Numerical Simulation of Hot Forging Using Taguchi Approach 215
 Sam Joshy, T. M. Anup Kumar, N. Nikhil Asok, R. Suraj, and Koshy P. Joseph

Selecting the Optimum Tool for Driving Performance Evaluation by Assessing the Ergonomic Methods—An Overview 227
 Arun Chand, H. Mannikandan, and A. B. Bhasi

Optimization of Geometrical Parameters in Magnetorheological Dampers Using Finite Element Modeling 239
 N. Nikhil Asok, Sam Joshy, R. Suraj, Anjana Viswanath, and A. Rakesh

Academic Performance Prediction of Postgraduate Students Using Artificial Neural Networks 253
 M. Varun, R. Sridharan, and K. K. Eldose

Internet of Things-Based Attendance Management System 263
 J. Anoj, R. Sridharan, and V. Karthikeyan

Patient Flow Optimization in an Emergency Department Using SimPy-Based Simulation Modeling and Analysis: A Case Study 271
 Anudeep Battu, S. Venkataramanaiah, and R. Sridharan

Computation in Fluid Flow and Heat Transfer

Comparison of Simple Probabilistic Approach with Deterministic Model for Predicting Surge and Leakage in Water Pipelines 283
 C. D. John Paul, P. Radhika, Ajith Kumar Arumugham-Achari, Anu Mol Joy, Abraham Thomas, and Dominic Mathew

Design and Analysis of Liquid-Cooled Battery Thermal Management System of Electric Vehicles 299
 Athul Rajeev Mundonkakkoth, Nandini Menon, and Thundil Karuppa Raj

Numerical Analysis to Investigate the Effect of Solidification Parameters on the Pull-In Effect of Continuous Casting 313
 Ritesh S. Fegade, Rajendrakumar G. Tated, and Rupendra S. Nehete

Mathematical Modeling of a Skin Condenser with Angular Contact for Domestic Refrigerator 327
 N. D. Shikalgar, S. N. Sapali, and A. B. Shinde

Aerodynamic Analysis of Deployable Wing Arrangement for Space Shuttle 337
 Vidya Chandran, Poornima Rajendran, Shabu Gopakumar, K. S. Arun Kumar, C. A. Nikhilraj, and Sheeja Janardhanan

Single Blow Characteristics of a Porous Spherical Bed Regenerator at Liquid Nitrogen Temperature 355
 V. M. Abhiroop, R. I. Vivek, K. E. Reby Roy, and B. R. Vishnu

Design, Development, and Numerical Analysis of Mist Nozzle and Its Impact on Performance Parameters of an Evaporative Cooler 371

Avinash M. Deshmukh, S. N. Sapali, Ajit B. Shinde,
and Niyaj D. Shikalgar

About the Editors

Prof. Dr. Ir. Dean Vučinić is professor at the Brussels School of Governance (BSoG) at Vrije Universiteit Brussel (VUB), which he joined in 2017, as adjunct Professor in Global Business and Entrepreneurship/Bachelors and Masters Preparatory Programmes. He is also visiting Full Professor at Faculty of Electrical Engineering, Computer Science and Information Technology (FERIT), University of Osijek and Technical Faculty, University of Pula (UNIPU), both in Croatia. His work is mostly related to Research and Development (R&D) projects, and his interest covers scientific visualization, modelling and simulation, optimization methodologies and techniques. His Ph.D. became a book, as in the early 90's he developed "CFView—Computational Field Visualization System", the first-time-ever interactive visualization software for numerical simulations, fully based on the object oriented technology. In his 30 years at VUB, he has successfully participated in over 20 European Commission R&D projects (FP, H2020, EUREKA/ITEA and Tempus/Erasmus+). He is author of over 70 scientific papers in international reviewed journals and conference proceedings, and several book chapters. He is member of International Boards of Journals and Conferences, acting as chair, session organizer, reviewer and editor. He is the European Commission expert in H2020 and member of international organizations: AIAA, IEEE, ACM, SAE and ASME.

Dr. Vidya Chandran is currently Associate Professor in the Department of Mechanical Engineering, SCMS School of Engineering and Technology, India, affiliated to A. P. J. Abdul Kalam Technological University, India. She earned her Ph.D. in Mechanical Engineering from the School of Mechanical Sciences, Karunya Institute of Technology and Sciences, India. She did her research in numerical prediction of vortex induced vibration of offshore structures. Dr. Chandran did her Bachelors and Master's degree in Thermal Engineering with specialization "Steam and Gas Turbines" from the Department of Thermal Engineering and Turbo-machinery, Peoples Friendship University of Russia, Moscow. She is presently focused on research related to fluid structure interaction of bluff bodies, hydrokinetic power generation and renewable energy. She has more than 15 published articles including journal publications. Hydro Vortex Power Generator developed by her research

team has attracted societal importance and was supported by Energy Management Centre, Government of Kerala, India. Dr. Chandran has received several awards including AEE's Asia Subcontinent Region Energy Professional Development Award 2022, Dr. E. C. George Sudharshan Endowment for academic excellence in 2000 and academic scholarship for professional education and higher studies in Russia in 2001 and 2005, consecutively.

Prof. Dr. Alam Md. Mahbub is a professor at the Shenzhen Graduate School of Harbin Institute of Technology (China) since 2012. He worked as a senior lecturer at the University of Pretoria (South Africa), research and postdoctoral fellows at the Hong Kong Polytechnic University, and lecturer at the Rajshahi University of Engineering and Technology, Bangladesh. He received M.Eng. and Ph.D. degrees from Kitami Institute of Technology, Japan, in 2001 and 2004, in Mechanical Engineering. More than 370 technical articles are authored and co-authored, including 175 journal papers, most of which have been published in journals of national and international repute. He is the author of two books and 20 chapters in books. He has delivered 25 Keynote speeches at international conferences. His research has mostly involved fluid dynamics around single and multiple cylinders, flow-induced vibrations, fluid-structure interactions, airfoil aerodynamics, renewable energy, and flow controls. He has secured a total of RMB 11 million research funding from national and international levels. Prof. Mahbub has received a number of awards: Japan Government Scholarship for Masters and Ph.D. studies, Japan Society for Promotion of Science Postdoctoral fellowship, South Africa National Research Foundation (NRF) rating 'Promising Young Researcher, Y1', Shenzhen High-Level Overseas Talent, Shenzhen High-Level Professional.

Dr. C. B. Sobhan currently teaches in the School of Materials Science and Engineering, National Institute of Technology (NIT) Calicut, India. He is also a research collaborator at the George W. Woodruff School of Mechanical Engineering, Georgia Institute of Technology, USA. Dr. Sobhan earned his Ph.D. from Indian Institute of Technology (IIT) Madras, India, in 1990 following his Master of Technology (1986) from the same institute, and Bachelor of Technology from Regional Engineering College Calicut (1984). He performed post-doctoral studies at Purdue University, Indiana, USA (1999–2000) and since then, is focusing on research in microscale and nanoscale heat transfer. He has over 100 international publications to his credit. He has served as keynote speaker and session chair at various international conferences and is also the reviewer of several technical journals of international repute.

Conceptual Design of Zero-Emission Sailing Ship Renewable Energy Challenges



Željko Hederić , Dean Vučinić , Mislav Brlić, Mislav Bezovnik, Ivan Rutnik, Marko Cuković, Mario Čačić, Antonio Hmura, Dina Jukić, Miljenko Švarcmajer, and Bojan Vučinić

Abstract The paper describes the conceptual design of the project: “Development of zero-emission passenger sailing ship”, as the breakthrough approach to use renewable energy sources (RES) for ship propulsion and other on-board operations. The project is co-financed by the European Union from the European Regional Development Operational Program “Competitiveness and Cohesion 2014–2020” and fully in line with the ongoing Horizon Europe Framework Programme for Green Maritime Transport. The electricity for the electric ship propulsion is stored in rechargeable batteries. The important research challenge is the recharging of batteries, applying the hybrid process of converting wind and solar energy using different technological solutions: propellers operating in the turbine mode as drive motors operate in generator mode, auxiliary hydrokinetic turbines, wind turbines, photovoltaic system, and connection to coastal power sources. These hybrid energy conversion options are promising, as they provide energy for the ship’s electrical propulsion motors and power all other on-board equipment. The project consortium is entirely Croatian consisting of shipbuilding industry members and academic partners, adopting a very “shipbuilding approach” by reusing the results from the already built sailing ship Klara, as a reference design with ICE drives, to design and build the new sailing ship LeDA with zero-emission propulsion. LeDA will be the full-scale prototype of a 3-masted cruising sailing ship for a maximum of 36 passengers, to be built

Ž. Hederić · M. Cuković · M. Čačić · A. Hmura · D. Jukić · M. Švarcmajer
Faculty of Electrical Engineering, Computer Science and Information Technology, J. J. Strossmayer University of Osijek, Osijek, Croatia
e-mail: zeljko.hederic@ferit.hr

D. Vučinić (✉)
Vrije Universiteit Brussel, Brussels School of Governance, Brussels, Belgium
e-mail: dean.vucinic@vub.be

M. Brlić · M. Bezovnik · I. Rutnik
Marine and Energy Solution DIV Doo, Zagreb, Croatia

B. Vučinić
MA-CAD, Menton, France

in the Croatian shipyard Brodosplit, and expected to empower the Croatian ship-building industry with such new products and their commercialization for the world waterborne transportation market.

Keywords Zero emission propulsion · Sailing ship · RES · Energy conversion

1 Introduction

The paper presents the conceptual design phase of building a zero emission sailing ship with focus on the generation and use of renewable energy sources, mainly wind energy. The encountered challenges are listed along with proposed solutions to define this first design step towards the production of a ship, which will not only be powered by wind, but goes a step further by recuperating part of the kinetic energy via the propeller(s), which in the turbine mode are driving the propulsion electric motor as generator(s) to produce electricity. This energy will be stored on board and used for propulsion during “no wind” periods, as well as, satisfying also, all other energy needs on board. This will make the new ship, fully energy self-sufficient, expecting to end the fossil fuel use.

The main objectives of the project “Development of a zero-emission passenger sailing ship”, co-financed by the European Regional Development Fund, contribute with their solutions to the overall goals of Maritime transport, aimed at reducing greenhouse gas (GHG) emissions, which account for about 3% of global emissions annually [1, 2]. Today, the sector is highly dependent on fossil fuels, counting approximately 100,000 ships that in the future, should be replaced by more energy efficient ships. Consequently, this will transform the entire fuel supply chain in the shipping industry.

The wind and hydrokinetic renewable energy sources [3] are in focus. However, in the future, the solar “photovoltaic” sources will also be considered to further improve the use of green energy to power the Croatian zero-emissions sailing ship [4, 5].

The conventional soft sails are experiencing revival, primarily through the development of super yachts and racing sailboats [5]. In this way, it is expected that the gained knowledge/solutions will be scaled up, to be used for the propulsion of larger ships, as an auxiliary propulsion option. In Fig. 1, several research projects are shown, to motivate the future ship designs, as follows: *Greenheart Project*—combination of PV energy produced on land that will be used as energy to power a coastal ship along with wind energy over sails; *B9 shipping*—combination of Dynarig solution of the sails with the biogas-powered engine; *Ecoliner*—combination of rounded Dynarig solution of the sails with the diesel-powered engine; *Seagate delta wing sail*—fast deployment delta wing sails on existing cargo ships offer higher efficiency over investment cost [6].

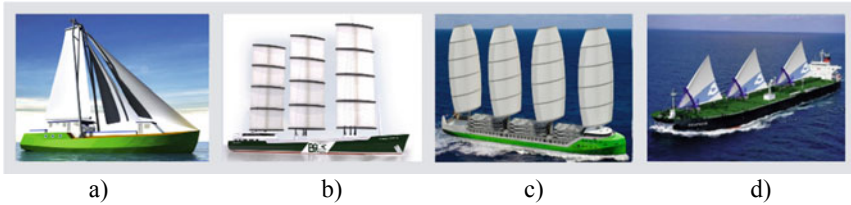


Fig. 1 Ship designs deploying soft-sail technology: **a** *Greenheart Project* (2012), **b** *B9 shipping* (2013), **c** *Ecoliner* (2015), **d** *Seagate delta wing sail* (2016)

1.1 On-Board Energy Storage (for ‘no Wind’ Periods)

The wind energy solutions for ship propulsion rely on relatively consistent winds, while in the high seas. The problem arises when ships enter bays and ports, and the electric energy storage systems are needed for the manoeuvring operations. Therefore, it is necessary to consider the use of electrical energy storage for the ship propulsion, which could be obtained from two different sources, as follows.

The first approach is to get electricity from the port infrastructure [5], see Fig. 2, where the electricity comes from the continent (not only RES sources). This approach is already in use for the electric vehicles and their charging stations. Thus, it needs to be scaled up for the electrical ships, where the challenge is to fulfil the huge energy demand within a relatively short charging time. This consequently leads to the technical design connections problem on how to provide very high charging currents [7], under increased humidity conditions (e.g. splashing waves on shore), see Fig. 3.

The port electrical infrastructure is a complex design problem [8], as we need the high-voltage installations appropriately located near the ship (transformation stations and underground cable routes) to be connected to the ship’s energy storage,

Fig. 2 In port exchanging batteries



Fig. 3 In port charging cables

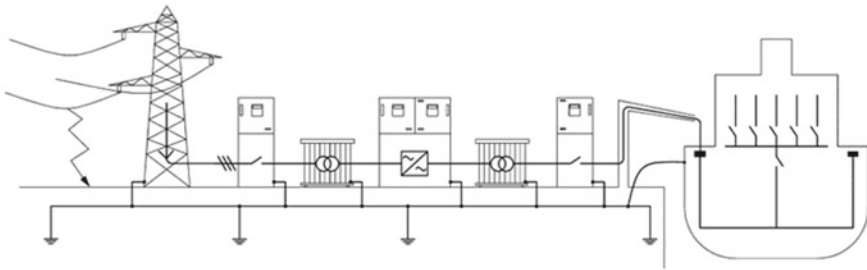


Fig. 4 Port with high-voltage shore connection (HVSC) system power supply by an HV > 100 kV primary line with a single-phase fault at the delivery point

see Fig. 4. The main problem is the handling of the heavy power cables under poor weather conditions (ship is floating, and hydrodynamic forces are critical to keep a safe distance for the connected cables). One possibility is to use cranes with robotic arms to assure the required distance.

To set a strong project baseline for our zero-emission sailing ship project, see Fig. 5, the state-of-the-art design is introduced with these two most advanced concepts found. The expected outcome will be the prototype ship, to be built in the Croatian shipyard Brodosplit.

2 Zero-Emission Passenger Sailing Ship Project

The Zero-Emission Passenger Sailing Ship Project addresses the overarching goals for the Maritime transport to prevent further climate change and environmental degradation fostering environmentally friendly ship propulsion by motivating the change of diesel propulsion to propulsion systems based on renewable energy sources.

Therefore, the construction of sailing ships, see Figs. 6 and 7, is in progress and will implement such new propulsion system, which is well aligned with the “Innovative



Fig. 5 Renewable energy sources

Green Initiatives” funded programme entitled: “Increasing the development of new products and services arising from R&D activities—Phase II” from 2019 [9].

The current development strategies have been analysed [10, 11] and resulted in the project based on the company management long-time vision to use the existing 3-masted sailing ship Klara, as a reference design, see Fig. 7, and build the new ship equipped with the innovative solutions for the ship propulsion and operations [12].



Fig. 6 Golden Horizon—speed 20 knots, length 162 m, weighs 24 tons, 5 masts with 36 cross sails, total area is 6347 m², total energy consumption ~4.2 kWh



Fig. 7 Three mast schooner passenger sailing ship Klara is 64 m long, 10 m wide, with the height of 5.35 m up to the main deck. Gross Tonnage: 497 t and max speed above 11 knots $2 \times$ ICE 368 kW, 8 sails with a total area of 845 m², and two 150 kW diesel generators

The key ship designers [13], members of the project consortium, and authors of this paper have brought in their extensive experience in the design, construction, and monitoring of naval and civilian ships, which made possible to produce such improved ship design in cooperation with the academic partners, as strong multidisciplinary effort, by converting the reference sailing ship Klara into the new zero-emission sailing ship LeDA, see Fig. 8, which is already in construction at the Brodosplit shipyard.

2.1 Design Challenges

As already discussed, the basic idea of “zero emissions” is to eliminate diesel propulsion by returning to sailing, the wind energy propulsion. The need for a propeller has raised the question: “What propulsion system can be an alternative to a diesel engine?” Considering the developments in electrical vehicles, electric propulsion is considered a suitable solution, becoming interesting even for sail-less ships due to its high efficiency, see Fig. 9.

The challenge in the sailing ship design is to use wind energy efficiently. Throughout history, the requirement for continuous navigation, when there was not enough wind, was met by using propellers for ship propulsion. Initially, steam engines were used, but with the development of the internal combustion engines, the era of sail-less ships began [14, 15].

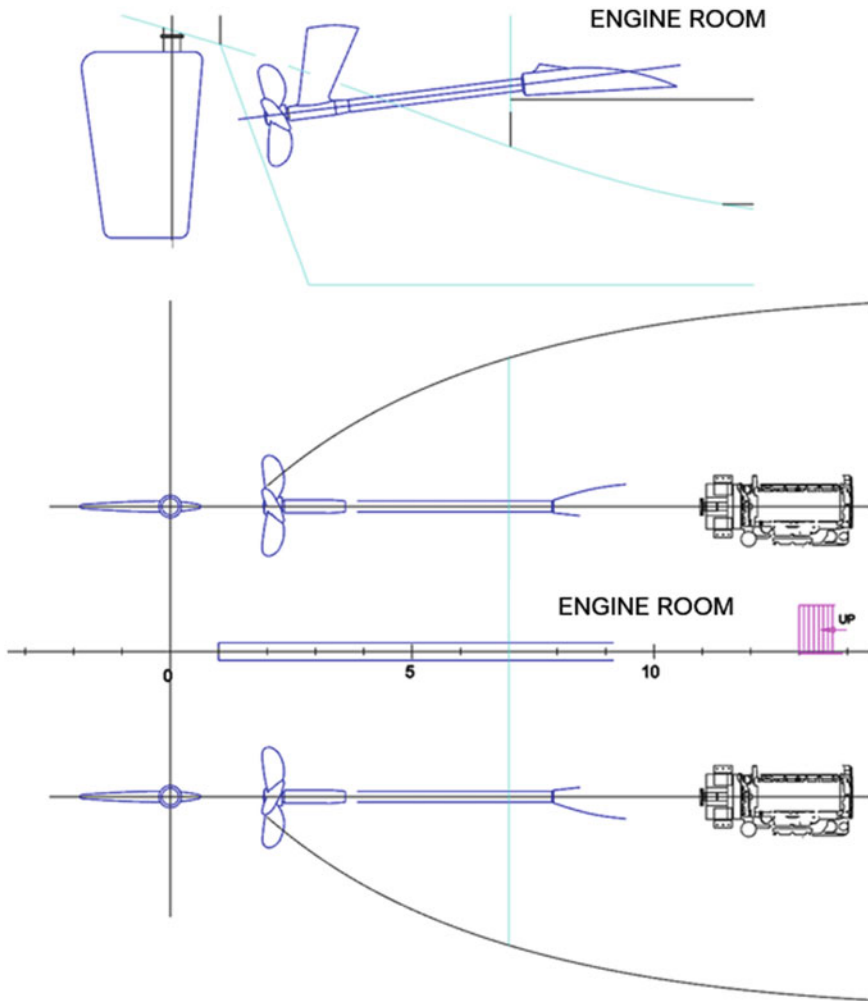


Fig. 8 Twin propellers configuration (Klara ship reference design). ICE as drive will be replaced with electric drive as more efficient solution that can use energy from RES and can produce energy via hydrokinetic recuperation

A safety regulation, dates from that period, still requires that sailing ships are equipped with the propeller propulsion. Today, the latest trend is that electric propulsion is the auxiliary sailing ship propulsion, combining the propeller with an electric drive [16].

During the sailing, the water stream under the ship can act on the existing propeller, which behaves as turbine driving the electrical generator. The same electric motor, used for the propulsion, becomes a generator in the turbine mode. The technical

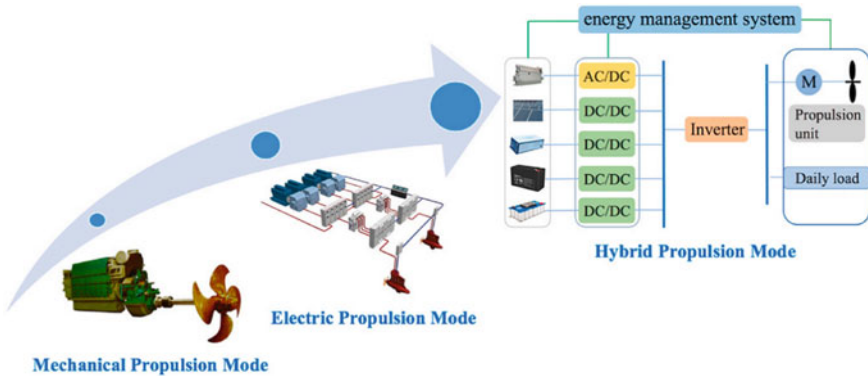


Fig. 9 Development of the propulsion system for ships

challenge is to optimise the amount of kinetic energy, which can be extracted, named “sea plowing”, to transform, even better, the available wind energy [3, 16].

The recovered energy ensures stability and comfort of navigation while maintaining the required ship cruising speed [9, 10]. The advantage of electric systems is that speed control is much faster than the navigation time constants, as the excitation of the generator can act as a “brake”. The advantage of such control system is that in the event of a sudden wind energy decreasing, the transition from generator to engine operation, and vice versa, is achieved practically instantaneously. This feature makes extremely smooth the entire control of the ship cruising speed, see Fig. 10 [17].

The computational fluid dynamics (CFD) analysis will simulate the sea hydrodynamic hull resistance, when sailing, as the basis for the required propulsion calculation [18, 19]. Primarily, the hybrid propulsion will be achieved from the wind acting on sails and secondarily from the propeller propulsion. In both cases, the CFD simulations of propellers performance are required. There are two basic propeller’s types

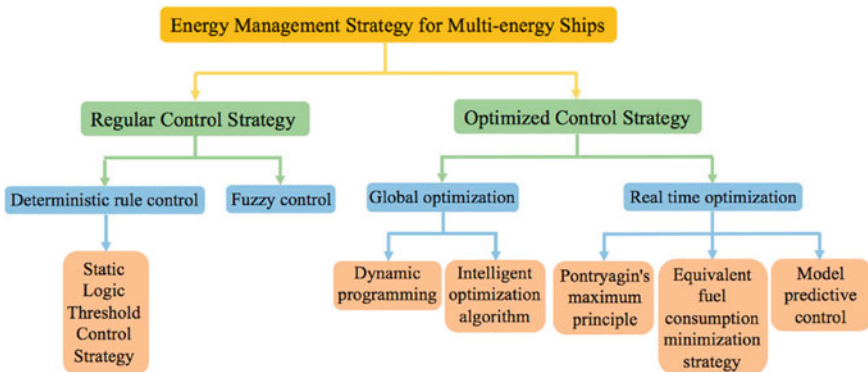


Fig. 10 Classification of the ships’ energy management strategies



Fig. 11 Ship Klara (left) and the conceptual new zero-emission sailing ship design

considered: fixed pitch propeller (FPP) and controlled pitch propeller (CPP). CPP (blades rotate around their axes) can achieve optimum performance under different water stream conditions, as the propeller pitch can be adjusted and thus the propellers thrust forces can be adjusted too.

In addition, the solution can be used to generate electricity when a ship is anchored in a location where coastal currents are present [20].

Since the wind turbines are also considered in the project, they are expected to be used when the ship is anchored in the harbour and there is wind (then the sails are lowered). Figure 11 shows one of the proposed wind turbine arrangements.

2.2 Energy Storage (Batteries)

The electricity storage is a key element in the design of hybrid systems, where different sources and consumers need to be combined [15]. To define such a topology, the electricity storage is usually connected to other systems via the DC bus. Figure 12 shows a common solution, where the parts of the power system operated by AC are separately connected.

In measuring the size of the battery's demand, as the power storage device, two important facts must be kept in mind: the battery is a chemical source that should never be fully charged, but neither should be fully discharged [21, 22]. In this respect, the battery's role is to temporarily store surplus energy from RES or possibly recovered energy from certain subsystems of the ship, representing the energy source, as backup option, when the ship systems need it (and RES is not available).

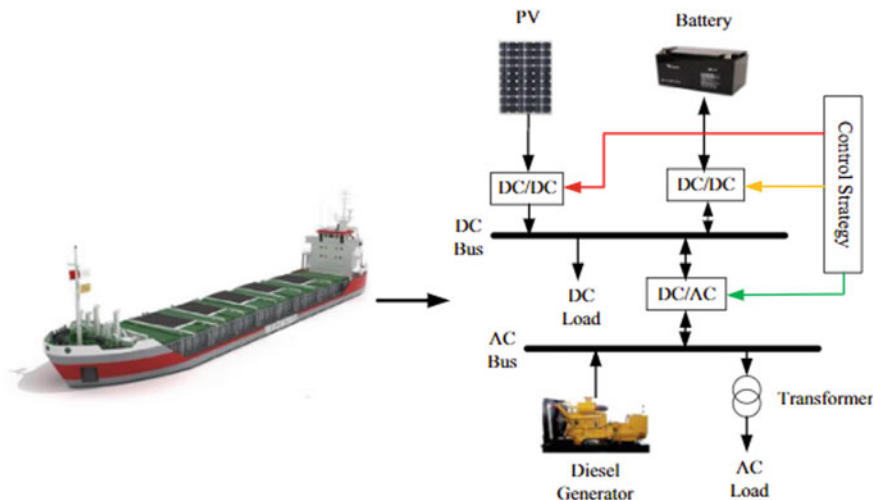


Fig. 12 Hybrid PV/diesel/ESS power system in an oil tanker ship

The aspect of the financial burden of the initial investment in the size of the battery, its maintenance, and optimization for the needs of the energy flows within the ship has been the subject of numerous studies, as shown in [23].

3 Conclusions

The paper describes the conceptual design of the “Development of a zero-emission passenger sailing ship” project, which represents an innovative use of renewable energy sources for ship propulsion and on-board operations. The project is funded by the EU and supported by the Horizon Europe’s Green Maritime Framework Programme, as the urgent action is needed to reduce carbon emissions to halt global warming, and shipping is no exception.

The International Maritime Organisation (IMO) strategy document points to the fossil fuels pollution from internal combustion engines (ICE) as destroying our environment and nature. Analyses have shown that up to 80% of the pollution is caused by the international container ships transport, which offers a unique opportunity to contribute to the decarbonisation of the shipping industry. It is well-known that the shipping classification societies are very strict with their rules and regulations. In recent years, they have already adopted guidelines for environmentally friendly maritime transport and are increasingly considering the possible application of wind energy for ship propulsion.

In line with the presented facts, the presented conceptual solution is well aligned with the overall objective of the underlying European project, which aim is to find an acceptable solution for maritime mobility by developing a clean integrated wind

energy use with the expectation of increasing the global competitiveness of the maritime sector and thus achieving the far-reaching goal to sustain a greener maritime transport of goods and passengers.

The presented conceptual design focuses on the use of wind energy, as the dominant available energy resource available on the high seas. Another form of wind energy use is the conversion of wind energy into electricity. The combination of these two approaches represents an interesting integrated solution, which makes possible: (1) to power the ships, (2) to reduce the high dependence on fossil fuels, (3) to reduce greenhouse gas emissions and thus contribute to a more environmentally friendly maritime transport.

3.1 Industry-Wide Cooperation

In order that such proposed design is implemented, the project coordinator, the DIV group, in close cooperation with scientific institutions has adopted the research and development cluster approach, i.e. creating an innovative platform for design, production of best practices for prototyping such solution, already applied in the design and construction of the Golden Horizon sailing ship, see Fig. 6, which received the highest possible class for noise and vibration classification, due to its superior design and construction quality. This conceptual design is part of the continuation effort underpinning the project consortium research and development approach, which is well aligned with the Horizon Europe Framework Programme for Green Maritime Transport objectives.

The design and build of such new generation ship, see Fig. 13, is motivated by the Golden Horizon success story, whose propulsion systems are based on renewable energy sources. Thus, in response to the proposals call for “Increasing the Development of New Products and Services Arising from Research and Development Activities”, a five-member project consortium was formed to achieve synergy in skills and expertise to cover the needed multidisciplinary areas required to implement the project objectives, see Fig. 14. The project coordinator is the DIV Group and together with the two industrial partners (i) MES DIV—a design and engineering company, and (ii) Brodosplit—a shipyard with almost 100 years ships production history.

3.2 Backed by Academia

For the project consortium, the two technical faculties are selected, as scientific partners, namely (i) the Faculty of Electrical Engineering, Mechanical Engineering and Naval Architecture (FESB) Split—for sailing innovations, and (ii) the Faculty of Electrical Engineering, Computer Science and Information Technology (FERIT)

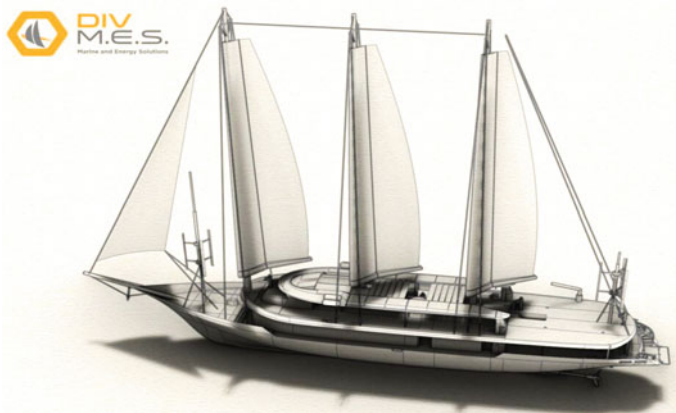


Fig. 13 First variant of the zero-emission sailing ship design



Fig. 14 Hybrid energy recuperation from different RES: wind energy during sailing on open sea (movement of ship, recuperation of kinetic energy via hydrokinetic turbine mode of ship main propellers), wind energy during anchored time with sails down via small wind turbines, sun energy via photovoltaic panels

Osijek—for innovations in the field of electrical propulsion and electrical subsystems designing ship energy flows, see Fig. 15.

Horizon Europe has defined the basic guidelines for climate-neutral, clean, smart, and competitive waterborne transport. In line with this intervention logic, this project is funded to improve the electrification of shipping and the overall energy efficiency of maritime transport.



Fig. 15 Ship propulsion and manoeuvrability research was presented by FESB to FERIT, during their project consortium meeting, in 2021

3.3 Establishment of the Digital Twin to Reach LeDA

The ship design must consider the entire life cycle of the ship, from the beginning of construction to the end when it is recycled. The energy consumption analysis is very important to determine the energy requirements for all the ship subsystems. The collected data is used for energy and exergy analysis. Usually, the results are presented with Sankey diagrams summarising the energy transfer during the ship's voyage. The well-known engineering practice was applied, by starting the project from a reference project, the designed and constructed sailing ship Klara, with diesel and sail propulsion. The new project (LeDA) aims to build a new ship with zero emissions, equipped with innovative renewable energy systems. The planned system analyses for propulsion, energy, and management are intended to improve the ship's key characteristics. The resulting data will enable the validation of the achieved results from the numerical simulations and to tune the numerical models (initial settings, parameters, and boundary conditions) to be more realistic and in line with the real data measurements. The verified and validated mathematical models of the ship systems (developed as part of the industrial research) form the important base for the virtual ship simulator (digital twin), which can model and simulate a variety of the ship physical objects and/or processes, in real time, as a digital equivalent.

3.4 Life Cycle Approach Starts at Conceptual Design

The goal is to minimise carbon emissions, for the entire shipbuilding process: starting with the extraction of raw materials, through the production of the basic materials used to build ships. Subsequently, this is linked to the operation and maintenance of ships, right through to the recycling and reusing of the existing materials. The zero-emission planning must consider the energy sources required to operate all the maritime systems that are available, in space and time, for the planned area of operation. Today, the main problem is on the coast supply chain for renewable

energy, and another problem is the maintenance of ships and the supply of spare parts. Therefore, the use of wind energy, as the dominant and available source, is fully considered, regardless of the position with the energy storage system for times when wind energy is not available. The results are expected to show that the electric propulsion is the most efficient and environmentally friendly propulsion.

3.5 On Sails Design

As a scientific partner, FESB Split has the task of developing an innovative sails design for the ship LeDA, together with the designers from MES DIV Zagreb. The latest findings, from this conceptual design phase, show that further studies are needed for the development of the sailing semi-rigid sails, with a system of rollers and leans on the mast. The multi-part wing sail, as the basic concept, is already in use for the fastest high-performance sailboats. To achieve the best possible sail performance, in-house numerical methods are being developed, applying the Finite Elements computational analysis of sails, and Computational Fluid Dynamics flows simulations under different environmental and technical conditions, to analyse hard and soft surfaces in contact with fluid that have specific dynamic behaviour and should achieve the optimum aerodynamic performance.

3.6 On Electricity Storage and Management

The electric ship propulsion uses electricity stored in rechargeable batteries. The batteries recharging is a hybrid process of converting wind and solar energy, using different technical solutions: propellers and main propulsion in reverse mode behaving like turbines and power generators, axillary hydrokinetic turbines, wind turbines, photovoltaic panels, and finally connection to energy sources on the coast. These energy conversion options are very promising, as they provide the necessary energy for the ship's electric propulsion motors and for all other equipment on board.

The project was submitted under the call for proposals to support the development of new products and services from research and development activities, co-financed by the European Union from the European Regional Development Fund. The most valuable outcome of the project will be a passenger ship in the form of a three-masted schooner, independently designed and built to prove the state of technological knowledge, but also to prove the use of renewable energy sources to obtain an efficient vehicle without greenhouse gas emissions.

The electricity storage is a key element in the design of hybrid systems, where different sources and consumers need to be combined.

Since the main propulsion of a sailboat is wind, which often exceeds the propulsion needs, one of the challenging objectives is to explore the possibility of using the main propellers to harvest hydrokinetic wind energy, as a function of the relative speed

between the ship and the sea. This part of the scientific research will be carried out by FERIT having expertise in electromechanical energy conversion and energy storage systems, as detailed in Sect. 2.1.

This process must be coordinated with the process of ship and sail management. When operating the propellers as turbines, it is important to control the generated propeller resistance, which slows down the ship speed, as well as the hydrokinetic energy of the water entering the turbine. This is done using the experience gained from the modern management development process, and in combination with different simulation techniques, primarily developed for use in electric vehicles and modified to be used in the development of electric marine propulsion systems.

3.7 *On Solar*

In parallel, the development of a system for observing and monitoring sailing systems, solar panels, and electric drives is being carried out, see Fig. 13. It is necessary to determine the parameters of the solar collector on the roof of the passenger cabin, which serves as an additional heat source for the ship's hot water needs. It is also being investigated whether small wind turbines can be installed above the deck to collect wind energy when the ship is anchored in port (as in this case, the sails cannot collect the available wind energy).

3.8 *Teamwork Towards Excellence*

The envisage main projects outcomes are as follows:

- Development and construction of an innovative zero-emission passenger sailing ship from renewable energy sources.
- Cooperation of regional industrial and scientific subjects in the development of a competitive product.

The specific objectives of the project, which this conceptual design has investigated, are as follows:

- Development of a hydrokinetic electric marine propulsion system for wind kinetic energy storage and propulsion redundancy.
- Integration of vertical wind turbines, hydro turbines, and solar panels for use on the existing diesel-powered vessels.

In this paper, the analysed design solutions contribute to the use of renewable energy sources for ship propulsion and other on-board operations, as the added value to the underlying research and innovation project in progress. The presented conceptual design is the integrated multidisciplinary teamwork, representing the unique know-how of this project consortium, well-balanced between shipbuilding industry

and academic partners. The novel ship design concept represents a strong engineering base for building such advanced ship prototype—the cruising emission-free sailing passenger ship with 3 masts—under construction in the Brodosplit shipyard, expected to strengthen the Croatian shipbuilding industry in the global water transport market.

Acknowledgements This research is supported by the European Union from the European Regional Development Fund within the Operational Program “Competitiveness and Cohesion 2014–2020”, under the project: “Development of zero-emission passenger sailing ship”, under the project number KK.01.2.1.02.0127.

References

1. https://ec.europa.eu/info/funding-tenders/opportunities/docs/2021-2027/horizon/wp-call/2021-2022/wp-8-climate-energy-and-mobility_horizon-2021-2022_en.pdf
2. Initial strategy on the reduction of greenhouse gas emissions from ships. UN International Maritime Organization (IMO) strategic document, April 2018
3. Laws ND, Epps BP (2016) Hydrokinetic energy conversion: technology, research, and outlook. *Renew Sustain Energy Rev* 57:1245–1259. <https://doi.org/10.1016/j.rser.2015.12.189>
4. Olatomiwa L, Mekhilef S, Ismail MS, Moghavvemi M (2016) Energy management strategies in hybrid renewable energy systems: a review. *Renew Sustain Energy Rev* 62:821–835. <https://doi.org/10.1016/j.rser.2016.05.040>
5. Renewable energy options for shipping, IRENA, January 2015
6. Sulligoi G, Bosich D, Pelaschiar R, Lipardi G, Tosato F (2015) Shore-to-ship power. *Proc IEEE* 103(12):2381–2400
7. <https://insideevs.com/news/466633/electric-ferry-26-plugs-dc-fast-charging/>
8. Smal V (2019) Electric container ships are stuck on the horizon. *IEEE Spectrum*
9. DIV Group research and development projects webpage. <https://www.divgroup.eu/en/research-and-development-projects/>. Last accessed 11 Jan 2022
10. Brodosplit Golden Horizon webpage. <https://www.brodosplit.hr/en/vessels/-golden-horizon/>. last accessed 11 Jan 2022
11. Brodosplit 3-mast schooner webpage. <https://www.brodosplit.hr/en/-shipbuilding/3-mast-schooner/>. Last accessed 11 Jan 2022
12. Smogeli Ø (2017) Digital twins at work in maritime and energy. DNV GL Feature
13. MES DIV official website. <http://www.mes.divgroup.eu/>. Last accessed 11 Jan 2022
14. Korberg AD, Brynolf S, Grahn M, Skov IR (2021) Techno-economic assessment of advanced fuels and propulsion systems in future fossil-free ships. *Renew Sustain Energy Rev* 142. <https://doi.org/10.1016/j.rser.2021.110861>
15. Lan H, Wen S, Hong Y-Y, Yu DC, Zhang L (2015) Optimal sizing of hybrid PV/diesel/battery in ship power system. *Appl Energy* 158:26–34. <https://doi.org/10.1016/j.apenergy.2015.08.031>
16. Yuan Y, Wang J, Yan X, Shen B, Long T (2020) A review of multi-energy hybrid power system for ships. *Renew Sustain Energy Rev Elsevier*, 132(C)
17. Seyyedi SM, Shafaghat R, Siavoshian M (2019) Experimental study of emmersion ratio and shaft inclination angle in the performance of a surface-piercing propeller. *Mech Sci* 10:153–167. <https://doi.org/10.5194/ms-10-153-2019>
18. Croatian Technical Encyclopedia (2018) Vučinič Alice, <https://tehnika.lzmk.hr/vucinic-alice/>
19. Alice V (1997) Hydrodynamics of vessels (resistance and propulsion). University of Rijeka, Faculty of Engineering. ISBN 953-6326-07-8
20. Platzer VF, Sarigul-Klijin N (2021) The green energy ship concept, 1st edn. Springer International Publishing

21. Baldi F, Ahlgren F, Nguyen TV, Thern M, Andersson K (2018) Energy and exergy analysis of a cruise ship. *Energies* 11(10):2508. <https://doi.org/10.3390/en11102508>
22. Li C, Wang H, Sun P (2020) Numerical investigation of a two-element Wingsail for ship auxiliary propulsion. *J Mar Sci Eng* 8:333. <https://doi.org/10.3390/jmse8050333>
23. Møller KT, Jensen TR, Akiba E, Li H-W (2017) Hydrogen—a sustainable energy carrier. *Prog Nat Sci Mater Int* 27(1):34–40. <https://doi.org/10.1016/j.pnsc.2016.12.014>

Modeling and Simulation in Materials and Manufacturing

Simulation Analysis of Composite Materials for Divergence Elimination



Kalaivanan , Ganesh Karthic , Vyas Jatinkumar Manubhai ,
N. P. Pavai , V. Aravinth, S. Poornachandran, and Naveen Velmurugan

Abstract The forward swept-wing aircraft is one of the most superior aircrafts in terms of both aerodynamics and structural configurations. This design has been consistently frustrated by the divergence problem. The divergence in the wing can be reduced by increasing the wing bending stiffness which in turn increases the weight of the wing. So, to accomplish both, composite materials are being employed in this analysis. The alteration of the fiber angle orientation enables the material to improve mechanical properties. This research has been conducted to analyze the buckling behavior of different materials with the various fiber angle orientation so that the material would be sufficient to alleviate divergence. A laminate of three different materials, carbon fiber, graphite epoxy and Kevlar epoxy for 20 different stacking sequences, each sequence consisting of 24 plies have been analyzed by using Fortran and Abaqus. The analysis results showed that the graphite epoxy has better mechanical property comparing to the other two materials, and it can be used for divergence elimination.

Keywords Forward swept wing · Divergence · Buckling behavior · ABAQUS · FORTRAN

1 Introduction

The wing behavior of an aircraft is characterized by the interaction between the material and shape of the wing. Material selection plays a prominent role in the design and wing behavior of an aircraft. If the material is not selected properly, the design may show poor performance and requires frequent maintenance. The

Kalaivanan · G. Karthic (✉) · N. P. Pavai
Department of Aeronautical, KCG College of Technology, Karapakkam, Chennai, India
e-mail: ganeskharthic103@gmail.com

V. J. Manubhai · V. Aravinth · S. Poornachandran
AU-FRG Institute for CAD/CAM, ANNA University, Chennai, India

N. Velmurugan
Mechanical Engineering, Loughborough University, Loughborough, England

structural failure of the wing may lead to injuries or fatalities [1]. The selection of the material is dependent upon the performance requirements of the aircraft [2]. Poor selection of the material leads to various modes of failure, namely buckling, excessive deflection, fatigue, creep, etc. [3]. The modulus and strength are the two basic material properties that are often considered in the preliminary selection of the material where structural integrity and design constraints are limited. The deformations occurring in the wing of an aircraft, which uses the composite laminate layups, indicate the modulus, and the utmost load-carrying capacity indicates the strength of the layup's orientation [4].

The forward-swept wings prove to have high aerodynamic efficiency if the divergence problem is eliminated. The major problem in the forward swept-wing aircraft is divergence. Generally, in the forward-swept wing, when the aircraft turns, it applies high G-loads on the wing, and this load causes the wingtip to bend upward which in turn leads to the twist of the leading edges in the upwards direction [5]. A catastrophic phenomenon called divergence occurs, when the angle of attack increases, due to the twisting of a wing. Moreover, the divergence in the wing can be reduced by increasing the wing bending stiffness which is in turn associated, with the increase in the weight of the wing that leads to an increase in the overall weight of the aircraft. Implementation of the advanced composite material using the laminate layup method helps the designer to overcome the weight constraint in the conventional metal wings [6].

The high strength-to-weight ratio, stiffness-to-weight ratio and lightweight tend to reduce the fuel cost as well as the increase in the payload capacity are the major reasons for employing composite material in aircraft applications [7]. It is evident from the literature that the laminate layups provided significant changes in the property of the material based on the orientation. The experimental evaluation of the different stacking sequences seems to provide the variation in the dynamic cracking behavior of the test specimen [8]. In this analysis, three different composite materials, namely carbon fiber, graphite epoxy and Kevlar epoxy, have been employed. These three materials are used in various parts of the aircraft majorly in the aircraft's wings [9]. The structural arrangement of an individual fiber in the material improvisation is called fiber angle orientation. The concept of the alteration of the fiber angle orientation enables the material with improved mechanical properties, so it can be used as a prominent key in avoiding divergence [10, 11].

2 Methodology

This research is all about simulation analysis of three different materials that exhibit different properties for 20 different stacking sequences. Each stacking sequence consists of 24 plies, of which 12 plies are symmetric. The sequences are organized in the order of combination of single angle, double angle, triple angle and even four angles. Carbon fiber, graphite epoxy and Kevlar epoxy having properties as shown in Table 1 [7, 12] were analyzed by using Fortran and Abaqus software. The buckling

Table 1 Properties of three materials

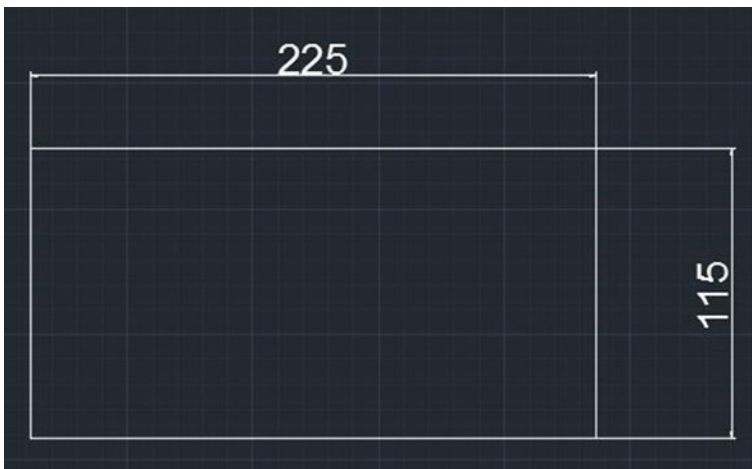
Carbon fiber	Graphite epoxy	Kevlar epoxy
$E_1 = 132 \text{ GPa}$	$E_1 = 181 \text{ GPa}$	$E_1 = 76 \text{ GPa}$
$E_2 = 11 \text{ GPa}$	$E_2 = 10.3 \text{ GPa}$	$E_2 = 5.5 \text{ GPa}$
$\nu_{12} = 0.3$	$\nu_{12} = 0.28$	$\nu_{12} = 0.34$
$G_{12} = 5.5 \text{ GPa}$	$G_{12} = 7.17 \text{ GPa}$	$G_{12} = 2.1 \text{ GPa}$

behavior of different materials for various orientations has been observed through this analysis, which in turn provides sufficient knowledge about the bending stiffness of material that varies for each orientation. By conducting this research, the proper selection of stacking sequence and material can be accomplished, through which divergence of the forward-swept wing can be alleviated.

A laminate of size $225 \times 115 \text{ mm}$ as shown in Fig. 1, with a single-ply thickness of 0.15 mm has been analyzed in Abaqus. The total thickness of 24 plies is 3.6 mm [12].

This analysis involves three primary steps, namely.

1. Calculation of extensional stiffness matrix, bending extension coupling stiffness matrix and bending stiffness matrix by using Fortran programming.
2. Calculation of buckling strength value (eigenvalue) through the simulation analysis of three materials for 20 different orientations in Abaqus software.
3. Calculation of buckling factor and displacement values by using Fortran programming.



All dimensions are in mm

Fig. 1 Geometry of panel

3 Computation of Buckling Factor and Displacement

Considering the carbon fiber material which has the following properties,

$$E_1 = 132 \text{ GPa}; E_2 = 11 \text{ GPa}; \nu_{12} = 0.3; G_{12} = 5.5 \text{ GPa}$$

Stacking sequence: $(-45^\circ/0^\circ/+45^\circ/90^\circ/-45^\circ/0^\circ/+45^\circ/90^\circ/-45^\circ/0^\circ/+45^\circ/90^\circ)_S$

4 Stiffness Matrix

The stiffness matrix, $[Q]$, can be calculated by using below-mentioned equation

$$[Q] = \begin{bmatrix} Q_{11} & Q_{12} & 0 \\ Q_{12} & Q_{22} & 0 \\ 0 & 0 & Q_{33} \end{bmatrix} = \begin{bmatrix} E_{11} - \nu_{21}\nu_{12} & \frac{\nu_{12}E_2}{1-\nu_{21}\nu_{12}} & 0 \\ \frac{\nu_{12}E_2}{1-\nu_{21}\nu_{12}} & E_{11} - \nu_{21}\nu_{12} & 0 \\ 0 & 0 & G_{12} \end{bmatrix}$$

(SEQ “equation”\n \ * MERGEFORMAT 1)

where $[Q]$ is the stiffness matrix in Pascal [7]

E_1 and E_2 are longitudinal and transverse modulus in Pascal

G_{12} is modulus of rigidity in Pascal

ν_{12} and ν_{21} are Poisson ratios (no unit)

$$\nu_{21} = E_2 E_1 \times \nu_{12} = 0.025; Q_{11} = E_{11} - \nu_{21}\nu_{12} = 132.997 \text{ GPa};$$

$$Q_{22} = E_{21} - \nu_{21}\nu_{12} = 11.083 \text{ GPa};$$

$$Q_{12} = \frac{\nu_{12}E_2}{1 - \nu_{21}\nu_{12}} = 3.324 \text{ GPa};$$

$$Q_{33} = G_{12} = 5.5 \text{ GPa};$$

$$Q_{13} = Q_{23} = 0 = Q_{31} = Q_{32}$$

$$[Q] = \begin{bmatrix} Q_{11} & Q_{12} & 0 \\ Q_{12} & Q_{22} & 0 \\ 0 & 0 & Q_{33} \end{bmatrix} = \begin{bmatrix} 132.997 & 3.324 & 0 \\ 3.324 & 11.083 & 0 \\ 0 & 0 & 5.5 \end{bmatrix} \text{ GPa}$$

4.1 Transformation Matrix

The transformation matrix $[T]$ can be calculated by using below-mentioned Eq. (2)

$$\begin{aligned}
[T] &= \begin{bmatrix} T_{11} & T_{12} & T_{13} \\ T_{21} & T_{22} & T_{23} \\ T_{31} & T_{32} & T_{33} \end{bmatrix} \\
&= \begin{bmatrix} \cos^2(x) & \sin^2(x) & -2 \cos(x) \sin(x) \\ \sin^2(x) & \cos^2(x) & 2 \cos(x) \sin(x) \\ \cos(x) \sin(x) & -\cos(x) \sin(x) & \cos^2(x) - \sin^2(x) \end{bmatrix}
\end{aligned}$$

(SEQ “equation” \n \ * MERGEFORMAT 2)

where $[T]$ is the transformation matrix (no unit) [13]

(x) is the fiber orientation angle in Radians

Initially, before calculating the transformation matrix, the degrees will be converted into radians, $x = (\pi/180) \times \theta$

$$\begin{aligned}
[T]_{0^\circ} &= \begin{bmatrix} 1 & 0 & 0 \\ 0 & 1 & 0 \\ 0 & 0 & 1 \end{bmatrix}; [T]_{45^\circ} = \begin{bmatrix} 0.5 & 0.5 & -1 \\ 0.5 & 0.5 & 1 \\ 0.5 & -0.5 & 0 \end{bmatrix}; \\
[T]_{-45^\circ} &= \begin{bmatrix} 0.5 & 0.5 & 1 \\ 0.5 & 0.5 & -1 \\ -0.5 & 0.5 & 0 \end{bmatrix}; [T]_{90^\circ} = \begin{bmatrix} 0 & 1 & 0 \\ 1 & 0 & 0 \\ 0 & 0 & -1 \end{bmatrix}
\end{aligned}$$

4.2 Transformed Stiffness Matrix

$$[\bar{Q}] = [T][Q][T]^T \text{ (SEQ “equation” \n \ * MERGEFORMAT 3)}$$

where $[\bar{Q}]$ is the transformed stiffness matrix in Pascal [13]

$[T]$ is the transformation matrix (no unit)

$[Q]$ is the stiffness matrix in Pascal

$[T]^T$ is the transpose of transformation matrix (no unit)

$$\begin{aligned}
[\bar{Q}]_{0^\circ} &= \begin{bmatrix} 132.997 & 3.324 & 0 \\ 3.324 & 11.083 & 0 \\ 0 & 0 & 5.5 \end{bmatrix} \text{ GPa;} \\
[\bar{Q}]_{45^\circ} &= \begin{bmatrix} 43.182 & 32.182 & 30.478 \\ 32.182 & 43.182 & 30.478 \\ 30.478 & 30.478 & 34.358 \end{bmatrix} \text{ GPa} \\
[\bar{Q}]_{-45^\circ} &= \begin{bmatrix} 43.182 & 32.182 & -30.478 \\ 32.182 & 43.182 & -30.478 \\ -30.478 & -30.478 & 34.358 \end{bmatrix} \text{ GPa;}
\end{aligned}$$

$$\overline{[Q]}_{90^\circ} = \begin{bmatrix} 11.083 & 3.324 & 0 \\ 3.324 & 132.997 & 0 \\ 0 & 0 & 5.5 \end{bmatrix} \text{GPa}$$

4.3 ABD Matrix Formula

$$A_{ij} = \sum_{K=1}^N \overline{Q}_{ij}^{(K)} (h_{K+1} - h_K) \quad (1)$$

$$B_{ij} = \frac{1}{2} \sum_{K=1}^N \overline{Q}_{ij}^{(K)} (h_{K+1}^2 - h_K^2) \quad (2)$$

$$D_{ij} = \frac{1}{3} \sum_{K=1}^N \overline{Q}_{ij}^{(K)} (h_{K+1}^3 - h_K^3) \quad (3)$$

where A_{ij} indicates the element of extensional stiffness matrix in Pascal [13]

B_{ij} indicates the element of bending extension coupling stiffness matrix in Pascal [13]

D_{ij} indicates the element of the bending stiffness matrix in Pascal [13]

$$[A] = \begin{bmatrix} 0.2073 & 0.0639 & 0 \\ 0.0639 & 0.2073 & 0 \\ 0 & 0 & 0.0717 \end{bmatrix} \text{GPa}; \quad [D] = \begin{bmatrix} 244.1 & 76.09 & -16.02 \\ 76.09 & 189.8 & -16.02 \\ -16.02 & -16.02 & 84.46 \end{bmatrix} \text{GPa};$$

$$[B] = \begin{bmatrix} 0 & 0 & 0 \\ 0 & 0 & 0 \\ 0 & 0 & 0 \end{bmatrix} \text{GPa}$$

During the flight, the top skin undergoes compressive loading which leads to buckling of the skin. It is essential to examine the buckling strength of the skin for an ultimate load. As the laminate has symmetric layers, there is no extensional-flexural coupling. The pre-buckling deformations are hence purely in-plane [14].

4.4 Buckling Factor

$$\lambda = \text{Buckling load} \div q_0 \text{ (SEQ "equation" \n \ * MERGEFORMAT 7)}$$

where λ is the buckling factor (No unit) [13]

Buckling load is in Newton

q_o is the applied load is in Newton

$$\text{Buckling Load} = \text{Buckling strength} * b \tag{4}$$

where buckling load is in Newton

Buckling strength is in Newton per meter

b is the width of the panel is in meter

Buckling strength = 1.4099E6 N/m; Buckling load = 1.4099E6 * 0.115 = 0.161E6 N; $q_o = 50\text{KN}$

$$\lambda = 0.161E6 \div 50E3 = 3.242 \text{ (No unit)}$$

It has no unit as both the loads have the unit of Newton (N). The buckling strength is the eigenvalues that are calculated through Abaqus. To obtain buckling load, the buckling strength is multiplied by the width of the panel since the panel is being compressed at the width section.

The compressive load applied or used has been considered from the critical load cases of a real-time aircraft wing at several flight conditions such as take-off, maneuvering, landing, etc., and it is applied on simply supported laminated skin. Assume the value of compressive load was 50,000 N [11].

4.5 Displacement

$$\text{Displacement} = \frac{a^4 q_{mn}}{\pi^4 [D_{11}m^4 + 2(D_{12} + 2D_{66})(mnR)^2 + D_{22}(Rn)^4]} \tag{5}$$

(SEQ “equation” \n \ * MERGEFORMAT 9)

where D_{11} , D_{12} , D_{22} , D_{66} are the elements of the bending stiffness matrix in Pascal

a is the length of the panel in meter

b is the width of the panel in meter

R is the ratio of length to width of the panel (no unit)

m and n are buckling mode shape parameters (no unit)

q_{mn} is the load applied for the corresponding buckling mode shape parameter in Newton, and it can be calculated by using the below [12],

$$q_{mn} = \frac{16 \times q_o}{\pi^2 mn} \text{ (SEQ “equation” \n \ * MERGEFORMAT 10)}$$

where q_o is the applied load in Newton

m and n are buckling mode shape parameters (no unit)

$m = 1; n = 1; q_o = 50 \text{ KN};$

$$q_{11} = \frac{16 \times 50000}{\pi^2 1 * 1} = 81056.946 \text{ N}$$

$$R = \frac{a}{b}; R = 0.225 \div 0.115 = 1.9565 \text{ (no unit)}$$

$$a = 0.225 \text{ m}; b = 0.115 \text{ m}$$

The elements of bending stiffness matrix of carbon fiber material for the stacking sequence $(-45^\circ/0^\circ/+45^\circ/90^\circ/-45^\circ/0^\circ/+45^\circ/90^\circ/-45^\circ/0^\circ/+45^\circ/90^\circ)_s$ are

$$D_{11} = 244.1 \text{ Pa}; D_{12} = 76.09 \text{ Pa}; D_{22} = 189.8 \text{ Pa}; D_{66} = 84.46 \text{ Pa}$$

$$\text{Displacement} = \frac{0.225^4 \times 81056.946}{\pi^4 [244.1 + 2(76.09 + (2 \times 84.46))(1.9565)^2 + (189.8 \times (1.9565)^4)]}$$

$$\text{Displacement} = 0.00044 \text{ m}$$

The edges apart from the loading direction are constrained in all translational degrees of freedom. The loading edges are constrained only in the z -direction. In short, the long edges of the panel are constrained in all translational degrees of freedom (Encastre condition), and the width edges of the panel are compressively loaded and constrained only in the z -direction.

5 Results and Discussions

The simulation analysis of carbon fiber, graphite epoxy and Kevlar epoxy for various ply angle orientations as shown in Table 2 produced results of different properties, namely displacement and buckling factor. Figure 2 displays the changes in the buckling behavior of each material at the same orientation $(-45^\circ/0^\circ/+45^\circ/90^\circ/-45^\circ/0^\circ/+45^\circ/90^\circ/-45^\circ/0^\circ/+45^\circ/90^\circ)_s$. For the 15 sets of the ply orientation that is considered for the divergence elimination purposes and their variations in the buckling factor for all the three materials is represented in Table 3.

The numbers (1 to 20) indicated in Table 2 specify the stacking sequence used in Figs. 3 and 4 graphs.

From Figs. 3 and 4, it can be observed that the increment order of the buckling factor values for three materials is in this hierarchy of graphite epoxy < carbon fiber < Kevlar epoxy and vice versa for displacement. As a result of comparing, all the three materials, the graphite epoxy shows the better buckling factor value with the least displacement value. All the three materials tend to exhibit different strength values based on the orientation, $(-45^\circ/0^\circ/+45^\circ/90^\circ/-45^\circ/0^\circ/+45^\circ/90^\circ/-45^\circ/0^\circ/+45^\circ/90^\circ)_s$ of the ply as mentioned in Table 4. Among all the four different plies, 0° tends to exhibit the least desirable characteristics in terms of buckling strength.

Table 2 Stacking sequences used in this research

Orientation	
1	$(0^\circ/0^\circ/0^\circ/0^\circ/0^\circ/0^\circ/0^\circ/0^\circ/0^\circ/0^\circ/0^\circ)_s$
2	$(90^\circ/90^\circ/90^\circ/90^\circ/90^\circ/90^\circ/90^\circ/90^\circ/90^\circ/90^\circ)_s$
3	$(+45^\circ/+45^\circ/+45^\circ/+45^\circ/+45^\circ/+45^\circ/+45^\circ/+45^\circ/+45^\circ/+45^\circ)_s$
4	$(-45^\circ/-45^\circ/-45^\circ/-45^\circ/-45^\circ/-45^\circ/-45^\circ/-45^\circ/-45^\circ/-45^\circ)_s$
5	$(-45^\circ/+45^\circ/-45^\circ/+45^\circ/-45^\circ/+45^\circ/-45^\circ/+45^\circ/-45^\circ/+45^\circ)_s$
6	$(90^\circ/+45^\circ/90^\circ/+45^\circ/90^\circ/+45^\circ/90^\circ/+45^\circ/90^\circ/+45^\circ)_s$
7	$(90^\circ/-45^\circ/90^\circ/-45^\circ/90^\circ/-45^\circ/90^\circ/-45^\circ/90^\circ/-45^\circ)_s$
8	$(90^\circ/0^\circ/90^\circ/0^\circ/90^\circ/0^\circ/90^\circ/0^\circ/90^\circ/0^\circ)_s$
9	$(-45^\circ/0^\circ/-45^\circ/0^\circ/-45^\circ/0^\circ/-45^\circ/0^\circ/-45^\circ/0^\circ)_s$
10	$(0^\circ/+45^\circ/0^\circ/+45^\circ/0^\circ/+45^\circ/0^\circ/+45^\circ/0^\circ/+45^\circ)_s$
11	$(+45^\circ/0^\circ/90^\circ/+45^\circ/0^\circ/90^\circ/+45^\circ/0^\circ/90^\circ/+45^\circ/0^\circ/90^\circ)_s$
12	$(-45^\circ/0^\circ/90^\circ/-45^\circ/0^\circ/90^\circ/-45^\circ/0^\circ/90^\circ/-45^\circ/0^\circ/90^\circ)_s$
13	$(90^\circ/-45^\circ/0^\circ/90^\circ/-45^\circ/0^\circ/90^\circ/-45^\circ/0^\circ/90^\circ/-45^\circ/0^\circ)_s$
14	$(0^\circ/90^\circ/+45^\circ/0^\circ/90^\circ/+45^\circ/0^\circ/90^\circ/+45^\circ/0^\circ/90^\circ/+45^\circ)_s$
15	$(-45^\circ/0^\circ/+45^\circ/90^\circ/-45^\circ/0^\circ/+45^\circ/90^\circ/-45^\circ/0^\circ/+45^\circ/90^\circ)_s$
16	$(90^\circ/0^\circ/+45^\circ/-45^\circ/90^\circ/0^\circ/+45^\circ/-45^\circ/90^\circ/0^\circ/+45^\circ/-45^\circ)_s$
17	$(+45^\circ/-45^\circ/+45^\circ/-45^\circ/0^\circ/90^\circ/+45^\circ/-45^\circ/+45^\circ/-45^\circ/0^\circ/90^\circ)_s$
18	$(-45^\circ/+45^\circ/-45^\circ/+45^\circ/0^\circ/90^\circ/0^\circ/90^\circ/-45^\circ/+45^\circ/-45^\circ/+45^\circ)_s$
19	$(-45^\circ/-45^\circ/0^\circ/0^\circ/+45^\circ/+45^\circ/0^\circ/0^\circ/90^\circ/90^\circ/-45^\circ/-45^\circ)_s$
20	$(+45^\circ/+45^\circ/90^\circ/90^\circ/-45^\circ/-45^\circ/90^\circ/90^\circ/0^\circ/0^\circ/+45^\circ/+45^\circ)_s$

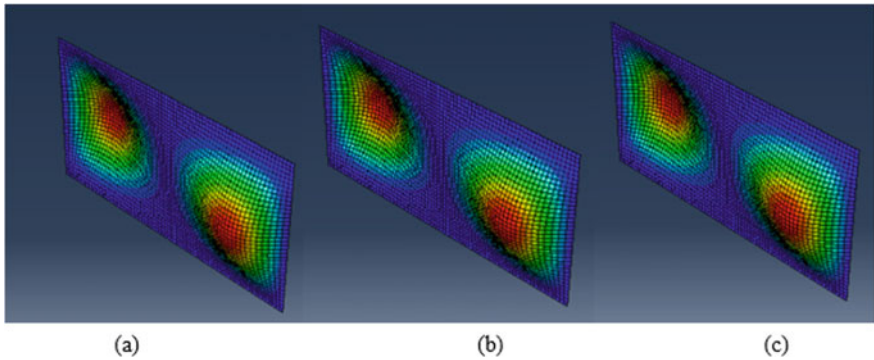


Fig. 2 Contours of carbon fiber (a), graphite epoxy (b) and Kevlar epoxy (c) for the stacking sequence, $(-45^\circ/0^\circ/+45^\circ/90^\circ/-45^\circ/0^\circ/+45^\circ/90^\circ/-45^\circ/0^\circ/+45^\circ/90^\circ)_s$

Table 3 Range of buckling factor

Material	Minimum buckling factor (no unit)	Maximum buckling factor (no unit)
Carbon fiber	3.17803	3.24298
Graphite epoxy	4.23488	4.32526
Kevlar epoxy	1.76296	1.79551

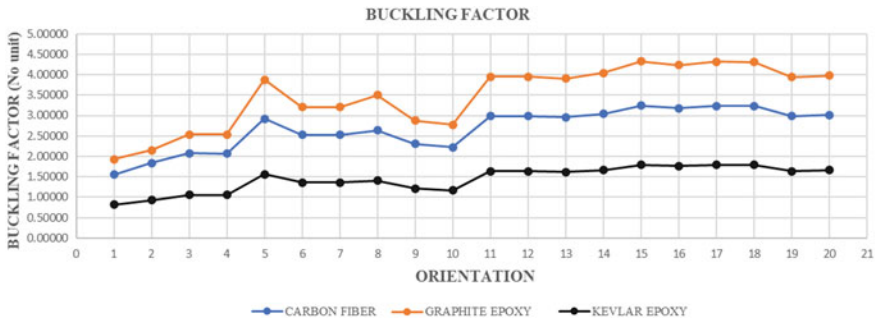


Fig. 3 Variation in the buckling factor values with respect to different stacking sequences

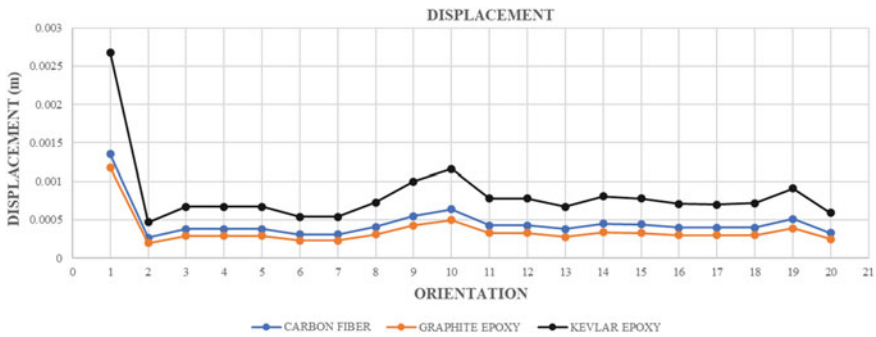


Fig. 4 Variation in the displacement values with respect to different stacking sequences

It is evident from Tables 4, 5 and 6 that the stacking sequences based on positive and negative 45° fiber angle orientation produce the same displacement and buckling factor values, irrespective of the material. Although the second stacking sequence, (90°/90°/90°/90°/90°/90°/90°/90°/90°/90°/90°/90°) _S orientation as indicated in Table 5, shows the least displacement value, it has a smaller buckling factor value. Hence, this stacking sequence cannot be considered the best one for divergence elimination. Considering the buckling factor values of the graphite epoxy material for the 15th to 18th stacking sequences holds values greater than 4. Hence, it is evident that among the four stacking sequences, the 15th stacking sequence provides the high buckling factor value.

Table 4 Buckling strength values of different stacking sequences

Buckling strength (N/m)		Carbon fiber	Graphite epoxy	Kevlar epoxy
Material/orientation				
$(0^\circ/0^\circ/0^\circ/0^\circ/0^\circ/0^\circ/0^\circ/0^\circ/0^\circ)$ s		6.76E + 05	8.37946E + 05	3.54607E + 05
$(90^\circ/90^\circ/90^\circ/90^\circ/90^\circ/90^\circ/90^\circ/90^\circ/90^\circ)$ s		7.99E + 05	9.34638E + 05	4.02429E + 05
$(+45^\circ/+45^\circ/+45^\circ/+45^\circ/+45^\circ/+45^\circ/+45^\circ/+45^\circ/+45^\circ)$ s		9.02E + 05	1.10294E + 06	4.59880E + 05
$(-45^\circ/-45^\circ/-45^\circ/-45^\circ/-45^\circ/-45^\circ/-45^\circ/-45^\circ/-45^\circ)$ s		8.98E + 05	1.10294E + 06	4.59880E + 05
$(-45^\circ/+45^\circ/-45^\circ/+45^\circ/-45^\circ/+45^\circ/-45^\circ/+45^\circ/-45^\circ/+45^\circ)$ s		1.2703E + 06	1.68493E + 06	6.81320E + 05
$(90^\circ/+45^\circ/90^\circ/+45^\circ/90^\circ/+45^\circ/90^\circ/+45^\circ/90^\circ/+45^\circ)$ s		1.1000E + 06	1.39514E + 06	5.89865E + 05
$(90^\circ/-45^\circ/90^\circ/-45^\circ/90^\circ/-45^\circ/90^\circ/-45^\circ/90^\circ/-45^\circ)$ s		1.1007E + 06	1.39514E + 06	5.89865E + 05
$(90^\circ/0^\circ/90^\circ/0^\circ/90^\circ/0^\circ/90^\circ/0^\circ/90^\circ/0^\circ)$ s		1.1479E + 06	1.52180E + 06	6.11702E + 05
$(-45^\circ/0^\circ/-45^\circ/0^\circ/-45^\circ/0^\circ/-45^\circ/0^\circ/-45^\circ/0^\circ)$ s		1.0023E + 06	1.24968E + 06	5.27369E + 05
$(0^\circ/+45^\circ/0^\circ/+45^\circ/0^\circ/+45^\circ/0^\circ/+45^\circ/0^\circ/+45^\circ)$ s		9.6741E + 05	1.20888E + 06	5.08972E + 05
$(+45^\circ/0^\circ/90^\circ/+45^\circ/0^\circ/90^\circ/+45^\circ/0^\circ/90^\circ/+45^\circ/0^\circ/90^\circ)$ s		1.3001E + 06	1.71888E + 06	7.11925E + 05
$(-45^\circ/0^\circ/90^\circ/-45^\circ/0^\circ/90^\circ/-45^\circ/0^\circ/90^\circ/-45^\circ/0^\circ/90^\circ)$ s		1.3001E + 06	1.71888E + 06	7.11924E + 05
$(90^\circ/-45^\circ/0^\circ/90^\circ/-45^\circ/0^\circ/90^\circ/-45^\circ/0^\circ/90^\circ/-45^\circ/0^\circ)$ s		1.2850E + 06	1.70024E + 06	7.05404E + 05
$(0^\circ/90^\circ/+45^\circ/0^\circ/90^\circ/+45^\circ/0^\circ/90^\circ/+45^\circ/0^\circ/90^\circ/+45^\circ)$ s		1.3226E + 06	1.75747E + 06	7.24884E + 05
$(-45^\circ/0^\circ/+45^\circ/90^\circ/-45^\circ/0^\circ/+45^\circ/90^\circ/-45^\circ/0^\circ/+45^\circ/90^\circ)$ s		1.4099E + 06	1.88055E + 06	7.80656E + 05
$(90^\circ/0^\circ/+45^\circ/-45^\circ/90^\circ/+45^\circ/-45^\circ/90^\circ/+45^\circ/-45^\circ/90^\circ/+45^\circ/-45^\circ)$ s		1.3820E + 06	1.84125E + 06	7.66503E + 05
$(+45^\circ/-45^\circ/+45^\circ/-45^\circ/0^\circ/90^\circ/+45^\circ/-45^\circ/+45^\circ/-45^\circ/0^\circ/90^\circ)$ s		1.4059E + 06	1.88002E + 06	7.81151E + 05
$(-45^\circ/+45^\circ/-45^\circ/+45^\circ/0^\circ/90^\circ/-45^\circ/+45^\circ/-45^\circ/+45^\circ/0^\circ/90^\circ)$ s		1.4065E + 06	1.87532E + 06	7.78893E + 05
$(-45^\circ/-45^\circ/0^\circ/+45^\circ/+45^\circ/0^\circ/90^\circ/90^\circ/-45^\circ/-45^\circ)$ s		1.2974E + 06	1.71393E + 06	7.11882E + 05
$(+45^\circ/+45^\circ/90^\circ/-45^\circ/-45^\circ/90^\circ/0^\circ/0^\circ/+45^\circ/+45^\circ)$ s		1.3125E + 06	1.72972E + 06	7.25210E + 05

Table 5 Displacement values of different stacking sequences

Displacement (m)	Carbon fiber	Graphite epoxy	Kevlar epoxy
Material/orientation			
(0°/0°/0°/0°/0°/0°/0°/0°/0°/0°) s	0.00135	0.00118	0.00268
(90°/90°/90°/90°/90°/90°/90°/90°/90°/90°) s	0.00027	0.0002	0.00047
(+45°/+45°/+45°/+45°/+45°/+45°/+45°/+45°/+45°/+45°) s	0.00038	0.00029	0.00067
(-45°/-45°/-45°/-45°/-45°/-45°/-45°/-45°/-45°/-45°) s	0.00038	0.00029	0.00067
(-45°/+45°/-45°/+45°/-45°/+45°/-45°/+45°/-45°/+45°) s	0.00031	0.00023	0.00054
(90°/+45°/90°/+45°/90°/+45°/90°/+45°/90°/+45°) s	0.00031	0.00023	0.00054
(90°/-45°/90°/-45°/90°/-45°/90°/-45°/90°/-45°) s	0.00041	0.00031	0.00073
(90°/0°/90°/0°/90°/0°/90°/0°/90°/0°) s	0.00055	0.00043	0.001
(-45°/0°/-45°/0°/-45°/0°/-45°/0°/-45°/0°/-45°/0°) s	0.00064	0.0005	0.00116
(0°/+45°/0°/+45°/0°/+45°/0°/+45°/0°/+45°/0°/+45°) s	0.00043	0.00033	0.00078
(+45°/0°/90°/+45°/0°/90°/+45°/0°/90°/+45°/0°/90°) s	0.00043	0.00033	0.00078
(-45°/0°/90°/-45°/0°/90°/-45°/0°/90°/-45°/0°/90°) s	0.00038	0.00028	0.00067
(90°/-45°/0°/90°/-45°/0°/90°/-45°/0°/90°/-45°/0°) s	0.00045	0.00034	0.00081
(0°/90°/+45°/0°/90°/+45°/0°/90°/+45°/0°/90°/+45°) s	0.00044	0.00033	0.00078
(-45°/0°/+45°/90°/-45°/0°/+45°/90°/-45°/0°/+45°/90°) s	0.0004	0.0003	0.00071
(90°/0°/+45°/-45°/90°/0°/+45°/-45°/90°/0°/+45°/-45°) s	0.0004	0.0003	0.0007
(+45°/-45°/+45°/-45°/0°/90°/+45°/-45°/+45°/-45°/0°/90°) s	0.0004	0.0003	0.00072
(-45°/+45°/-45°/+45°/0°/90°/-45°/+45°/-45°/+45°/0°/90°) s	0.00051	0.00039	0.00091
(-45°/-45°/0°/+45°/+45°/0°/90°/90°/-45°/-45°) s	0.00033	0.00025	0.00059
(+45°/+45°/90°/90°/-45°/-45°/90°/90°/0°/0°/+45°/+45°) s			

Table 6 Buckling factor values of different stacking sequences

Buckling factor (no unit)		Carbon fiber	Graphite epoxy	Kevlar epoxy
Material/orientation				
(0°/0°/0°/0°/0°/0°/0°/0°/0°)	s	1.55450	1.92728	0.8156
(90°/90°/90°/90°/90°/90°/90°/90°/90°)	s	1.83773	2.14967	0.92559
(+45°/+45°/+45°/+45°/+45°/+45°/+45°/+45°/+45°)	s	2.07562	2.53676	1.05772
(-45°/-45°/-45°/-45°/-45°/-45°/-45°/-45°/-45°)	s	2.06595	2.53676	1.05772
(-45°/+45°/-45°/+45°/-45°/+45°/-45°/+45°/-45°/+45°)	s	2.92282	3.87534	1.56704
(90°/+45°/90°/+45°/90°/+45°/90°/+45°/90°/+45°)	s	2.5317	3.20882	1.35669
(90°/-45°/90°/-45°/90°/-45°/90°/-45°/90°/-45°)	s	2.5317	3.20882	1.35669
(90°/0°/90°/0°/90°/0°/90°/0°/90°/0°)	s	2.64026	3.50014	1.40691
(-45°/0°/-45°/0°/-45°/0°/-45°/0°/-45°/0°/-45°/0°)	s	2.30527	2.87426	1.21295
(0°/+45°/0°/+45°/0°/+45°/0°/+45°/0°/+45°/0°/+45°)	s	2.22504	2.78042	1.17064
(+45°/0°/90°/+45°/0°/90°/+45°/0°/90°/+45°/0°/90°)	s	2.99016	3.95342	1.63743
(-45°/0°/90°/-45°/0°/90°/-45°/0°/90°/-45°/0°/90°)	s	2.99016	3.95342	1.63743
(90°/-45°/0°/90°/-45°/0°/90°/-45°/0°/90°/-45°/0°)	s	2.95559	3.91055	1.62243
(0°/90°/+45°/0°/90°/+45°/0°/90°/+45°/0°/90°/+45°)	s	3.04205	4.04218	1.66723
(-45°/0°/+45°/90°/-45°/0°/+45°/90°/-45°/0°/+45°/90°)	s	3.24298	4.32526	1.79551
(90°/0°/+45°/-45°/90°/0°/+45°/-45°/90°/0°/+45°/-45°)	s	3.17803	4.23488	1.76296
(+45°/-45°/+45°/-45°/0°/90°/+45°/-45°/+45°/-45°/0°/90°)	s	3.23364	4.32405	1.79665
(-45°/+45°/-45°/+45°/0°/90°/-45°/+45°/-45°/+45°/0°/90°)	s	3.23495	4.31324	1.79145
(-45°/-45°/0°/+45°/0°/90°/90°/-45°/-45°)	s	2.98397	3.94204	1.63733
(+45°/+45°/90°/90°/-45°/-45°/90°/90°/0°/0°/+45°/+45°)	s	3.0188	3.97836	1.66798

6 Conclusion

Higher the buckling factor, the possibility of material to withstand the divergence will be greater. From the above-obtained result, since the properties are varying in accordance with the ply angle orientations, it is obvious that the ply which shows the better buckling factor can be utilized to reduce the divergence on the aircraft wing. The 15th stacking sequence that has been mentioned below has the maximum buckling factor, and hence, it can opt for the elimination of divergence.

$$(-45^{\circ}/0^{\circ}/+45^{\circ}/90^{\circ}/-45^{\circ}/0^{\circ}/+45^{\circ}/90^{\circ}/-45^{\circ}/0^{\circ}/+45^{\circ}/90^{\circ})_s$$

From the obtained results, it is also evident that the graphite epoxy has moderate displacement and maximum buckling factor values when compared to the other two materials. Also, it shows enhanced properties than the other materials. Hence, graphite epoxy can be employed in the application of divergence elimination.

References

1. Williams JK (1969) Paper 31: major causes of failure—civil aircraft structure. Proc Inst Mech Eng Conf Proc 184(2):222–231. https://doi.org/10.1243/PIME_CONF_1969_184_063_02
2. Nassar A, Nassar E (2020) Effect of fiber orientation on the mechanical properties of multilayers laminate nanocomposites. Heliyon 6(1). <https://doi.org/10.1016/j.heliyon.2020.e03167>
3. Ahmad I, Baharum A, Abdullah I (2006) Effect of extrusion rate and fiber loading on mechanical properties of twaron Fiber-Thermoplastic Natural Rubber (TPNR) composites. J Reinf Plast Compos 25(9). <https://doi.org/10.1177/0731684406065082>
4. Mallick PK (2007) Fiber-reinforced composites. CRC Press. <https://doi.org/10.1201/9781420005981>
5. Hwu C, Tsai ZS (2002) Aeroelastic divergence of stiffened composite multicell wing structures. J Aircr 39(2). <https://doi.org/10.2514/2.2945>
6. Krone N (1975) Divergence elimination with advanced composites. Am Inst Aeronaut Astronaut J. <https://doi.org/10.2514/6.1975-1009>
7. Kaw AK (2005) Mechanics of composite materials, second edn
8. Ferrero JF, Tawk I, Rivallant S, Barrau JJ, Sudre M (2007) Fibre orientation effects on high strain rate of carbon/epoxy composites. Adv Compos Lett 16(1):096369350701600. <https://doi.org/10.1177/096369350701600103>
9. Mohammed TW, Taha DY, Abdul-Ilah RR (2018) Evaluation of composite material used in the wings of typical airplane based on stress analysis. Eur J Eng Res Sci 3(11). <https://doi.org/10.24018/ejers.2018.3.11.921>
10. Krone N Jr (1980) Forward swept-wing design. In: The evolution of aircraft wing design; proceedings of the symposium <https://doi.org/10.2514/6.1980-3047>
11. Weaver PM (2002) Designing composite structures: Lay-up selection. Proc Inst Mech Eng Part G J Aerosp Eng 216(2). <https://doi.org/10.1243/095441002760179807>
12. Rajappan R (2012) Finite element modeling and analysis of skin panel based on the fiber orientation and stacking sequence. IOSR J Mech Civil Eng 3(1). <https://doi.org/10.9790/1684-0310119>
13. Reddy JN (2003) Mechanics of laminated composite plates and shells. <https://doi.org/10.1201/b12409>
14. Jones RM (1999) Mechanics of composite materials Jones

Effect of Fiber Drawing on Tensile Strength of UHMWPE Single Fibers: Simulation via Von Mises Stress Criterion



Shubhanker Singh , Vishal Das , D. N. Tripathi, and N. Eswara Prasad

Abstract Ultra-high molecular weight polyethylene (UHMWPE) is an exceedingly strong and lightweight polymer owing to its extremely long-chain molecules and a very high average molecular weight. Consequently, it is the material of choice for lightweight high-performance fibers. In this study, the tensile strength of single UHMWPE fibers, i.e., undrawn, drawn and Dyneema[®] SK75, has been determined experimentally as well as through simulation using finite element analysis (FEA) via von Mises stress criterion to study the effect of fiber drawing on tensile properties. The requisite material properties of UHMWPE were fed in the simulation software (SolidWorks and ANSYS), and the tensile properties were extracted using linear elastic isotropic model. The simulation results agree with the experimental results and illustrate that the percentage error between the simulated and experimentally determined results reduces with the extent of fiber drawing which can be ascribed to the better alignment and close packing of polymer chains during fiber drawing. This observation has been complemented by relative crystallinity through X-ray diffraction studies and also through morphological studies of the fiber specimens examined through scanning electron microscopy.

Keywords Dyneema[®] SK75 · UHMWPE · Single fiber · ANSYS · SolidWorks

1 Introduction

Ultra-high molecular weight polyethylene (commonly termed as UHMWPE) is a subset of the family of polyethylene (PE) which has an exceedingly high molecular weight and exceptional molecular orientation. As per ASTM definition [1],

S. Singh (✉) · V. Das · D. N. Tripathi

Directorate of Polymers, Defence Materials and Stores Research and Development Establishment (DMSRDE), Defence Research and Development Organisation (DRDO), G.T. Road, Kanpur 208013, India
e-mail: shubhanker1990@gmail.com

N. Eswara Prasad

Defence Materials and Stores Research and Development Establishment (DMSRDE), Defence Research and Development Organisation (DRDO), G.T. Road, Kanpur 208013, India

the average molecular weight of UHMWPE should generally be more than 3.1×10^6 g/mol. There are commercial grades of UHMWPE with molecular weights in between 3 and 9×10^6 g/mole. UHMWPE is a class of polymer having unique specific properties (per unit density) and hence finds applications in areas requiring less abrasion, excellent impact strength, good chemical resistance, etc. [2–5]. UHMWPE gets its strength primarily from the extremely long linear molecules. The van der Waals forces in UHMWPE are rather weak for each atom of overlap between the molecules. However, large overlaps are created due to the extremely long molecules due to which polymer can bear more shear stresses. Thus, each UHMWPE chain is bonded to the others with a number of van der Waals bonds so that the overall inter-molecule strength is quite high. This results in UHMWPE fibers with extremely high specific tensile properties. Because of the extremely high molecular weight of UHMWPE, it is not possible to produce fibers through the conventional melt spinning process. Hence, the gel-spinning process followed by high temperature fiber stretching has been specifically adopted to produce extremely oriented, high-strength fibers [6]. During the production of UHMWPE fibers, the high orientation of fibrous structure through the application of high draw ratios is important for obtaining high specific tensile properties. To accomplish high draw ratios, an assortment of different techniques has been employed [7]. A commercial grade of UHMWPE fibers has been reported to have tensile strengths of about 3–4 GPa or lower, whereas some researchers have even reported tensile strengths of more than 6 GPa for fibers developed in their research work [8–10]. Thus, optimization of fiber production and processing stages is extremely important to maximize the strength characteristics of the developed UHMWPE fibers. There may be several aspects that finally govern the mechanical strength features of the gel-spun UHMWPE fibers [11, 12]. Fiber drawing just after the gel-spinning stage is one of the important aspects which govern the final mechanical strength of the UHMWPE fiber. The experimental determination of strength and modulus thus becomes imperative to comment on the effect of fiber drawing on the final properties of UHMWPE fibers. The conduct of several sets of experiments to draw a correlation data between the effect of fiber drawing and final properties of UHMWPE fibers may be lengthy and time consuming. On the other hand, the conduct of simulation through various finite element (FE) models presents a dependable and efficient way to report the effect of various processing parameters on the overall properties of the fiber [13, 14]. Commercial software like SolidWorks and ANSYS presents an efficient platform to virtually carry out physical tests under various simulated conditions to arrive at the final output which is extracted as meaningful data in the form of results [15, 16]. However, it is also pertinent to validate the simulated test results with the actual experimentally observed results so that the necessary confidence level can be generated [17, 18]. The work presented here describes the FE methodology to carry out the simulation of three different types of single UHMWPE fibers, i.e., undrawn, drawn and Dyneema® SK75 utilizing von Mises stress criterion. The deformation behavior of fibers is modeled with a linear elastic isotropic model based on tensile properties to study the effect of fiber drawing on tensile properties of UHMWPE fibers. The simulated results have also been correlated with the experimental results to study the level of agreement between these sets of results.

2 Experimental Details

2.1 Materials

The UHMWPE polymer used in this work was obtained from Reliance Industries Ltd., India (Grade–Relene[®] UHM 2504) in the form of powder and is associated with a viscosity average molecular weight (M_v) of more than 3×10^6 g/mol. Decalin (Decahydronaphthalene, mixture of cis and trans, purity > 98%, reagent grade) was obtained from Merck and used as such. n-Hexane (HPLC grade, purity > 95%) was obtained from Merck and was also used as such. Neat fibers were also taken from DSM Dyneema[®] SK75 grade and cleaned with xylene (Merck, purity > 95%) to be used as the reference UHMWPE fiber.

2.2 UHMWPE Fiber Spinning Through the Gel-Spinning Process

To gel-spin [19] the UHMWPE powders obtained, UHMWPE was first dissolved in decalin in stirred condition for about 60 min to form cakes which could then be fed into the extruder. The weight % of UHMWPE in decalin was maintained between 5 and 10%. A moderately low dilution level of homogeneous UHMWPE solution was prepared. This was done since the final mechanical properties of the fibers depend greatly on inhomogeneities present in the solution which may result in defects in the final fiber structure [20]. The cake which was prepared from the dissolution of UHMWPE in decalin was then fed into a lab size single screw extruder to obtain a single strand of UHMWPE with some amount of decalin trapped in the UHMWPE gel. Decalin was subsequently removed from the UHMWPE gel through several water baths during the continuous drawing process of UHMWPE. The as-spun and drawn fibers were dried in an air circulated oven at 80 °C for 4 h to remove the residual water and decalin. In this study, an as-spun fiber specimen was collected, and a drawn fiber specimen was also collected which was collected at a draw ratio of 10. The draw ratio (D_R) can be obtained from Eq. (1).

$$D_R = \frac{U_B}{U_A} \quad (1)$$

where U_A = winding speed (in m/min) of spool A (for as-spun fiber) and U_B = winding speed (in m/min) of spool B (for drawn fiber).

2.3 Measurement of UHMWPE Fiber Diameter

To study the morphology and diameter of the fibers, these fiber specimens were first cut, cleaned with xylene, dried and then sputter-coated with gold. These fibers were then observed on a TESCAN Field Emission Scanning Electron Microscope (FESEM). The fiber specimens used in the SEM analysis were as-spun fibers extruded through the gel-spinning process (ND), drawn fibers (*D*) attained through the hot stretch drawing procedure and cut from dried Dyneema[®] SK75 UHMWPE fiber (Dyneema) after cleaning with xylene.

2.4 Tensile Test of Single UHMWPE Fibers

Tensile tests were carried out on single UHMWPE fibers to study their tensile properties (ultimate tensile strength and tensile modulus) which were performed in accordance with ASTM D3379-75 [21]. The INSTRON 5900 Series Universal Testing Machine (UTM) was utilized with a load cell of 30 kN. The area of cross section of single UHMWPE fibers was evaluated using the mean observed diameter in the FESEM images. The support strip for fixing the fiber specimen in the UTM was fabricated out of thick paper. A rectangular slit of length that was equal to the gauge length was cut out in the middle of the support strip. A single fiber was pasted at both the ends of the slit in the paper support strip using a suitable adhesive. Utmost care was employed to verify that the axis of the UHMWPE single fiber was precisely aligned with the axis of the cross-head of UTM. This care was taken so that a uniform stress condition could be replicated over the entire cross section of the fiber. A load of 30 kN was set as the full-scale load. The cross-head velocity was set to 5 mm/min for all the types of UHMWPE fibers under study. Before the start of the tensile tests, both sides of the paper support strips were cut cautiously at the middle of the gauge section without unsettling the setup. The specimen fiber was then pulled under tension, and the test load and elongation were recorded until the test specimen failed. A total of four single fibers were tested, and the results were averaged for each type of UHMWPE fiber (ND, *D* and Dyneema).

2.5 Finite Element Modeling

Finite element analysis (FEA) is a universally employed methodology for studying structural properties of different engineering materials as well as structures [22–24]. The FE modeling in this work was carried out primarily in SolidWorks as it emphasizes more on rapidly generating 3D solid models of both intricate parts and assemblies which can be visually displayed. It hence aids in faster design development and communication and thus can evaluate efficient design functionality and performance

prior to the production of a prototype. With all component drawing views created from the original 3D model, SolidWorks can virtually confirm that any corrections made to the model are automatically updated within the drawing itself. FEA in this study was also done on ANSYS Workbench 15.0 as it was convenient to use a multi-purpose tool to solve complex structural engineering problems efficiently in a short time. The ANSYS Workbench 15.0 has the FEA solvers in its suite. Thus, it is easy to modify and automate solutions for structural mechanics problems and parameterize them to investigate multiple design setups [25]. Solid models were initially prepared on SolidWorks and then imported into ANSYS Workbench 15.0 as STEP files. The fibers were modeled as solid bodies with different diameters. These solid models were meshed with 6 node solid elements with a reduced integration scheme having hourglass control in the Lagrangian reference frame to capture the materials' nonlinearity. Computation time highly depends upon the size of the elements. Thus, to compensate for the trade-off between accuracy and computation time, program control element size was considered. All six degrees of freedom of the nodes of the outer periphery of the rigid ground, i.e., the x , y and z translations, as well as the rotational motions about these three axes were restricted to fix the rigid ground. To simulate the test condition, one end of the fiber was fixed, and force (which was obtained from experiments done on UTM) was applied on another end of the fiber. The tensile properties were extracted using linear elastic isotropic model. Some of the properties of fiber were fed into a system comprising the boundary conditions like axial tensile modulus and Poisson's ratio. Simulation results were compared with experimental tensile tests conducted on single fibers on UTM.

2.6 *X-Ray Diffraction (XRD) Studies of UHMWPE Single Fibers*

Studies were conducted on an XRD instrument to obtain the crystalline natures of the three single fibers. The XRD measurements of the UHMWPE fibers were recorded on a Bruker XRD system with Cu $K\alpha$ radiation of wavelength (λ) equal to 1.54 Å. The experiments were done in the 2θ range of 5° to 80°. A scan rate of 0.05°/s was set to record the XRD pattern.

3 Results and Discussion

The FESEM micrographs of the undrawn, drawn and Dyneema® SK75 UHMWPE fibers have been illustrated in Fig. 1a–c, respectively. It was obvious from the FESEM micrographs that the undrawn, un-stretched fiber extruded through the in-house developed gel-spinning process shown in Fig. 1a has a diameter of approximately 188–192 μm . When a similar fiber is drawn through the hot stretching process,

the diameter of the fiber is reduced to approximately 118–122 μm as evident from Fig. 1b. Dyneema[®] SK75 UHMWPE fiber shown in Fig. 1c has a diameter of approximately 19–21 μm as it is an extremely drawn, highly stretched fiber. Four single fibers of each type were measured to obtain the mean fiber diameter. Also, four different measuring points were taken along each fiber length. The disparity in the diameters measured at each measuring point along the fiber length was observed to be insignificant for each fiber specimen and each fiber type. Thus, the mean diameter of each specimen was taken as the average of diameters at the four measuring points. Furthermore, an insignificant variation in the diameters of various fiber specimens was seen for each fiber type. The mean and standard deviation in diameters for each type of fiber (ND, D and Dyneema) have been illustrated in Table 1. The diameters of undrawn, drawn and Dyneema were taken to be 190, 120 and 20 μm , respectively, for simplicity.

The simulation of stress conditions on the fibers is depicted in Figs. 2a–c, 3a–c and 4a–c for ND, D and Dyneema, respectively. Figure numbers 2a, 3a and 4a represent the solid body models of the three fibers, i.e., ND, D and Dyneema, correspondingly. Figure numbers 2b, 3b and 4b represent the solid body with meshing for ND, D and Dyneema fiber types in that order. Additionally, Figs. 2c, 3c and 4c represent the simulated value of the respective stresses obtained for ND, D and Dyneema single fibers acquired through the von Mises stress criterion. Comparative ultimate tensile strengths obtained experimentally as well as through simulation using FE analysis via von Mises stress criterion are depicted in Table 2. Results in Table 2 elucidate that the simulation results are close to experimental results and the percentage error between the experimental and simulated values reduces with the extent of fiber drawing.

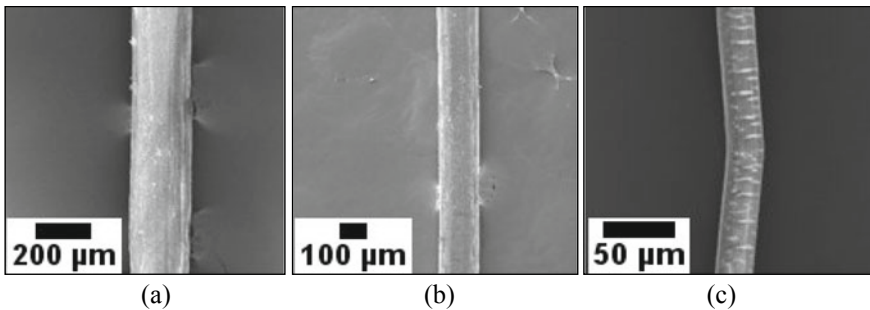
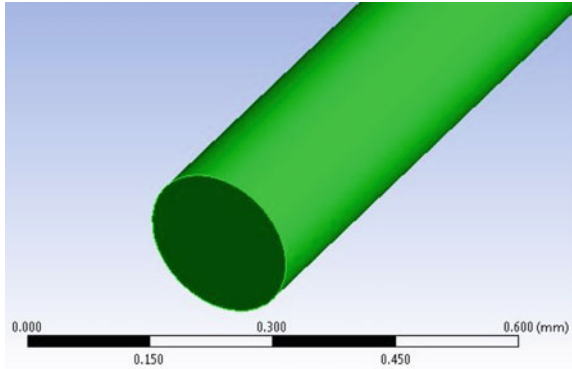


Fig. 1 FESEM images of **a** Undrawn (N); **b** Drawn (D); and **c** Dyneema[®] SK75 (Dyneema) UHMWPE fibers

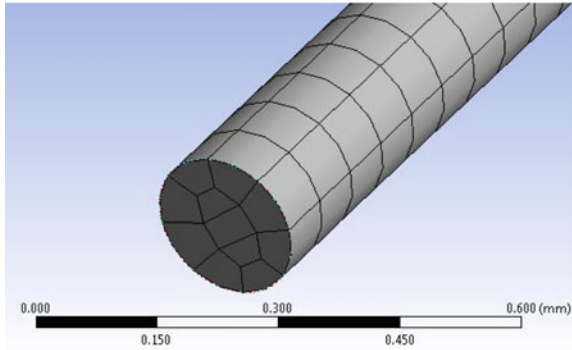
Table 1 Mean and standard deviation for diameters of each type of UHMWPE fibers

Fiber diameter	UNDRAWN	DRAWN	DYNEEMA [®] SK75
Mean (μm)	189.4	120.2	19.6
Standard deviation (μm)	1.6	1.8	0.9

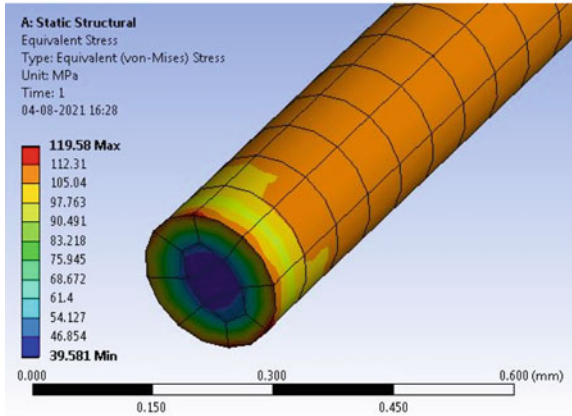
Fig. 2 Stress simulation of undrawn UHMWPE fiber (ND) **a** Solid body model of fiber; **b** Solid body of fiber with meshing and **c** von Mises stresses in the fiber



(a)



(b)



(c)

Fig. 3 Stress simulation of drawn UHMWPE fiber (D) **a** Solid body model of fiber; **b** Solid body of fiber with meshing and **c** von Mises stresses in the fiber

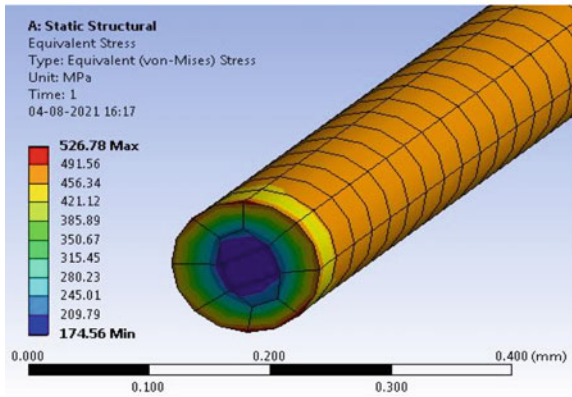
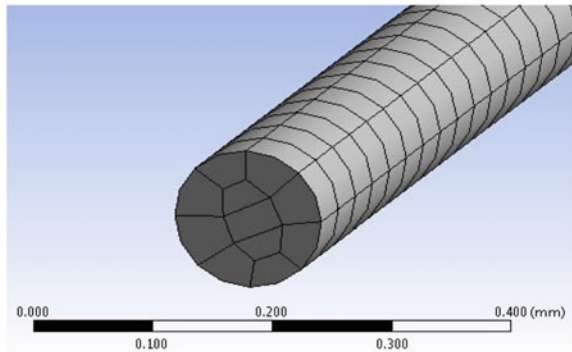
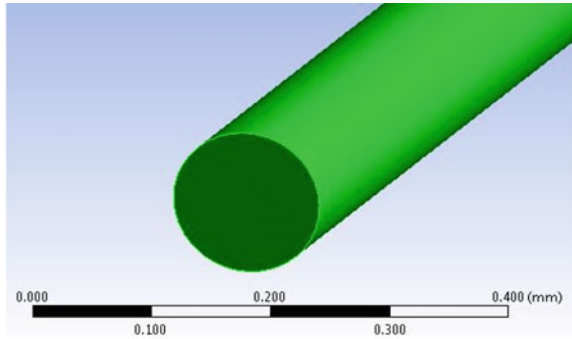
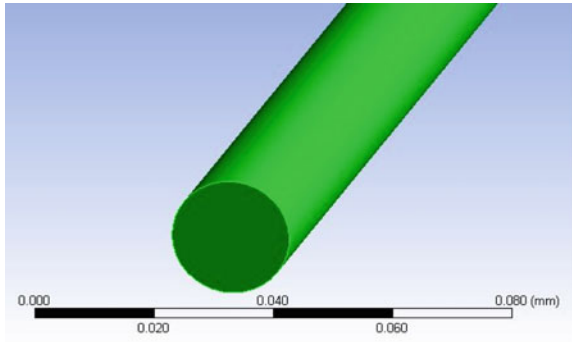
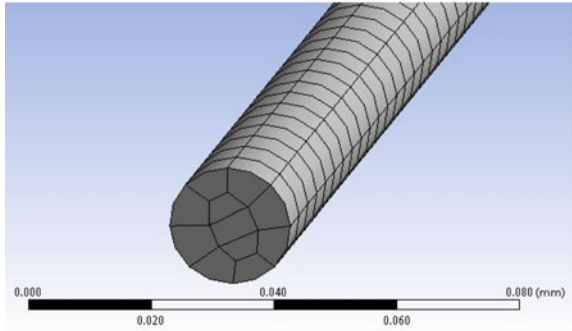


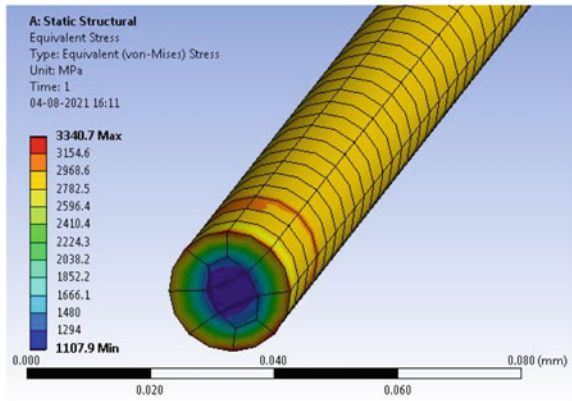
Fig. 4 Stress simulation of Dyneema® SK75 UHMWPE fiber (Dyneema) **a** Solid body model of fiber; **b** Solid body of fiber with meshing and **c** von Mises stresses in the fiber



(a)



(b)



(c)

Table 2 Properties of (a) Undrawn (N); (b) Drawn and (c) Dyneema® SK75 UHMWPE fibers

Properties	UHMWPE (ND)	UHMWPE (D)	Dyneema
Poissson's ratio (approx.)	0.4	0.4	0.4
Young's modulus (GPa) from UTM	0.301	10.746	122.107
Load (N) from UTM	3.24	6	1.035
Density (g/cm ³)	0.97	0.97	0.97
Specimen length (mm)	25	25	25
Tensile strength (MPa) (experimental)	115.89	515.31	3299.81
Tensile strength (MPa) (FEA value)	119.58	526.78	3340.7
Percentage error (%)	2.64	1.80	1.40

The XRD studies of the fibers give immensely valuable information about its crystalline nature and its consequent properties [26, 27]. There are a plethora of studies that have correlated the crystalline nature of a material to its tensile properties like tensile strength and modulus [28, 29]. In this study, the crystalline natures of the fibers have been correlated with its tensile properties. The XRD plots of the three types of UHMWPE fibers have been represented in Fig. 5. Similar to other polyethylenes with a different assortment of densities, UHMWPE has XRD peaks at practically the same position, indicating that they have typical crystal structures. As shown in Fig. 5, all plots contained two typical characteristic diffraction peaks at approximately 2θ angles of ca. 21.7° and ca. 24.1° , respectively. These peaks have generally been reported for UHMWPE fibers by many researchers. Also, these crystalline peaks are accompanied by amorphous halo at 2θ values around 12° and 30° which indicates that the fibers are all semi-crystalline in nature. The earliest evaluation of the crystallographic unit cell parameters for polyethylene (PE) was reported by Bunn et al. in 1944 [30] in which an orthorhombic unit cell was predicted through wide angle X-ray diffraction (WAXD). As can be seen in Fig. 5, few additional peaks at ca. 19° and ca. 37° have also been observed in the case of the ultra-drawn Dyneema® SK75 fiber and to some extent in the case of drawn UHMWPE fiber. It has been widely reported that during numerous researches conducted by varied groups in the 1950s, it was observed that WAXD patterns for PE films and filaments which were subjected to significant cold drawing demonstrated extra peaks which were absent in the orthorhombic unit cell proposed by Bunn et al. [31, 32]. Subsequently, these extra peaks have been reported to occur as a consequence of the metastable monoclinic unit cell which forms due to the deformation of the orthorhombic unit cell [33–35]. The percent crystallinity in the three types of fibers was evaluated from the XRD data using Eq. 2 [36].

$$X_c(\%) = \frac{\sum A_{\text{crystalline}}}{\sum A_{\text{crystalline}} + \sum A_{\text{amorphous}}} \times 100 \quad (2)$$

where X_c is the percentage crystallinity in (%), $\sum A_{\text{crystalline}}$ is the total integral area of the crystalline peaks, and $\sum A_{\text{amorphous}}$ is the total integral area of the amorphous phase.

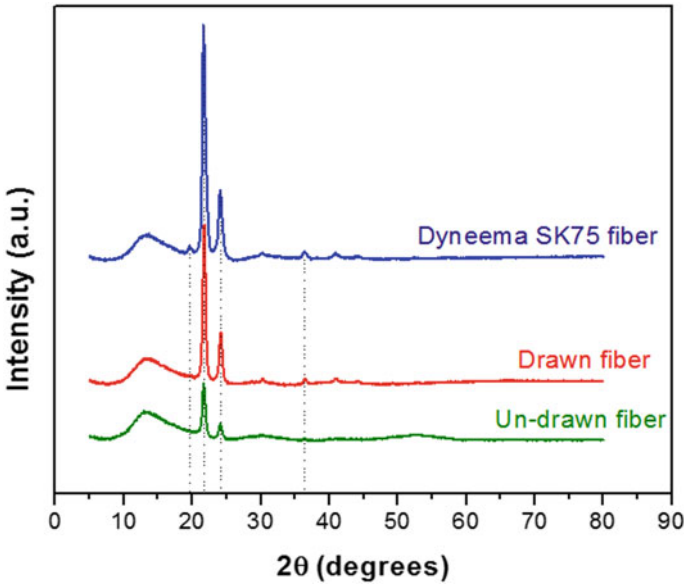


Fig. 5 XRD patterns of UHMWPE fibers

The crystalline natures of the three types of fibers under study have been illustrated in Table 3. It was observed that the percentage crystallinity (X_c) increased considerably with increased drawing and stretching involved in the processing of the gel-spun fibers. The trend in percentage crystallinity calculated from the XRD plots is in line with the findings reported earlier [37, 38] and also the technical brochure supplied by DSM Dyneema. This may be ascribed to better alignment and close packing of polymer chains during fiber drawing which can be supported by the relative crystallinity of the fibers studied through XRD (Fig. 5). One of the plausible explanations of this peculiar observation was provided by Xu et al. [39] where it was elucidated through the transformation of the shish-kebab type of crystalline structure seen in the case of the undrawn UHMWPE fiber; to that of the more compact type of shish-kebab type of crystalline structure perceived in case of the drawn UHMWPE fiber and finally to the purely microfibrillar type of extended chain crystalline structure depicted by the highly drawn and highly stretched Dyneema[®] SK75 fiber.

Table 3 Crystallinity of the three types of fibers under study

Fiber type	X_c (%)	$2\theta_{(110)}$ (degrees)	$2\theta_{(200)}$ (degrees)
Undrawn (ND)	51.96	21.73	24.15
Drawn (D)	65.94	21.67	24.10
Dyneema [®] SK75	82.07	21.69	24.09

Thus, it is observed that the tensile properties of the UHMWPE fibers are governed by their microstructure evolution during the processing stage which in turn is dependent on the crystalline nature of the fibers. In this study, it was evident that the undrawn UHMWPE fiber which has the lowest percentage crystallinity amongst the three types of fibers depicts the lowest axial tensile strength. Contrary to this, the more compact and larger number of crystalline phases present in the microstructure of the drawn fiber culminates into higher percentage crystallinity and provides the chain segments to bear more tensile loads before failure. The highly stretched highly drawn Dyneema fiber, because of its high percentage crystallinity, compact and extended chain crystal structure, has the ability to bear enormous amounts of tensile loads before failure.

4 Conclusions

This research work concludes the following:

- The percentage error between experimentally observed values and simulated values through FE analysis in respect of ultimate tensile strengths of undrawn, drawn and Dyneema fibers was found to be 2.64, 1.80 and 1.40 respectively, which are well within the acceptable limits.
- The ultimate tensile strength of fibers has been found to be dependent on the processing methodology (fiber drawing in particular) and thus the crystallinity of fibers.
- The simulation results corroborated well with the experimental results and illustrate that percentage error between the simulated and experimentally determined results reduces with the extent of fiber drawing which can be ascribed to the better alignment and close packing of polymer chains during fiber drawing.

Acknowledgements The authors would like to thank Dr. Kavita Agarwal and Mr. Rakesh Kumar for FESEM analysis; Mr. Sudhanshu Singh for XRD analysis and Mr. Harjeet Singh for his help during the tensile tests.

References

1. Annual Book of ASTM Standards, 1991, vol 08.03, Plastics, Method D4020
2. Ogawa T, Mukai H, Osawa S (1998) Mechanical properties of ultrahigh-molecular-weight polyethylene fiber-reinforced PE composites. *J Appl Polm Sci* 68(9):1431–1439
3. Kurtz SM, Muratoglu OK, Evans M, Edidin AA (1999) Advances in the processing, sterilization, and crosslinking of ultra-high molecular weight polyethylene for total joint arthroplasty. *Biomaterials* 20(18):1659–1688
4. Rose RM, Cimino WR, Ellis E, Crugnola AN (1982) Exploratory investigations on the structure dependence of the wear resistance of polyethylene. *Wear* 77(1):89–104

5. Nakayama K, Furumiya A, Okamoto T, Yag K, Kaito A, Choe CR, Wu L, Zhang G, Xiu L, Liu D, Masuda T, Nakajima A (1991) Structure and mechanical properties of ultrahigh molecular weight polyethylene deformed near melting temperature. *Pur Appl Chem* 63(2):1793–1804
6. Vlasblom MP, van Dingenen JJJ (2009) The manufacture, properties and applications of high strength, high modulus polyethylene fibers. In: *Handbook of tensile properties of textile and technical fibres*. Woodhead, pp 437–485
7. Bastiaansen CWM (1997) High-modulus and high strength fibers based on flexible macromolecules. In: *Materials science and technology*, vol 18, Part IV. John Wiley, ch 11
8. O'Connor TC, Robbins MO (2020) Molecular models for creep in oriented polyethylene fibers. *J Chem Phys* 153:144904
9. Pennings AJ, Roukema M, Van der Veen A (1990) Further studies on the high-speed gel-spinning of ultra-high molecular weight polyethylene. *Polym Bull* 23(3):353–359
10. Wang J, Smith KJ Jr (1999) The breaking strength of ultra-high molecular weight polyethylene fibers. *Polymer* 40(26):7261–7274
11. Lemstra PJ, Kirschbaum R, Ohta T, Yasuda H (1970) High strength/high modulus structures based on flexible macromolecules: Gel-spinning and related processes. In: *Developments in oriented polymers—2*. Elsevier Applied Science, pp 39–77
12. Ohta Y, Murase H, Hashimoto T (2005) Effects of spinning conditions on the mechanical properties of ultrahigh-molecular-weight polyethylene fibers. *J Polym Sci B* 43(19):2639–2652
13. Hutton DV (2004) *Fundamentals of finite element analysis*. Elizabeth A. Jones Publishers
14. Naveen J, Jawaid M, Vasanthanathan A, Chandrasekar (2019) *Finite element analysis of natural fiber-reinforced polymer composites*. Woodhead, pp 153–170
15. Islam MM, Chowdhury MA, Sayeed MA, Hossain EA, Ahmed SS, Siddique A (2014) Finite element analysis of steel fiber-reinforced concrete (SFRC): validation of experimental tensile capacity of dog-bone specimens. *Int J Adv Struct Eng* 6(63):1–8
16. Staszuk M, Nabiałek M (2017) Computer simulation of static tensile test using the finite elements method. *Mat Plast* 54:225–228
17. Okabe T, Takeda N (2002) Size effect on tensile strength of unidirectional CFRP composites—experiment and simulation. *Compos Sci Technol* 62(15):2053–2064
18. Okabe T, Ishii K, Nishikawa M, Takeda N (2010) Prediction of tensile strength of unidirectional CFRP composites. *Adv Compos Mat* 19(3):229–241
19. Pennings AJ, Hooft RJ, Postema AR, Hoogsteen W, Brinke G (1986) High-speed gel-spinning of ultra-high molecular weight polyethylene. *Polym Bull* 16(2–3):167–174
20. Kuo CJ, Lan WL (2014) Gel spinning of synthetic polymer fibers. In: *Advances in filament yarn spinning of textiles and polymers*. Woodhead Publishing, pp 100–112
21. ASTM D (1975) 3379: Standard test method for tensile strength and Young's modulus for high modulus single filament fibers. ASTM Standards
22. Stolarski T, Nakasone Y, Yoshimoto S (2018) Fundamentals of the finite element method, In: *Engineering analysis with ANSYS software*. Butterworth-Heinemann, pp 1–35
23. Khan HA, Hassan A, Saeed MB, Mazhar F, Chaudhary IA (2017) Finite element analysis of mechanical properties of woven composites through a micromechanics mode. *Sci Eng Compos Mat* 24(1):87–99
24. Joun M, Choi I, Eom J, Lee M (2007) Finite element analysis of tensile testing with emphasis on necking. *Comput Mat Sci* 41(1):63–69
25. Madenci E, Guven I (2015) *The finite element method and applications in engineering using ANSYS®*. Springer
26. Folomeshkin MS, Pisarevskiy YV, Prosekov PA, Volkovsky YA, Kumskov, AS, Grigoriev YV, Ligacheva EA, Targonskii AV, Blagov AE, Kovalchuk MV (2019) X-ray diffraction analysis and electron microscopy of the carbon fiber structure. *Crystallogr Rep* 64:1–5
27. Alwan TJ, Toma ZA, Kudhler MA, Ziadani KM (2016) Preparation and characterization of the PVA nanofibers produced by electrospinning. *J Nanotechnol Nanosci* 1(1):1–3
28. Wang ML, Bian WF (2020) The relationship between the mechanical properties and microstructures of carbon fibers. *New Carbon Mat* 35(1):42–49

29. Tanaka F, Okabe T, Okuda H, Ise M, Kinloch IA, Mori T, Young RJ (2013) The effect of nanostructure upon the deformation micromechanics of carbon fibers. *Carbon* 52:372–378
30. Bunn CW, Alcock TC (1945) The texture of polythene. *Tran Faraday Soc* 41:317–325
31. Natta G (1955) Polymeres isotactiques. *Makromol Chem* 16(1):213–237
32. McCall DW, Slichter WP (1957) Molecular motion in polyethylene. *J Polym Sci* 26(113):171–186
33. Teare PW, Holmes DR (1957) Extra reflections in the X-ray diffraction pattern of polyethylenes and polymethylenes. *J Polym Sci* 24(107):496–499
34. Walter ER, Reding FP (1956) The appearance of a new crystalline phase in stretched, linear polyethylene. *J Polym Sci* 21(99):557–559
35. Keller A (1952) Morphology of crystallizing polymers. *Nature* 169:913–914
36. Peterlin A (1987) Mechanical properties of fibrous structure. In: *Developments in oriented polymers*. Elsevier Applied Science, pp 279–318
37. Jian T, Shyu WD, Lin YT, Chen KN, Yeh JT (2003) Spinning and drawing properties of ultrahigh-molecular-weight polyethylene fibers prepared at varying concentrations and temperatures. *Polym Eng Sci* 43(11):1765–1777
38. Schaller R, Feldman K, Smith P, Tervoort TA (2015) High-performance polyethylene fibers “Al Dente”: improved gel-spinning of ultrahigh molecular weight polyethylene using vegetable oils. *Macromolecules* 48(24):8877–8884
39. Xu H, An M, Lv Y, Zhang L, Wang Z (2017) Structural development of gel-spinning UHMWPE fibers through industrial hot-drawing process analyzed by small/wide-angle X-ray scattering. *Polym Bull* 74:721–736

Prediction of In-Process Forces and Tool Durability in Stationary Shoulder Friction Stir Welding: A Process Modeling Approach



Vikash Kumar  and Buchibabu Vicharapu 

Abstract The conventional friction stir welding (FSW) of aluminum alloys is reasonably matured and most of the transportation industries integrated FSW in their production lines. The novel stationary shoulder friction stir welding (SSFSW) is a sister process of FSW, in which only tool probe rotates and linearly translates along the original weld joint interface to form a weld seam under much lesser heat input and lower peak temperature. The spindle torque and traverse force on the tool during SSFSW of a topical AA7075-T6 is important for the prior estimation of tool fracture but rarely reported in literature. An absolute comparison is made here between the SSFSW and FSW under the identical welding conditions using a finite element-based process model. The computed 3D temperature field, thermal cycle, spindle torque, traverse force, and tool durability index are reported here, and the model is thoroughly validated with the independent experimental results.

Keywords Stationary shoulder friction stir welding · Spindle torque · Traverse force · Tool durability index

1 Introduction

Stationary shoulder friction stir welding (SSFSW) process is an improved version of conventional friction stir welding (FSW) technology. In case of SSFSW, only tool probe rotates and shoulder remains stationary during welding. Sinhmar et al. [1] reported the lesser heat input and lower peak temperature due to the absence of heat generation component by stationary shoulder in SSFSW. Recently, Vicharapu et al. [2] reported the advantage of having improved mechanical properties and reduced residual stresses in SSFSW due to the lower heat input. Further, SSFSW offers weld nuggets with excellent surface finish, which found to enhance the fatigue life of the weld joint substantially. The SSFSW offers no excess flash unlike FSW that reduces the post-processing and cost of weld joint [3, 4].

V. Kumar · B. Vicharapu (✉)
Indian Institute of Technology, Palakkad, India
e-mail: buchibabu@iitpkd.ac.in

Barbini et al. [5] highlighted that the spindle torque was found to be lower in SSFSW unlike FSW. In addition, the tool probe experienced high traverse force due to the lack of pre-softening effect in SSFSW, while in conventional FSW, the additional heat generation by tool shoulder significantly reduces the traverse force on tool probe. DebRoy et al. [6] explained that the mechanical stress deriving from the combined effect of bending and torsion is the most anticipated cause for the tool probe failure. Trimble et al. [7] reported, substantial increase in tool traverse force with increase in welding speed for 5 mm thick AA2024 plate in FSW. Leitaoa et al. [8] also observed that higher tool traverse force and early tool failure during FSW of 5 mm thick AA5083 and 9.5 mm thick AA7075 plate at higher welding speed. Vicharapu et al. [9] reported higher tool traverse force and lower tool life in SSFSW compared to FSW process for 6.35 mm thick AA7010-T6 plate.

The effect of process conditions on in-process forces and tool failure are well reported in literature in case of FSW [10, 11], while such studies are rarely addressed in SSFSW [9]. Therefore, a comparative study between FSW and SSFSW of causative variables of tool failure, which include traverse force and shear stress induced in the tool for prior estimation of tool durability index in FSW and SSFSW of AA7075-T6 plate. AA7075-T6 is considered for the current study due to its high strength in comparison with other topical aluminum alloys.

2 Numerical Modeling

A transient 3D heat conduction Eq. (1) is solved in commercial finite element software, ABAQUS.

$$\frac{\partial}{\partial x} \left(K \frac{\partial T}{\partial x} \right) + \frac{\partial}{\partial y} \left(K \frac{\partial T}{\partial y} \right) + \frac{\partial}{\partial z} \left(K \frac{\partial T}{\partial z} \right) + Q = \rho C_p \frac{\partial T}{\partial t} \quad (1)$$

where K = thermal conductivity ($\text{Wm}^{-1} \text{K}^{-1}$), T = temperature (K), ρ = density (Kgm^{-3}), C_p = specific heat capacity ($\text{kJkg}^{-1} \text{K}^{-1}$), and t = time (s). The X -, Y -, and Z -directions represent along the length, width and thickness of the plate.

The rate of volumetric heat generation rate ($\text{Wm}^{-3} \text{s}^{-1}$) was estimated by Eq. (2), and the boundary conditions shown in Eqs. (3) and (4) are applied to solve Eq. (1) [2].

$$Q = \eta_n \times [\eta_m \times (1 - \delta) \tau_y + \delta \mu_f P_N] (\omega r - U \sin \theta) (A/V) \quad (2)$$

where η_n = fraction of heat transfer to workpiece, η_m = mechanical efficiency, δ = fractional sliding, τ_y = yield shear stress of workpiece (Nm^{-2}), μ_f = coefficient of friction between workpiece and tool, P_N = axial pressure (MPa), ω = angular speed of rotating tool (rad.s^{-1}), r and θ = radial distance (m) from axis of tool and its orientation (degree) with the welding speed, respectively. U = welding speed (m/s),

A/V = ratio of probe-workpiece contact area to the sheared volume around the probe (m^{-1}).

Fractional sliding (δ) and co-efficient of friction (μ_f) shown in Eq. (2) are estimated by using the following relations

$$\delta = 0.271 \times \exp\left(\frac{r\omega}{1.87}\right) - 0.026 \quad (3)$$

$$\mu_f = 0.54 \times (-\delta r\omega) \quad (4)$$

$$K \frac{\partial T}{\partial n} - Q_s + h(T - T_0) = 0 \quad (5)$$

$$h = h_b(T - T_0)^{0.25} \quad (6)$$

where K = thermal conductivity ($\text{Wm}^{-1} \text{K}^{-1}$), Q_s = surface heating by shoulder (W.m^{-2}), h = convective heat transfer coefficient ($\text{Wm}^{-2} \text{K}^{-1}$), and h_b = heat transfer parameter for bottom surface ($\text{Wm}^{-2} \text{K}^{-0.25}$).

The spindle torque (M_f), and traverse force (F_f) were calculated analytically using the Eq. (7) and Eq. (8), in which τ_y and σ are realized from the computed isotherms for both FSW and SSFSW [10]. First, second, and third terms of the Eq. (7) are the contribution of torque from shoulder, probe along the length and probe bottom. First, second, and third terms of Eq. (8) are the contribution traverse force from shoulder, probe along the length and probe bottom. Equations (9) and (10) are used to compute the spindle torque (M_s), traverse force (F_s) for SSFSW process, respectively.

$$M_f = \int_{R_p}^{R_s} r \times C \times (2\pi r dr) + \int_0^L r \times C \times (2\pi r dl) + \int_0^{R_p} r \times C \times (2\pi r dr) \quad (7)$$

$$F_f = \int_{R_p}^{R_s} [\delta\mu_f P_N] \times (2\pi r dr) + \int_0^L \sigma \times (dA) + \int_0^{R_p} [\delta\mu_f \sigma] \times (2\pi r dr) \quad (8)$$

$$M_s = \int_0^L r \times C \times (2\pi r dl) + \int_0^{R_p} r \times C \times (2\pi r dr) \quad (9)$$

$$F_s = \int_{R_p}^{R_s} [\delta\mu_f P_N] \times (2\pi r dr) + \int_0^L \sigma \times (dA) + \int_0^{R_p} [\delta\mu_f \sigma] \times (2\pi r dr) \quad (10)$$

where R_p , R_s , L , τ_y , and dA are the tool probe radius, shoulder radius, tool probe length, and projected are of tool probe. $C = [(1 - \delta)\tau_y + \delta\mu_f \sigma]$.

The linear and rotational motion of tool probe possess stresses due to combined effect of bending and torsion. Considering the tool as a cantilever, maximum shear stress can be calculated as per Tresca criterio by using below Eq. (11) [10, 11].

$$\tau_{\max} = \sqrt{\left(\frac{\sigma_B}{2}\right)^2 + (\tau_B + \tau_T \cos\beta)^2 + (\tau_T \sin\beta)^2} \quad (11)$$

where τ_{\max} = maximum shear stress experienced by tool probe (MPa), σ_B = normal stress due to bending, τ_B = shear stress due to bending (MPa), τ_T = shear stress due to bending (Mpa).

Tool durability index (I) can be defined as the ratio of yield shear stress (τ_{yp}) of tool probe corresponding to the peak temperature (T_p) to the maximum shear stress experienced by the tool probe during the welding process Eq. (12).

$$I = \frac{\tau_{yp}}{\tau_{\max}} \quad (12)$$

A half symmetric 3D FEM model of dimensions L (300) \times W (110) \times Th (6.3) mm³ was discretized in cuboidal element with eight nodes, the nodal temperature is considered as the nodal degree of freedom. Biased meshing with minimum seed size of 0.001 m was used near the weld region and kept increasing gradually in the transverse direction of weld joint for decreasing the computational time as shown in Fig. 2a. Heat transfer coefficients 100 W/m² at the bottom and 30 W/m² for rest of the surface are used for cooling the solution domain.

3 Materials and Methods

Table 1 shows the welding input process parameters and tool dimensions considered for comparative study between FSW and SSFSW [12, 13]. Figure 1 shows the thermo-physical properties of AA2024-T6 and AA7075-T6 plates considered for the current models [13, 14]. The solidus temperature of the AA7075-T6 and AA2024-T6 were considered as 749 K and 645 K, respectively, while density of the both the alloys assumed as 2800 kgm⁻³ [14]. The value of τ_{yp} for EN40 tool was calculated using $\tau_{yp} = (930.24 - 0.33 \times T_p)$ [15]. The thermocouple location considered for extracting thermal cycle was 11.0 mm at the transverse distance from the weld center line and 1.5 mm below the top surface of the plate [13].

4 Results and Discussion

Figure 2 shows the biased meshed model and computed isotherms for both the FSW and SSFSW under the welding condition for 3.0 mm thick AA2024-T4 plate. Both

Table 1 Welding input process parameters and tool dimensions considered for analysis

Material	Welding process	Dimensions of rotating tool (mm)				Welding conditions	
		D_{SH}	D_{PR}	D_{PT}	L_P	N (rpm)	U (mm/min)
AA2024-T6	FSW	10	4.5	3.5	2.7	800	50
	SSFSW						
AA7075-T6	FSW	18	6.2	4.0	5.8	1500	100, 400
	SSFSW						

where D_{SH} = Shoulder diameter, D_{PR} = diameter of tool probe at the root, D_{PT} = diameter of tool probe at the tip, L_P = length of the tool probe, N = tool rotational speed, and U = welding speed

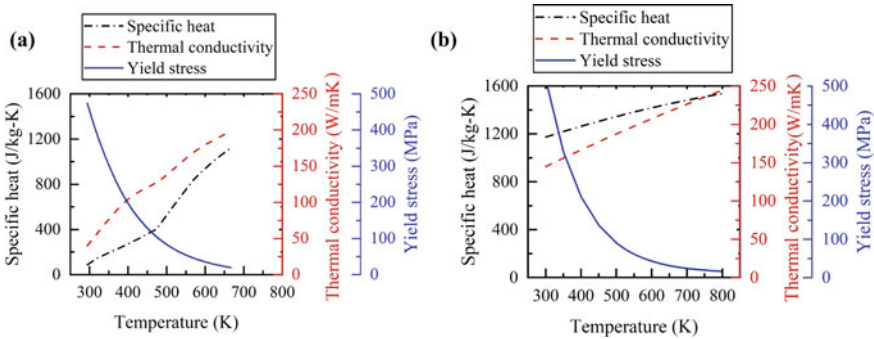


Fig. 1 Thermo-physical properties of **a** AA2024-T6, and **b** AA7075-T6

the processes were compared at the welding speed of 50 mm/min and tool rotational speed of 800 rpm. The isotherms corresponding to FSW exhibited higher temperatures as shown in Fig. 2a due to the heat generation by both tool shoulder and tool probe. At the same time, Fig. 2b depicts much lower peak temperatures under the same welding conditions due to the absence heat generation by tool shoulder, since it is stationary in SSFSW. As a result, high temperature zones appear to be narrower in SSFSW compared to FSW (Fig. 2).

Figure 3 depicts the computed thermal cycles and the same are validated with the independent experimental results [13]. The measured peak temperatures observed to be ~486 K and ~412 K, respectively, for the conventional FSW and SSFSW process. The numerically computed peak temperatures are 490 K and 410 K, for FSW and SSFSW, respectively. The computed results found to be in fair agreement with the corresponding measured results. The maximum error noted between the measured and computed results is much less than 1%. These FSW and SSFSW process models for AA2024-T6 are extended for AA7075-T6 material as well by simply replacing the thermal physical properties of AA2024-T6 with AA7075-T6. Here, AA7075-T6 workpiece material is considered for his high strength such that the tendency for the tool fracture is more in both FSW and SSFSW [9, 10].

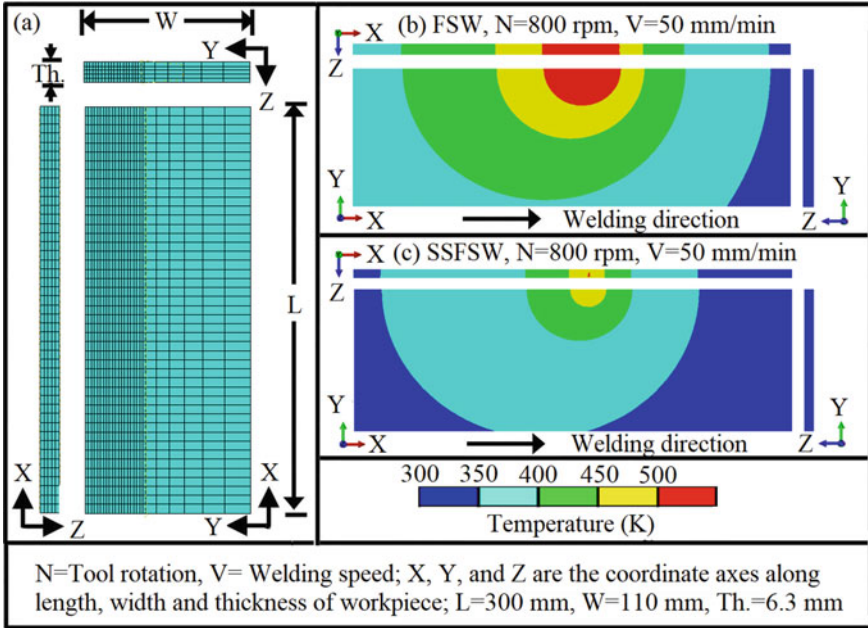


Fig. 2 a Biased meshed model and computed temperature field for b FSW, and c SSFSW at the welding speed of 50 mm/min and tool rotation of 800 rpm

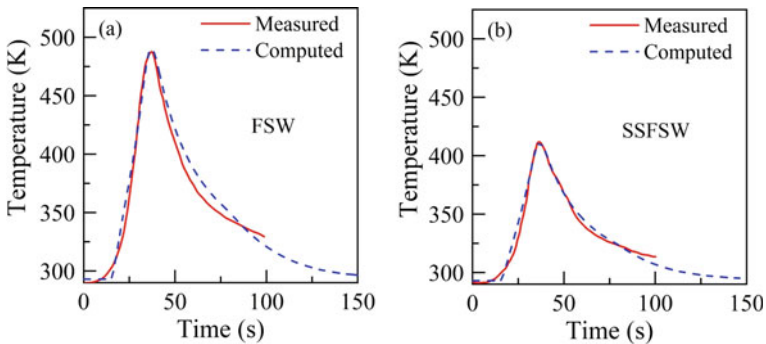


Fig. 3 Numerically computed and experimentally measured thermal cycles a FSW, and b SSFSW at the welding speed of 50 mm/min tool rotation of 800 rpm for 3.0 mm thick AA2024-T4 plate

The computed 3D temperature isotherms during FSW and SSFSW of 6.3 mm thick AA7075-T6 are used to estimate the spindle torque, traverse force and tool durability index following the methodology provided in section-2 for the process conditions shown in Table 1. The computed peak temperature calculated for SSFSW at the welding conditions of 1500 rpm rotational speed and 100 mm/min, 400 mm/min

welding speed are 684 K and 653 K, whereas for FSW the peak temperatures are calculated 749 K for both conditions.

The spindle torques were computed to be 8.44 N-m and 11.79 N-m in SSFSW for 6.3 mm AA7075-T6 plate, whereas in case of FSW found to be 26.63 N-m and 27.36 N-m for the identical welding conditions Table 2. The spindle torque observed lower in case of SSFSW as shoulder is stationary. At lower welding speed, the rate of heat generation is observed higher which further makes the material softer. Consequently, spindle torque decreases with decrease in welding speed.

The tool traverse forces were calculated 3.34 kN and 4.1 kN in SSFSW. On the other hand, tool traverse force was found in FSW to be 2.51 kN and 2.53 kN for the identical conditions Table 2. Traverse force was found to be higher in SSFSW and increasing with welding speed, as workpiece materials are relatively harder in SSFSW. The maximum probe forces obtained were 1.6 kN and 2.36 kN for SSFSW. However, the probe force found in FSW to be 0.81 kN and 0.83 kN for the same welding conditions Table 2. The maximum probe force was observed higher in SSFSW than FSW as probe resists relatively harder material as shown in Fig. 4.

Table 2 Numerically computed peak temperature, spindle torque, traverse force, maximum shear stress (τ_{max}), and tool durability index (I) in conventional FSW and SSFSW

Welding process	Welding speed (mm/min)	Peak temp (K)	Spindle torque (N-m)	Traverse force (kN)		τ_{max} (MPa)	I
				Tool	Probe		
FSW	100	749	26.63	2.51	0.81	195.75	2.01
SSFSW		684	8.44	3.34	1.6	407.62	0.99
FSW	400	749	27.36	2.53	0.83	196.76	2
SSFSW		653	11.79	4.1	2.36	583.66	0.71

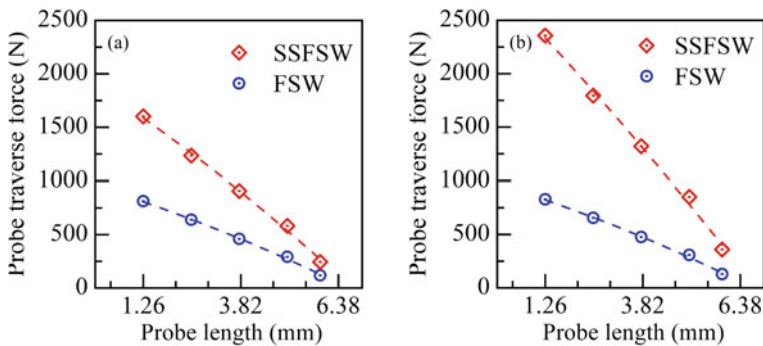


Fig. 4 Probe traverse force along the length in FSW and SSFSW at 1500 rpm rotational speed and welding speed (mm/min) of **a** 100, **b** 400

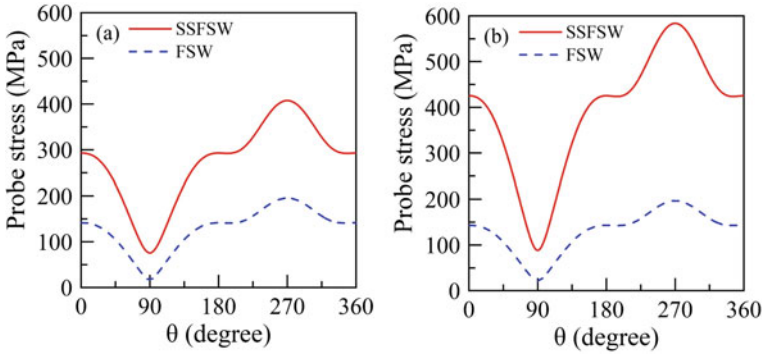


Fig. 5 Computed maximum shear stress (τ_{\max}) around the rotating tool probe in FSW and SSFSW at 1500 rpm rotational speed and welding speed of **a** 100 mm/min **b** 400 mm/min

The maximum shear stresses experienced by the tool probe in SSFSW were obtained 407.62 MPa and 583.66 MPa Table 2. The yield stress calculated corresponding to process peak temperatures in the vicinity of tool probe were 406.75 MPa and 412.67 MPa. The tool durability indexes were calculated using Eq. (12) and were found to be 0.99 and 0.71, respectively, Table 2. On the other hand, the maximum shear stress found to be 195.75 MPa and 196.76 MPa in FSW for the identical welding conditions Table 2. The yield stress calculated corresponding to process peak temperatures are 394.37 MPa for both conditions. The tool durability indexes found to be 2.01 and 2.0, respectively Table 2. The maximum shear stress experienced by the tool probe were calculated higher in case of SSFSW compared to FSW and found to be increasing with welding speed. Since, harder material possesses higher probe force as shown in Fig. 5 Hence, tool is less durable at higher welding speed Table 2.

5 Conclusion

Both SSFSW and FSW were compared in 6.3 mm thick AA7075-T6 plate for the same welding conditions based on spindle torque, traverse force, and maximum shear stress experienced by the tool. The spindle torque was observed to be ~57–68% lower in case of SSFSW. The computed traverse force reported ~33–62% higher in SSFSW unlike FSW. The maximum probe traverse force observed ~97–184% higher in SSFSW than FSW. The maximum shear stress experienced by the tool probe was reported ~99–197% higher in case of SSFSW compared to FSW process. Tool durability index found to be ~50–65% lower in SSFSW. It can be seen that tool is more susceptible to tool failure in SSFSW and is more vulnerable at higher welding speed for constant tool rotational speed.

References

1. Sinhmar S, Dwivedi DK (2020) Mechanical behaviour of FSW joint welded by a novel designed stationary shoulder tool. *J Mater Process Technol* 277:116482
2. Vicharapu B, Liu H, Fujii H, Narasaki K, Ma N, De A (2020) Probing residual stresses in stationary shoulder friction stir welding. *Int J Adv Manuf Technol* 106:1573–1586. <https://doi.org/10.1007/s00170-019-04570-9>
3. Ji S, Li Z, Zhou Z, Zhang L (2017) Microstructure and mechanical property differences between friction stir lap welded joints using rotating and stationary shoulders. *Int J Adv Manuf Technol* 90(9–12):3045–3053
4. Buffa G, Fratini L, Impero F, Masnata A, Scherillo F, Squillace A (2020) Surface and mechanical characterization of stationary shoulder friction stir welded lap joints: experimental and numerical approach. *Int J Mater Form* 1–12
5. Barbini A, Carstensen J, dos Santos JF (2018) Influence of a non-rotating shoulder on heat generation, microstructure and mechanical properties of dissimilar AA2024/AA7050 FSW joints. *J Mater Sci Technol* 34(1):119–127
6. DebRoy T, De A, Bhadeshia HKDH, Manvatkar VD, Arora A (2012) Tool durability maps for friction stir welding of an aluminium alloy. *Proc Royal Soc A Math Phys Eng Sci* 468(2147):3552–3570
7. Trimble D, Monaghan J, O'donnell GE (2012) Force generation during friction stir welding of AA2024-T3. *CIRP Ann* 61(1):9–12
8. Leitão C, Louro R, Rodrigues DM (2012) Using torque sensitivity analysis in accessing Friction Stir Welding/Processing conditions. *J Mater Process Technol* 212(10):2051–2057
9. Vicharapu B, Liu H, Fujii H, Ma N, De A (2019) Probing tool durability in stationary shoulder friction stir welding. In: *Friction stir welding and processing X*. Springer, Cham, pp 91–98
10. Buchibabu V, Reddy GM, De A (2017) Probing torque, traverse force and tool durability in friction stir welding of aluminum alloys. *J Mater Process Technol* 241:86–92
11. Arora A, Mehta M, De A, Debroy T (2012) Load bearing capacity of tool pin during friction stir welding. *Int J Adv Manuf Technol* 61(9):911–920
12. Wu H, Chen YC, Strong D, Prangnell P (2015) Stationary shoulder FSW for joining high strength aluminum alloys. *J Mater Process Technol* 221:187–196
13. He W, Li M, Song Q, Liu J, Hu W (2019) Efficacy of external stationary shoulder for controlling residual stress and distortion in friction stir welding. *Trans Indian Inst Met* 72(5):1349–1359
14. ASM Handbook (1992) Properties and selection, non-ferrous alloys and special purposes materials, vol 2
15. Woolman J, Mottram RA (1969) The mechanical and physical properties of the British standard En Steels (B.S. 970-1955) vol 3 (En 40 to En 363), 1st edn. Pergamon press, Oxford, pp 1–29

Wire Arc Additive Manufacturing of ATI 718PLUS[®]: A Process Modeling Approach



Mohammad Shabbar  and Buchibabu Vicharapu 

Abstract The wire arc additive manufacturing (WAAM) process is an emerging metal printing technique. The WAAM uses a typical arc welding power source for melting and deposition of metal wires as per the computer aided design model. The existing investigations highlight several critical issues in WAAM, which include deterioration of mechanical properties and excess distortion. These two problems can be addressed by a thorough understanding of the heat flow during the WAAM process. An attempt is made here for the development of a finite element-based 3D heat conduction process model for WAAM to analyze the heat transfer in the 3D domain. The effect of interlayer cooling time and substrate preheating temperature during the metal printing of ATI 718Plus[®], a derivative of Inconel 718, is studied as part of the current investigations. The computed thermal history from the model is in good agreement with the independently published experimental results. The thoroughly validated process model is extended further for the in-depth analysis of WAAM at different process conditions.

Keywords Additive manufacturing · Wire arc additive manufacturing · ATI 718Plus[®] · Numerical model · Thermal cycles · Metal printing

1 Introduction

The additive manufacturing (AM) technique is a promising technique for fabricating multi-layered, complex geometries covered in dense metal parts. In addition to its advantages over traditional manufacturing, additive manufacturing has great potential for a wide range of industrial applications. Several methods of metal additive manufacturing are currently available; in general, the powder bed fusion (PBF) process and directed energy deposition (DED) process are the most common. In the DED process, metal powder or wire is fed directly into a focal point of a laser, electron beam, or arc, resulting in a molten pool. A 3D-printing process such as

M. Shabbar · B. Vicharapu (✉)
Indian Institute of Technology, Palakkad, India
e-mail: buchibabu@iitpkd.ac.in

this can be scaled to produce extremely large components sooner than powder bed fusion, enabling fast build speeds. Wire and arc additive manufacturing (WAAM) is a DED technique that uses feed wire and arc welding sources equipped with a robotic arm to deposit a 3D geometry. The final part is formed completely from the deposited weld material. Compared to powder-based AM techniques, WAAM can build parts up to tens of meters tall, can fabricate fully dense and large-dimensional parts without high forming costs or inefficiencies. It has one of the highest deposition rates ($2\text{--}10 \text{ kg}\cdot\text{h}^{-1}$) [1].

Ogino et al. [2] developed a numerical model and studied the influence of interpass temperature and welding direction on deposition shape during the WAAM process. Ding et al. [3] developed a steady-state thermal model to predict the thermal fields during the WAAM process. Numerous works of researchers in numerical modeling establish it as a very efficient tool for analysis. In this paper, a 3D heat transfer finite element model of a multi-layer wall is developed. A study of the temperature distribution at the deposited layers and the effects of interlayer cooling and substrate preheating temperature is performed.

2 Modeling of WAAM Process

A finite element (FE) analysis method facilitated by ABAQUS© software was used to model the thermal behavior of a multi-layered thin-walled structure deposited by the WAAM process. A 3D heat conduction process model is developed without considering the heat transfer due to material flow. The temperature distribution resulting due to cyclic heating and cooling during the WAAM process has been predicted by this method. The heat transfer model solved the transient equation of conservation of energy in three dimensions to obtain the temperature distribution. The solution domain for this calculation includes a substrate, deposit, and heat transfer due to convection and radiation to the surrounding.

2.1 Heat Source Model

Most finite element analyses employ transient conduction models with a moving heat source. This heat source for the model is given with the DFLUX user subroutine. The Goldak double ellipsoidal model [4] was used to apply the heat to deposit material. This heat source model specifies a heat generation per unit volume in a moving frame of reference. This model gives Gaussian distribution and has good control of power density distribution in the weld pool. Power density for this model is determined separately for the region in front and behind the arc center using:

Table 1 Parameters used in Goldak model

a_f	a_r	b	c	f_f	f_r
3 mm	12 mm	3 mm	1.6 mm	1.4	0.6

Table 2 Process parameter values

Current	Voltage	Efficiency	Scanning speed
100 A	15 V	0.5	1.666 mm/s

$$Q_f = \frac{6\sqrt{3}Qf_f}{\pi\sqrt{\pi.a_f.b.c}} \exp\left[-3\left(\frac{x^2}{a_f^2} + \frac{y^2}{b^2} + \frac{z^2}{c^2}\right)\right] \quad (1)$$

$$Q_r = \frac{6\sqrt{3}Qf_r}{\pi\sqrt{\pi.a_r.b.c}} \exp\left[-3\left(\frac{x^2}{a_r^2} + \frac{y^2}{b^2} + \frac{z^2}{c^2}\right)\right] \quad (2)$$

$$f_f + f_r = 2 \quad (3)$$

$$Q = \eta VI \quad (4)$$

where a_f and a_r are the length of the front and the rear ellipsoid, respectively; b is the width and c is the depth of the heat source; f_f and f_r are the front and rear heat fraction coefficient, respectively, Q is the energy input considering the factor of efficiency (η), V is the voltage supplied, and I is the current. Table 1 gives the parameters used in the heat source model, and Table 2 gives the values of various process parameters.

2.2 Thermal Modelling

Modeling the deposition process was done as a multi-step transient heat transfer analysis, where every single step was further subdivided into smaller time increments. To model, the continuous deposition of material, a discrete set of elements was incrementally added at the starting of each time step in such a way that the arc travels a distance that is equal to a new set of activated elements. Transient thermal analysis within ABAQUS/CAE was applied to calculate the temperature history at each desired point of the deposited material.

Considering the melt generation and re-solidification caused by phase change in this analysis, specific material properties such as density, thermal conductivity, specific heat, latent heat for different temperature ranges. As adopted from Ref. [5], numerical values for thermal conductivity and specific heat are shown in Fig. 1. The latent heat was taken as 272 kJ/kg, between solidus temperature 1533 K and liquidus temperature of 1615 K.

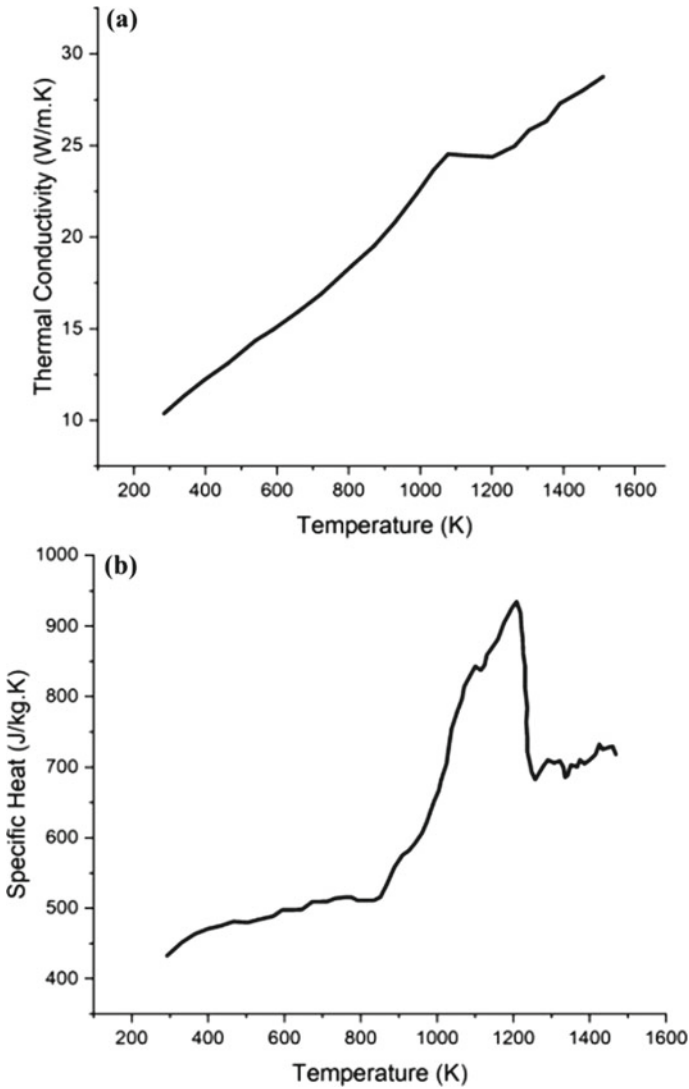


Fig. 1 Temperature-dependent properties of ATI 718Plus[®] **a** Thermal conductivity **b** Specific heat

To simulate material addition, the element birth and death technique in ABAQUS/CAE was used. Initially, all elements within the deposited path were deactivated. The time needed for the arc to travel along the deposited path of each layer was divided into multiple small-time steps. Elements set were activated at each time step. In subsequent steps, the model would use the previous results of the step as the initial condition for the new active element sets. The thermal model considers the heat flux losses by convection and radiation; thus, for the thermal analysis, a

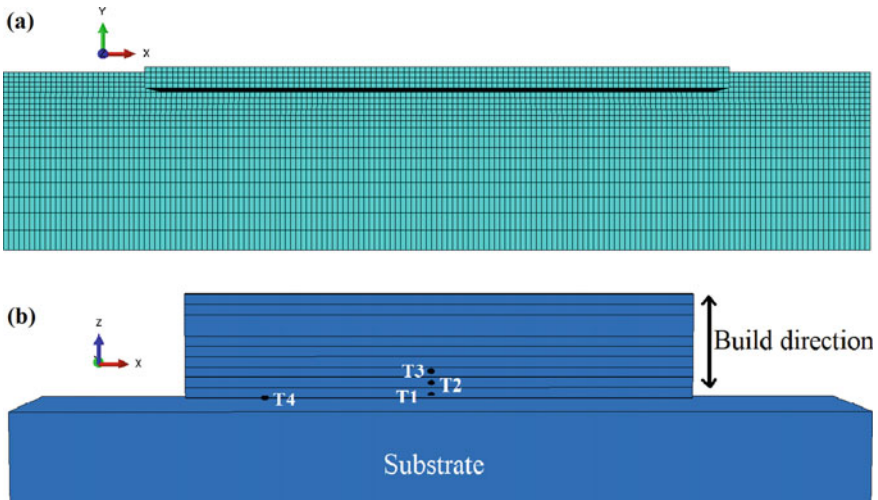


Fig. 2 a Meshing of the geometry (top view), b locations of temperature measurement

convective heat transfer coefficient of $10 \text{ W/m}^2\text{K}$, the Stefan-Boltzmann constant of $5.67 \times 10^{-8} \text{ Wm}^{-2} \text{ K}^{-4}$ and the radiative emissivity of 0.3 were applied to the exterior sides of the substrate and layers.

In this WAAM model, a symmetry plane (XZ -plane) was used to reduce computational time without compromising the physics of the process. The considered model has a substrate plate of dimensions ($110 \text{ mm} * 45 \text{ mm} * 12.5 \text{ mm}$), and a wall of dimensions ($70 \text{ mm} * 6 \text{ mm} * 6 \text{ mm}$) deposited over it. The deposit consists of ten layers. Mesh of the geometry, as shown in, Fig. 2a, representing a discretized form of the model, is made of DC3D8 element, which is an 8-node linear heat transfer brick. Severe temperature gradients are observed in the wall region where fusion occurs. So this region was given finer mesh and areas farther from the wall with a rather coarse mesh. Also, the locations at which the computed temperatures are extracted are shown in Fig. 2b. It shows the measurement of temperature at the center along the length of the deposit. Specific locations are chosen to analyze the peak temperatures at each layer separately.

3 Results and Discussions

Figure 3 shows the computed temperature distribution in a three-dimensional domain. The temperature ranges are represented by color bands in the figure legend. The region represented by the red color shows the fully melted portion of the weld called the fusion zone, as this region has a temperature above the liquidus temperature ($\sim 1615 \text{ K}$) of the material, whereas the yellow region, which has a temperature

below liquidus and higher than solidus temperature (~ 1533 K), represents the mushy zone.

Figure 4 shows the computed thermal cycle at a point T1 (at the center of the first layer) for the subsequent layers. As indicated at the center of the first layer, when the heat source approached, a sharp increase in temperature is seen. And, the cooling curve is observed as the heat source moved away. The thermal cycle curve has two peaks surpassing the melting point (~ 1533 K), indicating decent conditions for metallurgical bonding between two layers.

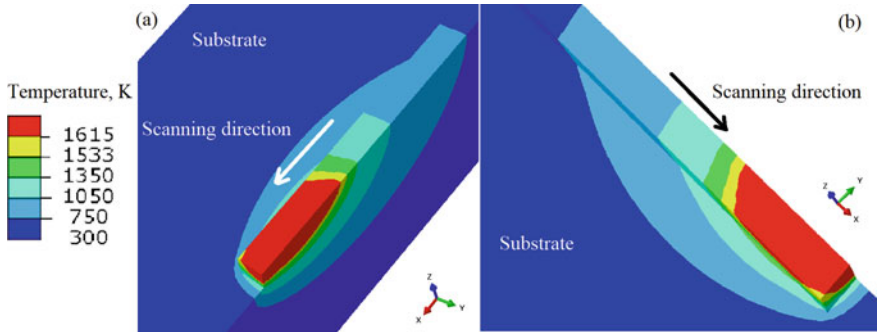


Fig. 3 Temperature distribution during WAAM in two isometric views (a) and (b), calculated using the thermal model

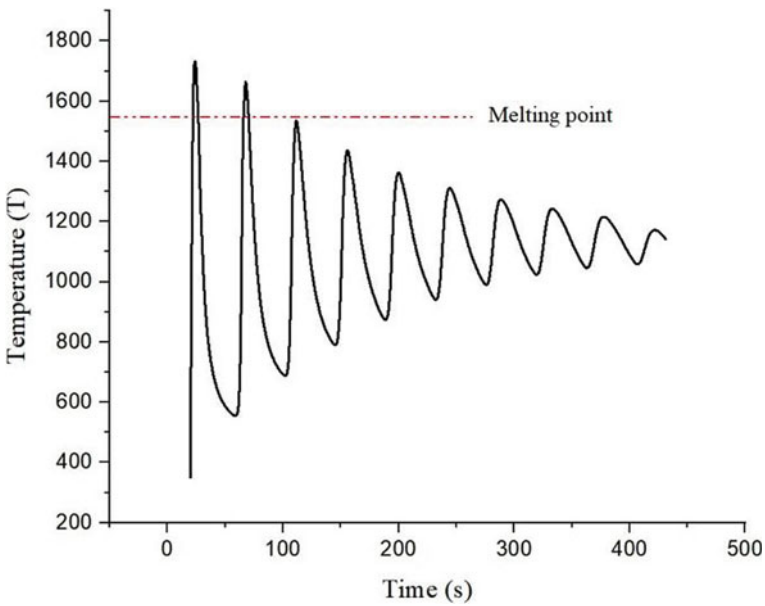


Fig. 4 Thermal cycle with no interlayer cooling time measured at T1

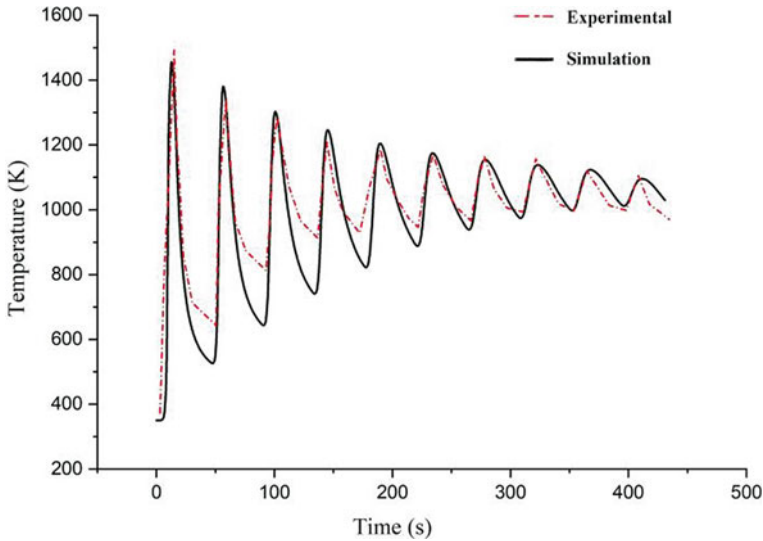


Fig. 5 Comparison of experimental versus simulation results measured at T4

The model was applied to simulate the experimental work on WAAM of ATI 718Plus® carried out by Asala et al. [6]. The experimental temperature measurement was done by the thermocouple at the bottom of the deposit protected by a Tantalum foil to prevent the thermocouple from the arc. The comparison between the computed and the experimental results are shown in Fig. 5. There is a good agreement between the computed and the experimental results. The graph shows a lower interpass temperature for the computed result. The reason for this could be not considering the fluid flow for the modeling.

There is an increase in peak temperature of subsequent layers as the deposition takes place, as shown in Fig. 6. The preheating of the previously deposited layer results in a significant rise in the peak temperature of the new layer in comparison to the previously deposited layer. This temperature rise can be attributed to the fact that, with the deposit height increasing, heat accumulates in the already deposited layer. Accumulation of heat is due to an increase in the deposit volume, while the contact area for conduction of heat from the deposit to the substrate remains roughly the same.

The effect of interlayer delay/cooling time on the temperature distribution during the WAAM process can be seen in Fig. 7. Shorter interlayer cooling time results in higher interpass temperatures of previously deposited layers and the substrate. For 1 s of interlayer cooling time, a very large portion of the deposit, as well as substrate, is at a higher temperature as compared to the interlayer cooling time of 120 s. The provision of appropriate interlayer cooling time can help to control the interpass temperature between consecutive layer deposition.

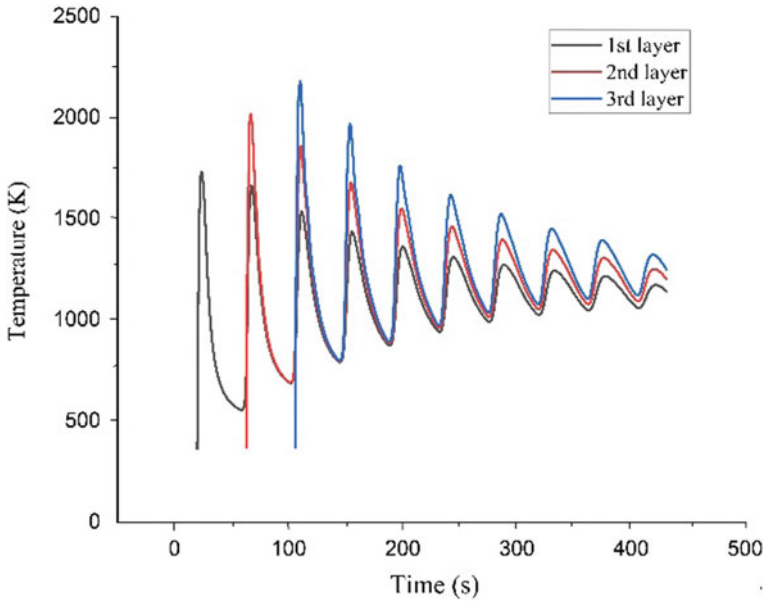


Fig. 6 Computed thermal cycles at T1, T2, and T3

Deposition of material on a substrate at room temperature results in a large temperature gradient, causing serious thermal stresses, cracking, and fracture of fabricated parts in some cases. This makes preheating of the substrate a very good option to minimize residual stresses. Debroy et al. [5] stated that the substrate preheat temperature can reduce the final residual stresses post-fabrication and the stresses during building. So, the effect of substrate preheating on the cooling rate as well as the thermal cycles was obtained and compared. Figure 8 shows the thermal cycles for deposition without substrate preheating and with substrate preheating. A higher peak temperature at each layer with substrate preheat temperature was observed, but a significant reduction of cooling rate was seen with preheating of the substrate. For the first layer, the average cooling rate without substrate preheating obtained was 33.49 K/s, whereas with preheating, the cooling rate was 30.24 K/s.

4 Conclusion

A thermal model was developed and compared with the independent experimental results from the published literature. A layer-by-layer heat transfer analysis was performed to understand the temperature evolution. The following are the findings of this work:

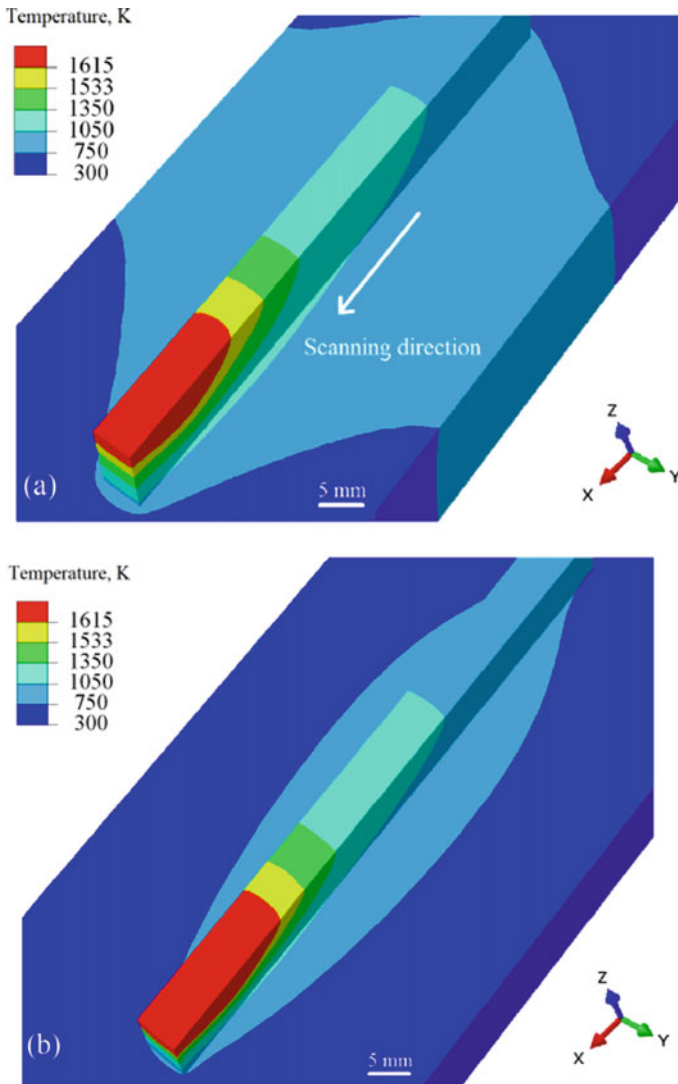


Fig. 7 Comparison of temperature distribution for interlayer cooling time (s) of **a** 1 and **b** 120

1. With an increase in build height, the interpass temperature was found to be higher. This is attributed to the accumulation of heat during material deposition.
2. Interlayer cooling also referred to as idle time between the deposition of the subsequent layer results in lower interpass temperatures. This would eventually enhance the dimensional accuracy of the metal prints.
3. The increase in substrate preheat temperature resulted in low cooling rates, which would lead to lower residual stresses.

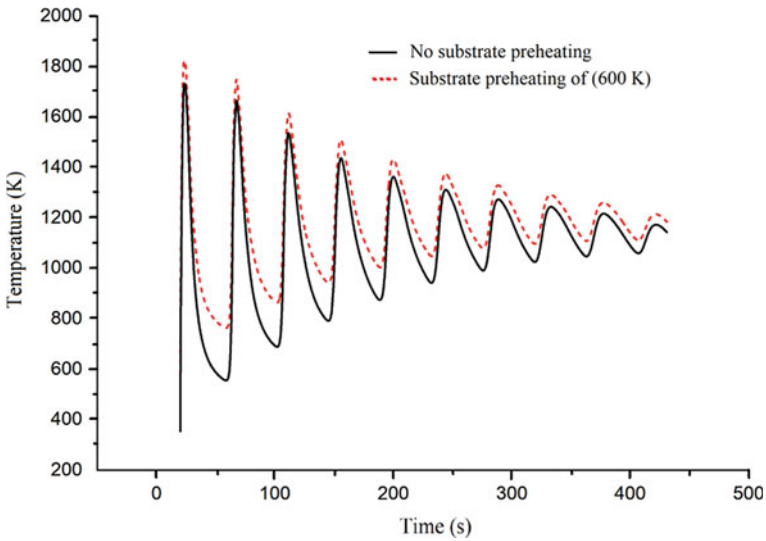


Fig. 8 Comparison between preheating the substrate (600 K) and no preheating

References

1. Ding D (2015) Wire-feed additive manufacturing of metal components: technologies developments and future interests. *Int J Adv Manuf Technol* 81(1):465–481
2. Ogino Y (2018) Numerical simulation of WAAM process by a GMAW weld pool model. *Weld World* 62(2):393–401
3. Ding J (2014) A computationally efficient finite element model of wire and arc additive manufacture. *Int J Adv Manuf Technol* 70(1–4):227–236
4. Goldak J (1984) A new finite element model for welding heat sources. *Metall Trans B* 15(2):299–305
5. ATI, https://www.atimetals.com/Products/Documents/datasheets/nickel-cobalt/nickel-based/ati_718plus_tds_en_v3.pdf. Last accessed 9 Aug 2021
6. Asala G (2017) Microstructural analyses of ATI 718Plus® produced by wire-ARC additive manufacturing process. *Metall Mater Trans A* 48(9):4211–4228
7. DebRoy T (2018) Additive manufacturing of metallic components—process, structure and properties. *Prog Mater Sci* 92:112–224

A Review on Computational Techniques for Nanostructured Polymer Composite Materials



G. R. Raghav , Gibin George , R. Sujith, and Nikhil Ashok

Abstract This paper summarizes recent advancements in computational analysis of nanoparticle/nanofibers reinforced polymer matrix composites. The reinforcements vary from particle to fibers of varying shapes and sizes. In this review, various computational techniques such as computational micromechanics, integrated computational materials engineering (ICME) framework, and algorithms are discussed in detail. The multiscale modeling of polymer composites which includes mesoscale, microscale, nanoscale, and electronic scale modeling techniques can be carried out using various software packages available in the market. This review aims to explore the various research activities in polymer matrix composites using computational techniques for studying the microstructures and other mechanical behaviors which enables the readers for further exploration in this field.

Keywords Computational techniques · Polymers · Micromechanics · FEM

1 Introduction

In recent years, the utilization of polymer-based composites has increased drastically in the field of coatings, electronic devices, automobile, construction, and aerospace applications. Even though polymer-based composite materials have been widely preferred it has its disadvantages. The polymer matrix composites exhibit very poor toughness and thermal properties. Hence, many researchers are working to discover better mechanical properties from polymer matrix composites. In this process, many methods have been employed by the researchers such as trying new reinforcements such as nanoparticles, nanofibers, and nano cellulose. The addition of reinforcements has resulted in improving the properties such as micro-hardness, toughness, tensile strength, and thermal resistant properties. Even though the experimental studies are important and more works are there in exploring the properties of polymer-based composites, it is difficult to predict the mechanical properties through experimental

G. R. Raghav (✉) · G. George · R. Sujith · N. Ashok
SCMS School of Engineering and Technology, Ernakulam, India
e-mail: raghavmechklnce@gmail.com

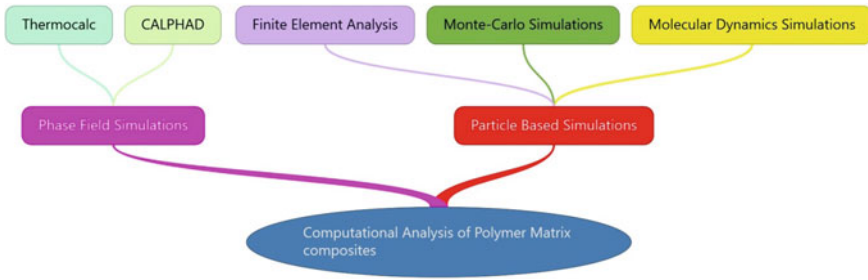


Fig. 1 Classification of different types of computational techniques

methods. Hence, the need for computational analysis of the composite materials in predicting the mechanical properties also increasing. So, the computational analysis was utilized by many researchers to forecast the important properties of the polymer-based composites. There are diverse types of computational techniques available such as micromechanics of composite materials, integrated computational materials engineering (ICME), and various algorithms as shown in Fig. 1.

2 Computational Analysis of Polymer Matrix Composites

Ever growing demand to amplify the different properties of polymer-based composites has made the researchers implement new computational techniques to predict and improve the mechanical properties of the polymer based composite materials. There are different types of simulation techniques such as particle-based simulations which include Monte Carlo simulations (MCS), molecular dynamics simulation, brownian dynamics (BD), dissipative particle dynamics (DPD), and field theory-based simulations such as CALPHAD and Thermocalc. These simulation techniques are considered widely to probe the structural, mechanical and thermal properties of polymer composite materials [1–3]. There are many particle-based simulation techniques which were considered by different researchers to develop models of polymer matrix composites. The above methods are so powerful in predicting the mechanical properties of polymer-based composites but these methods proved to be more expensive when simulating large scale models. The above said methods, in the recent past, have established themselves to be beneficial in gaining molecular insights and forecasting the different properties of polymeric systems. Conversely, the above methods are very expensive and sometimes difficult to simulate larger models [4–6]. The field theory-based methods are mostly analytical calculations from which we can predict mechanical properties for large scale models with ease compared to particle-based techniques [7, 8]. While predicting using computational methods it is necessary to assume the basic behavior of the materials. When the models are developed following assumptions are made. Both the reinforcement (particles/fibers) and the matrix will have linear elastic properties. There will be perfect bonding between the matrix and

the reinforcements. The reinforcements such as nanoparticles or fibers will have identical shapes and sizes [3]. Even though the following assumptions are made, most of the micromechanics simulations fail to calculate all the important properties of the polymer matrix composites [9]. Odegard et al. predicted the variation in mechanical properties of polymer matrix composites considering the size and volume of the reinforcements. To predict the mechanical properties, we require developing analytical or semi analytical computational or statistical methods to apply the micromechanical models for simulation of polymer matrix composites [10].

2.1 Types of Particle-Based Simulation Methods

2.1.1 Molecular Dynamics Simulations (MDS)

This is the method that is widely used to predict the properties of polymers and molecules [11, 12]. The interactions generally can be divided as non-bonded and bonded interactions as shown in Eq. (1). The harmonic potential represents the bonded interactions, which are premeditated by the summing up of different angles which includes dihedral angles, bond angles, and inappropriate angles as shown in Eq. (2). The electrostatic and Van der Waals forces represent the non-bonded interactions as shown in Eq. (3). It can be noted that in Eq. (2) [13]. Tang et al. have studied the relationship between the structure and properties of carbon fiber reinforced composites, which were fabricated using selective laser sintering. They developed a new framework to study the properties of carbon fiber reinforced composites (CFRP) using the representative volume element (RVE) model. Based on the voxel algorithm. The results revealed that the volume fraction of fiber can reach up to 38% when the diameter to length ratio is maintained as 15. The increase in the volume of fiber and direction of alignment together with the direction of loading can increase the stability of CFRP [14]. Sun et al. have explored the microscopic breakdown means of fiber reinforced polymer composites which have a unidirectional orientation. The molecular dynamic simulations are utilized to explore the interphase region of matrix and fiber. The outcome of this work exhibited the following properties: The composites have much improved young's modulus and flexural strength in comparison with the pure matrix. This combination of experimental and computational approaches was utilized to model and authenticate the various measurable values at the interface. The fallouts provided great insights about failure mechanisms and confirm that the CFRP composites have multiple failure mechanisms and are complex in nature based on the condition of loading [3, 15, 16].

$$U = U_{\text{Bonded}} + U_{\text{Nonbonded}} \quad (1)$$

$$U_{\text{Bonded}} = \sum_{\text{Bonds}} K_b (b - b_0) + \sum_{\text{Bonds}} K_\theta (\theta - \theta_0)^2$$

$$+ \sum_{\text{Dihedrals}} \frac{K\varphi}{2} (1 + \text{Cos}(n\varphi - \varphi_0)) + \sum_{\text{Impropers}} (K\vartheta - \vartheta_0)^2 \quad (2)$$

$$U_{\text{Nonbonded}} = \sum_{i=1}^{n-1} \sum_{j>i}^n \frac{q_i q_j}{4\pi r_{ij}} + \sum_{i=1}^{n-1} \sum_{j>1}^n 4 \in \left[\left(\frac{\sigma}{r_{ij}} \right)^{12} - \left(\frac{\sigma}{r_{ij}} \right)^6 \right] \quad (3)$$

2.1.2 Monte Carlo Simulations (MCS)

The random numbers are used to forecast the properties of polymeric materials using MCS, which is a stochastic approach [3, 17, 18]. In the MCS the forces are neglected, whereas the forces are considered in MDS. The statistical physics of materials can be analyzed using MCS which is not possible by MDS.

2.1.3 Finite Element Analysis (FEA)

The FEA is one of the numerical simulation methods and an adaptable tool for modeling a variety of problems. The FEA is a process in which we obtain solutions if there are initial and final boundary values. The entire model or domain is splitted or discretized into smaller subdomains as shown in Fig. 2. The nodes interconnect the subdomains. The limitation of FEA is that developing the maximum number of elements but has the advantage of solving more complex solutions. The FEA analysis can be used to solve more mechanical properties such as stiffness, elastic modulus properties of polymer matrix composites [19–22]. Mishnaevsky et al. has explored the effect of nanocellulose in polymer matrix composites and their relationship to structure and properties were studied. The FESEM image of snake-like nanocellulose fibrils is shown in Fig. 3. Figure 4 represents a snake-shaped nanocellulose fibrils 3D unit cell which was developed using Finite element analysis. The three-dimensional computational simulations of failure mechanisms were characterized by considering nanocellulose morphology. The results revealed that the nanocellulose fibrils have increased the stiffness of the composite materials and also reduces the brittleness of the polymer-based composites [23, 24]. Kempesis et al. investigated the Ultra-High-Molecular-Weight-Polyethylene (UHMEPE) composites through RVE [14]. The numerical models were developed using FEA code based on the fibrillar nature of the UHMEPE composites. The LS-DYNA software was utilized to develop and implement 3D models of fibrils. The 3D models were subjected to tensile, shear and compressive loads. This model has achieved to record exactly the mechanisms of experiments [16, 25, 26] (Fig. 5).

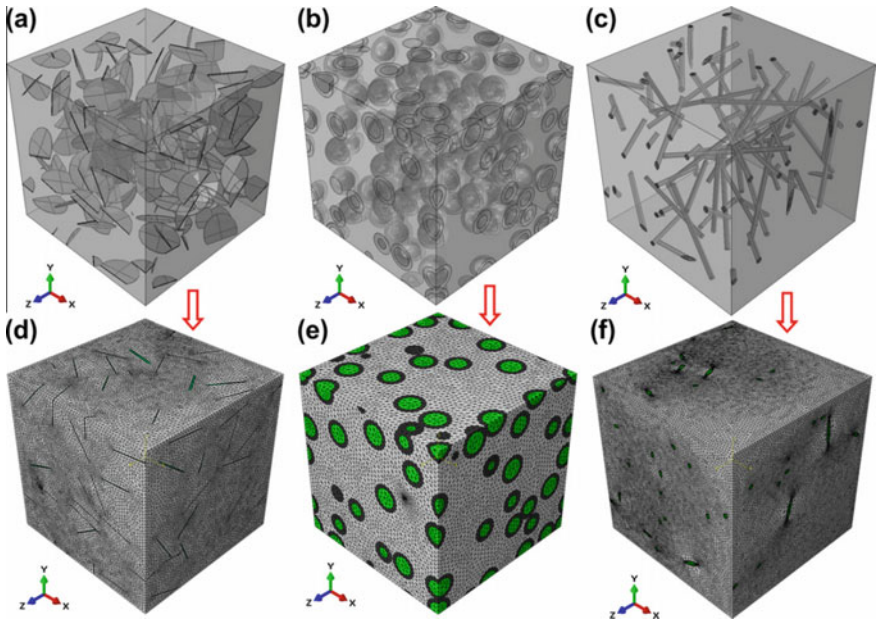


Fig. 2 Finite element 3D cubic models (RVE) of various geometries (adapted with permission from [21])

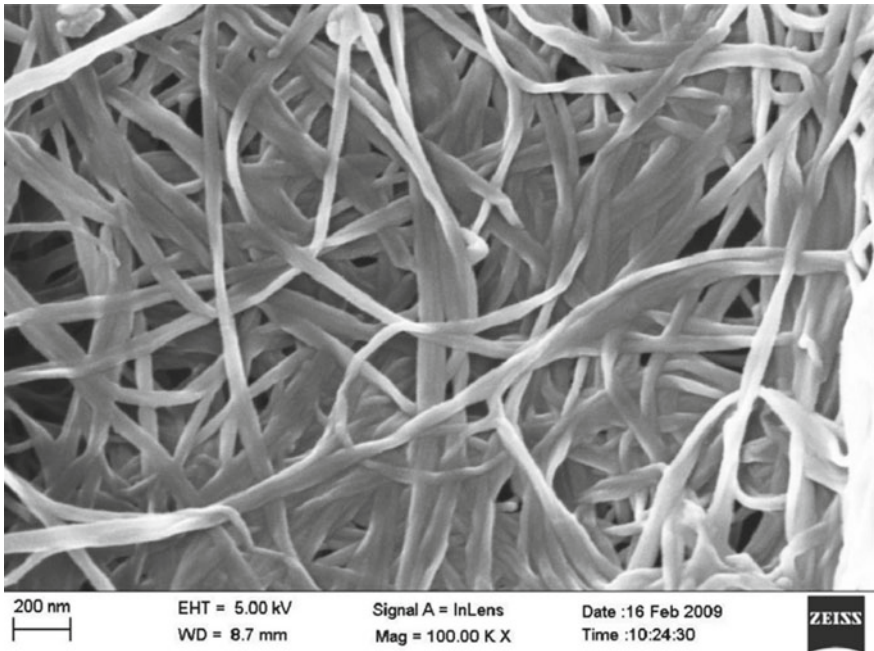


Fig. 3 The FESEM image of snake-like nanocellulose fibrils (adapted with permission from [23])

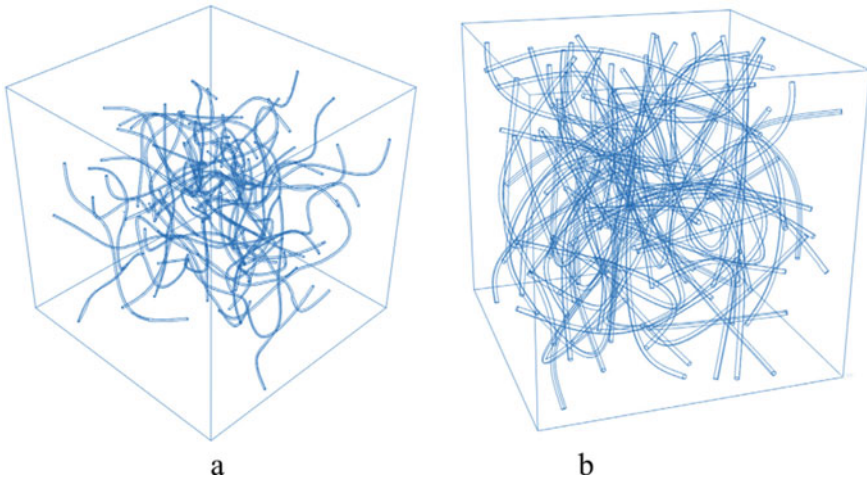


Fig. 4 Different types of 3D unit cells with nanocellulose fibrils **a** windows type **b** periodic type (adapted with permission from [23])

2.1.4 Phase Field Modeling

The phase field modeling is a model which can be used to solve interfacial solutions such as solidification dynamics, micromechanics and vesicle dynamics. Raj et al. reported crack propagation mechanisms of bio composites by employing phase field modeling. They concentrated on exploring crack propagation in spread out composites employing a mixed mode environment employing a phase field theory. The results show that the cracks can propagate in a straight manner or shall deflect or kink and travel along with organic-mineral interphases depending upon the elastic modulus mismatch and also due to mismatch of other mechanical parameters. It is also observed that the mixed mode environment has influenced the trajectory of crack propagation by shifting the strain energy density. This model has achieved good prediction on crack propagation in composites [27].

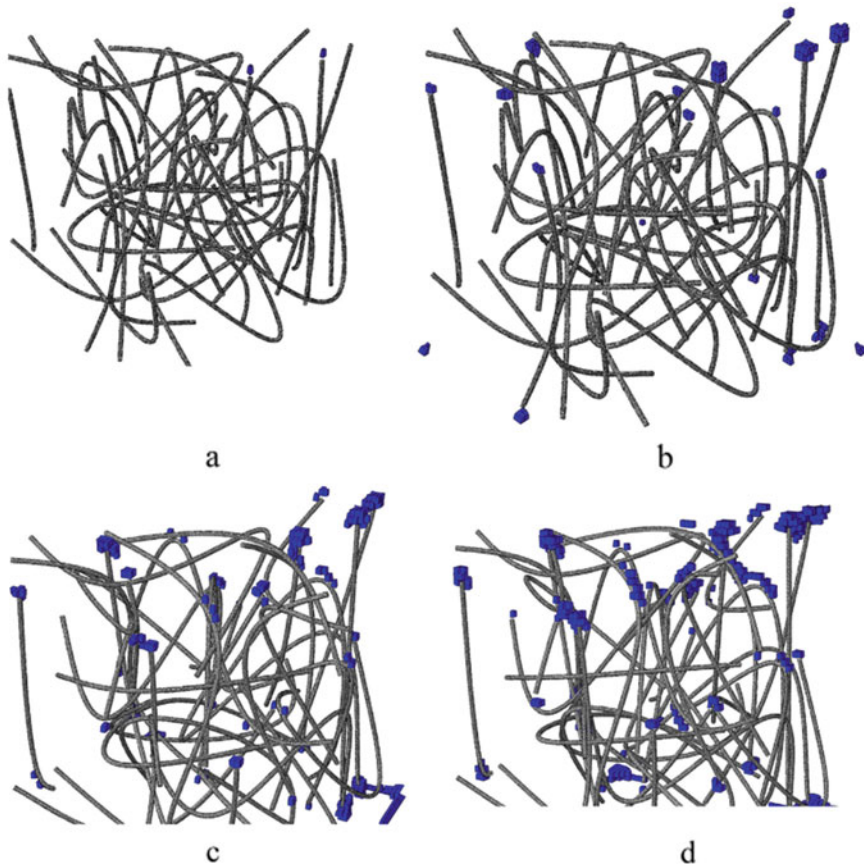


Fig. 5 Simulation results of FEA analysis which exhibits damage mechanisms (reproduced with permission from [23])

3 Conclusion

Currently, the application of polymer-based composites has increased in almost every field owing to their eco-friendly nature. Polymer-based composites can be produced at a low cost which has influenced the researchers to undergo research to improve the mechanical and thermal properties of polymer-based composites. Therefore, this review brings out the different studies carried out in the field of computational analysis of polymer matrix composites. Albeit many studies carried out in the field of computational analysis of polymer-based composites and also produced some useful results that are difficult to realize from existing experimental methods. There is another disadvantage in computational methods is the cost of producing complicated models hence the researchers opt for quite simple models which reduces the

efficiency of the predictions. On the other hand, incredible improvements in computational analysis techniques by utilization of sophisticated algorithms and precise models have made the researchers simulate the models more realistically with more accuracy. The purpose of this paper is to help researchers in understanding recent research trends in computational analysis of polymer-based composites.

References

1. Chen Y, Zhang X, Jiang Y (2020) The influence of side-chain conformations on the phase behavior of bottlebrush block polymers. *Soft Matter* 16:8047–8056. <https://doi.org/10.1039/D0SM00918K>
2. Sunday DF, Chang AB, Liman CD, Gann E, Delongchamp DM, Thomsen L, Matsen MW, Grubbs RH, Soles CL (2018) Self-assembly of ABC bottlebrush triblock terpolymers with evidence for looped backbone conformations. *Macromolecules* 51. <https://doi.org/10.1021/acs.macromol.8b01370>
3. Zeng QH, Yu AB, Lu GQ (2008) Multiscale modeling and simulation of polymer nanocomposites. *Prog Polym Sci* 33:191–269. <https://doi.org/10.1016/j.progpolymsci.2007.09.002>
4. Wells BA, Chaffee AL (2015) Ewald summation for molecular simulations. *J Chem Theory Comput* 11:3684–3695. <https://doi.org/10.1021/acs.jctc.5b00093>
5. Aguado A, Madden PA (2003) Ewald summation of electrostatic multipole interactions up to the quadrupolar level. *J Chem Phys* 119:7471–7483. <https://doi.org/10.1063/1.1605941>
6. Osyuchenko ON, Astrakharchik GE, Boronat J (2012) Ewald method for polytropic potentials in arbitrary dimensionality. *Null* 110:227–247. <https://doi.org/10.1080/00268976.2011.640291>
7. Spencer RKW, Matsen MW (2018) Field-theoretic simulations of bottlebrush copolymers. *J Chem Phys* 149:18490. <https://doi.org/10.1063/1.5051744>
8. Fredrickson G (2005) *The equilibrium theory of inhomogeneous polymers*. Oxford University Press, Oxford. <https://doi.org/10.1093/acprof:oso/9780198567295.001.0001>
9. Cannillo V, Bondioli F, Lusvarghi L, Montorsi M, Avella M, Errico ME, Malinconico M (2006) Modeling of ceramic particles filled polymer–matrix nanocomposites. *Compos Sci Technol* 66:1030–1037. <https://doi.org/10.1016/j.compscitech.2005.07.030>
10. Odegard GM, Clancy TC, Gates TS (2005) Modeling of the mechanical properties of nanoparticle/polymer composites. *Polymer* 46:553–562. <https://doi.org/10.1016/j.polymer.2004.11.022>
11. Karplus M, McCammon JA (2002) Molecular dynamics simulations of biomolecules. *Nat Struct Biol* 9:646–652. <https://doi.org/10.1038/nsb0902-646>
12. Procacci P, Darden T, Marchi M (1996) A very fast molecular dynamics method to simulate biomolecular systems with realistic electrostatic interactions. *J Phys Chem* 100:10464–10468. <https://doi.org/10.1021/jp960295w>
13. Rissanou AN, Harmandaris V (2013) Structure and dynamics of poly (methyl methacrylate)/graphene systems through atomistic molecular dynamics simulations. *J Nanopart Res* 15:1589. <https://doi.org/10.1007/s11051-013-1589-2>
14. Tang H, Chen H, Sun Q, Chen Z, Yan W (2021) Experimental and computational analysis of structure-property relationship in carbon fiber reinforced polymer composites fabricated by selective laser sintering. *Compos B Eng* 204:108499. <https://doi.org/10.1016/j.compositesb.2020.108499>
15. Sun Q, Meng Z, Zhou G, Lin S-P, Kang H, Keten S, Guo H, Su X (2018) Multi-scale computational analysis of unidirectional carbon fiber reinforced polymer composites under various loading conditions. *Compos Struct* 196:30–43. <https://doi.org/10.1016/j.compstruct.2018.05.025>

16. Fermiglia M, Mio A, Aulic S, Marson D, Laurini E, Pricl S (2020) Multiscale molecular modelling for the design of nanostructured polymer systems: industrial applications. *Mol Syst Des Eng* 5:1447–1476. <https://doi.org/10.1039/D0ME00109K>
17. Zhang Q, Lin J, Wang L, Xu Z (2017) Theoretical modeling and simulations of self-assembly of copolymers in solution. *Prog Polym Sci* 75:1–30. <https://doi.org/10.1016/j.progpolymsci.2017.04.003>
18. Sose AT, Cornell HD, Gibbons BJ, Burris AA, Morris AJ, Deshmukh SA (2021) Modelling drug adsorption in metal–organic frameworks: the role of solvent. *RSC Adv* 11:17064–17071. <https://doi.org/10.1039/D1RA01746B>
19. Chozhan CK, Alagar M, Sharmila RJ, Gnanasundaram P (2007) Thermomechanical behaviour of unsaturated polyester toughened epoxy–clay hybrid nanocomposites. *J Polym Res* 14:319–328. <https://doi.org/10.1007/s10965-007-9114-x>
20. Wang HW, Zhou HW, Peng RD, Mishnaevsky L (2011) Nanoreinforced polymer composites: 3D FEM modeling with effective interface concept. *Compos Sci Technol* 71:980–988. <https://doi.org/10.1016/j.compscitech.2011.03.003>
21. Mortazavi B, Bardon J, Ahzi S (2013) Interphase effect on the elastic and thermal conductivity response of polymer nanocomposite materials: 3D finite element study. *Comput Mater Sci* 69:100–106. <https://doi.org/10.1016/j.commatsci.2012.11.035>
22. Grandidier J-C, Channakeshava AB, Mazziotta R (2021) A non-local model to analyse 2D and 3D micro buckling of long carbon fiber epoxy material. *Compos Struct* 277:114531. <https://doi.org/10.1016/j.compstruct.2021.114531>
23. Mishnaevsky L, Mikkelsen LP, Gaduan AN, Lee K-Y, Madsen B (2019) Nanocellulose reinforced polymer composites: computational analysis of structure–mechanical properties relationships. *Compos Struct* 224:111024. <https://doi.org/10.1016/j.compstruct.2019.111024>
24. Wang X, Zhang J, Wang Z, Liang W, Zhou L (2013) Finite element simulation of the failure process of single fiber composites considering interface properties. *Compos B Eng* 45:573–580. <https://doi.org/10.1016/j.compositesb.2012.07.051>
25. Kempesis D, Iannucci L, Rosso SD, Curtis PT, Pope D, Duke PW (2021) A representative volume element model for ultra-high-molecular-weight-polyethylene composites. *Compos Struct* 262:113609. <https://doi.org/10.1016/j.compstruct.2021.113609>
26. Li Z, Liu Z, Lei Z, Zhu P (2021) An innovative computational framework for the analysis of complex mechanical behaviors of short fiber reinforced polymer composites. *Compos Struct* 277:114594. <https://doi.org/10.1016/j.compstruct.2021.114594>
27. Raj K, Murali P (2020) Mixed mode crack propagation in staggered biocomposites using phase field modelling. *J Mech Behav Biomed Mater* 101:103421. <https://doi.org/10.1016/j.jmbbm.2019.103421>

Design and Computational Analysis of DeusCell—A Piston Actuated Modular Reconfigurable Robot



Aaditya Radhakrishnan, Abel P. Johnson, Nikhil Roy, Ruben Geo Ribu, and B. Deepak

Abstract Modular Reconfigurable Robotics deals with the design and building of robots that can come together in versatile configurations to form a lattice shape to adapt to the task at hand. DeusCell is an MRR unit that runs on command to self-assemble into a desired structure or design with real-time adaptability and the capability to reconfigure themselves if an external deformation occurs. The paper will discuss the system's design, the new locomotion concept and its implementation, the actuation algorithm, and the analysis of the cube design. It reports on the hardware for locomotion.

Keywords Modular · Reconfigurable · Real-time adaptability

1 Introduction

In the 2014 Walt Disney movie “Big Hero 6”, Hiro Hamada develops an almost omnipotent system of microbots that can assemble into any shape with the help of mental commands. This inspired us to explore the possibilities of such a system in the current world and such robots are called Modular Reconfigurable robots (MRR). MRR systems are comprised of numerous individual modules (or units) that are rearrangeable or possess sufficient autonomy to rearrange themselves into different configurations based on the task the robot is required to perform at the time [1]. Modular self-reconfiguring robotic systems, also known as self-reconfigurable modular robots, are kinematic machines that are capable of such autonomy and, as a result, have a variety of morphologies. Self-reconfiguring robots are capable of modifying their own form by rearranging the connectivity in their parts, in addition to the standard actuation, sensing, and control found in fixed-morphology robots, to

A. Radhakrishnan (✉) · A. P. Johnson · N. Roy · R. G. Ribu · B. Deepak
Department of Mechanical Engineering, Mar Baselios College of Engineering and Technology,
Trivandrum, India
e-mail: adihagane20@gmail.com

B. Deepak
e-mail: deepak.b@mbcet.ac.in

adapt to new situations, perform new tasks, or recover from damage. The term “self-reconfiguring” or “self-reconfigurable” implies that the unit possesses the capability of utilizing its system of control such as with actuators or stochastic means to change its overall lattice structure [2].

MRR systems have three areas of promise—versatility, robustness, and low cost [3]. Regrettably, these three benefits have yet to be fully realized. The additional degrees of freedom make modular robots more flexible in terms of their probable capabilities, but they arrive at a cost in terms of performance and mechanical and computational intricacy. A modular robot will almost certainly be inferior to a single specialized robot built for a specific mission. As a result, the benefit of modular robotics is only apparent when considering many functions that would otherwise necessitate a variety of fixed-morphology robots, or when the essence of tasks cannot be fully determined before the robots are deployed. However, these research prototypes are fragile and their costs exorbitant, as expected in any initial development.

The DeusCell design has materialized a mechanical-based locomotion system [4], which is unique when compared to the earlier novel counterparts which employed a majorly electrical-based system. Through this mechanical working, we have achieved higher load-bearing capacities and strength for each cell.

2 Methodology

The methodology for this work is developed by considering the objectives and current trends, methods and materials used in this field obtained by an extensive review of various literature. Many existing MRR designs such as Mu cubes [5], M-block [6], CoBold [7], RoomBots [8], SwarmBots [9], EM cubes [10], and PolyBot [11], were referred to while designing the current cell. The main focus of the work was to design a robotic cell that was made majorly using mechanical components and would possess load-bearing capabilities. The product in an idea is a modular unit, which can reconfigure into shapes using multiple units to support unstable structures. Depending on the situation, the cells can be programmed to take on various morphologies. The setup consists of a piston actuator assembly that aids the movement of cells and magnets that help two different cells to interlock. The cell is coded to accept external commands and assemble into the required support and has reconfiguration capabilities in case of external forces.

The design aimed to improve its load-bearing capabilities as well as induce more mechanical, rather than electrical components within the cell. Designs for load-bearing MRR are rare, and hence methodologies that have been applied for their design and analysis are either undisclosed or non-existent. Therefore, the methodology applied for this design is based on the simple question, “how much can one cell carry and how much can it be improved?”.

In the first phase of design, cell locomotion was given priority to make sure that the cell can move with ease. Later, the focus was put on its load-bearing capabilities.

Bound by practical limitations, to understand the behavior of the design under loading conditions, computational analysis was preferred over experimental setups.

3 Design

The DeusCell can be described as a cube with curved edges, inspired by the designs in shadow metamorphosis [12] that has dimensions of 230 mm on each side. The components housed inside the cell aids in its locomotion. The Fig. 1 shown illustrates the model designed using SOLIDWORKS that was achieved after many design iterations to optimize the mechanism and functionality of this unit.

3.1 Inner Components

The rectangular 'Core' is a major component, which serves as the nucleus to house the essential units required for the coordinated working of the locomotion system and the power source. It consists of the PyBoard/Arduino, MPU6050 and the 9 V battery. The core consists of two parts made using ABS plastic. Pneumatic spring return actuators are connected perpendicular to each face of the core using piston mountings. Around each actuator, a 3-way 2-position directional control (DC) solenoid valve with spring return is held using a collar. The other end of the actuator is held to the inner membrane using the 'M-Halo', a disc with equally spaced holes that are also used to accommodate the face magnets used for climbing (Fig. 2).

Fig. 1 Open cell assembly

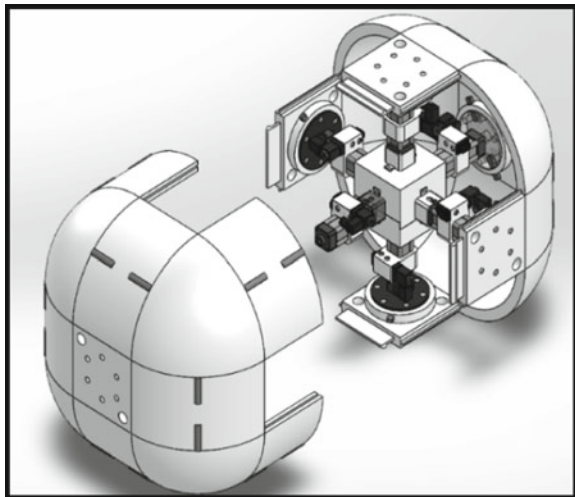
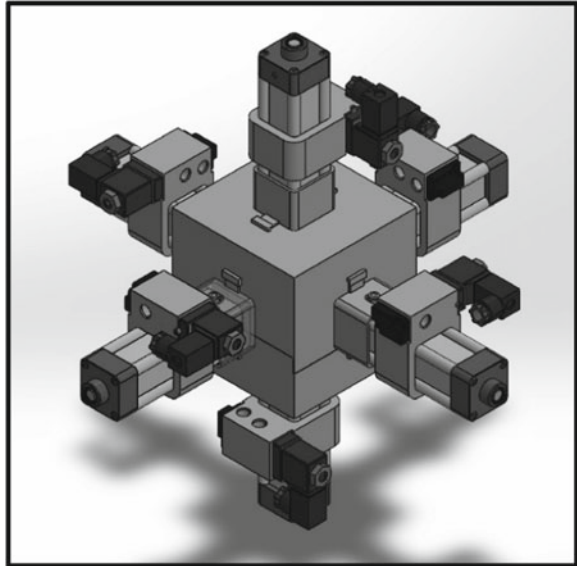


Fig. 2 Assembly of interior components excluding the shell



3.2 Shell

The entire outer membrane is created in such a way that it provides ease of locomotion as well as structural integrity. The membrane can be opened to have access to the internal parts. The two halves of the membrane are connected using snap-fit locking. The membranes can be released using slots given for releasing the snap-fit. There are also permanent magnets placed along the curved edges to allow the locomotion from one face to another smoothly. Along the 70×70 mm face we have also added two equally sized holes for the sole purpose of acting as the vents for the built-up air inside the cell. The shell/membrane is the main load-bearing component, and hence the material of this component is required to meet certain parameters and property specifications to ensure it is suitable for the assigned role, and ABS plastic was the appropriate material of choice for the shell/outer membrane. The shell also has holes on each face to accommodate the face magnets [5] for docking and climbing, and edge magnets along each of the curved edges to act as pivots to aid in the climbing motion. The edge magnets are diametrically polarized [6] and allowed to rotate within its cavity (Fig. 3).

4 Working

The activity of a DeusCell begins in the core/nucleus which houses the PyBoard which runs on micro-python. The pyboard initiates the motion of the unit by first

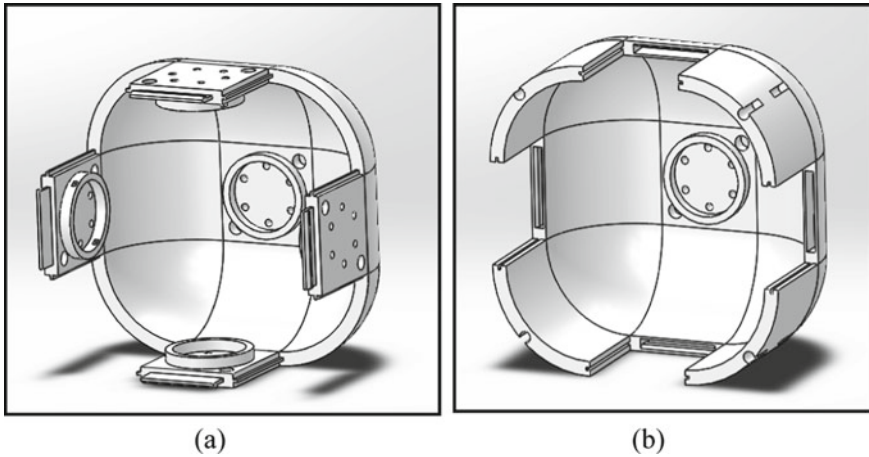


Fig. 3 The two halves of the shell. **a** The male half with the snap-fits; **b** The female half with the cavity for the snap-fits

reading the angle or orientation of the cell using the gyroscope. Then based on it sends a command/signal to the corresponding ‘3-way 2-position Directional Control (DC) Valve’. The valve by default is in exit or exhaust path, but when it receives the signal, it flips to supply path, this then allows for the input of compressed air from the compressor to flow through the DC Valve and to the ‘single acting pneumatic actuator with a spring return function’. The compressed air pushes the piston linearly which leads to an impact force on the inner wall of the unit cell membrane. The actuator works on a spring return function, and so using a spring the piston returns to its initial position. Due to this, the input air exits through the same air-port and is released out through the exit path of the valve (the signal to the valve will be absent by then) to the vacant space of the cell which will then gradually exit through the vents provided in the shell. This completes the major working for a quarter of the rotation of a single DeusCell unit.

5 Analysis

The software used is FUSION360, which is a potent analyzing platform for various types of finite element analysis. Fusion 360 is a cloud-based 3D modeling, CAD, CAM, CAE, and PCB software platform for product design and manufacturing.

Here only the shell is considered for analysis as it plays a vital role in the system by carrying the majority of the load on its faces as well as shielding the inner parts against external factors. The inner components are not considered to be carrying any load. The shell was analyzed with an increment of 100 up to 1000 N to ascertain the maximum load possible. Table 1 represents the result obtained.

Table 1 Factor of safety

Load applied (N)	Factor of safety (with snap-fit)	Factor of safety (without snap-fit)
100	15.00	15.00
200	15.00	14.65
300	10.01	9.78
400	7.51	7.34
500	6.01	5.87
600	5.01	4.90
700	4.03	4.20
800	3.76	3.67
900	3.34	3.27
1000	3.01	2.94

From the values, it is understood that the body can take up to 900 N, but it is not preferred, and the maximum load limit has been decided on 800 N.

The shell is analyzed in two cases—load applied on the face with snap-fit and load applied on face without the snap-fit. In both cases, the bottom surface was constrained, gravity was considered, and the top surface was given a uniaxial surface force of 800 N (downwards).

6 Results

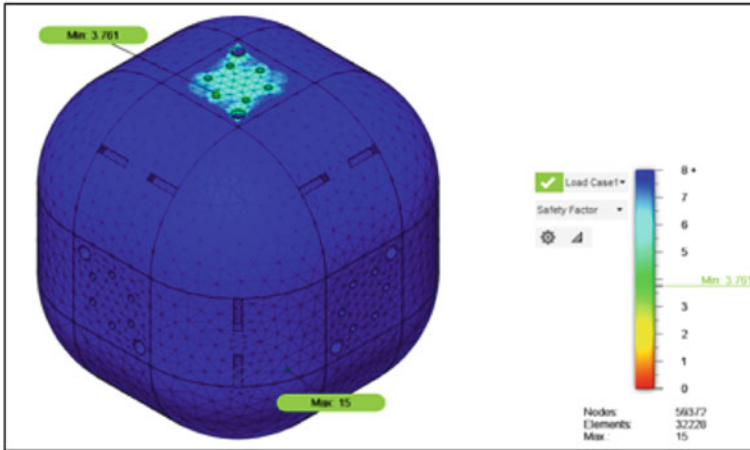
The results obtained are given below.

6.1 Factor of Safety

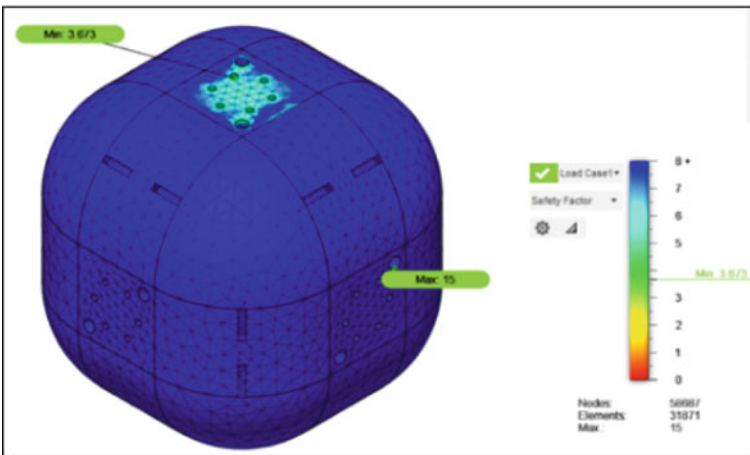
Under the given conditions the value of factor of safety obtained is 3.761, which means stress applied on the body is one-third the value of yield stress of ABS. Any value of stress greater than 800 N can cause the FOS value to go lower than 3 which can lead to failure of the design (Fig. 4).

6.2 Stress Analysis

Under these conditions, the maximum value of Von Mises stress obtained is 5.317 MPa in Case 1 and 5.445 MPa in Case 2. The maximum value is located near the holes (magnet holes and vents) because of stress concentration. Von Mises



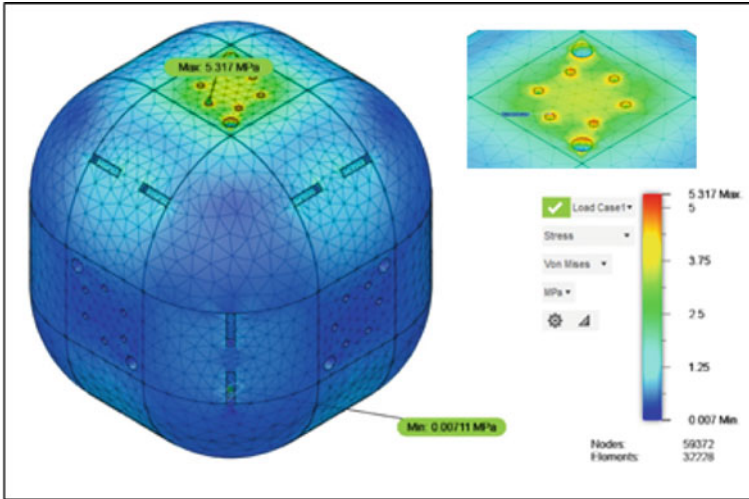
(a)



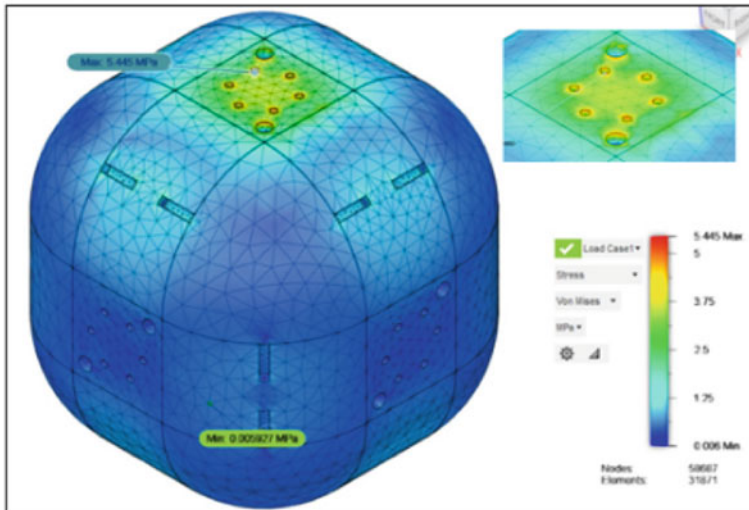
(b)

Fig. 4 Factory of safety analysis by applying load on **a** face with snap-fit, and **b** face without snap-fit

Criterion states that if Von Mises stress is equal or greater than the yield limit of material then the material will yield. Here, the material does not yield as the yield limit is greater than the stress value obtained (Fig. 5).



(a)

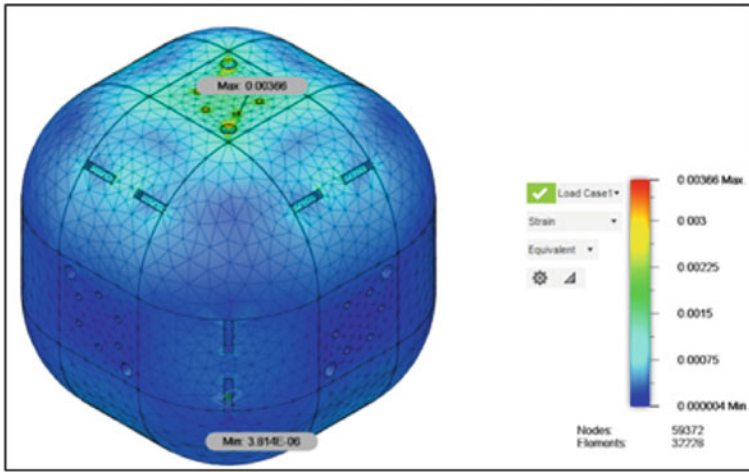


(b)

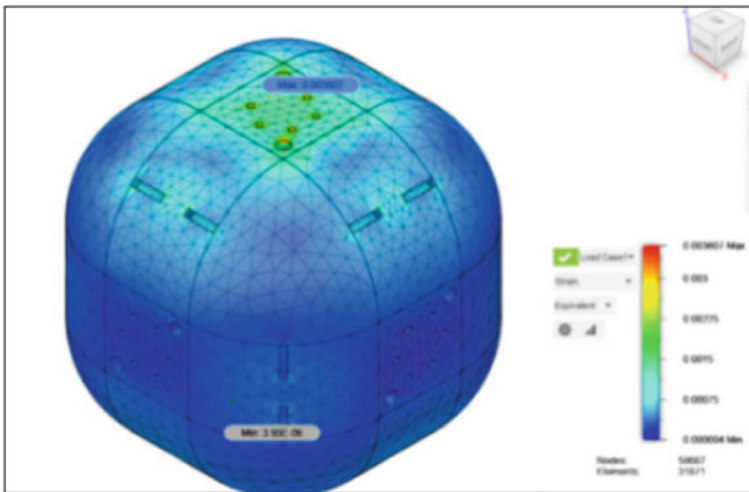
Fig. 5 Stress analysis by applying load on **a** face with snap-fit, and **b** face without snap-fit

6.3 Strain Analysis

Under these conditions, the maximum value of strain obtained in both cases is 0.0036. Strain is a value that represents the amount of distortion that occurs in a body. The value obtained is very low and hence the design is safe (Fig. 6).



(a)

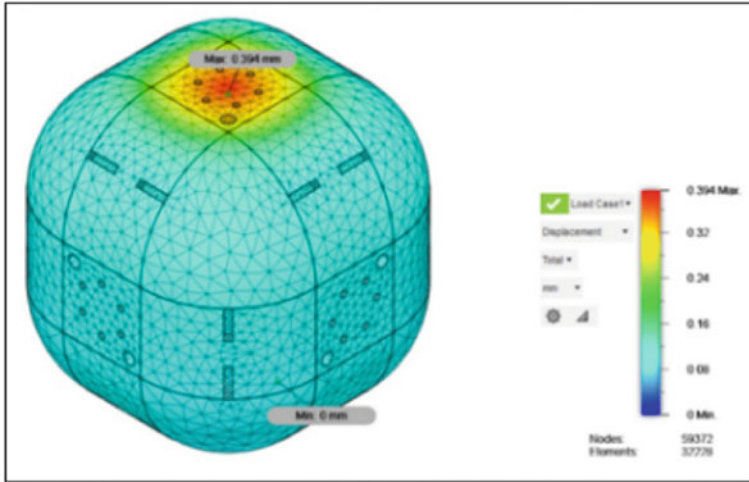


(b)

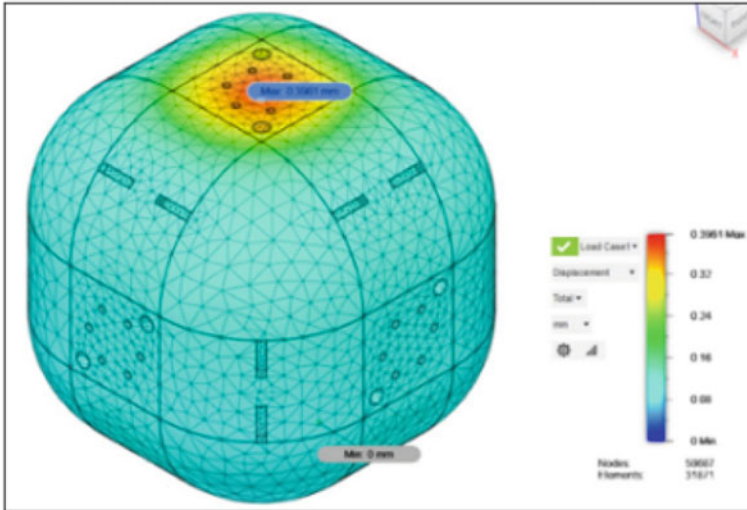
Fig. 6 Strain analysis by applying load on **a** face with snap-fit, and **b** face without snap-fit

6.4 Total Displacement

The maximum total displacement value obtained under applied load in both cases is 0.39 mm. This value is very small compared to the overall dimensions of the cells and hence the cell remains safe (Fig. 7).



(a)



(b)

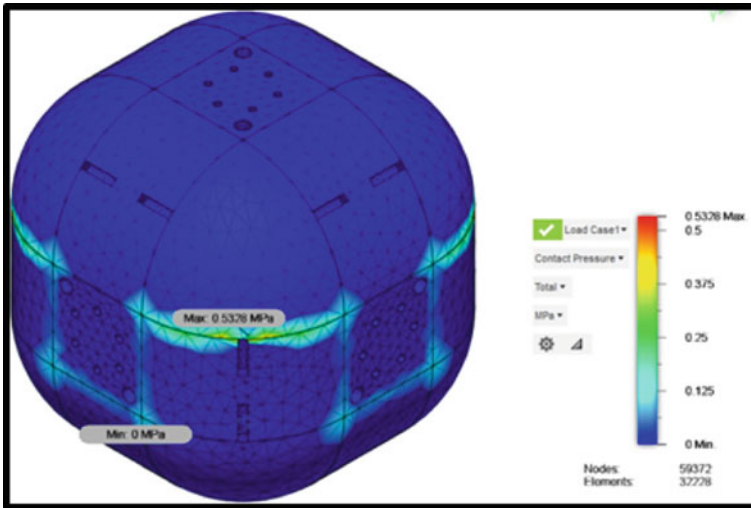
Fig. 7 Total displacement analysis by applying load on: **a** face with snap-fit, and **b** face without snap-fit

6.5 Contact Pressure

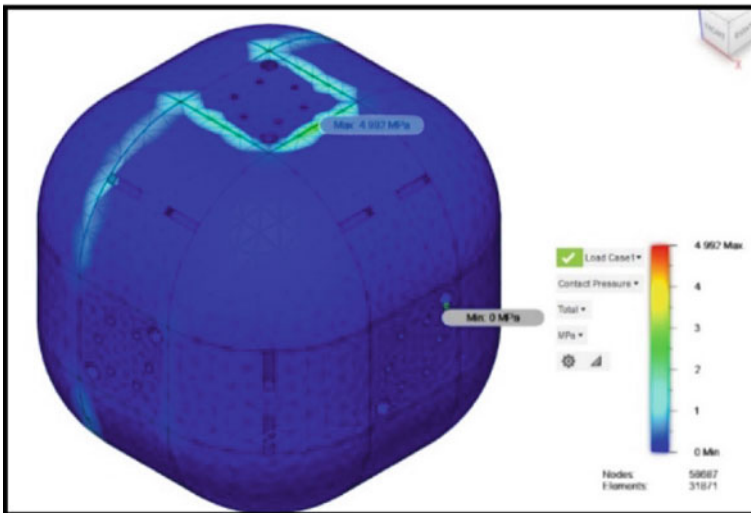
It refers to the pressure exerted between the contact surfaces of the two shell halves. The contact pressure is the ratio of the normal load to the true contact area. The maximum value of pressure is 0.532 MPa is obtained in case 1 and 4.992 MPa is

obtained in case 2. The value increases in case 2 as the load is directly applied on the snap-fit connection of the 2 cells (Fig. 8).

From the analysis, it is understood that the cell can handle a maximum load of 800 N. Table 2 depicts various values obtained in both cases for after mentioned load.



(a)



(b)

Fig. 8 Contact pressure analysis by applying load on: **a** face with snap-fit, and **b** face without snap-fit

Table 2 Values for maximum possible load

Analysis	On face with snap-fit		On the face without snap-fit	
	Maximum	Minimum	Maximum	Minimum
Von Mises stress	5.445 MPa	0.006 MPa	5.317 MPa	0.007 MPa
Strain	0.003607	3.95E – 06	0.00366	3.814E – 06
Displacement	0.3961 mm	0 mm	0.394 mm	0 mm
Contact pressure	4.992 MPa	0 MPa	0.5328 MPa	0 MPa
Reaction force	113.5 N	0 N	134.3 N	0 N

From the above analysis, the following can be inferred:

- From the above values, it is understood that the material ABS will suffice for our design and a single cell can carry a maximum load of 800 N without any deformation or failure.
- We can also understand that if a single cell is considered to carry a load it is always better to load the face without a snap-fit connection as it is safer than the face with snap-fit. This is due to the higher contact pressure that is exerted on the snap-fit joint when the load is applied on the face where the snap-fit.

7 Conclusion

The concept of using this new mechanical oriented locomotion system that employs pneumatic actuators, is plausible. This in turn can change how MRR will be seen as they will be capable to perform higher load-bearing tasks which are rarely seen in this field. The use of ABS plastic as the base for most of the components in the design makes it cost-effective and easier to manufacture using 3D printers. Based on the computational analysis performed on the two cases, it is evident that the deformation, on the face without the snap-fit locking mechanism, is substantially lesser than that on the face encasing the snap-fit. Irrespective of this, the design is capable of handling loads in both cases. This leads to the conclusion that it is relatively more feasible to use the faces that are void of the snap-fit for any loading purposes.

References

1. Seo J, Paik J, Yim M (2019) Modular reconfigurable robotics. *Annu Rev Control Robot Auton Syst* 2:4.1–4.26
2. Brunete A, Ranganath A, Segovia S, de Frutos JP, Hernando M, Gambao E (2017) Current trends in reconfigurable modular robot’s design. *Int J Advanced Robotics System* 1–21
3. Yim M, Shen W, Salemi B, Rus D, Moll M, Lipson H, Klavins E, Chirikjian G (2007) Modular self-reconfigurable robot systems-challenges and opportunities for the future. *IEEE Robot Automat Mag* 14:43–52

4. Dilip R, Milan K, Vajrangi A, Chavadi KS, Puneeth A (2021) Jumping robot: a pneumatic jumping locomotion across rough terrain. *J Phy: Conf Ser* 2115:012008
5. Zia AB, Abbas S, Ejaz SO, Ikram U, ur Rehman S (2017) Mu-cubes—modular, cube shaped, and self-reconfigurable robots, MIT
6. Romanishin J W, Gilpin K, Rus D (2013) M-block—momentum-driven, magnetic modular robots. In: *IEEE/RSJ international conference on intelligent robots and systems (IROS)*
7. Liedke J, Worn H (2011) CoBoLD—a bonding mechanism for modular self-reconfigurable mobile robots. In: *IEEE international conference on robotics and biomimetics, Phuket, Thailand, 7–11 Dec 2011*
8. Hauser S, Mutlu M, Léziart P-A, Khodr H, Bernardino A, Ijspeert AJ (2020) Roombots extended: challenges in the next generation of self-reconfigurable modular robots and their application in adaptive and assistive furniture. *Robotics and Autonomous Systems* 127:103467
9. Schranz M, Umlauf M, Sende M, Elmenreich W (2020) Swarm robotic behaviors and current applications. *Front Robot AI* 7. <https://doi.org/10.3389/frobt.2020.00036>
10. An BK (2008) EM-cube: cube-shaped, self-reconfigurable robots sliding on structure surfaces. In: *IEEE international conference on robotics and automation Pasadena, CA, USA.*
11. Yim M, Duff DG, Roufas K (2000) Modular reconfigurable robots, an approach to urban search and rescue. *International Journal of Human-friendly Welfare Robotic*
12. Klimmek B, Prautzsch H, Vahrenkamp N (2007) *Shadow metamorphosis*. Springer, Berlin

Structural Design of Ultimate Terrain Electric Vehicle Suspension System



Jerin Joseph, Justine Joseph, Karthik S. Rajendran, and M. S. Anoop 

Abstract The ultimate terrain vehicle (UTV) is a unique type of all-terrain vehicle (ATV) that can accommodate four passengers with enough storage spaces and is utilized for expeditions across tough terrain. Such vehicles are ideal for military surveillance, but they must be quiet during operation and have high initial torque. Both of these requirements are met by the UTV with an electric power train, resulting in the ultimate terrain electric vehicle (UTEV). This study explores the process of designing and analyzing a suspension system for a UTEV. This paper comprises objectives and different methodologies used for the calculation and design of the suspension components. For the simulation, designing, and analysis, software such as LOTUS, CATIA, and ANSYS was used. Necessary corrections in the designs were done after the analysis, and final evaluation of the outcomes of each component has been specified.

Keywords Ultimate terrain vehicle · Suspension system · Structural analysis

1 Introduction

ATVs are advanced vehicles that may be utilized on difficult terrain for adventure. This needs a huge amount of force to move the car across such difficult terrain [1]. These vehicles are only meant to carry a single passenger. The demand for special purpose vehicles with additional passenger and storage space has led to the creation of ultimate terrain vehicles (UTVs). These types of UTV are deployed for surveillance and transportation of equipment necessary through tough terrain. These vehicles can also be used in disaster-stricken areas as medical response vehicles. Such vehicles have to maneuver over unprecedented conditions and require high torque. These vehicles maneuver under severe conditions, demanding a large amount of torque. In

J. Joseph · J. Joseph · K. S. Rajendran · M. S. Anoop (✉)
Department of Mechanical Engineering, Sree Chitra Thirunal College of Engineering,
Thiruvananthapuram, Kerala, India
e-mail: anoopms@sctce.ac.in

A. P. J. Abdul, Kalam Technological University, Thiruvananthapuram, Kerala, India

such circumstances, an electric motor-driven power train is an excellent alternative to internal combustion (IC) engines [2]. Furthermore, such a power train is well suited to military surveillance applications that require quiet operation while still providing high-power navigation. The main objective of the study is to design an electric-powered UTV that will lead to the development of ultimate terrain electric vehicle (UTEV). As the power train switches to electric, the UTEV needs to be redesigned. The primary focus of this article is to design the suspension system of the UTEV catering to the specific requirements.

Depending on the operating conditions of the vehicle, the suspension system of the vehicle needs to satisfy many requirements. The basic functions of a suspension system are as follows: to improve the vehicle's handling and braking for better active safety and driving enjoyment and to keep the occupants comfortable and well separated from road noise, bumps, and vibrations [3]. The car and its associated systems are also protected by the suspension. Springs and associated linkages are all part of the suspension system that links a vehicle to its wheels. The design of the front and rear suspension of a vehicle is in most cases different, but there are similarities too [4].

When speaking about the suspension geometry, it means how the unsprung mass of the vehicle would be connected to the sprung mass. These linkages not only regulate the wheel's movement, but also the forces that are communicated between the sprung and unsprung masses [5]. The most important objective in the design of this suspension system was to ensure that the tyers have substantially good vertical wheel motion to tackle terrain roughness and undulations. If the suspension mechanism does not allow for efficient wheel motion, then when the wheels hit bumps or potholes, the wheels will continue upward or downward motion, dragging the chassis along with them at the same velocity. The major goal was to create a fully functional suspension system that would allow for efficient vertical wheel motion and hence give driving comfort and stability when traveling over rough terrain. Following a detailed review of the literature and analysis of the benefits and drawbacks of various suspension systems, as well as the criteria and limits, sufficient information was gained to properly design a suspension system for an all-terrain vehicle (ATV). The best solution for completing the design assignment was to build an independent suspension system [6].

The goal of this research is to build the UTEV's suspension system so that the road shocks are not transferred to the vehicle's components or its occupants. In pitching or rolling action, the suspension system should maintain the vehicle's stability. While traveling over rough terrain, it should limit torque, provide appropriate ride height, reduce brake reflexes, and keep the body level.

2 Methodology

The methodology followed for designing the suspension system of the UTEV is shown in Fig. 1. Designing the suspension system of a vehicle starts by deciding

on the requirements of the suspension system that is to be designed [7]. From the literature survey and industry knowledge, we need to select a suitable suspension system (independent or dependent) for the application. After selecting the suspension configuration, the basic parameters of the vehicle like wheelbase, estimated weight, suspension configuration, required wheel travel, and tire properties are entered into the Lotus suspension simulation software. Based on the load considerations, spring is designed. Considering the length and the features of the designed spring, the mounting points on the frame are located. Suspension geometry is analyzed in the Lotus software and is iterated again and again to find the optimum combination of the camber, toe, and caster angles [8]. Depending on the geometry obtained from the Lotus software, various components of the system are designed and modeled using 'CATIA' and 'SOLIDWORKS'. Integrity and the strength of the modeled components are analyzed using the 'Ansys Workbench'. If the component fails during the analysis, it is remodeled and is again iterated to check the integrity.

Springs are components that are engineered to have a lower stiffness than regular rigid members, which allows them to apply a force that changes in a regulated manner with the length of the member. Springs are segregated in general by the material they are made of and how the loads and stresses are applied. When it comes to vehicle handling, the apparent qualities of the spring, such as force, stiffness, inertia, friction, and so on, as perceived at the wheel, are more important than the specific mechanism in which those effects are accomplished. Therefore, the choice of a springing medium, such as nitrogen, rubber, or steel, does not in principle pre-empt the achievement of any particular handling qualities. The large diversity of systems in use today illustrates that no single form of spring has been shown to have an overwhelming advantage [9].

Fig. 1 Methodology adopted for designing the suspension system of UTEV

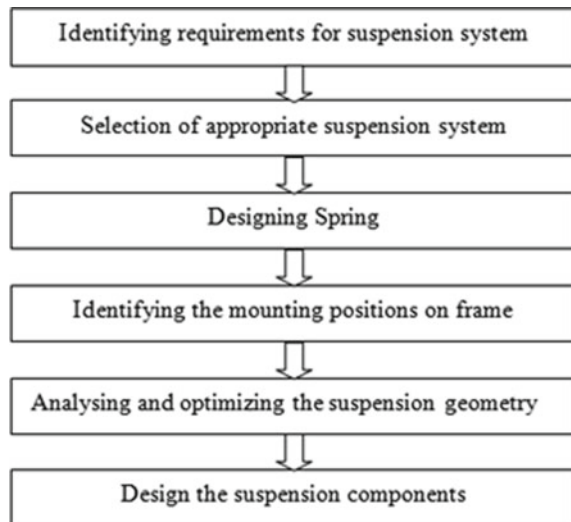


Table 1 Input values of front-end geometry

Bump travel	254 mm
Rebound travel	190 mm
Steer (rack) travel	65 mm
Wheelbase	3100 mm
Center of gravity height	700 mm
Braking on the front (%)	60
Drive on the front (%)	50
Weight on the front (%)	45
Wheel track	1840 mm
Tire rolling radius	410.20 mm
Tire width	261.6 mm

Coil springs utilize the elastic qualities of a wire in torsion to generate a rectilinear spring rate, and they are the most extensively used spring type in independent and solid axle suspensions for vehicles. The helix is the most frequent design, with a constant mean diameter. Other shapes include tapered coils (with a variable mean diameter) and coils with varied wire diameters. Coil springs are available in compression and tension designs.

Double-wishbone suspension geometry with a damper to upper wishbone configuration was selected for the front end. A double-wishbone suspension is an independent suspension design using two wishbone-shaped arms to locate the wheel. Engineers can precisely manage the motion of the wheel throughout suspension travel using double-wishbone designs, adjusting factors such as camber, caster, toe pattern, roll center height, and scrub radius [10]. The initial input geometry parameters adapted for the front-end and rear-end design are depicted in Tables 1 and 2. The mechanical properties of 300M steel is shown in (Table 3).

The hub is the section of the wheel that connects to the suspension through the knuckle, which is where the wheel is joined to the suspension. To install the wheel to the vehicle, a hub assembly comprising of the wheel bearing and hub kept between

Table 2 Input values of rear-geometry

Bump travel	254 mm
Rebound travel	190 mm
Wheelbase	3100 mm
Center of gravity height	700 mm
Braking on the rear (%)	40
Drive on the rear (%)	50
Weight on the rear (%)	55
Wheel track	1900 mm
Tire rolling radius	410.20
Tire width	261.6 mm

Table 3 Mechanical and physical properties of low-alloy steel 300M

Density	7.83 g/m ²
Tensile strength, ultimate	2030 MPa
Tensile strength, yield	1667 Mpa
Poisson's ratio	0.28
Young's Modulus	205 GPa

the brake rotor and the axle is employed [11]. A wheel hub is the mounting part for the wheel of a vehicle; it houses the wheel bearings as well as supports the lugs [12]. Knuckle and the hub assembly are used to provide support to the vertical load acting on the vehicle.

To increase purity, plasticity, and toughness, vacuum arc melting is commonly used in low-alloyed 300M steel. Non-vacuum smelting is used in the AMS 6416 standard, which is the general aviation quality level. It is frequently utilized in the aerospace industry due to its high strength, corrosion resistance, and other benefits. The following are the mechanical, physical, and chemical characteristics of low-alloy steel 300M.

The geometry of the suspension system and the steering geometry are the most important factors in determining the design of the steering knuckle [13]. This study involves modeling and analysis. First, the modeling of the steering knuckle component is done and then analysis of stresses under actual load conditions. The steering knuckle model of our vehicle is modeled in 'CATIA' based on the location of the hardpoints obtained from Lotus suspension geometry. The CAD model consists of suspension upper and lower arms mounting points, tie rod end mounting, and brake caliper mounting points. For the steering knuckle component, forged steel EN 47 was used since it has higher strength and is lighter [9]. 'Ansys Workbench 2020 R1' has been used to analyze the steering knuckle for the forces that are acting on it. Forces are due to the static load of the vehicle, steering effort, braking force, and constraints of the vehicle. The initial model was then reiterated based on the analysis results for further weight reduction and uniform stress distribution.

The methodology adopted for the design of components such as front-rear wheel hubs and upper-lower arms is as follows. The initial parameters such as pitch circle diameter, lug pattern, rotor mounting points, shaft diameter, and bearing size, an initial CAD model was developed on the software like 'CATIA' and 'SOLIDWORKS'. 300M steel is high-strength low-alloy steel was chosen due to its high strength, high corrosion resistance, good fatigue performance for the wheel hub component. After modeling, the 3D model was meshed in 'Ansys Workbench' and was analyzed based on our calculated loading conditions. Based on the analysis, the design was reiterated for further weight reduction and uniform stress distribution.

The double-wishbone suspension system is made up of two lateral control arms (upper and lower), which are normally of different lengths, as well as a coil over-spring and a shock absorber. There are two mounting locations on the chassis for each wishbone or arm, as well as one joint at the knuckle. To regulate vertical movement, the shock absorber and coil spring are attached to the wishbones. Engineers may

precisely regulate the motion of the wheel during suspension travel with double-wishbone designs [14].

The requirements of a suspension system include maintaining correct vehicle ride height, reducing the effect of shock forces so that they are not transmitted to the occupants, supporting the weight of the vehicle to provide a better ride, to maintain correct wheel alignment to provide better steering, braking, and reducing the uneven wearing of tires. Suspension requirements also include improved tyer contact with the road to improve road adhesion and manage the vehicle's direction of travel [15]. The caster, camber, and static toe angles are the most important suspension geometry features. When it comes to independent wheel suspension, the double-wishbone has a lot of benefits in terms of kinematics. The body roll center and variations in camber angle can be determined by the varied locations that the upper and lower control arms may have owed to differing lengths. Such properties are beneficial for off-road vehicles. Even though there are a lot of advantages to double-wishbone suspension system, there are some disadvantages too. The suspension geometry should be clearly defined and engineered to get the best performance from this system. Double wishbones are generally considered to have dynamic load handling capabilities, so they are used in most cases with various design changes to fit the requirements.

To design the semi-trailing arm, first of all, the problem statement and requirements were studied thoroughly, and the following methodology is adopted in the design. An initial 3D model is created based on the parameters obtained from the 'Lotus' such as wheelbase, track width, suspension hardpoints. After modeling, the 3D model was analyzed based on our calculated loading conditions assigning steel as material. Based on the analysis, the design was reiterated for further weight reduction and uniform stress distribution.

3 Results and Discussion

Coil springs employ the elastic characteristics of a wire in torsion to generate a rectilinear spring rate, and they are the most extensively used spring type in independent and solid axle suspensions for vehicles. The helix is the most frequent design, with a constant mean diameter. Other shapes include tapered coils (with a variable mean diameter) and coils with varied wire diameters. Coil springs are available in compression and extension designs. Table 4 shows the spring selection specification.

A double-wishbone suspension system provides more design choices. It takes up less space, and due to its unique geometry, the suspension setup can be tuned easily. The double-wishbone system provides increasing negative camber gain in jounce and is easy to work out the loads that different parts will be subjected to. It also provides the flexibility to adjust parameters like camber, caster, and toe. But, double-wishbone suspension systems are more complex and expensive when compared to other systems. They are heavier when compared with the MacPherson strut system. When compared with the much-advanced multilink suspension system, they offer less

Table 4 Spring properties

Properties	Front	Rear
Material	High carbon wire	High carbon wire
Torsional yield point	1100 N/mm ²	1100 N/mm ²
Torsional elastic limit	920 N/mm ²	920 N/mm ²
Factor of safety	1.25	1.25
Spring index	6	6
Ride frequency	1.35	1.5
Spring rate	25.8 N/mm	39.04 N/mm
Static deflection	136.74 mm	110.56 mm
Diameter of wire	16 mm	20 mm
Mean diameter	96 mm	120 mm
Maximum load	9030 N	13,664 N
No of active coils	28	24
Total no. of coils	30	26
Solid length	480 mm	520 mm
Total length	833.03	975.7 mm
Pitch	29.75 mm	mm

design choice. It takes longer to service a double-wishbone system. The suspension parameters are shown in (Figs. 2, 3 and 4). The static values are shown in (Table 5).

While deciding the rear-end geometry for a UTV, different criteria need to be satisfied. Criteria like space constraint, dynamic nature of wheel, unsprung weight, reliability, or even type of usage come into the picture. Several geometries were considered for installation at the rear. Finally, semi-trailing arm geometry was selected. As the name suggests ‘semi’, this geometry is half trailing and half transverse. This results in neutral steering response and controls both lateral and vertical motions. Thus,

Fig. 2 Camber change

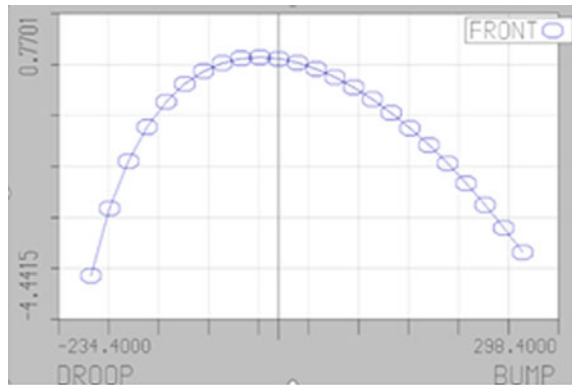


Fig. 3 Toe change

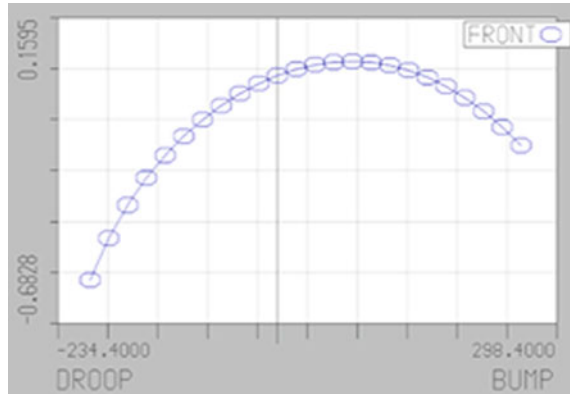


Fig. 4 King pin angle change

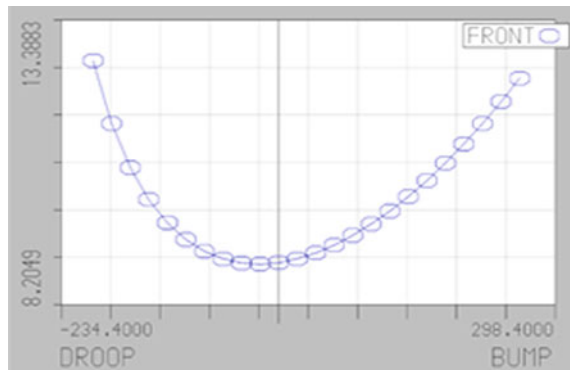


Table 5 Static values (front)

Camber angle	0°
Toe angle	0°
Caster angle	5.64°
Kingpin angle	8.97°
Scrub radius	4.31 mm
Mechanical trail	36.64 mm
Roll center height	355.28 mm

semi-trailing geometry was chosen for the rear. The results of the simulations are shown in Table 6. Figures 5, 6, and 7 represent the toe change and chamber change.

This is similar to the pure trailing arm; the only difference is that the bushing axis (and ‘instant axis’) now can run at an angle in all three views. The plan view angle means that the bushing axis will intersect the front-view plane at a point inboard of the wheel, thus establishing the front-view instant center. This instant center is fixed relative to the car, and therefore, the camber change is constant with wheel

Table 6 Static values (rear)

Camber angle	0°
Toe angle	0°
Roll center height	168.24 mm

Fig. 5 Camber change

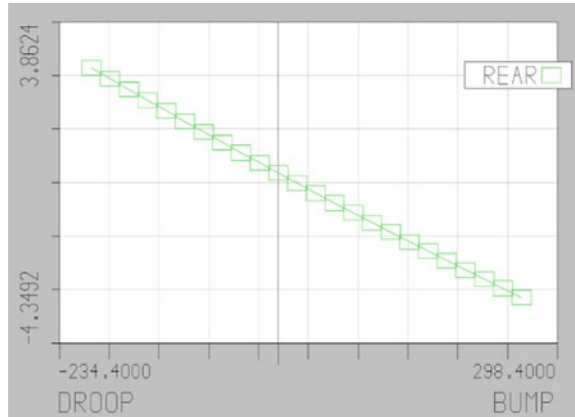
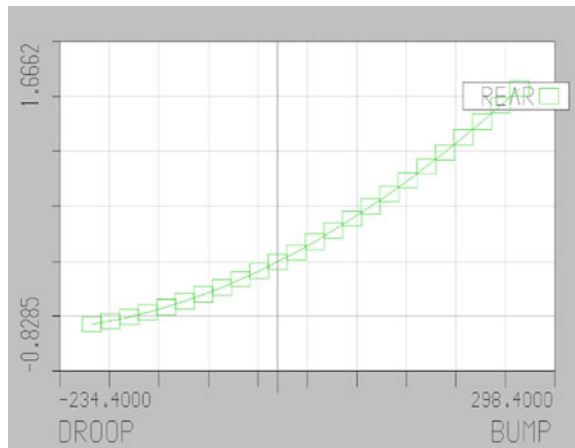


Fig. 6 Toe change



travel. The roll center is found by conventional means and can either be above or below ground level. With the instant axis angled in top view, the toe curve will never be a straight line; it will typically toe-in, both in bump and droop. The amount of toe change is a function of the plan view angle of the bushing pivot (instant) axis. Geometrically, this suspension has two basic faults: The camber change is a straight line, and the toe change is a curved line. We generally desire exactly the opposite in a good suspension.

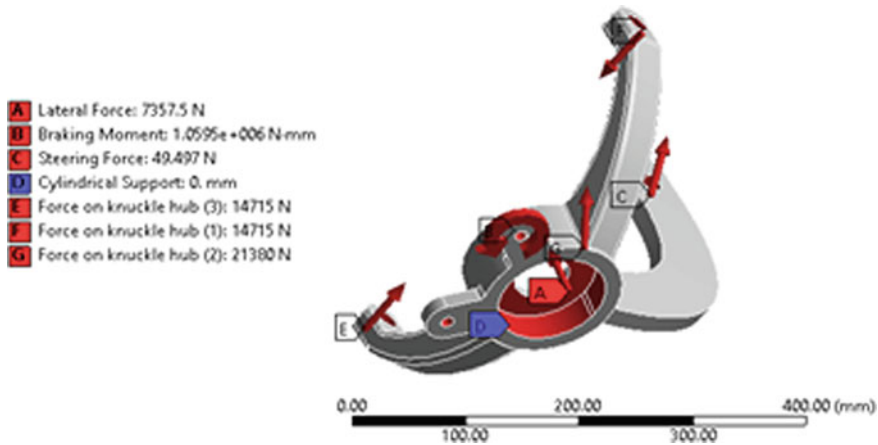


Fig. 7 Loading condition on the knuckle

The objective is the mass reduction of the steering knuckle of the UTEV. Material selection, shape optimization, and finite element analysis (FEA) have been used to maintain stress and deformation levels and achieve high stiffness. Shape optimization has been done by using analysis ‘ANSYS’ software. The CAD model of the steering knuckle is shown in the figure.

The steering knuckle is usually made out of a variety of materials, including cast iron, mild steel, and aluminum. Cast iron and mild steel are strong, but they add to the vehicle’s weight. In the future, forged steel will be the most demanding material for steering knuckles. Fuel utilization may be stretched to the maximum limit due to the lightweight of the materials. For the steering knuckle component, forged steel EN 47 was used since it has higher strength and is lighter. Table 7 lists the mechanical and physical characteristics of forge steel materials. Table 8 shows the necessary load for the steering knuckle component, as estimated from several research articles. The analysis’s optimum results are shown in Table 9.

The decrease in the hub’s rotating mass and the total weight of the ATV resulted in increased acceleration. Due to the motion of the ATV, such as braking, turning, and a six-foot fall, the hub is subjected to continual pressures and impacts. As a result, the hub should be constructed with low weight and high strength in mind. This is made to perform better acceleration, braking, and cornering. Wheel hub located at a driven axle of the car transfers torque from the driveline to the wheel; thus, it should

Table 7 Material properties of forge steel (EN 47)

Density	7.7 g/m ²
Tensile strength, ultimate	650 GPa
Tensile strength, yield	350 GPa
Young’s Modulus	200 GPa
Poisson ratio	0.3

Table 8 Forces acting on the knuckle

Braking force	1.5 mg	7357.5 N
Lateral force	1.5 mg	7375.5 N
Steering force	45–50 N	50 N
<i>Force on the knuckle hub:</i>		
In x-direction	3 mg	14,715 N
In y-direction	3 mg	14,715 N
In z-direction	1 mg	4905 N

Table 9 Results obtained through engineering analysis

Parameters	Initial model	Final model
Mass	14.914 kg	9.946 kg
Total deformation	2.5871 mm	1.8724 mm
Equivalent stress	1187.2 MPa	415.15 MPa

be strong enough to withstand the torque generated at the wheels. The results from analysis are shown in (Figs. 8, 9, 10 and 11). Loading conditions and results are shown in (Tables 10, 11).

The arm design is shown in Fig. 12. The CAD model is imported into ‘Ansys Workbench’ for analysis. The maximum stress and maximum deflection for the wishbone were calculated using a set of boundary conditions and load scenarios. Table 12 shows the input parameters. The inserted parameters and results are shown in (Tables 13, 14).

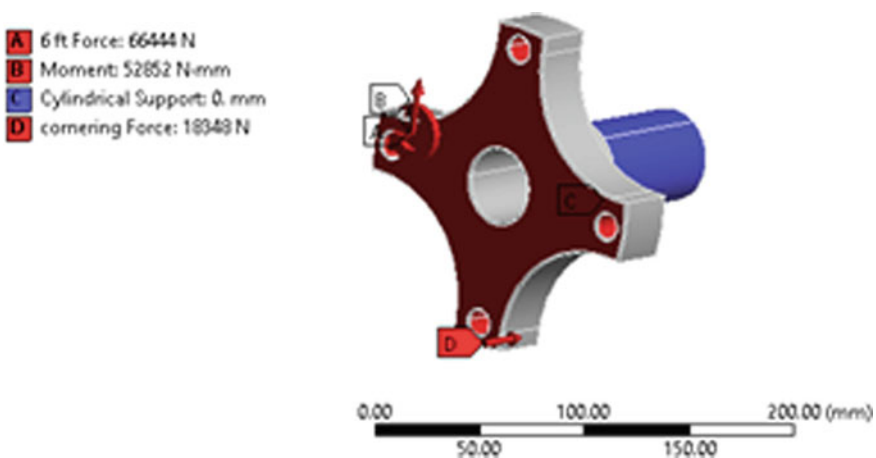


Fig. 8 Loading condition on front wheel hub

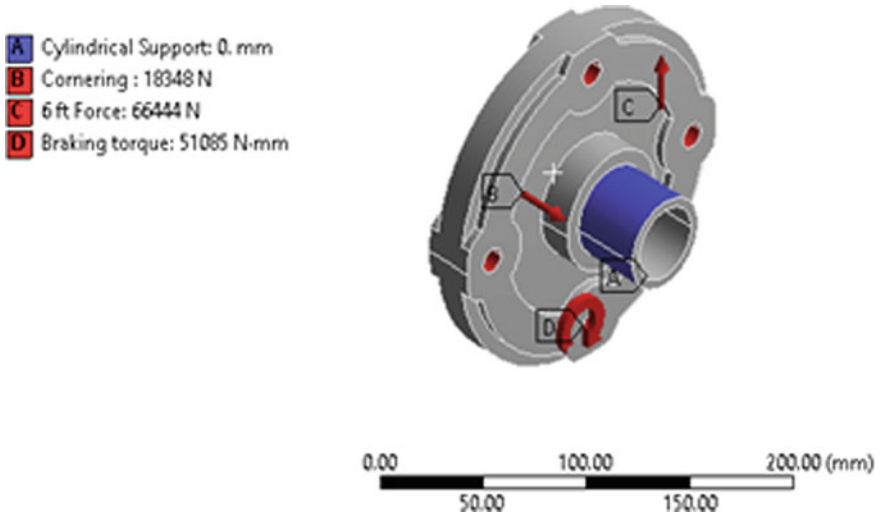


Fig. 9 Loading condition on rear wheel hub

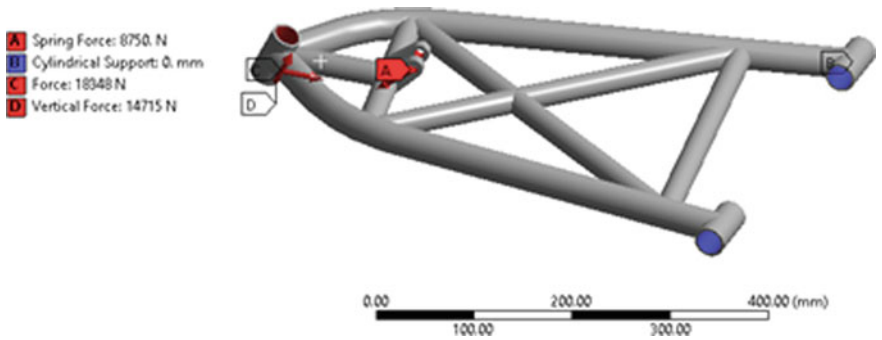


Fig. 10 Loading conditions on upper A-arm

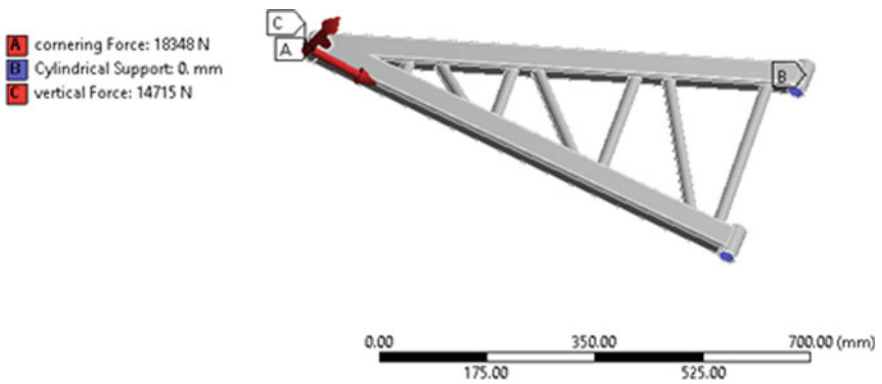


Fig. 11 Forces acting on lower A-arm

Table 10 Loading conditions (wheel hub)

Braking torque	52,861.5 Nm
(1) Front wheel	51,084.8 Nm
(2) Rear wheel	
Six feet fall	66,444.4 N
Cornering force	18,347 N

Table 11 Results obtained through engineering analysis (wheel hub)

Parameters	Front	Rear
Mass	2.8916 kg	4.3253 kg
Total deformation	666.55 MPa	0.096403 mm
Equivalent stress	666.55 MPa	207.47 MPa

- A** Normal load: 30000 N
- B** Cylindrical Support: 0. m
- C** Spring force: 13664 N
- D** Cornering force: 20000 N

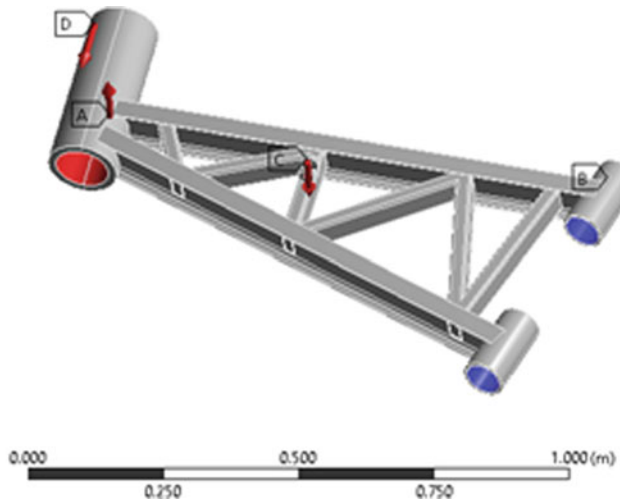


Fig. 12 Loading conditions on semi-trailing arm

Table 12 Loading conditions (A-arms)

Vertical loading	14,715 N
Spring force	8750 N
Cornering force	18,347 N

Table 13 Results obtained through engineering analysis (A-arms)

Parameters	Upper	Lower
Mass	5.2029 kg	6.4794 kg
Total deformation	36.366 mm	50.534 mm
Equivalent stress	1553.8 MPa	941.06 MPa

Table 14 Loading conditions (semi-trailing arm)

Vertical loading	14,715 N
Spring force	8750 N
Cornering force	18,347 N

Parameters	Arm
Mass	32.887 kg
Total deformation	33 mm
Equivalent stress	832 MPa

4 Conclusion

The suspension geometry was simulated using 'LOTUS' and the points from the same wire used for modeling the components in 'CATIA' and 'Solidworks'. The springs (front and rear) have been designed taking a static deflection, ride frequency, etc., into consideration. The bearing was designed to calculate the radial and axial forces acting on the bearing. Then, it was selected from the 'SKF' bearings Web site.

The component design involved modeling an initial prototype and refining the design using analysis results. The loads acting on each component were calculated from the cited reference journals and other calculations as mentioned in the appendix of this report. The components were then analyzed using static structural in 'Ansys'. The total deformation and von Mises stress values were found to be within limits for all components. The models were finalized.

References

1. Thosar A (2014) Design, analysis and fabrication of rear suspension system for an all terrain vehicle. *Int J Sci Eng Res* 5(11):258–263
2. Meghashyam P, Naidu SG, Baba NS (2013) Design and analysis of wheel rim using CATIA & ANSYS. *International Journal of Application or Innovation in Engineering and Management* 2(8):14–20
3. Gillespie TD (1999) *Fundamentals of vehicle dynamics*, SAE Inc
4. Vivekanandan N, Gunaki A, Acharya C, Gilbert S, Bodake R (2014) Design, analysis and simulation of double wishbone suspension system. *IPASJ International Journal of Mechanical Engineering* 2(6):1–7
5. Milliken WF, Milliken DL (1992) *Race car vehicle dynamics*, SAE International
6. Upadhyay P, Deep M, Dwivedi A, Agarwal A, Bansal P, Sharma P (2020) Design and analysis of double wishbone suspension system. *International Conference on Mechanical and Energy Technologies* 748:1–8
7. Shelar ML, Khairnar HP (2014) Design analysis and optimization of steering knuckle using numerical methods and design of experiments. *International Journal of Engineering Development and Research* 2(3):2958–2967

8. Sinha A, Jagtap A, Deshpande S (2018) Design, analysis and simulation of double wishbone suspension system for formula student vehicle. *International Research Journal of Engineering and Technology* 5(1):1427–1431
9. Verma H, Kumar S, Bharj RS, Kumar R (2020) Design and development of the front wheel hub for all-terrain vehicle (ATV). *Journal of Mechanical Engineering* 17(1):49–62
10. Mishra R, Baghel A (2016) Design, analysis and optimization of front suspension wishbone of BAJA 2016 of all terrain vehicle—a review. *IJRMMAE* 2(4):40–52
11. Shrivastava D (2014) Designing of all-terrain vehicle (ATV). *Int J Sci Res Publ* 4(12):1–16
12. Shaisundaram VS, Karikalan L, Vignesh V, Tamilmani R, Akash M (2018) Design and analysis of steering knuckle component for terrain vehicle. *International Journal of Recent Trends in Engineering and Research* 4(2)
13. Yadav S, Mishra RK, Ansari V, Lal SB (2016) Design and analysis of steering knuckle component. *International Journal of Engineering Research and Technology* 5(4):457–463
14. Suni K, Kiran JK (2017) Suspension system for an all-terrain vehicle. *IJMET* 8(6):85–95
15. Dixon JC (2009) Suspension analysis and computation geometry

Modal Analysis of Motorcycle Handlebar



T. G. Ajay Krishnan , R. Ajay Krishna , S. Akash ,
Akhildev K. Vasudevan , and B. Rajesh Menon 

Abstract India is the largest motorcycle manufacturers in the world, where majority of the population prefer motorcycles for their daily commutation. As a motorcycle is an open type vehicle, the riders are exposed to many uncomfortable conditions. The vibrations in the motorcycle are one of such concern. This project focuses on the vibration analysis of a motorcycle handlebar. Vibrations are induced from engine and road surface. A modal analysis simulation is performed in ANSYS to find natural frequencies and then handlebar is subjected to a free vibration test (impact hammer test) using MEScope visual SDM software to verify the natural frequencies. The 3D model required for modal analysis is created by reverse engineering tools like hexagon portable 3D scanner and GOM 3D software. From an article published on Academic Press, London, it is found that most hand arm vibrations come in the range of 50–150 Hz frequency range. The modification of the handlebar is made so that the natural frequencies coming in this range will be bypassed. To validate the modifications, modal analysis is repeated for these modifications.

Keywords Motorcycle handlebar · Impact hammer test · MEScope visual SDM · Hexagon portable 3D scanner and GOM 3D software · Modal analysis in ANSYS

1 Introduction

Vibrations in motorcycles are always an overlooked problem. Many factors like the low fuel consumption, easy maintenance and affordability outweigh the problem on hand. The vibration transmitted through the handlebars can cause several health issues like vibration-induced white finger in long term [1]. Hence, it is very much important to perform vibration analysis of the handlebar. These issues are often overlooked because of the design constraints. In this study, focus is to improve the design by breaking such constraints using various computer-based mechanical

T. G. A. Krishnan (✉) · R. A. Krishna · S. Akash · A. K. Vasudevan · B. R. Menon
NSS College of Engineering, Akathethara, Palakkad, India
e-mail: brmenonnsce@gmail.com

engineering tools. The motivation behind the study is for the improvement of overall comfort by reducing these damaging effects.

In this project, the stock handlebar of Royal Enfield Classic 350 is selected. This is a chump type handlebar and is widely used in many different models of Royal Enfield, Bajaj and Yamaha. The vibrations coming from the engine are mainly due to the imbalances in the engine, different motions in the drive line and the gas forces inside the cylinder [2]. From an available literature [3], it was found that most hand arm vibrations come in the range of 50–150 Hz. Appropriate analysis should be performed to make sure that the frequencies of the handlebar do not line up with the frequencies of operating range. The natural frequencies and mode shapes are determined and compared with engine excitation frequency for resonance [4]. The natural frequencies of the current model are found through modal analysis simulation. The simulation results are verified by conducting free vibration test of the handlebar. The 3D model required to perform modal analysis simulation is reverse engineered using hexagon 3D scanner and GOM 3D software. Afterward, the modification should be done such that frequency range susceptible for resonance is bypassed. The natural frequency of a structure can be modified by changing the mass or by changing the rigidity.

2 Method

2.1 *Impact Hammer Test*

Impact hammer test is a free vibration test to find the natural frequencies of a structure [5]. With help of software program called MEScope visual SDM, natural frequencies can be found by providing an input and output. Using impact hammer force, inputs are given and the vibrations induced in the freely hanging structure are measured as output using an accelerometer. The input and output are solved to obtain the natural frequencies. The experimental setup is shown in Fig. 1 and the results are given in Table 1.

The objective of the impact hammer test is to obtain the real natural frequencies at different modes so that most suitable analysis settings can be applied in the ANSYS modal analysis by relating the results of simulation and real-world experiment.

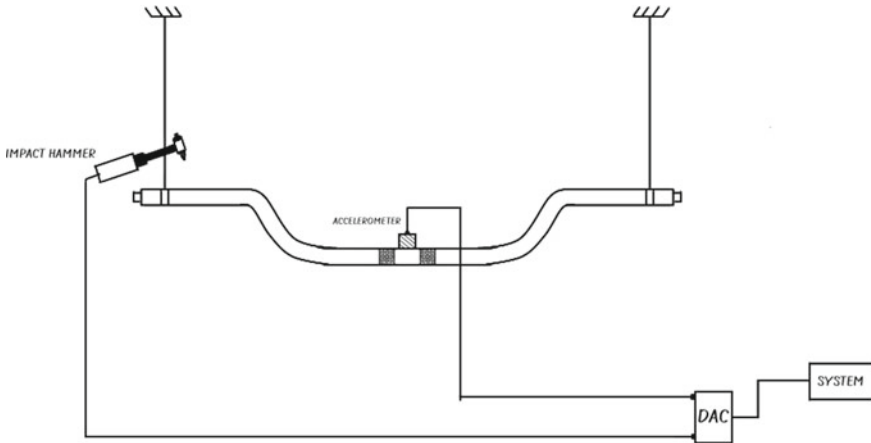


Fig. 1 Test setup for impact hammer test

Table 1 Natural frequency (impact hammer test)

Mode number	Natural frequency (Hz)
1	156
2	351
3	439
4	465
5	701

2.2 Reverse Engineering of Handlebar

Handlebar 3D model is created by scanning the model using hexagon portable 3D scanner and GOM3D software. The prepared 3D model (Fig. 2) is modified in fusion 360 software and saved as step file.

2.3 Modal Analysis

The modal analysis simulation helps find the dynamic properties of a structure [6, 7]. The handlebar geometry is imported in ANSYS design modeler and required repairs are done. Adaptive size function is used in the simulation which generates different shaped meshes (Fig. 3) depending on the nature of a face [8]. The modal is solved for free-free vibration condition and the results are given in Table 2.

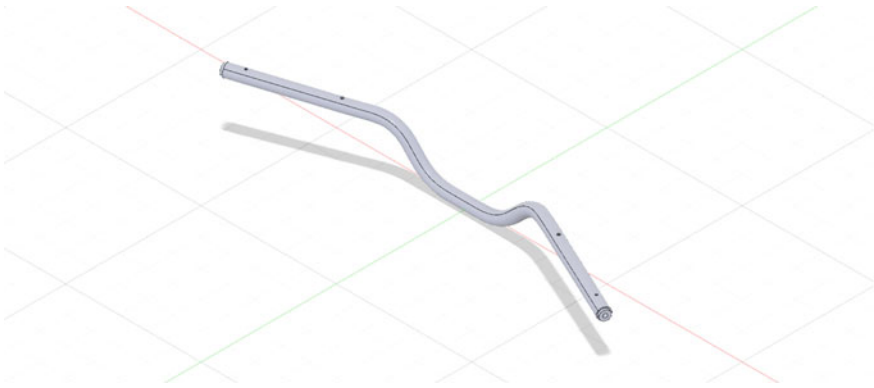


Fig. 2 3D CAD model of handlebar (reverse engineered)

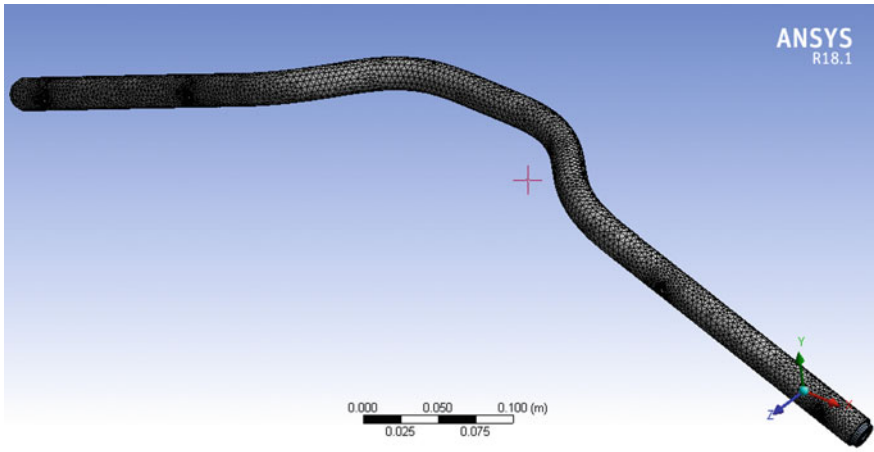


Fig. 3 Meshed handlebar model

Table 2 Natural frequency (modal)

Mode number	Natural frequency (Hz)
1	150.9
2	352.54
3	428.67
4	449.89
5	692.22

2.4 *Modification of Handlebar*

As the problematic frequencies lie in the range of 50–150 Hz, the modifications should be such that the natural frequencies will bypass this range. Here, we got the natural frequency at the first mode as 150.9 Hz. Natural frequency of a body depends on its stiffness and mass. The modifications done here are based on that. Three different modifications are made, reducing the mass, and replaced material of end blocks at the ends of the handlebar to attach the end caps, length of this block is reduced which resulted in decrease in mass (Fig. 4a). The next modification was to change the material of end blocks (Fig. 4b) The third modification was to increase the thickness of the handlebar pipe by 1 mm (Fig. 4c). All these modifications gave desired result for our objective.

3 Results

By conducting modal analyses and test, it is established that the natural frequency of the handlebar is in the problematic range. The graph in Fig. 5 shows that both the results are almost same. The excitations reaching the handlebar from the engine were also found [9]. All the procured data indicates that the rider is exposed to hazardous vibrations from the handlebar [10]. Hence, the primary objective of the project, which is to unveil the handlebar vibrations as a concern of importance, is achieved.

All the above modifications are validated by conducting modal analysis simulation and the obtained results are found satisfying. The results obtained are given in Table 3, and the variations are shown in Fig. 6. It can be found that with the specified modifications, a desired change, i.e., to bypass the particular frequency of 150 Hz is achieved. This particular problematic frequency range was mentioned in the paper [3].

Each of these modifications poses certain new drawbacks, like when thickness is increased, the overall weight has also increased. But considering the improvement in the desired property it can be neglected. The second modification of the material change of the end blocks has provided the expected result without any other side effects.

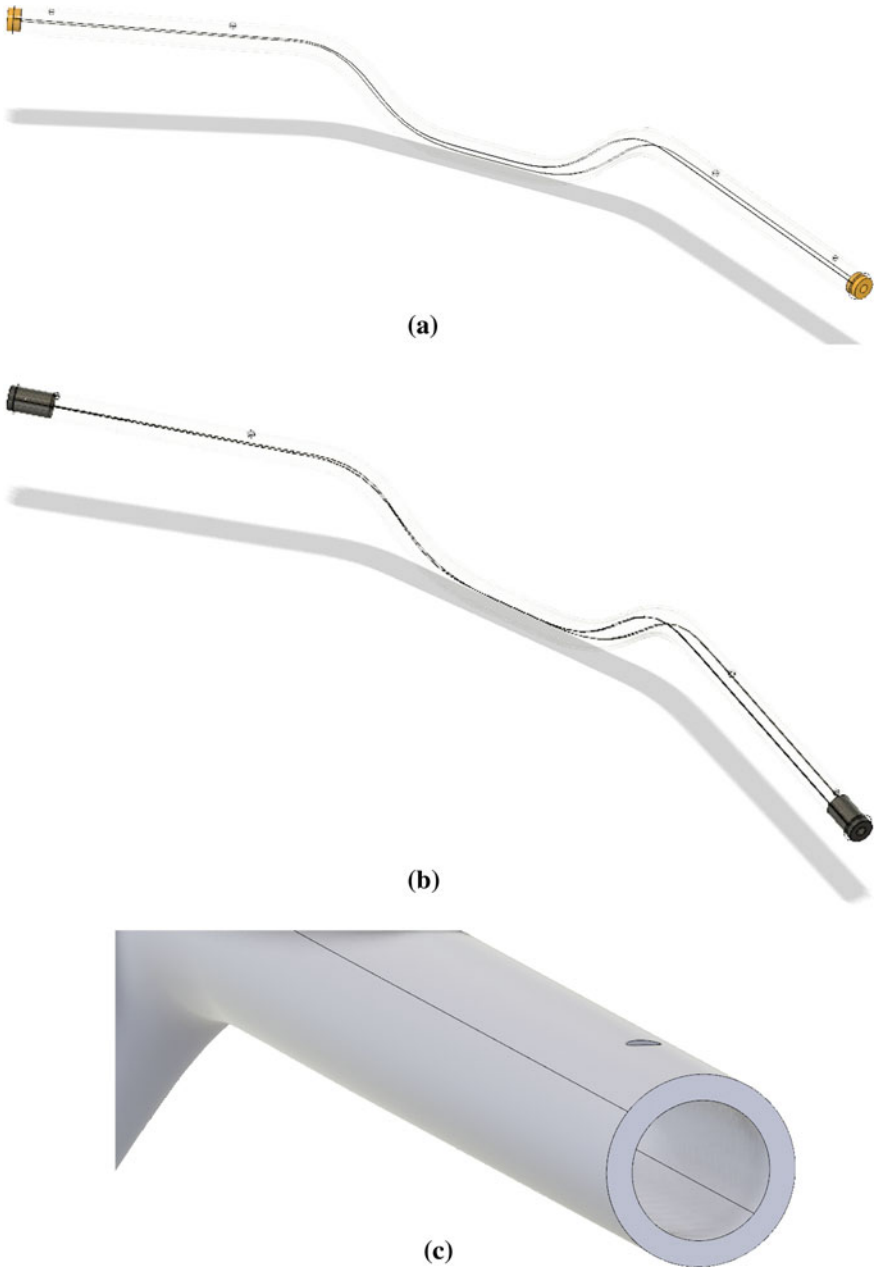


Fig. 4 **a** Length of block reduced. **b** Material of end block changed (carbon fiber). **c** Thickness of handlebar pipe increased

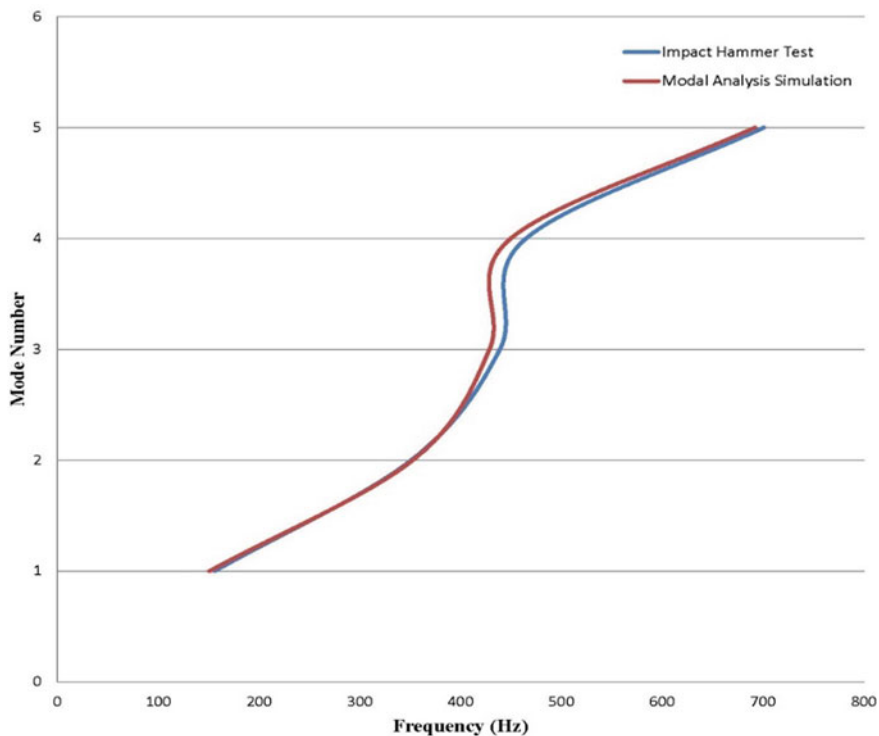


Fig. 5 Variation of natural frequency in impact hammer test and modal analysis

Table 3 Comparison of stock and modified handlebar natural frequency

Mode number	Stock model (Hz)	Modification 1 (Hz)	Modification 2 (Hz)	Modification 3 (Hz)
1	150.9	166.8	160.02	174.88
2	352.54	368.13	363.9	380.81
3	428.67	454.18	439.19	475.09
4	449.89	479.25	465.68	500.75
5	692.22	735.37	710.87	764.38

Bold represents it is the first mode (important and most common)

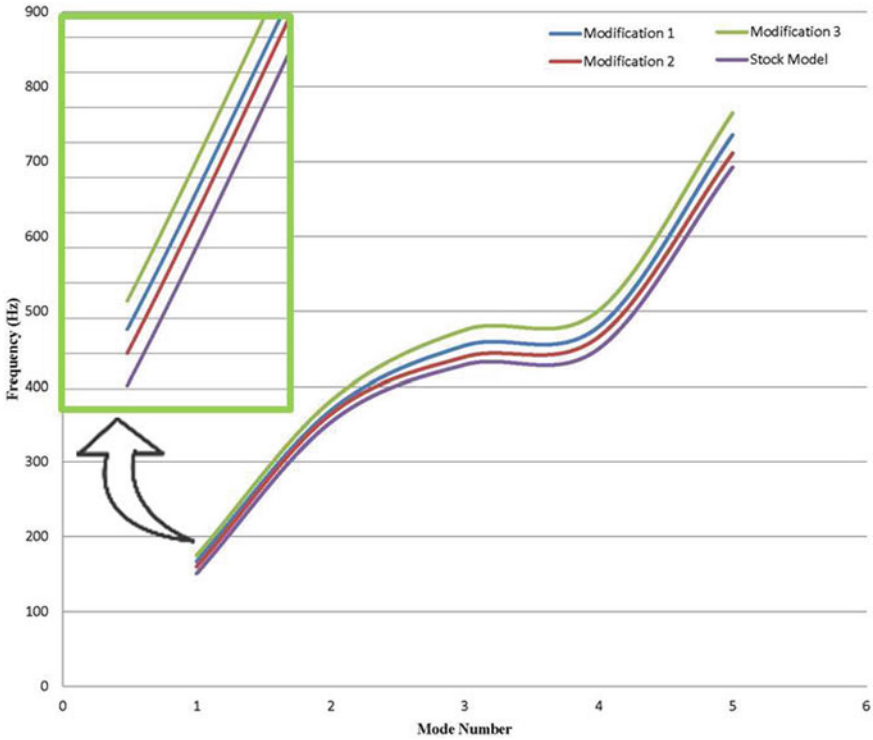


Fig. 6 Variation of natural frequency for different modifications

4 Conclusion

The proper and most suitable mesh settings were established by validating the simulation results with the actual experimental results. This helps to find the correct settings to get natural frequencies in further analysis for modified handlebar. The 3D CAD model of the handlebar is created by reverse engineering tools like 3D scanner and GOM suite. Thus, obtained a near net shape of the handlebar in the 3D model as well. Further, modal analysis is done on the stock model and modified models and desired results are obtained. Major conclusions derived from the study are:

1. The natural frequency of the handlebar is found through experiment and simulation.
2. Handlebar is modified so that the particular range of 50–150 Hz is bypassed.
3. The modified models are validated by repeating the modal analysis with same mesh settings.
4. Once the natural frequencies are found, a vibration control device can be created using a piezoelectric device and feedback circuit to counter the unbalanced excitations.

References

1. Griffin MJ (1990) Handbook of human vibration. Academic Press, London
2. Baad SM, Qaimi MG (2016) Estimation of natural frequency of motorcycle handlebar. *International Research Journal of Engineering and Technology (IRJET)* 3(7):807–811
3. Borse PA, Desale PS (2017) Effect of motor vehicle structural vibration on human body—review. *International Advanced Research Journal in Science, Engineering and Technology* 4(7):145–149
4. Borse PA, Desale PS (2017) Design and vibrational analysis of motorcycle handlebar by FEA method and correlating it with test results. *International Advanced Research Journal in Science, Engineering and Technology* 4(7):291–296
5. Shivraj H (2012) N, Gyanendra Roy “vibration analysis of 2-wheeler handle-bar assembly” Mahindra 2 Wheelers Ltd. Mahindra 2 Wheelers Ltd., pp 1–7
6. Agostoni S, Barbera A, Leo E, Pezzola M, Vanali M (2009) Investigation on motor vehicle structural vibrations caused by engine unbalances (1st part-handlebar). In: *Proceedings of the society for experimental mechanics annual conference*, 1–4 June 2009
7. Shamasundar R, Doddabasappa AS, Patil SS (2011) Structural modification and frequency-structure correlation to optimize handlebar performance. *International Journal of Advanced Engineering Technology* 2
8. Kalsule DJ, Askhedkar RR, Sajanpawar PR (1999) Engine induced vibration control for a motorcycle chassis frame by right combination of finite element method and experimental techniques. *SAE Technical Paper Series*
9. Bovenzi M (2005) Health effects of mechanical vibration. *G Ital Med Lav Erg* 27(1):58–64
10. Gençoğlu C, Gürel AA, Koç EC (2016) Utilization of modal test techniques for quality control of mass manufactured parts. In: *International Mechanical Engineering Congress and Exposition*

Computing in Medicine and Biology

CFD Analysis to Minimize the Spread of COVID-19 Virus in Air-Conditioned Classroom



Adnan Memon  and Balkrushna Shah 

Abstract The COVID-19 which is a respiratory disease spread by a virus of the coronavirus family has become a big problem leading to the closure of all academic as well as economic activities due to its capability to spread fast. In this study, we have investigated the effect to mix a disinfectant in aerosol form with air coming out from the air conditioning machine so it can reach all parts of the room to remove the virus and prevent the closure of certain necessary teaching–learning activities in the classroom. For this, the k - ϵ model which consists of two equations is used to numerically model the turbulent flow in the classroom. From the analysis, it can be found that high turbulent zones are formed in the room which can be an effective way of distributing the aerosol-based disinfectant in the classroom and from the particle tracker we can see the aerosol-based disinfectant reaching every corner.

Keywords COVID-19 · Air-conditioning · CFD

1 Introduction

The COVID-19 also called coronavirus named after the coronavirus family [1, 2] has become a global pandemic. Even after a year of the declaration of a pandemic by the World Health Organization (WHO), the condition has not improved much, one after other waves are striking and resulting in the loss of millions of lives since its start. The virus has a high infection rate due to which it rapidly infects many people at a time. Mostly the spread takes place through contact of an infected person or indirect contact from his/her clothes, utensils, etc. [3, 4]. Studies also show airborne transmission of virus when droplets from sneeze and cough travel through the air in an isolated space [2, 5, 6]. The symptoms mainly include fever headache, cough, weakness at its initial stage, which further leads to severe respiratory illness like pneumonia and severe damage to lungs and other respiratory organs [7, 8].

A. Memon · B. Shah (✉)
Nirma University, Ahmedabad, India
e-mail: balkrushna.shah@nirmauni.ac.in

As per the WHO weekly epidemiological update of 6 April [9], the second wave was more devastating than the earlier one, especially in the areas of South-East Asia (notably India) and Western Pacific regions leading to a high number of infections rates and mortalities. Due to this high infection rate, the government had to implement strict lockdowns in the country to prevent more fatalities. This affected the economy of the country as well as day to day life works of people. Academic institutes were also affected by this as all teaching–learning activities were needed to be carried out on online platforms. Sometimes some core subjects need on hand experience for the students so it becomes important to conduct a few offline classes as the situation is normalizing so institutions will also reopen and to prevent the third wave it is important to prevent large scale spread of this virus.

Many researchers around the globe use computational fluid dynamics (CFD) tools to study the room parameters of air like temperature, velocity, contamination level, HVAC efficiency, etc. [1, 10–12]. It is a very powerful tool to study internal airflow where multiple parameters are to be studied. We can also use the same to study the airflow pattern and particles in the air inside the classroom through particle tracking methods along with the study of the process like velocity movement, temperature contour, streamline flow and path lines. As medical treatments are evolving and vaccination being a long and tedious process, it is helpful and reasonable to study the possibilities of disinfecting the air inside a closed air-conditioned room where a machine delivers an aerosol-based disinfectant and air-conditioned air helping it spread across the room which will kill the virus and thus preventing the spread of infection and continuing our teaching–learning activities.

Bhattacharyya et al. [13] have done similar research where sanitiser was used as a disinfectant to kill the virus in the ICU rooms so that infection can be prevented from patient to patient and especially the doctors and nurses working in the ICU dedicated for COVID-19 patients. We have adopted a similar concept; in our case, the need is to prevent the spread of the virus and continue teaching–learning activities in the classroom. Dwivedi and Shah [14] concluded that cellulose cooling pad coupled with ODU of split air conditioner results in about 5% reduction in energy consumption. Chung and Hsu [15] in their research have studied how ventilation pattern is affected by the location of the diffuser, and this study can be considered for validating the numerical model for our analysis. Not much work was done in this field but from a few works, we can say that more investigation is needed in this so we tried to apply a similar concept to our case of classroom disinfection and applied particle tracking to it to study coverage of disinfectant throughout the classroom in depth. This computational model can also be applied to various other places like malls or theatres which can help control the spread and not hamper the economic and academic activities.

2 Computational Methodology

2.1 Specification of CAD Model and Numerical Model

Figure 1 shows the CAD model of the classroom which is in the A block of Nirma University which include 13 people and infrastructure like teacher's desk, student desk, inlet-outlet vent for air conditioning, aerosol disinfectant machine, etc. For ease of analysis, the students are considered sitting and the desk on which they work are clubbed together as a single solid block keeping in mind necessary dimensions.

The dimensions of the classroom are length 8940 mm, breadth 6840 mm and height 3660 mm. Working fluid in this analysis is considered as air. The definite dimensions of the other parts of the room are clubbed entity of student and desk (1220 mm × 610 mm × 1000 mm), exhaust vent (1800 mm × 300 mm), inlet vent (1000 mm × 1000 mm), aerosol disinfectant machine (1300 mm × 500 mm × 800 mm) and disinfectant air inlet (700 mm × 200 mm).

For grid generation, fluid volume is extracted from this CAD model, Fig. 2 shows the meshing of the model, along with a cross-section view of meshing, Tetrahedral meshing elements are used to generate meshing, triangle meshing elements are used at some parts where tetrahedral cannot be formed. For the CFD analysis, a commercial software package called fluent developed by Ansys Inc. is used. The simulations were carried out in a Quad-Core Ryzen 5 processor with 8 GB of RAM.

Boundary conditions are one of the most important aspects of CFD analysis, in our analysis, the inlet velocity for the air-conditioner air is taken as 3.9 m/s and at a temperature of 297 K, for the exit of air, no temperature jump, no-slip condition with

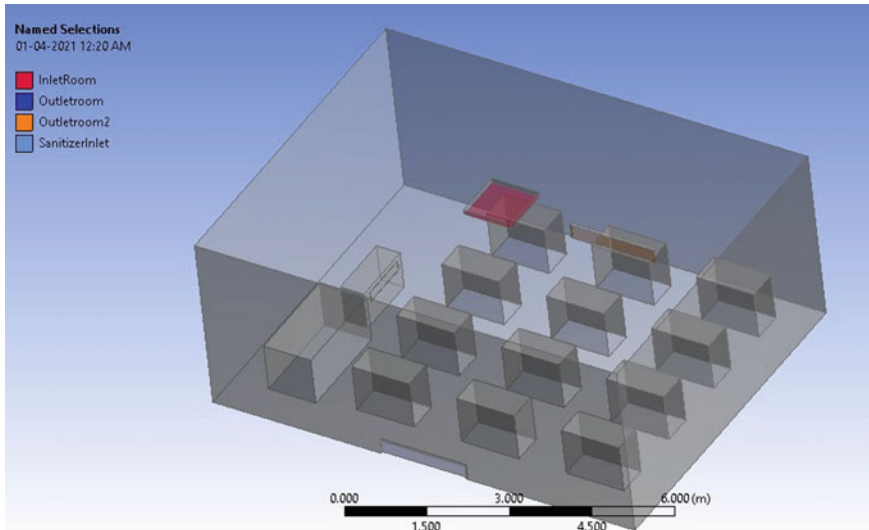


Fig. 1 Solid model of classroom

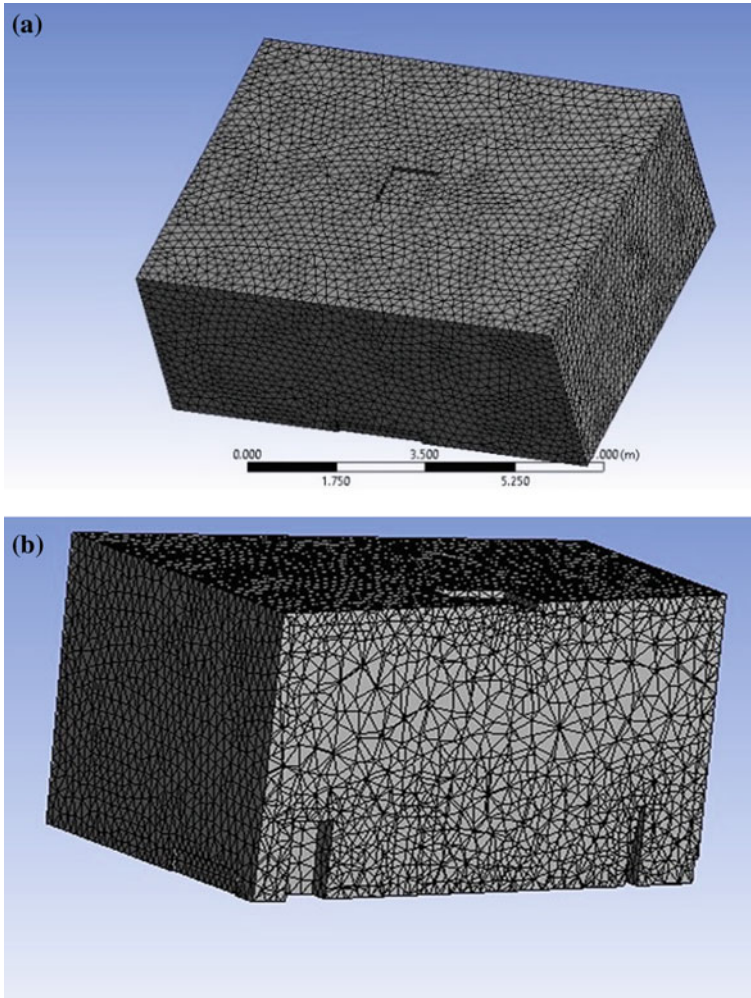


Fig. 2 Meshing view of classroom **a** isometric view and **b** section view

pressure outlet is considered. The initial temperature of room air is 303 K, and the ambient air temperature is 307 K. Aerosol-based disinfectant is injected at a speed of 1.5 m/s having a temperature of 303 K. For the sake of simplicity in analysis, continuous flow of disinfectant is considered.

For numerically modelling of the system $k-\epsilon$, turbulent model is used which consist of two-equation, the first transport variable is turbulent kinetic energy and the second transport variable is the rate of dissipation of turbulent kinetic energy. Figure 3 shows a schematic view of the inlet, outlet and location of other parts in the classroom.

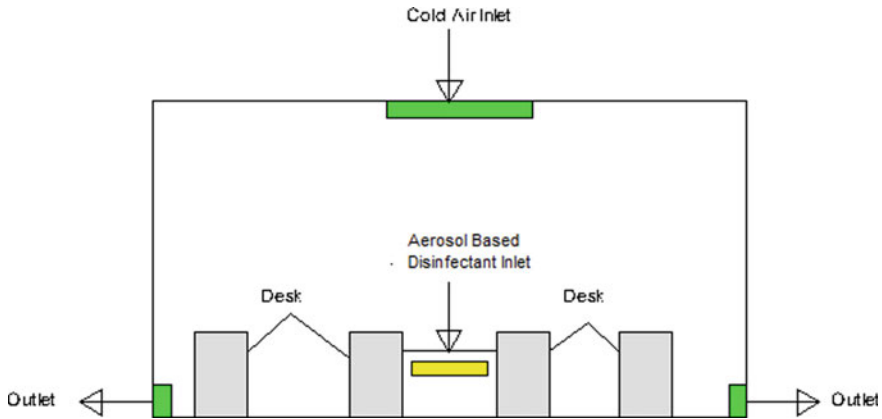


Fig. 3 Outlet and inlet for the classroom model

2.2 Validation of Numerical Model with Literature

Before studying the fluid pattern of the classroom, the present model is validated for methodology and numerical model with published and validated experiments and numerical model works. Figure 4a shows the model and Fig. 4b shows several locations where the velocity is measured, and Fig. 5 shows a comparison graph of this literature with the present model, and we can see it is in good agreement.

3 Results and Discussion

3.1 Investigation of a Classroom with a Central Air Conditioning System and Aerosol-Based Disinfectant Machine

Initially, the influence of air released from the air conditioner alone as a transient flow is studied at a time step of 3000 with a step size of 0.01 s. As shown in Fig. 6a, the streamlines are falling and strikes the floor, further, the flow rebounds from the floor and subsequently spreads towards the wall. From the top view indicated in Fig. 6b, we can see the ever-changing streamlines indicating fluid flow in the room is influenced by air originating from the air conditioning openings which are positioned at the top part of the classroom. The streamlines indicate that flow unsteadiness is established and we can move our investigation deeper in direction of mixing the aerosol-based disinfectant with this flow.

A temperature contour plot shown in Fig. 7 for the classroom depicts that aerosol-based disinfectant is released at a relatively higher temperature than of classroom,

Fig. 4 a Computational domain and b points at which velocity is measured inside the room

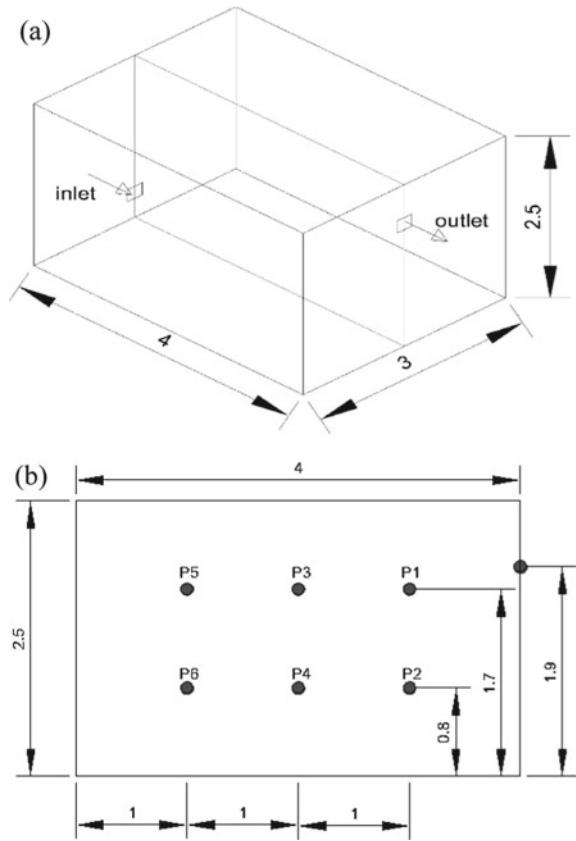
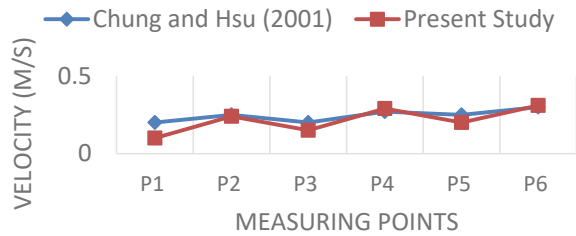


Fig. 5 Distribution of velocity at different points inside the test room at an inlet speed of 1.36 m/s



i.e. 30 °C. Better mixing can be assured due to the velocity and temperature gradient available between the air can disinfectant flow [16]. Figure 8 shows the velocity vector plot of the classroom where we can see the flow pattern is asymmetric, this asymmetry is due to the influence of temperature and velocity gradient from the disinfectant machine. It is seen from Fig. 8 that air flows from the top comes down touches the floor and slows down, then it meets disinfectant flow and mixes. It can also be seen that when it touches the floor it slows down.

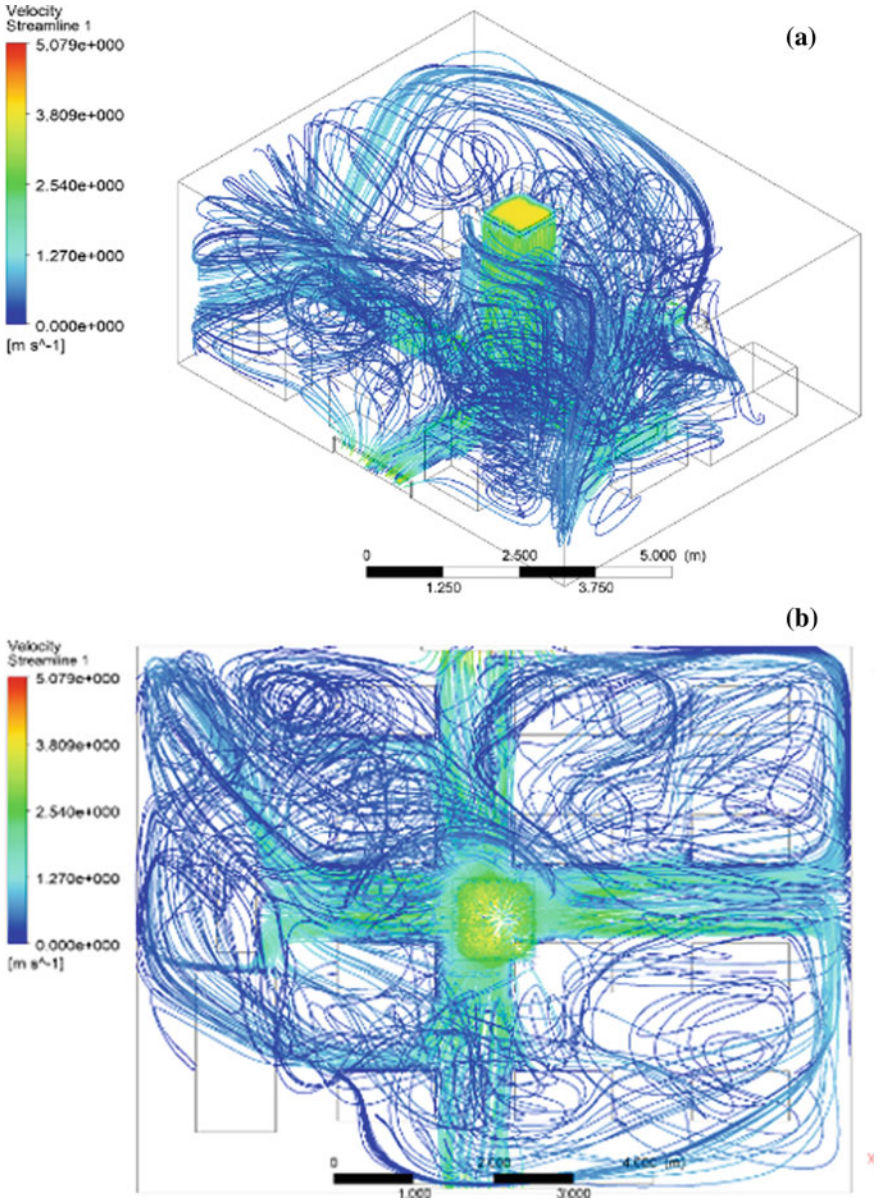


Fig. 6 Streamline flow of air-conditioner air a isometric view b top view

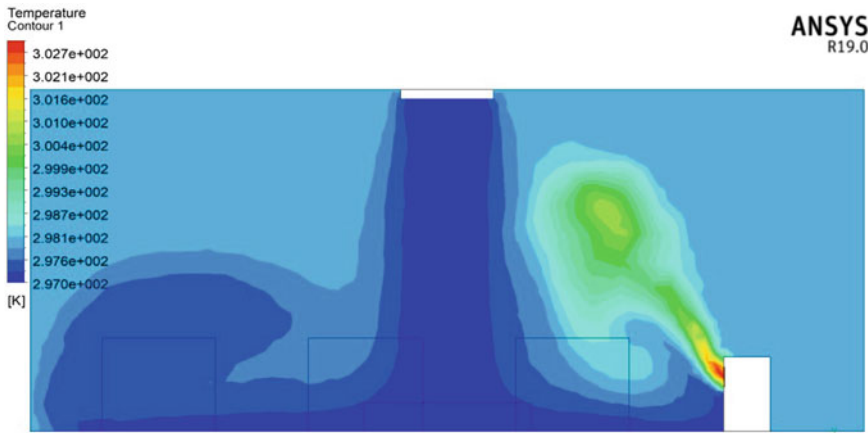


Fig. 7 Temperature contour plot

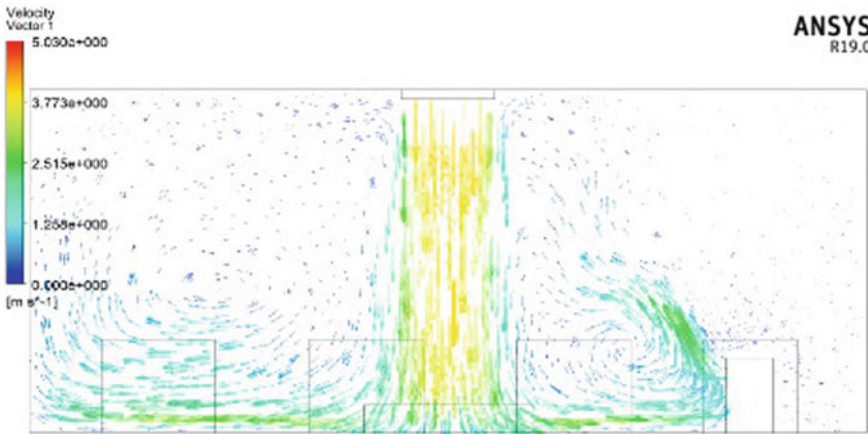


Fig. 8 Velocity vector plot

When this mixing of disinfectant and cool air takes place, large scale eddies are formed due to these eddies proper mixing of disinfectant, with cool air takes place and we can expect a spread of disinfectant across the classroom, the eddies generated can be seen and understood from turbulent kinetic energy contour plot, high turbulent zones indicate that large scale eddies formation is taking place as seen in the turbulent kinetic energy contour plot of the classroom in Fig. 9. We can see that from the figure that a high turbulent zone is created at the mixing of two flows (having turbulence kinetic energy of $0.4067 \text{ m}^2/\text{s}^2$), which indicates that a high amount of mixing will take place and ensures disinfection of airborne virus/germs with the help of disinfectant laden air.

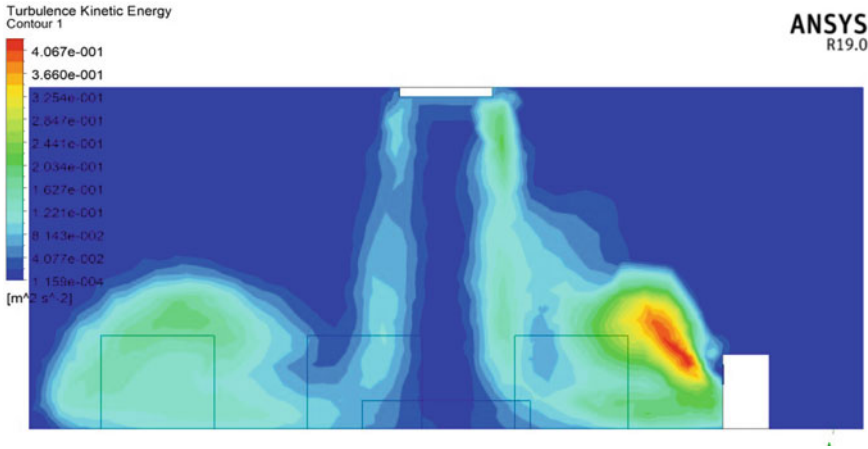


Fig. 9 Turbulent kinetic energy contour plot of the classroom

For a detailed investigation, we performed a particle tracking analysis using the DPM tool in the fluent software package. Particles of inert material with a density like aerosol-based disinfectant (700 kg/m^3) were released from the inlet of aerosol-based disinfectant, and its movements were tracked. Figure 10 shows that particles that are spreading around the machine and as they reach towards the air conditioner flow, they tend to spread across the classroom with the influence of the air conditioner flow, we can see that almost all the classroom area except the area behind the machine on the corner side is covered, and this area is not much used and with more and more circulation of air in the classroom eventually with the time that area will also get disinfected.

3.2 Investigation of the Classroom with Split Air Conditioning System and Parallel Flow Aerosol-Based Disinfectant Machine

In the Indian, subcontinent use of a split air conditioner is more than central air conditioning system, a similar investigation was also performed with two possibilities, i.e. the parallel flow of disinfectant and counter flow of disinfectant with a split air conditioning system.

Figure 11 shows a velocity vector plot of the classroom with an air conditioner where both the flows are parallel to each other, we can see that the vectors approach the floor, they tend to put down the flow of disinfectant rather than mixing. This results in disinfectant being remained stagnant near to the floor rather than mixing with air and disinfecting the classroom. To add to support of this, Fig. 12 indicates in turbulent kinetic energy contour that no eddies are formed to generate a proper

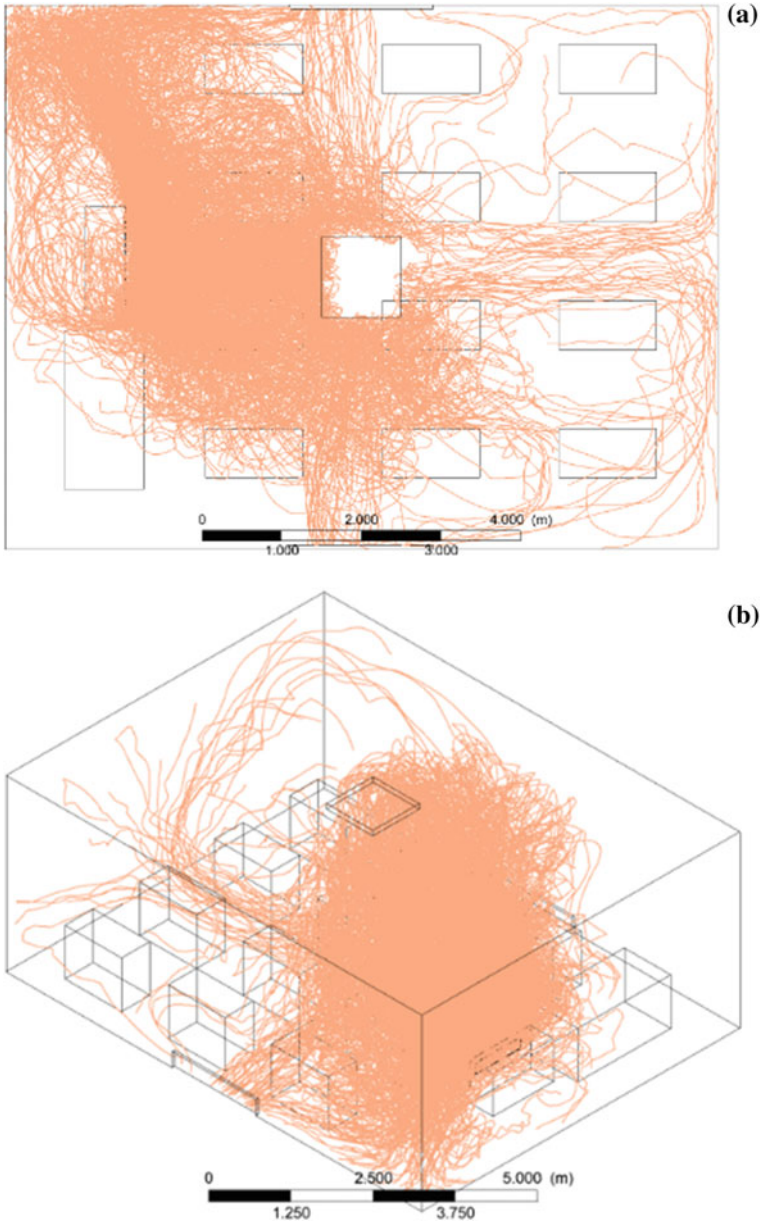


Fig. 10 Particle tracking from disinfectant machine inlet for central air conditioning system **a** top view and **b** isometric view

mixing phenomenon. This setup does not fulfil our purpose of disinfecting all areas of the classroom.

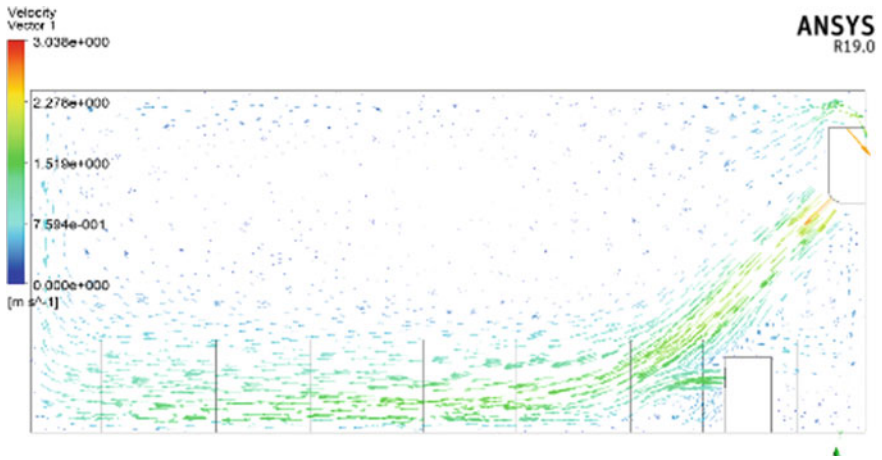


Fig. 11 Velocity vector plot for parallel flow

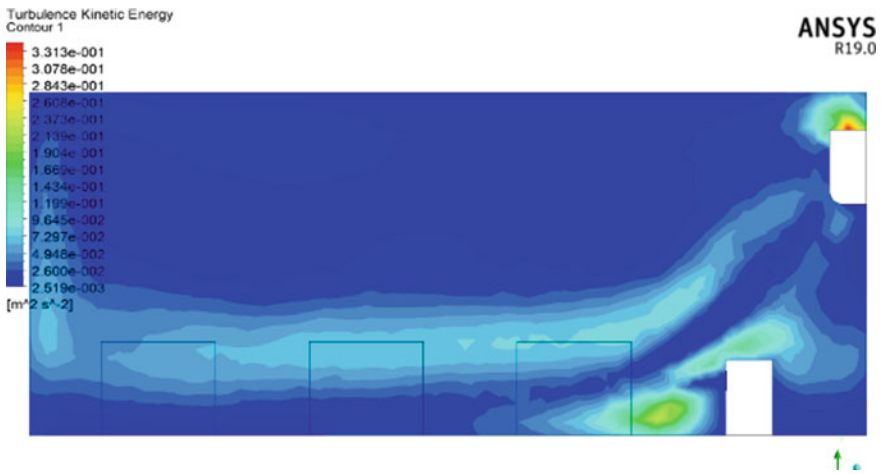


Fig. 12 Turbulent kinetic energy contour for parallel flow

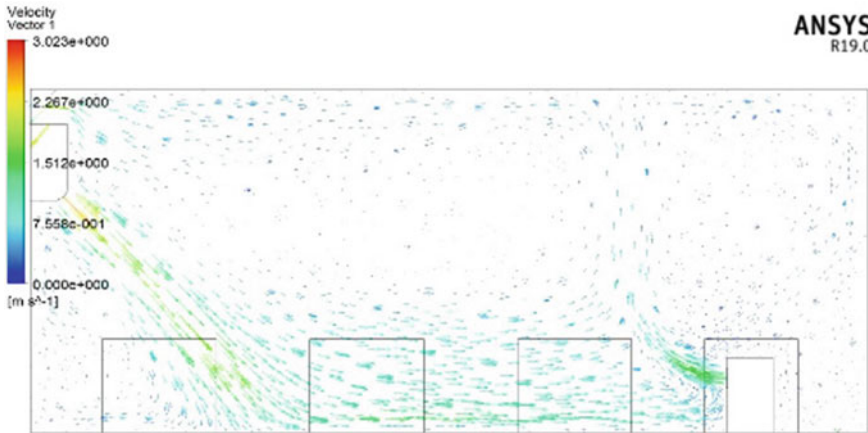


Fig. 13 Velocity vector plot for counterflow

3.3 Investigation of a Classroom with a Split Air Conditioning System and Counterflow Aerosol-Based Disinfectant Machine

Figure 13 shows velocity vectors released from the air-conditioning unit flow downwards due to the swing motion and then touches the floor where it tends to mix with the disinfectant flow which is further uplifted due to high velocity. Similar points can be noted from Fig. 14 that at the mixing region, high turbulent zones are created which suggest that eddies are formed after the flow moves upward approaches the classroom wall.

In the case of parallel flow, the disinfectant flow was made to push downwards, and hence, there will be no spreading in the classroom so no particle tracking analysis was carried out, but for counter flow particle tracking analysis was carried out as shown in Fig. 15, where it is seen that particles released from the disinfectant machine are spread moving towards the roof of room due to influence of air-conditioner air, and then, it tends to spread across the room. Further, it moves towards the outlet port of the air conditioning machine due to negative pressure at that point. We can see that almost all areas of the room are covered, there might be a little less coverage of floor part due to upliftment of disinfectant.

The biggest problem with the split air conditioner is the recirculation of air inside the room, and this contaminated air may recirculate throughout the room many times. This may lead to more spread of the virus within the room.

It is not desirable to use a split air conditioner system with recirculation of air in this situation; however, there may arise need to use this air conditioner due to unbearable heat or to keep computing system cool for its better performance, we can do a few things to keep a check on the spread of the virus.

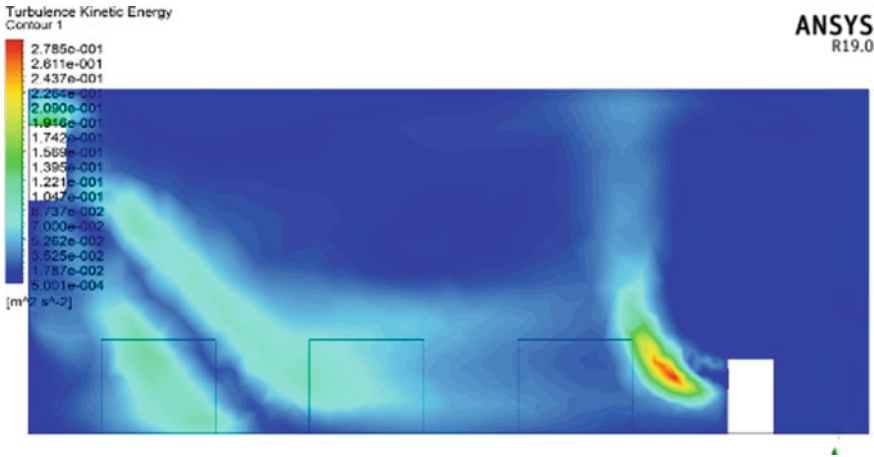


Fig. 14 Turbulent kinetic energy contour for counterflow

- Using air conditioning system with filters pre-installed or installing air filters as per guidelines from reliable organizations.
- External air can be provided in the room through the opening of one window which will help in air change in the room, this may lead to higher thermal load on the system but it can prevent frequent recirculation of air.
- Adding gable/exhaust fan to get maximum air circulation.

4 Conclusion

In the time of COVID-19, as the situation is going out of control for many countries, it has become most important to prevent the airborne transmission of the virus. This is done by implementing restrictions on all types of activities including academics where there is a chance of crowd gathering, this leads to many difficulties, to overcome this and continue some important gatherings we have proposed this solution, especially for teaching–learning activities.

The main objective of this investigation was to study that proper mixing of both air-conditioned air and aerosol-based disinfectant takes place so that all parts of the room can be sanitiser, in the present study, a CFD analysis is carried out to study this. For numerically modelling, the turbulent flow in the classroom k- ϵ turbulent model is used which involves two equations. This study was carried out considering a central air conditioning system as well as a split air conditioning system.

From this analysis, we can say that zones having high turbulency generated inside the room may be an efficient way to distribute disinfectant to every corner of the classroom. A high level of mixing can be seen from flow visualization and kinetic energy contour. To investigate, it further we did a particle tracking that shows that disinfectant flow will cover the entire room due to the influence of air-conditioned

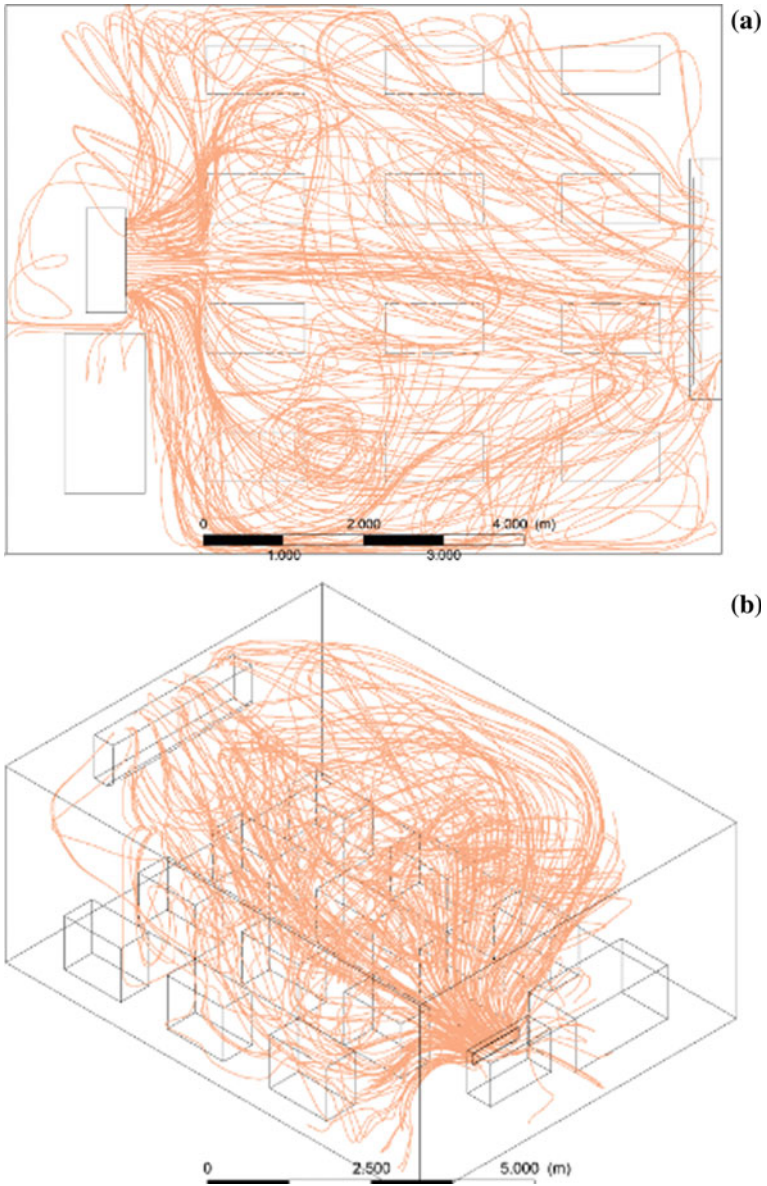


Fig. 15 Particle tracking from disinfectant machine inlet for split air conditioning system and counter flow **a** top view and **b** isometric view

air. So, we can say that a good amount of mixing of both the flows take place and it also covers all areas of the room. A similar study was done with a split air conditioning system where both parallel and counterflow patterns were considered, counterflow pattern yields better as compared to parallel flow which tends to push the disinfectant downwards instead of spreading it everywhere. Particle tracking of counterflow pattern was also done which shows disinfectant covering all areas of the whole classroom.

The numerical model can also be used for any other places like shopping malls, theatres, etc. Results from this can also be used to optimize the design of ducting for the central air conditioning system.

Our study was limited with many assumptions like we considered the flow of disinfectant as continuous, as a part of future work we think that this study can be more accurate to real-world if the flow of disinfectant can be considered intermittent and investigated further. Furthermore, investigation of multiple aerosol-based disinfectant machines can also be done along with various swing angles of air-conditioner air flows.

References

1. Rui Z, Guangbei T, Jihong L (2008) Study on biological contaminant control strategies under different ventilation models in hospital operating room. *Build Environ* 43(5):793–803
2. Zu ZY et al (2020) Coronavirus disease 2019 (COVID-19): a perspective from China. *Radiology* 296(2):E15–E25
3. Burkett J (2021) Defining viruses and droplet release. *ASHRAE Journal*
4. Ahmadi M, Sharifi A, Dorosti S, Ghouschi SJ, Ghanbari N (2020) Investigation of effective climatology parameters on COVID-19 outbreak in Iran. *Sci Total Environ* 729:138705
5. Setti L et al. (2020) The potential role of particulate matter in the spreading of COVID-19 in Northern Italy: first evidence-based research hypotheses. *medRxiv*, p 2020.04.11.20061713
6. Burkett J (2021) Airborne transmission and distribution. *ASHRAE Journal*
7. Peng PWH, Ho P-L, Hota SS (2020) Outbreak of a new coronavirus: what anaesthetists should know. *Br J Anaesth* 124(5):497–501
8. Huang C et al (2020) Clinical features of patients infected with 2019 novel coronavirus in Wuhan, China'. *The Lancet* 395(10223):497–506
9. Weekly epidemiological update on COVID-19—6 April 2021. <https://www.who.int/publications/m/item/weekly-epidemiological-update-on-covid-19---6-april-2021>. Accessed 18 April 2021
10. Jacob S, Yadav SS, Sikarwar BS (2019) Design and simulation of isolation room for a hospital. Springer, Singapore
11. Memarzadeh F (2011) Improved strategy to control aerosol-transmitted infections in a hospital suite. Conference proceedings by ASHRAE 2011:1–10
12. Peng S, Chen Q, Liu E (2020) The role of computational fluid dynamics tools on investigation of pathogen transmission: prevention and control. *Sci Total Environ* 746:142090
13. Bhattacharyya S, Dey K, Paul AR, Biswas R (2020) A novel CFD analysis to minimize the spread of COVID-19 virus in hospital isolation room. *Chaos, Solitons Fractals* 139:110294
14. Dwivedi S, Shah BA (2020) Review and experimental study on performance improvement of split air conditioner by reducing inlet air temperature to the ODU. *J Phys: Conf Ser* 1706(1):012211

15. Chung KC, Hsu SP (2001) Effect of ventilation pattern on room air and contaminant distribution. *Build Environ* 36(9):989–998
16. Wang SJ, Devahastin S, Mujumdar AS (2006) Effect of temperature difference on flow and mixing characteristics of laminar confined opposing jets. *Appl Therm Eng* 26(5–6):519–529

A Viable Approach to Medical Image Processing for CFD Simulations of the Upper Respiratory Tract



Akash James , Joshua Mathew Jacob , Liza Mathew ,
and Ajith Kumar Arumugham-Achari 

Abstract We discuss a fast and easy approach to create the upper airway geometry of human lungs from medical images to perform Computational Fluid Dynamics (CFD) simulations. We have employed a combination of open-source and commercial image processing and CFD applications. From Computed Tomographic (CT) images of lungs available in the public medical repository, we were able to recreate the 3D structure of the upper airways up to 6 generations, which after postprocessing was used to investigate the flow pattern during respiration. The uneven surface of the real geometry, the curvature of the flow paths and asymmetric bifurcations lead to definite and distinguishable variation in flow pattern unlike that in studies with idealized lung geometries, such as that with the Weibel model. The nature of flow at various positions along the airways was investigated employing simple boundary conditions of constant inlet velocity at the truncated trachea and constant outlet pressure at the truncated bronchi (fourth generation). For the preliminary simulations, we could observe the presence of counter-rotating vortices (Dean flow) as well as asymmetric flow rate across the left and right lung (a 50% more flow toward the right bronchus).

Keywords Medical imaging · Image segmentation · Airway tree · Human lung · Respiration · CFD · Respiratory tract · 3D Slicer · Autodesk® Meshmixer™ · Ansys Fluent®

1 Introduction

The human lung is one of the most intriguing and complex organs. Apart from oxygenation of the blood, it plays a pivotal role in thermoregulation of the body and filtration of the systemic circulation [1]. For centuries, its complexity has captured

A. James · J. M. Jacob · L. Mathew · A. K. Arumugham-Achari (✉)
Department of Mechanical Engineering, Rajagiri School of Engineering and Technology, Cochin,
Kerala, India
e-mail: ajithk@rajagiritech.edu.in

A. James
e-mail: akashj@rajagiritech.edu.in

the imagination of not only physicians but scientists and mathematicians as well. There have been innumerable attempts to decipher the enigma of respiration. For a long time, scientists relied on in vitro studies performed on cadaver lungs. Weibel's [2] pioneering studies into the morphology of the lung shed light on its structural complexities. Based on his studies, he was also able to propose a simplified set of geometrical models for the airway tree structure. Scholars around the world have relied on such simplified models to investigate the flow characteristics inside the human lung [3–5]. In addition to helping physicians understand the working of the lung, the study of flow characteristics will also help us predict aerosol transport and deposition in the lung. This will help analyze the effect of air pollution on human health, the efficacy of aerosol drug delivery, etc. Despite the unrealistic nature, simple geometric models such as Weibel's were relied on, mostly because of their computational attractiveness and the impracticality of in vivo experiments. But with the advancements in medical imaging technology and computing power, it is becoming ever easier to perform realistic modeling of the lung and computational analysis of the flow within it. To model the lung, its entirety is still a gargantuan task [6] and one can only hope that with the present pace of advancements, the task will become even handier in the decades to come. In this paper, we are discussing, a viable, off-the-shelf approach to generate a realistic upper airway geometry by medical image segmentation of the CT image of a human lung and performing preliminary CFD simulation of a steady flow through the geometry.

2 Methodology

We adopt a feasible approach of obtaining actual CT images from open-source platforms, thereafter, processing them to create an airway geometry of acceptable quality. Subsequently, a computational grid for flow simulation is carefully generated taking into consideration the CFL number (pertaining to a minimum cell size of 6.2×10^{-06} m, the software tool Ansys Fluent[®] being a transient finite volume solver).

2.1 *Upper Airway Segmentation*

We seek to obtain a realistic geometry of the upper airway by segmentation of a CT image. With better resolution images and a greater number of slices, the airway geometry becomes more resolved and realistic. We have chosen the best available image for this purpose.

Image Acquisition. Hundreds of medical images (redacting patient details) are now available to the public to facilitate scientific research. A few repositories are, VIA/I-ELCAP Public Lung Image Database [7], the Lung Image Database Consortium (LIDC), and the Image Database Resource Initiative (IDRI): A completed reference

database of lung nodules on CT scans [8], The Cancer Imaging Archive (TCIA) [9], Harmonized Cancer Datasets: Genomic Data Commons Data Portal (U.S. Department of Health and Human Services), etc. In this study, we have made use of a Computed Tomographic (CT) image of a thorax obtained from the VIA/I-ELCAP database. CT imaging makes use of X-Rays (slightly more powerful than the standard X-Ray machines) to differentially highlight various elements based on their density [10]. Inside of the airway tree and the lung parenchyma (being more sponge-like), it consists of mostly air and thus allows the rays to pass right through (radiolucent). Thus, these parts appear darker in the images (which are negatives of the original). A typical CT imaging produces multiple such images which are slices of the part being imaged (sample slices shown in Fig. 1). As the technology is maturing, the number of slices and the resolution is improving, we can image the thinnest of slices with the highest resolutions. CT images are typically stored in Digital Imaging and Communications in Medicine (DICOM) format, which apart from the pixel data, stores the patient information within its header [11]. The image used for this study is generated by GE Light Speed Ultra 8 Slice CT (276 Slices, Slice thickness of 1.25 mm, and 120 kVp).

3D Image Segmentation. Segmentation is commonly performed using techniques like thresholding, region growing, active contour segmentation, etc. [12–14]. Open-source image processing platforms such as 3D Slicer [15] and ITK-SNAP are equally equipped for the task, though we employed the former. Commercial packages such as Mimics[®] Innovation Suite offer more functionality, which has a section dedicated to pulmonary segmentation that employs advanced region growing and leak detection algorithms to segment the airway tree.

Here we segmented the upper airway geometry from the CT images by a process known as region growing in which a seed point for the region to be segmented is manually selected and adjacent voxels meeting predefined criteria are added to the region. This helped us create a geometry that resembled the vast network of air pockets within the lung, from which the airway tree was isolated by slicing, removing, and erasing the rest of the parenchyma.

Postprocessing of the 3D Geometry. The geometry thus created has a highly irregular surface topology. Most of the irregularities, though not all, are anatomically accurate. Some irregularities seep in due to the limitations of the imaging (viz. limitation to perform higher resolution imaging due to risk of high radiation intensities, availability of images having lower resolution, and lower number of slices in public repositories, etc.) and processing techniques (For example, limitations in the algorithm to exactly delineating sporadic regions of noise). Thus, some smoothening of the surface is essential to deliver accurate models and to ease the grid generation process. This was performed using open-source software Autodesk[®] Meshmixer[™]. The segmented geometry was exported as an STL file into the software. Meshmixer[™] allows us to sculpt the surface to get rid of some of the anatomically inaccurate irregularities such as peaks, holes, etc. Further smoothening of the surface for the ease of grid generation was done in Ansys SpaceClaim[®].

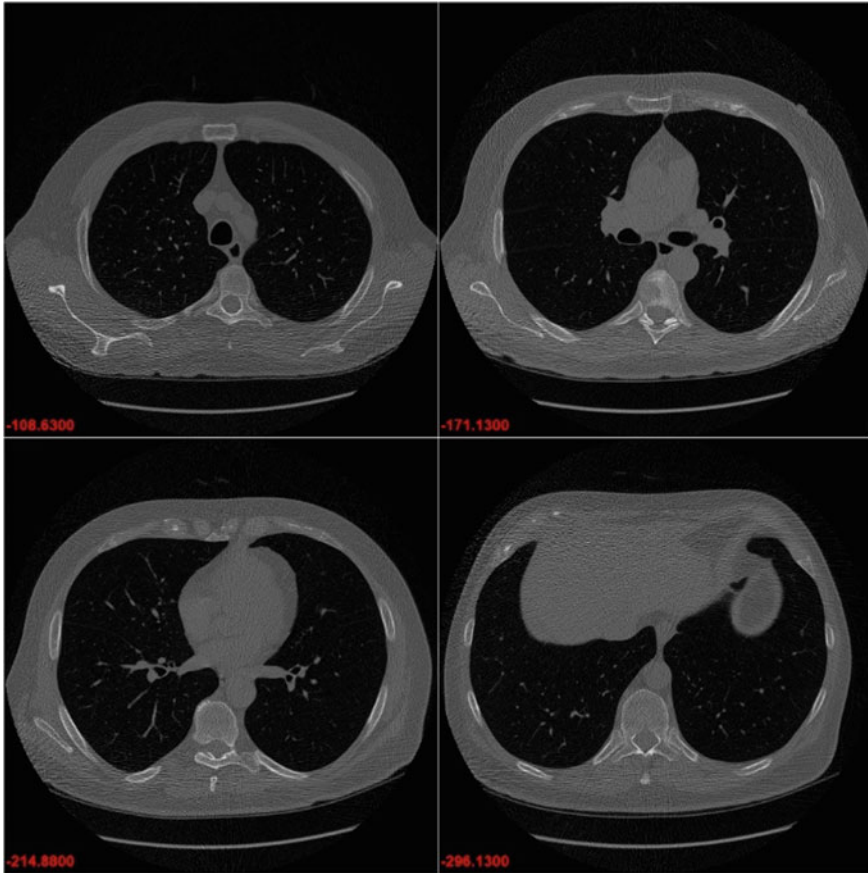


Fig. 1 Four representative slices of the CT image of the thorax that is used in the study (the slice position is indicated in the lower-left corner, the number decreasing from top to bottom)

2.2 CFD Analysis

A steady flow simulation is only envisaged for the present study because we aim to test the feasibility of the mentioned combination rather than employing realistic boundary conditions.

Mesh Generation. Generating computational grids for the respiratory tract is equally, if not more, challenging than segmentation, mostly because of the irregularities in the surface. Even an unstructured tetrahedral mesh for such complex geometry is challenging, time-consuming, and takes multiple attempts to create. The polyhedral meshing scheme available in Ansys Fluent[®] is an improvisation over the tetrahedral meshing, and it offers better computational efficiency, stability, convergence, and mesh quality control [16].

Governing Equations. For this preliminary analysis, we assumed a steady, laminar, and incompressible flow in a gravitational field. The conservation of mass and momentum is given by:

$$\nabla \cdot \vec{v} = 0 \quad (1)$$

$$\rho \frac{d\vec{v}}{dt} = -\nabla p + \rho \vec{g} + \mu \nabla^2 \vec{v} \quad (2)$$

where \vec{v} is the air velocity, p is the air pressure, μ is the dynamic viscosity, ρ is the air density, and \vec{g} is the constant gravitational acceleration. The air is assumed as a Newtonian fluid with a constant density of 1.225 kg/m^3 and viscosity of $1.7984 \times 10^{-05} \text{ kg/m s}$, referring to the physical air properties given by the Ansys Fluent® database.

Steady-State Analysis. The flow through the lung was simulated with a constant inlet velocity that represents a lightly active minute volume ventilation of a healthy adult male (18 l/min). The outlets were assumed to be at ambient pressure conditions. A no-slip boundary condition was enforced at the walls to capture the viscous effects. As opposed to this, some studies had tried to enforce the non-uniform lobar distribution of flow through boundary conditions [17]. But Elcner et al. [18] showed that it had minimal effect on the velocity profile throughout the geometry.

After obtaining the grids, a steady-state laminar flow was sought with uniform inlet velocity. Semi-Implicit Method for Pressure-Linked Equations (SIMPLE) scheme was adopted for the pressure–velocity coupling and a residual of under 10^{-06} was set as convergence criteria. Computation was performed at the Sunya Labs High-Performance Computing Facility, Rajagiri School of Engineering and Technology. The flowchart of the methodology is shown in Fig. 2.

3 Results

3.1 Segmented Geometry

In the airway, each branching produces a new generation dichotomously (exception rather than a rule), with one parent and two children [2]. The trachea is typically designated as the zeroth generation [1]. By the process of segmentation explained earlier, we were able to obtain a minimum of 4 generations along all the branches and up to 6 in some distal ones (refer Fig. 3.). Some of these flow paths were trimmed at fourth generation (using Ansys SpaceClaim®) for uniformity across all paths, thus reducing the total outlets to 18. The trimming was also done at the inlet to the trachea to help in clearly defining a plane surface at the inlet and outlets for the convenience of applying the boundary conditions. For a more advanced study, the segmented

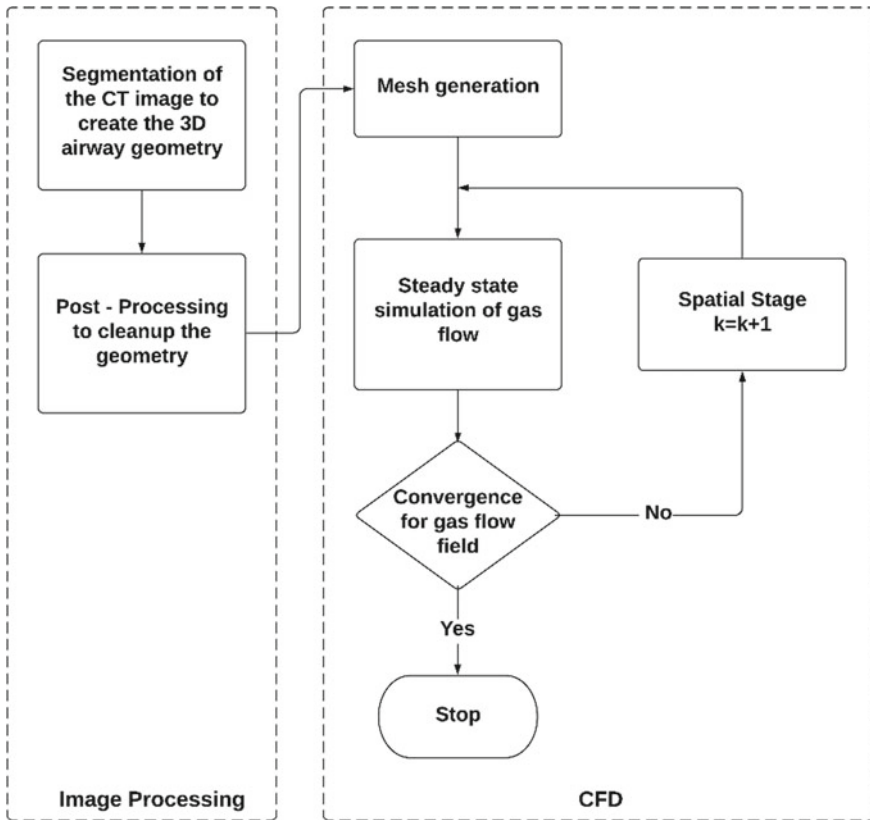


Fig. 2 Process flowchart

geometry could be compared with the ground truth through the Dice Similarity Coefficient in the software itself. Thaha et al. [19] have proposed a more robust evaluation tool for 3D medical image segmentation employing different evaluation metrics.

3.2 Meshing

The segmented geometry was meshed by using polyhedral meshing in Ansys Fluent[®], generating up to 4.2×10^5 cells at which we were able to obtain grid-independent results with acceptable orthogonal quality and aspect ratio as recommended by the solver (refer Fig. 4).

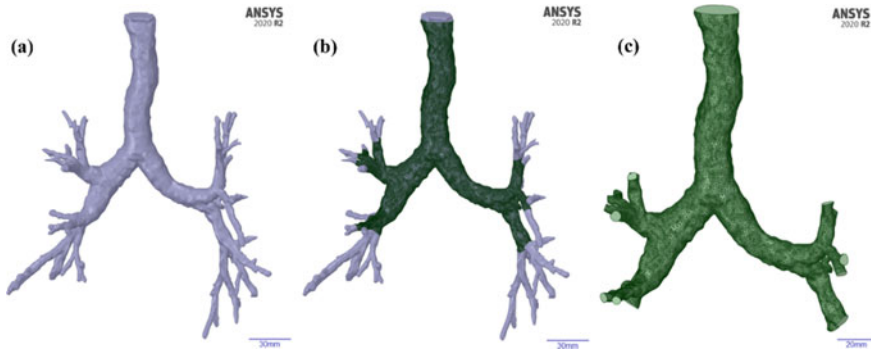


Fig. 3 Upper airway geometry (anterior view) generated from CT image segmentation, **a** has around 6 generations toward the lower lobes on either side. Some of these flow paths were trimmed at the fourth generation for uniformity along all the flow paths, **c** shows the resulting geometry, and **b** is a comparison of both

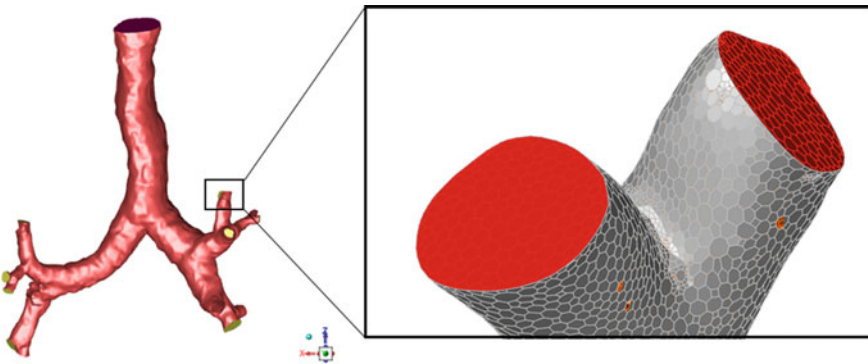


Fig. 4 Computational grid generated with Ansys Fluent® polyhedral scheme (airway viewed posteriorly)

3.3 Flow Pattern

Flow patterns corresponding to breathing during light activity were obtained. The irregular geometry of the airway results in an asymmetric flow distribution as one would expect. From the measurements taken at approximate midsections of both main bronchi, it is evident that the cross-sectional area of the right bronchi is significantly larger than that of the left. For this reason, the area-averaged flow through the right bronchi at 0.18 l/s, is around 50% more than that through the left (0.12 l/s), even though the average velocity through the left bronchi is slightly (around 6.5% at the selected section) greater. The velocity vector plots on the cross-sectional planes along different generations are shown in Fig. 5. The centripetal force when the

flow is bent toward either of the main bronchi is large enough to create counter-rotating vortices (Dean flow). Other studies on realistic geometries have noted that this may not always be the case. With low Reynolds number flows, smaller angles of bifurcation, or shorter bronchi lengths, Dean flow may not develop in the first branching [20, 21]. The flow asymmetry, as mentioned earlier, is also evident from the velocity and pressure contours on a coronal plane shown in Fig. 6. Though flow asymmetry and Dean flow pattern are reported in studies on realistic geometries [20, 21], it is not advisable to compare the magnitude of those, as the geometries would be unique to the individual and the exact values may not agree with the present findings. Nevertheless, it would be interesting to see patterns/similarities, if any, that would emerge from a study conducted on a broader collection of images. Such a study is beyond the scope of the present work.

4 Conclusion

A viable method for obtaining a realistic 3D geometry for CFD studies is laid out in this work. After obtaining a CT image of the lung from an online repository, we were able to segment the same to obtain an airway tree up to around the 6th generation. The geometry after necessary postprocessing was used for preliminary computational studies of flow. The results revealed asymmetric flow and secondary Dean flow patterns akin to results available in the literature. The comparison with other studies involving realistic lung geometries also suggests intersubject variability of such flow patterns.

The quality of the image plays a pivotal role in the ease of segmenting an airway volume. As imaging technologies evolve, delivering better resolution images, we are being better equipped to derive more detailed segmentation of pulmonary structures. Online repositories of such images, segmentation algorithms, and computational power are also poised to grow more robust empowering researchers even more.

The scope of the work can be expanded on several fronts to deliver more accurate predictions. A transient condition across the boundaries is necessary for more sensible and realistic results. The flow through the more distal and narrower airways and the lung parenchyma can be modeled as a flow across a porous media as proposed by DeGroot and Straatman [22]. The transportation and deposition of aerosols along the airway will also be interesting from a pharmaceutical (finding optimal particle size distribution for patient-specific and efficient drug delivery) and public health (determining the effect of pollutant aerosols on the health of individuals) standpoint. This is possible through broadening the spectrum of biomedical computations on aerosol inhalation, incorporating a broader patient database (combinations specific to age group, medical history, drug particulate size distribution, etc.)

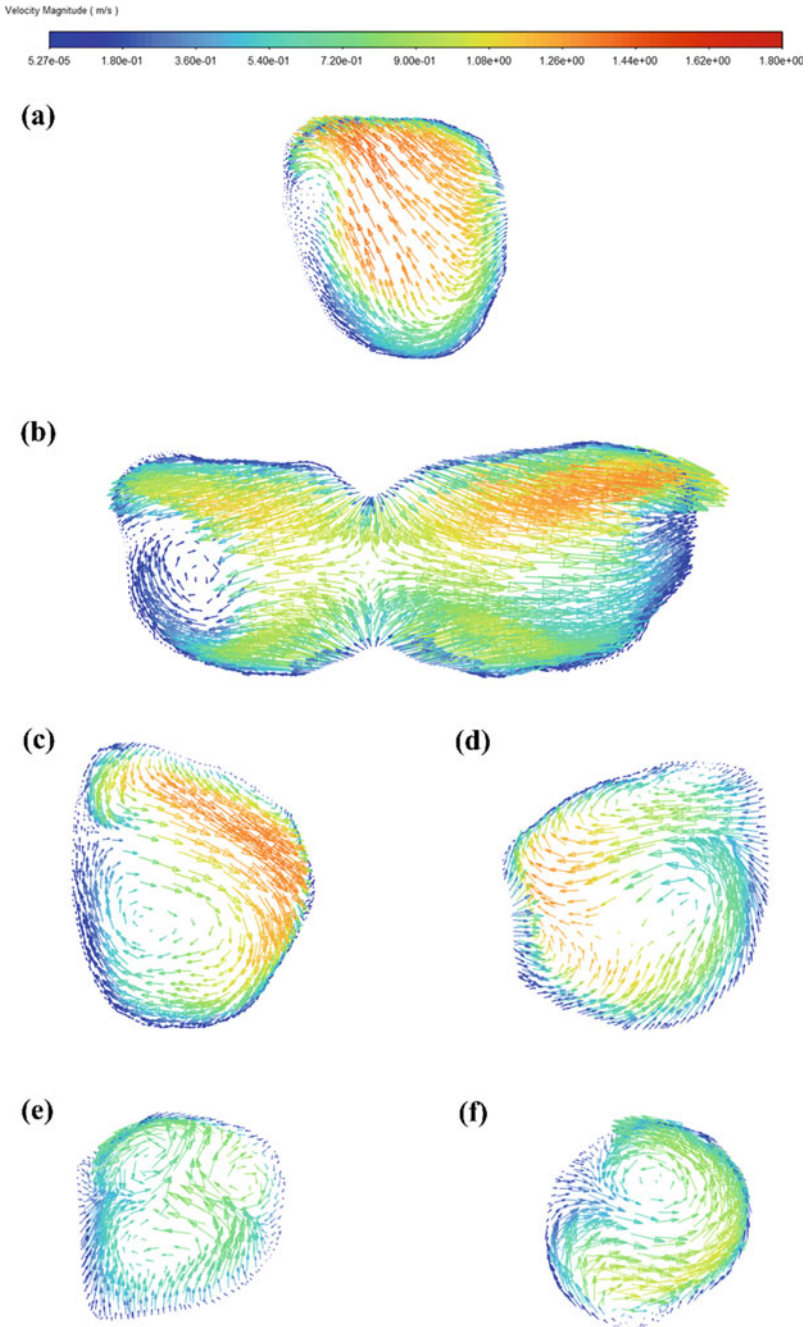


Fig. 5 Planar velocity vector plots along the cross-section of **a** trachea, **b** carina, **c** right main bronchus, **d** left main bronchus, **e** one of the right lobar bronchi (second generation), and **f** one of the left lobar bronchi (second generation)

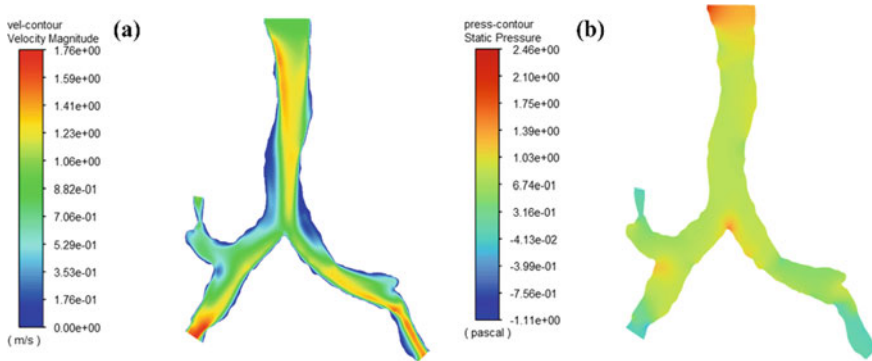


Fig. 6 Velocity **a** and pressure **b** contour plots in the coronal plane reveal the asymmetric flow distribution across the branches

References

1. Lumb AB (2017) Nunn's applied respiratory physiology, 8th edn. Elsevier Health Sciences, Amsterdam
2. Weibel ER (1963) Morphometry of the human lung. Springer, Berlin
3. Zhang Z, Kleinstreuer C, Kim CS (2001) Flow structure and particle transport in a triple bifurcation airway model. *J Fluids Eng* 123(2):320–330
4. Liu Y, So RMC, Zhang CH (2002) Modeling the bifurcating flow in a human lung airway. *J Biomech* 35(4):465–473
5. Liu Y, So RMC, Zhang CH (2003) Modeling the bifurcating flow in an asymmetric human lung airway. *J Biomech* 36(7):951–959
6. Walters DK, Luke WH (2010) A method for three-dimensional Navier–Stokes simulations of large-scale regions of the human lung airway. *Journal of Fluids Engineering* 132(5). <https://doi.org/10.1115/1.4001448>
7. VIA Research Group, Cornell University: Public Lung Image Database. VIA/I-ELCAP Public Access Research Database (2010)
8. Armato SG 3rd, McLennan G et al (2011) The lung image database consortium (LIDC) and image database resource initiative (IDRI): a completed reference database of lung nodules on CT scans. *Med Phys* 38:915–931
9. Clark K et al (2013) The cancer imaging archive (TCIA): maintaining and operating a public information repository. *J Digit Imaging* 26(6):1045–1057
10. Caldemeyer KS, Buckwalter KA (1999) The basic principles of computed tomography and magnetic resonance imaging. *J Am Acad Dermatol* 41(5):768–771
11. Varma DR (2012) Managing DICOM images: tips and tricks for the radiologist. *The Indian Journal of Radiology and Imaging* 22(1):4–13
12. Rosell J, Cabras P (2013) A three-stage method for the 3D reconstruction of the tracheo-bronchial tree from CT scans. *Comput Med Imaging Graph* 37(7–8):430–437
13. Aykac D et al (2003) Segmentation and analysis of the human airway tree from three-dimensional X-ray CT images. *IEEE Trans Med Imaging* 22(8):940–950
14. Van Ginneken B, Baggerman W, van Rikxoort EM (2008) Robust segmentation and anatomical labeling of the airway tree from thoracic CT scans. In: International conference on medical image computing and computer-assisted intervention. Springer, Berlin
15. Fedorov A et al (2012) 3D slicer as an image computing platform for the quantitative imaging network. *Magn Reson Imaging* 30(9):1323–1341

16. Yu F et al (2021) Tutorial: understanding the transport, deposition, and translocation of particles in human respiratory systems using computational fluid-particle dynamics and physiologically based toxicokinetic models. *J Aerosol Sci* 151:105672
17. Yin Y et al (2010) Simulation of pulmonary air flow with a subject-specific boundary condition. *J Biomech* 43(11):2159–2163
18. Elcner J, Chovancova M, Jichal M (2014) The influence of boundary conditions to the flow through model of upper part of human respiratory system. *EPJ Web of Conferences* 67:02025
19. Taha AA, Hanbury A (2015) Metrics for evaluating 3D medical image segmentation: analysis, selection, and tool. *BMC Med Imaging* 15:29
20. Luo HY, Liu Y (2008) Modeling the bifurcating flow in a CT-scanned human lung airway. *J Biomech* 41:2681–2688
21. Kakade PP, Mishchiy N, Annapragada AV (2002) Computational fluid dynamics simulation of airflow and aerosol deposition in human lungs. *Annu Int Conf IEEE Eng Med Biol—Proc* 2:1493–1494
22. DeGroot CT, Straatman AG (2016) A conjugate fluid–porous approach for simulating airflow in realistic geometric representations of the human respiratory system. *Journal of Biomechanical Engineering, American Society of Mechanical Engineers Digital Collection* 138(3). <https://doi.org/10.1115/1.4032113>

Evaluation of Hemodynamics Parameters in Carotid Bifurcation System using Numerical Simulation



H. N. Abhilash , S. M. Abdul Khader , Raghuvir Pai , Nitesh Kumar ,
Mohammad Zuber , John Corda, and Masaaki Tamagawa 

Abstract Hemodynamics plays a major role in the development of numerous diseases and disorders, including atherosclerosis and stroke. Hemodynamic forces must be adequately mapped to precisely predict and avoid various illnesses and disorders. Blood is a complicated biological fluid that contains constituents, such as erythrocytes that cause it to behave in a non-Newtonian manner. This component is usually overlooked while studying carotid blood flow, and blood is modeled as a Newtonian fluid with constant viscosity. In the present study comparison of hemodynamics in carotid artery for Newtonian viscosity model and non-Newtonian Carreau-Yasuda (CY) viscosity model is done. Computational fluid dynamics analysis is carried out for four patient-specific healthy carotid artery models. The geometry of the carotid artery is obtained from a CT scan and a 3D model is generated using MIMICS. Blood enters the carotid artery through a common carotid artery (CCA) and splits into two arteries named internal carotid artery (ICA) and external carotid artery (ECA). The pulsatile velocity boundary condition is considered at CCA, and the pulsatile pressure boundary condition is considered for both ICA and ECA. The results obtained for both Newtonian and Carreau Yasuda's viscosity models are

H. N. Abhilash (✉) · S. M. A. Khader · R. Pai · N. Kumar · M. Zuber · J. Corda
Manipal Academy of Higher Education, Manipal, India
e-mail: abhilash.n2@learner.manipal.edu

S. M. A. Khader
e-mail: smak.quadri@manipal.edu

R. Pai
e-mail: raghuvir.pai@manipal.edu

N. Kumar
e-mail: nitesh.naik@manipal.edu

M. Zuber
e-mail: mohammad.zuber@manipal.edu

J. Corda
e-mail: john.corda@learner.manipal.edu

M. Tamagawa
Kyushu Institute of Technology, Kyushu, Japan
e-mail: tama@life.kyutech.ac.jp

studied and compared. Wall shear stress is calculated and when compared, results obtained from the Newtonian viscosity model overestimates WSS in certain regions like CCA, ICA, and ECA.

Keywords Carotid artery · Newtonian and Carreau-Yasuda · Wall shear stress

1 Introduction

The study of developing interdisciplinary topics has been made easier due to recent developments in the computing domain. Currently, computer simulations in the biomedical field assist physicians in making decisions. Simulations are used in a wide range of applications, assisting in prognosis, and complementing current diagnostic techniques. Simulations of blood flow in flexible arteries using computational fluid dynamics (CFD) and fluid–structure interaction (FSI) give a quantitative picture of flow in the cardiovascular system, assisting researchers, and clinicians in better understanding cardiovascular disease [1, 2]. By some days nearer, radiological data acquired from patients, along with post-computational simulation processing, will aid clinicians in determining treatment decisions. CFD has become a prominent non-invasive approach for accessing hemodynamics, offering evaluation information on blood pressure, velocity, shear stress, and other factors that may be used to predict illness start and development. The carotid arteries provide blood to the brain and are divided into the internal carotid artery (ICA) and external carotid artery (ECA). They begin as the common carotid artery (CCA) and branch into the internal carotid artery (ICA) and external carotid artery (ECA) at the plane of the throat (ECA). The ICA is responsible for delivering blood to the brain, whereas the ECA is in charge of supplying blood to the face and neck. The left carotid artery is located on the left side of the neck, whereas the right carotid artery is located on the right side. The arteries expand at the point where the CCA bifurcates, forming a distinct bulb known as the carotid sinus. Approximately 80% of strokes are caused by stenosis in the carotid artery [3]. Plaque deposits are often soft formations that create an irregular and arbitrary region inside arteries. Platelets fill up the cracks and abnormalities in the artery, causing blood clots in the artery or its branches, which leads to atherosclerosis. Atherosclerotic plaque forms best at the bifurcation zone and the inner curvature of the vasculature, as well as in areas with low wall shear stress (WSS) [4]. A location with a high WSS is resistant to atherosclerosis, whereas a region with a less WSS is susceptible to atherosclerosis. As a result, the thickening of the artery wall begins in an area with low WSS [5–9]. The WSS is calculated by multiplying the known dynamic viscosity of blood and blood velocities. The Navier–Stokes equation is solved iteratively, and velocities are determined using CFD techniques. CFD, on the other hand, needs precise boundary conditions, clinical experience, and computing time. Blood velocities can also be measured using the phase-contrast MRI (PC-MRI) method. Due to a lack of spatial resolution, the PC-MRI method was shown to underestimate velocity and WSS magnitude [10]. However, both MRI and

CFD are qualitatively comparable. Pulsatile pressure, bifurcation geometry, artery wall characteristics, and blood rheology are all factors that influence local hemodynamic parameters [11]. Many studies have looked at the flow of blood in the carotid artery [12–15]. Blood was modelled as a Newtonian fluid in these researches, with shear-thinning features neglected, claiming that the shear rate in big arteries is high, and blood viscosity is equivalent to the high shear rate viscosity limit. Additionally, using computational models to mimic blood flow, several researchers have explored simplified geometry of actual arteries [1, 16].

Blood is a complex body fluid that consists of different particles like plasma, erythrocytes, erythrocytes, and platelets. About 40% of the blood is composed of plasma, which is a Newtonian fluid, but the presence of other particles in the blood may behave as a non-Newtonian fluid. Blood is considered a shear-thinning fluid in which viscosity of the blood decreases with an increase in shear and strain rate, this is due to the alignment of the hematocrit which is having a capsule shape along the direction of the flow [17]. The blood flow in a larger artery can be considered as Newtonian flow but flow in the regions like small arteries, stenosis, curve the flow turns into non-Newtonian flow [18]. So, the viscosity of the blood is to be considered as non-Newtonian fluid. There are different blood viscosity models often used to mimic blood flow. The most suitable model is the CY model which is a four parameters model that compensates for a large range of shear rates.

MIMICS is being used in the current study to reconstruct CT pictures of the carotid artery in a patient. Using the rebuilt 3D model, which is exported to ANSYS Fluent, the impact of non-Newtonian blood viscosity on the velocity distribution, WSS, and shear strain rate in a stiff carotid artery bifurcation model under transient circumstances is studied. The Carreau-Yasuda blood viscosity model is used to account for the shear-thinning feature of blood, and a comprehensive comparison of Newtonian and non-Newtonian models is provided.

2 Methods

2.1 Acquisition of Images and Reconstruction

For this study, four carotid models from two patients are considered. Using CT scan a set of 2D images were obtained in the DICOM format. DICOM files were imported to MIMICS (Materialize, Leuven, Belgium) for the processing of images. The region near the carotid artery was selected as a region of interest and approximately 120–150 Hounsfield range was used as the threshold. Using vessel segmentation tool 3D geometry is obtained and smoothing of obtained geometry is done to remove unwanted irregularities in the model as shown in Fig. 1a. In the figure, axial, sagittal and coronal views of the human head are shown, and carotid artery obtained after vessel segmentation is shown.

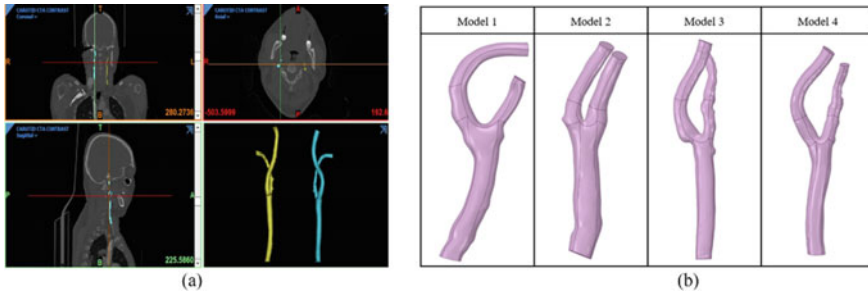


Fig. 1 **a** Vessel segmentation of carotid artery, **b** carotid geometry selected for analysis

Then obtained 3D model is exported to ANSYS 2020 in STL format. The 3D models obtained are shown in Fig. 1b. For the analysis, four geometry of carotid artery is considered obtained from two patients including both right and left carotid artery. The obtained geometries differ from each other with respect to diameter, bifurcation angle, and tortuosity.

2.2 Computational Setup and Flow Modelling

A Newtonian fluid has a constant viscosity that is proportional to the shear stress and shearing rate. It signifies that the viscosity of the fluid does not change with the shearing rate.

Effective viscosity,

$$\mu = \mu_{\infty} \quad (1)$$

where μ is effective viscosity in Pa-s and μ_{∞} is the viscosity at the infinite shear rate, $\mu_{\infty} = 0.00345$ Pa-s [19].

CY model combines Newtonian and Power law models to solve both shear thinning and thickening fluid problems. In contrast to the power-law model, this model works in both high and low shear rate situations [20]. It is necessary to include the viscosity values at zero shear and infinite shear in the formulation at extremely high and very low shear rates. The equation for effective viscosity for the CY model is as described below.

$$\eta(\gamma) = \mu_{\infty} + (\mu_0 - \mu_{\infty}) \left[1 + (\lambda \dot{\gamma})^a \right]^{\frac{n-1}{a}} \quad (2)$$

where γ is the shear rate, η is the viscosity, μ_0 is the viscosity at zero shear rate, μ_{∞} is the viscosity at infinite shear rate, λ , α , and n are material coefficients ($\lambda = 1.902$ s, $\alpha = 1.25$, $n = 0.22$), a is Yasuda constant ($a = 1.25$). For blood, $\mu_{\infty} = 0.00345$ Pa s, $\mu_0 = 0.056$ Pa s [21, 22].

The comparison of the Newtonian and CY model is done, dynamic viscosity is plotted against shear rate as shown in Fig. 2a. Ansys Fluent (with meshing) module is used for further analysis. Meshing is done as shown in Fig. 2b.

Meshing is done using Ansys Fluent with meshing module, Grid Independence test carried out by considering two parameters, like element size and the number of Inflation layer at the wall. Figure 3 represents the plot of velocity, pressure and number of inflation layers, the value of the inflation layer considered are 3, 5, 7, 10, and 15. The velocity and pressure value at four different planes of the carotid artery is calculated and plotted. As the number of inflation layers is increased the value of velocity and pressure remains constant. Hence, there is no significance in considering a high number of inflation layers, so the number of inflation layers is five.

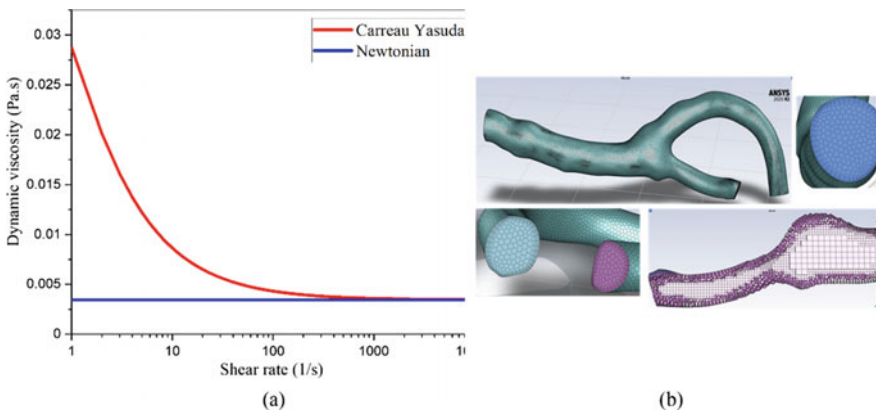


Fig. 2 a Comparison of Newtonian and Carreau-Yasuda viscosity model, b meshing of geometry using polyhexacore elements

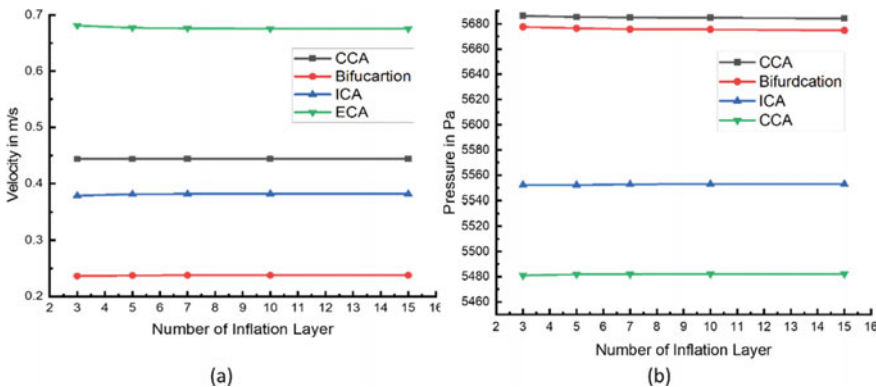


Fig. 3 Grid independency study, a velocity versus no. of boundary layer, b pressure versus no. of boundary layer

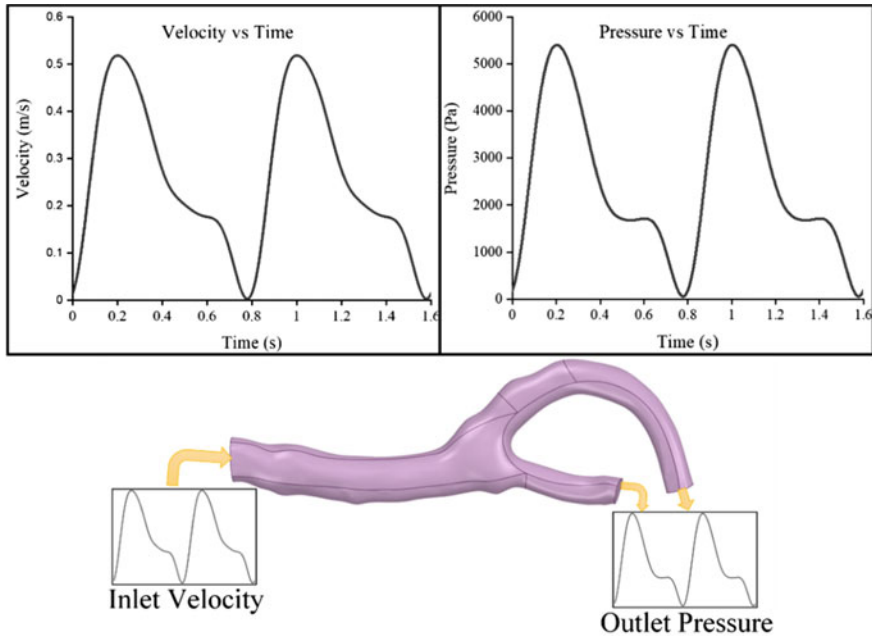


Fig. 4 Velocity and pressure waveform considered for the analysis

In the present study, the time-varying velocity boundary condition is applied at the inlet section of CCA. A pulsatile pressure waveform is applied at the exit of both ICA, ECA and for artery wall, stationary condition is selected. The velocity and pressure waveform is having a time period of 0.8 s, and analysis is carried out for four pulse cycles to get a stable solution. The velocity, pressure waveform, and implication of boundary condition are shown in Fig. 4.

3 Results and Discussion

Results obtained from numerical simulation of blood flow in carotid artery for Newtonian and CY viscosity model are compared by considering velocity contours, pressure contours, vorticity, and wall shear stress (WSS). For comparison of WSS along four regions of the carotid artery, four section planes are created in CCA, bifurcation, ICA and ECA as shown in Fig. 5.

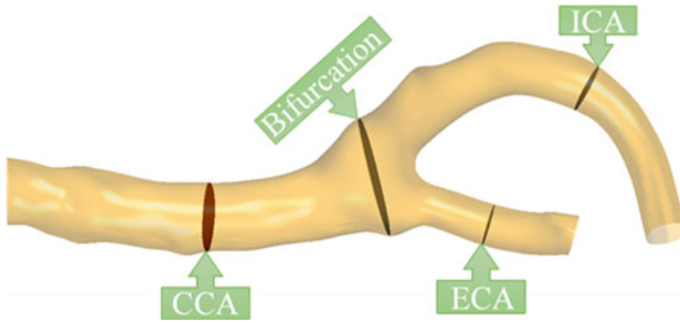


Fig. 5 Different planes selected for plotting of results

3.1 Velocity

Velocity contours are mapped using streamline plot, vectors starting from the inlet of CCA. In Fig. 6, streamline plot for model 1 for Newtonian and CY viscosity model is shown, and a bar graph is used to represent velocity magnitude for the rest of the models.

From the velocity streamline plot, it can be observed that early systole and peak diastole flow will be having some disturbance and recirculation for both Newtonian and CY models. In early systole cavitation can be observed in the region of bifurcation this is due sudden opening of CCA which creates a large sinus structure. During peak systole condition flow will be normal and no recirculation is observed. When the maximum value of velocity is compared for Newtonian and CY model, during early systole and peak diastole CY model is lesser than Newtonian by 7%, while for peak systole it is 2% lesser.

3.2 Pressure

Pressure contour is plotted at the wall region of the carotid artery as shown in Fig. 7. From the contour plot which represents the pressure plot for model 2 doesn't show any differentiation for Newtonian and CY models. It can be observed that during early systole maximum pressure can be observed near the inlet of CCA and during peak diastole in the exit of both ICA and ECA. During peak systole pressure will be maximum compared to early systole and peak systole.

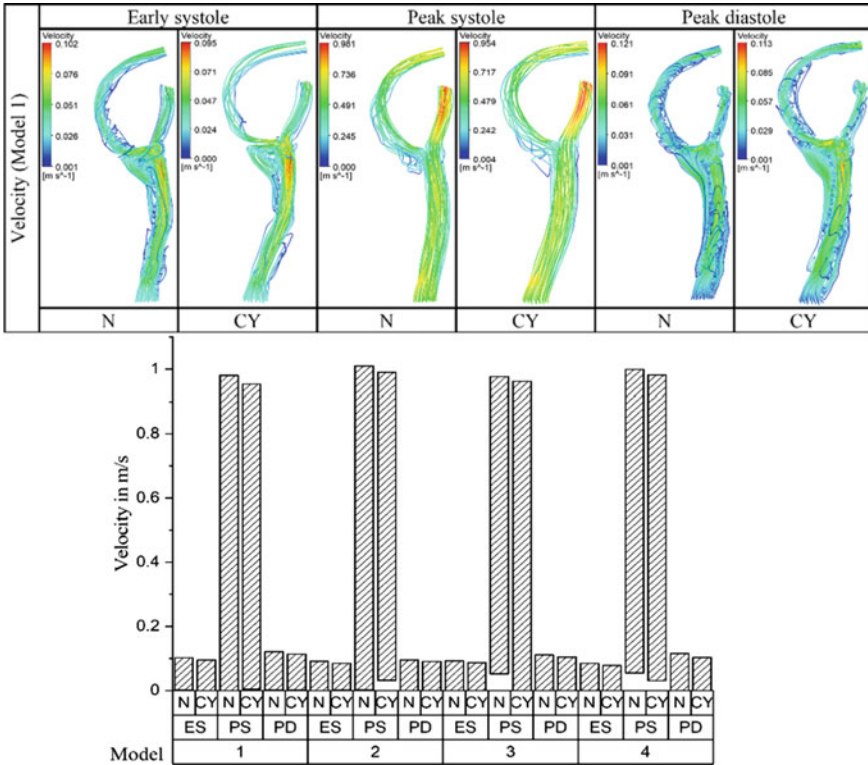


Fig. 6 Velocity streamline plot of model 1 (top), variation of velocity for 4 models represented in the bar graph

3.3 Vorticity

Figure 8 depicts the contours of vorticity in carotid artery models. Understanding the flow patterns in the arterial tree requires a thorough understanding of vorticity contours, which are the absolute value of the dot product of velocity and vorticity vector. The emergence of secondary flow is a significant phenomenon, and the emergence of three-dimensional flow fields has an impact on near-wall flow properties [23, 24]. A vortex zone forms when the flow recirculates downstream of the separation line. The flow diverges into opposite directions perpendicular to its initial course as it approaches the peak of the bifurcation zone, exhibiting vortex generation. As a result, it was discovered that flow separation occurs at the ICA’s lateral wall near the apex, where the ECA splits out. When Newtonian and CY model is compared there was no significant difference was observed and the difference was below 3%.

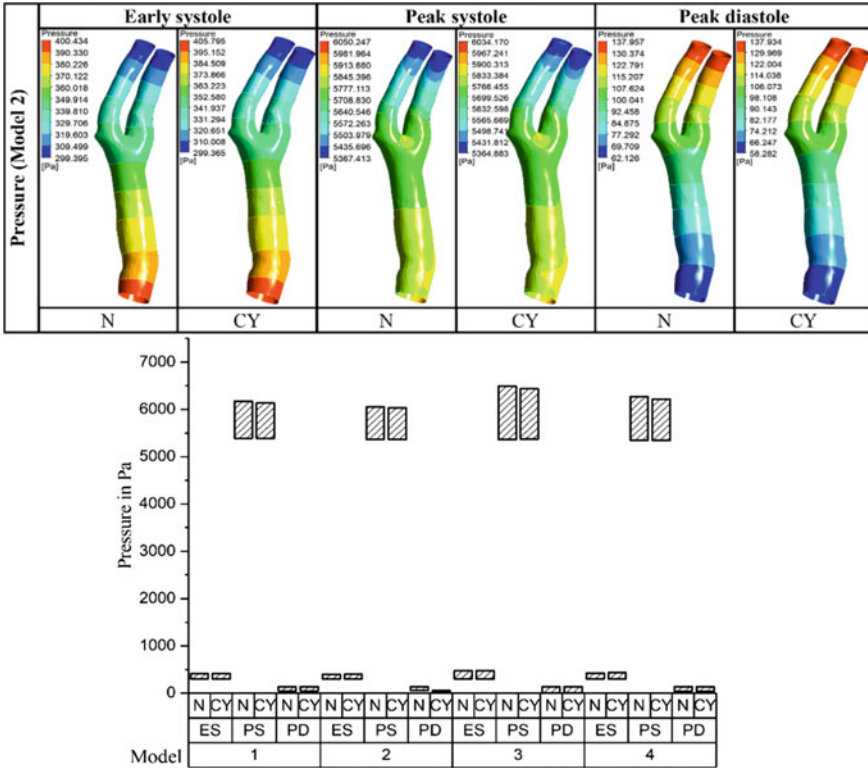


Fig. 7 Pressure plot of model 1 (top), variation of pressure for 4 models represented in the bar graph

3.4 Wall Shear Stress

The tangential force of flowing blood on the endothelium surface of a blood artery is known as wall shear stress. Wall shear stress is a force that has both a magnitude and a direction and is formally represented as a vector. Blood flow and fluid viscosity are directly proportional to the magnitude of the shear stress vector, whereas vessel radius is indirectly proportional [25]. Figure 9 represents the variation of WSS for Newtonian and CY model plotted using polar plot at four different planes along the interaction of plane and wall. The four planes selected are shown in Fig. 7. From the polar plot, it is observed that the Newtonian model overestimates the WSS in most of the planes like CCA, ICA, and ECA. Lower WSS leads to the formation of plaque, so accurate estimation of WSS is important for the study of blood flow.

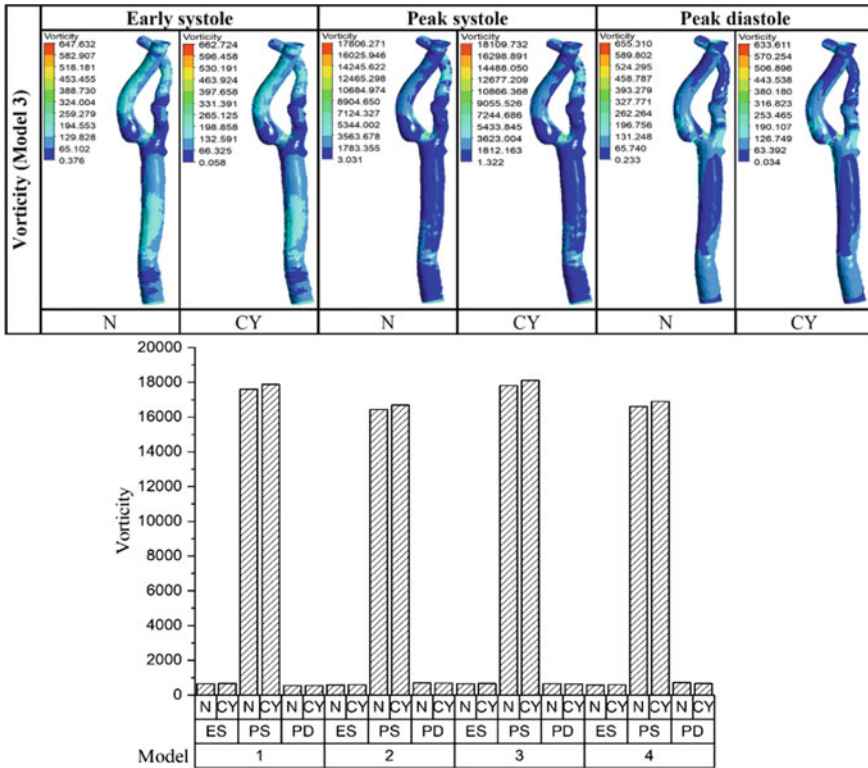


Fig. 8 Vorticity plot of model 1 (top), variation of vorticity for 4 models represented in the bar graph

4 Conclusion

In large arteries, the impact of blood shear thinning characteristics on hemodynamic parameters is not particularly substantial, according to the findings. Even in big arteries, when the WSS is low, causing reversals inflow, and the small diameter is owing to the stenosis, the Newtonian model amplifies the hemodynamic parameters and fails to properly forecast the outcome. Many studies believe that in the carotid sinus rapid expansion of the lumen due to plaque deposits, causes flow recirculation. But in the present study, estimation of flow recirculation is quantified using a velocity streamline plot. Comparing of pressure and vorticity plot didn't show any significant changes. But in the WSS plot, it is observed that the Newtonian model overestimates the values of WSS in most of the regions of the carotid artery. The formation of atherosclerosis can be determined by observing the region with low WSS since the Newtonian model overestimates WSS values it is better to consider the CY model for the calculation of WSS in an artery. Considering the rigid artery on blood flow is one of the limitations of the present study. Furthermore, the temporal changes of

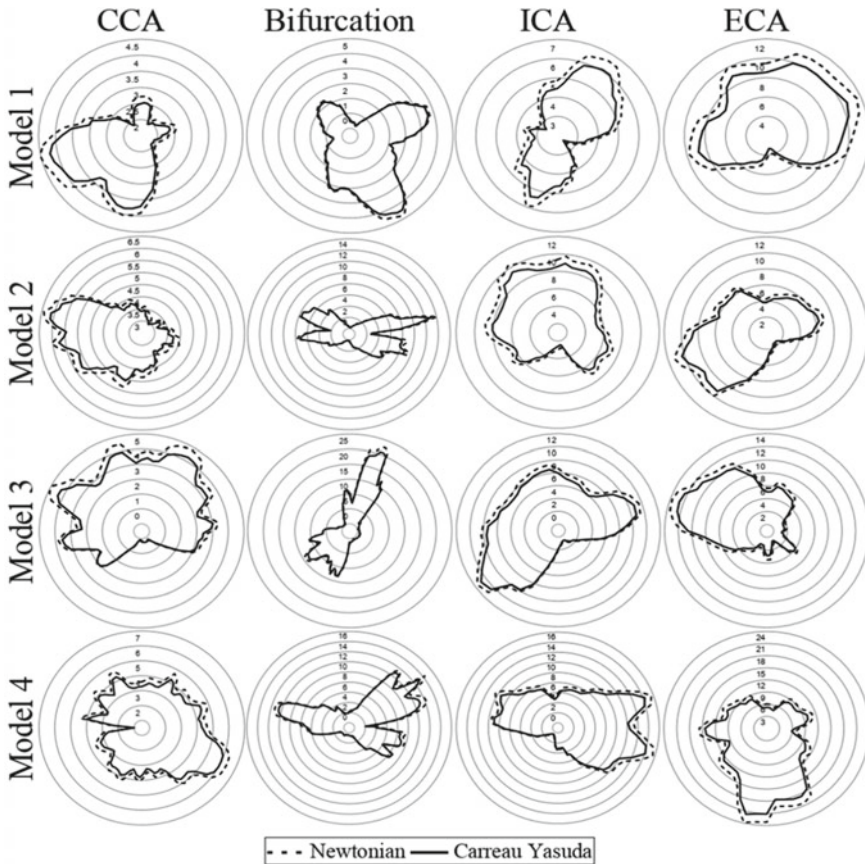


Fig. 9 Wall shear stress polar plot for Newtonian and Carreau-Yasuda viscosity model during peak systole

the parameters, as well as the precise rheological characteristics of blood, are not addressed.

References

1. Perktold K, Rappitsch G (1995) Computer simulation of local blood flow and vessel mechanics in a compliant carotid artery bifurcation model. *Biomechanics* 28(7)
2. Bathe RKM (1999) Computer simulation of local blood flow and vessel mechanics in a compliant carotid artery bifurcation model. *J Biomech Eng Trans ASME* 121:361–369
3. Flaherty ML et al (2012) Carotid artery stenosis as a cause of stroke. *Neuroepidemiology* 40(1):36–41. <https://doi.org/10.1159/000341410>

4. Liesch D, Balasso A, Berger H, Eckstein HH (2012) How local hemodynamics at the carotid bifurcation influence the development of carotid plaques. *Perspect Med* 1–12(1–12):132–136. <https://doi.org/10.1016/j.permed.2012.04.005>
5. Shaaban AM, Duerinckx AJ (2000) Wall shear stress and early atherosclerosis: a review. *Am J Roentgenol* 174(6):1657–1665. <https://doi.org/10.2214/ajr.174.6.1741657>
6. Slagger CJ et al (2005) The role of shear stress in the destabilization of vulnerable plaques and related therapeutic implications. *Nat Clin Pract Cardiovasc Med* 2(9):456–464. <https://doi.org/10.1038/ncpcardio0298>
7. VanderLaan PA, Reardon CA, Getz GS (2004) Site specificity of atherosclerosis: site-selective responses to atherosclerotic modulators. *Arterioscler Thromb Vasc Biol* 24(1):12–22. <https://doi.org/10.1161/01.ATV.0000105054.43931.f0>
8. Cecchi E et al (2011) Role of hemodynamic shear stress in cardiovascular disease. *Atherosclerosis* 214(2):249–256. <https://doi.org/10.1016/j.atherosclerosis.2010.09.008>
9. Malek AM, Alper SL (1999) Hemodynamic shear stress and its role in atherosclerosis. *Stress Int J Biol Stress* 282(21):2035–2042
10. Cibis M et al (2014) Wall shear stress calculations based on 3D cine phase contrast MRI and computational fluid dynamics: a comparison study in healthy carotid arteries, no March, 2014. <https://doi.org/10.1002/nbm.3126>
11. Gijsen FJH, Allanic E, Van De Vosse FN, Janssen JD (1999) The influence of the non-Newtonian properties of blood on the flow in large arteries: unsteady flow in a 90° curved tube. *J Biomech* 32(7):705–713. [https://doi.org/10.1016/S0021-9290\(99\)00014-7](https://doi.org/10.1016/S0021-9290(99)00014-7)
12. Perktold K, Hilbert D (1986) Numerical simulation of pulsatile flow in a carotid bifurcation model. *J Biomed Eng* 8(3):193–199. [https://doi.org/10.1016/0141-5425\(86\)90083-X](https://doi.org/10.1016/0141-5425(86)90083-X)
13. Bharadvaj BK, Mabon RF, Giddens DP (1982) Steady flow in a model of the human carotid bifurcation. Part I-flow visualization. *J Biomech* 15(5):349–362. [https://doi.org/10.1016/0021-9290\(82\)90057-4](https://doi.org/10.1016/0021-9290(82)90057-4)
14. Zarins CK, Giddens DP, Bharadvaj BK, Sottiurai VS, Mabon RF, Glagov S (1983) Carotid bifurcation atherosclerosis. quantitative correlation of plaque localization with flow velocity profiles and wall shear stress. *Circ Res* 53(4):502–514. <https://doi.org/10.1161/01.RES.53.4.502>
15. Li G, Chen B, Zhou G (2013) Unsteady non-Newtonian solver on unstructured grid for the simulation of blood flow. *Adv Mech Eng* 2013. <https://doi.org/10.1155/2013/596172>
16. van de Vosse FN et al (2003) Finite-element-based computational methods for cardiovascular fluid-structure interaction. *J Eng Math* 47(3–4):335–368. <https://doi.org/10.1023/B:ENGI.0000007985.17625.43>
17. Fung YC. *Biodynamics circulation*. Springer Verlag, New York Inc
18. Lopes D, Puga H, Teixeira J, Lima R (2020) Blood flow simulations in patient-specific geometries of the carotid artery: a systematic review. *J Biomech* 111:110019. <https://doi.org/10.1016/j.jbiomech.2020.110019>
19. Jahangiri M, Haghani A, Ghaderi R, Hosseini Harat SM (2018) Effect of non-Newtonian models on blood flow in artery with different consecutive stenosis. *Int J Adv Des Manuf Technol* 11(1):89–96. <https://www.researchgate.net/publication/323294878>
20. Khan M, Sardar H, Gulzar MM, Alshomrani AS (2018) On multiple solutions of non-Newtonian Carreau fluid flow over an inclined shrinking sheet. *Results Phys* 8:926–932. <https://doi.org/10.1016/j.rinp.2018.01.021>
21. Weddell JC, Kwack JH, Imoukhuede PI, Masud A (2015) Hemodynamic analysis in an idealized artery tree: differences in wall shear stress between Newtonian and non-Newtonian blood models. *PLoS ONE* 10(4):1–23. <https://doi.org/10.1371/journal.pone.0124575>
22. Lee SH, Han KS, Hur N, Cho YI, Jeong SK (2019) The effect of patient-specific non-Newtonian blood viscosity on arterial hemodynamics predictions. *J Mech Med Biol* 19(8):1–15. <https://doi.org/10.1142/S0219519419400542>

23. Domanin M, Bissacco D, Le Van D, Vergara C (2018) Computational fluid dynamic comparison between patch-based and primary closure techniques after. *J Vasc Surg* 67(3):887–897. <https://doi.org/10.1016/j.jvs.2017.08.094>
24. Guerciotti B, Vergara C (2018) Computational comparison between Newtonian and non-Newtonian blood rheologies in stenotic vessels, vol 84. Springer, pp 169–183
25. Paszkowiak JJ, Dardik A (2003) Arterial wall shear stress: observations from the bench to the bedside. *Vasc Endovascular Surg* 37(1):47–57. <https://doi.org/10.1177/153857440303700107>

Comparison of Newtonian and Non-Newtonian Flow in Abdominal Aorta and Renal Artery Using Numerical Simulation



B. Gowrava Shenoy , Nitesh Kumar , A. B. V. Barbouza ,
S. M. Abdul Khader , A. Ravindra Prabhu , Masaaki Tamagawa,
and B. Raghuvir Pai 

Abstract Numerical simulations of cardiovascular flows have emphasized investigating the mechanics of blood flow in arteries. The objective of the current study is to examine the effect of Newtonian and non-Newtonian flow models in flow simulation to analyze for hemodynamic behavior. CFD analysis was performed on an idealized healthy abdominal aorta with renal branching using ANSYS Fluent solver. The discretized mesh was obtained having polyhedral and hexahedral grid ensured the capture of gradients with a sufficient number of grids. Transient analysis was performed using pulsatile flow boundary conditions. Velocity plots obtained from the analysis predict the recirculation zone in the Ostia of the renal artery. TAWSS observed to be maximum at the infrarenal aorta. And Newtonian model predicted higher TAWSS. Oscillatory shearing index calculated to be maximum at the bifurcation. The result of this analysis will be helping in understanding the flow behavior in idealized cases and further extended to stenosed cases.

Keywords Renal artery · Abdominal aorta · Newtonian flow · Carreau-Yasuda flow model

B. G. Shenoy (✉) · N. Kumar · A. B. V. Barbouza · S. M. A. Khader · B. R. Pai
Department of Mechanical Engineering and Manufacturing Engineering, Manipal Institute of Technology, Manipal Academy of Higher Education, Manipal, Karnataka 576104, India
e-mail: gowrav.shenoy@manipal.edu

A. R. Prabhu
Department of Nephrology, Kasturba Medical College, Manipal Academy of Higher Education, Manipal, Karnataka 576104, India

M. Tamagawa
Department of Biological Functions Engineering, Graduate School of Life Science and Systems Engineering, Kyushu Institute of Technology, Kitakyushu 808-0196, Fukuoka, Japan

1 Introduction

The upsurge in reported cases of cardiovascular diseases worldwide has resulted in a significant increase in mortality. At birth, the probability of eventual cardiovascular disease-related death is 47% [5, 15]. The main reasons are atherosclerosis and chronic heart disease. Important regions of interest such as bifurcation or branching or curvature in the arteries are having greater susceptibility to plaque formation due to recirculation [9]. Physiologically, flow in the abdominal aorta is significant as it is supplying the oxygenated blood from the thoracic region to various functioning parts in the lower abdominal region and legs. The renal arteries are an important branch of the abdominal aorta which supplies blood to the kidneys. Atherosclerosis in the renal artery is directly linked with secondary hypertension and reduced renal function. However, the numerical study of blood flow in the abdominal aorta and its branches is limited [2]. The distribution of shear stress on the arterial walls has always been linked with atherogenesis. Wall shear stress (WSS) force exerted by the wall on the arterial flow. The lower value of localized WSS gives rise to recirculation and hence increasing the chances of plaque deposition thereby stenosis formation. Literature finds that low and oscillating WSS are directly linked to pathogenesis [18]. Zones of low and oscillating wall shear stress are being key hemodynamic markers in the evaluation of atherosclerosis [5]. The application of numerical methods in hemodynamics can achieve a better understanding of atherosclerosis thereby aiding prognosis on plaque formation and progression-related events [17]. Computational fluid dynamics (CFD) is widely used as complementary to clinical modalities like computerised tomography (CT) imaging, magneto resonance imaging, etc. [16]. This study focuses on hemodynamics investigation of the idealistic abdominal aorta and renal artery branching is performed using Newtonian and non-Newtonian models for possible key locations of low wall shear stress and oscillatory shearing index. The viscosity of blood mainly depends on shear rate, in larger arteries and aorta blood flow is considered as Newtonian having a shear rate over 100 s^{-1} and viscosity is calculated based on Newton's viscosity model [12]. Some literature also emphasizes on shear-thinning behavior of blood in which a nonlinear relation with shear rate and applied load is established. Non-newtonian model like Carreau-Yashuda Models are also considered to have a comparison with Newtonian viscosity [1, 3, 10, 11].

2 Methodology

2.1 Governing Equation of Fluid Flow

The simulation of blood flow in the abdominal aorta-renal artery systems is done with the consideration that the flow of blood is Newtonian, incompressible, and laminar. The governing equations used are the continuity and the incompressible Navier–Stokes equation shown in Eqs. (1) and (2).

$$\nabla \cdot v = 0 \quad (1)$$

$$\rho \left(\frac{\partial v}{\partial t} + v \cdot \nabla v \right) = -\nabla p + \mu \nabla^2 v \quad (2)$$

In the above equation, v represents flow velocity, ρ is the density, and μ represents the dynamic viscosity of blood. The notation P refers to the pressure of the system. Newtonian fluid conjecture considers density as 1050 kg/m^3 , viscosity as 0.004 kg/m.s . Newtonian model establishes a relation with viscosity η and shear rate γ given in Eq. (3).

$$\tau = \eta \dot{\gamma} \quad (3)$$

$$\frac{\eta - \eta_\infty}{\eta_0 - \eta_\infty} = \left[1 + (\lambda \dot{\gamma})^a \right]^{\frac{(n-1)}{a}} \quad (4)$$

Equation (4) is a generalization of the Newtonian model and describes the variation of viscosity η with shear rate γ than other rheological models. The fundamental characteristic of this formulation is that the Carreau-Yasuda equation involves five parameters, viz, η_0 —viscosity at the minimum shear rate, η_∞ —viscosity at the maximum shear rate, λ —time constant, a —Yasuda exponent, and n —Power-law index to describe the fluid rheology. Constants of Carreau-Yasuda Model were taken from available literature [10, 13].

2.2 Geometric Model

The objective of geometric modeling is to create a three-dimensional computational domain of interest. The dimensions of the CAD model are obtained from CT DICOM images, using the CATIA V5 software. Initially, standard computerized tomography slices of the renal artery system were obtained, which were subjected to reconstruction using the materialize MIMICS tool. The reconstructed models were defeaturized using the CATIA V5 computer-aided design tool. The simplification and defeaturization are done in such a way that the accuracy of the model isn't affected. The aortal and renal diameter along with the location of the Ostia is taken as it is. Geometrical simplification of the model aids in analyzing blood flow in idealized conditions. Crucial geometric parameters like diameter at various sections, lengths, and bifurcation zone were modeled by the measurements from CT data. Idealized models from the literature were considered in the study for the validation of the tool [6].

2.3 Meshing

Poly-hexcore mesh as it is known in the ANSYS Fluent meshing software consists of octahedral elements at the periphery and hexahedral elements at the interior. By incorporating mosaic technology, different types of meshes are automatically connected with polyhedral elements, thereby filling the region with hexahedral elements. This is known to make the mesh computationally efficient, increase the accuracy and decrease the simulation time of the solution.

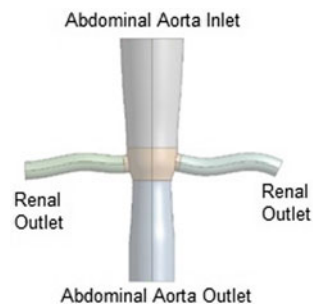
2.4 Boundary Conditions and Solver Settings

As shown in Fig. 1 Inlet boundary is assigned with pulsatile velocity taken from Refs. [4, 6, 7]. In similar way renal outlets and abdominal aorta outlets are assigned with corresponding arterial and aortic pressure [6, 14]. Pulse cycle of 0.9 s is taken for reference. Blood pressure reference is taken as a healthy condition under rest having 80–110 mmHg. The outer periphery of the artery and aorta is assigned with no-slip conditions. ANSYS Fluent solver was used on four core Xeon Processor, with 32 GB RAM, capacity for computation. Flow is analyzed for three complete pulses, considering the smaller time step 0.018 s to have 50 timesteps in a pulse cycle to capture the transience in each step [13]. Pulsatile wave in puts are enabled using user-defined function coded using fourier series for three pulses to ensure minimized numerical errors.

3 Result and Discussion

The results of the CFD analysis were compared with studies published for the same input conditions in a renal artery branching, showing a close match between the pressure, velocity, and wall shear results [13].

Fig. 1 Geometric model of abdominal aorta and renal artery



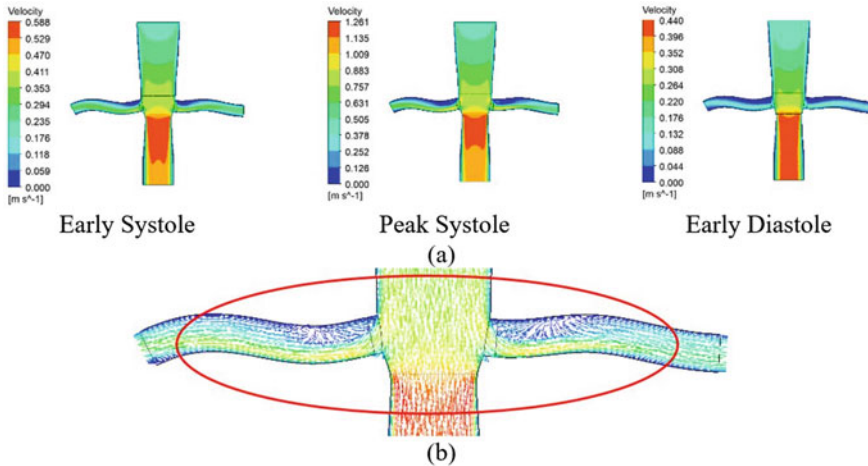


Fig. 2 **a** Midplane-velocity distribution abdominal aorta-renal artery **b** velocity vector plot showing possible recirculation zone

3.1 Velocity Distribution

Velocity plots are shown in Fig. 2 to find velocity distribution in the aorta, origins, and courses of the renal artery. Plots were taken during early systole, peak systole, and early diastole of velocity wave in normal conditions. During early systole, minimum velocity was observed proximal region of branching in the upper Ostia portion and the maximum value of velocity is observed in the infrarenal abdominal aorta. During peak systole, low-velocity values were observed in the same region without significant change in the velocity magnitude. In peak systole fluid layers immediate to the renal artery wall along the length had minimum velocity and maximum velocity was spread along the length of the infrarenal abdominal aorta. Velocity plots allow us to know the possible recirculation zones within the artery after the stenosis. This study finds the possible recirculation zones immediately after renal branching due to curvature and reduced velocity. Velocity plots of Newtonian and non-Newtonian flow were almost the same as they are reflecting the same boundary conditions.

3.2 Pressure Distribution

The variation of pressure in the renal artery is given in Fig. 3. The peaks represent higher values in pressure wave inputs. During early systole, peak systole, and early diastole of the pulse normal healthy artery has shown varying wall pressure distribution. At the beginning of the pressure wave, the inlet portion of the abdominal aorta had a larger pressure value, whereas the infrarenal aorta had the minimum pressure

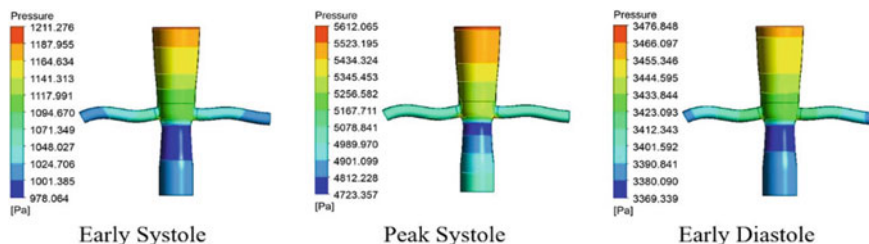


Fig. 3 Wall pressure distribution in abdominal aorta-renal artery

on the wall. The maximum value of pressure is observed during the peak systole phase of the pulse. Wall pressure is the factor directly linked with arterial distensibility, and it will be the input for interaction analysis. Pressure distribution in cases of Newtonian and non-Newtonian flow was almost similar as they are reflecting the same boundary conditions.

3.3 Wall Shear Stress Distribution

In Fig. 4 it can be seen that during the entire pulse high WSS remains the zone of the wall of the aorta immediately after the renal branching. At renal bifurcation also slightly, the larger value of WSS was observed. Higher amounts of shear stress in areas subjected to incoming flow impingement at the junction such as the distal wall, often cause shear thinning in said regions and other regions downstream where Non-Newtonian consideration becomes more important. Wall shear stress distribution in the case of Newtonian and Carreau-Yasuda model showed a similar trend with marginal difference in the magnitude of the WSS which are shown in plots.

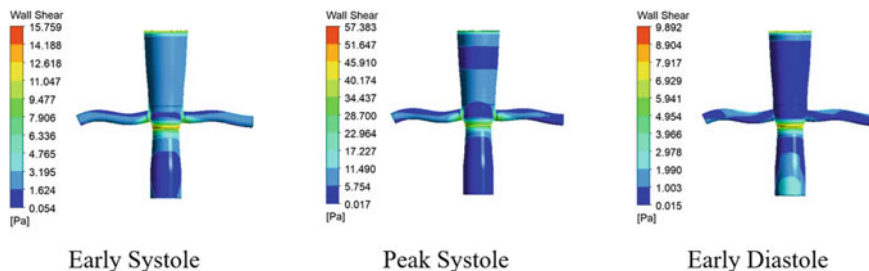


Fig. 4 Wall shear stress distribution in abdominal aorta-renal artery

3.4 Time Averaged Wall Shear Stress

Time-averaged wall shear stress (TAWSS) is a function of wall shear stress (WSS) averaged over the entire period T . The expression for the parameter is given in the equation below [8].

$$TAWSS = \frac{1}{T} \int_0^T (|WSS_x| + |WSS_y| + |WSS_z|) dt \tag{5}$$

where WSS_x , WSS_y and WSS_z are the WSS values resolved at x , y , and z directions, respectively.

Figures 5 and 6 exhibit the WSS contours on the idealized abdominal aorta and renal artery model over the entire time duration of 0.9 s pulse cycle. Shear stress along the length of the abdominal aorta increased till the region of bifurcation, where it is highest and lowered further upstream. In normal renal arteries, the distal walls experienced higher amounts of stress compared to proximal walls.

Fig. 5 TAWSS distribution in abdominal aorta renal artery for Carreau-Yasuda model

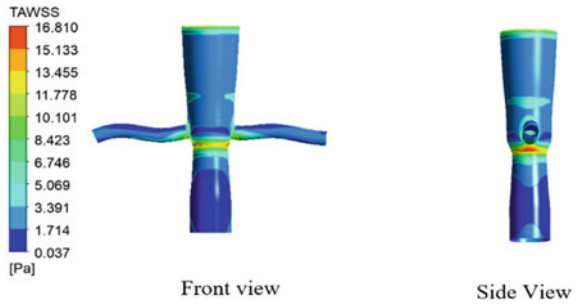
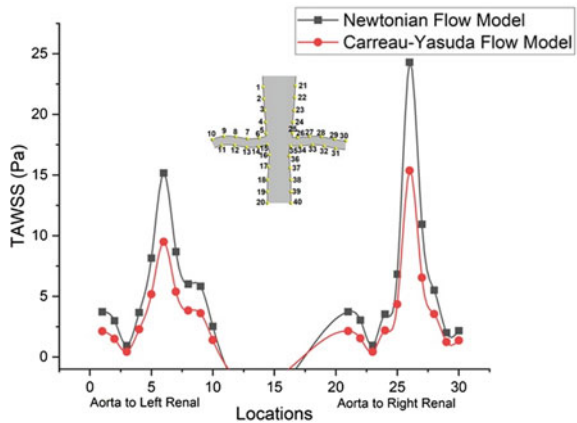


Fig. 6 Time averaged wall shear stress variation along the length of the abdominal aorta and renal artery



3.5 Oscillatory Shearing Index

Oscillatory shear index (OSI) was derived to consider the cyclic movement of the wall shear stress vector from the axis reference [14]. The oscillatory shear index can be calculated using the following equation which considers the value over the entire pulse rather than at an instance.

$$\text{OSI} = 0.5 \left[1 - \left(\frac{\left| \int_0^T \text{WSS} dt \right|}{\int_0^T |\text{WSS}| dt} \right) \right] \quad (6)$$

Figure 7 shows the variation of OSI on the wall for the idealized abdominal aorta and renal artery model. The value of OSI ranges from 0 to 0.5. Literature mentions locations with OSI over 0.15 with low TAWSS less than 0.4 Pa are more prone to rupture. In Fig. 7, it is observed that the highest value of OSI was observed near the bifurcation. However, in some portions of the infrarenal aorta, there are localized high OSI values observed. When compared with the Newtonian model, the Carreau-Yasuda model exhibited larger OSI in some locations and almost the same values in major points.

4 Conclusion

The present study of the idealized abdominal aorta and renal artery model using computational fluid dynamics focuses on comparing the Newtonian flow and Non-Newtonian shear thinning Carreau-Yasuda model under normal pressure and rest conditions. It has been observed that velocity distribution remains the same in Newtonian and Carreau-Yasuda models having the highest value in the infrarenal region and lowest in renal branching with possible recirculation zone. Pressure distribution remained uniform in Newtonian and Carreau-Yasuda models. However, TAWSS plots have shown an increase in peak value at branching and while compared with the Carreau-Yasuda model, the Newtonian model shows the highest value of TAWSS for the same input. OSI distribution and plots have shown maximum OSI immediately after branching. The present study identifies these regions as they are more susceptible to atherosclerosis due to flow behavior and geometry properties.

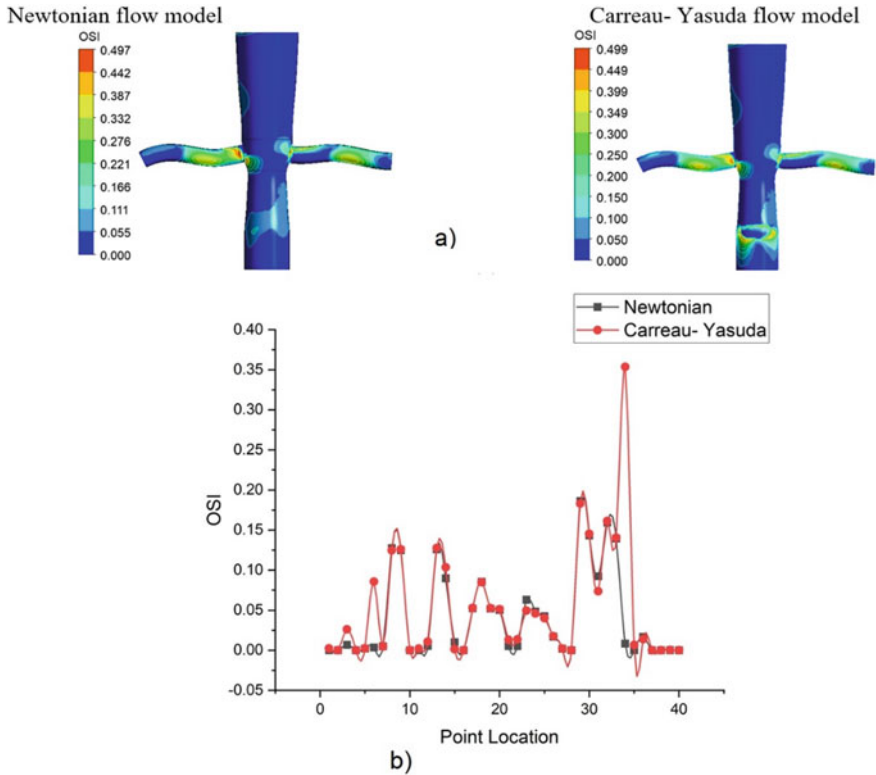


Fig. 7 a Oscillatory shearing index variation on the wall in case of Newtonian and Carreau-Yasuda flow model b OSI variation along the length of the abdominal aorta and renal artery

References

1. Abbasian M, Shams M, Valizadeh Z, Moshfeqh A, Javadzadegan A, Cheng S (2020) Effects of different non-Newtonian models on unsteady blood flow hemodynamics in patient-specific arterial models with in-vivo validation. *Comput Methods Programs Biomed* 186:105185. <https://doi.org/10.1016/j.cmpb.2019.105185>
2. Abdul Khader SM, Raghuvir Pai B, Srikanth Rao D, Prakashini K (2021) Numerical investigation of blood flow in idealized abdominal aorta with renal bifurcation using fluid–structure interaction. In: *Lecture notes in mechanical engineering*. Springer, Singapore. https://doi.org/10.1007/978-981-15-4308-1_39
3. Ashrafizaadeh M, Bakhshaei H (2009) A comparison of non-Newtonian models for lattice Boltzmann blood flow simulations. *Comput Math Appl* 58(5):1045–1054. <https://doi.org/10.1016/j.camwa.2009.02.021>
4. Azriff A, Johny C, Abdul Khader SM, Raghuvir Pai B, Zuber M, Ahmed KA, Ahmad Z (2018) Numerical study of haemodynamics in abdominal aorta with renal branches using fluid–structure interaction under rest and exercise conditions. *Int J Recent Technol Eng* 7(4):23–27
5. Bantwal A, Singh A, Menon AR, Kumar N (2021) Pathogenesis of atherosclerosis and its influence on local hemodynamics: a comparative FSI study in healthy and mildly stenosed carotid arteries. *Int J Eng Sci* 167:103525. <https://doi.org/10.1016/j.ijengsci.2021.103525>

6. Basri AA, Khader SA, Johny C, Pai R, Zuber M, Ahmad Z, Ahmad KA (2019) Effect of single and double stenosed on renal arteries of abdominal aorta: a computational fluid dynamics. *CFD Lett* 12(1):87–97
7. Basri AA, Khader SMA, Johny C, Raghuvir Pai B, Zuber M, Ahmad Z, Ahmad KA (2020) Fluid structure interaction of renal arteries of abdominal aorta subjected to single and double stenosed complication. *Malays J Med Health Sci* 16:35–41
8. Fuchs A, Berg N, Wittberg LP (2019) Stenosis indicators applied to patient-specific renal arteries without and with stenosis. *Fluids* 4(1). <https://doi.org/10.3390/fluids4010026>
9. Fung YC (1997) *Biomechanics*. Springer, New York. <https://doi.org/10.1007/978-1-4757-2696-1>
10. Gijssen FJH, Allanic E, Van De Vosse FN, Janssen JD (1999) The influence of the non-Newtonian properties of blood on the flow in large arteries: Unsteady flow in a 90° curved tube. *J Biomech* 32(7):705–713. [https://doi.org/10.1016/S0021-9290\(99\)00014-7](https://doi.org/10.1016/S0021-9290(99)00014-7)
11. Husain I, Labropulu F, Langdon C, Schwark J (2020) A comparison of Newtonian and non-Newtonian models for pulsatile blood flow simulations. *J Mech Behav Mater* 21(5–6):147–153. <https://doi.org/10.1515/jmbm-2013-0001>
12. Jahangiri M, Saghaian M, Sadeghi MR (2017) Numerical simulation of non-Newtonian models effect on hemodynamic factors of pulsatile blood flow in elastic stenosed artery. *J Mech Sci Technol* 31(2):1003–1013. <https://doi.org/10.1007/s12206-017-0153-x>
13. Khader SMA, Azriff A, Pai R, Zubair M, Ahmad KA, Ahmad Z, Prakashini K (2018) Haemodynamics study in subject-specific abdominal aorta with renal bifurcation using CFD—a case study. *J Adv Res Fluid Mech Therm Sci* 50(2):118–121
14. Moore JE Jr, Xu C, Glagov S, Zarins CK, Ku DN (1994) Fluid wall shear stress measurements in a model of the human abdominal aorta: oscillatory behavior and relationship to atherosclerosis. *Atherosclerosis* 110(2):225–240
15. Roquer J, Ois A (2010) Atherosclerotic burden and mortality. In: *Handbook of disease burdens and quality of life measures*, vol 51. Springer, New York, pp 899–918. https://doi.org/10.1007/978-0-387-78665-0_51
16. Suh GY, Les AS, Tenforde AS, Shadden SC, Spilker RL, Yeung JJ, Cheng CP, Herfkens RJ, Dalman RL, Taylor CA (2011) Hemodynamic changes quantified in abdominal aortic aneurysms with increasing exercise intensity using MR exercise imaging and image-based computational fluid dynamics. *Ann Biomed Eng* 39(8):2186–2202. <https://doi.org/10.1007/s10439-011-0313-6>
17. Taylor CA, Hughes TJR, Zarins CK (1998) Finite element modeling of three-dimensional pulsatile flow in the abdominal aorta: relevance to atherosclerosis. *Ann Biomed Eng* 26(6):975–987. <https://doi.org/10.1114/1.140>
18. Tse KM, Chang R, Lee HP, Lim SP, Venkatesh SK, Ho P (2013) A computational fluid dynamics study on geometrical influence of the aorta on haemodynamics. *Eur J Cardiothorac Surg* 43(4):829–838. <https://doi.org/10.1093/ejcts/ezs388>

Analysis and Prediction of COVID-19 Spread in Ernakulam District, Kerala



Serin Kuriakose , Zarin Pilakkadavath , C. Rohini, and S. Sreedevi

Abstract The world is witnessing a pandemic of SARS-CoV2 infection since the first quarter of the twenty-first century. Ever since the first case was reported in Wuhan city of China in December 2019, the virus has spread over 223 countries. Understanding and predicting the dynamics of COVID-19 spread through data analysis will empower our administrations with insights for better planning and response against the burden inflicted on our health care infrastructure and economy. The aim of the study was to analyze and predict COVID-19 spread in Ernakulam district of Kerala. Data was extracted from lab data management system (LDMS), a government portal to enter all the COVID-19 testing details. Using the EpiModel package of R-mathematical modeling of infectious disease dynamics, the predictive analysis for hospitalization rate, percentage of patients requiring oxygen and ICU admission, percentage of patients getting admitted, duration of hospital stay, case fatality rate, age group and gender-wise fatality rate, and hospitalization rate were computed. While calculating the above-said variables, the percentage of vaccinated population, breakthrough infections, and percentage of hospitalization among the vaccinated was also taken into consideration. The time trend of patients in ICU showed men outnumbered women. Positive cases were more among 20–30 years, while 61–70 years age group had more risk for ICU admission. An increase in CFR with advancing age and also a higher CFR among males were seen. Conclusions: Analyzing and predicting the trend of COVID-19 would help the governments to better utilize their limited healthcare resources and adopt timely measures to contain the virus.

Keywords COVID-19 · Prediction model · Data analysis

S. Kuriakose (✉) · C. Rohini

Data Management and Analysis Team, District Surveillance Unit, Kerala Government Health Services, Ernakulam, India

e-mail: dr.serinkuriakose@gmail.com

Z. Pilakkadavath

Boston, USA

S. Sreedevi

Kerala Government Health Services, Ernakulam, India

Abbreviations

TRP	Test Positivity Rate
LSGD	Local Self Government Department
DCC	Domiciliary Care Centre
FLTC	First-Line Treatment Centre
SLTC	Second-Line Treatment Centre
ICU	Intensive Care Unit
CFR	Case Fatality Rate

1 Introduction

The world is witnessing a pandemic of SARS-CoV2 infection since the first quarter of the twenty-first century. Ever since the first case was reported in Wuhan city of China in December 2019, the virus has spread over 223 countries. Globally, there had been 187 million confirmed cases of COVID-19 as of 12 July 2021 [1]. The pandemic had also created global health, economic and political crises of which the consequences are yet to be determined. The spread of COVID-19 caused a huge disruption in our day-to-day activities which we never experienced in our lifetime. The mandatory social distancing norms and usage of face masks, temporary suspension of business activities and travel restrictions were new to the entire world. The pandemic also created an additional burden on the health care system. The first case of COVID-19 reported in India was in the Trichur district of Kerala on 30 January 2020. As on 12 July 2021, the number of cases in India is 30,904,734 and Kerala has 3,073,134 cases [2]. Ernakulam, the district in our focus, reported having 369,260 cases and 1446 deaths as of 12 July 2021.

In this scenario, the use of data analysis is more important than ever. Understanding and predicting the dynamics of COVID-19 spread through the analysis of the available data will empower our administrations with insights and can serve as useful tools for better planning and response against the burden inflicted on our health care infrastructure, emergency systems, and the overall economy. Thus, data analysis on COVID-19 is critical not only to protect the public health system but also to save lives.

2 Epidemiology of COVID-19

The predominant mode of transmission of SARS-CoV2 is through direct and indirect droplets [3]. The virus has also been identified from the stool samples of both symptomatic and convalescing patients but the risk of feco-oral transmission is unclear. The incubation period for the virus is 14 days, and the median incubation period is

4–5 days. The presentation varies from asymptomatic to symptoms like fever, dry cough, breathlessness, anosmia, loss of taste, anorexia, myalgia, and gastrointestinal symptoms like diarrhea, abdominal pain, vomiting, and nausea [4].

3 Methodology

Data is extracted from lab data management system (LDMS) which is a government portal to enter all the COVID testing details. Approximately, 15,000–35,000 tests are done daily in the district and the positive, negative and total number of tests done is taken from this portal. Complete demographic data of positive patients are also entered into the system. Daily reports of TPR, active cases, cases per million, etc. are calculated based on this data. Data from all the 124 peripheral government institutions are also entered into a google spreadsheet by the concerned authority and shared with the data management analysis team. The data collected include the number of new cases, active cases, test positive health care workers, antenatal COVID-19 cases and deaths including covid and non-covid deaths which get reported under the concerned institution.

When a patient is tested positive, the details of the patient are also entered into a google spreadsheet of positive case line list. Multiple google sheets are shared with peripheral institutions and the concerned authority in each institution is required to fill in the respective spreadsheets and share them with the data management analysis team of the District Surveillance Unit.

The members of the data analysis team combine the spreadsheets and sort the data using R software daily. The final detailed line list is a list with 58 columns, and a master line list is generated into which details of all COVID-19 positive patients are uploaded. As the number of cases is very high, the volume of data fed into the spreadsheets will also be high. Hence, the line list is split into 35 parts. For the ease of documentation and analysis, these 35 parts are combined into one part using the R software and all data analyzes are done using R. For a daily generation of various reports and a daily bulletin, a dedicated R script is written by the data team. Depending on the various parameters required to be plotted on a day, the R code is modified and then shared with the data management analysis team.

4 Data Analysis

The presenting author, part of the COVID-19 surveillance team of Ernakulam district had access to the data and conducted the data analysis. This article shares how the data analyzes had been an insightful resource to plan response measures against this pandemic in our district. All the analyzes were done using R software, version 1.4.1103. Tidyverse, ggplot2, dplyr, rlang, Googlesheets4, etc., are some of the main

packages used during the analysis. The different types of data analyzes conducted are mentioned briefly below (Fig. 1).

Ernakulam district has an estimated population of 3,811,430 and a population density of 1072/km². The time trend of COVID-19 cases-gender wise, category wise (history of contacts, health care workers, travelers, and unknown sources of infection) is being analyzed daily.

Males (51%) outnumbered females (49%) in the proportion of active cases and also in cumulative cases. Those with a history of contact with a confirmed case were the most among the positive cases.

Daily analysis of the time trend of patients who were isolated at their own houses and those getting admitted to various treatment facilities like DCCs, ICUs, FLTCs, CSLTCs, Government Medical College, and private hospitals are also done routinely. Biweekly projection of the expected cases is done, and the occupancy anticipated at various COVID treatment facilities is also calculated. Evaluation of these projections is done daily, and any variation will be noted and corrective measures are undertaken. Hence, we could anticipate the need for an additional requirement of hospital beds, beds with oxygen supply, ICU beds, and ventilators quite early and be prepared to address the rise in the number of cases (Fig. 2).

The time trend of TPR of the previous 1 year, previous 6 months, rolling TPR of previous 6 months, and last 2 weeks TPR are also analyzed. The test positivity rate (TPR) is one of the indexes used for monitoring the progression of the COVID-19 pandemic in the community. By observing this trend, it was also possible for us to forecast the course of patients admitted in hospitals and intensive care units. For example, when the TPR reaches a peak value, growth in COVID-19 hospitalizations lasting 12–15 days can be inferred. But, with the current testing strategy in which most of the tests being done in symptomatic and high-risk primary contacts and not in a random sample from the community; TPR doesn't translate to the real situation and imposing restrictions based on TPR alone will not help in containing the spread

Time trend of COVID 19 cases: Cumulative data

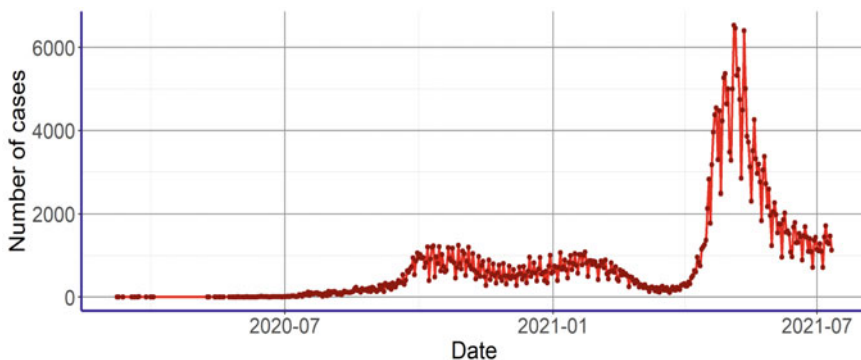


Fig. 1 Time trend of COVID-19 cases in Ernakulam district, Kerala

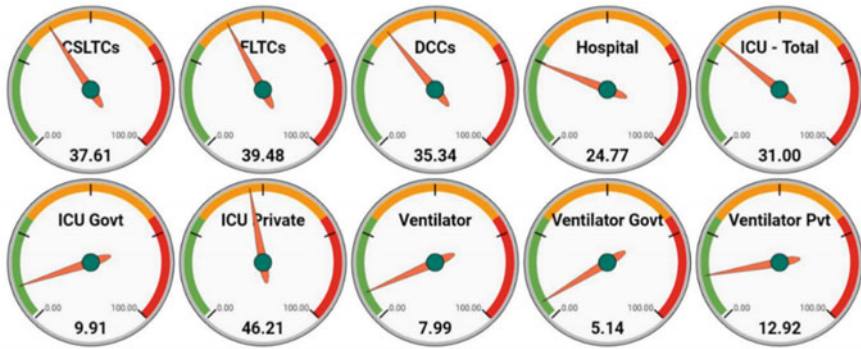


Fig. 2 Occupancy graph: district dashboard

of the virus. Some LSGDs had TPR less than 30 and most had TPR between 10 and 15% and only six LSGDs had TPR less than 5% at the time of writing this article (Fig. 3).

Plotting the seven-day moving average of cases provided us with a smoother curve of case trend without any drastic ups and downs spikes, which can occur due to fluctuations in daily test numbers and thus case numbers. The seven-day moving average in our data shows a steady plateauing trend, and this is expected to continue for 2–3 weeks (Fig. 4).

Fatal cases were analyzed age-wise and gender-wise and also CFR was calculated. CFR is the number of reported deaths per reported case. The analysis showed an increase in CFR with advancing age and also a higher CFR among males (Fig. 5).

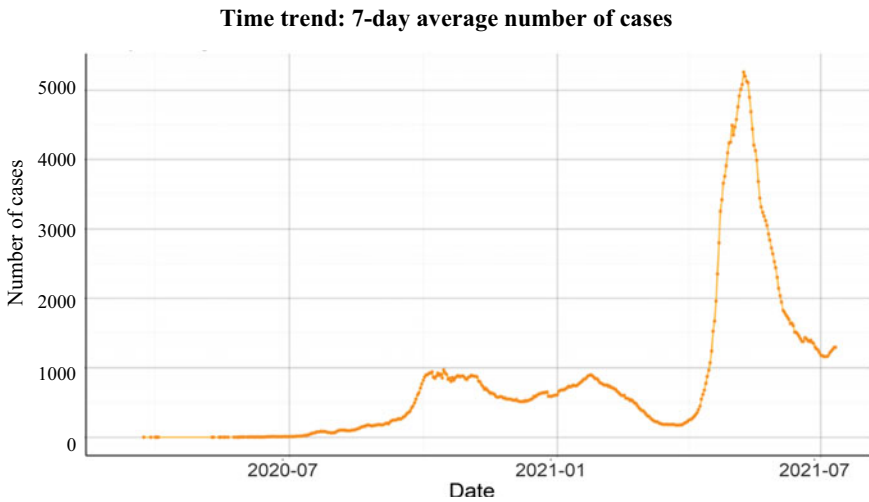


Fig. 3 Time trend of COVID-19 cases: 7 days rolling average

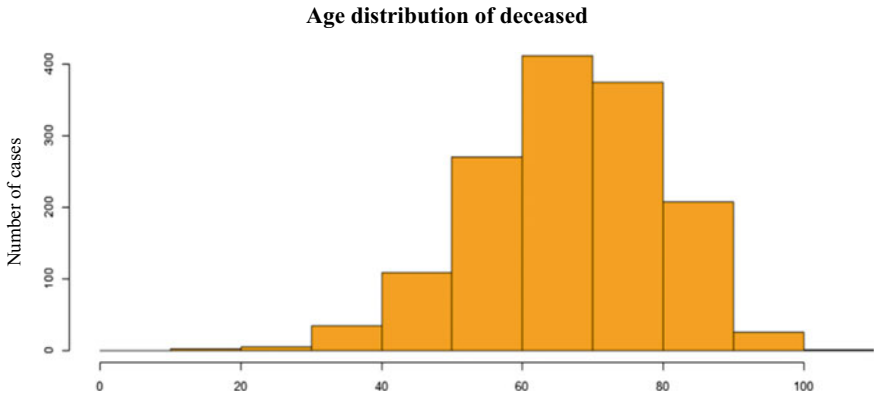


Fig. 4 Age distribution of deceased

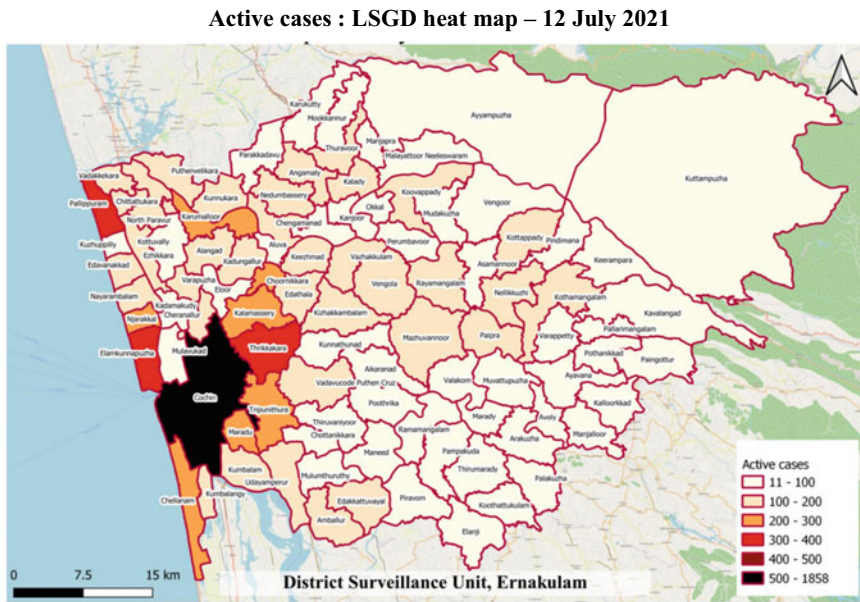


Fig. 5 Active cases heat map

LSGD heat maps for active cases, active cases per million, and TPR were also done which helped in focused intervention in places that had increasing active cases (Fig. 6).

As mentioned earlier, weekly TPR, active cases in each LSGD, and active cases per million in each LSGD were calculated. Using QGIS 3.5 mapping software, all these details are entered into the shapefile of Ernakulam District and a heat map based on colour grading is created. The heat map also allowed policymakers to make informed

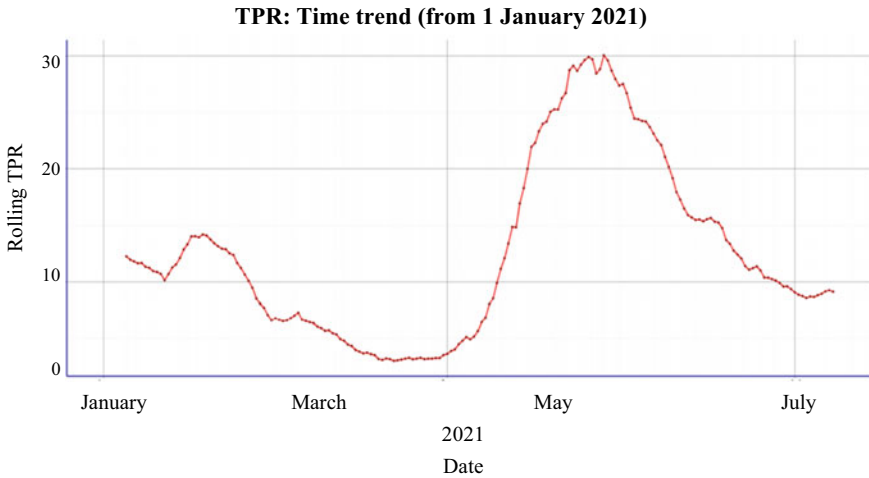


Fig. 6 Time trend of TPR

decisions since a piece of vital information was displayed in an easily comprehensible way. By looking at the heat maps, policymakers were able to quickly assess the areas which come under red and green zones and take appropriate data-driven decisions.

Time trend of patients in ICU showed that men outnumbered women and 61–70 years age group were more in number while the number of positive cases reported was more in 20–30 years age group. The average age of COVID-19 patients admitted in ICU was 57 years and the average age of the positive cases in the ongoing wave was found to be 39 years.

Dowd et al. found that the case fatality rate in COVID-19 increases as age advances [5]. In Ernakulam district also, the case fatality rate increased as the age advanced, and it goes significantly high above the age of 40 years. Most of the deaths are in the age group of above 60 years. Figure 4 shows the number of deceased across age groups. The fall in the number of deaths beyond the age group of 60–70 is due to the relatively lower number of COVID-19 cases in the respective age groups.

Studies from across the globe show that females have lesser fatality when infected with SARS-CoV2 [6–8]. In Ernakulam also females were found to have a lesser fatality. Females contribute to less than 40% of all COVID-19-related fatalities. The number of primary and secondary contacts for each case and each category of patients (health care workers, travelers, etc.) for the last 14 days and cumulative data was also analyzed.

Projection of cases for every upcoming 2 weeks and the next peak was also done. This data helps in the preparedness and to track the impact of the outbreak and facilitate infrastructure planning like arranging hospital beds and planning the daily required number of ICU beds, oxygen supply, and ventilators necessary to accommodate patients. The projection graph also helps to plan enforcement measures

TPR: LSGD heat map: 12 July 2021

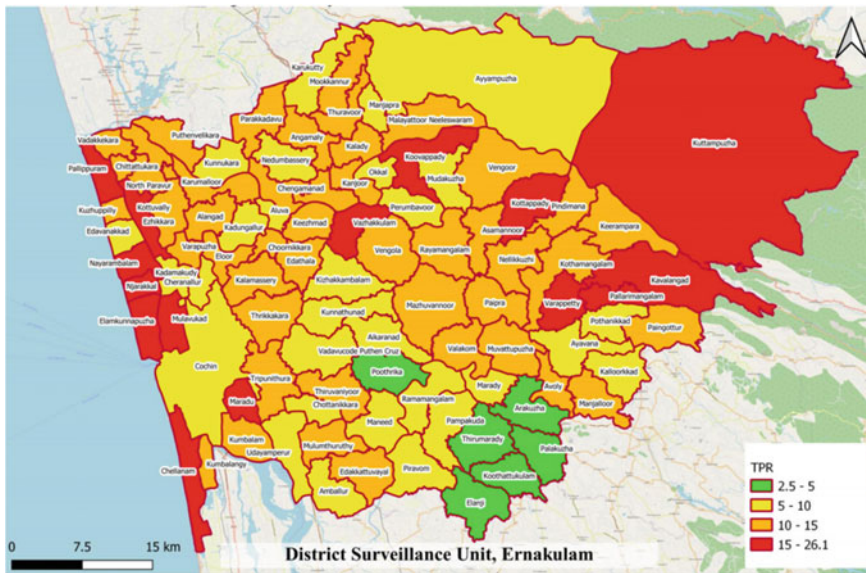


Fig. 7 LSGD heat map based on TPR

like imposing/withdrawing lockdown, intensifying social distancing measures, and opening of institutions and other business establishments (Fig. 7).

As there were many hues and cries in media over the rise in reported cases of invasive fungal infections among COVID-19 patients, we also analysed the mucormycosis cases reported in the district. Though 16 cases of mucormycosis got treated in the district (10 were Ernakulam natives), we found that the incidence of it was not different from the precovid days (2.8 per 100,000).

5 Cases Among Vaccinated

At the time of writing this article, 41% of individuals in the district are vaccinated with at least one dose and 11.34% of the population is fully vaccinated. As of July 12, 2021, 10,523 cases were reported among the first dose vaccinated individuals and 2692 infections were reported among the fully vaccinated. Breakthrough infections show an increasing trend, but studies from other parts of the world have shown that breakthrough infections have less mortality [9]. But, attaining a greater vaccination coverage should not be a reason to relax social distancing norms, usage of masks, or sanitization of hands. At the same time, an upward trend of breakthrough infections need not be taken as a failure of vaccination drive.

6 Prediction Model

Using the package ‘EpiModel’ of R-mathematical modeling of Infectious disease dynamics, we did the predictive analysis for hospitalization rate, percentage of patients requiring oxygen and ICU admission, percentage of patients getting admitted to first-line and second-line treatment centers, duration of hospital stay, duration of stay in first-line and second-line treatment centers, case fatality rate, age group and gender-wise fatality rate and hospitalization rate. While calculating the above-said variables, we had also taken into consideration the percentage of vaccinated population, breakthrough infections and percentage of hospitalization among the vaccinated.

We used four parameters in the model:

R0—the initial reproductive number

e.dur—duration of the exposed state

i.dur—duration of the infectious state

cfr—case fatality rate expressed as a proportion of those who will die among those infected.

Based on the above model described, we did a predictive analysis in July 2021 to look for the expected cases in September 2021. The results are summarized in Table 1 and Fig. 8.

Only a few studies have been conducted on predictive models of COVID-19 in India. A study conducted by Mandal et al. analyzed the predictive behaviour of COVID-19 cases in Maharashtra, New Delhi and Tamil Nadu. The authors used a classical SEIR type mathematical model to predict the daily active infected and confirmed (cumulative) infected COVID-19 cases in these three states using the software Mathematica. These models were used to impose testing strategies and lockdown measures in the three states [10].

Table 1 Expected cases based on the predictive model

Indicators	Numbers
Expected number of new cases—rolling average by 15 September 2021	2619–3143
Expected cases during (1–15 September 2021)	44,610–54,523
Number of active cases expected by 15 September 2021	35,000–44,000
ICU admissions expected by 15 September 2021	357–600
Hospitalisation: Expected by 15 September 2021	2114–2818
Expected deaths during 1–15 September 2021	268–327

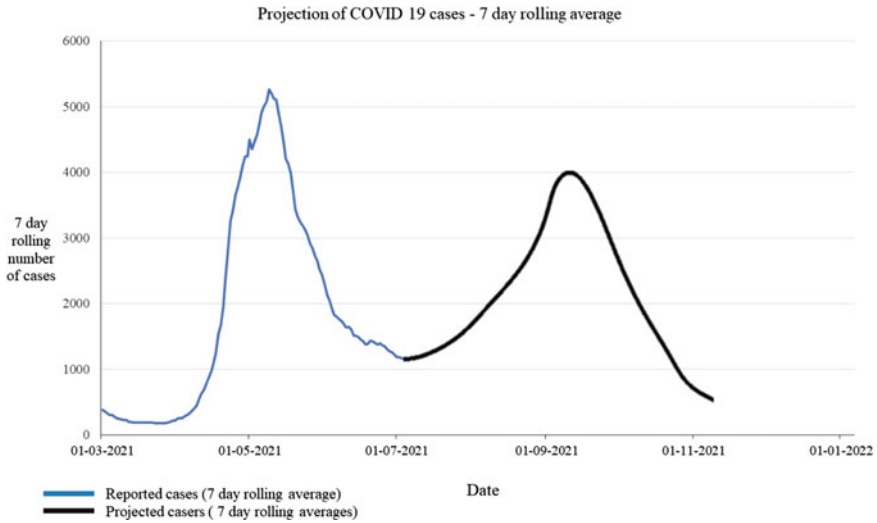


Fig. 8 Projection of COVID-19 cases—7 days rolling average

7 Conclusion

Although the epidemic situation in Kerala is not yet alarming, strengthening the mitigation efforts and increasing the vaccination drive is necessary to keep the transmission rate as low as possible. A comprehensive approach needs to be adopted to contain the virus. This can be achieved through aggressive testing, early diagnosis isolation and treatment with adherence to the updated protocols. Analysing and predicting the trend of COVID-19 would help the governments to better utilize their limited healthcare resources and adopt timely measures to stop the spread of the virus. The severity of SARS-CoV2 infection goes up as age advances, especially in patients with comorbidities. Prioritizing target treatment groups based on age and comorbidity status will help in better utilization of healthcare facilities and will reduce the fatalities due to COVID 19. Complications and fatalities are extremely rare below 20 years of age and vaccination can be prioritized to other age groups. Due to the dynamic nature of the virus, more epidemiological models are required for forecasting and preparedness for the pandemic. This can be achieved by utilizing the raw data and secondary data for analysis and conducting more research.

Acknowledgements Data collection and compilation:

Dr Vinu M Satheesh, District Surveillance Unit, Ernakulam

Dr Shima Salim, District Surveillance Unit, Ernakulam

Ms. Anjaly Roni, Data Entry Operator, District Surveillance Unit, Ernakulam

Ms. Lincy Mary, Data Entry Operator, District Surveillance Unit, Ernakulam

References

1. COVID-19 map—Johns Hopkins coronavirus resource center. Johns Hopkins Coronavirus Resource Center. Published 2021. Accessed 13 July 2021. <https://coronavirus.jhu.edu/map.html>
2. MoHFW. Home. Mohfw.gov.in. Published 2020. Accessed 12 July 2021. <https://www.mohfw.gov.in/>
3. Cheung KS, Hung IFN, Chan PPY et al (2020) Gastrointestinal manifestations of SARS-CoV-2 infection and virus load in fecal samples from a Hong Kong Cohort: systematic review and meta-analysis. *Gastroenterology* 159(1):81–95. <https://doi.org/10.1053/j.gastro.2020.03.065>
4. World Health Organization: WHO. Transmission of SARS-CoV-2: implications for infection prevention precautions. Who.int. Published July 9, 2020. Accessed 12 July 2021. <https://www.who.int/news-room/commentaries/detail/transmission-of-sars-cov-2-implications-for-infection-prevention-precautions>
5. Dowd JB, Andriano L, Brazel DM, Rotondi V, Block P, Ding X et al (2020) Demographic science aids in understanding the spread and fatality rates of COVID-19. *Proc Natl Acad Sci USA* 117(18):9696–9698
6. [Internet]. Epicentro.iss.it. 2021 [cited 30 October 2021]. Available from: https://www.epicentro.iss.it/en/coronavirus/bollettino/Report-COVID-2019_5_october_2021.pdf
7. Coronavirus (COVID-19) case numbers and statistics [Internet]. Australian Government Department of Health. 2021 [cited 5 October 2021]. Available from: <https://www.health.gov.au/>
8. Alkhouli M, Nanjundappa A, Annie F, Bates MC, Bhatt DL (2020) Sex differences in case fatality rate of COVID-19: insights from a multinational registry. *Mayo Clin Proc* 95(8):1613–1620
9. COVID-19 vaccine breakthrough cases: data from the states [Internet]. KFF. 2021 [cited 2021 Aug 14]. Available from: <https://www.kff.org/policy-watch/covid-19-vaccine-breakthrough-cases-data-from-the-states/>
10. Mandal M, Jana S, Nandi SK, Khatua A, Adak S, Kar TK. A model based study on the dynamics of COVID-19: prediction and control. *Chaos, Solitons & Fractals* [Internet]. 2020 Jul [cited 2022 Jan 9];136:109889. Available from: <https://www.ncbi.nlm.nih.gov/pmc/articles/PMC7218394/>

Optimization Techniques

Solar Water Pumping System Design and Analysis-A Numerical Study at Dum Dum, Kolkata



A. Kr. Roy  and S. Dutta 

Abstract Solar water pumping system is one of the engineering marvels, which uses solar energy to pump underground water for irrigation, agricultural and drinking purposes in India and most importantly it does not utilize the traditional fuels which are responsible for polluting the environment. In the following research article, we carry out a technical analysis of pumping water by utilizing solar systems for agricultural irrigation needs and fresh drinking water supply for a project located at Dum Dum, Kolkata (chosen as per the nearest location available in software) by execution of simulations utilizing photovoltaic system software. Accordingly in the research paper, we present the results in terms of water delivered for human uses, the water volume which is absent or missing, the additional (underutilized) solar energy, and the entire calendar yearly generated photovoltaic system efficiency. The results of the simulations display that investment in photovoltaic solar technologies could be highly beneficial for this site location, as the amount of pump operation energy was found to be maximum in the month of June (6454 Kwh), while the monthly performance ratio was found to be 55.3% and the efficiency of the system was found to be 15.22%.

Keywords PV panel · Solar pump · Irrigation · Solar inverter · Photovoltaic system

1 Introduction

The solar irrigation system mostly utilized by society and human needs comprises the photovoltaic system array and pumping components such as motor, positive displacement pump and a control system. The intention for this project work is that some rural areas of West Bengal, India are currently suffering from acute power crises because of recent cyclones. Nonrenewable energy sources are the main energy source of India and the power generation sector is heavily dependent on that. The

A. Kr. Roy (✉) · S. Dutta
Elite College of Engineering, Kolkata, West Bengal 700113, India
e-mail: royarnb93@gmail.com

price of fossil fuel and pollution level is increasing rapidly. Due to these problems, the farmers in the rural areas are not able to irrigate the crops properly. In this paper, we aim to design an optimized solar water pumping system in photovoltaic system software for irrigation purposes.

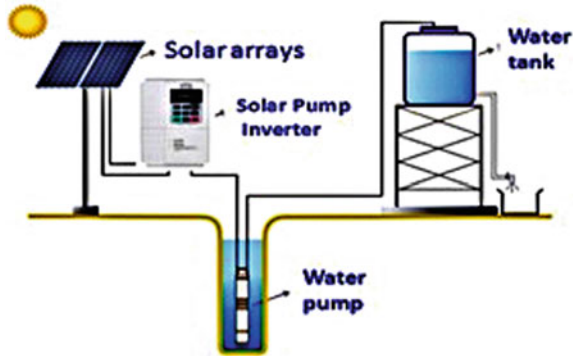
A critical literature survey analysis reveals that Arab et al. [1] has presented a method for doing estimation regarding the probability of loss load (PLL) pertaining to photovoltaic water system centrifugal pumping by choosing regarding constant profile, and utilizing a water tank with an autonomy capacity of maximum 2 (two) days and also considering two pumping heads when applied to a centralized system of centrifugal pumping. Abu-Aligah [2] had carried out research work pointing out the fact that in localized areas where electricity was unavailable, other measures were of necessity to pump water pertaining for human consumption. One option proposed by them was a photovoltaic (PV) pumping system. Sudhakar et al. [3] had investigated the solar water pump for lift irrigation. A “modified pump” was also suggested by them, which could have been beneficial to rural requirements of water. The authors had presented the thermodynamic analysis of the pumps. The authors had also presented the results pertaining to the solar water pump being operational with solar collectors having flat-plate, but it was also analyzed by them whether the same pump could be run more efficiently by utilizing concentrating coupled solar collectors. Barua and Prasath [4] had carried out simulations pertaining to an academic campus utilizing the grid-connected solar photovoltaic top roofing system and accordingly the feasibility and the design study of the solar photovoltaic rooftop system project was presented by them after the authors inspected their project viable area by critical utilization of specific NASA meteorological surface data points in the photovoltaic system. Sharma et al. [5] studied solar photovoltaic system design and the performance depends on geographical location and solar irradiation using a photovoltaic system. Matchanov et al. [6] studied a 2.24 kW grid-connected micro-inverter system output by photovoltaic system software. Another well-known research article presented by Shrivastava et al. [7] used photovoltaic system software evaluation of a grid-connected standalone system consisting of 20.8 kW 10 PV modules was also referred to.

2 Methodology

The solar water pumping system runs on electricity generated by solar panels. (Please refer to Fig. 1). A submersible pump is used in the simulations, which is used to pump water from a well and stored in an overhead tank for irrigation, drinking and other household purposes. Solar panels generate an electric charge and the solar pump inverter controls the charge for the smooth running of the pump. Further, the pump is placed in a well to pump the well water to a tank for future use.

PVsyst is the most sought-after software analysis utilized in the critical investigation and modeling examination of photovoltaic solar structural schemes for several practical applications (be it standalone, or water pumping and grid-connected). A

Fig. 1 Deep well solar water pumping diagram



huge database is inbuilt in the software analysis with the simulation tool closely associated with the photovoltaic solar structural synthesis that is currently in demand for day-to-day analysis and commercial market applications. Photovoltaic system simulation can also lead to a detailed eco-commercial analysis too. The solar water pumping system runs on electricity stemming from the solar panelized cabinets. A submersible pump is used in the simulations, which is used to pump water from a well and stored in an overhead tank. Solar panels generate an electric charge and the solar pump inverter controls the charge for the smooth running of the pump. It should also be mentioned in this context that the photovoltaic system software runs on an hour-to-hour criterion and measure.

In this project, we have utilized, the photovoltaic system 6.88 [8] for utilizing the simulations obtained by the photovoltaic system software for deepwater pumping criterion and measure for two water levels of 40 m and 60 m, but we have presented the results for 60 m only, because of paper length constraints. The inputs of this software are irradiation energy (Avg. monthly and solar), average everyday water requirements, the depth of the water well or reservoir indications, exact selection of the pump and photovoltaic system solar modules. The final relevant results include mainly the delivery of exact water transported for human uses, the loss of water data, the additional (underused) solar power available, and most importantly the exact ratio of performance (PR) measured to calculate the photovoltaic system software efficiency which we can calculate either monthly or yearly.

In this research paper, we chose the geographical location from the software database, the meteo data for the location was provided by the software (Metronome 7.2). The tilt and azimuth angle can be ascertained from the latitude and longitude of the located place. We had also chosen the angle of inclination which yields maximized system output. Also, in this context, it is important to note that the angle of azimuth is defined as that angle that is calculated intervening the south/north and the plane of solar collectors. In this PVsyst software simulated input value, the angle of inclination in summer is assumed 22 and in winter it is 42°, and the azimuth angle was chosen as Zero (0°) degrees. The software also provides a huge number of different kinds of solar panels based on material, output and quality. In this simulation, we used

250-W si-poly photovoltaic system modules accordingly which were chosen to give the best possible results and maximize the output obtained. The inverter used in this simulation is an maximum power point tracker (MPPT)-AC inverter for power conditioning of this system and is also provided by the photovoltaic system software and has a large number of choices.

3 Validation

Extensive research work was carried out by concentrating upon the dataset of NASA surface meteorology utilized via the coordination of geographical viewpoints of several project places before embarking on the simulations on this research paper. The research papers which we had referred to compare the research results are the system efficiency (during the entire year), effectiveness and array global energy.

We had carried out two validations from the previously published research work. The 1st validation was from the research paper of Touahri et al. [9] who analyzed a design of a 3 MW grid which consisted of 245 W, 12,244 photovoltaic panels and 500 kW, 6 inverters, and had a cumulative total output of 5980 MWh during the year using photovoltaic system software. The 2nd validation was carried out by comparing the published results pertaining to the paper of Kumar et al. [10] who presented a work of requirements of power in the department of mechanical engineering office at a Bikaner based reputed engineering college, Rajasthan by designing and installing the standalone solar photovoltaic system. The validation results are now compared in the present manuscript from Touahri et al. [9]

Figure 2a–c are the figures of simulations that was achieved by present photovoltaic system simulation software for normalized productions and performance ratio, loss diagram, and the main simulation results of 3 MW system by PVsyst software (connection achieved by grid) and it is validated and compared from Touahri et al. [9] who presented results for Kabertene in the NE of Adrar state, conforming to latitude $28^{\circ} 27'04.8''$ N, and longitude of $0^{\circ} 02'49.8''$ W. The balances and main results as carried out from the present photovoltaic system of 3 MW grid-connected PVsyst is also presented in Fig. 3.

From the simulations carried out, it is found that the normalized productions (per installed Kwp), performance ratio, loss diagram of the present simulations are closely matching the published results. The balances and main results are presented in Fig. 3, and it should be mentioned in this context that the present authors had simulated the E_array and E_grid results in MWh whereas Touahri et al. [9] had presented those in KWh.

The validation results of Kumar et al. [10] are now presented in Fig. 4a, b and when we compare the published results of Kumar et al. [10] suiting to Engineering College Bikaner it's found that the Normalized productions (per installed Kwp), performance ratio, loss diagram of the present simulations are closely matching the published results.

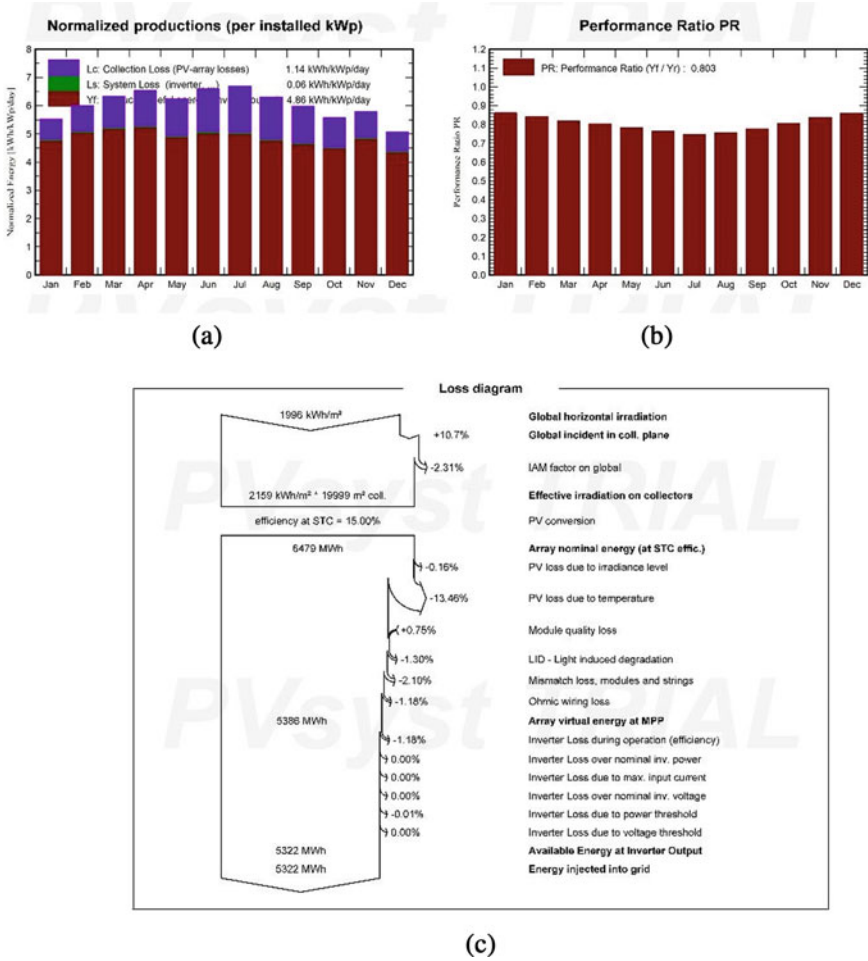


Fig. 2 a, b and c From our present simulation (PVsyst V7.2.8) and validated from Touahri et al. [9]

4 Result and Discussion

4.1 Site Location

To start with this research paper, we have carried out simulations of the solar photovoltaic pumping water systems by selecting one potential site. The region selected by us is Gauripur, Dumdum (Latitude 22.6420° N, Longitude 88.4312° E) located in West Bengal, the eastern part of India and it is the closest site of meteo data available in the photovoltaic system database. We also present here solar energy (radiation) set

Balances and main results								
	GlobHor	DiffHor	T_Amb	GlobInc	GlobEff	EArray	E_Grid	PR
	kWh/m ²	kWh/m ²	°C	kWh/m ²	kWh/m ²	MWh	MWh	ratio
January	116.8	37.27	12.32	171.7	168.2	449.4	444.3	0.863
February	128.9	45.41	15.62	168.0	164.9	430.3	425.3	0.844
March	171.5	68.74	20.93	196.6	192.5	488.8	483.0	0.819
April	192.0	82.78	25.32	196.0	191.2	477.7	472.2	0.803
May	207.2	97.02	30.82	193.7	188.3	461.0	455.3	0.784
June	219.3	99.35	34.76	197.7	192.0	459.0	453.2	0.764
July	226.6	99.72	38.39	207.7	201.9	471.8	465.9	0.748
August	198.7	99.46	37.53	195.6	191.0	450.0	444.7	0.758
September	165.4	76.16	33.15	179.7	175.6	423.3	418.4	0.776
October	143.1	69.05	27.30	172.7	169.3	422.8	417.8	0.806
November	122.1	39.83	18.50	173.6	170.3	440.9	435.8	0.837
December	104.8	35.97	13.55	157.3	154.1	410.5	405.7	0.850
Year	1996.5	650.75	25.74	2210.3	2159.3	5385.7	5321.6	0.803

Legends	
GlobHor	Global horizontal irradiation
DiffHor	Horizontal diffuse irradiation
T_Amb	Ambient Temperature
GlobInc	Global incident in coll. plane
GlobEff	Effective Global, corr. for IAM and shadings
EArray	Effective energy at the output of the array
E_Grid	Energy injected into grid
PR	Performance Ratio

Fig. 3 From our present simulation (PVsyst V7.2.8) and validated from Touahri et al. [9]

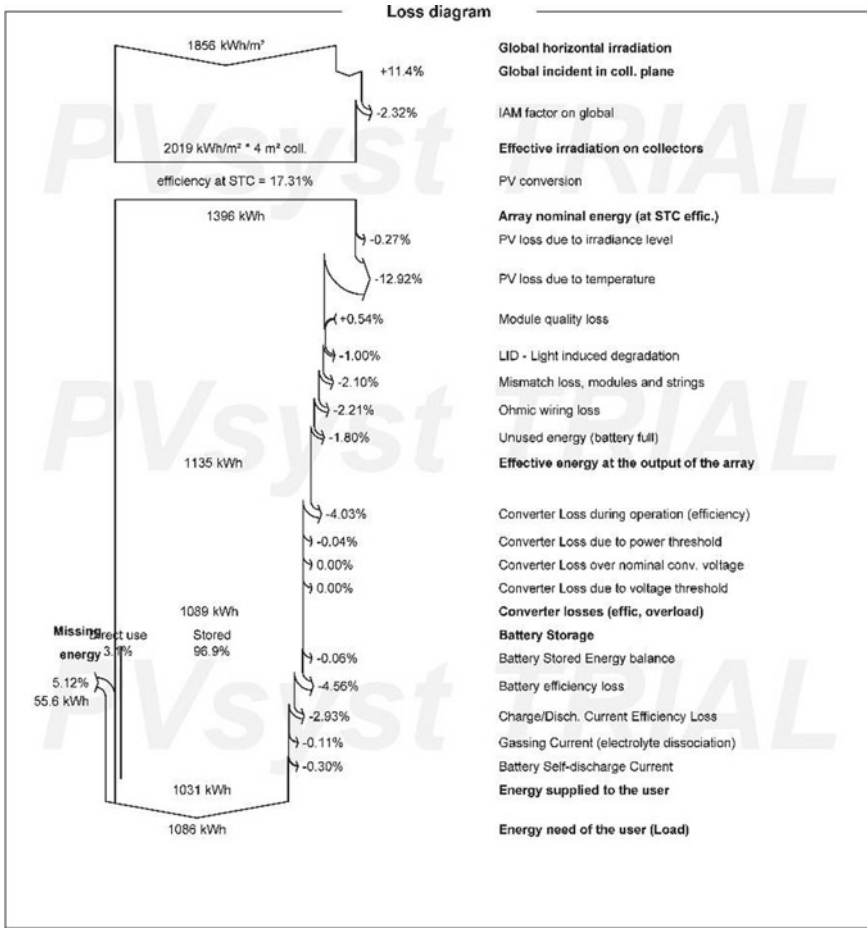
of data according to geographical location which is collected from the photovoltaic system software database (Metronome 7.2, 1981–1990) as shown in Fig. 5.

4.2 Simulation Input Parameter

While critical analysis of the present design and the simulation results of the system, some assumptions were done accordingly and results presented. The primary among those was that the panels of solar cells were considered un-shaded and with the pump working at the fullest consideration of water extraction to meet the annual summer months demand. We have tried to present the important design main input values and the chosen simulation parameter in Table 1 which was selected as per our choice of parameters. This table represents the details of 60 m well simulation parameters and components, also their manufacturer power rating and model name. It is important to mention that changing these parameters will change the simulation results too. Simulations corresponding to 60 m deep well are presented in Table 2. It can be seen from the simulation values that it selected photovoltaic size and pump power too. Pump efficiency is pegged at 67.7% which is a healthy ratio.

For the following paper and in this section, we now present the results of the simulations for the proposed photovoltaic system.

Here we can see how much water is pumped than needed, energy at the pump, pump efficiency, unused PV energy are presented for 60 m deep well PV pumping systems as done by design simulation result. The ratio of water pumped vs. water needs is found to be 46.9%.



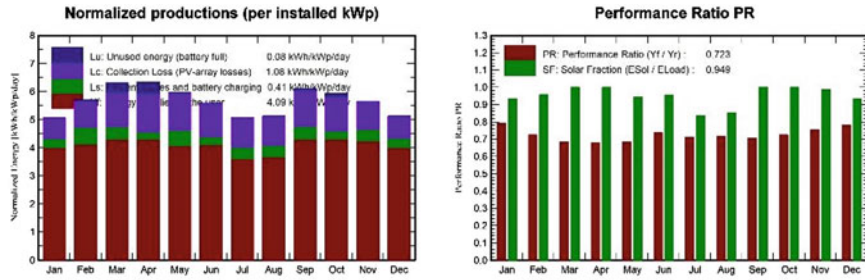
(a)

Fig. 4 a, b Simulations carried through PVsyst by a present photovoltaic system and suiting to Kumar et al. [10] for Engineering College Bikaner at 28.060 N latitude and 73.300 E longitude

And it can be seen that the results enumerated are energy production, production specified energy along with the performance ratio and loss diagrams. Accordingly, we now present the entire simulation main and balance data results of the photovoltaic systems in Table 3.

Here we can see that the system balances consist of the global effect, array virtual energy, pump operation energy, unused energy, average total head of the pump, water pumped, water drawn by the user, missing water.

Legends and abbreviation used: G_{eff} = Effective global energy, E_{ArrMPP} = Array virtual energy at MPP, $E_{\text{Pmp Op.}}$ = Pump operation energy, ETK_{Full} =



Balances and main results

	GlobHor	GlobEff	E_Avail	EUnused	E_Miss	E_User	E_Load	SolFrac
	kWh/m ²	kWh/m ²	kWh	kWh	kWh	kWh	kWh	ratio
January	111.5	153.7	89.3	0.000	6.34	85.92	92.26	0.931
February	125.4	156.3	88.9	0.609	3.56	79.77	83.33	0.957
March	171.7	191.6	105.2	7.249	0.00	92.26	92.26	1.000
April	185.5	186.0	100.0	8.762	0.00	89.28	89.28	1.000
May	197.0	179.9	95.1	0.146	5.18	87.08	92.26	0.944
June	183.3	162.9	87.3	0.000	4.11	85.17	89.28	0.954
July	169.4	152.6	82.3	0.000	15.17	77.08	92.26	0.836
August	162.1	154.7	84.1	0.002	13.60	78.66	92.26	0.853
September	168.4	178.9	96.5	1.208	0.00	89.28	89.28	1.000
October	150.8	180.6	97.9	2.770	0.00	92.26	92.26	1.000
November	122.3	166.2	92.9	0.000	1.30	87.98	89.28	0.985
December	108.3	155.7	89.9	0.013	6.36	85.89	92.26	0.931
Year	1855.7	2019.3	1109.4	20.760	55.62	1030.62	1086.24	0.949

Legends

- GlobHor Global horizontal irradiation
- GlobEff Effective Global, corr. for IAM and shadings
- E_Avail Available Solar Energy
- EUnused Unused energy (battery full)
- E_Miss Missing energy
- E_User Energy supplied to the user
- E_Load Energy need of the user (Load)
- SolFrac Solar fraction (EUsed / ELoad)

(b)

Fig. 4 (continued)

Unused energy (full Tank), H_{Pump} = Avg. total head of the pump, W_{Pumped} = Water pumped, W_{used} = Water drawn by the user, W_{miss} = Missing water.

It can be observed that January records the highest effective global energy and the Array virtual energy at Multiple Maximum PowerPoints (MPP). The yearly effective global energy was found to be 1829.1 Kwh/m². The pump operation energy was found to be maximum in June (6454 Kwh). We now analyze Fig. 6 which shows the simulations of produced normalized energy and measured in terms of unused energy ($L_u = 1.27$ kWh), collective energy loss obtained ($L_c = 0.58$ kWh), photovoltaic system's loss obtained ($L_s = 0.45$ kWh), and effective energy at the pump ($Y_f = 2.85$ kWh) installed and measured in kWp/day per pump for the entire year. Figure 7 represents the monthly performance ratio and it is found to be 55.3%.

It can also be seen from the simulation results that the system's unused energy is not low while the collective losses in the system are on the higher side. This can be attributed to the fact that we had designed the system in such a manner so that the

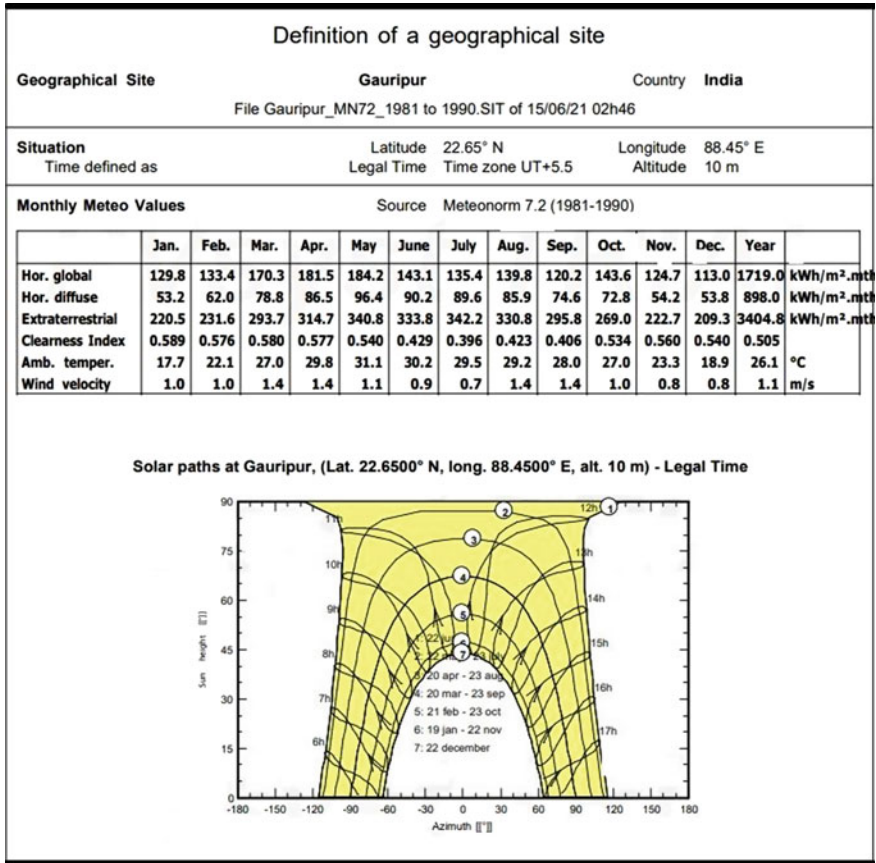


Fig. 5 Solar radiation data of the site

motor and pump unit pumps out the maximum water possible and the production accordingly maximizes and happens by reducing this is what leads to the collective losses. Minimization of losses and unused systems will be catapulted and this has to happen if we reduce water pump capacity. In Fig. 8 we can refer to the loss diagram for the entire year for the present preposition of the chosen grid. It has been found that the global irradiance (horizontal parameter) is pegged at 1719 KW/m² while the irradiance (as effective on collector) is 1829 KWh/m². The maximum loss that is encountered here is the loss in the array which has a value of 11.8% and the converter loss reached 3.21%. The efficiency of the system is thus obtained as 15.22%. The efficiency can be increased by reducing the array losses which will be our target for a better system design.

Table 1 Design simulation input parameters

Input parameters	Specifications
Total requirement of water	1200 m ³ /day
Water head (Total)	67 m
The tank storage volume of water	240 m ³
Well depth	60 m
Borehole diameter	40 cm
Length of the pipes	70 m
Summer sun angle (tilt)	22°
Winter sun angle (tilt)	42°
Consideration of Azimuth angle	0°
Types of solar panel	Model: TSM-310PD14, 250w, si-poly, manuf. Trina solar
Pump manufacturing type	Model: SP 95-7, 37 kW, ac motor, Manufacturer Grundfos
Control device	Model: ACSM1, 45 kw 440 vac, MTTP AC inverter, manuf. ABB

Table 2 Simulation result of 60 m deep well

Simulation result	
Pumped water	205,493 m ³
Water needed	438,000 m ³
Pump energy	56,217 kWh
PV energy underutilized (for full tank conditions)	20,154 kWh
System efficiency//pump efficiency	65.6 and 67.7%
Missing water//unused fraction	53.1 and 23.5%

5 Conclusion

For the present research paper, solar photovoltaic-based water pumping has been designed and presented for a rural **project located at Dum Dum, Kolkata**. In this research paper, we have accordingly presented the results such as the effective global energy and the Array virtual energy at MPP, pump operation energy and the system efficiency during the year. The lifespan of solar pumping systems is more than 20 years and is also reliable too. It is more cost-effective than conventional diesel-powered systems. Efforts should be made to reduce the array losses which will make this system more feasible in the long run. In today's world, pollution is a very big problem to mankind, and by replacing diesel or fossil fuel systems with solar pumping systems, pollution can be controlled at a great point.

The main summary of this research paper was:

Table 3 Entire simulation main and balance data results of the photovoltaic systems

	Globe kWh/m ²	EArr _{MPP} kWh	E_Pmp Op K	ETK _{Full} kWh	H_Pump Meter (W)	W_Pumped m ³	W_used m ³	W_miss m ³
January	175.9	8461	4057	4112	47.84	21,458	21,578	15,622
February	157.7	7453	3674	3505	47.80	19,663	19,663	13,937
March	175.6	8132	4052	3695	47.78	21,795	21,795	15,405
April	177.2	8090	4044	3688	47.73	21,462	21,462	14,538
May	168.0	7697	4056	3261	47.63	21,234	21,234	15,966
June	127.8	5971	6454	2017	47.52	17,794	17,794	18,206
July	121.7	5752	3268	1734	47.48	17,961	17,961	19,239
August	132.0	6173	3443	2217	47.59	18,153	18,153	19,047
September	120.0	5640	3261	1882	47.51	16,772	16,772	19,228
October	159.7	7459	3868	3173	47.72	20,733	20,733	16,467
November	161.0	7548	3765	3472	47.82	20,167	20,167	15,833
December	152.4	7332	3732	3318	47.83	20,231	20,231	16,969
Year	1829.1	85,709	44,875	36,075	47.68	237,423	237,523	200,457

Normalized productions (per installed kWp): Nominal power 54.0 kWp

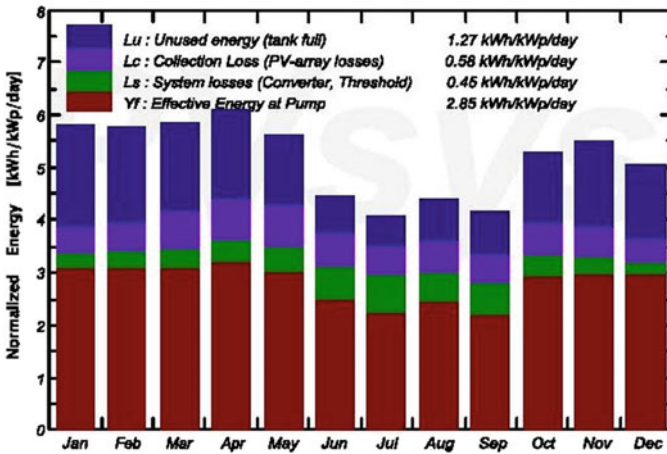


Fig. 6 Normalized energy production of the system

- The month of January records the highest effective global energy and the Array virtual energy at Multiple Maximum PowerPoints (MPP).
- The pump operation energy was found to be maximum for June (6454 Kwh) while the monthly performance ratio was found to be 55.3%.

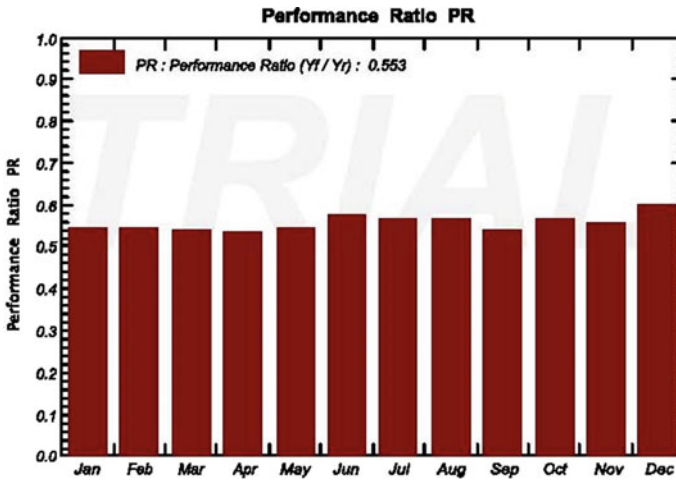


Fig. 7 Monthly performance ratio

- The unused energy was found to be ($L_u = 1.27$ kWh), the collective loss was pegged to be: ($L_c = 0.58$ kWh), the loss of the system performance was ($L_s = 0.45$ kWh) and effective energy at the pump was found to be ($Y_f = 2.85$ kWh).
- The horizontal global irradiance found from simulations was found to be 1719 KW/m² while it was found that the irradiance (effective collector value) to be 1829 kWh/m².
- The efficiency of the system is thus obtained as 15.22% . The lifespan of solar pumping systems is more than 20 years and is also reliable.
- From the analysis it can be concluded that if we can install a similar machine in the present location then it will be more cost-effective than conventional diesel-powered systems. However, care should be taken to take care about the efforts to be made to reduce the array losses which will make this system more feasible in the long run.

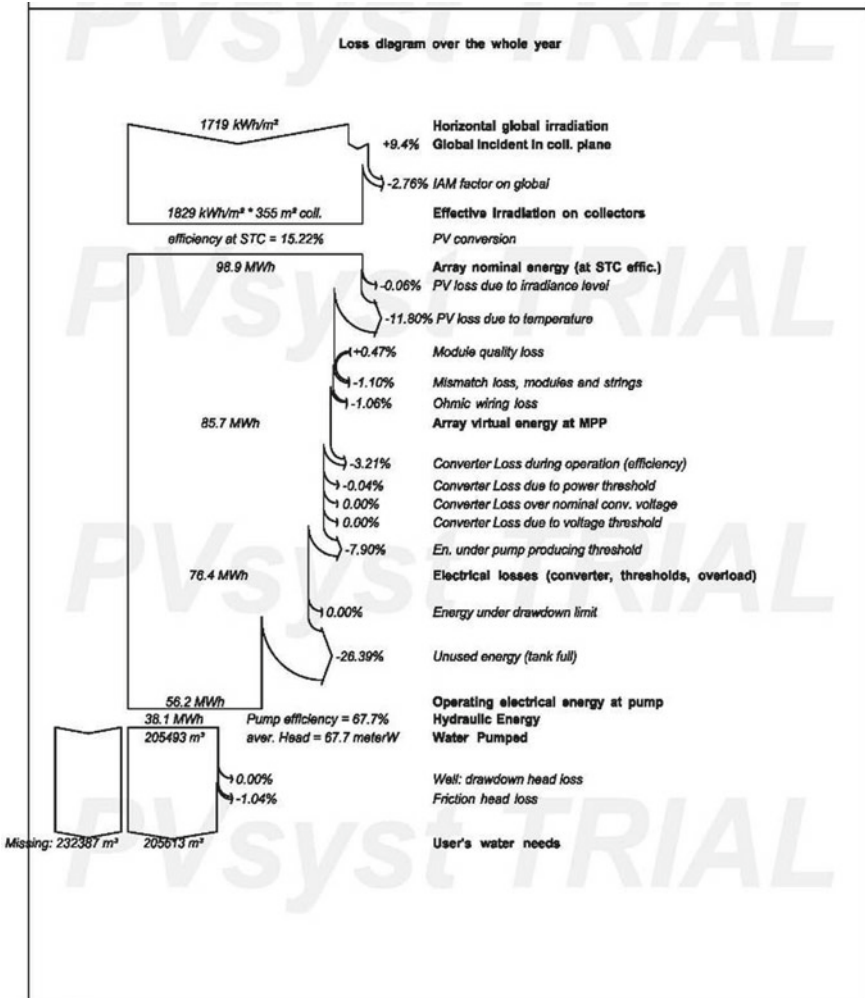


Fig. 8 Loss diagram of the present PV system

References

1. Hadj Arab A, Chenlo F, Benganem M (2004) Loss-of-load probability of photovoltaic water pumping systems. Solar Energy 76:713–723
2. Abu-Aligah M (2011) Design of photovoltaic water pumping system and compare it with diesel powered pump. Jordan J Mech Indus Eng 5:273–280
3. Sudhakar K, Murli Krishna M, Rao DP, Soin RS (1980) Analysis and simulation of a solar water pump for lift irrigation. Solar Energy 24:71–82
4. Barua S, Prasath RA (2017) Rooftop solar photovoltaic system design and assessment for the academic campus using PVsyst software. Int J Electron Electr Eng 5

5. Sharma S, Kurian CP, Paragond LS (2018) Solar PV system design using PVsyst. In: 2018 International conference on control, power, communication and computing technologies
6. Matchanov NA, Seok KO, Mirzaev AA, Maikov MA, Saidov DSH (2020) Study of energy yield on grid connected micro-inverter type 2.24 kW PV system using PVsyst simulation software. *Appl Solar Energy* 56:263–269
7. Shrivastava A, Sharma R, Saxena MK, Shanmugasundaram V, Rinawa MK, Ankit (2021) Solar energy capacity assessment and performance evaluation of a standalone PV system using PVsyst. *Mater Today: Proc*
8. PVsyst photovoltaic software (2021). <https://www.PVsyst.com/>
9. Touahri T, Larabi S, Maouedj R, Ghaitaoui T (2019) Feasibility analysis of a solar PV grid-connected system using PVsyst software tools. In: Hatti M (eds) *Smart energy empowerment in smart and resilient cities. ICAIRES 2019. Lecture notes in networks and systems*, vol 102. Springer, Cham
10. Kumar R, Rajoria CS, Sharma A, Suhag (2021) Design and simulation of standalone solar PV system using PVsyst software: a case study. *Mater Today: Proc* 46:5322–5328

A Model for Prediction of Water Level and Pressure in an Industrial Boiler Using Multivariate Regression



V. K. Haribhakta , R. S. Jha , A. K. Kelkar , A. N. Khairnar ,
and H. S. Khade 

Abstract During the operation of an industrial boiler, it is subjected to huge variations in pressure as well as water level which lead to a decrease in the performance of a boiler. This decline in performance can be avoided by minimizing these variations with the help of a control system. However, the conventional control system used by a boiler accounts for a significant time lag which in turn affects the performance negatively. Hence, in this study, predictive models of water level and pressure developed using mass and energy balance equations of the boiler are presented, which can be utilized in minimizing these variations by determining the fluctuations beforehand. The predictions made by these models can be used in adjusting the inputs such as feedwater rate and fuel input rate to avoid the impending changes in pressure and water level. The concept of multivariate regression has been implemented in developing these models that have an average error of 0.0243% in water level predictions and 8.0525% in pressure predictions. This regression algorithm deals with a water level range of 64.525%, pressure range of 0.467 MPa, and steam load range of 70%.

Keywords Boiler dynamics · Multivariate regression · Water level · Void fraction · Pressure · Prediction

V. K. Haribhakta · A. K. Kelkar (✉) · A. N. Khairnar (✉) · H. S. Khade
Department of Mechanical Engineering, College of Engineering, Pune, India
e-mail: kelkarak17.mech@coep.ac.in

A. N. Khairnar
e-mail: khairnar17.mech@coep.ac.in

V. K. Haribhakta
e-mail: vkh.mech@coep.ac.in

H. S. Khade
e-mail: khadehs17.mech@coep.ac.in

R. S. Jha
Thermax Ltd., Chinchwad, Pune, India
e-mail: r.jha@thermaxglobal.com

1 Introduction

Since, the industrial revolution, the power requirement of the world has been increasing at an unprecedented rate. This has made thermal power plants one of the main sources of power generation today. The changing output requirements lead to a changing load on the boiler. Hence, the input parameters of the boiler have to be changed accordingly. Controlling parameters such as pressure, temperature, fuel input rate, feedwater flow rate, and net air quantity have to be modified to meet the output requirements. The conventional control systems implemented in an industrial boiler are PID controlled and have a significant time lag in modifying the inputs. By the time inputs change, the output requirements vary and a new set of inputs is needed to maintain the efficiency of the boiler. Such rapid variations in the boiler affect the performance of the boiler. Hence, a faster control system is required.

The recent developments in storage capacities and faster computing abilities of computers have widened the scope of artificial intelligence (AI) and machine learning (ML) to various fields. Various ML algorithms can be used to model a system that helps in making useful predictions. Hence, such a control system can be developed for an industrial boiler with the help of ML algorithms. The impending water level variations in a boiler can be predicted using one model and another model can be used to change the inputs to the boiler to avoid these predicted variations. This paper presents such a model that has been developed using multivariate regression. The process of multivariate regression has been performed on the mass balance equation and energy balance equation of the boiler [1] using the SLSQP minimizer from SciPy.

2 Literature Review

Neural networks (NN) are good at establishing relations between multiple variables, which comes in handy in boiler dynamics, with complex dependencies of numerous variables. The equations formed by a trained NN also help give insight into these dependencies in a system. A user-friendly approach involving no complex expressions and transparent calculations was proposed in [2] to determine the Silica level in the steam inside the boiler. Silica (SiO_2) formation on boiler walls is a major problem, and a simple correlation between pressure, density, and temperature of steam and scale formation was used to predict the solubility of silica. There may be erosive wear on the metal surfaces along the flow field due to entrained fly ash particles in the flue gas as presented in [3]. The areas in a boiler that are likely to be subjected to erosion have been identified with computational fluid dynamics (CFD) based code. Here, ANSYS Fluent was used in conjunction with a developed erosion model for a large-scale furnace to understand the flow field. The temperature inside a boiler plays an important role in boiler dynamics. With inputs of fluid pressure, fluid temperature, a product of mass flux and diameter, and heat flux, an artificial neural network (ANN) was modeled that outputs the wall temperature with a prediction accuracy

of 100% for the experimental data and 81.94% for the literature data at a deviation level of ± 7 °C in [4]. According to Romeo and Garetta [5], it was concluded that a NN is a stronger tool for monitoring than equation-based monitoring in control and minimizing the effect of fouling in biomass boilers. The operational performance of a boiler is crucial to engineers and to improve the energy efficiency in process industries, predicting the appropriate inputs, viz., temperature, pressure, and mass flow rate of steam are of importance. Artificial neural networks can efficiently predict the data on steam properties and could serve as a good tool to monitor boiler behavior under real-time conditions [6].

As mentioned earlier, process knowledge can be understood from simple NN models. Methods for model-based control have seen significant developments. The complexity of static models is complex and does not account for dynamics. System identification techniques are hence required to obtain insight into the system under various operating conditions, which is where AI models like [7–9] come in. The drum level control is an important problem for conventional as well as nuclear plants as proposed in [10, 11]. Further, Parry et al. [12] demonstrated that poor level control of water level caused about 30% of the emergency shutdowns in French PWR plants. Uncertainty in the phase behavior changes significantly with operating conditions. The steam inside the boiler is present in the form of bubbles in the water leading to false water level measurements. This is one reason for the complexity in control problems, the shrink and swells dynamics inside the boiler as presented in [1].

Multivariate regression serves as a good tool for applications such as the ones referred to above. Essential dynamics in boilers could be captured by simple models, as is indicated in the results of system identification experiments from Behera et al. [6]. In [13] multiple regression analysis was performed for predicting the energy consumption of a supermarket in the UK, based on gas and electricity data for the year 2012. Furthermore, in [14] multi-stage regression on thermodynamic equations was used to model room temperature in office buildings. In [15] too logarithmic regression predicted the temperature of block heaters based on the resistance of sensors, which is used to control the generation of power. With major boiler losses at the input, a statistical model for boiler efficiency was established in [16]. Here, it can be exploited for the prediction of boiler parameters.

It can be observed that the application of regression analysis in the controlling water and pressure variations inside a boiler is a lesser-explored domain as compared to NNs. Hence, this study proposes such an application that would predict these variations and these predictions can then be used in controlling the inputs to the boiler.

3 Methodology

Figure 1 shows a flowchart of the methodology implemented in developing the predictive water level and pressure model. It utilizes the concept of balancing the mass and energy in a boiler.



Fig. 1 Flowchart of methodology

Table 1 specifies the symbols used for designating certain parameters in this study.

The data for this study was collected from a horizontal, multi-tubular, shell type, and smoke tube boiler with a water wall furnace (Courtesy: Thermax Ltd., Chinchwad, Pune, India) with the specifications as tabulated in Table 2.

Initially, the input and output parameters of this boiler are recorded at an interval of 1 min over 24 h. This data is then filtered to obtain the parameters required for this study. Parameters such as pressure inside the boiler p , feed water rate q_f , steam flow rate q_s , water level and steam load are extracted from raw data over 6138 min. Further, mathematical operations are carried out on this data to obtain the volumes of steam and water present in the boiler along with fuel consumption. The formulae used for this purpose are mentioned below. Moreover, properties such as density and

Table 1 Symbols used in this study

Symbol	Description	Symbol	Description
r	The inner radius of the boiler (cm)	V_{wt}	The true volume of water (m ³)
l	Length of the boiler drum (m)	V_{st}	True volume of steam (m ³)
t	Time (s)	V	Volume of boiler (m ³)
p	Pressure inside the boiler (Pa)	ρ_w	Density of water in kg/m ³
$\frac{dp}{dr}$	Pressure differential (Pa/s)	ρ_s	Density of steam in kg/m ³
WL	Water level inside the boiler as a percentage of level gage height	H_w	Specific enthalpy of water in kJ/kg
Q_s	Steam flow rate (kg/hr)	h_s	Specific enthalpy of steam in kJ/kg
q_f	Feed water flow rate (kg/hr)	$\frac{d\rho_s}{dp}$	Change in density of steam with respect to pressure
V_s	Apparent volume of steam (m ³)	$\frac{d\rho_w}{dp}$	Change in density of water with respect to pressure
V_{w1}	Apparent volume of water excluding that in tubes (m ³)	$\frac{dh_w}{dp}$	Change in specific enthalpy of water with respect to pressure
V_t	Volume of water present in the tubes (m ³)	$\frac{dh_s}{dp}$	Change in specific enthalpy of steam with respect to pressure
V_w	Total apparent volume of water (m ³)		

Table 2 Specifications of the boiler

Outer diameter of drum	1900 mm
Inner diameter of drum	1880 mm
Length of drum	3750 mm
Number of tubes	255
Radius of each tube	32 mm
Efficiency of boiler	85%
Design steam load	8000 kg/h
Design steam pressure	10.54 kg(f)/cm ²
Heating surface area	254.28 m ²

specific enthalpy of steam and water are determined for the given conditions using the steam table.

$$WL(\text{cm}) = 200 \times \frac{WL(\%)}{100} \tag{1}$$

Here, 200 is the height of the level gauge in cm. The water level calculated in Eq. (1) only accounts for the height of water in the level gauge. The amount of water above the center of the boiler is calculated using Eq. (2).

$$\text{Height of water above center(cm)} = H = 390 + \text{WL(cm)} \quad (2)$$

The length of the chord present at height of water level is denoted as L and expressed as follows

$$L = 2\sqrt{r^2 - H^2} \quad (3)$$

The angle formed by the chord mentioned in Eq. (3) is determined using Eq. (4)

$$\theta(\text{rad}) = \sin^{-1}\left(\frac{\left(\frac{L}{2}\right)}{r}\right) \quad (4)$$

The part of the cross-sectional area covered in steam is calculated using Eq. (5) and denoted as A_s

$$A_s = \left(\pi\left(\frac{r}{1000}\right)^2 \times \left(\frac{2\theta}{2\pi}\right)\right) - \left(\frac{1}{2} \times \frac{H}{1000} \times \frac{L}{1000}\right) \quad (5)$$

$$V_s = A_s \times l \quad (6)$$

$$V_{w1} = \left(\pi\left(\frac{r}{1000}\right)^2 - A_s\right) \times l \quad (7)$$

$$V_t = 255\left(\frac{\pi}{4} \times 0.0635^2\right) \times l \quad (8)$$

$$V_w = V_{w1} - V_t + 0.55671 \quad (9)$$

where the volume of water present in tubes running into the boiler drum is 0.55671 m³.

To predict the water level variation in the boiler, firstly the relationship between water level and the remaining parameters was derived with the help of the mass balance equation [1]. It is given as follows:

$$(\rho_w - \rho_s) \times \frac{dV_{wt}}{dt} + \left(V_{st} \frac{\partial \rho_s}{\partial p} - V_{wt} \frac{\partial \rho_w}{\partial p}\right) \times \frac{dp}{dt} = q_f - q_s \quad (10)$$

Here, V_{wt} and V_{st} refer to the actual volume of water and steam present in the boiler, respectively. These volumes are calculated using void fraction (ϕ) and water level. The apparent volumes of water (V_w) and steam (V_s) are determined from the water level indicator reading and substituted in the following equations:

$$V_{wt} = V_w(1 - \phi) \quad (11)$$

$$V_{st} = V_w \phi + V_s \quad (12)$$

However, the void fraction cannot be measured directly and needs to be calculated using the following equation:

$$\phi = \frac{A}{p} + B.q_s + C.q_f^2 + D.e^{-\left(\frac{dp}{dt}\right)^2} + E \quad (13)$$

The unknown constants A , B , C , D , and E are assumed to be -1 each to determine the value of ϕ . Since, $\frac{dp}{dt}$ cannot be computed for $t = 1$, the initial guess for ϕ is taken as 0.5. The values of ϕ obtained from Eq. (13) are substituted in Eqs. (11) and (12). The values of V_{wt} and V_{st} obtained from Eqs. (11), (12) are substituted in Eq. (10). This was followed by minimizing the sum of squares of errors between the LHS and RHS of Eq. (10). This minimization was performed using the SLSQP optimizer from the SciPy library in Python.

Since the conditions inside a boiler vary rapidly, the predictive model needs to account for these variations. Such an adaptive model can be developed by performing regression on the newly fed data as well and changing the regression coefficients accordingly. To achieve this dynamism, the multivariate regression is performed on sets of 100 data samples. That is, the first set consists of samples from $t = 1$ to $t = 100$, the second set ranges from $t = 2$ to $t = 101$, and so on. The regression coefficients obtained after each iteration are used to obtain the void fraction at the last time step. Using this value, the apparent volume of water at the next time step is calculated and compared with the original value to determine the error. For example, after performing regression on the first set $\{t = 1 : 100\}$, the values of regression coefficients obtained are used to calculate V_w for the 101st time step. Using the V_{wt} and V_{st} values obtained from this process were substituted in the energy balance Eqn. [1] of boiler which is expressed as follows:

$$e_1 \times \frac{dV_{wt}}{dt} + e_2 \times \frac{dp}{dt} = q_f h_f - q_s h_s + Q \quad (14)$$

where

$$e_1 = \rho_w h_w - \rho_s h_s \quad (15)$$

$$e_2 = V_{st} \frac{\partial \rho_s h_s}{\partial p} - V_{wt} \frac{\partial \rho_w h_w}{\partial p} \quad (16)$$

Now, after determining the LHS, the only unknown in Eq. (14) is the heat of combustion, i.e., Q . Since Q cannot be measured, the amount of heat available at an instant is expressed as the sum of fractions of fuel consumptions over a certain period of time. Through trial and error this period was determined to be 25 min. Hence, the amount of heat available at an instant is expressed as:

$$Q = \sum_{t=1}^{25} Q_t (F \ln(t) + G) \quad (17)$$

where Q_t is the amount of fuel consumed, in kJ/s. Considering SL as steam load (%), q as design steam flow rate (kg/h), LH as latent heat in kJ/kg, and CV as the calorific value of fuel in kJ/kg, Q_t is given as:

$$Q_t = \frac{SL \times q_s \times LH}{100 \times 3600} \quad (18)$$

Moreover, the sum of all these fractions from 1 to 25 is unity and results in the following Eqn.,

$$\sum_{t=1}^{25} (F \ln(t) + G) = 58.02F + 25G = 1 \quad (19)$$

$$G = 0.04 - 2.320144F \quad (20)$$

This value of B is substituted in Eq. (17), which is further substituted in Eq. (14). The error here is then considered as the difference between Q and remaining terms from energy balance Eqn. [1]. On taking the partial derivative of the sum of squares of such 100 errors the following equation is obtained,

$$\sum_{t=26}^{125} k_i m_i = 0 \quad (21)$$

In Eq. (21) m_i is

$$m_i = (\text{EBT} - F \times p_i) \quad (22)$$

where

$$p_i = \left(\sum_{m=t-25}^t Q_m (\ln(m) + 2.32) \right) - 0.04 \left(\sum_{m=t-25}^t Q_m \right) \quad (23)$$

where EBT refers to the remaining terms of the energy balance equation [1] and

$$k_i = 2.32 \sum_{m=t-25}^t Q_m - \sum_{m=t-25}^t Q_m \ln(m) \quad (24)$$

From Eqs. (21–23),

$$F = \frac{\sum_{t=26}^{125} k_i (\text{EBT} - 0.04 (\sum_{m=t-25}^t Q_m))}{\sum_{t=26}^{125} k_i (\sum_{m=t-25}^t Q_m (\ln(m) + 2.32))} \quad (25)$$

Using this value of F and that of G from Eq. (20) the combustion heat Q is calculated for the 126th time step. This Q is substituted in Eq. (14) and $\frac{dp}{dt}$ is determined. The pressure for the 126th time step is predicted using this $\frac{dp}{dt}$.

This entire process is repeated for regression datasets of sizes 200, 300, 400 and 500 samples. That is, dynamic regression is performed on datasets of the form $\{t = n : n + 100\}$, $\{t = n : n + 200\}$, $\{t = n : n + 300\}$, $\{t = n : n + 400\}$, and $\{t = n : n + 500\}$ for obtaining coefficients of Eqs. (13) and (17). After comparing the results of all five processes statistically, the dataset of size 500 is taken as the final size and its results are presented in the following section.

4 Results and Discussions

After implementing the methodology from Sect. 3 the mean error, variance, etc. statistical properties of the predicted and actual values of water level and pressure were compared for different sizes of regression data sets. Table 3 summarizes this comparison.

From Table 3, it is observed that the predictive water model was developed by performing multivariate regression on mass balance Eqn. [1] of boiler has a minimum error of 0.0198% when the size of the dataset is taken as 300. It renders a maximum error of 0.0277% for the dataset of size 100. Moreover, the error in the mean of V_w is minimum (0.0285%) for size 400 and maximum (0.0384%) at 100. In case of the standard deviation of V_w , size 100 gives the maximum error of 35.3473% and size 400 gives the minimum error of 10.9612%. Similarly, in the Pressure model developed after minimizing the error in energy balance Eqn. [1] of boiler has a minimum error (3.7630%) when the size of regression dataset was taken as 200 samples and maximum error (13.3018%) when this size corresponds to 400 samples. Furthermore, minimum error (3.9475%) in the mean of pressure readings occurs at size 200 and maximum error (12.3908%) occurs at size 300. Minimum error (762.8552%) in the standard deviation of pressure readings is observed at size 100 and maximum error (5708.0029%) at size 200. Hence, to avoid overfitting and underfitting, the size 500 is considered the optimum for both models.

In total, 5637 iterations were carried out for predicting V_w over a dataset of 6138 min. The values of regression coefficients A , B , C , D , and E (Eq. 13) were obtained after carrying out regression over the mass balance Eqn. [1] are as shown in Table 4.

In Table 4, the 'Time' column indicates the time for which the regression coefficients are being used for prediction. For example, the coefficients obtained after performing regression from $t = 2$ to $t = 501$ are used for predicting V_w for $t = 502$ min.

Table 3 Summary of iterations

Number of samples in the dataset	100	200	300	400	500
<i>Water level model</i>					
Mean error in the Water level model	0.027789	0.020988	0.019869	0.020125	0.024365
Mean of Actual V_w readings	5.589937	5.589937	5.589937	5.589937	5.589937
Mean of Predicted V_w readings	5.587788	5.588294	5.588337	5.588340	5.588128
Error in mean (V_w)	0.038444	0.029394	0.028616	0.028570	0.032353
Standard deviation of actual V_w readings	0.098646	0.098646	0.098646	0.098646	0.098646
Standard deviation of predicted V_w readings	0.133514	0.114600	0.111502	0.109459	0.120199
Error in standard deviation (V_w)	35.34733	16.17332	13.03277	10.96126	21.84934
<i>Pressure level model</i>					
Mean error in the Pressure model	10.70815	3.763053	12.43353	13.30183	8.216613
Mean of actual pressure readings	793,751.79	793,751.79	793,751.79	793,751.79	793,751.79
Mean of predicted pressure readings	710,708.0	762,417.98	695,399.46	695,437.06	729,834.66
Error in mean (P)	10,46218	3,94756	12,39082	12,38608	8,052533
Standard deviation of actual pressure readings	60,883.69	60,883.69	60,883.69	60,883.69	60,883.69
Standard deviation of predicted pressure readings	525,338.1	3,536,126.89	2,795,392.63	3,405,874.25	2,686,099.70
Error in standard deviation (P)	762.8552	5708.0029	4491.3648	5494.0661	4311.8538

Table 4 Regression coefficients of Eq. (13)

Time (min)	<i>A</i>	<i>B</i>	<i>C</i>	<i>D</i>	<i>E</i>
502	-1	0.059469	-0.00318	0.000249	0.406366
503	-0.99991	0.060881	-0.00389	0.0000198	0.169291
504	-0.99991	0.060355	-0.00393	-0.0000196	0.162426
...
6137	-1.01504	0.052846	-0.00285	-0.00162	0.312294
6138	-1.01481	0.053267	-0.00287	-0.00165	0.319818
6139	-1.01481	0.053266	-0.00287	-0.00165	0.319818

Following Fig. 2 displays the variation of actual and predicted water levels over the entire dataset of 6138 min.

Similar to the water level model, 5613 iterations were carried out over 6138 min for predicting the values of pressure. The coefficients *F* and *G* (Eq. 17) obtained after performing dynamic regression over the energy balance Eqn. [1] are shown in Table 5.

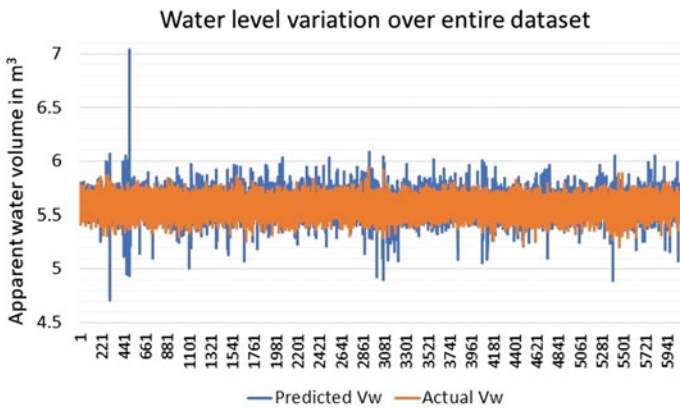


Fig. 2 Variation of predicted and actual water level over 6138 min

Table 5 Regression coefficients of Eq. (17)

Time (min)	<i>F</i>	<i>G</i>
526	0.006454607	0.025024382
527	0.006775862	0.024279024
528	0.006996788	0.023766445
...
6137	0.003327385	0.032279988
6138	0.006255549	0.025486225
6139	0.00739753	0.022836666

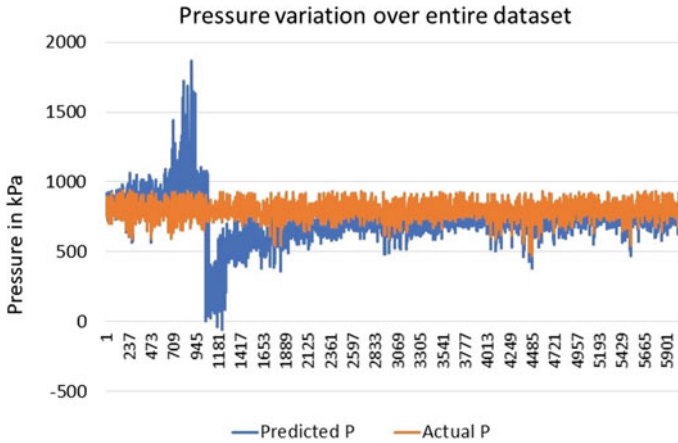


Fig. 3 Variation of predicted and actual pressure over 6112 min

In Table 5, like Table 4, the ‘Time’ column corresponds to the time for which pressure is predicted. In the above table, the regression coefficients are displayed from $t = 526$ min instead of 501 min. This is because the first 25-time steps have been excluded from the calculation as the heat available at a time instant is the sum of contributions of fuel over the last 25 min. That is why regression is carried out on the data ranging from $t = 26$ to $t = 525$.

The variation of pressure values determined using the coefficients from Table 5 can be seen in Fig. 3 along with the variation of actual pressure over 6112 (6138-25) minutes.

The predictive water level and pressure models presented above had an average error of 0.0243% and 8.0525%, respectively, after performing dynamic regression on the mass and energy balance Eqns. [1] of the boiler using 500 samples for each iteration.

5 Conclusion

In this study, predictive models for water level and pressure variations in the boiler are presented. These models have been developed using the mass balance as well as energy balance Eqns. [1] of the boiler. Prediction is done by performing multivariate regression on these Eqns. using SLSQP minimizer from SciPy. Furthermore, these models give insights on the dependency of water level and pressure variations on void fraction, steam flow rate, water flow rate, steam load, and the properties of steam and water. Regression is performed in five different ways by varying the size of the regression data set from 100 to 500. The results of each of these sets are compared with each other and the set giving the optimum error and optimum variance is presented as the final result.

These models can further be used in improving the existing control systems of industrial boilers. The inputs to the boiler such as feedwater rate and fuel input rate can be adjusted to avoid the predicted variations inside the boiler. Such an application can help in preventing the decline in the performance of a boiler occurring due to these variations.

Acknowledgements This work has been supported by Thermax Ltd. Chinchwad, Pune, India and College of Engineering, Pune, India. The authors are grateful for the valuable data shared by Thermax Ltd. Chinchwad, Pune, India. The authors are also thankful to Dr. B.B Ahuja, director, College of Engineering, Pune, India, and the Department of Mechanical Engineering, College of Engineering, Pune, India.

References

1. Åström KJ, Bell RD (2000) Drum-boiler dynamics. *Automatica* 36:363–378
2. Bahadori A, Vuthaluru HB (2010) Prediction of silica carry-over and solubility in steam of boilers using simple correlation. *Appl Therm Eng* 30:250–253
3. Gandhi MB, Vuthaluru R, Vuthaluru H, French D, Shah K (2012) CFD-based prediction of erosion rate in large scale wall-fired boiler. *Appl Therm Eng* 42:90–100
4. Dhanuskodi R, Kaliappan R, Suresh S, Anantharaman N, Arunagiri A, Krishnaiah J (2015) Artificial neural networks model for predicting wall temperature of supercritical boilers. *Appl Therm Eng* 90:749–753
5. Romeo LM, Garetta R (2006) Neural network for evaluating boiler behaviour. *Appl Therm Eng* 26:1530–1536
6. Behera SK, Rene ER, Kim MC, Park HS (2014) Performance prediction of an RPF-fired boiler using artificial neural networks. *Int J Energy Res* 38:995–1007
7. Garcia CE, Prett DM, Morari M (1989) Model predictive control: theory and practice—a survey. *Automatica* 25:335–348
8. Mayne DQ, Rawlings JB, Rao CV, Sokaert POM (2000) Constrained model predictive control: stability and optimality. *Automatica* 36:789–814
9. Qin SJ, Badgwell TA (1997) An overview of industrial model predictive control technology. In: AIChE symposium series
10. Kwatny HG, Berg J (1993) Drum level regulation at all loads. In: 12th Triennial world congress of the international federation of automatic control, Sydney, Australia, 18–23 July, 1993
11. Ambos P, Duc G, Falinower CM (1996) Loop shaping H_{∞} design applied to the steam generator level control in EDF nuclear power plant. In: Proceeding of the IEEE international conference on control applications held together with IEEE international symposium on intelligent control, Dearborn, MI, USA, 15 September–18 November, 1996
12. Parry A, Petrot JF, Vivier MJ (1985) Recent progress in SG level control in French PWR plants, In: 3rd International conference on boiler dynamics and control in nuclear power stations, Harrogate, UK, 21–25 October, 1985
13. Braun MR, Altan H, Beck SBM (2014) Using regression analysis to predict the future energy consumption of a supermarket in the UK. *Appl Energy* 130:305–313
14. Wu S, Sun JQ (2012) Multi-stage regression linear parametric models of room temperature in office buildings. *Build Environ* 56:69–77
15. Al-Sahib NKA, Hameed HS (2014) Monitoring and wireless controlling of power generation by labview. *Control Theory Inform* 4:1–13
16. Chayalakshmi CL, Jangamshetti DS, Sonoli S (2018) Multiple linear regression analysis for prediction of boiler losses and boiler efficiency. *Int J Instrum Control Syst* 8:1–9

Optimisation of Parameters in Numerical Simulation of Hot Forging Using Taguchi Approach



Sam Joshy, T. M. Anup Kumar, N. Nikhil Asok, R. Suraj,
and Koshy P. Joseph

Abstract Finite element analysis (FEA) is performed on the hot forging of a sample using DEFORM™ 3D in this research. The Taguchi method and Deform 3D simulation software was used to optimize the forging process. The responses to die stress in the hot forging process are investigated using Taguchi's L_9 orthogonal array to find the interactions and influences on the design parameters and process parameters such as die temperature, sliding velocity, and friction coefficient. For the simulations in Deform 3D, a design of experiment based on Taguchi's three-level, the three-parameter approach was used and was carried out on AISI 1025 steel, which is commonly used in making bolts. To ascertain the significant parameters of this operation, the Analysis of Variance (ANOVA) is utilized, and it was seen that the optimal factor settings for each performance characteristic were different. The results show that die temperature and die speed has the highest contribution in reducing die stress.

Keywords Forging · Deform 3D · Optimization · Taguchi analysis

1 Introduction

Forging, extrusion, and rolling are the most preferred manufacturing processes used for producing structural components [8, 13]. Forging is widely used to make near-net-shape parts with optimum material utilisation and superior mechanical properties.

S. Joshy · T. M. A. Kumar · N. N. Asok · R. Suraj · K. P. Joseph (✉)
SCMS School of Engineering and Technology, Ernakulam, India
e-mail: koshy@scmsgroup.org

S. Joshy
e-mail: samjoshy@scmsgroup.org

T. M. A. Kumar
e-mail: anupkumartm@scmsgroup.org

N. N. Asok
e-mail: nikhil@scmsgroup.org

R. Suraj
e-mail: surajr@scmsgroup.org

Forged parts find applications in sectors like automotive, aerospace, and power plants [13]. Based on the temperature of the billet, the forging process can be classified as hot, warm, and cold forging. During hot forging, billets are heated above their recrystallization temperature, whereas warm and cold forging is performed below recrystallization and room temperature, respectively. Previous research has found that temperature at the die surface can increase up to 800 °C. Further, the mechanical stress can go beyond 1000 MPa. The large in-service thermomechanical stress during the forging process severely affects the property of the material [21]. Mainly due to the focused application of axial forces, which results in a multi-axial stress condition [3]. Because of the variation in strain and stress distribution, metal flow exhibits complex behaviour [10, 19]. Metal flow dynamics are influenced significantly by forging parameters such as coefficient of friction, die speed, and temperature [7]. The above-stated forging parameters control the quality of the final product [1]. Detailed knowledge of the metal flow pattern would help in the manufacture of high-quality goods [7]. Therefore, optimizing the forging parameters is critical for enhancing the production process.

In the former years, forged component production was done by experimentation, with the expertise of professional designers [14, 16]. However, this process is costly and time-consuming [14]. Consequently, to improve product consistency and efficiency, computer and physical simulations have replaced older technologies [1, 17]. The behavior of hot metal flow is analyzed using laboratory specimens in physical simulation. The deformation mechanism can be streamlined and projected using the flow stress collected data [23]. Interfacial friction induces increased flow stress, resulting in metal flow inhomogeneity [11, 12, 18]. Therefore, this method necessitates more tests to establish the optimal forging conditions. Consequently, several trial-and-error samples are needed, resulting in a long procedure. In the present competitive market, the only way to increase profit is to reduce the cost of production. To minimize production costs, commercial simulation software for metal forming processes has been developed [6, 15]. The simulation software with finite element analysis (FEA) tools supplies a valid and low-cost process of optimization. Deform 3D has been widely used for optimizing the industrial forming process [24]. It requires several simulations to get an optimized set of conditions for the forming process. The design of the experiment (DoE) uses numerical methods like Taguchi's experimental design which can be used to minimise the number of simulations. The effects of metal forming process parameters and variables were studied using this approach [9, 20]. The Taguchi design technique was identified as a useful tool for optimizing manufacturing processes in the literature [9]. Deform™ 3D program has been used to model the forging process of different alloys and metals, according to the literature [24]. As a result, Taguchi's experimental method and Deform™ 3D simulation were used in this research to effectively study and refine the forging process, resulting in a reduction in simulation time.

In industries, dies are preheated before each forging cycle [4]. This helps to reduce thermal gradients and improves die service life. The proper preheating of forging dies helps to reduce thermal stresses and prevent brittle fracture [2]. There is much research on the preheating of dies. Studies conducted by Kellow et al. [5] have found

that dies should be preheated to 100 to 200 °C. However, a more contemporary work suggests 205 to 260 °C. Thus, there is a lack of general understanding of the amount of preheating, and according to the authors' knowledge, there has been very limited work on optimization of die temperature on reducing the die stress. This research aims to optimize the die stress based on the factors die temperature, sliding velocity, and coefficient of friction.

2 Simulation Modeling

2.1 Forging Material

Finite element approaches have recently been used to model and optimize the forging process. Deform™ 3D FEM software was used to model the forging process in this report. A 3D solid model of die made of AISI H13 hot work die steel was used to obtain simulation data. The Deform™ 3D database includes the material properties. This work uses an axisymmetric die model; hence, a quarter model was used for the simulation.

2.2 Design of Experiment

The Taguchi design methodology is a detailed and effective way of understanding parameter interrelationships and their effect on the process. As a result, by defining a series of criteria that will increase product consistency, this method allows for the improvement of the manufacturing process. The collection of control/independent variables is a crucial phase in the design process. The die speed and temperature along with the friction coefficient are the key control variables during the forging process. Table 1 lists the control variables and variables used in the simulation forging process. A three-level, three-parameter design is selected. Levels 1, 2, and 3 represent the lower, middle, and upper levels respectively. The range of die temperature is selected based on the die temperature used in the hot forging industries. Based on these control variables, an L9 array was selected from the Taguchi approach. The different combinations for the simulation trials as obtained from the Taguchi approach are shown in Table 2.

Nine sets of simulations were generated using a three-level Orthogonal Array (OA).

Table 1 Input parameters

Factor	Units	Levels		
		1	2	3
Die temperature	°C	150	250	350
Die speed	m/s	0.5	1	1.5
Coefficient of friction		0.3	0.5	0.7

Table 2 Design of experiments

Analysis No:	Die temperature	Die speed	Coefficient of friction
1	150	0.5	0.3
2	150	1	0.5
3	150	1.5	0.7
4	250	0.5	0.5
5	250	1	0.7
6	250	1.5	0.3
7	350	0.5	0.7
8	350	1	0.3
9	350	1.5	0.5

2.3 Forging Simulation Model

In this research, the FEM Deform™ 3D program was used in the simulation of hot working systems. The figure shows the steps in the simulation of the forging process. The simulation is performed in three stages, viz., preprocessing, simulation, and post-processing. The steps in each stage are also shown in Fig. 1.

The object (die and billet) geometries are modelled in onshape. The dies are designed as per the standards. The geometry in ‘STL’ format is loaded in the pre-processor module. Further, the materials for the billet were selected. The material properties of AISI 1025 steel were chosen for the billet, from a database in the software. The following are the mechanical properties of AISI 1025 steel: The Young’s modulus is 200 GPa, the Poisson’s ratio is 0.33, the elongation is 16%, and the density is 7.7 g/mm³. The billet temperature is 1200 °C. Figure 2 shows the dies and billet. In this figure, dies are designed and rigid bodies and the billet is modeled as plastic. The billet is meshed using the following parameters. The objects are positioned using the object positioning. The interference approach is selected to keep the dies in contact with the workpiece. Further, simulation controls are set in the software. The stopping distance, convection coefficients are set in this step. Lagrangian interpolation is used for iteration.

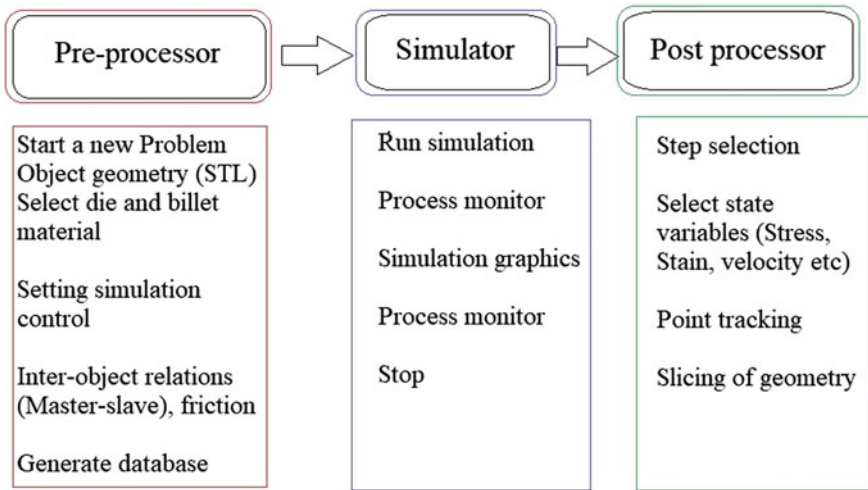


Fig. 1 Analysis in deform 3D

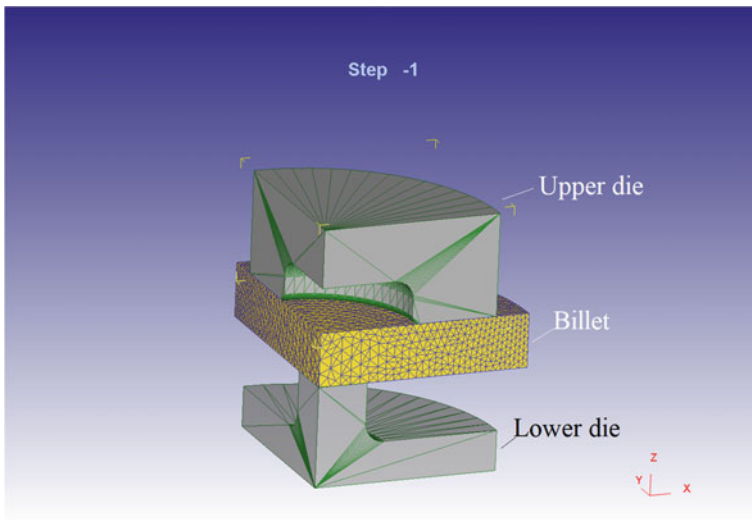
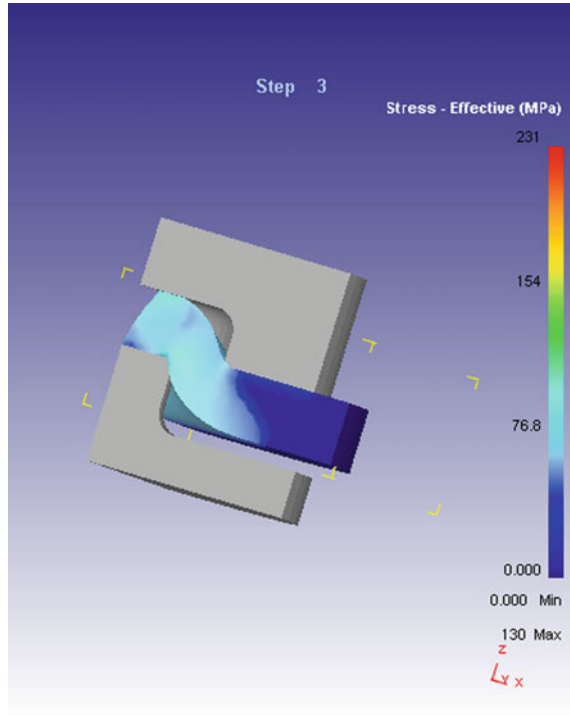


Fig. 2 Quarter model of die and billet geometry

Further, the database is generated and is run in the software. This generates a deformation database. The deformed billet geometry (see Fig. 3) can be observed in the simulation graphics monitor.

The deformation data base is generated in the pre-processor of the software. Further, this database is loaded in the 'Die stress' module. In this step, dies and the billet is modeled as elastic members. The upper die and lower die are selected as the

Fig. 3 Object geometry with deformed billet



master and slave, respectively. The dies are meshed, and the forces are interpolated on the dies (refer Fig. 4). Thus, the forces on the dies are loaded. Figure 4 shows the interpolation of forces on the upper die. The force vectors can be observed in the figure.

Further, die stress analysis is performed.

2.4 Main Effects Plot and S/N Ratio

The Taguchi results are shown in the main effects plot and *S/N* ratio. The main effect is an attribute that represents the influence of a factor on the result. This plot illustrates the variance of the response variable in contrast to the change in control factors and is used to determine the variations between the level means for variables. If the line plotted is horizontal and there is no change in reaction with the change in factor, the factor is said to be negligible. A high slope, on the other hand, suggests that the aspect has a major effect on the response.

The *S/N* ratio is the proportion of the signal factor to the noise factor in the Taguchi approach. In this method, the three stages of *S/N* ratio, viz., smaller the best, nominal the best, and larger the best are used. The objective of this work is to

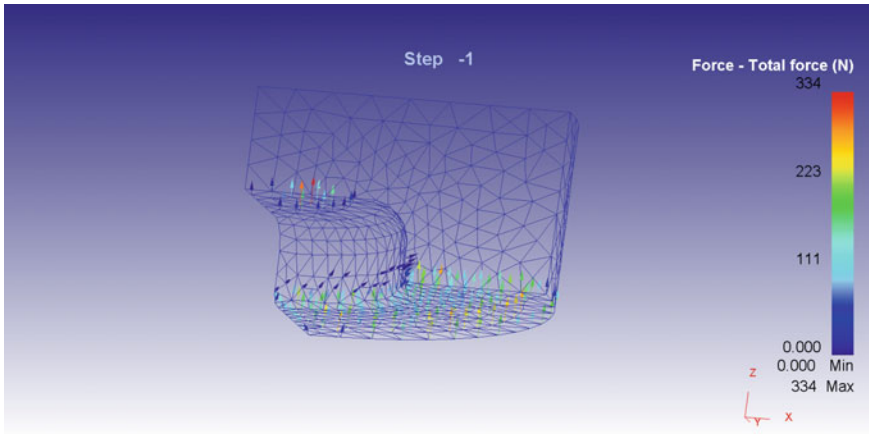


Fig. 4 Upper die with force interpolation

optimize the geometric parameters to maximise the magnetic flux density, and thus the latter option is selected.

The higher *S/N* ratio reflects a higher quality technique. This means that it is possible to achieve a high-quality product by Taguchi analysis, the mixture indicates a higher *S/N* ratio. The *S/N* ratio can be maximized, minimized, or held at nominal values as the primary goal of optimization. This allows in the selection of control levels capable of fully compensating for noise effects. In this work, *S/N* ratio is chosen to be kept to the minimum, as the goal of the design is to minimize the maximum tensile stress.

It is necessary to determine the statistically important parameters, which has the highest influence on the response parameter, and ANOVA analysis is performed, Further, a confidence level of 95% is used for analysis purposes, thus a *p*-value less than 0.05 will ascertain the significance of factor.

In addition, the percentage of influence of each parameter on output factors can be defined using ANOVA. As a consequence, if the *p*-value is less than 0.05, the null hypothesis for the whole population is ignored, and the parameters are considered significant. On the other hand, the null hypothesis is not discarded, and the parameters are irrelevant if the *p*-value is greater than 0.05.

3 Results and Discussion

Following the completion of all simulations, the maximum tensile stresses were reported for further study and optimization. The response die stress (maximum tensile) has been calculated using the experimental layout shown in Table 3. The basic Taguchi procedure transforms the target parameters to the signal-to-noise (*S/N*) ratio,

which is then used to quantify performance characteristics. To find the configuration with the least variance and the maximum efficiency, the S/N ratio is used. The performance would be more reliable if the S/N ratio were higher. There are usually three types of consistency properties in the analysis of the S/N ratio: the-lower-the-better, the-higher-the-better, and the-nominal-the-better.

In this analysis, tension is a consistency trait with the target of “the lower, the better.” As a consequence, the S/N ratio is defined as,

$$\frac{S}{N} = -10 \log_{10} \frac{\sum y^2}{n}$$

From the table, it can be observed that optimum die stress is obtained with Analysis No. 9. The optimum parameters combination for die stress is die temperature = 350 °C, sliding velocity = 1.5 m/s, and $\mu = 0.5$ corresponding to the highest values of S/N ratio for all control parameters. This is followed by die temperature = 350 °C, sliding velocity = 0.5 m/s, and $\mu = 0.7$. Statistical analysis of the main effects plot (see Fig. 5) shows the change in control factors with the levels. It may be observed that the die stress decreases with an increase in die temperature. Thus, it can be inferred that with an increase in die temperature, the thermal gradient with the hot billet reduces, which lowers the heat transfer from the billet to the dies. This helps to maintain the billet at lower flow stress during forging, and thus lower forming forces are required to forge the billet. As a result, die stress gets reduced with an increase in die preheat temperature. Further, it can be observed that the die stress increase with an increase in sliding velocity up to 1 m/s. This initial increase in flow stress is due to an increase in dislocation density due to strain hardening. However, with an increase in die speed, the strain rate increases, which increases the flow stress. As a result, dynamic recovery and recrystallization occur resulting in thermal softening behavior at higher strain rates [22]. Thus, the die stress decreases with an increase in die speed up to 1.5 m/s.

Table 3 Responses and S/N ratio

Analysis No:	Die temperature	Die speed	Coefficient of friction	Die stress (MPa)	S/N ratio
1	150	0.5	0.3	440	-52.87
2	150	1	0.5	460	-53.25
3	150	1.5	0.7	410	-52.26
4	250	0.5	0.5	385	-51.98
5	250	1	0.7	435	-52.25
6	250	1.5	0.3	341	-51.48
7	350	0.5	0.7	352	-50.98
8	350	1	0.3	384	-51.47
9	350	1.5	0.5	325	-50.23

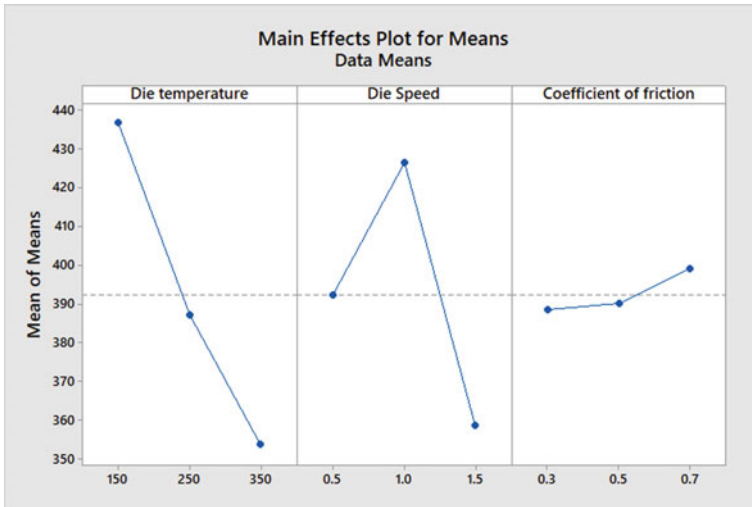


Fig. 5 Main effects plot

Thus, it can be inferred that at constant die temperature, an increase in die speed should be compensated with a decrease in coefficient of friction to lower the die stress. At a higher die speed, the strain rate increase, which results in dynamic recrystallization, leading to thermal softening. As a result, the coefficient of friction increases apparently. Thus, a decrease in the coefficient of friction by applying lubrication is required for minimising the die stress (Fig. 6).

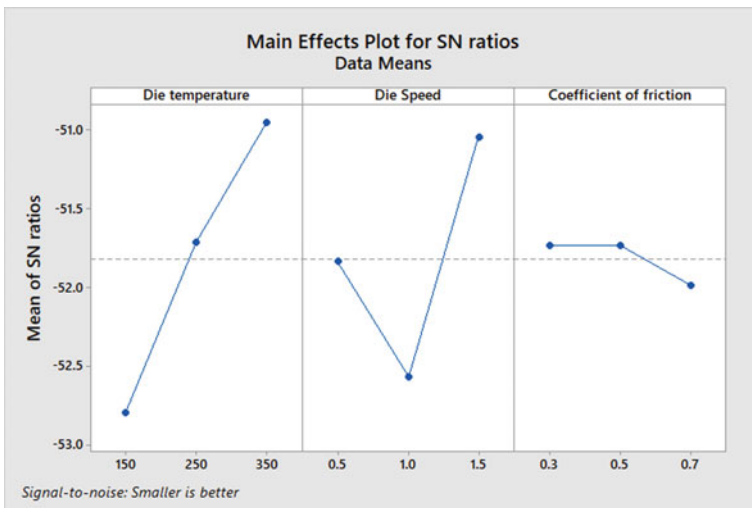


Fig. 6 S/N ratio plot for die stress

Table 4 Contribution of factors

Source	DF	Seq SS	Contribution (%)	Adj SS	Adj MS	F-value	p-value
Die temperature	2	10,466.9	58.47	10,466.9	5233.44	28.32	0.034
Die speed	2	6868.2	38.37	6868.2	3434.11	18.59	0.049
Coefficient of friction	2	197.6	1.10	197.6	98.78	0.53	0.652
Error	2	369.6	2.06	369.6	184.78		
Total	8	17,902.2	100.00				

The analysis of variance method (ANOVA) was used to assess the relative effect of each component, and the results are described in Table 4. The F -value is a metric that is used to measure when all the factor level means are equal. It is determined by dividing the factor's mean square by the error's mean square.

The percent contribution is measured using F . Under the 95% confidence level, ANOVA reveals that the process parameters of die temperature are the most important parameter influencing the die stress. This factor is followed by die speed. Both factors have a p -value less than 0.05, which establishes the significance level of these factors at a 95% confidence level.

4 Conclusion

The study looked at the effects of die temperature, sliding velocity, and friction coefficient on the response (die stress) during the forging process. The closed die forging mechanism was simulated using three-dimensional finite element (FE) analysis and the Taguchi procedure, followed by a sequence of optimization iterations. To evaluate significant parameters, an analysis of variance (ANOVA) is used. The most important parameters influencing the response were found to die temperature and die speed.

References

1. Babu PA, Saraf MR, Vora KC, Chaurasiya SM, Kuppam P (2015) Influence of forging parameters on the mechanical behavior and hot forgeability of aluminium alloy. *Mater Today: Proc*:3238–3244
2. Brockhaus HW, Guderjahn A, Schruoff I (2002) Improving the performance of forging tools—a case study. In: 6th International tooling conference, Karlstad University, Sweden, vol 1, pp 95–108
3. Dieter GE, Bacon D (1988) *Mechanical metallurgy*. McGraw-Hill Book Company, New York
4. Hawryluk M, Widomski P, Kaszuba M, Krawczyk J (2020) Development of new preheating methods for hot forging tools based on industrial case studies and numerical modeling. *Metall Mater Trans A* 51(9):4753–4764

5. Kellow MA, Bramley AN, Bannister FK (1969) The measurement of temperatures in forging dies. *Int J Mach Tool Des Res* 9(3):239–260
6. Ketabchi M, Mohammadi H, Izadi M (2012) Finite-element simulation and experimental investigation of isothermal backward extrusion of 7075 Al alloy. *Arab J Sci Eng* 37(8):2287–2296
7. Kingkam W, Li N, Zhang HX, Zhao CZ (2017) Hot deformation behavior of high strength low alloy steel by thermo mechanical simulator and finite element method. *IOP Conf Ser: Mater Sci Eng*:012001
8. Osakada K (2007) Effects of strain rate and temperature in forming processes of metals. *Le J Phys IV* 07(C3):C3-XXXVII–C3-XLIV
9. Kumar SD, Karthik D, Mandal A, Kumar JP (2017) Optimization of thixoforging process parameters of A356 alloy using Taguchi's experimental design and DEFORM simulation. *Mater Today: Proc* 4(9):9987–9991
10. Lin YC, Chen MS, Zhong J (2008) Numerical simulation for stress/strain distribution and microstructural evolution in 42CrMo steel during hot upsetting process. *Comput Mater Sci* 43(4):1117–1122
11. Lin SY (1995) An investigation of die-workpiece interface friction during the upsetting process. *J Mater Process Technol* 54(1–4):239–248
12. Li YP, Onodera E, Matsumoto H, Chiba A (2009) Correcting the stress-strain curve in hot compression process to high strain level. *Metall Mater Trans A* 40(4):982–990
13. Lu SQ, Xin LI, Wang KL, Liu SB, Fu MW (2013) A method for prediction of unstable deformation in hot forging process by simulation. *Trans Nonferrous Met Soc China* 23(12):3739–3747
14. Maarefdoust M (2012) Simulation of finite volume of hot forging process of industrial gear. In: *International proceedings of computer science and information technology*, pp 57, 111
15. Mohapatra SK, Maity KP (2016, February). Parametric optimization of simulated extrusion of square to square section through linear converging die. *Parametric optimization of simulated extrusion of square to square section through linear converging die*. *IOP Conf Ser: Mater Sci Eng* 115(1):012031
16. Moraes AL, Balancin O (2015) Numerical simulation of hot closed die forging of a low carbon steel coupled with microstructure evolution. *Mater Res* 18:92–97
17. Na YS, Yeom JT, Park NK, Lee JY (2003) Simulation of microstructures for Alloy 718 blade forging using 3D FEM simulator. *J Mater Process Technol* 141(3):337–342
18. Obiko J, Mwema F, Akinlabi E (2019) Strain rate-strain/stress relationship during isothermal forging: a deform-3D FEM. *Eng Solid Mech* 8:1–6
19. Obiko JO, Mwema FM, Bodunrin MO (2019) Finite element simulation of X20CrMoV121 steel billet forging process using the Deform 3D software. *SN Appl Sci* 1(9):1–10
20. Ohdar R, Equbal MI, Kumar V (2013) Die stress optimization using finite element and Taguchi method. *Mater Sci Forum*:319–324
21. Rasti J, Najafzadeh A, Meratian M (2011) Correcting the stress strain curve in hot compression test using finite element analysis and Taguchi method. *Int J ISSI* 8(1):26–33
22. Shahriari D, Sadeghi MH, Ebrahimi GR, Kim KT (2011) Effects of lubricant and temperature on friction coefficient during hot forging of Nimonic 115 superalloy. *Kovove Mater* 49(5):375–383
23. Shi L, Yang H, Guo LG, Zhang J (2014) Constitutive modeling of deformation in high temperature of a forging 6005A aluminum alloy. *Mater Des* 54:576–581
24. Zhang ZJ, Dai GZ, Wu SN, Dong LX, Liu LL (2009) Simulation of 42CrMo steel billet upsetting and its defects analyses during forming process based on the software DEFORM-3D. *Mater Sci Eng*:49–52

Selecting the Optimum Tool for Driving Performance Evaluation by Assessing the Ergonomic Methods—An Overview



Arun Chand , H. Mannikandan , and A. B. Bhasi

Abstract Ergonomic analysis of the driving environment is very essential for enhancing productivity and reducing musculoskeletal disorders (MSDs) of drivers. The proposed driver distraction model for heavy vehicles examines the influence of environmental, psychological, and vehicle design factors on driver performance. The main ergonomic risk factors include long driving hours, poor human–machine interface, incorrect driving posture, vibration due to bad road conditions, driver sleepiness and age. To evaluate the effect of these factors on driving performance which leads to MSDs, different ergonomic methods/techniques are available. Selecting a single tool from these methods is quite difficult due to the heterogeneity of driver ergonomic parameters. To find the optimum tool, different features of the ergonomic methods were identified and compared. Integration of these tools used for ergonomic analysis was an outcome of the advancements in machine learning technology which resulted in digital human modelling (DHM). DHM combines computer-aided design, human factors management, and risk evaluation.

Keywords Human factors · Musculoskeletal disorders · Driver fatigue · Ergonomic tools · Digital human modelling

1 Introduction

Subsequent paragraphs, however, are indented. Driver ergonomics have been identified as a source of concern that contributes significantly to traffic accidents. Driver fatigue is a function of ergonomic issues related to driving. Fatigue is a state of exhaustion caused by extended periods of driving, tedious road conditions, and a poor environment or the driver's features [1]. Driver fatigue caused by ergonomic issues also leads to a reluctance to drive and a complete withdrawal of attention

A. Chand (✉) · A. B. Bhasi
School of Engineering, CUSAT, Kochi, Kerala, India
e-mail: arunchand@cusat.ac.in

H. Mannikandan
SCMS School of Engineering and Technology, Kochi, Kerala, India

from traffic and road conditions [2]. Although previous researchers have debated the matter in numerous domains, they have still come up with the importance of driver ergonomics and its effects on driving performance.

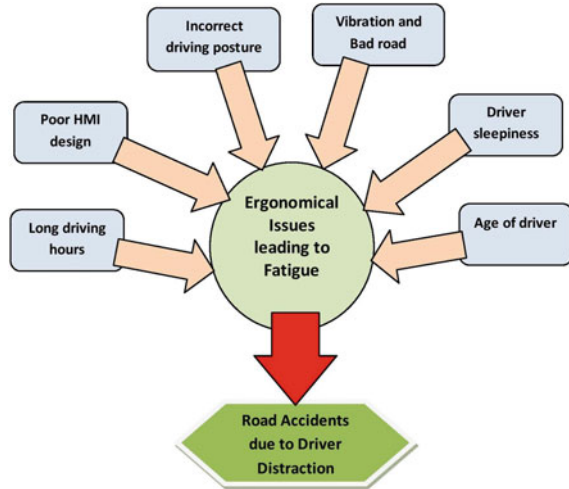
One of the most critical safety concerns in reducing road transport accidents is the management of heavy-truck driver ergonomic issues. Heavy vehicle drivers are responsible for 25% of traffic accident deaths on highways, worldwide [3]. It is found that personal fatalities are more than any other type of vehicle accident, in each heavy-duty accident [4]. Driver associated factors are determined to be significant causes in most accidents. Major health problems like musculoskeletal disorders (MSDs) are a common health concern and a major source of occupational illness of heavy-duty drivers [5]. Many researchers have examined heavy-duty driver fatigue, its roots and effects, as well as solutions for reducing the frequency of accidents caused by it [6–8]. The best technique to evaluate driver ergonomic issues has been a long history of incoherence in the transportation sector even though it is critical for the health and safety of heavy-duty drivers. It is critical to accurately assess a driver's exposure to ergonomic factors that may lead to the growth of MSDs. Various methods and mechanisms for evaluating exposure to ergonomic risk factors for driving-related MSDs have been developed. According to the measurement technique, they can be grouped into self-report, direct measurement, and observational methods [9]. However, these three divisions have their pros and cons when dealing with the assessment settings.

Most of the countries have spent decades attempting to understand the issues and reasons underlying driver ergonomic health impacts. There is a dearth of study on ergonomic impacts on driving performance in developing countries, especially India [10, 11]. Limited data is available to address the ergonomic concerns of heavy-duty drivers, indicating a significant gap in the literature that needs to be addressed. This study paves the way for the inquiry into the impacts of factors affecting driver ergonomics and discusses the issues that should be considered when selecting and using an assessment instrument. The significance of developing the optimal tool for resolving ergonomic challenges of heavy-duty drivers is also presented.

2 Human Factors in Heavy-Duty Vehicle Driving

The importance of human factors in safe driving identifies that a combination of environmental, psychological, and vehicle design factors influence driver performance [12]. In contrast to normal, drivers of heavy vehicles are more exposed to the road because of the lengthy travel schedules and distances [13]. Driver ergonomics and fatigue management is tough issue, especially if the aim is to preserve public safety on the road. But a little data is available which could reveal the influence of ergonomic factors on the heavy-duty vehicle driver's safety, especially in developing countries like India. This is because multiple aspects have to be examined and understood simultaneously for recording the effect of the driver ergonomic scenario. A driver distraction model for heavy vehicles is developed from the literature survey, and it focuses on the research gaps connected to driver ergonomics and regulations

Fig. 1 Factors affecting the driver ergonomics



impacting driver fatigue. This model is divided into six major areas: long driving hours, poor human–machine interface, incorrect driving posture, vibration due to bad road, driver sleepiness, and age of the driver (Fig. 1).

2.1 Long Driving Hours

Abledu et al. [14] used a Nordic-musculoskeletal semistructured questionnaire to inspect the frequency and consequences of long driving hours related MSDs among 148 commercial bus drivers in Ghana. The results showed that 116 (78.4%) participants had experienced MSDs in the past twelve months. Neck pain (25%), low back pain (59%), shoulder pain (18%), upper back pain (22%), ankle pain (10%), knee pain (15%), elbow pain (5%), thigh pain (3%), and wrist pain (7%) were the most predominant MSD areas. Multiple-logistic regression investigation adjusted for probable confounders exhibited that fewer physical movements (OR = 4.9; 95% CI = 1.5–16.5; P = 0.010), driving over 12 h in a day (OR = 2.9; 95% CI = 1.1–7.8; P = 0.037), and driving not less than 5 days in a week (OR = 3.7; 95% CI = 1.4–9.4; P = 0.007) were particularly related with MSDs amongst the group of bus drivers. Wise et al. [15] found from their concept analysis research that long-distance heavy-truck drivers are at risk of cognitive, psychological, and physical fatigue. This influences the safe travelling of long-distance heavy-truck drivers and other stakeholders of roadways also.

2.2 Poor Human–Machine Interface (HMI)

Pickering et al. [16] developed a test environment to ascertain driver preferences regarding dashboard and console designs, as well as attention performance and appropriate real-time responses for various driver demographics. The test environment was capable of providing speed, position, acceleration, and rear proximity sensing, in a 25-min test drive route. The most prevalent cause found was an operational error, such as a failure to grasp or act on information presented on the vehicle console, or an inability to handle the vehicle properly. The driver's abilities could be showcased from the test data results. Additionally, the platform features driver-selectable instrument clusters and LCD panel configurations. The findings demonstrated the critical role of HMI design in promoting physical ergonomics and reducing musculoskeletal diseases.

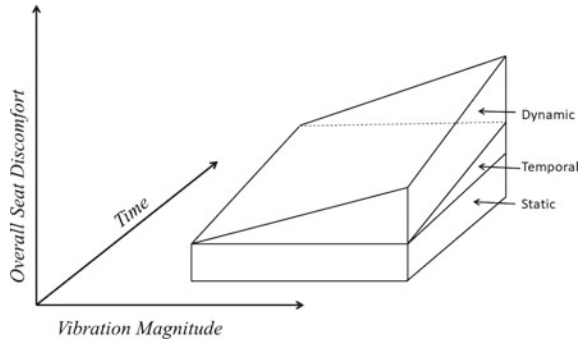
2.3 Incorrect Driving Posture

In a year, truck drivers spend nearly 2400 h on the road [17]. Physical injuries and the development of MSDs can be avoided, and vehicle drivers can stay comfortable and healthy by selecting the right position for the body and avoid stretching regularly. Through a virtual test, Xing et al. [18] quantified the stability of the driving posture and the driver's subjective evaluation of modules and seat supportive qualities, as well as the efficiency of the enhanced seat models. The findings of the study could be used to strengthen basic investigations into the stability of the driving posture and pedal controls, as well as trunk and thigh angles. Also, guidelines were established for the creation of a seat support design for truck drivers' upright seated postures.

2.4 Vibration and Bad Roads

Raffler et al. [19] used direct field assessments and self-reported data from 45 truck drivers to compare the physical burdens of whole-body vibration (WBV) and inconvenient posture. Also, manual materials handling and MSDs were examined to determine their effect on drivers' perceptions. While the measured WBV exposure levels were quite similar among the drivers, the respondents' perceptions varied significantly. With regard to posture, respondents appeared to estimate far more accurately when the variation in exposure was high. The percentages of the awkward trunk and head inclination evaluated in WBV overestimating drivers were significantly greater than in non-overestimating drivers; 77 and 80% versus 36 and 33%, respectively. Other health issues with the spine (42%), neck (67%), and the upper arm (50%) were substantially more frequently reported by WBV-overestimating drivers as opposed to non-overestimated drivers (0.25%, 13%, and 0%). The study used a comparison of

Fig. 2 An improved model of car seat discomfort including static, dynamic, and temporal element



field and questionnaire data to identify the elements influencing drivers’ perceptions of WBV exposure and found that musculoskeletal and posture issues significantly influenced the opinion of WBV-exposed drivers. Previously, a hybrid theoretical model for predicting overall discomfort was proposed [20], a schematic of which is presented in Fig. 2. Static, dynamic, and temporal elements are used in the model to provide the complete assessment of overall discomfort.

2.5 Driver Sleepiness

Bener et al. [21] used the multivariate logistic regression to show that driving-related fatigue, excessive speed, lapses, Epworth sleepiness score, and errors were all significantly related to the probability of a motor vehicle accident, once demographic factors were taken into consideration. The research also analysed that fatigued drivers, who have both chronic sleepiness and abnormal exhaustion, substantially increase their chances of a traffic accident which can result in severe injuries. Zhang et al. [22] conducted a naturalistic driving study (NDS), with the data collected from 34 professional drivers. After determining the level of fatigue in all drivers using the Karolinska sleepiness scale (KSS), the KSS data was transformed to successive values and modelled using curve fitting techniques. The findings indicated that fatigue prediction results are strongly related to driving performance by predicting the risk driving period and the maximum repeated driving time once the driving schedule is determined. The fatigue due to driving can be avoided or mitigated through optimization of the driving and break work schedule.

2.6 Age of the Driver

Depestele et al. [23] showed through statistical results that middle-aged drivers are less inclined to read an SMS/email or check online social media while driving. Heavy

vehicle drivers aged 20–25 have reported steadily increased driving distraction and fatigue rates and higher positive rates of societal and individual acceptance than drivers from 35 to 54 years of age. Elder drivers aged 65 and over reported reduced rates and acceptability of these practices. Many researchers have shown that younger drivers are more prone than non-lane-hanging drivers to be involved in accidents while changing lanes. The decrease in cognitive, sensory, and motor abilities could be the main reason that older persons are more sensitive to driver distraction.

3 Ergonomic Methods for Assessing Exposure to Driving Risk Factors

Numerous ergonomic assessment techniques have been created and classified into three broad groups. Selecting the most appropriate technique or combination of methods from this spectrum of existing methodologies poses a major difficulty. To provide an effective and healthy driving environment, it is important to combine these approaches with the understanding of the anatomy of the body and how it reacts to loads. The three sets of methods, as well as the names of the techniques and their features, to evaluate if drivers are at risk when engaging with the vehicle environment, are listed in Table 1.

The approaches presented in Table 1 could be found in many of the independent software applications and design packages. Design software such as Delmia, Jack, winOWAS, CATIA, HSE.Ergo.QEC, ProE, ViveLab, 3DSSPP, ErgoSoft includes OWAS, REBA, RULA, ROSA, MAPO, QEC, NIOSH lifting equation, APSA, EAWS, KIM-MHO, NPW, WERA, cognitive databases and strain index. Ergo-Plus, ViveLab, and ErgoSoft are major video-based ergonomic analysis software that is used for action detection and exploratory risk assessment of musculoskeletal disorders.

4 The Development of an Integrated Ergonomic Tool—Digital Human Model (DHM)

The input to the ergonomic analysis is highly reliant on the technique of observation or sensitivity measurement used. Thus, the structure of ergonomic evaluation is dependent on the available resources and the features of the driving environment. The hybrid character of ergonomic issues requires the use of various instruments for a complete ergonomic evaluation. Digital human modelling techniques incorporate a variety of strategies that integrate different ergonomic tools to evaluate driving environment design, analyse human–machine interface compatibility, and determine risks of musculoskeletal disorders. Modern technology offers analysis methods for dynamic human modelling and problem identification by combining

Table 1 Ergonomic methods for evaluating risk factors for MSDs associated with driving [24, 25]

Types of methods	Name of techniques	Main features
1. Self-reports	1. VIDAR-Self-evaluation of the driver using videos of the driving process 2. Interview, category data, and visual analog scales 3. Evaluation of possible ergonomic risks employing a web-based tracking system	1. Driver load ratings and associated pain and discomfort estimations 2. Identification of variables that increase a driver’s psychosocial risk for shoulder and neck pain 3. List of comfortable ergonomic positions that might help prevent discomfort, workplace stress, and functional restrictions
2. Observational methods	1. RULA 2. REBA 3. OWLS 4. QEC 5. LUBA 6. Checklist 7. NIOSH lifting equation	1. Concepts like body postures and force, together with action levels for evaluation 2. Elements of biomechanics include body postures and force, with activity levels for assessment 3. Force and body posture evaluation 4. Driver reactions to major body areas, as well as scores to suggest intervention 5. Angular displacement of the joint from neutral and discomfort evaluation 6. Displacement of neck, legs and trunk for repeated tasks 7. Driving posture is associated with biomechanical stress
2.a. Advanced observational methods	1. Video analysis 2. ROTA 3. TRAC 4. HARBO 5. SIMI motion	1. Hand/finger posture assessment, repetitiveness, force, velocity, and body postures are computed. Task evaluations, both static and dynamic 2. Static and dynamic task evaluation 3. Posture and activity analysis 4. Observation of different driving activities over a long period 5. Dynamic movements of the limbs and upper body are assessed

(continued)

Table 1 (continued)

Types of methods	Name of techniques	Main features
2.b. Productivity analysis	<ol style="list-style-type: none"> 1. ErgoSoft 2. ErgoMOST 3. EMA 	<ol style="list-style-type: none"> 1. Motion analysis evaluation and early risk assessment for musculoskeletal disorders 2. The neck, upper limbs, lower limbs, and back are evaluated for risk 3. Virtual ergonomics, the collaboration between humans and robots, three-dimensional production planning, and human simulation
3. Direct methods	<ol style="list-style-type: none"> 1. LMM 2. Body posture scanning systems 3. EMG 4. Cyberglove 5. Inclinometers 6. Electronic goniometry 	<ol style="list-style-type: none"> 1. Assessment of back posture and motion 2. Measurements of displacements, velocities and accelerations of a body segment 3. Estimation of variation in muscle tension and force application 4. Measurement of the wrist, hand and finger motion with superimposed grip pressure 5. Measurement of postures and movement of the head, back and upper limbs 6. Measurement of angular displacement of upper extremity postures
3.a. Biomechanical models	<ol style="list-style-type: none"> 1. Evaluation of Muscle effort and back stress 2. Static strength prediction programme—3D 	<ol style="list-style-type: none"> 1. Estimation of driving-related internal exposures 2. Body-integrated segmental representations
3.b. Psychophysical indices	<ol style="list-style-type: none"> 1. Psychophysical databases; 2. Borgs scale of perceived exertion 3. Body part discomfort scale 	<ol style="list-style-type: none"> 1. Assessment of quantitative and qualitative variation in individual human reactions (heart rate variability, eye blink rate, etc.) to mental load 2. Measurement of high heart and respiration rate, profuse perspiration and muscle exertion 3. Evaluation of driver’s direct experience of discomfort at different body parts

(continued)

Table 1 (continued)

Types of methods	Name of techniques	Main features
3.c. Cognitive tools	<ol style="list-style-type: none"> 1. GSR 2. Heart rate variability (HRV) 3. EEG 4. NASA TLX 5. RSME 6. SWAT 	<ol style="list-style-type: none"> 1. Evaluating accuracy and reaction time 2. Assessment of mental demand, decision-making and skilled performance 3. Detection of abnormalities in brain waves and electrical activity of the brain 4. Assessment of time load, mental effort load and stress load 5. Assessment of reaction time, correct action and ratings 6. Assessing driving activity laps and errors

powerful CAD tools. DHM combines CAD, human factors management, and risk evaluation. Computer-generated human models, called computer manikins, are used to augment the computer software with algorithms for ergonomics assessments. RAMSIS, human builder, V5 HUMAN, Delmia, and JACK are some modern DHM software programmes that include CAD packages for simulating body positions, physiological parameters and inspecting ergonomic challenges [26].

Using DHMs, designers can render a digital representation of human beings in software that has all or part of the human qualities and abilities, hence eliminating the iterations of the design. DHMs are beneficial for design ideas in the CAD environment, as they assist designers to visualize driver-machine interaction, driver engagement, and aid in making design adjustments early on in the design process. DHMs are generally utilized in tandem with CAD systems to allow designers to conduct ergonomic analyses of driver-vehicle interactions and examine how vehicle design factors affect human occupants [27, 28].

5 Conclusions

Ergonomics and driving environment design issues in heavy-duty drivers play a significant impact in traffic fatalities. Several countries have not yet taken this issue as a major concern and casualties are growing. Both driver and vehicle-related ergonomic issues are prominently affected by heavy vehicle drivers. The different ways to measure the ergonomic aspects of drivers were identified, and these methods will help in finding the importance of the scenario. Choosing the most appropriate technique or combination of methods from the vast array of current approaches would help in assessing and determining the risks of musculoskeletal difficulties of drivers.

Digital human modelling is found to be the optimum solution that integrates most of the ergonomic assessment techniques.

References

1. Matthews G (2002) Towards a transactional ergonomics for driver stress and fatigue. *Theor Issues Ergon Sci* 3(2):195–211. <https://doi.org/10.1080/14639220210124120>
2. Brown ID (1994) Driver fatigue. *Hum Factors* 36(2):298–314. <https://doi.org/10.1177/001872089403600210>
3. Ameratunga S, Hijar M, Norton R (2006) Road-traffic injuries: confronting disparities to address a global-health problem. *The Lancet* 367(9521):1533–1540. [https://doi.org/10.1016/S0140-6736\(06\)68654-6](https://doi.org/10.1016/S0140-6736(06)68654-6)
4. Kockelman K, Kweon YJ (2002) Driver injury severity: an application of ordered probit models. *Accident Analysis Prevention* 34(4):313–321. [https://doi.org/10.1016/S0001-4575\(01\)00028-8](https://doi.org/10.1016/S0001-4575(01)00028-8).
5. Lee J-H, Bogak H (2014) Effects of self stretching on pain and musculoskeletal symptom of bus drivers. *J Phys Ther Sci*. <https://doi.org/10.1589/jpts.26.1911>
6. Chand A, Bhasi AB (2019) Effect of driver distraction contributing factors on accident causations—a review. *AIP Conf Proc* 2134(August). <https://doi.org/10.1063/1.5120229>
7. Arippa F, Leban B, Pau M (2019) Postural strategies of bus drivers during a regular work shift in urban area: a pilot study. *Proc Hum Factors Ergon Soc Annu Meet* 63(1):967–971. <https://doi.org/10.1177/1071181319631429>
8. Madhan Chandran SY (2015) Are bus drivers at an increased risk for developing musculoskeletal disorders? An ergonomic risk assessment study. *J Ergon s3*. <https://doi.org/10.4172/2165-7556.s3-011>
9. Fredricks J, McColskey H (2012) The measurement of student engagement: a comparative analysis of various methods and student self-report instruments. In: *Handbook of research on student engagement*. Springer, pp 763–782. https://doi.org/10.1007/978-1-4614-2018-7_37
10. Gastaldi M, Rossi R, Gecchele G (2014) Effects of driver task-related fatigue on driving performance. *Procedia Soc Behav Sci* 111:955–964. <https://doi.org/10.1016/j.sbspro.2014.01.130>
11. Chand A, Jayesh S, Bhasi AB (2021) Road traffic accidents: an overview of data sources, analysis techniques and contributing factors. *Mater Today Proc*. <https://doi.org/10.1016/j.matpr.2021.05.415>
12. Chen C, Zhang J (2016) Exploring background risk factors for fatigue crashes involving truck drivers on regional roadway networks: a case control study in Jiangxi and Shaanxi, China. *Springerplus* 5(1):1–12. <https://doi.org/10.1186/s40064-016-2261-y>
13. Perttula P, Ojala T, Kuosma E (2011) Factors in the fatigue of heavy vehicle drivers. *Psychol Rep* 108(2):507–514. <https://doi.org/10.2466/06.13.22.PR0.108.2.507-514>
14. Abledu JK, Offei EB, Abledu GK (2014) Predictors of work-related musculoskeletal disorders among commercial minibuss drivers in Accra metropolis, Ghana. *Adv Epidemiol* 2014:1–5. <https://doi.org/10.1155/2014/384279>
15. Wise JM, Heaton K, Patrician P (2019) Fatigue in long-haul truck drivers: a concept analysis. *Work Heal Saf* 67(2):68–77. <https://doi.org/10.1177/2165079918800509>
16. Pickering CA, Burnham KJ, Richardson MJ (2007) A review of automotive human machine interface technologies and techniques to reduce driver distraction. *IET Conf Publ* 532 CP:223–228. <https://doi.org/10.1049/cp:20070468>
17. Dalziel JR, Job RFS (1997) Motor vehicle accidents, fatigue and optimism bias in taxi drivers. *Accid Anal Prev* 29(4):489–494. [https://doi.org/10.1016/S0001-4575\(97\)00028-6](https://doi.org/10.1016/S0001-4575(97)00028-6)
18. Kim HM (2018) A study on improvement of sitting posture stability for heavy truck drivers. *SAE Tech Pap* 2018-April:1–7. <https://doi.org/10.4271/2018-01-1319>

19. Raffler N, Ellegast R, Kraus T, Ochsman E (2016) Factors affecting the perception of whole-body vibration of occupational drivers: an analysis of posture and manual materials handling and musculoskeletal disorders. . <https://doi.org/10.1080/00140139.2015.1051598>
20. Mansfield NJ, Mackrill J, Rimell AN, MacMull SJ (2014) Combined effects of long-term sitting and whole-body vibration on discomfort onset for vehicle occupants. *ISRN Automot Eng* 2014:1–8. <https://doi.org/10.1155/2014/852607>
21. Bener A, Yildirim E, Özkan T, Lajunen T (2017) Driver sleepiness, fatigue, careless behavior and risk of motor vehicle crash and injury: population based case and control study. *J Traffic Transp Eng (English Ed)* 4(5):496–502. <https://doi.org/10.1016/j.jtte.2017.07.005>
22. Zhang Q, Wu C, Zhang H (2020) Driving fatigue prediction model considering schedule and circadian rhythm. *J Adv Transp* 2020(Figure 1). <https://doi.org/10.1155/2020/9496259>
23. Depestele S et al (2020) The impact of cognitive functioning on driving performance of older persons in comparison to younger age groups: a systematic review. *Transp Res Part F Traffic Psychol Behav* 73:433–452. <https://doi.org/10.1016/J.TRF.2020.07.009>
24. David GC (2005) Ergonomic methods for assessing exposure to risk factors for work-related musculoskeletal disorders. *Occup Med (Chic Ill)* 55(3):190–199. <https://doi.org/10.1093/occmed/kqi082>
25. Raghunathan R, Srinath R (2016) Review of recent developments in ergonomic design and digital human models. *Ind Eng Manag* 5(2). <https://doi.org/10.4172/2169-0316.1000186>
26. Schaub KG et al (2012) Ergonomic assessment of automotive assembly tasks with digital human modelling and the ‘ergonomics assessment worksheet’ (EAWS). *Int J Hum Factors Model Simul* 3(3/4):398. <https://doi.org/10.1504/ijhfm.2012.051581>
27. Peng J, Wang X, Denninger L (2018) Effects of anthropometric variables and seat height on automobile drivers’ preferred posture with the presence of the clutch. *Hum Factors* 60(2):172–190. <https://doi.org/10.1177/0018720817741040>
28. Wolf A, Miehling J, Wartzack S (2020) Challenges in interaction modelling with digital human models—a systematic literature review of interaction modelling approaches. *Ergonomics* 1442–1458. <https://doi.org/10.1080/00140139.2020.1786606>

Optimization of Geometrical Parameters in Magnetorheological Dampers Using Finite Element Modeling



N. Nikhil Asok , Sam Joshy , R. Suraj , Anjana Viswanath, and A. Rakesh

Abstract Magnetorheological (MR) dampers is widely used in semiactive vibration control in automobile suspension systems. The vibration control depends on the electromagnetic circuit used in these damping systems. To achieve the maximum damping performance, the geometric parameters of the piston is optimized. In the present work, a compact design of MR damper is presented, and optimization of geometric dimensions of the electromagnetic circuit is performed using design of experiments techniques. The pole length, inner radius and MR fluid gap are selected as factors, and the magnetic field density is taken as the response parameter. Amongst these factors, pole length has the highest contribution of 74.34 requires lower values of MR gap to produce highest damping characteristics.

Keywords Magnetorheological damper · Anova · Design of experiments · Taguchi · Optimization.

1 Introduction

Automobiles uses active suspension, in which these suspension systems uses an on-board system which responds according to the vertical movement of the body with respect to the chassis as against the passive systems which uses springs, the movement of which is controlled by road surface, whereas semi-active or adaptive suspension systems controls the damper properties to match with the road conditions. Such dampers uses solenoid valves (electrohydraulic dampers), and the damping is controlled by using fluids with controllable viscosity. Semi suspension systems offers higher reliability, versatility and adaptability of fully active damper, with a cost that is comparable to that of a passive system. Semi-active systems uses magnetorheological (MR) dampers. In these dampers, MR fluids are used to control damped vibration. These fluids comes under smart fluids, which allow electric or magnetic

N. Nikhil Asok (✉) · S. Joshy · R. Suraj · A. Viswanath · A. Rakesh
SCMS School of Engineering and Technology, Karukutty, India
e-mail: nikhil@scmsgroup.org

fields to regulate rheological properties. These properties are useful in the construction of a variable force damper. MR fluids consist of ferrous particles (particle size in the order of micrometers) dispersed in the carrier medium. In presence of a magnetic field, these particles get magnetized, the rheological properties of the fluid change. Thus, the ferrous particles form into chain-like structures, which get aligned in the direction of the magnetic field lines. As a result, a yield stress develops inside the fluid, which resists the fluid flow. This yield stress is a function of magnetic field density. The resulting interaction between the particles increases the viscosity of MR fluids. The viscosity of such fluids depends on the strength of the magnetic field. The applications of MR dampers include suspensions in railway carriages [1], washing machines [2], seismic dampers in structural engineering [3, 4], automotive dampers [5–7], and aircraft landing gear systems [8]. Several investigations have been reported on the nature and characterization of MR dampers to maximize their efficiency. Researchers Yasrebi et al. used CFD analysis to predict the effectiveness of MR dampers [9]. A quasi-static model generated using the Bingham fluid model was investigated by Nguyen et al. rheological properties and geometric design parameters were optimized to maximize damping force [2]. Research conducted by Djavareshkian et al. by analytical method, defined the influence of design factors on MR damper and offered design parameter optimization using the method of response surface to minimize power consumption and optimize response time [10]. Magnetostatic analysis, computational fluid dynamics analysis, and heat transfer analysis were used in previous research to develop an electromechanical brake device using magnetorheological fluid [11]. Various rheological models for the MR fluid viz., Bingham plastic, Casson, Biviscous, Biplastic Bingham, and Papanastasiou models were developed in previous research [12]. In order to study the magnetic field dependent flow behavior of fluids in MR dampers, most of the literature uses the linear Bingham plastic (BP) fluid model. This work uses the Bingham model for MR fluid. Further, Mangal and Kumar [13] used statistical methods for the geometric optimization of MR damper. Parlak et al. [14] proposed design of experiments based on Taguchi approach and conducted geometric optimization of MR damper. Ferdaus et al. [15] developed an optimal design of MR damper using finite element method considering various geometric configurations of all components. These researchers used the pole length as 23 mm, and the MR gap as 1–2 mm. The overall length of the damper is 68 mm. Recently, research conducted by Olivier et al. [16] used a pole length in the range of 11–12 mm for the design of hybrid dampers, reducing the overall length to 50 mm. Thus, reducing the pole length will reduce the length of the damper, and helps to improve the compactness. As per the authors' understanding, hardly any research has been conducted to optimize the conventional MR geometry with a shorter pole length, with magnetic flux as its objective functions.

The major focus of this research is to design a compact MR damper and to present a methodology for optimizing MR damper geometry with the sole aim of optimizing magnetic flux using design of experiments (DoE) and finite element analysis. On basis of the literature survey, three geometric parameters of the MR damper, which has the highest influence on the magnetic flux density were selected. Thus, pole length, inner radius and MR gap were selected as the study parameters. DoE analysis was

performed to obtain the combinations of parameters. Finite element analysis of MR dampers was performed using parameter combinations. Further, optimization was performed using Taguchi approach and ANOVA analysis.

2 Magnetorheological Damper

2.1 Magnetorheological Fluids

Magnetorheological fluids, discovered by Jacob Rabinow, consist of magnetically polarizable particles dispersed in a non-polar carrier fluid. In general, iron particles (micron-sized particles) produced by decomposition of iron pentacarbonyl are used as particles [17–19]. In essence, the carrier fluid should have good thermal stability, so that at varying temperatures it exhibits steady rheological behavior. Carrier fluids include petroleum-based oils, silicone, mineral oils, polyesters, polyethers, water, and synthetic hydrocarbon oils [18, 20–22]. In addition, stabilizers and surfactants will be added. These include xanthan gum, stearates, carboxylic acids, and silica gel [23]. These additives prevent particles in the carrier fluid matrix from being sedimented.

2.2 MR Dampers

The MR damper works similar to a conventional damper in spite of differences in the constructional features [1]. These dampers use the basic piston cylinder assembly construction. MR dampers have a distinct orifice geometry and provisions for mounting an electromagnetic coil as opposed to conventional dampers. MR dampers have an annular orifice rather than a spherical orifice, as is the case for conventional dampers [2, 24]. The magnetic flux circulating through the MR fluid can be completely used due to this annular orifice. In these dampers, the outer cylinder acts as a flux return path. The magnetic flux circulating through the MR fluid can be completely used due to this annular orifice. In these dampers, the outer cylinder acts as a flux return path [2]. The electromagnetic coil conducts the electric current, creating a magnetic field that travels from the inner pole to the outer pole, jumping over the MR fluid flow distance. This fluid flow gap is designed to be within 0.5–2 mm, beyond which complete utilization of magnetorheological properties is limited.

2.3 *Developing Yield Stress in MR Fluid*

On applying the magnetic field, the ferrous particles present in the magnetorheological fluid get aligned along the field direction to form chain-like structures. This result in the increase of yield stress [16, 25, 26]. However, on removing this magnetic field, the chain formation collapses, and the MR fluid returns to its original state, which helps in faster phase transition. These phase transitions occur in the order of microseconds, which makes it popular to control damping properties in semi-active damping systems. The solid structures created during the operation of the magnetic field determine the yield stress of the magnetorheological fluid. Thick columnar structures increase yield stress, while single/few columnar structures result in lower yield stress [20]. By applying compressive force to the magnetorheological fluid along with the application of the magnetic field, this yield pressure can be further increased.

3 Methodology

3.1 *Modeling and Analysis of a MR Damper*

The damping force produced by the MR damper is directly proportional to the magnetic field induced by the working fluid and the piston cylinder clearance [27, 28]. The finite element models of these MR dampers were developed using ANSYS Workbench to study the magnetic flux density in various combinations of control parameters. The 3D model of the MR Damper was developed using ANSYS Design Modeler. The MR damper is considered as an axisymmetrical solid, and the modeling is performed assuming that the magnetic loop is fully formed with the magnetic material [29–31]. Further, MR damper is modelled considering negligible leakage of magnetic flux. Figure 1 shows the structural design of the MR damper.

In the FEM analysis, cylinder, piston, and the MR fluid gap are designed as stationary components. Each component was meshed with quadratic elements having a size of 5 mm. The core/piston and the outer cylinder are made of SA 1008 Steel, a magnetic soft iron which is widely used as core in motors, transformers, and inductors. The electromagnetic coils are made of copper alloy. The magnetorheological fluid, Lord MRF 132 DG. MRF 132 DG is a hydrocarbon-based magnetorheological fluid, which is commonly used in dampers and brakes is used in this work. The MRF 132 DG contains micron-sized magnetic particles suspended in a carrier fluid. It is suitable for operating in both valve mode and shear mode. In the absence of magnetic field, the MR fluid flows freely. The exposure to a magnetic field aligns the magnetic particles in a chain like fashion. This creates a resistance to the flow of carrier fluid. The magnetization properties of SA 1008 steel (Fig. 2) and MRF 132 DG (Fig. 3) are described by a nonlinear B-H curve. The properties of the materials considered in this work are shown in the Table 1.

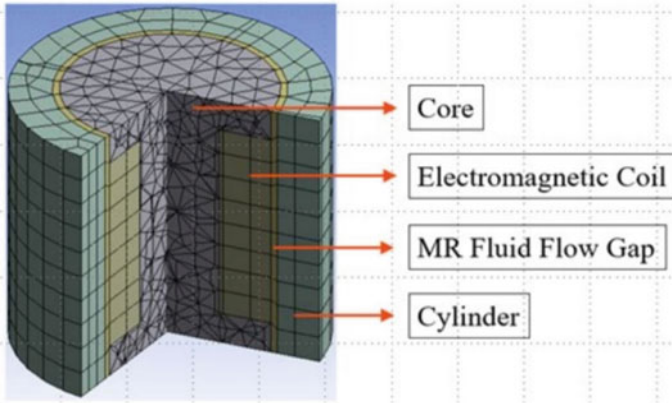


Fig. 1 Model used for numerical analysis in ANSYS

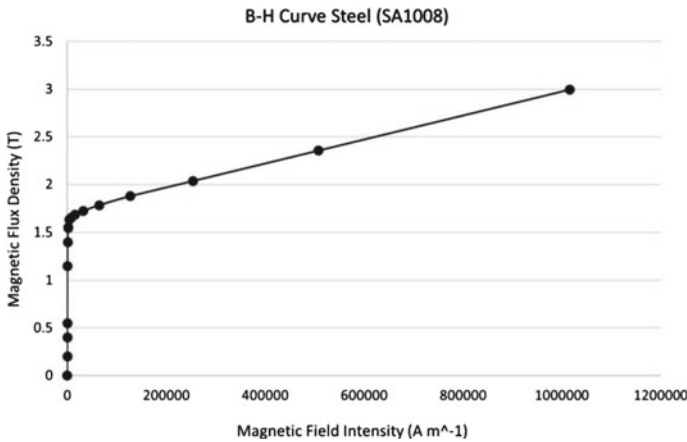


Fig. 2 Magnetization properties of SA 1008 steel

The electromagnet is modelled with 350 turns wrapped over the piston and the magnetic flux is found. A cylindrical coordinate system is assigned to the EM coil apart from the global cartesian coordinate system. A current of magnitude 1A is applied to the EM coil. A stranded type of source conductor was selected. The conducting area was calculated according to the model in consideration. A grid independence test was carried out in the MR damper. The results show that 40,000 nodes are optimum for this analysis.

The magnetic flux in the MR damper is influenced by a number of geometric characteristics. This includes pole length, piston rod to coil radial width, piston to cylinder radial clearance, and cylinder thickness. From these, three parameters that have highest influence on the damping force are chosen. The possible combinations of design points are chosen and analysis series are run within the ranges defined within

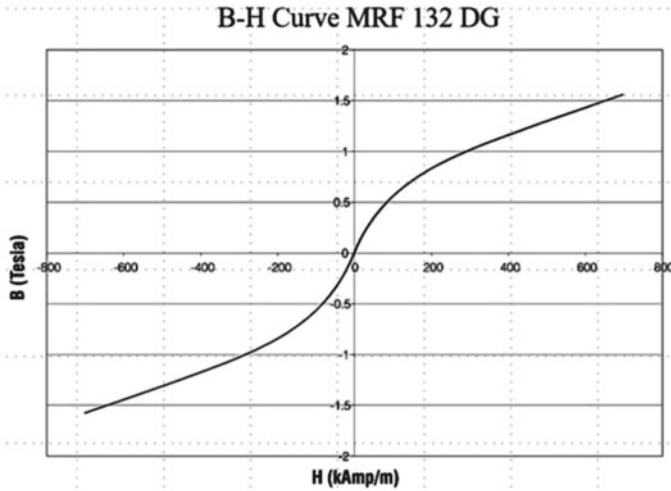


Fig. 3 Magnetization properties of MRF 132 DG

Table 1 Typical properties of MRF 132 DG

Viscosity at 400 °C	0.112 Pas
Density	2.95–3.15 gm/cu.cm
Solid content by weight	80.98%
Flash Point	>150 °C
Operating temperature	–40 to 130 °C

the established set of parameters. Between the upper and lower bounds of variables, the range is set. Table 2 summarizes these input parameters and their ranges. The aim of this research is to optimize the geometric parameters to maximize the magnetic flux with reduced pole length. To this end, the pole length was chosen between 6 to 10 mm (Table 2). Further, the inner radius and MR gap were selected. MR gap of the dampers was selected between 1 mm to 1.6 mm, because an increase in MR gap will reduce the magnetic flux.

Table 2 Factors used in design of experiments

Sl. No.	Parameter	Lower range	Mid range	Upper range
		All dimensions in mm		
1	Pole length	6	8	10
2	Inner radius	8	10	12
3	M R Gap	1.0	1.3	1.6

The effect of these geometric damper parameters on the damping force (response parameter) is established, and Taguchi technique designs and optimizes the experiments. The orthogonal array and the SN ratio are two important tools in the Taguchi technique. The best feasible design variables impacting the performance of the optimization problem are provided by design of experiment. This statistical approach is employed in design problems where more than one input parameter affects a response or output. In this method, different combinations of parameters are identified; and these are referred to as design points.

The responses in the orthogonal array can be obtained using real life experiments or numerical analysis using finite element methods. However, numerical analysis using FEM reduces the experimentation cost. Furthermore, the numerical analytical results are very similar to the experimental results. The factors are taken in three levels, viz., upper, middle and lower levels. Since the L9 array was defined, the degree of freedom (DOF) for the selected three levels is $3 - 1 = 2$, and for three variables, the total DOF is $3 \times 2 = 6$. In accordance with Taguchi's L9 array, nine damper models were examined. This array consists of the nine combinations of three geometric variables. These factors are used for the FEM analysis, and the results from the analysis are taken as the response for Taguchi analysis. The maximum S/N ratio reflects greater performance, according to the Taguchi method. This suggests that it is necessary to achieve a high-quality product by In the Taguchi analysis, this combination indicates a higher S/N ratio. The S/N ratio of quality characteristic analysis for the parameters (pole length, inner radius and MR gap) with the objective of 'the larger-the better' was performed.

The following parameters are used for the modeling.

- Magnetic reluctance R_i
- Magnetic flux density ϕ

$$F = R_i \phi \quad (1)$$

where F is magnetic potential ($F = NI$), where N is the number of turns of the coil, and I is the current that is passing through the coil. The magnetic reluctance, R_i , is given as

$$R_i = \frac{L_i}{A_i \mu_i} \quad (2)$$

where L_i is the length of the component (mean direction of magnetic flux lines), A_i is the cross-sectional area, and μ_i is the permeability of the i th portion of the magnetic flux path and so on. Magnetic flux ϕ and magnetic flux density B are determined as follows:

$$B = \frac{\phi}{A} \quad (3)$$

3.2 Main Effects Plot and S/N Ratio

The Taguchi results are shown in main effects plot and SN ratio. A value that reflects the impact of a factor on the response is the main effect. The variance of the response variable with the variation in control factors is represented by this plot and is used to find the differences between the level means for variables. If the line plotted is horizontal and there is no change in response with the change in factor, the factor is said to be insignificant. A high slope, on the other hand, indicates that the factor has a significant impact on the response.

The S/N ratio is the proportion of the signal factor to the noise factor in the Taguchi approach. In this method, the three stages of S/N ratio, viz., smaller the best, nominal the best, and larger the best are used. The objective of this work is to optimize the geometric parameters to maximize the magnetic flux, and thus the latter option is selected. The mathematical expression for larger the best approach is

$$\frac{S}{N} = -10 \log_{10} \frac{1}{n} \sum_{i=1}^n \frac{i}{y^2} \quad (4)$$

where n is the number of replications and y_i is observed response value. The higher S/N ratio reflects a higher quality technique. This means that it is possible to achieve a high-quality product by Taguchi analysis, the mixture indicates a higher S/N ratio. As the primary goal of optimization, the SN ratio can be maximized, minimized, or held at nominal values. This allows in the selection of control levels capable of fully compensating for noise effects. In this work, SN ratio is chosen to be kept the maximum, as the goal of the design is to maximize the magnetic flux in the MR damper, ultimately maximizing the damping force.

It is necessary to determine the statistically important parameters, which has the highest influence on the response parameter, and ANOVA analysis is performed. Further, confidence level of 95 thus p value less than 0.05 will ascertain the significance of factor. In addition, the percentage of influence of each parameter on output factors can be defined using ANOVA. As a result, the null hypothesis for the entire population is ignored if the p value is less than 0.05, and the parameters are judged significant. If the P value is greater than 0.05, the null hypothesis is not discarded, and the parameters are irrelevant.

4 Results and Discussion

Figure 4 shows the typical image showing the intensity of magnetic flux. The magnetic flux is observed to be highest at regions closer to the pole. It may also be observed that the magnetic flux is minimum toward the central region (shown in blue color).

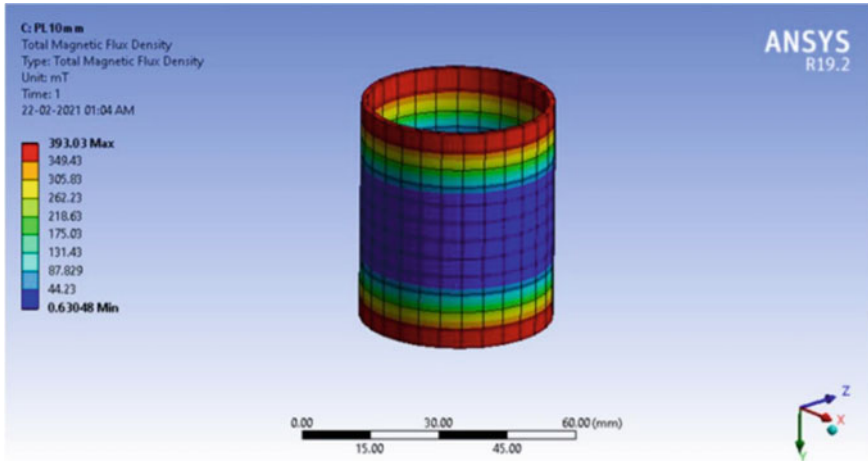


Fig. 4 Typical results of numerical analysis in ANSYS

The responses from numerical analysis are solved in Minitab, and the results are shown in Table.3. The S/N responses for pole length, inner radius, and MR gap are shown in this table, and the results show the optimum control factor levels for both dependent parameters. The magnetic flux is obtained in between 0.395 T and 0.560 T. In general, it may be observed that the magnetic flux density reduces with increase in pole length. This observation is in line with the results of similar research conducted by Nanthakumar and Jancirani [32]. With increase in pole length, the magnetic flux distribution gets lowered. Considering the pole length and MR gap, it may be observed that with lower pole length of 6 mm, the increase in MR gap reduces the magnetic flux. On the other hand, with increase in pole length to the 8 mm, the highest magnetic flux is obtained with MR gap of 1.6 mm. Thus, it can be inferred that up to 8 mm, the increase in pole length and MR gap will increase the magnetic flux. The increase in pole length increases the magnetic to However, with further increase in pole length to 10 mm, the magnetic flux increase up to 1.3 mm. With further increase in MR gap, the magnetic flux decreases. This shows that at higher values of pole length, the highest damping performance is obtained corresponding to MR gaps ranging between 1.3 mm and 1.6 mm. These values are in line with the previous research conducted by Mangal and Kumar [13]. It may be observed from this table that the parameters used in the Analysis No. 2 has the highest S/N ratio. Figures 5 and 6 present these findings in graphical form. The optimal control parameters for maximizing the magnetic flux in the MR damper may be easily found using these graphs. The optimum level for the geometric parameters was obtained at pole length of 6 mm, Inner radius of 10 mm and MR gap of 1.3 mm according to these results. These parameters had the highest S/N ratio as compared to that of other levels.

As shown in Table 4, the effect of geometric parameters was further investigated using analysis of variance (ANOVA). With multivariate data, this technique can be

Table 3 Results of DOE

Analysis No.	Pole length	Inner radius	MR gap	Magnetic flux	S/N ratio
	All dimensions in mm			T	
1	6	8	1.0	0.5370	-5.40051
2	6	10	1.3	0.5600	-5.03624
3	6	12	1.6	0.5120	-5.81460
4	8	12	1.3	0.4670	-6.61366
5	8	10	1.6	0.4870	-6.24942
6	8	8	1.0	0.5359	-5.41832
7	10	8	1.6	0.4684	-6.58766
8	10	10	1.0	0.5153	-5.75880
9	10	12	1.3	0.5249	-5.59847

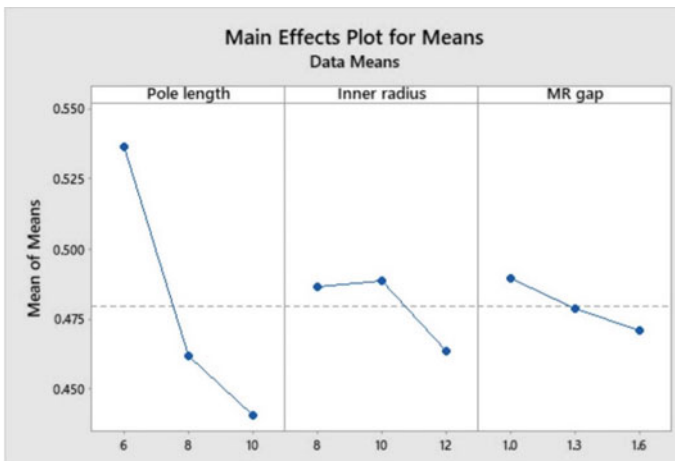


Fig. 5 Main effects plots for means during simulation

used to test the statistical hypothesis of complicated occurrences. The *p*-value shows the differences in the geometric factors, as shown in the table. In contrast to the other variables, the pole length had the highest percent contribution of 74.34%, means that the pole length has the highest significance; while the *p*-value of the inner radius and MR gap that is greater than 0.10, which suggests that these model terms are not significant. The results show that the differences in the factors had a significant impact on the pole length.

A normality test was performed to analyze the distributed population of the data points. In Fig. 7, the standard residuals are plotted against the MR damper’s percentage probability distribution.

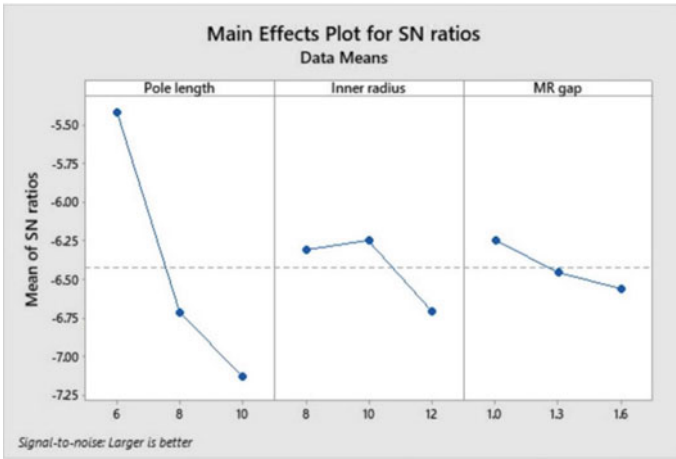


Fig. 6 Main effects plots for S/N ratios during simulation

Table 4 Significance analysis using ANOVA

Source	DF	Contribution	F-Value	P-Value
Pole length	2	74.34%	32.54	0.030
Inner radius	2	8.52%	6.70	0.130
MR gap	2	14.85%	6.50	0.133
Error	2	2.28%		
Total	8	100%		

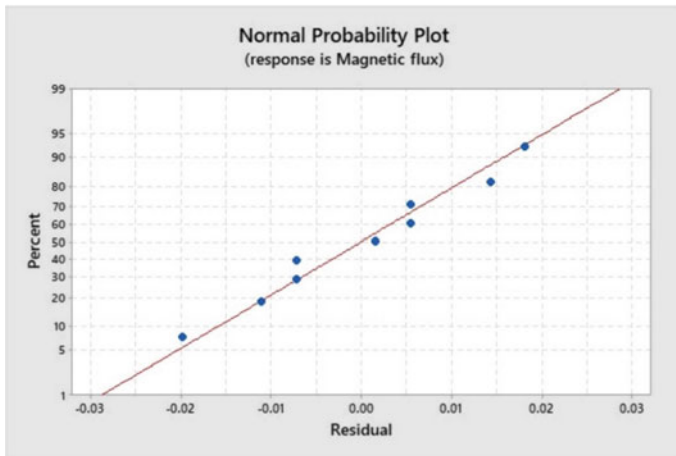


Fig. 7 Normal plot of a model MR damper

The straight reference line depicts the real normal distribution, whereas the points distributed are residual data points. The residual data points are closely fitted, as can be shown. Thus, it can be found that the data points follow normal distribution.

5 Conclusion

By optimizing the geometric factors of the MR damper, the magnetic flux density at the fluid flow gap is maximized. Optimization is performed using Taguchi approach, and it was observed that the lowest pole length of 6 mm, along with inner radius of 10 mm and MR gap of 1.3 mm gives the highest value of magnetic flux. Further, these responses were analyzed for significance analysis in ANOVA approach. The significance of the parameter and their interactions is analyzed using ANOVA. The results from the numerical analysis and ANOVA shows that the contribution of pole length is 94.42% as against the 2.86% and 2.59% contribution of inner radius and MR gap, respectively.

References

1. Lau Y, Liao W (2005) Design and analysis of magnetorheological dampers for train suspension. *Proc Inst Mech Eng Part F: J Rail Rapid Transit* 219:261–276
2. Nguyen QH et al (2007) Geometry optimization of MR valves constrained in a specific volume using the finite element method. *Smart Mater Struct* 16(6):2242–52. <https://doi.org/10.1088/0964-1726/16/6/027>
3. Jung HJ, Spencer BF, Ni YQ et al (2004) State-of-the-art of semiactive control systems using MR fluid dampers in civil engineering applications. *Struct Eng Mech* 17(3–4):493–526
4. Elsaady W, Oyadiji SO, Nasser A (2020) A review on multi-physics numerical modelling in different applications of magnetorheological fluids. *J Intell Mater Syst Struct* 31(16):1855–1897. <https://doi.org/10.1177/1045389X20935632>
5. Sassi S, Cherif K, Mezghani L, Thomas M, Kotrane A (2005) An innovative magnetorheological damper for automotive suspension: from design to experimental characterization. *Smart Mater Struct* 14:811
6. Xiao P, Gao H, Niu L (2017) Research on magnetorheological damper suspension with permanent magnet and magnetic valve based on developed FOA-optimal control algorithm. *J Mech Sci Technol* 31(7):3109–3119. <https://doi.org/10.1007/s12206-017-0601-7>
7. Khot SM (2019) Design and analysis of magneto-rheological (MR) damper amey pramod marathe. 2019 Int Conf Nascent Technol Eng (Icnte):1–6
8. Batterbee D, Sims N, Stanway R, Wolejsza Z (2007) Magnetorheological landing gear: 1. a design methodology. *Smart Mater Struct* 16:2429
9. Yasrebi N, Ghazavi A, Mashhadi M, Yousefi-Koma A (2006) Magnetorheological fluid dampers modeling: numerical and experimental. In: *Proceeding of the 17th IASTED international conference modeling and simulation*
10. Safarzadeh H, Djavareshkian MH, Esmaeili A (2015) Optimal design of magnetorheological fluid damper based on response surface method. *Int J Eng* 28:1359–1367
11. Park EJ, da Luz LF, Suleman A (2008) Multidisciplinary design optimization of an automotive magnetorheological brake design. *Comput Struct* 86:207–216

12. Ghaffari A, Hashemabadi SH, Ashtiani M (2015) A review on the simulation and modeling of magnetorheological fluids. *J Intell Mater Syst Struct* 26:881–904
13. Mangal S, Kumar A (2015) Geometric parameter optimization of magnetorheological damper using design of experiment technique. *Int J Mech Mater Eng* 10:1–9
14. Parlak Z, Tahsin IE (2012) Optimal design of mr damper via finite element analyses of fluid dynamic and magnetic field. *Mechatronics* 22:890–903
15. Ferdaus MM, Rashid MM, Hasan MH, Rahman MA (2014) Optimal design of magneto-rheological damper comparing different configurations by finite element analysis. *J Mech Sci Technol* 28:3667–3677
16. Olivier M, Sohn JW (2020) Design and geometric parameter optimization of hybrid magnetorheological fluid damper. *J Mech Sci Technol* 34:2953–2960
17. Swaroop KV et al (2020) Investigation of steady state rheological properties and sedimentation of coated and pure carbonyl iron particles based magneto-rheological fluids. In: *Materials today: proceedings*, Elsevier Ltd. <https://doi.org/10.1016/j.matpr.2020.05.364>
18. Swaroop KV, Aruna MN, Kumar H, Rahman MR (2020) Investigation of steady state rheological properties and sedimentation of coated and pure carbonyl iron particles based magneto-rheological fluids. *Mater Today Proc.* <https://doi.org/10.1016/j.matpr.2020.05.364>
19. Raeesi F, Azar BF, Veladi H, Talatahari S (2020) An inverse TSK model of MR damper for vibration control of nonlinear structures using an improved grasshopper optimization algorithm. *Structures* 26(March):406–416. <https://doi.org/10.1016/j.istruc.2020.04.026>
20. De Vicente J et al (2011) Magnetorheological fluids: a review. *Soft Matter* 7(8):3701–10. <https://doi.org/10.1039/c0sm01221a>
21. Utami D, Ubaidillah, Mazlan SA et al (2018) Material characterization of a magnetorheological fluid subjected to long-term operation in damper. *Materials (Basel)* 11(11). <https://doi.org/10.3390/ma11112195>
22. Sternberg A, Zemp R, de la Llera JC (2014) Multiphysics behavior of a magneto-rheological damper and experimental validation. *Eng Struct* 69:194–205. <https://doi.org/10.1016/j.engstruct.2014.03.016>
23. Sukhwani VK, Hirani H (2007) Synthesis and characterization of low cost magnetorheological (MR) fluids. In: *Behavior and mechanics of multifunctional and composite materials 2007*, vol 6526. International Society for Optics and Photonics, p 65262R
24. Kumar Kariganaur A, Kumar H (2020) Effect of magnetic permeability, shearing length, and shear gap on magnetic flux density of the magnetorheological damper through finite element analysis. *Mater Today Proc.* <https://doi.org/10.1016/j.matpr.2020.05.714>
25. Case D, Taheri B, Richer E (2013) Multiphysics modeling of magnetorheological dampers. *Int J Multiphys* 7(1):61–76. <https://doi.org/10.1260/1750-9548.7.1.61>
26. Susan-Resiga D (2009) A rheological model for magneto-rheological fluids. *J Intell Mater Syst Struct* 20(8):1001–1010. <https://doi.org/10.1177/1045389X08100979>
27. Zambare H et al (2021) MR damper modeling performance comparison including hysteresis and damper optimization. *IEEE Access* XX:1–1. <https://doi.org/10.1109/access.2021.3057174>
28. Purandare S, Zambare H, Razban A (2019) Analysis of magnetic flux in magneto-rheological damper. *J Phys Commun* 3(7). <https://doi.org/10.1088/2399-6528/ab33d7>
29. Lee TH, Han C, Choi SB (2018) Design and damping force characterization of a new magnetorheological damper activated by permanent magnet flux dispersion. *Smart Mater Struct* 27(1). <https://doi.org/10.1088/1361-665X/aa9ad6>
30. Özsoy K, Usal MR (2018) A mathematical model for the magnetorheological materials and magneto rheological devices. *Eng Sci Technol Int J* 21(6):1143–1151. <https://doi.org/10.1016/j.jestch.2018.07.019>
31. Seid S, Chandramohan S, Sujatha S (2018) Optimal design of an MR damper valve for prosthetic knee application. *J Mech Sci Technol* 32(6):2959–2965. <https://doi.org/10.1007/s12206-018-0552-7>
32. Nanthakumar A, Jancirani J (2019) Design optimization of magnetorheological damper geometry using response surface method for achieving maximum yield stress. *J Mech Sci Technol* 33:4319–4329

Academic Performance Prediction of Postgraduate Students Using Artificial Neural Networks



M. Varun , R. Sridharan , and K. K. Eldose 

Abstract Institutions of higher learning operate in a highly competitive environment. To compete with world-class institutions, institutes must adapt their strategy to increase overall performance. Academic achievement of students is one of the most important factors in improving an institution's ranking and recognition. Performance of students in an academic program depends upon several aspects of their previous academic performance and family background. In the present study, an artificial neural network (ANN) is developed using Python programming language to predict students' performance and to determine the outcome of students' performance. Students' data were collected through a questionnaire-based survey from postgraduate students of technical education institutions all over India. The appropriate ANN model is identified, and the Python code for the same is developed with the help of Keras library. The developed model did not have the expected accuracy due to lack of adequate number of responses required for deep learning techniques, but still valuable results are obtained such as that of identifying some crucial factors.

Keywords Machine learning · SVM · Performance prediction · ANN · Deep learning

1 Introduction

The academic performance of students at higher institutions is a subject of tremendous concern and curiosity for most researchers, as well as parents, universities/colleges and governments around the world. These institutions need to evaluate their students' performance in order to develop a strategy for improving the institute's reputation and obtaining funding for initiatives from a variety of sources. As a result, educational institutions must keep track of how students are doing and where they

M. Varun · R. Sridharan (✉)

Department of Mechanical, National Institute of Technology Calicut, Calicut, India

e-mail: sreedhar@nitc.ac.in

K. K. Eldose

Department of Mechanical, Adi Shankara Institute of Engineering and Technology, Kalady, India

need to improve. Institutions would be able to monitor students' future performance by using previous knowledge/past recordings of their details. This projection will help educational institutions evaluate and assess student induction into the university programme or plan to help slow learners at the beginning of the semester (poor performers).

The performance of students depends on a number of parameters that can directly or indirectly influence their performance. These parameters are the features of the students, which needs rework so that these metrics are comparable to that of the better performers. The analysis of past performance and some background information of admitted students is essential in order to get a better view of student performance in future.

The consequence of adopting the methodology briefed above is that educators will be able to comprehend the obstacles that students face in their studies. So, an educator may teach students better and intervene when they do poorly. The procedure for adopting machine learning techniques such as artificial neural networks (ANN) and support vector machines (SVM) for performance prediction and generating intended outputs is presented in this paper. As a result, the current study focuses on the application of performance prediction approaches and provides information about machine learning techniques' great potential.

Students who underperform need to be spotted at the earliest, and necessary steps have to be provided to boost their performance. This study focuses on identifying the vital attributes and its influence on the students' performance to formulate an appropriate strategy.

- Predict students' academic performance from the different factors that shaped their background.
- To analyse various ANN and SVM models for predicting the academic performance.

2 Background of the Study

Several investigators have studied the prediction of the performance of students. The present research is based on a brief review of the relevant studies, the background of which is given below.

Kotsiantis et al. [1] researched student performance using six machine learning algorithms in the correspondence learning mode. The researchers conclude that for a software's easier implementation, effective application of the Naïve Bayes' algorithm would suffice. Slim et al. [2] presented a study wherein Markov networks were able to predict students' performance with high accuracy, which shows that a detailed dataframe consisting of present performance was able to predict the future performance. Over the six same methods in Kotsiantis et al. [1], Koutina et al. [3] propose models to compare the most effective technique using an open-source software package called Waikato Environment for Knowledge Analysis (WEKA). The results show the best prediction of the Bay of Naïve and k-NN, while it is less likely

to be predicted by the decision tree algorithm. They suggest that the presence in the class and undergraduate programmes is the most effective effect on attributes.

Sahu et al. [4] performed an analysis in identifying the critical factors that affect the success in technical education scenario using total quality management (TQM) approach and found that the study's model matched the results of the previously existing literatures' quality improvement measures. This piece of literature throws light at the success of the institution itself which might help the current study on predicting the academic performance by diversifying the components of the research. Naser and al. [5] use the ANN technique to forecast the performance of sophomore students by taking into account their previous year's grades and the corresponding personal/background information of that time. The researchers conclude that the model developed is able to predict the students' academic performance with 80% accuracy. The study splits the dataset in three ways and assigns 60% for training, 30% for testing and the rest for validation.

Ajibade et al. [6] used five predictive analytics which fall under the category of subsets of artificial intelligence, for predicting the academic performance of students. Ensemble techniques are used to improve the predictive model efficiency. The results show that students' academic performance and their behaviour are in stark correlation. The model has been found to be less exact while only taking into account students' academic performance. Lau et al. [7] bring to the table, a statistical model and a neural network model to predict the academic performance of students. Factor analysis has been applied to understand the influencing variables and the neural network Marquardt algorithm as the back-propagation training rule. The researcher concludes that with certain restrictions the overall performance of the neural network is better.

The academic performance of students plays an important role in assessing an institutes' reputation. The academic performance of students, however, depends on various factors. Academic performance prediction will help to develop and implement improvement programmes. The current research focuses on applying ANNs and SVMs to model students' academic performance. The following sections contain details of the study.

However, not many research studies exist for academic performance prediction in Indian technical education scenario and the previous studies are not exhaustive when considering factors for different algorithms. Also, there is nowhere in the literature had there been reported performance improvement measures that have been confirmed to do the same.

3 Methodology

In the present study, several artificial neural network (ANN) models and other machine learning models were developed using Python programming language to predict students' performance, and the models were compared to one another. Various ANNs were created by changing certain parameters (like kernel initialiser, activation function, loss function, optimiser, etc.) in the multilayer perceptron (MLP) base model. The only other model developed other than the above-mentioned ANNs is a support vector machine (SVM). Before the SVM model was developed, exploratory factor analysis has been performed on the collected data which reveals important attributes that affect the model. This gives insights into the factors that the attributes share which makes the model more dependent on the said attributes (Fig. 1).

3.1 Data Preprocessing

The goal of this research is to create a model that relates the specified characteristics to the students' performance. The prior performance of students as well as their living situation should be examined for this study in order to gain insight into performance trends. The attributes considered for this study were chosen from existing literature, as well as some new attributes added as a contribution, and these newly added attributes were checked. A total of 54 attributes were taken into account, and 65 questions

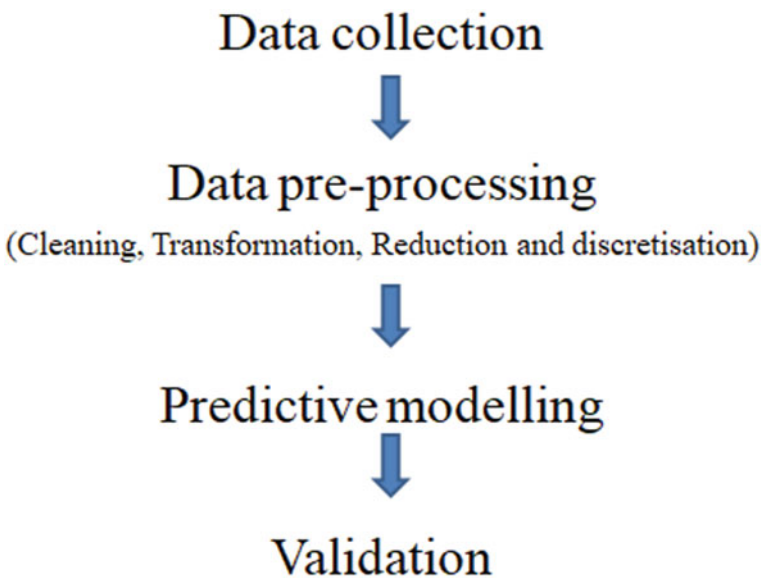


Fig. 1 Methodology overview

were created using Google Forms based on these 54 attributes. This questionnaire is divided into two sections: the first comprises questions about personal information, and the second has questions about educational performance at various levels of examination.

After the initial preparation of questionnaire, the questions were checked for independency, precision and adequacy for another two rounds. Any repetition or imperfections were removed after academic consultation. Finally, the questionnaire was circulated to the target group, viz. the postgraduate students of technical education (including management studies) throughout India. About 393 students participated in the survey. Since the target audience contained diverse features, the questionnaire was created to accommodate the pupil specific question without collecting unnecessary data. The questionnaire was designed such that it extracted data in nominal ordinal and interval scale. So response from the nine sections of the questionnaire needed to be encoded numerically to provide as input to the Python code.

Participants skipped some items in the questionnaire-based survey, which resulted in missing data. Cleaning the data and performing other preprocessing steps to the raw data collected from the survey has a major role to play in the accuracy of the model.

- Missing data are corrected by filling it with mean value of the particular feature.
- Since the nominal missing data are hard to rectify, the questionnaire mandates the respondent to fill the field. So those mandatory questions must be suitable for every eligible respondent which is why a conditional question is included before such questions, which skips the question depending on the response to that particular field.

3.2 Factor Analysis

An exploratory factor analysis (EFA) was performed to identify the critical factors that affect the students' academic performance by using principal component analysis with varimax rotation in Jamovi 2 software. The factor loading's minimum threshold was set at 0.5. The uniqueness of the attributes was computed, and the attributes with acceptable level of uniqueness are retained to ensure acceptable levels of explanation (less than 0.4). EFA requires several assumptions to be met. An important step involved is Bartlett's test of sphericity, which tests whether the variables are correlated perfectly to itself in which case the factor analysis need not be performed. The statistic showed that the p-value (0.001) is less than the level of significance (0.05), which shows that the correlation matrix is not an identity matrix. Another important step is the Kaiser–Meyer–Olkin (KMO) measure of sampling adequacy which showed that appropriateness of the data for factor analysis is 0.625 which is not considered good as the KMO statistic is supposed to have a value more than 0.8 for this type of problem even though the theoretically acceptable threshold is 0.5.

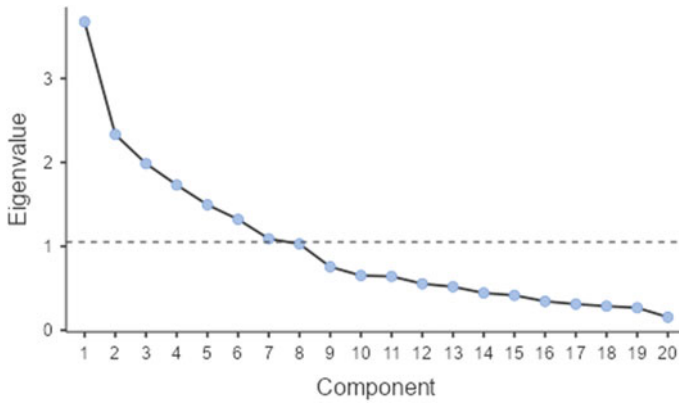


Fig. 2 Scree plot

Out of the 54 attributes extracted from the pupil data, seven components were considered based on eigenvalue which explains the variance explained by each component; the lower limit of the eigenvalue is set to 1.05 so that the components having a higher value are only considered. It is also to be noted that seven components were identified from a set of 20 attributes (from the total 54), which were deemed suitable as the uniqueness for each variable falls in the required range. These seven factors accounted for 68.1% of the total variation in the data. These factors were identified (from the attributes) and ranked as:

- (1) Past performance
- (2) Gender
- (3) Medium of instruction
- (4) Academic break
- (5) Financial pressure
- (6) Study hours
- (7) Family size (Fig. 2).

3.3 ANN Model Development

The prediction of the output data, i.e. second semester marks, is done after developing the model. For the model development, the input (various attributes obtained from the questionnaire) and the output are trained together. The model developed after feeding the encoded data was found not to be accurate but after reducing the dimensionality of the data, i.e. selecting fewer attributes that gives more accuracy, the accuracy of the model improved. The attribute selection was aided by reviewing the literature and factor analysis.

As mentioned above, various ANNs were created by changing certain parameters like kernel initialiser, activation function, loss function, optimiser, etc., in the multilayer perceptron (MLP) base model with one hidden layer.

Kernelinitialiser

- Uniform
- Normal

Optimiser

- Adam
- NAdam
- Adamax

Loss function

- Mean absolute error
- Mean squared error
- Huber

Activation function

- Sigmoid
- Relu
- Softmax

All of the above parameters have been used in combination exhaustively, and it has been found that model with uniform Kernel initialiser, Adam optimiser, mean squared error loss function and sigmoid activation function gave the best result; (i.e.) the loss function in the last iteration gave the least value of 6 which is not close to the ideally accepted value of 1 due to small dataset.

4 Results and Discussion

Data obtained from students were consolidated via an online survey in the form of a questionnaire, specifically catered from postgraduate (PG) students of technical education of institutions all over India. The appropriate machine learning model is identified, and the Python code for the same is developed with the help of Keras library. Some of the developed models (all the ANN models) did not have the expected accuracy due to lack of adequate number of responses required for deep learning techniques, but still valuable results were obtained such as that of identifying some crucial factors.

The parameter that governs the accuracy of the ANN model is mean squared error (MSE) whereas root mean squared error (RMSE) governs the accuracy of support vector machine (SVM) model (although these two measures cannot be compared directly, it can be compared after taking square root of the MSE). After comparing models to one another, it was found that the SVM model (developed using radial basis

function as kernel) fits the best for this scenario (smaller sample size, regression/non-classifier). Along with identifying the model for this aspect, it is also found that certain models suit certain problems; such as MLP are found to be best suited for classifier rather than regression problems. The other take away of this study is the ANN models in spite of having data adequacy issues, did not fall behind much when compared to SVM (SVM had 16% more data accuracy); although its (loss/error) is considered huge in terms of prediction, it is considerably lower than other ANNs (from the literature) that have similar dataset and similar dimension.

5 Conclusion

This study presents valuable insights into prediction of students' performance especially in the postgraduate scenario. The data were collected in the form of questionnaires from the target students of the case institution. The raw data collected were then processed for removal of any flaws and then encoded to be fit for feeding into the model algorithm. There were 54 variables in the final dataset. Following a thorough examination, seven variables were chosen for future investigation. As a result, the current study provides substantial proof that student academic performance can be predicted.

The proposed model needs correction in the form of higher data points in the training dataset, which due to the ensuing pandemic was hard to obtain. It can also be said that SVMs and other machine learning models are suitable for smaller datasets with fewer attributes, while ANNs are suitable for models of larger datasets.

The present study can aid the administration and the academics department in identifying the factors that contribute for enhancing students' performance, and appropriate actions can be made for such purpose.

Future studies can explore the possibility of performing Markov's analysis of student retention rate before being subjected to model training.

References

1. Kotsiantis S, Pierrakeas C, Pintelas P (2004) Predicting students' performance in distance learning using machine learning techniques. *Appl Artif Intell* 18:411–426
2. Slim A, Heileman GL, Kozlick J, Abdallah CT (2014) Employing markov networks on curriculumgraphs to predict student performance. In: 13th International conference on machine learning and applications
3. Koutina M, Kermanidis KL (2011) Predicting postgraduate students' performance using machine learning techniques. Ionian University, Department of Informatics
4. Sahu AP, Shrivatsava RR, Shrivatsava RL (2014) Development and validation of an instrument for measuring critical success factors (CSFs) of technical education—a TQM approach. *Int J Prod Qual Manage* 11(1):201

5. Naser AN, Zaqout I, Ghosh MA, Atallah R, Alajrami E (2015) Predicting student performance using artificial neural network: in the faculty of engineering and information technology. *Int J Hybrid Inf Technol* 8(2):221–228
6. Ajibade SSM, Ahmad NB, Shamsuddin SM (2018) A data mining approach to predict academic performance of students using ensemble techniques. In: *International conference on intelligent systems design and applications*. Springer, Cham, pp 749–760
7. Lau ET, Sun L, Yang Q (2019) Modelling, prediction and classification of student academic performance using artificial neural networks. *SN Appl Sci* 1(9):982

Internet of Things-Based Attendance Management System



J. Anoj , R. Sridharan , and V. Karthikeyan 

Abstract The project's purpose is to develop biometrics and facial detection-based attendance register for educational institution such as colleges and schools. This project combines engineering techniques of both hardware component and software skills to create a product that alternate the present method of attendance recording. This project makes use of Internet of Things for data transport, storage, and presentation. Face detection and fingerprint detection were integrated into a gateway with a Wi-Fi module that is connected to a cloud server to construct the system. The output can be received using a mobile application that is available whenever the faculty needed also faculty can have the provision to enter attendance manually if there is any mismatch.

Keywords Internet of Things · Fingerprint sensor · Face detection

1 Introduction

1.1 Salient Aspects of Attendance Management System

In today's world, precise data collection is critical for sustaining a system's integrity. Errors are less likely to occur when the appropriate method and device are utilized for data collecting. Attendance is used to maintain track of the number of pupils in a school, institution, or other organization. The attendance percentage is more crucial since students who consistently attend class are more likely to thrive academically.

J. Anoj (✉) · R. Sridharan
Department of Mechanical Engineering, National Institute of Technology Calicut, Calicut, India
e-mail: anoj94@gmail.com

R. Sridharan
e-mail: sreedhar@nitc.ac.in

V. Karthikeyan
Department of Electrical Engineering, National Institute of Technology Calicut, Calicut, India
e-mail: karthikeyan@nitc.ac.in

However, if a big number of students are usually missing, it is difficult for a faculty to compute manually or input data by typing.

The professor then manually enters data into an excel spreadsheet or an Internet database. Even though this system has been in operation for a prolonged time, this approach still has a lot of fundamental faults that can be easily fixed with technology.

Rather than relying on the traditional marking attendance system, the complete procedure of attendance recording and maintenance is handled by a smart gadget with help of the Internet of Things. This system effectively uses the principles of hardware and software incorporated with IoT networking.

1.2 IoT–Internet of Things

Internet of Things is a system of interrelated computers, mechanical equipment digital devices, objects, or persons which have unique identifiers and can transfer data over a network without interaction between humans to humans or humans to computers.

1.3 Major Components of IoT

Data and sensors are the important factors for the initial level of an IoT system to ensure data accuracy and credibility. This essential component is composed of physical and micro appliances that are integrated into IoT devices, responsible for the collection of or mechanism control.

After collecting the data from the sensors, transportation media is required. Only if two devices are securely connected, data can be transmitted online through IoT protocols. Network choices depend on factors such as bandwidth, electricity consumption, transfer of data speed, range, and overall efficiency. Bluetooth, ZigBee, and Wi-Fi are popular IoT Wireless protocols.

After collecting data, it is processed to the cloud. The cloud plays a vital role and it is the place for “intelligent things!” This powerful facility mainly connects the components of the IoT system. Cloud is used to handle, store, and manage data. All of this is done in milliseconds for massive volumes of data—time is important for IoT.

IoT analytical techniques are employed to make sense of massive volumes of analog data. The primary responsibility is to examine a situation and make a judgment based on that analysis. Predictive analysis can be done with a model from deep learning. The data is perhaps used for the prediction of trends, future planning, and intelligent business decisions. To make sense of any data, analytics necessitates a large amount of storage and cognitive computing.

The user interface is the apparent part of the system from which IoT user can approach and operate. In this stage, a user has proficiency to control of the system and customize their settings.

2 Background Study

2.1 *Highlights from the Background Research*

To ease the burden of attendance tracking and storage, a variety of approaches have been implemented. Nonetheless, they have their own virtues and flaws.

Jeong et al. [1] used a capturing device that collected student picture data and verified who is in class and sends information through the mail. But this system fails to explain alternate methods if there is an issue in a face detection system.

Jinushia et al. [2] used RFID cards to track the attendance of students since RFID usage depends on lecture attendance, and it has a limitation on providing accurate information on other events of attendance.

Dastidar et al. [3] have presented a good idea for collecting and storing attendance data, however, their system has not been well implemented. There is also no mention of how they intend to collect and sort the data before sending it to an online database. Furthermore, there is not enough detail for what happens to the data received if there is not a good Internet connection.

Vinay et al. [4] used a transparent system of attendance and the maintenance of real-time information present in online display for parents and other purposes of academic are the goal of this project. The author developed a system that maintains user data of fingerprints in a database and matches to fingerprints collected through the attendance period using an 8051 microcontroller. A web page can access the student's attendance record. But it involves a security risk in storing data of fingerprints in the database. However, it has a major disadvantage that this setup needs a direct connection with the PC to transfer data of fingerprint to the database.

Vishal et al. [5] have study the use of arm7-based processor in conjunction with a biometric sensor and an LCD screen, all of which are connected from JAVA API to a PC. Even though this approach is effective at representing data, it is cumbersome.

2.2 *Inference Drawn from Background Study*

Research studies reported have not integrated biometric and face detection/recognition to have more accurate data. Absence of an instant mobile notification alerts to concerned faculty.

Students could have access to a mobile phone application that allows them to simply track their attendance.

3 Proposed System Methodology

3.1 Components

Having a biometric and video sequence as input to the system consist of IoT and integration of fingerprint and face detection are described below:

- Raspberry 3 pi
- Camera for face detection
- Fingerprint scanner
- Cloud server account
- Power unit

3.2 Fingerprint Recognition

Initially, we must store the information of student's detail and fingerprint, respectively. At the very first period of the class, the students are required to give attendance through biometric and it will be valid throughout the day and the count was stored in the cloud server which will be used to check the face detection count.

Fingerprint sensors programmed in Python language have import two libraries time and serial. This serial library package is used to connect the serial port connection with the fingerprint sensor and Raspberry pi, thereby it exchanges data from the sensor to the Raspberry pi. Initially, it was used to scan the pupil's fingerprint and save it in a database, with the stored pattern comparing the obtained fingerprint every day and validating the fingerprint result.

3.3 Face Detection

Humans can quickly discern faces in a photograph, but computers have historically struggled to do so due to continuous changes of faces. For instance, must be detected independently of their hair color, beards, cosmetics, and age.

Face detection is the problem of detecting and localizing one or more faces in an image in computer vision. Localization refers to marking the extent of the face, and it is generally through a bounding box around the face, whereas locating the coordinate of a face in a photograph refers to identifying the coordinate of the face in the image. Then, generate zero or more bounding boxes including faces.

Face identification may be processed by two methods either by feature or image-based method.

The *multi-task cascaded convolutional neural network* (MTCNN) technique used to detect the face detection if an input photograph is given which recognizes other facial characteristics such as the eyes and mouth. By varying image size, the MTCNN

recognizes the face. The smaller the image size, the easier the box is to find contour characteristics and features.

The face is first recognized using P-net after the scale has been reduced. The face recognized on the P-net is then scaled up on the R-net, followed by the detection of a more complex portion. The scale has been enhanced for a feature in the most recent O-net to detect the facial characteristics like eyes, nose, and lips.

4 Working Process

4.1 System Configuration

Python language is used for developing face recognition and fingerprint detection. To facilitate the deployment of a global server, a flask framework is used, while MTCNN is used for face recognition. Hardware such as Raspberry Pi 3 model B is utilized. It contains four USB ports, an HDMI port for connecting with the display. Camera as per user convince resolution, AS608 optical fingerprint sensor, is used for biometric mounted on every class outside wall and DC power supply battery for power supply. A cloud server is used for database management with each class having its own separate database that can further split into the required period-wise database, where students' data is stored based on their roll number.

The webpage was developed in Flask Framework in Python language it connected to mobile applications. The mobile application was developed through Java Programming language which acts as a user interface.

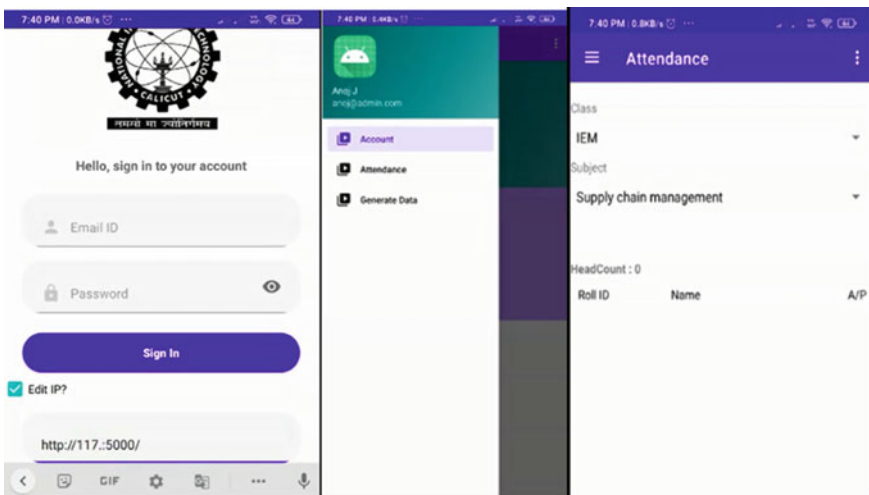


Fig. 1 Screenshot home page of mobile application

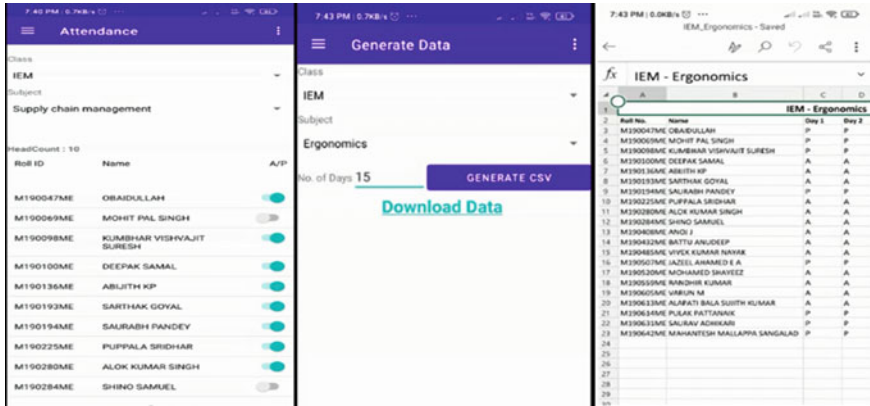


Fig. 2 Screenshot of generating attendance record in excel sheet

This system can read the fingerprints of the students at the beginning of the day. Then, after by using the camera, the faces of the students in the classroom during the class period are captured. Then, at the end of the period, the number of fingerprints counted in prior will be compared with the count of faces detected by the camera. If the count is the same, the system summarizes the attendance of the students for the period; otherwise, the faculties can inspect the faults and manage them, if necessary, via mobile application.

Mobile application facilities the faculty to ensure the obvious attendance marking system which also helps the faculty to calculate the attendance percentage easily. This UI has slide button to mark the attendance manually also have the option of printing the attendance in the excel sheet which was explained in Figs. 1 and 2.

This application came up with class and subject category which faculty can be able to choose option of concern class period. Therefore, faculty can user their login ID for each class period.

5 Conclusion

5.1 Highlight of the Work

The shortcomings of existing system manual operations are addressed by an automatic attendance management system. The project’s purpose is to have precise data to provide an accurate attendance management system, which might be performed via IoT and the integration of a fingerprint scanner and facial recognition. A superior system, which incorporates a completely automated attendance mechanism, has replaced the manual calculation of attendance.

An IoT-based advanced attendance system will be an evolutionary attendance marking technique. The proposed state-of-the-art system shows the higher effectiveness and efficiency over the existing systems by avoiding, if not eliminate, fake attendance entries as per the proposed system. Teachers will have less work keeping attendance records up to date. Moreover, the system makes the attendance summary easier when compared to manual attendance management systems. It had been implemented face detection using the MTCNN algorithm, which can also perform face recognition, resulting in a high-accuracy attendance system.

5.2 *Scope for Future Work*

The future work of the system can involve recognizing the faces of the students, which can determine the students who are present and absent from class. Such face recognition method can aid in getting a high accuracy of automated attendance. Faculty can find the students absents list immediately via mobile application.

References

1. Jeong JP, Kim M, Lee Y, Lingga P (2020) IAAS: IoT-based automatic attendance system with photo face recognition in smart campus. *Int Conf Inf Commun Technol Conv (ICTC) 2020*:363–366. <https://doi.org/10.1109/ICTC49870.2020.9289276>
2. Jinushia R, Senthilkumar S, Bhuvaneswari S, Clapton E (2020) Smart monitoring system using RFID technology. In: 2020 6th international conference on advanced computing and communication systems (ICACCS), pp 1430–1433. <https://doi.org/10.1109/ICACCS48705.2020.9074448>
3. Dastidar UG, Jogi N, Bansod M, Madamwar P, Jalan P (2017) Fingerprint sensor based attendance system using atmega 328 and ESP8266. *Int J Res Sci Eng* 3(2):471–475, ISSN 2394–8299
4. Suryawanshi V, Aundhakar S, Mane N, Kamble R (2017) Attendance system using fingerprint identification with GUI, Department of electronics & telecommunication engineering Shivaji University Kolhapur Maharashtra. *Int J Eng Dev Res* 5(2):2321–9939
5. Suryawanshi V, Puri K, Devkar P, Tiwari KS (2017) Attendance monitoring system-automation-using-fingerprint-module ISSN (Online) 5(1):2347–2820

Patient Flow Optimization in an Emergency Department Using SimPy-Based Simulation Modeling and Analysis: A Case Study



Anudeep Battu, S. Venkataramanaiah, and R. Sridharan

Abstract Long waiting times and patient congestion are common problems faced by emergency departments (EDs) worldwide. During pandemics like COVID-19, EDs worldwide start to be flooded with patients and hospitals find it very challenging to provide good treatment to the large number of patients visiting the EDs with their current allocation of resources. Hospitals are in need of a decision support system (DSS) which can predict the excess demand and suggest the appropriate quantity of resources to be allocated at each point of care. The present research focuses on an ED of a large public hospital in India and explores in finding a solution for the long patient waiting time problem experienced by the hospital. This study extends the application domain of SimPy-based simulation modeling with integrated metamodeling and optimization to optimally allocate the resources in the ED. This can be used as a novel DSS which is relatively faster and needs less human interaction by the hospital management compared to the existing methods. The proposed resource allocation by this model reduced the patient waiting time by 44% in the case hospital being studied. Hospitals may use the proposed methodology to appropriately allocate their resources in times of excess demand.

Keywords Emergency department · Bottlenecks · Discrete event system simulation · Multiple linear regression · Optimization · SimPy

A. Battu (✉) · R. Sridharan
Department of Mechanical Engineering, National Institute of Technology Calicut, Calicut, India
e-mail: anudeep_m190432me@nitc.ac.in

R. Sridharan
e-mail: sreedhar@nitc.ac.in

S. Venkataramanaiah
Indian Institute of Management Lucknow, Lucknow, India
e-mail: svenkat@iiml.ac.in

1 Introduction

Reduced waiting time of patients and management of resources in the emergency departments (EDs) is very crucial for any hospital. In recent years, people started giving more priority to health care than anything else. During the recent COVID-19 pandemic, many countries have failed in managing their COVID-19 cases and the hospitals started flooding with emergency patients who need critical treatment and resources like ventilators and oxygen support. The emergency departments never experienced such a situation before. Hence, the patients had to wait for a long time and many patients have died due to lack of proper treatment and resources in hospitals. Long waiting times and patient's congestion are few of the biggest problems faced by hospitals worldwide. In the recent times, the number of patients visiting the EDs has also increased drastically. Thus, there is a need for finding a solution to this problem.

According to the literature review, the most appropriate methodology for determining optimal resource allocation and reducing patient waiting time in EDs is simulation modeling. Simulation modeling helps in assessing the consequences of making changes in the system without disturbing the system.

The remaining portion of the paper is organized in the following way. In the next section, salient and relevant literature belonging to the present research domain is reviewed briefly. In Sect. 3, the research methodology is presented. The details of the simulation model are presented in Sect. 4. Metamodel-based optimization is described in detail in Sect. 5. Results and interpretation are provided in the next section. Finally, in the last section, conclusions and scope for future work are articulated.

2 Literature Review

Several researchers have adopted simulation modeling for investigating the health-care services. Khekale et al. [1] provided an extensive review on the use of simulation models in reducing the patient waiting times in the EDs. The researchers describe the salient aspects of the analysis of various studies based on their modeling techniques, data sources, collection methods and study findings. A comprehensive review of published studies from each category along with a discussion on their important features is furnished.

Ahmed et al. [2] presented a study in which a decision support tool is designed by integrating simulation with optimization. The optimum number of resources required such as the nurses, laboratory technicians, doctors, etc., can be found out using the simulation-based optimization methodology proposed in this study. Using the proposed method, optimization can be done to improve the patient throughput and to reduce the time patient spends in the system considering the budget constraints.

Cabreraa et al. [3] adopted simulation and agent-based modeling to design a decision support system which optimizes the processes, resources and operations of

emergency departments and aids the hospital management in formulating strategies for optimization.

Lin et al. [4] conducted a study in which the power of genetic algorithm (GA) and data envelopment analysis (DEA) are used for proposing a multiobjective simulation and optimization framework. This method can be used for searching very large design spaces effectively. In this method, GA is selected using the fitness value as the value obtained from the relative efficiency score of design point from data envelopment analysis. Then, the algorithm is applied for optimization of resources in surgical services.

Zeinali et al. [5] carried out a work which portrays a novel tool which can be used for decision support in all the three levels (i.e.,) strategic, tactical and operational. The model proposed by the authors can be used to reduce the total average waiting time of ED patients taking budget and capacity constraints into consideration.

Thim et al. [6] investigated the significant factors affecting the length of stay of patient in the hospital, and the findings suggest the use of lean principles for process improvement in the EDs in hospitals. They propose setting up referral processes, using third-party coordinators and setting up 24-h ambulance services for integrating the processes from the site at which the accident occurred to the emergency department in the hospital.

From the literature review, the following inferences can be drawn:

- Although several studies have been reported on simulation of emergency departments, there are only a few studies on trauma care in Indian hospitals. Indian healthcare system is different from others because low-cost trauma care is to be provided to geographically large and populated areas.
- Reducing patient waiting time is the primary objective in most studies performed.
- Data collected in most studies for simulation modeling involves patient interarrival times, healthcare service times, length of stay, volume and mix of patients. Data collection in most studies uses time and motion studies.
- The findings from most studies can be categorized in two ways: resource related and process related. Optimization of resource allocation has been pursued in relatively more studies than optimization of process.

3 Research Methodology

The objective of the present study is to develop a novel decision support system to reduce the patient waiting time in emergency departments of hospitals. In this study, firstly data regarding various parameters to be input in the simulation model such as patient arrival rate, service times at various points of care and transit times is obtained from a previous study performed in the hospital. In the next step, a simulation model is developed using SimPy library in Python programming language. The results are compared with that obtained from a simulation model developed using the process-oriented simulation package, Arena. In the next step, the simulation model is run for different configuration of resources and the average patient waiting time is obtained

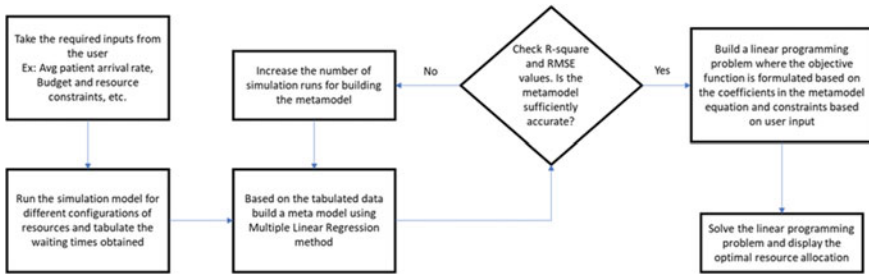


Fig. 1 Simulation-based metamodeling and optimization using SimPy

for each configuration. This data is tabulated into a data frame in Python. Based on the tabulated data, a multiple linear regression (MLR) metamodel is developed and the accuracy of the model is checked. Using the coefficient values obtained from MLR, a metamodel equation is obtained. In the next step, a linear optimization problem is formulated based on the metamodel equation and resource and budget constraints specified by the hospital management with the objective of reducing the average patient waiting time. The quantity of resources to be allocated at various points of care is the decision variables. The present study focuses on obtaining the optimal resource allocation at all points of care in the ED using this research methodology (Fig. 1).

4 Simulation Model Development

The emergency department of a large public hospital located in the northern part of India is considered in the present study. When a patient enters the emergency department, a stretcher is located and brought to the entrance of the emergency department. The patient is then kept over the stretcher and moved to the emergency room. In the emergency room, an ED doctor and paramedical staff examine the patient for movements and the patient is later sent for laboratory investigations (X-ray, MRI and ultrasound). The attendants accompanying the patient are issued the bill for laboratory investigations in the cash counter. After the laboratory investigation, the patients are re-examined by an ED doctor and paramedical staff. The patients are then sent to the surgery ward for opinion. The surgeon inspects and sends the patient to the specialty ward. Specialists check the patient and send him to the operation theater. The orthodoctor performs the surgery, and a bed is allocated to the patient in the in-patient department. After observation and treatment for a few days, the patient is discharged. In this study, the objective is to reduce the patient waiting time from the entry stage to the surgery stage. The process chart of processes followed by various types of patients from entry to surgery is shown in Fig. 2.

The main resources and their quantities used in the emergency department are as follows:

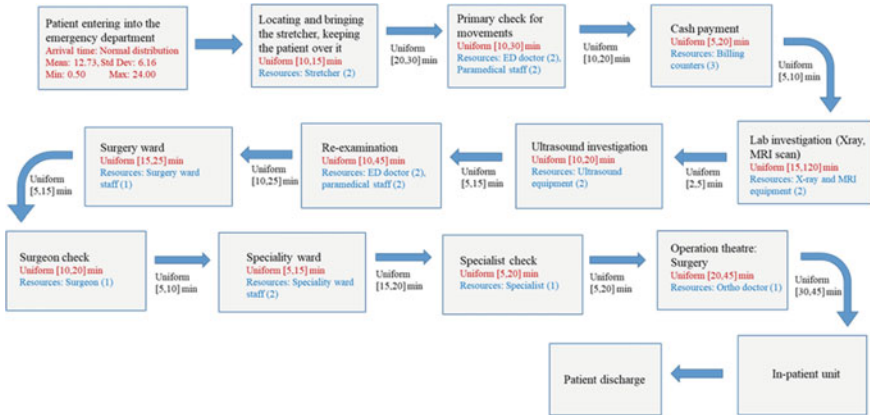


Fig. 2 Process flowchart of the emergency department

- Stretcher (2)
- ED doctor (2) and paramedical staff (2)
- Billing counters (3)
- X-ray, ultrasound and MRI equipment (2)
- Surgeon (1) and surgery ward staff (1)
- Specialist (1) and specialty ward staff (2)
- Orthodoctor (1) and operation theater staff (1)

Two simulation models of the emergency department were developed, one using Arena 15.0 simulation package and the other using SimPy library in Python. The key inputs required for the simulation model are the following: (1) interarrival time distribution, (2) service time distribution at various points of care, (3) transit time distribution between various points of care and (4) quantity of resources used at each point of care. Many of the inputs were collected from a previous study done in the emergency department. In the present study, around 104 patients were given a questionnaire survey and data regarding their arrival time service times, transit times and wait times at various points of care was obtained. Distributions regarding the inputs in the simulation model were obtained using the data collected. The interarrival time, the service and the transit time distribution at various points of care are specified in Fig. 2.

The warm-up period was derived as 160 days using the Welch’s method [7]. The warm-up period is set as 160 days before collecting the results from the model for the queues to settle into normal running conditions. The run length and number of replications were derived using the desired half-width of 5% of the average length of stay (LOS). Accordingly, the simulation models were run for 360 days with 100 replications.

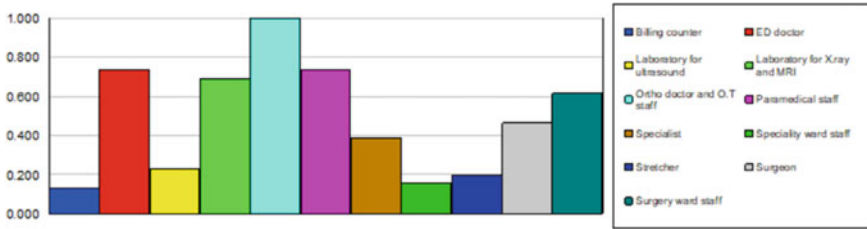


Fig. 3 Utilization rates of various resources

Verification is the process of ensuring that the model is built correctly. In the present study, verification is done by comparing the results obtained from the simulation models to the performance data obtained from the actual emergency department. Moreover, the hospital managers have confirmed that the simulation model is able to accurately represent the emergency department and can be used to assess the changes in the system to make managerial decisions.

Validation is the process of determining whether the right model is built for the right problem. The simulation model is run using different data and different configurations of resources, and the model is found to be sufficiently accurate.

5 Metamodel-Based Optimization

5.1 Multiple Linear Regression Metamodel

Multiple linear regression (MLR) models are widely used to determine the relationship between a single dependent variable and two or more independent variables. By using MLR models, results can be tabulated and the hospital management can draw inferences without much prior knowledge in statistical methods. In this study, linear regression is used to determine the effect of altering the quantity of resources at various stages on the total average length of stay (LOS) of a patient. The aim of linear regression is to construct the best-fitting straight-line to the observed data and using least squares method to determine the regression coefficients which define the line. A multiple linear regression equation with three independent variables and one target variable can be described as follows:

$$Y = \beta_0 + \beta_1x_1 + \beta_2x_2 + \beta_3x_3 + e$$

where Y is the target variable, β_0 is the y -intercept, $\beta_1, \beta_2, \beta_3$ are the regression coefficients, x_1, x_2, x_3 are the independent variables and e is the error term. The data required for building the metamodel was collected from the SimPy simulation model by repeatedly running the model and collecting the results for different sets of resource configurations. The dataset was divided into training data and testing

data using Scikit-learn library by taking 80% data for training and 20% for testing. The multiple linear regression model was fit using Statsmodels library in Python, and results were obtained in a tabular form. From the results, different regression coefficients were obtained and the model is derived. The measures, namely coefficient of determination (R^2) and root mean square error (RMSE) of the multiple linear regression models, were obtained for verifying the accuracy of the model.

5.2 Optimization

Linear optimization is done using PuLP library in Python to obtain the optimal resource allocation to reduce the waiting time of patients in the emergency department subject to various capacity and budget constraints of the department. The mathematical model of the optimization problem is as follows:

$$\begin{aligned} & \text{Minimize } Z = f(X_1, X_2, X_3, \dots, X_n) \\ & \text{Subject to} \\ & \sum C_i X_i \leq B \\ & L_i \leq X_i \leq U_i \quad \text{for } i = 1 \text{ to } n \\ & X_i \text{ is an integer for } i = 1 \text{ to } n \end{aligned}$$

This is an integer programming problem where Z represents the objective function value, i.e., the total average length of stay (LOS) of a patient, X_i represents the quantity of resources at the i th point of care and n represents the total number of points of care in the ED, C_i represents the cost incurred by the hospital in increasing the corresponding resource by 1 unit at the i th point of care, L_i and U_i represent the minimum and maximum quantities of resources feasible by the hospital at the i th point of care and $f(X_i)$ represents the metamodel equation derived using the coefficients obtained from the MLR model.

6 Results and Discussion

It is observed from the simulation results in Table 1 and (Fig. 3) that the average waiting time of patients and utilization rates of resources are very high at various points of care in the ED. The significant bottlenecks identified in the ED are at the laboratory investigation stage, surgery ward stage, specialty ward stage and operation theater stage with waiting time of more than 1 h. The total average waiting time by patients is observed to be around 2.27 days. Table 2 provides the results of the MLR metamodel. From Fig. 4, the condition that the error terms in the MLR model are normally distributed is supported as the normal probability plot is approximately linear. The R -square and adjusted R -square values for the MLR model are obtained

Table 1 Waiting times at various points of care

Point of care (POC)	Average waiting time (minutes)
Stretcher	25
primary check	45
Cash payment	30
Laboratory investigation	180
Ultrasound Investigation	20
Re-examination	30
Surgery ward	110
Surgeon check	75
Specialty ward	185
Specialist check	52.5
Operation theater	2520

as 0.710 and 0.684, respectively, which implies that there are only small differences between the observed and the fitted values. Thus, the model is sufficiently accurate. Table 3 provides the details of the proposed resource allocation obtained from the model. The proposed resource allocation reduces the total average patient waiting time by almost 1 day, i.e., 44% reduction in total waiting time. The results from the SimPy-based metamodeling and optimization model are validated by comparing that obtained from the model developed for the proposed resource configuration using the simulation software Arena. Furthermore, the proposed system is observed to be faster and inexpensive because SimPy is a library in a popular programming language named Python. The Simpy software can be used and distributed freely (even for commercial use) since it is developed under open-source license approved by the open-source initiative.

7 Conclusion

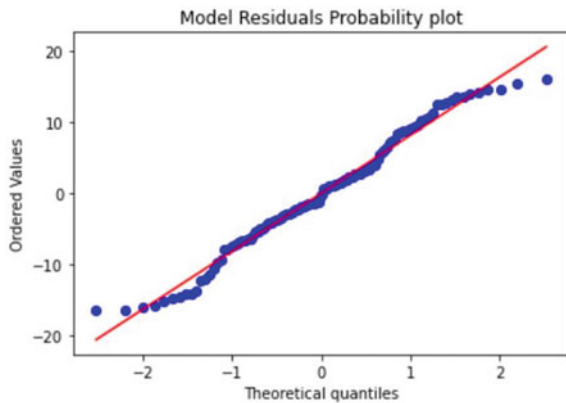
The present study applies simulation, metamodeling and optimization for appropriate resource allocation in hospital EDs. The simulation model is developed, tested and analyzed using the simulation software Arena and SimPy library in Python. The performance measure considered for investigation in the present study is the total patient length of stay which is directly related to patient waiting time and patient satisfaction in the ED. The simulation model was built for the ED of a hospital, and the various bottlenecks in the ED are identified. An integrated metamodel is built in the same Python program using multiple linear regression method. The results are verified and validated. An integrated linear optimization model is developed from the metamodel using PuLP library in Python. The optimal resource allocation is obtained with the objective of reducing the patient length of stay to the desired level within the capacity and budget constraints of the hospital.

It is found that the proposed methodology based on SimPy is comparatively faster than the simulation software Arena. Further, it has the feature of integrating the functions such as simulation, metamodeling and optimization within a single program.

Table 2 Results of MLR model: average waiting time of patients

Model	Unstandardized Coefficients		<i>t</i>	Sig.	95% Confidence Interval for B	
	<i>B</i>	Std. Error			Lower bound	Upper bound
Constant	54.5621	5.7302	9.5219	0.0000	43.2051	65.9191
Billing counters	0.2438	0.9665	0.2522	0.8013	-1.6718	2.1594
Ultrasound equipment	-0.8748	1.0717	-0.8163	0.4161	-2.9990	1.2493
X-ray, MRI equipment	-13.2730	0.9629	-13.7848	0.0000	-15.1814	-11.3646
Paramedical staff ED doctor	-6.9695	0.9945	-7.0080	0.0000	-8.9406	-4.9984
Stretcher	-0.0519	0.9883	-0.0525	0.9582	-2.0106	1.9068
Surgery ward staff	0.5317	1.0062	0.5284	0.5983	-1.4626	2.5260
Surgeon	0.0706	0.9716	0.0727	0.9422	-1.8551	1.9964
Specialty ward staff	0.1907	0.9650	0.1976	0.8437	-1.7219	2.1033
Specialist	1.7972	1.0053	1.7877	0.0766	-0.1953	3.7896
Orthodoctor and operation theatre staff	-0.1843	1.0013	-0.1840	0.8543	-2.1689	1.8003

Fig. 4 Normal probability plot of residuals



Thus, it requires minimal interaction from the hospital management staff and aids them in taking quick decisions in times of excess demand. The only input required by the model is the patient inflow data, resource and budget constraints of the hospital. This study can help hospitals in situation like COVID-19 pandemic when the demand grows exponentially. In the future, a time series analysis model can also be integrated

Table 3 Optimal allocation suggested by the model

Name of the resource	Existing quantity	Suggested quantity
Billing counters	3	1
Ultrasound equipment	2	3
X-ray, MRI equipment	2	3
Paramedical staff and	2	2
ED doctor	2	3
Stretcher	1	1
Surgery ward staff	1	1
Surgeon	2	1
Specialty ward staff	1	1
Specialist	1	1
Orthodoctor and operation theatre staff		

with the proposed model to predict the daily patient inflow into the emergency department and to propose the resource allocation for the proceeding days accordingly. Advanced metamodeling techniques like artificial neural networks can be used for more precise results. A significant portion of the patients arriving is related to medico-legal cases which further increases the congestion and waiting time in emergency departments. Applying lean techniques to identify the non-value adding activities at each stage and eliminating them can be performed in the future. The present study is conducted in the emergency department of only one large public hospital in India. The present study can be extended to various other hospitals in different locations.

References

1. Khakale SN, Askhedkar RD, Parikh RH (2020) An analysis for the use of simulation modeling in reducing patient waiting time in emergency departments (EDs) in hospitals. *Int J Appl Ind Eng (IJAIE)* 7(1):52–64
2. Ahmed MA, Alkhamis TM (2009) Simulation optimization for an emergency department healthcare unit in Kuwait. *Eur J Oper Res* 198(3):936–942
3. Cabrera E, Taboada M, Iglesias ML, Epelde F, Luque E (2011) Optimization of healthcare emergency departments by agent-based simulation. *Procedia Comput Sci* 4:1880–1889
4. Lin R-C, Sir MY, Pasupathy KS (2013) Multi-objective simulation optimization using data envelopment analysis and genetic algorithm: Specific application to determining optimal resource levels in surgical services. *Omega* 41(5):881–892
5. Zeinali F, Mahootchi M, Sepehri MM (2015) Resource planning in the emergency departments: a simulation-based metamodeling approach. *Simul Modell Pract Theory* 53:123–138
6. Prætorius T, Chaudhuri A, Venkataramanaiah S, Hasle P, Singh A (2018) Achieving better integration in trauma care delivery in India: insights from a patient survey. *J Health Manage* 20(3):234–254
7. Salmon A, Rachuba S, Briscoe S, Pitt M (2018) A structured literature review of simulation modelling applied to emergency departments: current patterns and emerging trends. *Oper Res Health Care* 19:1–13

Computation in Fluid Flow and Heat Transfer

Comparison of Simple Probabilistic Approach with Deterministic Model for Predicting Surge and Leakage in Water Pipelines



C. D. John Paul, P. Radhika, Ajith Kumar Arumugham-Achari, Anu Mol Joy, Abraham Thomas, and Dominic Mathew

Abstract Pipe flows are highly nonlinear and the related structural failure and leakage thereafter may arise from fluid pressures of various nature. Burst leakage may result from high local pressure heads causing circumferential (hoop) stress or longitudinal (axial) stress being larger than the material yield stress. Boiling or cavitation effect in regions of fluid pressure drops below its vapor pressure, which in turn develop as air bubbles and get transported through the pipeline may also cause burst at remote locations. In a multiple pipeline network, such information may be available as an overlapping set of noisy signals. This calls for advanced signal processing, and a reduction in complexity of deducing the signals to be processed would be favorable in a computational environment. Hence as a preliminary step, we investigate the extent to which a simple probabilistic model would better a purely deterministic hydraulic model when employed for the same. We initially developed a purely deterministic hydraulic model with method of characteristics to simulate burst failure and leakage in a pipeline, and further extended it with a simple probabilistic model coupled into the scheme. A detailed investigation of the influence of successive over relaxation (SOR) on the simulated transients revealed that the use of variable local relaxation techniques could alleviate false numerical oscillations at the interior nodes. We also observed that the simple probabilistic model was only marginally different in its prediction of the transients when compared with the fully deterministic hydraulic model.

Keywords Method of characteristics · Signal processing · CFD · Pipe burst · Numerical simulation · Probability · SOR

C. D. John Paul · A. K. Arumugham-Achari (✉) · A. Thomas · D. Mathew
Rajagiri School of Engineering and Technology, Cochin, India
e-mail: ajithk@rajagiritech.edu.in

P. Radhika
MGM CEPS, Calicut, India

A. M. Joy
Lambton College, Sarnia, Canada

1 Introduction

Effective water conservation calls for the minimization of leakage in distribution systems. However, detection of leakages is usually difficult not only due to the complexity of the supply network but also because many leakages are small and can go unnoticed. Large pipeline networks can be further challenging since multiple leaks can offer a noisy environment for leak detection technology. An apt solution can be the adoption of a predictive-corrective methodology using CFD before project implementation, while it is still on the drawing board. Here, we present the results from our CFD-based simulations using our code developed in MATLAB[®], wherein we compare the pros and cons of a probabilistic numerical model over a deterministic fluid dynamic model, while implemented in a noisy environment (multi-leak system).

Many different technologies have been used for detecting leaks in water distribution systems. Hargesheimer tried a method to find water leaks by using trihalomethanes (THMs) chloroform and dichlorobromomethane [1]. THM analysis, he claims, is a precise and sensitive method of identifying treated municipal water samples in seepage. This method only works with treated water and only provides a general location for the leak, not its magnitude. In a single-stage evaporator, DalleMolle and Himmelblau used the Kalman Filter to detect faults [2]. In a closed-loop nonlinear distillation process, Li and Olson used Extended Kalman Filter [3]. Using transient flow simulations, Liou and Tian developed a model for a single pipeline [4]. They considered data noise in pressure and flow measurements and found noise limits leak detectability.

Brunone devised a method for detecting leaks in outfall pipes based on transient pressure wave properties [5]. The occurrence of transient damping indicated the presence of a leak, while the timing of the damping indicated the location of the leak.

Vitkovsky et al., detected leaks in water distribution systems using the genetic algorithm (GA) technique in conjunction with the inverse transient method (ITM) [6]. The slow rate of convergence within complex systems is a disadvantage of this method. Mpesha tried a leak detection frequency response method [7]. This method required measuring pressure and discharge at one location in the pipeline.

Buchberger has devised a technique for determining the magnitude of leaks in pipe networks [8]. The mean and standard deviation of the measured flows are calculated, and when the flow values depart from the statistical curves the maximum network leakage rate is determined. But, this method does not locate the position of the leak.

Verde devised a system for locating a pipeline leak that relied solely on flow and pressure sensors at the pipeline's ends [9]. According to him, it can be solved by combining a static relationship between residual components and leak position error with a basic nonlinear flow model that assumes leak location with uncertainty.

Misiunas tried a method for detecting pipeline leaks that involved sensing pressure in one location and detecting the negative pressure wave that happened when a break occurred [10]. The position was determined by the timing of the break's initial and

reflected transient waves. The speed with which the break opens is a shortcoming of this method.

Lesyshen used a model-based estimation process for leakage detection [11]. The goal of this project was to determine the effectiveness of the Extended Kalman Filter for leak detection through simulations.

Doney also tested the model's ability to detect a pipeline leakage using a model-based method [12]. Once four pressure measurements were entered into the EKF, the model accurately detected the location and magnitude of a leak in a pipeline.

Andrea Cataldo presents time-domain reflectometry (TDR)-based system for leak detection in underground metal pipes [13]. The proposed system dramatically reduces the inspection time required by other methods.

Marcia Golmohamadi used two leak detecting techniques in pipelines [14]. There was a hardware-based method and a software-based method. In the first method, for pipeline inspection, ultrasonic wave emission is used. The software-based method is based on the transient model of the pipeline. A hardware-based method is very reliable; however, it is very expensive in leak detection and is applicable only in shorter ranges compared to the model-based approach.

While using the explicit finite difference method of the MOC model, Nerella, and Venkata Rathnam have observed peak pressure fluctuations with flow variations for the case of a sudden closure of a valve on the downstream side of the complex pipe system [15]. The peak pressure variation during the sudden closure of the valve is observed to have a repetitive pattern.

The remainder of this paper is organized as follows. The theory of transient fluid modeling is presented in Sect. 2 and the method of characteristics, which is a solution method for partial differential equations of motion and continuity. The methodology is discussed in Sect. 4 and the results are given in Sect. 5.

2 Transient Pipe Flow Equations

Fluid dynamics for pipe flow is governed by the continuity equation and Navier-stokes (momentum) equation [16].

2.1 Continuity Equations

The continuity equation is derived from the principle of mass conservation and it is given by,

$$\frac{a^2}{gA} \frac{\partial Q}{\partial x} + \frac{\partial H}{\partial t} = 0 \quad (1)$$

where Q is the flow rate [m^3/s], H is the hydraulic head [m], A is the pipe cross-sectional area [m^2], g is the acceleration due to gravity [m/s^2], and a is the wave speed of the fluid [m/s] within the pipe and it's given by,

$$a = \sqrt{\frac{\beta/\rho}{1 + (\beta/E)(D/e)c_1}} \quad (2)$$

in which β is the bulk modulus of water [N/m^2], ρ is the density of the fluid [kg/m^3], E is the Youngs modulus [N/m], D is the pipe diameter (inner) [m], c_1 is a constant, and e represents the thickness of the pipe walls [m].

2.2 Transient Momentum Equation

$$\frac{\partial Q}{\partial t} + gA \frac{\partial H}{\partial x} + \frac{f}{2DA} Q|Q| = 0 \quad (3)$$

where f is the friction factor, and D is the pipe diameter (inner) [m].

2.3 The Method of Characteristics

Using the method of characteristics, the two partial differential equations of momentum and continuity can be converted into four ordinary differential equations [16].

$$\frac{dQ}{dt} + \frac{gA}{a} \frac{dH}{dt} + \frac{f}{2DA} Q|Q| = 0 \quad (4)$$

if

$$\frac{dx}{dt} = a \quad (5)$$

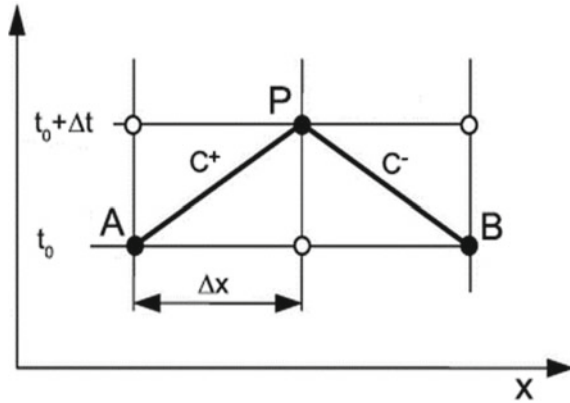
and

$$\frac{dQ}{dt} - \frac{gA}{a} \frac{dH}{dt} + \frac{f}{2DA} Q|Q| = 0 \quad (6)$$

if

$$\frac{dx}{dt} = -a \quad (7)$$

Fig. 1 Characteristic lines in the x-t plane



Equations 4 and 6 are called compatibility equations. They are also known as the C+ and C- equations as they both exist only along with so-called C+ and C- characteristic lines. The idea of characteristic lines is given in Fig. 1.

The physical relevance of characteristic lines is that they allow Eq. 4 to be integrated from point A to point P if the pressure head and flow at point A are known. The equation that results will be expressed in terms of an unknown pressure head and flow at point P. Similarly, if you know the pressure head and flow at point B, you can integrate Eq. 6 along line BP to get an equation that relates the pressure head and flow at point P. As a result, two equations and two unknowns (pressure head and flow) can be solved at point P. In this way, pressure head and flow at each point can be calculated throughout time.

2.4 Discretization

Integrating Eq. 4 along the C+ characteristic line (AP) and solving for flow at point P gives,

$$Q_P = C_p - C_a H_P \tag{8}$$

where,

$$C_p = Q_A + \frac{gA}{a} H_A - \frac{f \Delta t}{2DA} Q_A |Q_A| \tag{9}$$

Similarly, integrating Eq. 6 along with the C- characteristic line (BP) and solving for flow at point P gives,

$$Q_P = C_n + C_a H_P \tag{10}$$

where,

$$C_n = Q_B - \frac{gA}{a} H_B - \frac{f \Delta t}{2DA} Q_B |Q_B| \tag{11}$$

and

$$C_a = \frac{gA}{a} \tag{12}$$

where C_p and C_n are constants for each timestep and the constant C_a depends on pipe properties. The values of two unknowns (Q_P and H_P) can be determined by simultaneously solving these equations, i.e.

$$Q_P = \frac{C_p + C_n}{2} \tag{13}$$

And, the value of H_P can be determined using Eqs. 8 or 10. Thus, by using Eqs. 8 and 10, conditions at all interior points at the end of each time step can be determined. However, at the boundaries, either Eqs. 8 or 10 is available. So, special conditions are needed to determine the parameters at the boundaries at time $t_0 + \Delta t$.

3 Test Model for Pipe Flow Computations

The test model comprises a long pipeline of length 600 [m] and diameter 0.5 [m] connecting two reservoirs (maintained at constant heads of 40 [m] upstream and 30 [m] downstream), and a gate valve located at the entry to downstream reservoir. Starting at the upstream reservoir, computational node locations along the pipeline are equally spaced at every 100 [m], thus dividing it into six equal parts. The test configuration to implement the numerical codes for the water transmission system, is as shown in Fig. 2.

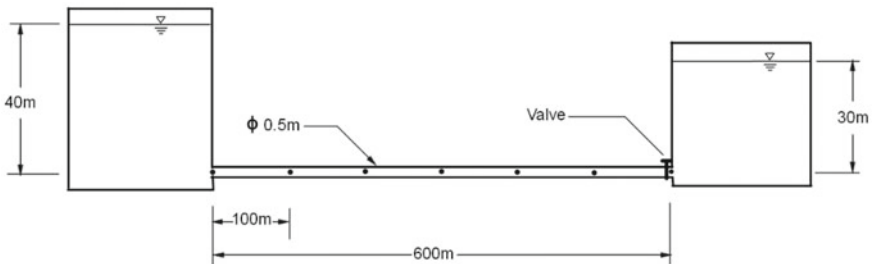
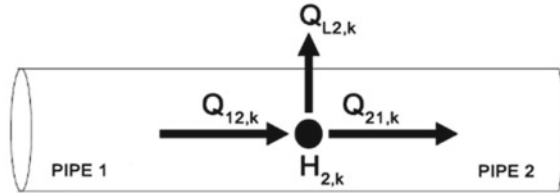


Fig. 2 Two-reservoir pipeline test configuration

Fig. 3 Notation for flow and pressure at step k , following the original nomenclature of Lesyshen [11]



The flow along the pipeline is assumed one-dimensional, and any parameter in the flow direction is assigned its sign positive. The initial configuration of the flow system is estimated at its steady state condition. The steady-state of a hydraulic numerical model is one in which the flow variables do not change over time, while the flow and pressure distribution can be quantitatively expressed by the laws of conservation of mass, momentum and energy. The discharge through the pipeline, Q , and the total pressure head at each junction node, H , are the unknowns in the present steady-state hydraulic analysis.

The flowrate through the pipeline is represented in the form, $Q_{ij,k}$. Here, the first two-digit subscript ij represents the spatial position in the system (j th node of the i th pipe-segment), while the second subscript, k represents the temporal instant of computation. For example, refer Fig. 3. flow at the entry to the second segment in the pipeline, at the time step k will be represented as $Q_{21,k}$. The instantaneous head and leakage at this node 2 will be denoted as $H_{2,k}$ and $Q_{L2,k}$ respectively. It may be noted that the head at the second node to the first pipe-segment, is the same as the head at first node to the second pipe-segment. However the flow rates would differ by the leak rate, if any. Also, the model assumes a non-leakage condition at the boundary nodes for simplicity, i.e., $Q_{L1} = Q_{L7} = 0$.

3.1 Boundary Conditions

The boundary condition at the upstream reservoir is defined using the energy equation and the boundary condition at the downstream reservoir is defined using the valve equation. However the valve equation will be different from the model of Lesyshen [11], and its formulation is explained in the following section.

The Supply Reservoir. There is a pump and/or upstream reservoir (Node 1) at the beginning of the water distribution line. The water level in the reservoir is assumed to remain constant because the upstream reservoir is assumed to have a large cross-sectional area. The energy equation gives a relationship between the head and the flow at the upstream reservoir. The boundary condition of the upstream reservoir is stated below:

$$H_{1,k} = H_{R1} - (1 + \eta) \frac{Q_{11,k}^2}{2gA^2} \tag{14}$$

$$Q_{11,k} = \frac{-1 + \sqrt{1 + 4K_1(C_p + C_a H_{R1})}}{2K_1} \quad (15)$$

in which

$$K_1 = C_a \frac{(1 + \eta)}{2gA^2} \quad (16)$$

Here, H_{R1} is the supply reservoir head and η represents the entrance loss coefficient. The entrance loss coefficient is chosen to be 0.5.

The Downstream Reservoir and Valve. There is a valve at the downstream reservoir (Node 7) and the valve equation by Chaudhry [16] is used to model the boundary condition for the downstream reservoir. The orifice equation for steady state flow through a valve is:

$$Q_{62,0} = (C_{do}A_{vo})\sqrt{2g(H_{6,0} - H_{R2})} \quad (17)$$

where $Q_{62,0}$ is the steady state flow through the valve, $(H_{6,0} - H_{R2})$ is the steady state head loss across the valve, H_{R2} is the downstream reservoir head, C_{do} is the steady state discharge coefficient, and here it is chosen as 0.6 and A_{vo} is the full valve opening area. For a general opening the flow may be described as:

$$Q_{62,k} = (C_d A_v)\sqrt{2g(H_{6,k} - H_{R2})} \quad (18)$$

Here, A_v is the current valve opening area, and C_d is the normal flow discharge coefficient [17] that is used to characterize the flow and pressure head behavior at the orifices and it is given by,

$$C_d = 0.05959 + 0.0312\alpha^{2.1} - 0.184\alpha^6 \quad (19)$$

where α is the area ratio (D_0^2/D_1^2), D_1 is the full pipe diameter, and D_0 is the constricted diameter. Solving for flow at the valve ($Q_{62,k}$) gives

$$Q_{62,k} = \frac{-C_v + \sqrt{C_v^2 - 4C_v(C_a H_{R2} - C_p)}}{2} \quad (20)$$

in which,

$$C_v = \frac{(\tau Q_o)^2}{C_a(H_{6,0} - H_{R2})} \quad (21)$$

Here, τ is the dimensionless valve opening and it is given by

$$\tau = \frac{(C_d A_v)}{(C_{do} A_{vo})} \quad (22)$$

For a fully open valve, as in this case, $\tau = 1$

4 Methodology

Fluid transients (unsteady pressure head and flow rates) in the pipe flow were allowed to develop from an initial steady state condition, due to the sudden closure of a gate valve at a downstream reservoir. The diameter of the pipe, length of the pipe, pipe wall thickness were assigned and the CFL number of computations was fine-tuned with the calculated wave speed within the pipe. The resulting local burst-leakages themselves will generate further transient signals. This coupled complex phenomena being highly non-linear is essentially a problem of fluid–structure interaction and signal processing. We have carefully included a water hammer in the hydraulic model since it can generate pressure transients of exorbitant magnitudes (*surge*) causing pipe bursts.

For the hydraulic modeling of the transmission line, we adopted the Method of Characteristics (MOC), which offers a robust finite-difference solution to the governing partial differential equations. Initially, a deterministic model with full numerical control on the breakage was developed based on hoop stress characteristics alone. The model was analyzed for the significance of the relaxation factor and the selection of a suitable method. Further, we developed a simple probabilistic model and compared the results with the purely deterministic hydraulic model.

4.1 Deterministic Model

Burst leakage can be caused by high pressure heads that create circumferential (hoop) or longitudinal (axial) stress greater than the material yield stress. We have considered a threshold for failure at a node, when either of the above stress reaches 80% of material yield stress, to account for the factor of safety.

4.2 Probabilistic Model

The probabilistic model is based on merely a coin-tossing probability to assign its(their) eligibility of being the breaking node(s) from among the group of potentially plausible nodes. Potential breakage nodes are identified based on the same threshold of 80% of material yield stress.

4.3 Inner Nodes with Leakage

When a leak is detected in the pipeline through either of the above methods, the transients generated will be different from the no-leak situation. The leakage at each interior node is now modeled using an orifice equation (Eq. 25). For e.g., a leakage detected at node 5, will be solved numerically with MOC as

$$Q_{42,k} = Q_{32,k-1} + C_a H_{4,k-1} - \frac{f \Delta t}{2DA} \times Q_{32,k-1} |Q_{32,k-1}| - C_a H_{5,k} \quad (23)$$

$$Q_{51,k} = Q_{52,k-1} - C_a H_{6,k-1} - \frac{f \Delta t}{2DA} \times Q_{52,k-1} |Q_{52,k-1}| + C_a H_{5,k} \quad (24)$$

$$Q_{L5} = \lambda \sqrt{H_{5,k}} \quad (25)$$

where λ represents the unknown area constant of leakage for node 5 and experimentally it is chosen as 0.01. Solving for Head at node 5 gives,

$$H_{5,k} = \left(\frac{\lambda^2}{8C_a^2} \right) + \frac{1}{2C_a} (C_p + C_n) - \frac{\lambda}{8C_a^2} \times \sqrt{\lambda^2 + 8C_a (C_p + C_n)} \quad (26)$$

where,

$$C_n = Q_{52,k-1} - C_a H_{6,k-1} - \frac{f \Delta t}{2DA} \times Q_{52,k-1} |Q_{52,k-1}| \quad (27)$$

$$C_p = Q_{32,k-1} - C_a H_{4,k-1} - \frac{f \Delta t}{2DA} \times Q_{32,k-1} |Q_{32,k-1}| \quad (28)$$

5 Results

5.1 Transients on Valve Closure

An important observation we made is the influence of the Successive Over Relaxation factor (SOR) on the simulated transients. For the interior nodes, numerical oscillations in the recorded head with a repetitive pattern are observed if SOR is not employed. A similar oscillatory pattern in the transients has been reported by Nerella and Venkata Rathnam [15], who also used MOC without SOR. They had incorrectly attributed these oscillations to the sudden closure of the valve, which we consider is not the true reason for the same. A qualitative comparison of the same is presented in Figs. 4 and 5.

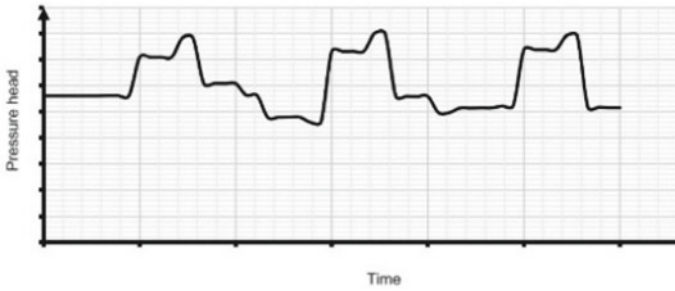


Fig. 4 Numerical oscillations in simulated pressure on valve closure (sans SOR)—Nerella’s model [15]

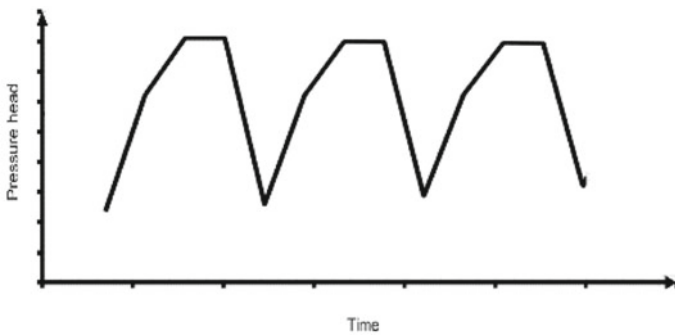


Fig. 5 Numerical oscillations in simulated pressure on valve closure (sans SOR) for an interior node—our model

Following this, we applied a constant successive under relaxation factor (0.6) to study its influence on the fluctuations, to no avail. Later, on applying the *Variable Local Relaxation Technique* [18], these initial oscillations could be completely rectified (Fig. 6). Hence, we attribute this phenomenon to the numerical discrepancies which warrant the implementation of a correct SOR in the scheme.

The validation of the numerical method without leakage was further carried out against the work of Lesyshen [11]. Close qualitative agreement in result was obtained (refer Fig. 7). Lesyshen has mentioned that his model overpredicts peak pressure since it is a fully transient model which always considers compressibility effects, while TransAM[®] moves to rigid column theory when compressibility effects are minimal. We consider that the quantitative discrepancy and resulting phase lag in signals predicted by our model in comparison with the former two are primarily due to the difference in an exact recreation of non-dimensional opening area (τ) as in the literature considered for validation. It may be noted that the term is directly linked with C_d of Eq. 19.

In the present model, we calculate the non-dimensional valve opening area (τ) of Eq. 22 by geometrically defining instantaneous valve opening area (A_v) as

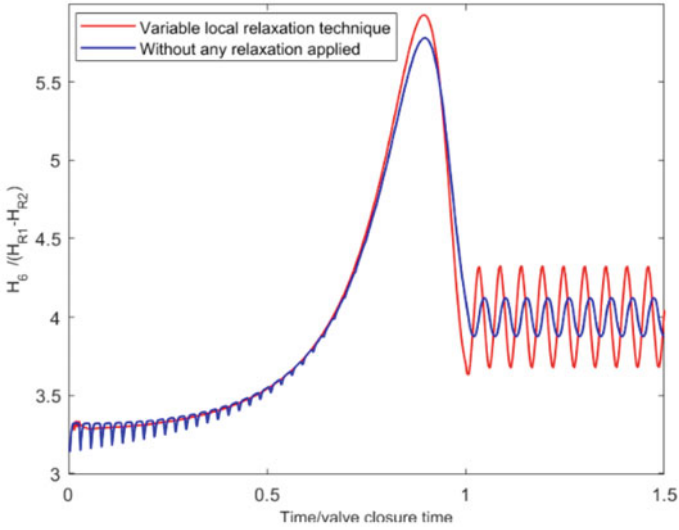


Fig. 6 Comparison of simulated transients with and without applying variable local relaxation factor at interior node (Here, for node 6)

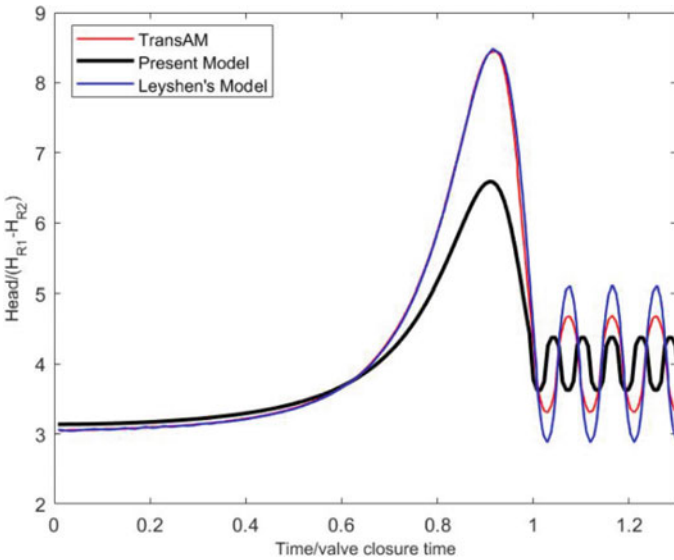


Fig. 7 Fluid transients developed through valve closure, with no burst leakage: validation

$$A_v = \pi R^2 - (R^2 \cos^{-1}\left(\frac{R-h}{R}\right) - (R-h)\sqrt{2Rh-h^2}) \tag{29}$$

Here, R is the internal radius of pipe and h is the sector height of the gate which varies as $0 < h < R$ through its limiting positions. However, Lesyshen [11] had calculated τ by defining it as a simple function of time alone as

$$\tau = \left(1 - \frac{T_k}{T_c}\right)^{\frac{3}{2}} \tag{30}$$

Here, T_k is the current time and T_c is the time required for full closure. A comparison of values for τ , thus employed in both methods is shown in Fig. 8.

Following the above, a deterministic model with full numerical control on the breakage was developed to simulate a fictitious burstleakage on a selected node (Here, node 6) (refer Fig. 9).

Further, this numerical scheme was extended to include the simple probabilistic model for all the nodes eligible for burst based on hoop stress characteristic alone (Fig. 10a–c). It may be noted that we had allowed failure only to those nodes with the highest probability, whose eligibility was assigned based on simple random coin tossing probability. Close observation reveals that the instantaneous pipe burst is characterized by sudden variation in the recorded pressure head, as clearly evident in the simulated plots. We also observe that the transients tend to die out faster as expected, due to the sudden release in pressure in the event of a burst leakage.

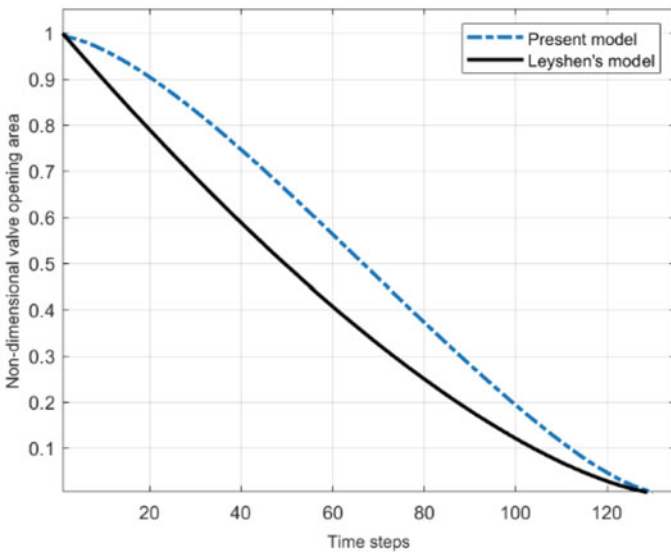


Fig. 8 Comparison of non-dimensional valve opening area

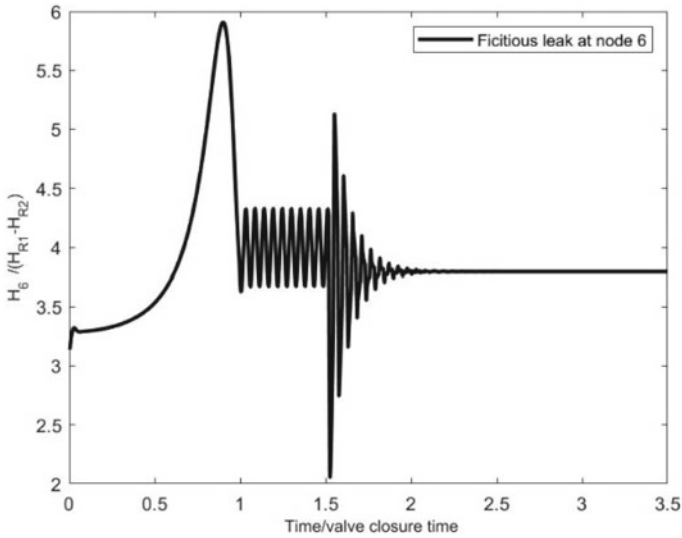


Fig. 9 Simulation of controlled fictitious burst-leakage at a node through a deterministic model

6 Conclusion

A numerical model for pipe burst leakage was developed based on the Method of Characteristics. We found that the transients developed are greatly influenced by the nature of the equation chosen for the coefficient of discharge for flow through controlled restrictions such as valves in the pipeline. Also, important is the correct implementation of an appropriate relaxation factor (such as a *Variable Local Relaxation Technique*) in the simulations, to alleviate the occurrence of false numerical oscillations at interior nodes.

Setting a pressure threshold of 80% to material yield stress as an eligibility-to-fail criteria, and allowing only selected nodes to leak based on a simple probabilistic method, we found it performed only marginally different from a purely deterministic hydraulic model. This calls for improved probabilistic methods based on reliable distribution functions to be introduced into a hydraulic model to improve its predictive capability. We are extending the current study to include filter-based signal processing techniques, in an attempt to favorably reduce the complexity of deducing the indicative signals for pipe failure, in a noisy computational environment such as a larger network.

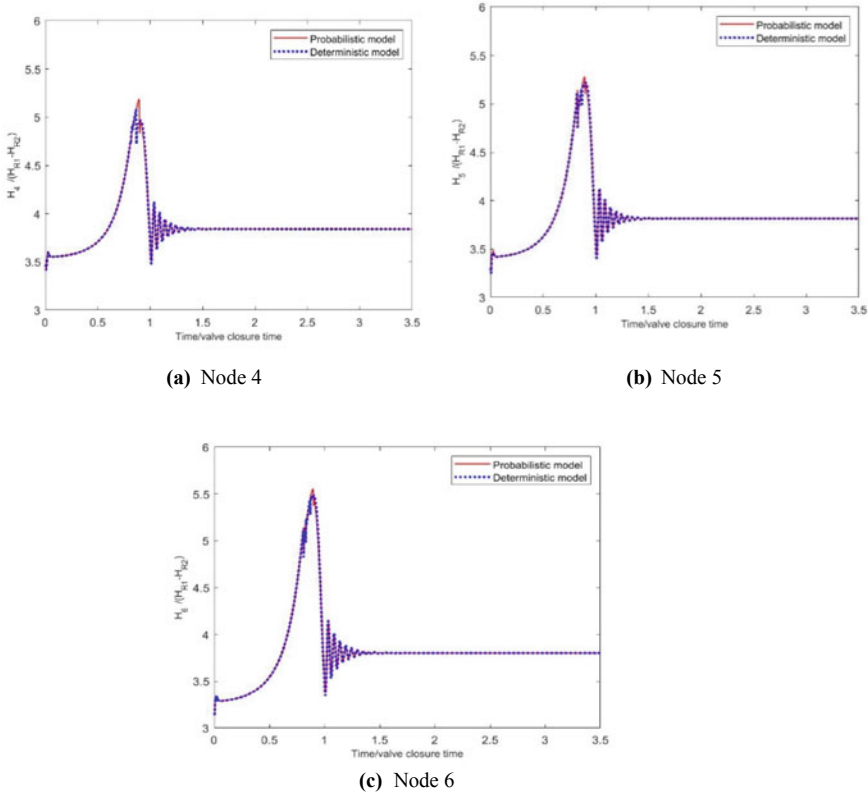


Fig. 10 Comparison of transients predicted by the two models at interior nodes

References

1. Hargesheimer EE (1985) Identifying water main leaks with trihalomethane tracers. *Am Water Works Assoc J* 77:71–75
2. DalleMolle DT, Himmelblau DM (1987) Fault detection in a single-stage evaporator via parameter estimation using the kalman filter. *Ind Eng Chem Res* 26:2482–2489
3. Li R, Olson JH (1991) Fault detection and diagnosis in a closed-loop nonlinear distillation process: application of extended kalman filters. *Ind Eng Chem Res* 30:898–908
4. Liou CP, Tian J (1995) Leak detection—transient flow simulation approaches. *J Energy Resour Technol* 117:243–248
5. Brunone B (1999) Transient test-based techniques for leak detection in outfall pipes. *J Water Resour Plan Manag* 125:302–306
6. Vitkovsky JP, Simpson AR, Lambert MF (2000) Leak detection and calibration using transients and genetic algorithms. *J Water Resour Plan Manag* 126:262–265
7. Mpesha W, Gassman SL, Chaudhry MH (2001) Leak detection in pipes by frequency response method. *J Hydraul Eng* 127:134–147
8. Buchberger SG, Nadimpalli G (2004) Leak Estimation in water distribution systems by statistical analysis of flow readings. *J Water Resour Plan Manag* 130:321–329

9. Verde C (2004) Minimal order nonlinear observer for leak detection. *J Dyn Syst Measur Control* 126:467–472
10. Misiunas D, Vitkovsky J, Olsson G, Simpson A, Lambert M (2005) Pipeline break detection using pressure transient monitoring. *J Water Resour Plan Manag* 131:316–325
11. Lesyshen RM (2005) Water distribution line leak detection using extended kalman filtering. University of Saskatchewan, Thesis
12. Doney KL (2007) Leak detection in pipelines using the extended kalman filter and the extended boundary approach. Thesis. University of Saskatchewan
13. Cataldo A, Cannazza G (2012) A new method for detecting leaks in underground water pipelines. *IEEE Sens J* 12(6)
14. Golmohamadi M (2015) Pipeline leak detection. The University of Missouri, IThesis
15. Nerella R, Venkata Rathnam E (2015) Fluid transients and wave propagation in pressurized conduits due to valve closure. In: International conference on computational heat and mass transfer-2015, procedia engineering vol 127, pp 1158–1164
16. Chaudhry MH (1987) Applied hydraulic transients. Van Nostrand Reinhold Company Inc., New York
17. <https://neutrium.net>. Fluid flow discharge-coefficient-for nozzles-and-orifices. Last Accessed on 17 March 2021
18. Bastos JPA, Ida N, Mesquita RC (1995) A variable local relaxation technique in nonlinear problems. *IEEE Trans Magnet* 31:1733–1736
19. Wylie EB, Streeter VL (1983) Fluid transients. Feb Press, Ann Arbor, Michigan

Design and Analysis of Liquid-Cooled Battery Thermal Management System of Electric Vehicles



Athul Rajeev Mundonkakkoth , Nandini Menon ,
and Thundil Karuppa Raj 

Abstract The thermal management of lithium-ion batteries plays an indispensable role in preventing thermal runaway and cold start in battery-powered electric (BEV) and hybrid electric vehicles (HEV) during on-road or fast charging conditions. The functioning of a battery depends on its thermal behavior. The life cycle and charging speeds are the optimizing factors of an EV battery pack. Higher charge rates translate to higher heat generation. At higher temperatures, it delivers an increased charge capacity but reduced longevity. But at lower temperatures, there is a higher electric resistance leading to lower efficiency and reduced total capacity of the battery. So the battery must be run at an optimal temperature range of 22–30 °C to improve performance and maintain its state of health (SOH). With the current battery technology, a battery pack is incomparable to gasoline in terms of energy density. So for an equivalent battery pack, the packing efficiency of the cylindrical battery assembly must be high, while preventing heat accumulation during high charge–discharge operations. Asymmetric thermal distribution can cause variation in the current discharge and the cell operating behavior, so a BTMS based on the thermal nature of the cells is designed. In this paper, we study the effects of a tab cooling BTMS on an anisotropic battery arrangement at different charge–discharge cycles.

Keywords COMSOL · Cooling system · Electric vehicles · Heat generation rate · Lithium-ion batteries · Simulation · Temperature distribution

A. R. Mundonkakkoth (✉)

Department of Manufacturing Engineering, School of Mechanical, VIT University, Vellore, India
e-mail: athulrmk@gmail.com

N. Menon

Department of Thermal and Energy Engineering, School of Mechanical, VIT University, Vellore, India
e-mail: nandinimenon05@gmail.com

T. K. Raj

Department of Automotive, School of Mechanical, VIT University, Vellore, India
e-mail: thundil.rajagopal@vit.ac.in

1 Introduction

The EV industry relies on lithium-ion batteries for modern electric vehicles because of their high-temperature performance and energy efficiency. Combined with the high efficiency of EV powertrains, they are unparalleled to gasoline engines. Most EV motors achieve 90% of efficiency, while most IC engines are 15% [1]. However, the downside of lithium-ion batteries is its lower energy density. Gasoline has an energy density of 47.5 MJ/L or 34.6 MJ/L. But a Li-ion battery pack has around 0.3 MJ/kg or 0.4 MJ/L. Hence, gasoline is 100 times denser than Li-ion battery packs [1]. Even though batteries cannot be compared with gasoline in terms of energy density, the high efficiency of the EV powertrain and the low energy density of the battery go hand in hand to make a fair candidate to replace IC engines.

The battery pack in a BEV should supply energy to the motors over its full range of about 300–500 km, compared to a PHEV or an HEV. It should have a higher storage capacity and a moderate charge–discharge rate without overheating. Hence, it will occupy a lot of space. So, the pack must be dense and should store as much energy as possible without compromising passenger space. Its major limitation is the high responsiveness of lifecycle and battery performance to operating temperature. Numerous studies have shown that increased temperature leads to an increase in the rate of degradation of the battery pack [2]. A typical BEV battery pack will reach its end cycle after a few thousand charge cycles. A BTMS maintains the optimal battery operation temperature by regulating the heat generated during its operations and increasing the lifetime performance. Nur Ismail and Siti Toha [2] developed a simplified heat generation model in a Li-ion battery to deal with the thermal issues related to the same. Capacity fade, self-discharge, pack electrical imbalance are a few issues that lead to battery degradation. The heat transfer is of three parts: the heat generated by the internal resistance of the cell, the change in entropy in the cell components while charging and discharging [3], and the convective transfer of heat to the ambient conditions. Zareer has proposed a design based on the advantageous option of using a low thermal conductivity polymer. The paper uses a novel technique to manufacture battery housings using a specified BASF polymer following additive manufacturing techniques [4]. Simulation analysis on the prototype will help to understand the performance of the 3D printed polymer in a high-density Li-ion battery. Using a coolant with a high heat transfer coefficient compensates for the low cooling effects of a lower thermally conducting polymer. The 3D printing methodology allowed the introduction of fins into the polymer for better heat transfer. The polymer uses its design complexity and structural architecture to make up for the poor material properties. The design is least sensitive to changing flow rates, especially when the inlet temperature of the coolant is similar to that of the surrounding. But the cooling solution maintains the operating temperature of batteries at discharge rates of 2C and 3C. Different configurations of the cooling channels promise to be a field of investigation. All these cooling solutions make use of a common design language; the batteries are maintained at an optimal temperature by cooling their lateral surfaces.

However, Zhao and Hunt [5] explain how cell tab cooling is a better option for long-term battery health when compared to surface cooling. There is little to no difference in the battery life between the cooling methods at lower C rates. However, when the cell discharges at a higher rate in under 10 min, there seems to be a significant loss in usable battery capacity up to 9.2% compared to 1.2% for tab cooling. The battery capacity loss due to surface cooling was three times higher than tab cooling after 1000 charge/discharge cycles [5]. The reason is that since battery cells have layers of cathode and anode material, the middle layer generates heat, and the ones closer to the surface get cooled better than the inner layers. The latter affects the current discharge from each layer as well, as the surface layer is the coldest hits the voltage cutoff sooner. In tab cooling, all the layers cool at the same rate from both ends. Hence, current discharge is homogeneous from all layers. Also, the axial thermal conductivity of a battery is more than the radial value, so heat is transferred axially at a higher rate. In the automotive sector, a cycle ends when the maximum usable battery capacity of an EV battery pack reaches 80%. In effect, tab cooling realizes to improve the useful life of a battery by three times. Wei et al. explain how thermal conductivity plays a pivotal role in deciding the right BTMS solution and the cooling effectiveness [6]. The key factors defining the thermal characteristics of batteries are maximum temperature, temperature difference, and temperature distribution. For a cylindrical battery system, thermal conductivity mainly depends on the effective thermal conductivities of its internal components such as electrodes, separator, and current collectors and the volume fractions of the electrolytes and solid materials [6]. In isotropic thermal conductivity, heat is uniform across all directions. Since thermal conductivity is the same in all orientations, the thermal resistance along the radial direction is lesser than axial. So, the cooling solution along the lateral surface of the battery is much more efficient. However, in anisotropic thermal conductivity, thermal distribution along the axial direction is more uniform than radial. Even though the lateral surface area is higher than the tab surface area, the difference in thermal distribution is associated with the excellent thermal conductivity along axial direction [6]. Drake et al. [7] explain how a cylindrical lithium-ion battery shows large anisotropy in its thermal conductivity. The spiral electrode construction results in several interfaces between the layers of electrode and electrolyte. And this adds to the thermal resistance in the radial direction [7]. In this paper, we simulate an anisotropic, lumped heat generation model of a battery pack and study the thermal performance of a tab cooling battery thermal management system. Thermal compound technology plays an important role to decide upon the best thermal management material for specific cooling applications. In a case study conducted by Parker Lord Corporation [8], the liquid dispense gap fillers and pre-cured thermal pads were compared with respect to their thermal performance and contact efficiency [8]. The interface between the battery pack and the cold plate is the limiting factor for heat dissipation through conduction. When the substrates come into contact, their surfaces may appear to be in perfect thermal connection with each other. However, at a microscopic level, these surfaces are rough, and only a minor fraction of the total surface comes in contact. The air entrapped in these spaces results in increased thermal resistance [8]. In such cases, thermal pads or a cured-in-place thermal compound facilitates efficient heat

transfer from the battery surface to the cold plates. According to the case study, a liquid gap filler offers lesser thermal impedance than a solid thermal pad for a comparable thermal conductivity value and thickness and, as a result, minimizes the formation of local hot spots. Its ability to conform into the microscopic hills and valleys of the rough surfaces reflects its low interfacial impedance and higher heat dissipation [8]. A thermal pad and its properties are sensitive to the applied pressure, as the thermal impedance decreases with an increase in pressure. Any local differences in them due to an uneven surface can cause heat accumulation in the corresponding regions. The thermal pad should be pressed to 650 kPa of pressure and compressed from 1 to 0.64 mm of thickness to gain comparable impedance with their SC-1200 gap filler. Applying such high pressures to obtain lower impedance is highly impractical. The design freedom of a liquid gap filler helps to use as little material as possible on any complex surface until they cure fully. Large thermal pads are difficult to handle as it tends to trap air during automated application [8].

2 Methodology

2.1 Design

A low-profile battery housing made of BASF polymer material [4] ensures the tight packing of batteries and reduces voids. Tab cooling allows us to pack the batteries together without sacrificing lateral space.

Six 18650 Li-ion batteries inserted in a BASF polymer housing ensure perfect insulation of the battery surface and prevent shorting of the individual cells. Table 1 shows the material specifications of the polymer used. A dielectric thermal compound, either liquid adhesive or a solid thermal pad, fills the gap between the interface. It facilitates heat transfer between the battery and the cold plate and displaces the air entrapped between them [8] (Figs. 1 and 2).

The bottom of the battery pack directly bonds to the liquid cooling plate for maximum heat dissipation, as the positive and negative terminals can be connected from the top surface of the battery while the side walls are insulated using the polymer cover. As mentioned previously, a pre-cured thermal pad or a cured-in-place liquid gap filler works. However, most prefer the latter due to its flexibility, negligible air entrapment, and overall better heat dissipation. Nickel 200 strips of 0.5 mm thickness represent the contact points between the battery terminals. It is necessary to make

Table 1 Material specifications of BASF polymer

Parameter	Value	Unit	Symbol
Specific heat	1500	J/Kg.K	c_p
Thermal conductivity	0.3	W/m.K	k
Density	1200	Kg/m ³	ρ

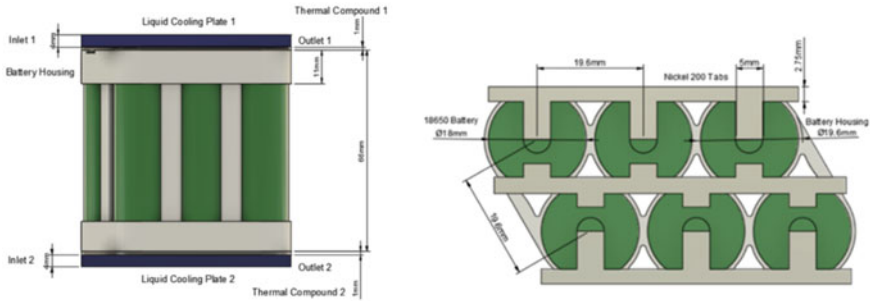


Fig. 1 Schematic diagram of the assembly consisting of six batteries

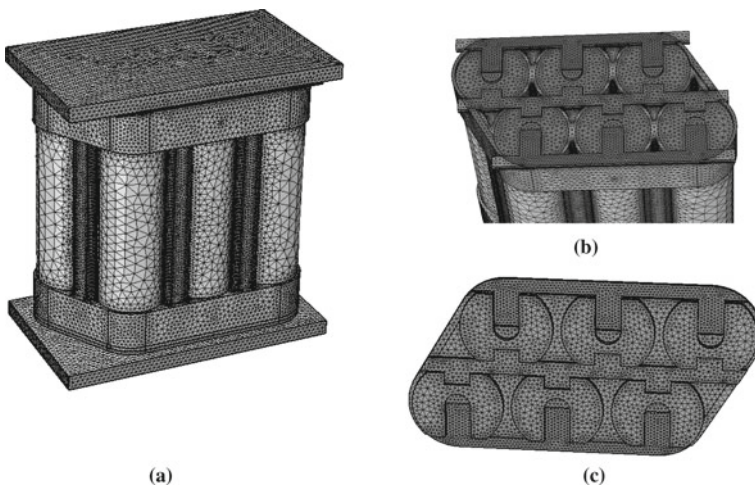


Fig. 2 Schematic diagram of the variation of mesh size **a** full assembly **b** nickel tab assembly **c** cold plate (top)

sure that the terminals are insulated from one another to prevent short circuits. The material properties are taken from the COMSOL built-in materials library (Fig. 3).

The design uses SC-1500 cure-in-place thermally conductive silicone gap filler, with thermal conductivity of 3.8 W/m.K [8]. The cold plates are then laid on top and bottom of the battery packs ensuring that the dielectric thermal compound insulates the nickel tabs and the terminals. Table 2 shows the specifications of the gap filler used.

The battery parameters used in the definition of the lumped system are from the COMSOL Multiphysics public library. The initial temperature of the battery module and the coolant are set as 20 °C. The coolant used is a 50:50 volume fraction solution of ethylene glycol and water. Properties such as density, thermal conductivity, specific heat capacity at constant pressure, the ratio of specific heat, and dynamic viscosity are determined by the thermodynamics and chemistry modules in COMSOL. The

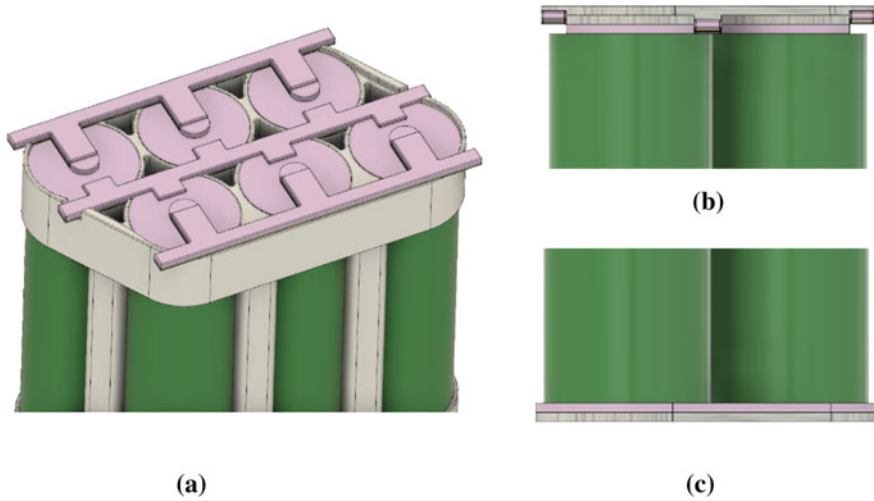


Fig. 3 **a** Isometric view of the pack with six batteries, nickel tabs and thermal compound **b** batteries, compound, nickel tabs and cold plate assembly (right view) **c** bottom cold plate and thermal compound (right view)

Table 2 Specifications of the cooltherm SC-1500 gap filler

Parameter	Value	Unit	Symbol
Thermal conductivity	3.8	W/(m.K)	K
Density	3300	Kg/m ³	ρ
Specific heat capacity	1000	J/(Kg.K)	c_p

cold plates used to transfer heat from the battery to the coolant is aluminum taken from the built-in materials library of COMSOL. Table 3 shows the specifications of the Li-ion battery used. These values are taken from the COMSOL public library.

Table 3 Specifications of the Li-ion battery used for the project

Parameter	Symbol	Value	Unit
Overpotential—ohmic (1C)	η_{ohm}	4.5	mV
Diffusion time constant	π	1000	S
Exchange current value (dimensionless)	J_0	8.5×10^{-1}	–
Thermal conductivity—axial	k_{axial}	30	W/m.K
Thermal conductivity—radial	k_{radial}	1	W/m.K
Specific heat capacity	C_p	1400	J/Kg.K
Density	P_b	2000	Kg/m ³

2.2 Simulation

For the project development, validation and proper understanding of the industry requirements is necessary. For this, the two methods followed are electrochemical analysis and lumped heat analysis. The electrochemical model recreates the lithium-ion battery behavior using the chemical characteristics and design parameters [9]. However, an electrochemical model accounting for the cell details is not practicable due to the lack of cell material and architectural specifications [3, 4]. To validate the chosen research work, we have implemented the lumped electrochemical analysis method. The lumped single-particle model (LSPM) elucidates the disparities in cell voltage of the battery set-up to a load current that is time-dependent [4]. Lithium-ion batteries are modelled using a specific set of parameters, namely open-circuit voltage (OCV) and the temperature derivative of the OCV at reference temperature versus battery state of charge (SOC) (Fig. 4).

2.2.1 Procedure for Lumped Analysis

The lumped battery heat generation model is an effective method to estimate heat generation and model the temperature distribution in a battery while charging and

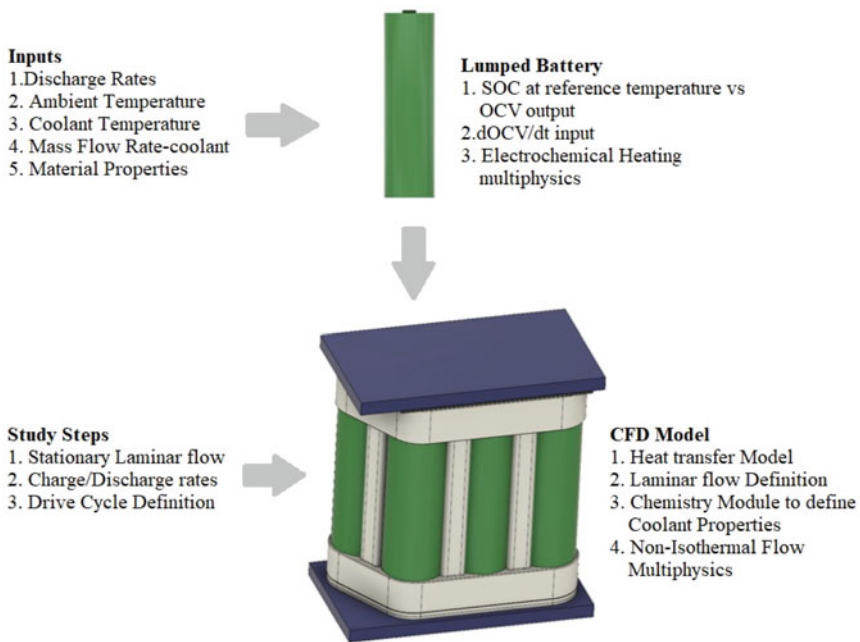


Fig. 4 Pictorial methodology chart

discharging. Instead of laying out the various electrochemical processes in the negative and positive electrodes of a battery, the lumped system makes use of the total of the voltage lost along with the cell equilibrium voltage. This voids the requirement to study the internal structure and the chemistry of the battery.

In a lumped battery system, the two defining factors are the cell equilibrium potential and the voltage losses. This solves for the state of charge of the battery as a dependent variable. The cell equilibrium voltage as a function of SOC and temperature is defined as:

$$E_{OCV}(SOC, T) = E_{OCV}(SOC) + (T - T_{ref}) \frac{\partial E_{OCV}(SOC)}{\partial t} \quad (1)$$

The interpolation function defines the OCV at the reference temperature and the temperature derivative of OCV. The SOC and OCV parameters that define the problem are derived experimentally and entered as inputs for the $E_{OCV,SOC}$ interpolation function.

Here, the temperature derivative of open-circuit voltage $E_{OCV}(SOC)$ is used to calculate the temperature dependence of the OCV and the heat of mixing that contributes to the total heat source.

The $E_{OCV}(SOC)$ is defined in COMSOL as an interpolation function using the state of charge and the corresponding open-circuit voltage values. (from COMSOL library).

The mathematical equation for the open-circuit voltage of a battery is:

$$E_{cell} = E_{OCV}(SOC, T) + \eta_{ohm} + \eta_{act} + \eta_{conc} \quad (2)$$

η_{ohm} , η_{act} , and η_{conc} are the over-potential losses in a battery.

The three overpotentials, namely ohmic (η_{ohm}), activation (η_{act}), and concentration (η_{conc}), account for the voltage losses in the battery [4]. The voltage losses that amount to the heat output are defined using the Arrhenius equations as a function of activation energy and temperature. The Arrhenius equation defines the temperature-dependent ohmic resistance, exchange current, and diffusion time-constant parameters.

The ohmic overpotential represents the value of ohmic voltage loss for a battery current of 1C rate.

$$\eta_{ohm} = \eta_{1C} \frac{I_{batt}}{I_{1C}} \quad (3)$$

η_{1C} is the ohmic potential at 1C, I_{1C} is the current at 1C.

The activation overpotential shows the voltage loss related to the charge transfer process.

The activation overpotential losses is defined as:

$$\eta_{act} = \frac{2R_i T}{F} \sinh^{-1} \left(\frac{I_{batt}}{2J_0 I_{1C}} \right) \quad (4)$$

F —Faraday's value, R_i —molar ideal gas constant, T is the temperature in kelvin, and J_0 is a dimensionless constant.

The SOC as a function of the battery current is:

$$\frac{dSOC}{dt} = \frac{I_{batt}}{Q_{batt}} \quad (5)$$

Q_{batt} represents the battery capacity.

The above equation is an inverted form of the Butler–Volmer equation. Here, the anodic and cathodic factors are 0.5 [10].

To find the LSPM over-potential, defining the Fickian diffusion of a local SOC on a 1D particle length of 0 to 1 on the x -axis is as follows:

$$\tau \frac{dS}{dt} + \nabla \cdot (-\nabla S) = 0 \quad (6)$$

τ is the diffusion time constant.

Subjecting the above equation to the stated boundary conditions.

$$(-\nabla S) = 0, x = 0 \quad (7)$$

$$(-\nabla S) = \tau \frac{dI_{batt}}{Q_d}, x = 1 \quad (8)$$

Here, d takes positive integer values for Cartesian, cylindrical, and spherical coordinates. The battery SOC and local SOC (particle) relate by the equation:

$$SOC = s \int_0^1 S x^{d-1} dx \quad (9)$$

At the same time, the concentration overpotential is:

$$\eta_{act} = K(S_{x=1} - SOC) \quad (10)$$

K is the parameter representing the variation when S deviates from SOC (battery). At this time, R_{ohm} , I_0 , and τ act as fitting parameters.

The numerical representation of heat generation rate for the analysis is as:

$$\dot{Q}_{gen} = (\eta_{act} + \eta_{ohm})I_{batt} + \frac{dQ_{cell}}{\tau} \int_0^1 \frac{dVOC(S)}{ds} \frac{dS}{dx} \frac{dd}{dx} x^{d-1} dx \quad (11)$$

2.2.2 Procedure for CFD and Heat Transfer Method

An electrochemical heating multi-physics node generates the heat in a lumped battery. The heat source then couples with the heat transfer in the solids and fluids module to design the cooling solution. Both conduction of heat through the thermal compound and cold plate and convection by the coolant helps with the heat transfer.

The coolant flow is assumed to be laminar and fully developed since the flow enters and exists through a long straight channel as previously shown. The flow rate is equally divided on the top and bottom domains. The flow is incompressible with no-slip boundary conditions assumed at the walls. The operating pressure is taken as 1 atm and an initial coolant temperature of 20 °C. The velocity of the fluid is in terms of mass flow rate (g/s). Outlet conditions are assumed to be a zero pressure outlet at normal flow where no tangential stress condition is changed to a no tangential velocity condition. The flow is assumed to be forced to exit the domain perpendicularly to the outlet boundary. Backflow is suppressed to prevent fluid from entering the domain through the boundary. The operating conditions are 2C discharge rate at 10 g/s coolant flow rate and 3C discharge rate with 15 g/s coolant flow rate. The coolant used is a 50:50 volume fraction solution of ethylene glycol and water. In addition, a charge–discharge model proposes to test the performance of BTMS, where the battery is discharged first at a 3C discharge rate from 100 to 0% SOC, then charged back to a 100% SOC at a 2.5C charge rate. Unlike the previous discharge-only setup, the heat generated will be immense. The coolant flow rate is set at 15 and 20 g/s to compare the effect of flow rate on cooling performance.

3 Results and Discussion

Under the operating conditions, we have generated a maximum module temperature vs. time graph and the module temperature difference vs. time graph in all cases. The BTMS performance is compared based on these plots. The initial temperature of the setup is at 20 °C.

3.1 Discharge Only

3.1.1 Insulated Batteries

Initially, the batteries are thermally insulated to find the peak temperature without a thermal management system. This helps to compare the performance of the BTMS system used. Initial temperatures are setup at 20 °C and discharge from 100 to 80% for 2C and 3C rates. At a 2C discharge rate, the peak temperature at the end of the cycle is 38.832 °C. The value is 18.832 °C higher than the initial pack temperature.

At a 3C discharge rate, the peak temperature at the end of the cycle is 42.533 °C. The value is 22.533 °C, more than the initial pack temperature.

3.1.2 BTMS

The boundary conditions are identical to the validation model [1] to maintain consistency. However, we did an additional charge–discharge cycle to measure the performance of the BTMS. As mentioned in the paper, the effect of increased flow rate is minimal. So, in our model, two sets of flow rate/discharge rate conditions along with a 3C–2.5C cycle at 12g/s coolant flow rate are selected for comparison. When discharged at a 2C discharge rate and 10g/s coolant flow rate, the peak temperature is measured to be 22.475 °C at 1096.3 seconds, which is only 2.475 °C higher than the initial coolant temperature and below the recorded temperature in the validation model [1]. At a 3C discharge rate and 15g/s coolant flow rate, the peak temperature is 24.07 °C at 720.37 seconds which is only 2.07 °C above the initial coolant temperature and below the resultant validation temperature [1] (Figs. 5, 6 and 7).

Fig. 5 Maximum temperature graph for 2C, 10 g/s and 3C, 15 g/s—battery only with BTMS

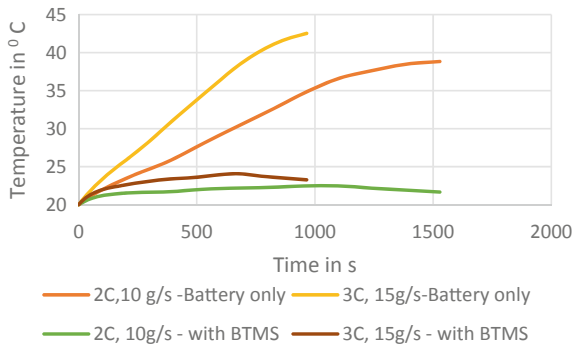
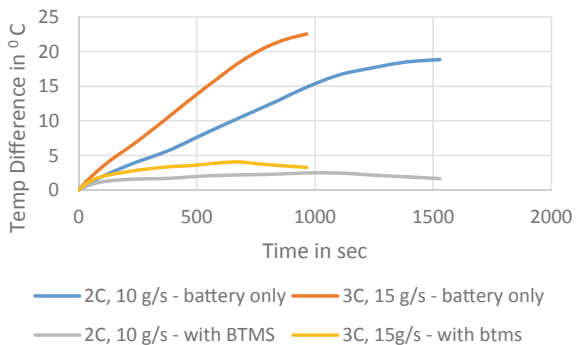


Fig. 6 Maximum temperature difference graph for 2C, 10 g/s and 3C, 15 g/s—battery only and with BTMS



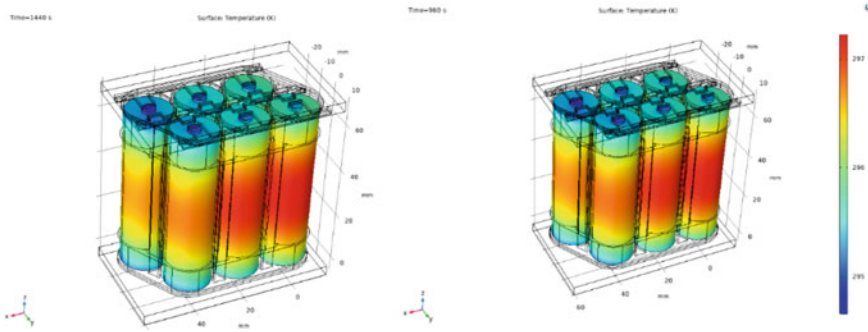


Fig. 7 Surface temperature contour of the batteries at a 2C and b 3C discharge rates

3.2 Charge–Discharge Cycle

3.2.1 Insulated Batteries

When the batteries are insulated, the peak temperature at the end of the cycle is 58.914 °C at 3C–2.5C discharge–charge cycle (100–0% and vice versa) at 1883.8 s. The value is 38.914 °C, more than the initial temperature of the batteries.

3.2.2 BTMS

When discharged from 100 to 0%, at a 3C discharge rate and charged 0 to 100% at a 2.5C charge rate with a 12g/s coolant flow rate, the peak temperature is measured to be 32.15 °C at 1320.3 seconds. However, at 1800 s, the temperatures drop back to 22.43 °C; that is, within 8 min, the batteries come back to an ideal temperature (Figs. 8, 9 and 10).

Fig. 8 Maximum temperature graph for 3C–2.5C charge–discharge cycle (100–0% and vice versa)–battery only and with BTMS

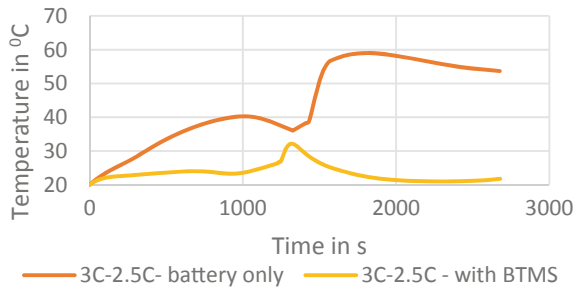


Fig. 9 Maximum temperature difference graph for 3C–2.5C charge–discharge cycle (100–0% and vice versa)—battery only and with BTMS

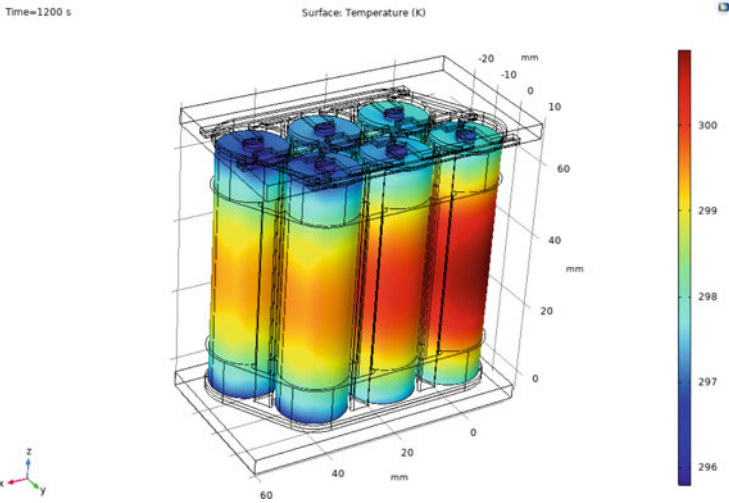
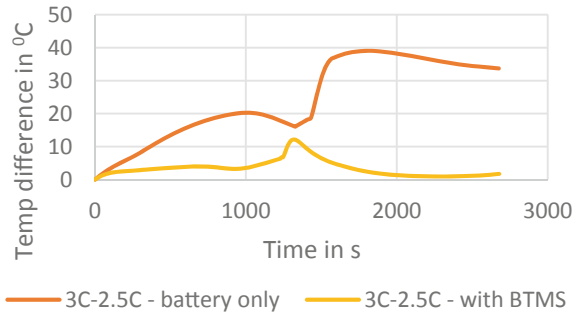


Fig. 10 Surface temperature contour of the batteries at 3C discharge and 2.5C charge rate

4 Conclusion

The use of a tab-cooling liquid-based battery thermal management system is investigated and compared to the surface cooling method. For the same battery setup and charge–discharge rates, the tab cooling setup showcased a reduction in maximum temperature and an ideal trend overall. The design is more compact than the surface cooling thermal management solution. The reason behind this is that a lithium-ion battery does not conduct heat uniformly in all directions, unlike other solid bodies. The anisotropic thermal conductivity is caused by the internal jelly-roll packing of the anode, cathode, and separator layers sandwiched together, causing internal thermal resistance between each layer of the battery material. Despite the smaller contact area between the battery tabs and the cold plate, the battery manages to remain cool during

the entire operation. A dielectric thermal gap filler is used to electrically insulate the battery tabs from the cold plate and transfer the heat efficiently.

Since it is extruded as a semi-solid material before cure, it achieves perfect thermal contact between the tabs and the cold plate. Altogether, the BTMS manages to keep the batteries in optimal operating temperatures. Small changes in the flow rate do not affect the cooling performance of the BTMS for the same current discharge rates. Hence, the BTMS using tab cooling methods needs more attention in the automotive industry, as it manages to improve the longevity of the battery by three times than the surface cooling methods. This reduces the degradation and waste of batteries in automotive applications, which translates to reduced costs of production. It will further empower the economy to become greener and more sustainable.

References

1. Schlachter F (2012) APS news. APS Physics, US
2. Al-Hallaj S, Selman J (2002) Thermal modeling of secondary lithium batteries for electric vehicle/hybrid electric vehicle applications. *J Power Sources: Science Direct* 110(2)
3. Ismail NH, Toha SF, Azubir NA, Ishak NH, Hassan MK, Ibrahim BS (2013) Simplified heat generation model for lithium-ion battery used in electric vehicle. *IOP Conf Ser Mater Sci Eng* 53:012014
4. Al-Zareer M (2020) Numerical study of flow and heat transfer performance of 3d-printed polymer-based battery thermal management. *Science Direct, Canada*
5. Hunt A, Zhao I, Patel Y, Offer GJ (2016) Surface cooling causes accelerated degradation compared to tab cooling for lithium-ion pouch cells. *IOP Sci*
6. Wei L, Lu Z, Cao F, Zhang L, Yang X, Yu X, Jin L (2020) A comprehensive study on thermal conductivity of the lithium-ion battery. *Wiley Online library*
7. Drake SJ, Wetz DA, Ostanek JK, Miller SP, Heinzl JM, Jain A (2014) Measurement of anisotropic thermophysical properties of cylindrical Li-ion cells. *J Power Sources: Science Direct*
8. Parker Lord (2021) Liquid-dispense gap fillers vs. thermal pads. A case study on thermal performance. *Lord.com, US*
9. Falconi A (2017) Electrochemical Li-Ion battery modeling for electric vehicles. In: *Material chemistry. Communauté université grenoble alpes.*
10. Ekström H, Fridholm B, Lindbergh G (2018) Comparison of lumped diffusion models for voltage prediction of a lithium-ion battery cell during dynamic loads. *J Power Sources: Science Direct*

Numerical Analysis to Investigate the Effect of Solidification Parameters on the Pull-In Effect of Continuous Casting



Ritesh S. Fegade, Rajendrakumar G. Tated, and Rupendra S. Nehete

Abstract Direct chill (DC) casting is a method of solidifying molten metal into a semi-finished billet, bloom, or slab prior to rolling in finishing mills using an external continuous chilling technology. However, its operational improvement remains a focus of researches due to the ingot curve formed at bottom and side. The purpose of this research is to examine the thermal and mechanical properties created during the direct chill casting process in order to determine the base and side curvature using a CFD technique. The effect of vertical pull-in direct chill casting of aluminum ingots was investigated using a numerical model based on multiple physics. Thermal and mechanical simulations are performed using ANSYS mechanical software. The development of the ingot during the transient solidification process is aided by the use of a dynamic mesh method. The element kills, and generated concepts are utilized to determine the ingot's deformation. The results demonstrate that the developed model may be utilized to forecast deformations in ingots caused due to thermo-mechanical characteristics throughout the direct chill casting process. The deflection of the slab increases as the molten metal temperature and casting speed decrease. The maximum deflection was determined to be 23.34 mm for the case at a molten temperature of 715 °C and a casting speed of 75 mm/min.

Keywords Continuous casting · Coupled finite element modeling · Element birth and death mesh · Computational fluid dynamics

R. S. Fegade (✉)

Department of Mechanical Engineering, Genba Sopanrao Moze College of Engineering, Balewadi, Pune, India
e-mail: riteshfegade@gmail.com

R. G. Tated

Department of Mechanical, SNJB's Late Sau Kantabai Bhavarlalji Jain College of Engineering, Chandwad, Nashik, India

R. S. Nehete

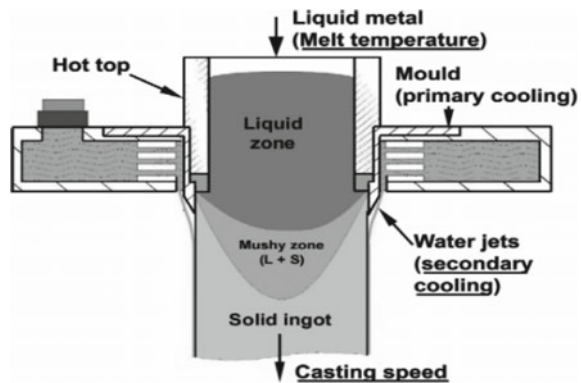
Department of Mechanical Engineering, SIES Graduate School of Technology, Navi Mumbai, India

1 Introduction

Continuous casting is a method of solidifying molten metal into a semi-finished billet, bloom, or slab that is then rolled in finishing mills. It has evolved to attain higher yields, higher quality, increased productivity and greater cost-efficiency. It enables lower-cost manufacturing of metal sections with higher quality, owing to the intrinsic cost savings associated with continuous, standardized production, as well as greater process control provided by automation. Aluminum alloys are typically cast using shape casting or direct casting processes. Several basic concepts such as solidification phenomenon, analysis of macroscopic heat transfer, deformation and flow characteristics are common in shape casting and direct chill casting process. Sand casting, die-casting, permanent mold casting and investment casting are the subsidiaries of the shape casting process. The direct chill casting process is most commonly used commercially to create wrought alloys. The billets formed with the extrusion method and slabs formed with rolling can be categorized into vertical and horizontal methods of direct chill casting. The vertical direct chill casting process is schematically shown in Fig. 1.

Throughout the initial phase, the ingot cools quicker than it does during the steady-state regime. Rapid cooling results in significant thermal stresses, which cause the ingot's first section to bow. This is referred to as the "butt curl." The phrase "butt swell" refers to an area of the ingot's butt that is thicker than the rest of the slab. As a result, the ingot contracts less and the slab approaches the nominal size of the mold. In continuous slab casting, increasing productivity and yield through the application of techniques such as high-speed casting, mold width variation and sequential casting of diverse chemical compositions has significantly lowered production costs. Breakout and surface defects of slabs are more likely to occur during high-speed casting, which is an efficient method of producing slabs at high temperatures, as a result of the more active flow of liquid steel and the thinner solidified shell creation in the mold.

Fig. 1 Direct chill casting process schematics



The quality of continuously cast steel is highly dependent on the flow of fluid within the mold, particularly near the meniscus [1]. Steel characteristics have a significant influence on solidification behavior. Chemical studies of carbon steels affect the solidus and liquidus temperatures, affecting the computed values. Nonetheless, the numerical solution of the governing heat-transfer differential equation with appropriate beginning and boundary conditions remains critical for the fundamental understanding of the entire solidification process. Numerous academics addressed the issues in their research articles; the majority of them focused on steel casting [1–3]. The molding temperature and casting speed are two crucial characteristics that impact the quality of the finished product, particularly the solidification and cross section. In continuous casting, the cross section has a significant influence on the yield. Although researchers attempted to solve the problem using a computational fluid dynamics (CFD) or a finite element analysis (ANSYS parametric design) solidification approach for steel casting, there is ample opportunity to develop modeling for a variety of aluminum alloy casting grades. Williams et al. [1] developed a simulated analytical model of the process that incorporates fluid flow and thermo-mechanical analysis in direct chill casting. He discovered that even for very high vertical intake velocities does not appear to be responsive to the input flow conditions of direct cold casting. He advised that stress levels be reduced by using a metal inflow distribution bag design. Nadella et al. [2] investigated the evolution of macrosegregation during the ingot production process. They separated the effects of several macro segregation methods using computer simulations. One of the primary reasons for macrosegregation is the movement of the solid and liquid phases relative to one another. Macrosegregation Due to Thermal Convection and Contraction-Driven Flow in Direct Chill was explored by Reddy and Beckermann [3]. By mathematical model, continuous casting of an Al-Cu rounded ingot. The findings indicate that the grain density and permeability of the mush define whether the segregation created is positive or negative. Contraction during solidification also results in segregation at the surface of ingots, which has a considerable effect on macrosegregation over the ingot's core section. Miha and Bozidar [4] investigated the effect of direct cold casting settings on macrosegregation. The results indicate that casting process factors affect macrosegregation by directly affecting the liquid pool and mushy zone. In direct cold casting, Eskin [5] studied the effect of macrosegregation, shrinkage and sump profile (DC). They concluded that the distance between the solidus and liquidus isotherms in casting billets defines the macrosegregation amount in the process. Turski et al. [6] used an analytical model and experimental data to predict residual stresses within a direct chill cast magnesium alloy slab. Alvarez et al. [7] used a mathematical model to investigate ways to avoid or minimize unwanted shrinkage in casting ingots. Lee et al. [8] used a mathematical model to investigate the emergence of porosity during the direct chill casting process of aluminum and magnesium alloys. The model was used to forecast the size, shape, distribution and percentage of porosity of pores. The model well anticipated the experimentally observed trends, with a strong link to the percentage porosity measurements. Fegade et al. [9, 10] discussed the pull-in procedure utilized in aluminum continuous casting. Additionally, they used a variety of

quality improvement approaches, including TQM, why-why analysis, standard operating procedures and the fishbone diagram, to eliminate faults during the aluminum continuous casting process. Fegade et al. [11] determined the thermal and mechanical stresses created during direct chill casting using a finite element method based on the element birth and death concept. Batwara and Shrivastav [12] investigated the effect of process factors on casting solidification using the computational fluid dynamics (CFD) software ANSYS FLUENT. They employed a surface approach with the MINITAB programmed to determine the relationship between factors and their responses. Maurya and Jha [13] developed a three-dimensional mathematical model to examine the influence of casting speed and superheat on steel slabs in continuous casting. According to the study, casting speed has a significant effect on temperature distribution, whereas superheat has a negligible effect on metallurgical strand length and temperature distribution. Amin and Gawas [14] demonstrated the effect of interfacial flux on the casting mold during the solidification phase of continuous casting. Luo and Zhang [15] investigated the uniform direct chill casting process, which incorporates annular electromagnetic casting and intercooling. He showed that annular electromagnetic stirring is effective in increasing temperature homogeneity throughout the casting process, but intercooling has an effect on temperature homogeneity and sump depth reduction. Hao et al. [16] employed a mathematical model to predict the thermal behavior of magnesium billets during direct chill casting. The results demonstrate that the model is capable of reproducing the heat transfer that occurs during this process precisely over a range of casting conditions. Hongjun et al. [17] used ANSYS to simulate a two-dimensional mathematical model to forecast the thermal and mechanical states of solidification of ingots during direct chill casting. They reported that the stress and strain levels are greater at the top of the crystallizer's web than in other regions. The quality of the surface has a significant effect on temperature changes during secondary cooling. Hao et al. [18] used a mathematical model to analyze the stress-strain behavior and hot ripping during the direct chill casting process on an AZ31 magnesium billet. The results indicated that the model was capable of describing the evolution of billet temperature and forecasting the rise of residual stresses/strains during the direct chill casting process. Zuidema et al. [19] used a mathematical model and an experiment to investigate secondary cooling in direct chill casting. Hallvard and Jensen [20] studied the deformation of ingots' butt curls using a mathematical model. They reported that the butt curl is insensitive to alloy composition modification. Barral and Quintela [21] used an analytical model to investigate thermal stresses caused during the casting process of an aluminum slab. Begum and Hasan [22] conducted a three-dimensional CFD simulation of aluminum AA-1050 alloy in a vertical direct chill slab caster equipped with a submerged nozzle and a porous filter supply system, as well as turbulent melt flow and heat transfer during solidification. They discovered that a low porosity filter results in nearly uniform flow in the mold zone, which is an admirable result for casting aluminum ingots. Weckman and Niessen [23] numerically studied the phenomenon of continuous casting in the direct chill casting process along with nucleate boiling heat transfer. To analyze boundary conditions in the ingot's sub

mold region, a theory of forced convection nucleate boiling and film cooling was created.

2 Methodology

During the DC casting process, a finite element method is used to predict the temperature profile and residual stress in rectangular shaped aluminum alloy ingots. The completed ingot generated in a direct chill casting process is meant to be relatively large than the material’s original elasticity, which allows thermal stress relief through the viscoelastic mechanism [2]. Transient structural–thermal models of the direct chill casting process are used to investigate ingot shrinkage. Table 1 shows the structural and thermal parameters of the aluminum alloys used in the finite element analysis. Figure 1 shows the three phases involved in FEA simulation. Quarter symmetric modeling is used in the simulation process. This method is used to cut down on computation time. The element birth and death principle are used in FEA simulations.

Table 1 Structural and thermal parameters of the aluminum alloys

Solidus temperature	630 °C		Youngs modulus	68.2 GPa	≤25 °C
Liquidus temperature	658 °C			60.6 GPa	200 °C
Density	2650 kg/m ³			51.8 GPa	400 °C
Dynamic viscosity	1 × 10 ² Pa/s			41.8 GPa	630 °C
Thermal conductivity	226 W/mK	≤630 °C		40.0 GPa	650 °C
	90 W/mK	≥658 °C	0.1 MPa	≥650.1 °C	
Specific heat	905 J/kgK	≤27 °C	Poissons ratio	0.37	
	950 J/kgK	127 °C		3 × 10 ⁵ /°C	≤650 °C
	998 J/kgK	227 °C		0	≥650.1 °C
	1043 J/kgK	327 °C	Yield stress	500 MPa	≤25 °C
	1090 J/kgK	427 °C		10 MPa	≥650.1 °C
	1135 J/kgK	≥527 °C	Fluidity	1.0 × 10 ⁶ s ⁻¹	≤25 °C
	1181 J/kgK	630 °C		3.7 × 10 ³ s ⁻¹	≥650.1 °C
	1086 J/kgK	≥658 °C	Strain-rate sensitivity	50	≤25 °C
Latent heat	358 kJ/kg			5	≥650.1 °C

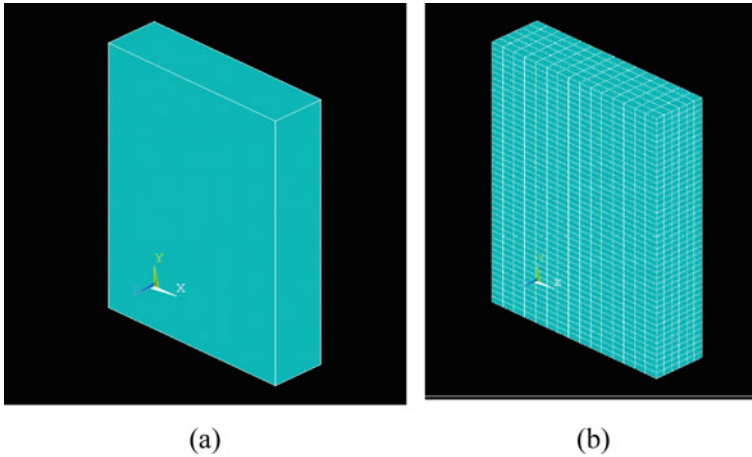


Fig. 2 **a** Domain used in the numerical investigation; **b** meshed model of computational domain in ANSYS

2.1 Computational Domain and Mesh

Figure 2a illustrates the domain used for numerical investigation of direct cold casting. As an asymmetrical alternative, aluminum ingots with a rectangular form will be investigated. As a result, approximately one-quarter of the overall ingot geometry is represented by computational geometry. The ingot generation process is modeled using a dynamic mesh method. The initial mesh of the ingot is chosen in advance to allow compression in the casting direction while maintaining the top side. The mesh lowers in lockstep with the speed of the casting. For every time step, the mesh gap can be raised while retaining the thickness and width. The meshed model of the computational domain in ANSYS is depicted in Fig. 2b.

2.2 Governing Equations and Boundary Condition

The fluid flow and solidification processes involved in a direct chill (DC) casting process can be modeled by solving continuity equations, Navier–Stokes equations, the volume of fluid-fraction equations and energy equations. The time-dependent structural and thermal analysis is performed with the help of the following governing equations.

A. Continuity equation

$$D = \frac{\partial u}{\partial x} + \frac{\partial v}{\partial y} + \frac{\partial w}{\partial z} = 0 \quad (1)$$

B. Navier–stokes equations

$$\begin{aligned}\rho\left(\frac{\partial u}{\partial t} + u\frac{\partial u}{\partial x} + v\frac{\partial u}{\partial y} + w\frac{\partial u}{\partial z}\right) &= -\frac{\partial p}{\partial x} + \rho g_x + \mu\nabla^2 u \\ \rho\left(\frac{\partial v}{\partial t} + u\frac{\partial v}{\partial x} + v\frac{\partial v}{\partial y} + w\frac{\partial v}{\partial z}\right) &= -\frac{\partial p}{\partial y} + \rho g_y + \mu\nabla^2 v \\ \rho\left(\frac{\partial w}{\partial t} + u\frac{\partial w}{\partial x} + v\frac{\partial w}{\partial y} + w\frac{\partial w}{\partial z}\right) &= -\frac{\partial p}{\partial z} + \rho g_z + \mu\nabla^2 w\end{aligned}\quad (2)$$

where p is pressure (Pa), μ is dynamic viscosity, t is the filling time.

C. Energy equation

$$\rho c \frac{\partial T}{\partial t} = \frac{\partial}{\partial x}\left(k_x \frac{\partial T}{\partial x}\right) + \frac{\partial}{\partial y}\left(k_y \frac{\partial T}{\partial y}\right) + \frac{\partial}{\partial z}\left(k_z \frac{\partial T}{\partial z}\right) + S \quad (3)$$

where c is specific heat capacity, S is the heat source term, k is the thermal conductivity.

D. Volume of fluid-fraction

$$\frac{\partial F}{\partial t} + u\frac{\partial F}{\partial x} + v\frac{\partial F}{\partial y} + w\frac{\partial F}{\partial z} = 0 \quad (4)$$

where F is the volume function for each grid and can be expressed as

$$F = \frac{f_v}{A_v}$$

where f_v is the volume of fluid in one grid and A_v is the volume of one grid. A fully fluid occupied grid has the unity F values.

A series of simulations with varying boundary conditions is used to study the manufacture of ingots and their thermo-structural behavior. The coupled field simulation imposes structural–thermal boundary conditions as illustrated in Fig. 5. The values for convection at the ingot's base and side faces are shown in Table 2.

3 Results and Discussion

The governing equations are solved using the FEM and FVM methods, which are implemented in the commercial program ANSYS APDL. It is assumed in this research that an individual material layer emerges and then begins to harden. The

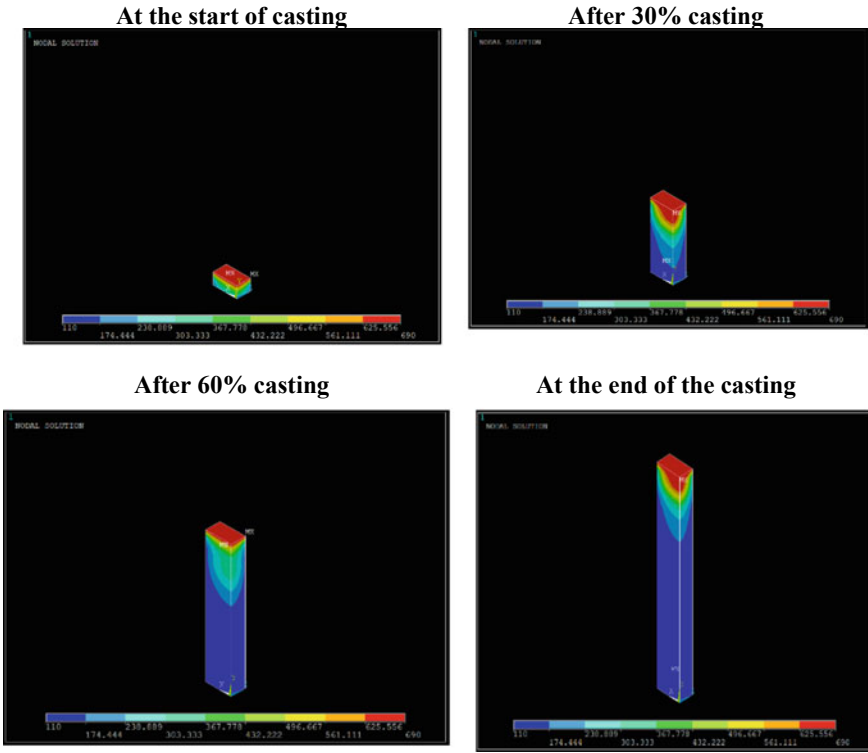


Fig. 3 Temperature distribution during casting process (quarter model)

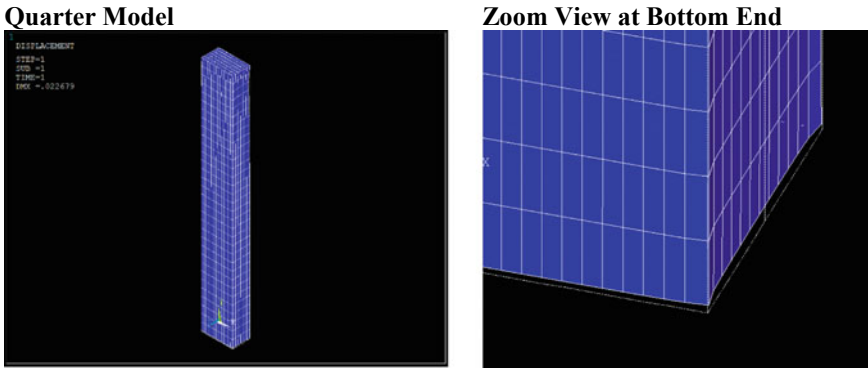


Fig. 4 Deflection contour plots

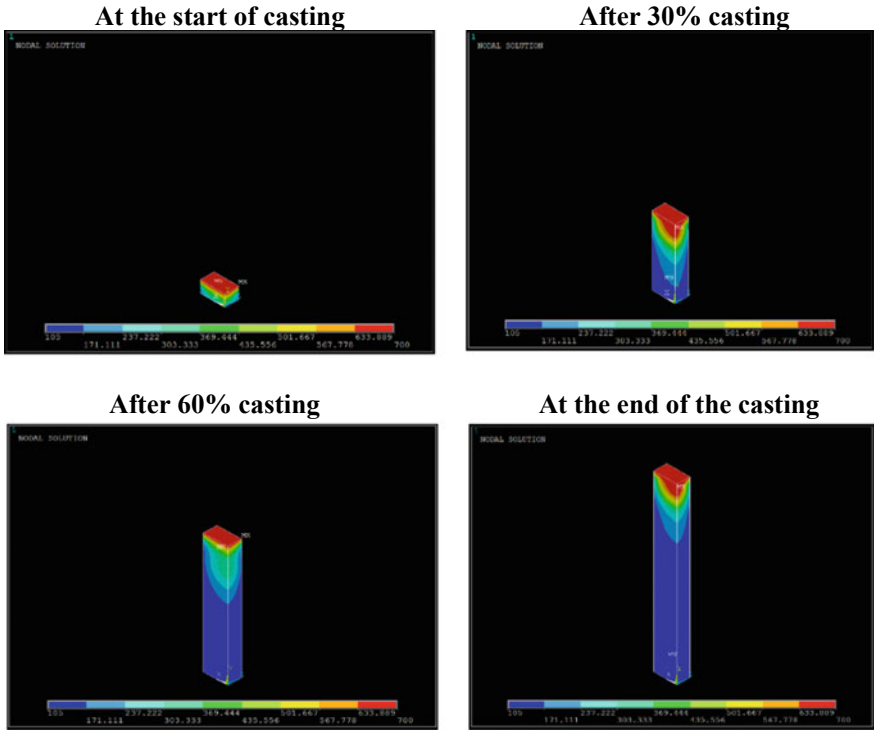


Fig. 5 Temperature distribution during casting process (quarter model)

Table 2 Thermal properties at base (h_{base}) and water cooling (h_{sides})

T (°C)	0	100	130	150	200	300	500	550	600	650
h_{base} (W/m ² K)	500	500	500	500	400	300	300	500	800	4000
h_{sides} (W/m ² k)	5000	8000	25,000	25,000	18,000	10,000	10,000	10,000	10,000	10,000

numerical model maintains the same speed of cast layer development as the actual casting process ($t = 25$ min). The element birth concept is implemented to describe the ingot layer formation process by adjusting the solidification temperature of the aluminum alloy ($T_s = 630$ °C). The simulation was performed in three different temperature ranges 690 °C, 700 °C and 715 °C and three different casting speed 65, 55 and 75 mm/min. The simulation process uses a quarter symmetric modeling approach. This approach is used to save computational time. FEA simulations are based on the element birth and death concept.

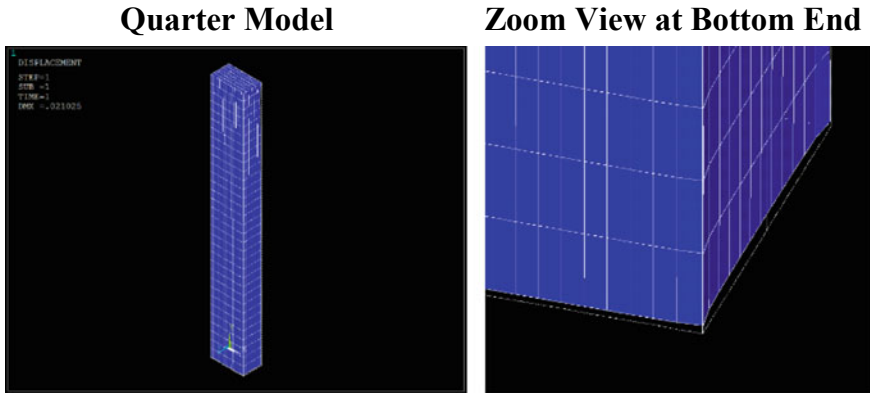


Fig. 6 Deflection contour plots

3.1 Temperature 690 °C and Casting Speed 65 mm/min

Figure 3 shows temperature distribution during the casting process using the quarter model. As layer forms, boundary conditions as explained in the earlier section are enabled for exposed faces. Temperature is observed between 108 and 690 °C.

Figure 4 shows the deflection curve after cooling for which maximum deflection is observed as **22.68** mm.

3.2 Temperature 700 °C and Casting Speed 55 mm/min

Figure 5 shows temperature distribution during the casting process using the quarter model. As layer forms, boundary conditions as explained in the earlier section are enabled for exposed faces. Temperature is observed between 105 and 700 °C.

Figure 6 shows the deflection curve after cooling for which maximum deflection is observed as 21.02 mm.

3.3 Temperature 715 °C and Casting Speed 75 mm/min

Figure 7 shows temperature distribution during the casting process using the quarter model. As layer forms, boundary conditions as explained in the earlier section are enabled for exposed faces. Temperature is observed between 110 and 715 °C.

Figure 8 shows the deflection curve after cooling for which Maximum deflection is observed as 23.34 mm.

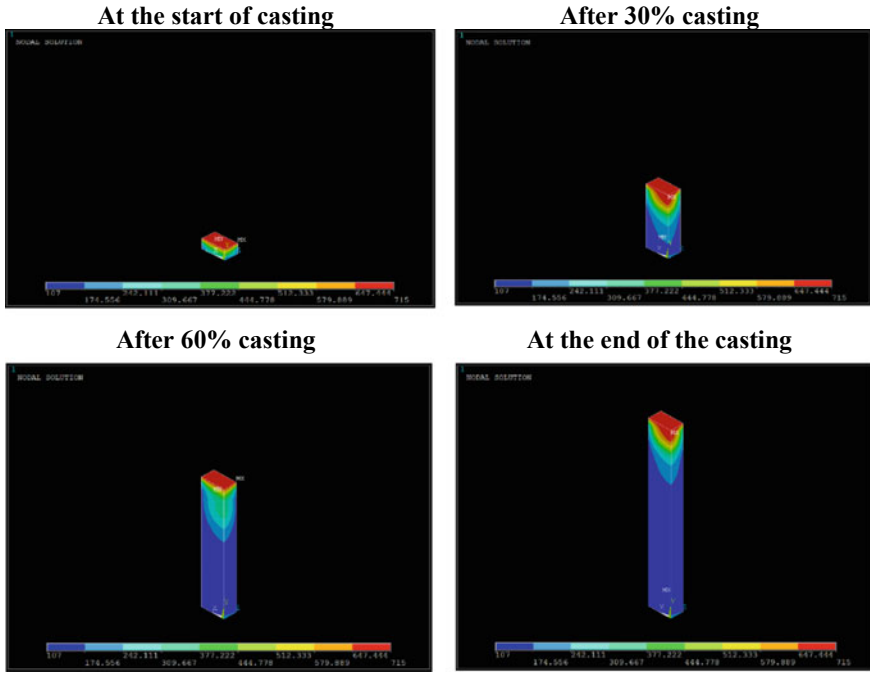


Fig. 7 Temperature distribution during casting process (quarter model)

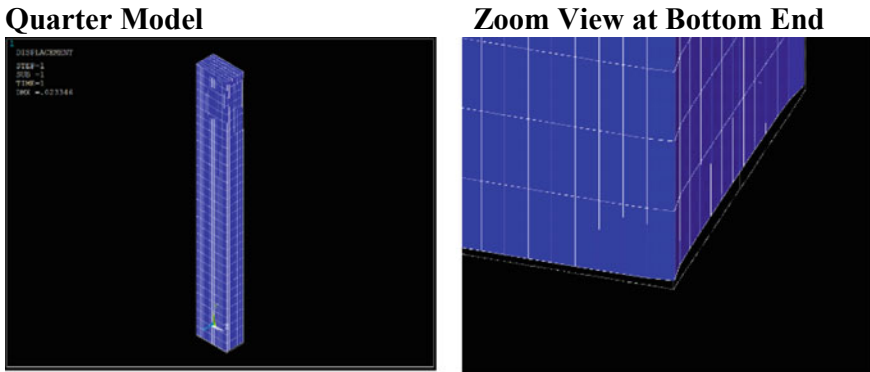


Fig. 8 Deflection contour plots

4 Conclusion

A numerical analysis of pull-in effect during the direct chill casting process has been done using a CFD tool with a death and birth concept. The mass, momentum and energy-governing equations were solved with time to predict the temperature

profile ingot formation process. The results of temperature profile and deflection for different operating conditions were plotted. From the results, it is concluded that a newly developed numerical model has shown the exceptional capability to solve the thermal and mechanical performance of the direct chill casting process. The model used in the research is capable of producing good grids with minimum error in the solution. The following conclusions have been drawn from the analysis.

The side pull-in effect has a great impact with change in molten metal temperature, casting speed and also on the convection rate over the outer surface of the mold.

The deflection of the slab increases with an increase in the molten metal temperature as well as casting speed.

The maximum deflection was found to be 23.34 mm for the case with 715 °C molten temperature and 75 mm/min casting speed.

References

1. Williams AJ, Croft TN, Cross M (2003) Modeling of ingot development during the start-up phase of direct chill casting. *Metall Mater Trans B* 34(5):727–734
2. Nadella R, Eskin DG, Du Q, Katgerman L (2008) Macrosegregation in direct-chill casting of aluminium alloys. *Prog Mater Sci* 53(3):421–480
3. Reddy AV, Beckermann NC (1997) Modeling of macrosegregation due to thermosolutal convection and contraction-driven flow in direct chill continuous casting of an Al-Cu round ingot. *Metall Mater Trans B* 28(3):479–489
4. Založnik M, Šarler B (2005) Modeling of macrosegregation in direct-chill casting of aluminum alloys: estimating the influence of casting parameters. *Mater Sci Eng, A* 413:85–91
5. Eskin DG (2008) *Physical metallurgy of direct chill casting of aluminum alloys*. CRC Press
6. Turski M, Paradowska A, Zhang SY, Mortensen D, Fjaer H, Grandfield J, DeLorme R (2012) Validation of predicted residual stresses within direct chill cast magnesium alloy slab. *Metall Mater Trans A* 43(5):1547–1557
7. Alvarez BD, Martínez JF, Martín MG, Quintana JC (1999) Mathematical modelling of the process of continuous casting of aluminium and its alloys. *Finite Elements Anal Des* 33(1):43–59
8. Lee PD, Atwood RC, Dashwood RJ, Nagaumi H (2002) Modeling of porosity formation in direct chill cast aluminum–magnesium alloys. *Mater Sci Eng, A* 328(1–2):213–222
9. Feagde R, Tated R, Nehete R (2019) Critical review on pull-in of aluminium in continuous casting. *Int J Scien Technol Res* 8(11):1950–1959
10. Fegade R, Tated R, Nehete R (2019) Improving the aluminium rolling ingot recovery using TQM technique. *Int J Inno Technol Explor Eng (IJITEE)* 8(12):282–289
11. Fegade R, Tated R, Nehete R, Parle DG (2009) Finite element analysis of direct chill casting using concept of element birth and death. *Int J Recent Technol Eng (IJRTE)* 8(4):2967–2975
12. Batwara A, Shrivastav S (2015) Effect of process parameters on continuous casting products solidification using surface response methodology: a numerical study. *Eur J Adv Eng Technol* 2(10):36–42
13. Maurya A, Jha PK (2014) Effect of casting speed on continuous casting of steel slab. *Int J Mech Eng Robot Res* 1(1):13–21
14. Amin MR, Gawas NL (2003) Conjugate heat transfer and effects of interfacial heat flux during the solidification process of continuous castings. *J Heat Transfer* 125(2):339–348
15. Luo Y, Zhang Z (2019) Numerical modeling of annular electromagnetic stirring with inter-cooling in direct chill casting of 7005 aluminum alloy billet. *Progr Nat Sci: Mater Int* 29(1):81–87

16. Hao H, Maijer DM, Wells MA, Cockcroft SL, Sediako D, Hibbins S (2004) Development and validation of a thermal model of the direct chill casting of AZ31 magnesium billets. *Metall and Mater Trans A* 35(12):3843–3854
17. Hongjun HU, Zhang D, Fusheng PAN, Mingbo YANG (2009) Analysis of the cracks formation on surface of extruded magnesium rod based on numerical modeling and experimental verification. *Acta Metall Sin (English Letters)* 22(5):353–364
18. Hao H, Maijer DM, Wells MA, Phillion A, Cockcroft SL (2010) Modeling the stress-strain behavior and hot tearing during direct chill casting of an AZ31 magnesium billet. *Metall and Mater Trans A* 41(8):2067–2077
19. Eskin DG, Zuidema J Jr, Savran VI, Katgerman L (2004) Structure formation and macrosegregation under different process conditions during DC casting. *Mater Sci Eng, A* 384(1–2):232–244
20. Fjaer HG, Mortensen D, Håkonsen A, Sørheim EA (2016) Coupled stress, thermal and fluid flow modelling of the start-up phase of aluminium sheet ingot casting. In: *Essential readings in light metals*. Springer, Cham, pp 737–742
21. Barral P, Quintela P (1999) A numerical method for simulation of thermal stresses during casting of aluminium slabs. *Comput Methods Appl Mech Eng* 178(1–2):69–88
22. Begum L, Hasan M (2014) 3-D CFD simulation of a vertical direct chill slab caster with a submerged nozzle and a porous filter delivery system. *Int J Heat Mass Transf* 73:42–58
23. Weckman DC, Niessen P (1982) A numerical simulation of the DC continuous casting process including nucleate boiling heat transfer. *Metall Trans B* 13(4):593–602

Mathematical Modeling of a Skin Condenser with Angular Contact for Domestic Refrigerator



N. D. Shikalgar , S. N. Sapali , and A. B. Shinde 

Abstract The refrigerator in the home is a necessary item. As a result, with being built each year, it is critical to account for such a big number of refrigerators refrigerator's energy use. The purpose of this research is to improve the thermal efficiency from the condenser tube to the refrigerator's metallic wall. Wire tube condensers were used in older refrigerators. Manufacturers have replaced the wire tube condenser with a skin condenser due to the likelihood of leaking during shipping and a loss in heat transmission due to fouling. The average heat flow from the skin condenser to the atmosphere is between 135 and 142 W/m², with a temperature gradient of 10–43/m along the skin condenser's surface. The mathematical model presented is used to predict the rate of heat transfer from a condenser tube with angular contact. To expand the surface area of the condenser tube, it is supported by a hemispherical cross-sectioned plate. The simulation result shows a 9.3% increase in heat transfer through the walls and a 50% reduction in the temperature of the polystyrene surface. The heat load on the refrigerator is lowered by 2 to 4% as a result of the skin condenser.

Keywords Refrigerator · Numerical simulation · Skin condenser · Heat transfer

1 Introduction

In the refrigeration cycle, there are six basic components compressor, evaporator, capillary tube, condenser and polyurethane foam. Two types of condensers are often used in small-to-medium-sized residential refrigerators. Condenser tubes with welded wires (fins) situated outside the cabinet are known as external condensers. Condenser tubes are attached to the inside surface of the outer wall and are not visible from the outside in the second form known as a “skin condenser.” In current refrigerators, a skin condenser, also known as a hot-wall condenser, has replaced the wire

N. D. Shikalgar (✉) · S. N. Sapali · A. B. Shinde

Department of Mechanical Engineering, College of Engineering Pune, Pune, Maharashtra, India
e-mail: nds.mech@coep.ac.in

S. N. Sapali

e-mail: sns.mech@coep.ac.in

tube condenser. The geometry of the skin condenser is a simple heat exchanger. The aluminum foil, as an adhesive tape as shown in Fig. 1, holds the condenser tube with a galvanized plate, which acts like a fin to increase the heat transfer area. Aluminum tapes were widely used in the appliance industry to adhere to tubes inside refrigerators to optimize the production process and increase the thermal performance of refrigerators. It is very important to ensure that the tubes are in contact with the wall of the refrigerator before injecting the polyurethane (PU) so that it will not be able to enter between the tube and the wall, which would fail the heat exchange system.

The polyurethane foam (PUF) acts as insulation and prevents the amount of heat transfer to the refrigerator. The biggest benefit of skin condensers is low manufacturing costs and a slight profile. The skin condensers are installed at the three sides of the refrigerator. The cross-section of the actual skin condenser used in the domestic refrigerator is shown in Fig. 2. The materials used for the skin condenser tube are copper, steel, or aluminum. They are in direct contact with the iron plate and on the sidewalls of the refrigerator, which acts as a fin.

The mathematical model of a skin condenser is developed by Bansal and Chin [1], and they were able to validate the experimental results. Banal has carried out a simulation study [2] on a hot-wall condenser with a finite-element method. Numerical and

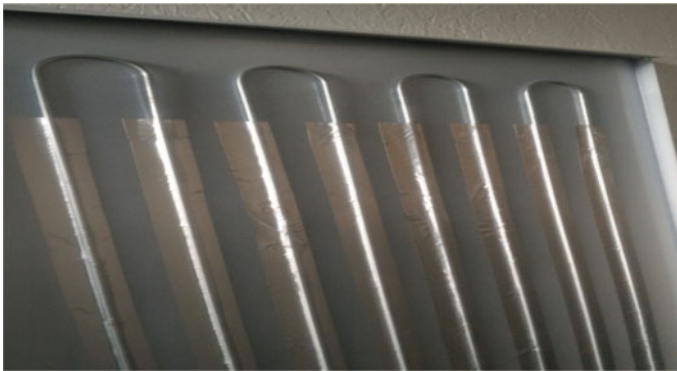


Fig. 1 Aluminum foil as an adhesive tape

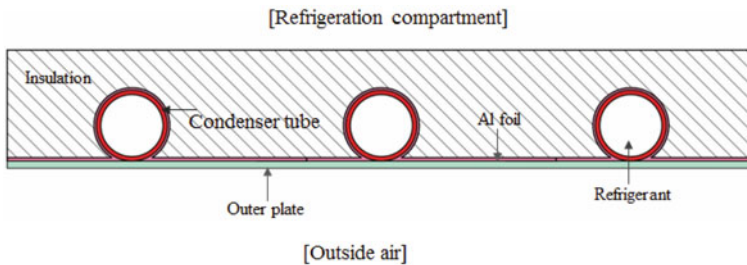


Fig. 2 Cut sectional model skin condenser used in the refrigerator

experimental data anticipated the skin condenser’s performance. The mathematical model is presented by Elias Gava based on Colombo heat diffusion equation [3], with the aluminum halt in its tracks and steel plate serving as fins. Experiments are used to corroborate the analytical results. Gupta and Gopal [4] have proposed a mathematical model of hot-wall condensers to predict the heat transfer characteristics of the condenser. Raiyani et al. [5] has studied the effect of geometrical parameter on thermal performance of condenser by changing the contact between tube and plate by line contact between plate and tube. Modeling and simulation of a hot-wall condenser applied to domestic refrigerator is presented by Sapali [6]. Lorbek et al. [7] have developed an analytical model and numerical simulation of heat transfer in a skin evaporator. He represented a simplified methodology for analytical modeling of skin evaporators based on diffusion equations assuming a two-dimensional case. A numerical simulation was done in ANSYS Fluent. The focus of this research is on the condenser wall’s composite construction and the influence of the parameter on heat transfer. The numerical simulation in ANSYS yielded the following findings. The results are presented fluently and analytically.

The temperature distribution is calculated using the steady-state energy conservation equation using aluminum foil. The fin model of a single element is presented in Fig. 3. The model consists of an aluminum foil, which is divided into two sections. The path of heat transfer to Sects. 1-2 is from the refrigerant to condensing tube by convection and then condenser tube to aluminum foil by conduction. Section 2 consists of aluminum foil in contact with the outer metal sheet on one side and insulation on the other side. The heat in Sects. 2-3 is carried out by conduction in aluminum foil and passed to ambient through outer metal sheet by convection. In Sects. 3-4, heat is transferred to the atmosphere.

The heat transfer in Sect. (1-1’) to (2-2’) is from the refrigerant to condensing tube by convection and then condenser tube to aluminum foil by conduction. The second section consists of an aluminum foil that is in contact with an outside plate on one side and PUF on the other side. The heat is carried out from the third section to the ambient through the outer metal sheet. The heat transfer in the various sections is presented in Fig. 4.

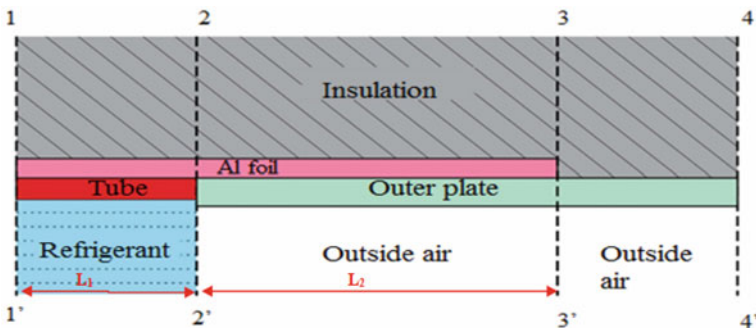
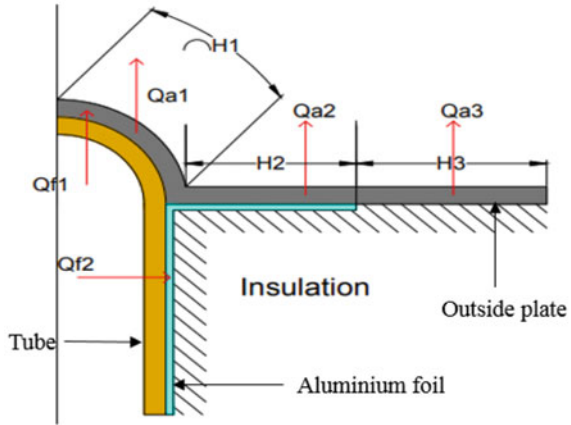


Fig. 3 Fin model of half part of a single element

Fig. 4 Actual model of an elemental section



The values of temperature at the interface are calculated using equating heat transfer rates at different sections. The energy-balance equations represent a system of linear equations. To obtain the values of the constant and junction temperature of the system, equations are solved in MATLAB code. The heat transferred from the condenser tube to the air is composed of three parts. It can be then expressed by Eq. 1.

$$Q_{ae} = Q_{a1} + Q_{a2} + Q_{a3} \tag{1}$$

The heat transfer from section (Q_{a1}) to air is calculated by Eq. 2.

$$Q_{a1} = \frac{(T_r - T_{\infty}) \times A_{A-2}}{(R_r + R_t + R_p + R_{\infty})} \tag{2}$$

The heat transfer from section (Q_{a2}) to air is calculated by Eq. 3.

$$Q_{a2} = \frac{(T_{f23} - T_{\infty}) \times A_{2-3}}{(R_p + R_{\infty})} \tag{3}$$

The heat transfer from section (Q_{a3}) to air is calculated by Eq. 4.

$$Q_{a3} = \frac{(T_{p23} - T_{\infty}) \times A_{3-4}}{(R_{\infty})} \tag{4}$$

Convection and radiation are used to transport heat from the outer layer to the surrounding environment. As a result, the total of convection and radiation heat transfer coefficients is the outer heat transfer coefficient [8].

$$H_{C_{total}} = H_{C_o} + H_{O_r} \tag{5}$$

Nusselt number is used to calculate average convective heat transfer.

$$Hc_o = \frac{Nu_0}{L_{c0}} K_0 \tag{6}$$

In the case of natural convection, the average Nusselt number correlation for a vertical flat plate is given by,

$$Nu_0 = \left[0.825 + \frac{0.387Ra_o^{1/6}}{\left[1 + (0.492/Pr)^{9/16} \right]^{8/27}} \right] \tag{7}$$

where

$$Pr = \frac{\mu_{air} C_{p,air}}{K_{air}} \tag{8}$$

The convective heat transfer coefficient for single-phase flow varies depending on whether the flow is laminar or turbulent. When the flow is turbulent, the Nusselt number correlates. The convective heat transfer coefficient is computed using equation employing the Nusselt number from Eq. 9.

$$Hc_{ref} = \frac{Nu_{ref}}{d_i} K_{ref} \tag{9}$$

2 Heat Path Analysis of Skin Condenser

ANSYS Fluent is used to do steady-state numerical simulations of two-dimensional heat transfers inside a skin condenser. Mesh independence shows that for condenser tube element size is 0.135 mm and for Metal sheet—0.2 mm, aluminum tape—0.0333 mm, PUF—0.5 mm and Polystyrene—0.2 mm. Heat transfer rate is depending upon the heat transfer area, the width of the heat transferring element, and the temperature gradient occurs. In this analysis, as mostly concentrate on heat transfer through composite wall element, hence variation in other parameters like the diameter of condenser tube and length of condenser tube is not considered. As the refrigerant is having a constant temperature in a particular region, hence we assume that constant temperature input at the inner surface of the tube. The outer surface of the back panel is exposed to the environment. From the literature survey, it is observed that for a vertical plate with natural flow heat transfer coefficient value for air is varying between 6 and 9 W/m²K. The average value of heat transfer coefficient 7.89 W/m²K at an ambient temperature of 28 °C is considered. Heat transfer takes place in radial direction hence all the surfaces in the normal direction is having symmetric wall boundary conditions that are all normal direction walls are insulated. The value of

the heat transfer coefficient inside the refrigerator is equal to $2 \text{ W/m}^2\text{K}$ at $50 \text{ }^\circ\text{C}$ average temperature refrigerator compartment. The outer steel plate works as a fin in the meshing of the hot-wall condenser, as seen in Fig. 5. The plate is provided for an increase in the contact area in convective heat transfer. By the use of fins, the contact area of the tube to air is increased; therefore, the heat transfers rate increase. In skin condense composite structure, heat is dissipated from refrigerant to aluminum tube, aluminum foil, air cavity, PUF insulation, steel plate and atmosphere by conduction and convection. The thermal analysis is shown in Fig. 8.

The simulation model for a skin condenser is developed using a finite-element variable conductance approach [2]. The simulation model is used to characterize the heat transfer analysis of the condenser. The simulation is carried out under certain assumptions, which includes the geometrical dimensions of the refrigerator and saturation temperature ($T_{\text{sat}} = 46 \text{ }^\circ\text{C}$).

The heat is conducted from flowing refrigerant to condenser tube and then rejected to the environment through rear and side panels of a refrigerator. A small amount of heat conduction takes place from the aluminum tape to the foam insulation and then it leaks into the refrigerator compartment. The thermal analysis is carried out on a simulation model by using the finite element method. The results of the thermal analysis show the variation in temperature gradient and heat flux concerning PUF insulation thickness as shown in Fig. 6.

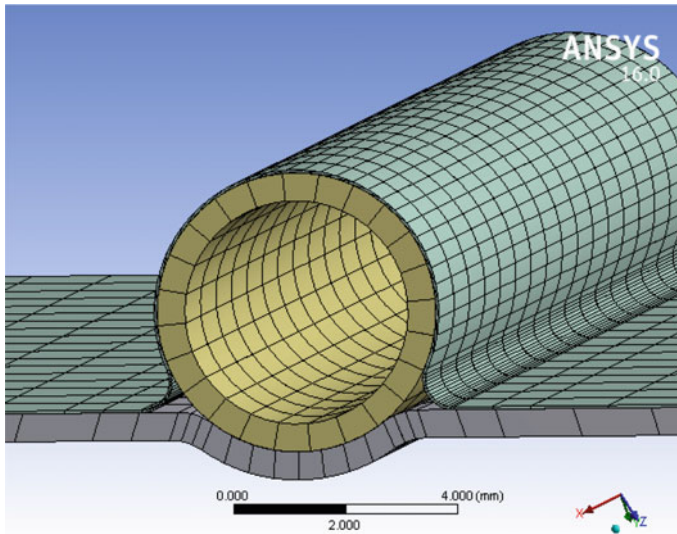


Fig. 5 Meshing of a single element with foil

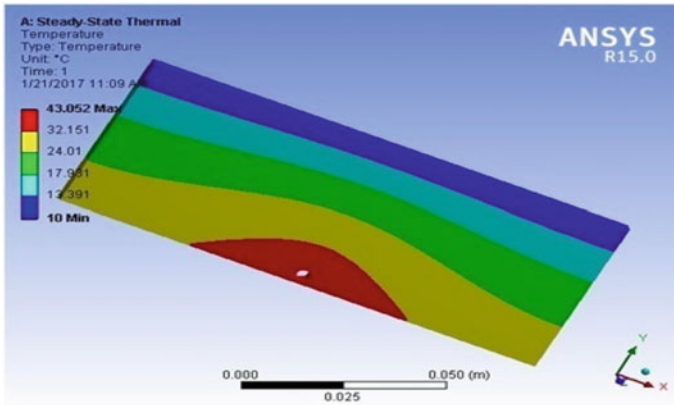


Fig. 6 Heat distribution along with the element of condenser tube

3 Heat Path Analysis of Skin Condenser with Angle

Total heat flux without aluminum foil with $h = 6 \text{ W/m}^2\text{K}$. The result of heat flux is almost the same throughout the whole tube plate configuration. The value of average heat flux is within the range of $42.5\text{--}68.5 \text{ W/m}^2$ for the backplate. The effect of change in contact angle on outside heat flux within skin condenser is presented in Fig. 7. The results show that the outside heat flux is a minimum of 143.38 W/m^2 with point contact and the heat flux is increasing to 156 W/m^2 at a 180° contact angle. The heat flux is increased due to the increase in contact surface area of the condenser tube with the plate. The effect of an increase in heat flux reduces the condenser tube length is by 5 m. As given in Table 1, the heat flux at a point of contact with 0° on the surface of the refrigerator compartment equals 18.0248 W/m^2 (Fig. 8).

It is clear that as contact between tube and plate is changed from point contact to angular contact, inside heat flux decreases. The variation in the inside heat flux is shown in Fig. 9. The net heat load in the refrigerator is reduced by 4 W/m^2 .

The influence of condenser pipes contact angle on the heat transfer performance of hot-wall condenser is studied. When the pipe's contact angle is increased from 0° to 45° , the hot-wall condenser has almost the same heat flux. From the present work, it is stated that if the contact angle is increased from 60° to 180° , there is an increase in heat flux.

4 Conclusion

The paper proposes a mathematical model that uses basic heat transfer equations to unravel the heat flow in a skin condenser structure, with numerical simulation serving as a reference for the analytical model. The mathematical models and simulation

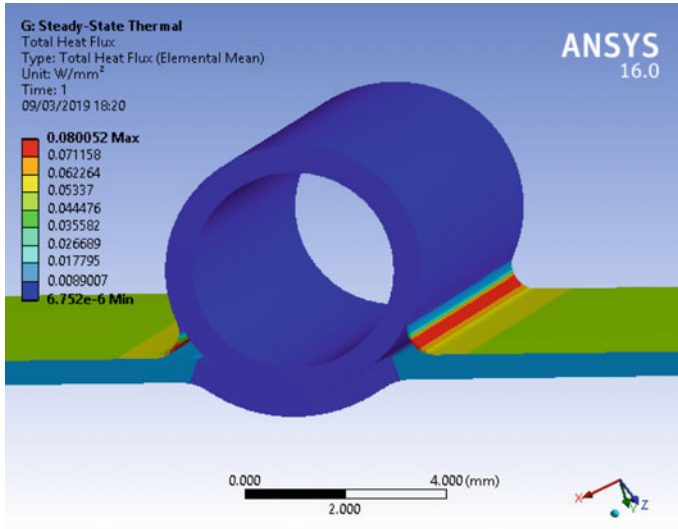


Fig. 7 Heat flux of an element with aluminum foil

Fig. 8 Deviation of outside heat flux with an angular contact

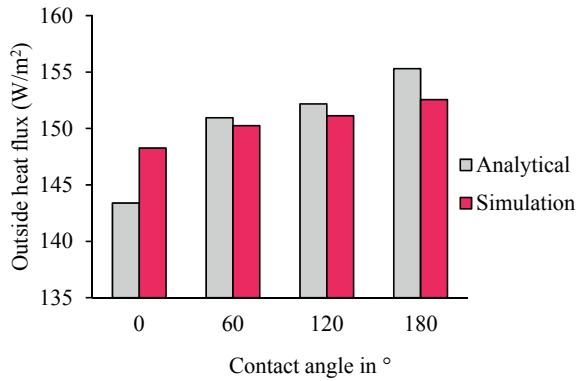
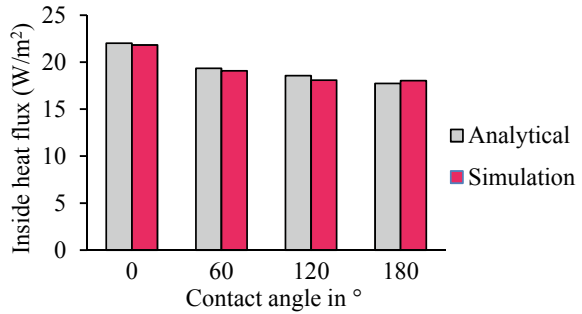


Table 1 Comparison of performance of the condenser for different cases

Sr. No.	Configuration of skin condenser	Outside heat flux (W/m ²)	Inside heat flux (W/m ²)
1	0° contact angle without aluminum foil	131.654	23.0462
2	0° contact angle with aluminum foil	148.310	21.820
3	60° contact angle	150.246	19.070
4	120° contact angle	151.134	18.078
5	180° contact angle	152.564	18.025

Fig. 9 Deviation of inside heat flux with an angular contact



outcomes were found to agree. The study’s findings are used to draw the following conclusions.

1. The slight temperature differential, along with the aluminum foil, can be attributed to heat conduction, demonstrating the need to include that parameter in the calculation.
2. When compared to the existing hot-wall condenser, the heat flow of the skin condenser with the atmosphere is increased by 8–10%.
3. The quantity of heat that enters the refrigerator compartment through the skin condenser is lowered by 2–4%.
4. A skin condenser with angular contact reduces the necessary condenser cooling length by 4 m for the same condenser cooling.

References

1. Bansal PK, Chin TC (2002) Design and modelling of hot-wall condensers in domestic refrigerators. *Appl Therm Eng* 22(14):1601–1617
2. Bansal PK, Chin T (2003) Heat transfer characteristics of wire-and-tube and hot-wall condensers. *HVAC&R Res* 9(3):277–290
3. Colombo EG, da Silva Espíndola R, Knabben FT, Melo C (2016) A numerical and experimental study on skin condensers applied to household refrigerators. In: 16th International refrigeration and air conditioning conference at Purdue, 11–14 July 2016
4. Gupta JK, Gopal MR (2008) Modeling of hot-wall condensers for domestic refrigerators. *Int J Refrig* 31(6):979–988
5. Raiyani AD, Sheth NR, Mehta NC (2014) Thermal analysis of hot wall condenser for domestic refrigerator. *Int J Sci Res* 3(7):622–626
6. Shikalgar ND, Sapali SN (2019) Energy and exergy analysis of a domestic refrigerator: approaching a sustainable refrigerator. *J Therm Eng* 5(5):469–481
7. Lorbek L, Poredoš P, Kitanovski A, Poredoš A (2018) Analytical modeling and numerical simulation of heat transfer in a skin evaporator. *Int J Refrig* 88:195–203
8. Bergman TL, Incropera FP, DeWitt DP, Lavine AS (2011, Apr 12) *Fundamentals of heat and mass transfer*. John Wiley & Sons

Aerodynamic Analysis of Deployable Wing Arrangement for Space Shuttle



Vidya Chandran , Poornima Rajendran, Shabu Gopakumar, K. S. Arun Kumar, C. A. Nikhilraj, and Sheeja Janardhanan 

Abstract The study space for morphing wings is astonishingly wide and provides ample scope for enhancements up against fixed wings. Morphing-wing research has accumulated considerable recognition in the aerospace community over the last decade, and a folding wing is a promising approach that can improve aircraft proficiency over multiple varieties of missions which conclusively enhance the capability of the space shuttle. In this paper, the conventional shape of the wings is being refashioned to serve the requirements for maintaining the flight and also for navigation. The idea was sparked by the traditional Japanese fan and has a hinged mechanism similar to that of the fan. This work introduces a novel concept for retractable dynamic wings on a space shuttle. Modeling of the spacecraft with modified wings is done in SOLIDWORKS. The aerodynamic analysis is performed using the computational fluid dynamics (CFD) method with ANSYS FLUENT® (2020 R1) as the solver. The aerodynamic force coefficients are estimated for five different specific deployment phases, viz., zeroth (0°), one quarter (7.5°), half (15°), three-quarter (22.5°), and full (30°) phases. The result reveals that the coefficient of drag drops and the coefficient of lift rises from the primary phase to the final phase providing promising inputs into the idea of retractable wings.

Keywords Space shuttle · Retractable dynamic wings · CFD · Wing deployment

V. Chandran · P. Rajendran (✉) · S. Gopakumar · K. S. A. Kumar · C. A. Nikhilraj
Department of Mechanical Engineering, SCMS School of Engineering and Technology,
Ernakulam, Kerala 683576, India
e-mail: poornimamar@gmail.com

V. Chandran
e-mail: vidyachandran@scmsgroup.org

S. Janardhanan
School of Naval Architecture and Ocean Engineering, Indian Maritime University,
Visakhapatnam, Andhra Pradesh, India
e-mail: sheeja@imu.ac.in

1 Introduction

A space shuttle is a partially reusable rocket-launch vehicle meant to go into orbit about Earth, to transport people and cargo to and from orbiting spacecraft. Recent years have displayed increasing study and advancement in reusable and low-cost space travel with an uptick in the commercial space launch market. A considerable factor for the increase in the expense of space travel is the non-reusability of the space shuttle. During the re-entry of a space shuttle, a substantial amount of heat is generated as it reaches the atmosphere of the earth from space [1]. Temperatures exceeding 2000 K are produced due to the friction between vehicle and air. Since most metals and alloys cannot withstand these temperatures, a special class of materials known as ablators that act as heat shields are used. The ablator will be consumed in the heat, thus dissipating a large amount of heat. However, these conventional wing designs have numerous limitations. Due to the large number of forces acting on the wing during re-entry, the reusability is limited as the wing material gets consumed during re-entry [2]. Also, the wing can get damaged due to the same.

To overcome this, we have developed a new retractable wing mechanism that resembles the Japanese hand-fan, such that the wings of the space shuttle will be completely ducked inside the fuselage during re-entry, thus minimizing the influence of forces (here, the forces of gravity, drag, lift, etc., are considered) acting on the wings, which can result in a safer and economic space journey. The aerodynamic force coefficients of drag and lift forces are estimated numerically using CFD tools for five different deploying phases to study the effectiveness of the novel design. Based on the above analysis, this paper studies the aerodynamic performance of a space shuttle equipped with deployable wings, with an expectation of proving theoretical foundation and technical base for conceptual space shuttle design.

2 Materials and Methods

2.1 Geometry Acquisition

The conceptual modeling was performed in SOLIDWORKS 2016. The material selected for the model is a composite material using a heterogeneous composite material bonded by adhesives for making the wing structure lighter [3, 4]. The dimensions of the model were inherited from the famous Russian space shuttle BURAN, and the wing cross-section was modeled based on NACA 4412 aerofoil profile. It has a maximum thickness of 12% at 30% chord and maximum camber of 4% at 40% chord length, and a side view of the wing profile is presented in Fig. 1. The wingspan is 23.9 m which is equivalent to the BURAN space shuttle wingspan.

Fig. 1 Side view of the designed wing



2.2 Mesh Generation

The modeling and meshing were performed in ANSYS WORKBENCH[®] (2020 R2), and the flow analysis was performed using ANSYS FLUENT[®]. The flow around the space shuttle while deployed at different phases is simulated using RANS solver with $k-\epsilon$ as the turbulence model which assumes the turbulent viscosity is isotropic. In the standard $k-\epsilon$ model, the eddy viscosity is resolved from a single turbulence length scale, so the calculated turbulent diffusion is that which occurs only at indicated scale, whereas in reality, all scales of the motion will contribute to turbulent diffusion. The three-dimensional computational domain for the space shuttle used in the simulation is as shown in Fig. 2. The turbulence intensity is taken to be 5%. The flow direction is taken parallel to the z -axis with an inlet velocity of 150 ms^{-1} at the inlet. The size of the domain is chosen to be $80 \text{ m} \times 80 \text{ m} \times 120 \text{ m}$ in dimension for capturing the flow. The nose of the shuttle is modeled 21.6 m from the inlet boundary of the domain. Figure 2 shows the computation domain used in the present simulations.

The origin of the cartesian coordinate system is at the center of the space shuttle. The distance from the inlet of the domain to the outlet of the coordinate system is 120 m , and the distance from the inlet and the outlet to the origin, located at the

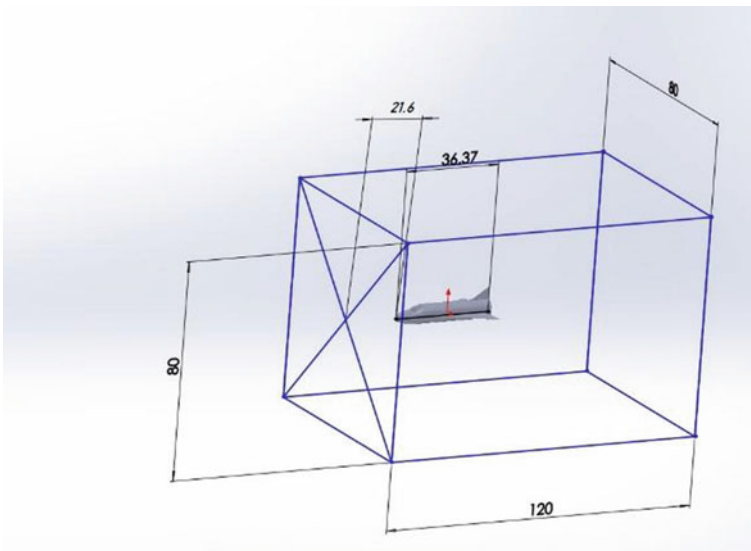


Fig. 2 Computational domain

geometric center of the space shuttle, is 40 m and 80 m, respectively. An unstructured grid consisting of tetrahedral elements was generated with a maximum element size of 0.3 m in the region of spacecraft and the rest of the domain meshed with elements having a maximum size of 2.3 m.

2.3 Flow Analysis

Analysis of the different deployment phases was performed in ANSYS FLUENT®. This renormalization group (RNG) approach of $k-\epsilon$ can be applied to conclude a turbulence model that results in a revised form of the epsilon equation which endeavors to sum for various scales of movement through changes in the production term. Equations (1) through (5) give the transport equation for k and ϵ as a simple interpretation where buoyancy is disregarded. Here, k connotes the turbulent kinetic energy, while the ϵ identifies with the pace of dispersal of turbulent kinetic energy [5, 6].

$$\frac{\partial}{\partial t}(\rho k) + \frac{\partial}{\partial x_i}(\rho k u_i) = \frac{\partial}{\partial x_j} \left[\left(\mu + \frac{\mu_t}{\sigma_k} \right) \frac{\partial k}{\partial x_j} \right] + P_k - \rho \epsilon \quad (1)$$

$$\frac{\partial}{\partial t}(\rho \epsilon) + \frac{\partial}{\partial x_i}(\rho \epsilon u_i) = \frac{\partial}{\partial x_j} \left[\left(\mu + \frac{\mu_t}{\sigma_f} \right) \frac{\partial \epsilon}{\partial x_j} \right] + C_{1\epsilon} \frac{\epsilon}{k} P_k - C_{2\epsilon}^* \rho \frac{\epsilon^2}{k} \quad (2)$$

where

$$C_{2\epsilon}^* = C_{2\epsilon} + \frac{C_\mu \eta^3 (1 - \eta/\eta_0)}{1 + \beta \eta^3} \quad (3)$$

$$\eta = S k / \epsilon \quad (4)$$

$$S = (2 S_{ij} S_{ij})^{1/2} \quad (5)$$

The velocities and other solution variables in the preceding equation represent the time-averaged values. The $k-\epsilon$ model which is designed specifically for planar shear layers and recirculating flows and can be used in this application since it effectively resolves free-shear layer flow. $k-\epsilon$ SST model is capable of simulating the flow characteristics for turbulent flow conditions. The simulations were performed for five specific deployment phases 0° , 7.5° , 15° , 22.5° , and 30° . For the sidewalls of the domain, a wall boundary with the specified shear condition is applied assuming the surfaces to be smooth. Specified velocity inlet boundary condition is employed at the inlet boundary of the domain, and the outlet boundary is treated as a pressure outlet.

2.4 Grid Independency Analysis

The grid independency study performed shows the following results as presented in Table 2 for the fully deployed phase. Grid 3 consisting of 502,302 elements that could successfully predict the aerodynamics lift coefficient (C_L) with 99.2% accuracy was considered for performing further analysis for the other phases. The lift values predicted by Grid 3 are verified by the experimental/numerical analysis performed for a similar spacecraft referred to in previously published work [7] where the value of the lift was determined as in Table 1.

3 Wing Design

The wing mechanism is inspired by Japanese hand-fans, a model of which is shown in Fig. 3.

The idea is to incorporate the entire design to the wings of a space shuttle while retaining the aerodynamic characteristics of the traditional wings in a fully deployed

Table 1 Comparison from wing profile

Derived from	C_L
NACA 4412 profile	0.5
Fully deployed condition	0.506

Table 2 Results of grid independency study

	Re	Phase	Number of elements	C_L
Grid 1	10^6	Deployed fully	254,234	0.527
Grid 2			365,903	0.511
Grid 3			502,302	0.506
Grid 4			702,053	0.505

Fig. 3 Traditional Japanese hand-fan





Fig. 4 Wing design and arrangement of leaves

configuration. In the pre-deployment phase, the entire wing structure will be stored inside the fuselage of the space shuttle. During landing, the wing will be deployed replicating the opening and closing action of a Japanese hand-fan. After several initial design concepts, through iterative designing, the design presented in Fig. 4 has been arrived at.

3.1 Deployment Mechanism

The wing consists of three segments called “leaves” as shown in Fig. 3. Each leaf operates in a manner to provide an increase in lift and reduction in drag as the deployment progresses, and this idea for deploying the wing was made from analyzing the morphing wing [8, 9] technologies currently in use, but with a different approach to the scenario [10, 11].

The wing is operated by a shaft driven by a multidrive mechanism consisting of an electric motor and hydraulic lift. The wings are initially held inside the body of the space shuttle, and each leaf is deployed at a slow pace such that the leaves are not subjected to shock waves. The first leaf which is fixed to the shaft deploys from the spacecraft fuselage through an angular displacement about the shaft. Progressive deployment phases of the wing leaves are presented in Figs. 5 and 6.

Fig. 5 First leaf deployment and second leaf initiation

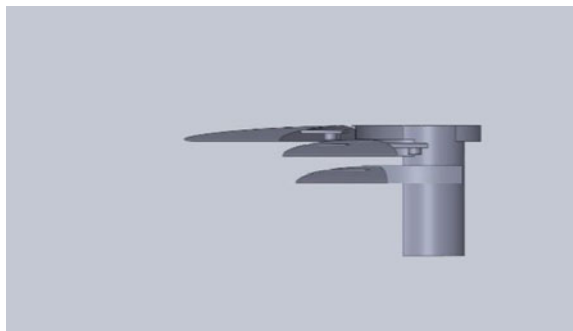


Fig. 6 Second leaf deployment and third leaf initiation

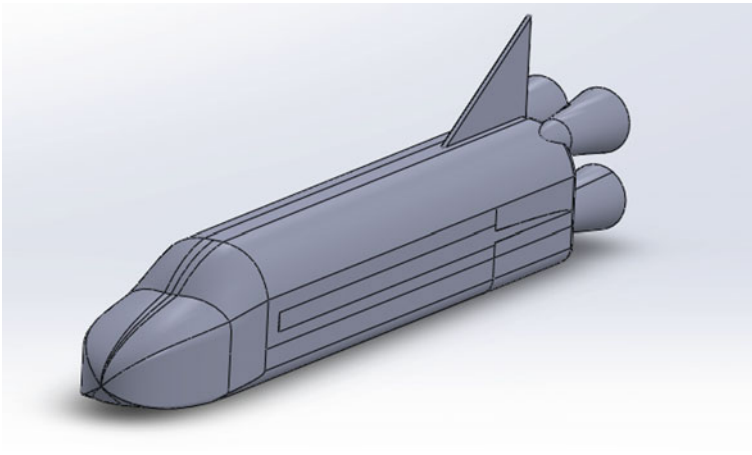


Fig. 7 Bare space shuttle

The second leaf, when deployed, initially is lifted with the help of a shaft driven by the motor to the level of the first leaf and interlocks with it and rotates out of the body. This process is repeated similarly for the third leaf where it lifts and advances out. The third leaf is accompanied by a hydraulic lift which is positioned beneath it, which also acts as a backing structure for the entire leaf setup against the pressure, while the shuttle orients for landing. A model of the bare space shuttle that re-enters the atmosphere without wings and the one with a fully deployed wing during landing is shown in Figs. 7 and 8.

3.2 Wing Deployment—Phases

The complete deployment of the wing happens through five phases, each of which is accomplished through a specific angle of deployment. They can be listed as:

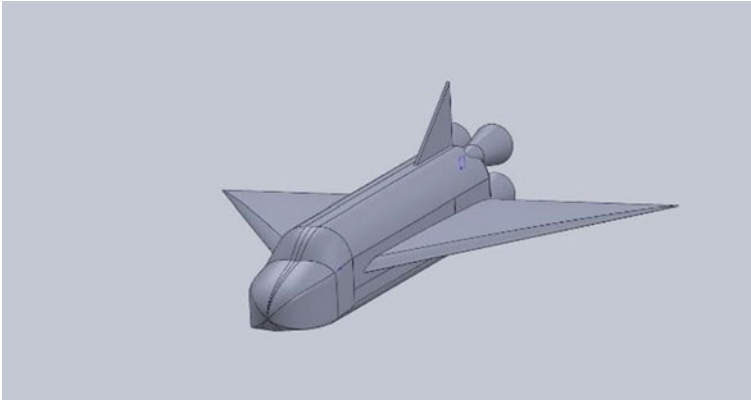


Fig. 8 Shuttle after full deployment

- Zeroth phase—no deployment (0°) (Bare spacecraft)
- One-quarter phase—wing deployed through 7.5 degrees (7.5°)
- Half phase—wing deployed through 15 degrees (15°)
- Three-quarter phase—wing deployed through 22.5 degrees (22.5°)
- Full phase—full deployment of the wing (30°).

The spacecraft model at each phase of deployment is modeled and analyzed for the lift and drag generated during various deployment phases using ANSYS FLUENT®.

3.3 Estimation of Wing Deployment Rate (WWR)

The atmospheric air interference prompts the object to undergo drag, or air resistance, which hinders down the object to a more reliable entry speed, generating intense heat. The heat will either blend or sublimate any material exposed to the shock wave, and since aluminum alloys are employed mostly [12] for the construction of spacecraft, in most cases, the spacecraft wing is damaged due to this high pressure and temperature during the re-entry. When an object with the blunt-shaped frontal area re-enters into the Earth's atmosphere, a shock wave is formed ahead of the vehicle. As the shock wave keeps the heat at a range from the object, the blunt shape also stalls the object's descent. The Apollo program, which operated several manned ships back and forth from space during the 1960s and 1970s, coated the command module with special ablative material that flared up upon re-entry, absorbing heat [2].

Deployable wings are needed to reduce friction and also offer a large wingspan for long endurance flights. This system also provides potential space savings due to function sharing of components.

Maneuvering takes place once the shuttle travels sub-sonically before landing. During maneuvering, the crew takes control of the flight. The approach and landing

phase begins when the shuttle is at an altitude of 4000 m (13,000 ft) and traveling at 150 m/s. The vehicle follows either a -20° or -18° glideslope and descends at approximately 51 m/s (167 ft/s) [13]. The speed brake is used to keep a continuous speed with touchdown occurring at 100–150 m/s, depending on the weight of the vehicle. After the landing gear touches down, the crew deploys a drag chute out of the vertical stabilizer and begins wheel braking when the vehicle is traveling slower than 72 m/s. After the wheels halt, the crew deactivates the flight components and prepares to exit [14].

In the proposed deployment landing, the space shuttle wing deployment starts at a height of 4000 m above the earth's surface since the deployment is supposed to happen in a subsonic region, where the crew takes control over the flight. The wing deployment rate is optimized for the proper functioning of the wings.

Considering full deployment before the vehicle lands, the range between 4000 and 2000 m is taken for the calculation of the wing deployment rate. The velocity of the vehicle during this range is 150 m/s. Time taken for full deployment, T_d is given by Eq. (6).

$$T_d = \frac{H}{U} \quad (6)$$

where H is the altitude above the mean sea level and U is the vehicle velocity at that altitude. Thus, the time taken for the full deployment of the wing will be 13.34 s. The total angular measurement of the wing is 30° . Therefore,

$$\dot{\psi} = \frac{\psi}{T_d} \quad (7)$$

where $\dot{\psi}$ is the rate of deployment and ψ is the total angle of deployment.

Finally, the deployment rate is calculated as 2.25°/s.

4 Space Shuttle Conceptual Design

The exact parameters of the BURAN space shuttle were preferred as the reference parameters for the simulation. The BURAN was selected out of all shuttles owing to its simplified design listed as follows [15]:

- Main rocket engine is not present on the shuttle. The main engine was mounted on the central block of ENERGIA, the rocket carrier which launched 120 tons payload into the orbit against 30 tons the shuttle.
- Maximum ratio of lift to drag is 6.5 for BURAN, while it is 5.5 for the space shuttle.
- The payload returned by BURAN from an orbit to the aerodrome is 20 tons and that for the space shuttle, it is only 15 tons.

Table 3 Dimensions of BURAN

Length	36.37 m (119.3 ft)
Wingspan	23.92 m (78.5 ft)
Height on gear	16.35 m (53.6 ft)
Payload bay length	18.55 m (60.9 ft)
Payload bay diameter	4.65 m (15.3 ft)

Fig. 9 BURAN top view

- The thermal protection tiles of Buran have optimal cutting layout design.
- The automated landing of Buran from orbit onto an airdrome.

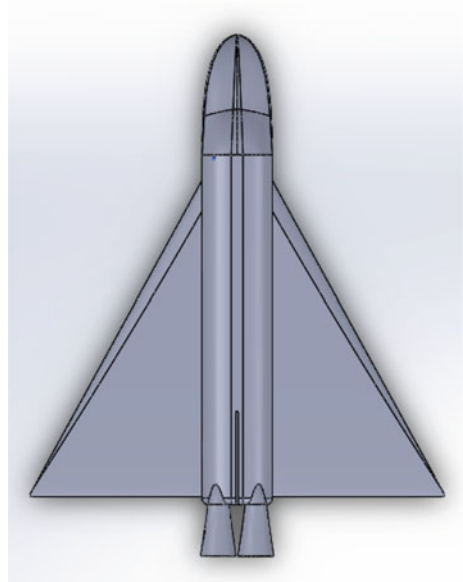
The dimensions of BURAN are given in Table 3.

The modeling of the space shuttle with modified wings is done in SOLIDWORKS. A representation of the model generated is shown in Fig. 10 and original BURAN reference in Fig. 9.

5 Results and Discussions

The origin of the space shuttle lies inside the domain at 40 m from the inlet and 80 m away from the outlet. The width of the domain is 40 m, and the geometry is placed with its nose pointing in the positive direction of the Z -axis, while the tail of the space shuttle points to the negative Z -axis. As a result, the drag force was developed in the negative Z -axis, while the lift was generated in the positive Y -axis. The following results were obtained after the analysis of each phase. Models of the space shuttle

Fig. 10 Top view of the conceptual design of a fully deployed wing



during various phases of the deployment are shown in Figs. 11 and 12. Computed coefficients of drag and lift are tabulated and presented in Table 4.

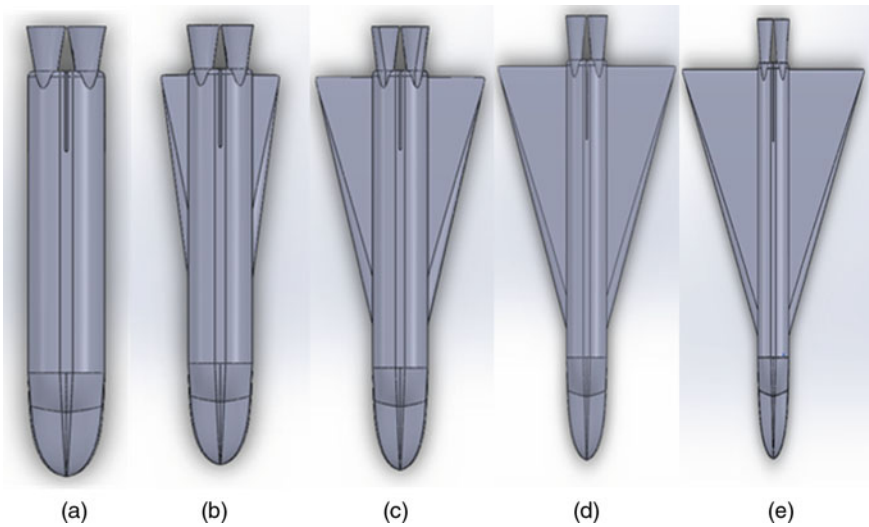


Fig. 11 Top view of the modeled space shuttle at various phases of wing deployment **a** zeroth phase **b** one-quarter phase **c** half phase **d** three-quarter phase **e** full phase

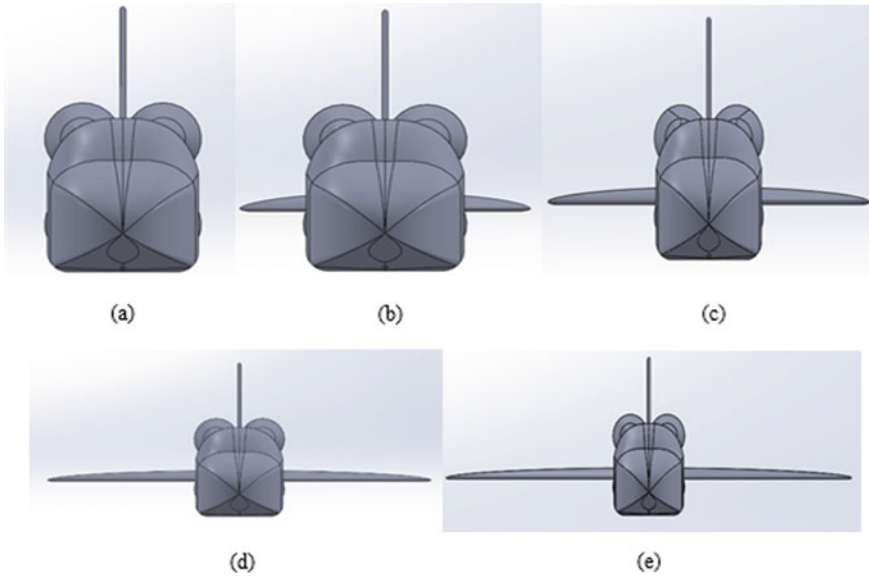


Fig. 12 Front view of the modeled space shuttle at various phase **a** zeroth phase **b** one-quarter phase **c** half phase **d** three-quarter phase **e** full phase

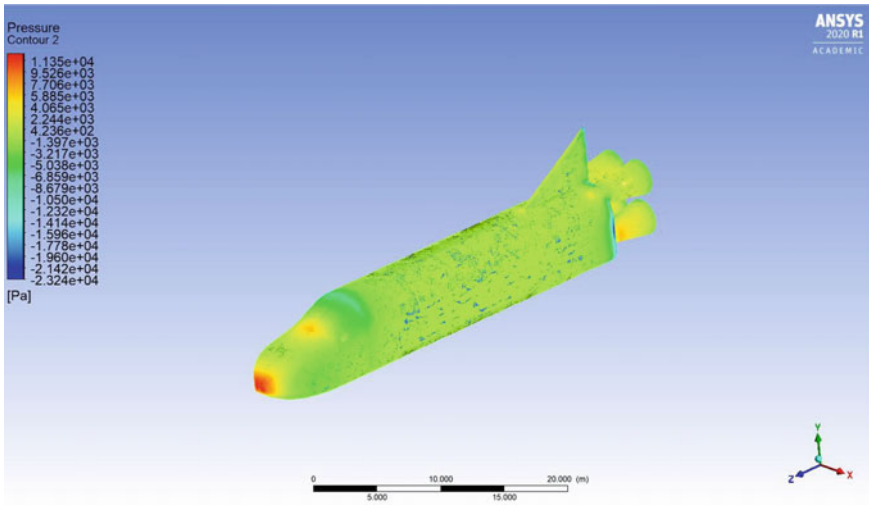
Table 4 Simulation results for various phases from numerical simulation

Phases	Coefficient of drag	Coefficient of lift
0	0.32	-0.12
7.5	0.28	-0.01
15	0.26	0.22
22.5	0.20	0.37
30	0.18	0.51

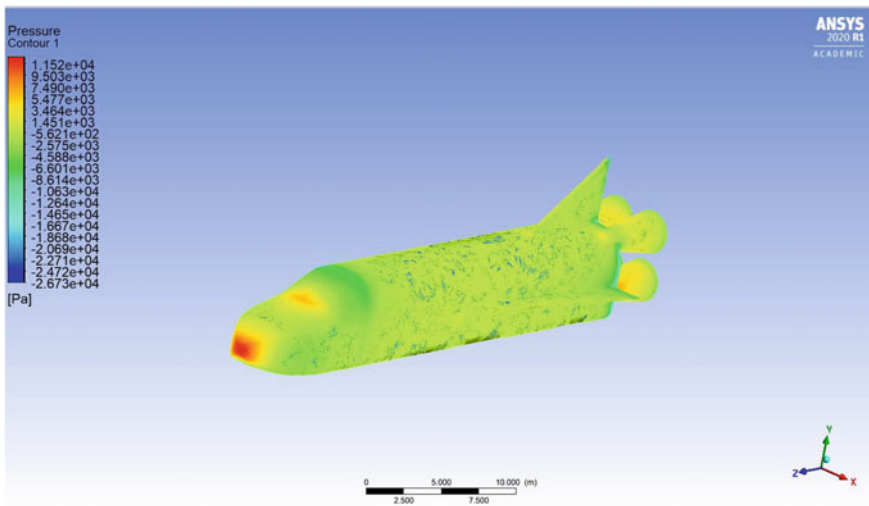
5.1 Zeroth Phase (0°)

In this phase, the wings are stacked inside the body of the space shuttle. It is the pre-deployment phase. The meshing contains 92,427 nodes and 502,302 elements.

It is observed from the simulation results that the bare shuttle has a drag coefficient of 0.32, and there is no lift force due to the more or less asymmetrical shape of the fuselage in the absence of wings. During this phase, a negative lift coefficient indicates an added component force that helps in the landing of the aircraft. The pressure distribution on the body of the space shuttle during the zeroth phase of deployment is presented in Fig. 13a.



(a)

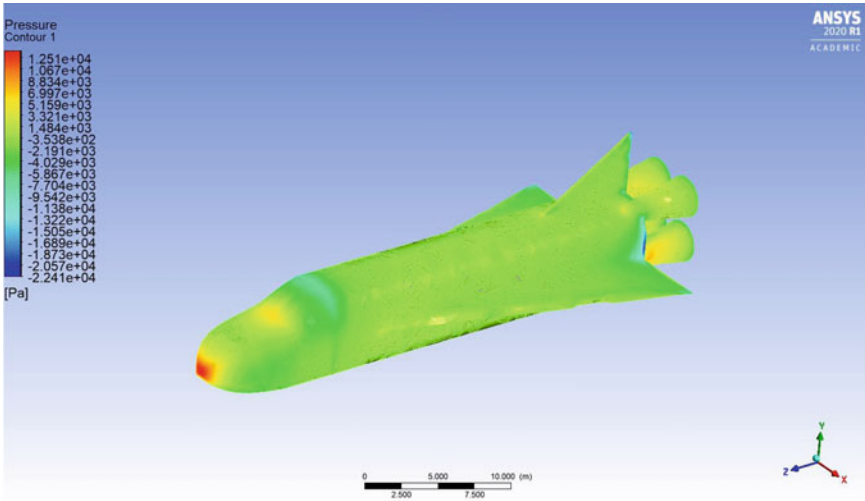


(b)

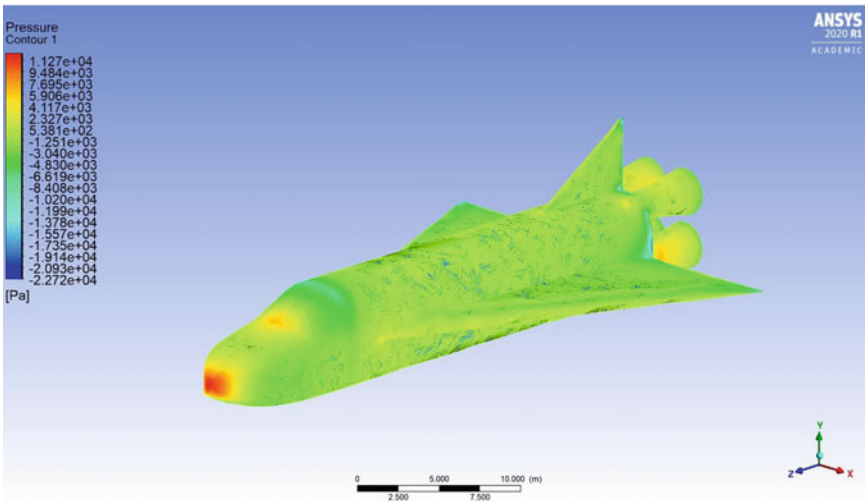
Fig. 13 Pressure contours of the modeled space shuttle at various phase **a** zeroth phase **b** one-quarter phase **c** half phase **d** three-quarter phase **e** full phase

5.2 One-Quarter Phase (7.5°)

In this phase, the first leaf starts to deploy and comes out of the space shuttle. The mesh contains 93,023 nodes and 509,754 elements. Due to the protrusion of the wing



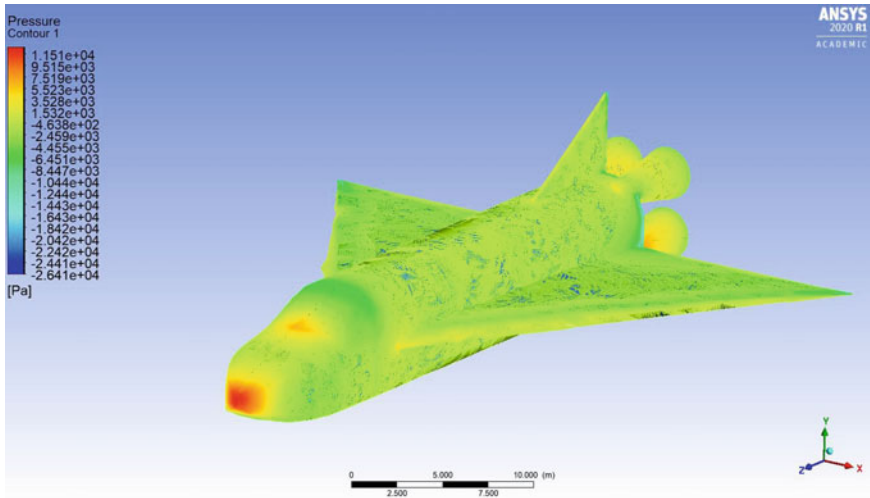
(c)



(d)

Fig. 13 (continued)

out of the body, a change in drag and lift is observed. Drag has shown a decrease with a coefficient value of 0.28 obtained from the simulation. The lift has not yet been generated considerably showing a slightly negative value for the coefficient. From the comparison with C_L obtained from zeroth phase analysis, the current phase showed a reduction in the component force directed in the vertically downward direction showing an almost zero lift generated. This condition is expected to give the crew



(e)

Fig. 13 (continued)

an upper hand in the maneuvering of the craft safely. This change is a result of the increased effective wingspan. The wing being an aerofoil is supposed to generate a pressure difference above and below the profile thus giving rise to lift forces. But, the current phase shows only a negligible lift generated, which demands further analysis of flight in this regime. The total air drag on the space shuttle considerably decreased as the wingspan increased. Pressure distribution during the current phase is shown in Fig. 13b.

5.3 Half Phase (15°)

In this analysis, the shuttle is modeled with its wings half deployed. The grid generated has 93,115 nodes and 510, 847 elements. From the results, it is observed that with halfway deployment of the wing has initiated the purpose for which it is meant to. The lift coefficient is observed to have drastically increased from almost zero value at quarter deployment to 0.22 when the wing is half deployed. During this transition regime from the quarter way deployment to halfway deployment of the wing, the space shuttle switches its state of motion from the freely falling state to a controlled flight. Pressure distribution on the shuttle with its wing half deployed is presented in Fig. 13c. Also, during this regime of flight, it is observed that the drag force has further decreased. The coefficient of drag (C_D) obtained from the half deployment simulation is 0.26, which is slightly lesser than the previous case.

5.4 *Three-Quarter Phase (22.5°)*

During the three-quarter phase, a further increase in the lift is observed for the space shuttle with C_L value of 0.36. The grid generated for this simulation has 93,244 nodes and 510,769 elements. Along with the increase in the lift, we can also observe a drastic reduction in the drag force with C_D value of 0.2 from the simulation. The notable reduction in drag force during the shift from half wing deployment flight to three-quarter wing deployment flight indicates the possibility of controllability and maneuverability to be gained by the space shuttle which was otherwise a freely falling body during this regime. At this phase of deployment, the aerodynamic force acting on the space shuttle is favorable to prepare for a controlled landing. The pressure distribution on the shuttle body obtained from the simulation is presented in Fig. 13d.

5.5 *Full Phase (30°)*

This is the fully deployed phase of the space shuttle. The entire wing that was stacked inside the body has finally come out making a much more favorable lift and drag distribution for the landing. The grid used for the full phase consists of 92,945 nodes and 510,146 elements. Values of coefficients of aerodynamic lift and drag obtained for each phase from simulations are presented in Table 4. Pressure distribution obtained from the full-phase simulation is presented in Fig. 13e.

Taking all the deployment phases into consideration, the trend was plotted to represent the variation of lift and drag during the deployment period. The graph shown in Fig. 14 represents the variation of drag force and lift force. It is observed that there exists a linear relationship between drag and lift coefficients during the deployment period. The values of drag and lift coefficients that are obtained from the present analysis for the full deployment phase is compared with results from the previously published analysis [7] on a NACA-profiled wing which gives the value of the coefficient of lift to be 0.5, while the lift is 0.01 for the NACA-profiled wing where the experimental value after considering the drag on the entire shuttle came to a conclusion of 0.5 coefficient of lift at 0.1 coefficient of drag.

Figure 15 represents the variation of the ratio of the drag coefficient to lift coefficient with degrees of wing deployment. The process of deployment can be divided into two separate phases. Phase A can be defined from the wing deployment initiation to the completion of the quarter deployment. During this phase, the shuttle is in a state of freely falling motion with a negligible wingspan to provide lift force. Phase B is defined from the initiation of half-phased deployment to the end of full-phase deployment. During phase B, the shuttle shifts its flight mode from a freely falling object to a more controlled flight. The slope of the relationship curves for phases A and B as observed from Fig. 15 shows a clear distinction between the two flight modes.

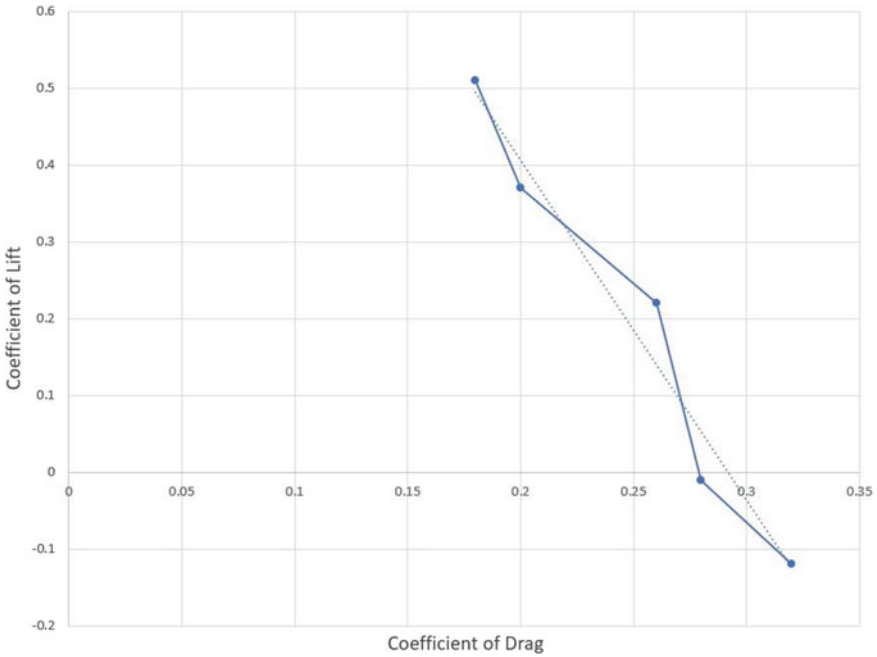


Fig. 14 Coefficient of drag versus coefficient of lift graph

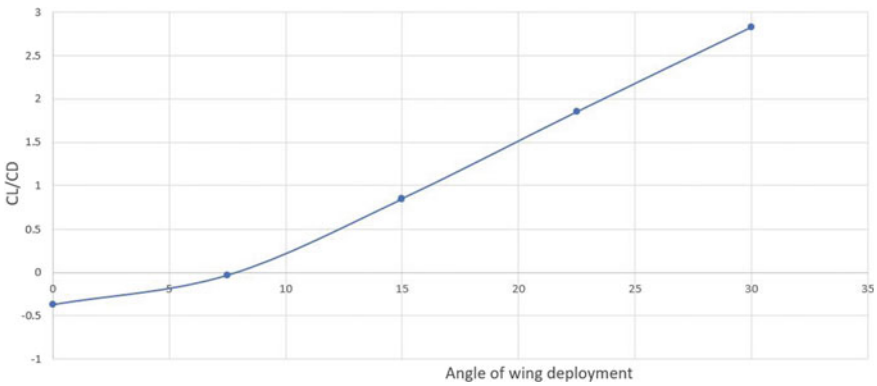


Fig. 15 C_L/C_D versus angle of wing deployment graph

6 Conclusion

This conceptual design, its modeling and simulation have put forward the fundamental theory and base for the development of a reusable wing for a space shuttle. As the shuttle passes from Phase A to Phase B, there is a drastic improvement in the

lift force generated by the wing. 43% of the total lift force generated by the wing develops on the shuttle during the deployment from the quarter angle phase to the half-angle phase. But, it is to be noted that during this phase transition, there is only a negligible reduction in the drag. Even though a 50% reduction is observed in the drag force from the bare shuttle to the full deployment phase, during the deployment period from quarter angle to half-angle, the drag remains almost constant. This phenomenon can be viewed as an indication of the shift from Phase A to Phase B as defined during which the space shuttle gains increased controllability and maneuverability.

The proposed design of the space shuttle could be made to glide with the mechanism of the dynamic fan wings. The drag and lift forces were comparably more favorable than with fixed wing design. The destruction of the wings by heating due to the re-entry can be avoided. This also tends to reduce the damage taken by the wings during the re-entry, thus making safer, economic, and reusable space travel.

References

1. Fuller M et al. Proposal for two-part recoverable launch system for unmanned payloads to LEO and GTO
2. Patera RP, Ailor WH (1998) The realities of reentry disposal. *Adv Astronaut Sci* 99:1059–1071
3. Diaconu CG, Weaver PM, Mattioni F (2008) Concepts for morphing airfoil sections using bi-stable laminated composite structures. *Thin-Walled Struct* 46(6):689–701
4. Lee J-H, Lee J-I, Cho J-U (2020) A research on strength characteristics of compact tension specimens with heterogeneous composite materials bonded by adhesives. *J Comput Theor Nanosci* 17(7):3218–3223
5. Mawat MJ (2018) Simulation of cylindrical body structure subjected to flow in different reynolds number regimes. *Muthanna J Eng Technol (MJET)* 6(1)
6. Papageorgakis GC, Assanis DN (1999) Comparison of linear and nonlinear RNG-based k-epsilon models for incompressible turbulent flows. *Num Heat Transf: Part B: Fundamentals* 35(1):1–22
7. Petinrin MO, Onoja VA (2017) Computational study of aerodynamic flow over NACA 4412 airfoil. *Br J Appl Sci Technol* 21(3):1–11
8. Colorado J et al (2012) Inertial attitude control of a bat-like morphing-wing air vehicle. *Bioinspir Biomim* 8(1):016001
9. Supekar AH (2007) Design, analysis and development of a morphable wing structure for unmanned aerial vehicle performance augmentation. The University of Texas at Arlington
10. Rodrigue H et al (2016) Effect of twist morphing wing segment on aerodynamic performance of UAV. *J Mech Sci Technol* 30(1):229–236
11. Vos R, Grdal Z, Abdalla M (2010) Mechanism for warp-controlled twist of a morphing wing. *J Aircr* 47(2):450–457
12. Launius RD, Jenkins DR (2012) Coming home: reentry and recovery from space. Government Printing Office
13. Icardi U, Ferrero L (2009) Preliminary study of an adaptive wing with shape memory alloy torsion actuators. *Mater Des* 30(10):4200–4210
14. Jones H (2018) The recent large reduction in space launch cost. In: 48th International conference on environmental systems
15. <https://www.buran-energia.com/documentation/documentation-akc-aerodynamic-designing.php>. Accessed on 4 April 2021

Single Blow Characteristics of a Porous Spherical Bed Regenerator at Liquid Nitrogen Temperature



V. M. Abhiroop, R. I. Vivek, K. E. Reby Roy, and B. R. Vishnu

Abstract The thermal–hydraulic performance of porous spherical bed regenerator was investigated in the present study. For this, a laboratory apparatus was developed with a passive system for evaluating the performance of a spherical bed regenerator at liquid nitrogen temperature with different porosities and mass flow rates of (0.4, 0.5, 0.6) and (2.29 g/s, 2.813 g/s, 3.33 g/s), respectively. The effectiveness of the regenerator was found to improve with increasing mass flow rate and decreasing porosity. The regenerator performed best with a mass flow rate and porosity of 2.29 g/s and 0.4, respectively.

Keywords Passive regenerator · Porosity · Chill down

1 Introduction

A regenerator is a type of heat exchanger with a high heat capacity porous matrix that stores and releases energy during alternate half cycles and is widely used for thermal energy storage in both high and low temperature applications. Electrocaloric, elastocaloric, magnetocaloric and magnetic systems are the most common applications utilizing active liquid regenerators [1–3]. In addition to the above, solar heat storage, metallurgical industries and glass industries are some of the applications of high temperature regenerators [4–6].

The thermal–hydraulic performance of spherical bed regenerators using water as the heat transfer fluid was investigated for stainless steel, lead and gadolinium spheres, and minimum axial flow conduction in a stainless steel matrix was found [7]. Thermal performance studies on regenerators also revealed their reliance on pressure drop and heat transfer effectiveness, as well as the importance of lower aspect ratios when considering viscous and axial conduction losses [7–9]. In addition

V. M. Abhiroop (✉) · R. I. Vivek · K. E. R. Roy
TKM College of Engineering, Kollam, India
e-mail: abhiroop.v.m@gmail.com

B. R. Vishnu
National Institute of Technology, Trichy, India

to the above, the reports indicated that large-sized regenerator bed can enhance the thermal performance of regenerators, which, on the other hand, increases pressure drop and matrix volume [8]. Despite of the fact that various regenerator beds such as packed spheres and parallel plates are widely used with different heat transfer fluids, the effect of porosity on regenerators with working fluid at cryogenic temperatures are least explored, and satisfactory improvements in heat transfer and viscous drops are not yet achieved [10]. Another factor that influences the overall performance of the regenerator at low Reynolds number and capacity applications is the effect of the regenerator's heat capacity [11].

The regenerator geometry, flow characteristics and nature of the device also play a significant role in thermal performance. The use of a passive device with conventional materials allows for a more cost-effective investigation of the effect of regenerator geometry on heat transfer and pressure drop [12]. The flow through the cryogenic regenerators is mostly unsteady, and the ratio of pressure drop for unsteady flow is about 2.5 times the steady flow pressure drop [13, 14]. Therefore, in the present paper, investigation on heat transfer characteristics of the spherical bed regenerator with various porosities was done with a passive experimental setup for single blow steady flow at liquid nitrogen temperatures.

2 Materials and Methods

The experiment setup consisted of a nitrogen gas cylinder, Dewar vessel, flow control valves, data acquisition system, heater, flow meter, transfer lines, regenerator and thermocouples. Figure 1 shows the experimental setup used in the study.

The regenerator pipe has an l/d ratio of 4.43 and a wall thickness of 1.2 mm, and it has a spherical bed matrix with varying porosities. The outer wall temperatures were

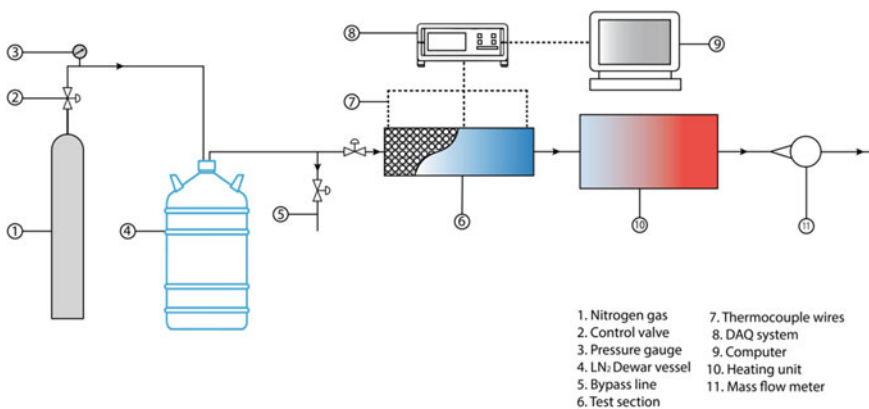


Fig. 1 Experiment setup

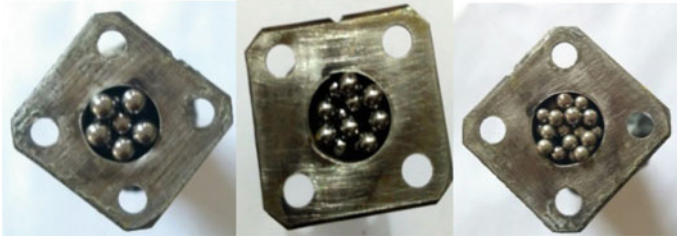


Fig. 2 Fabricated spherical bed regenerator

measured using thermocouples which were placed at three different x/l positions 0.1, 0.5 and 0.9, where x is the distance from inlet and l is the length of regenerator.

At each location, 3 T-type thermocouples were fixed circumferentially at equal angles for the temperature measurement. Uniform stainless steel spheres of grade SS304 were used as the storage matrix in experimentation. The ratio of the diameter of the sphere to the inner diameter of regenerator housing were 0.19, 0.28 and 0.33, making the porosity of the regenerator bed 0.4, 0.5 and 0.6 as illustrated by Fig. 2.

Liquid nitrogen was used as the working fluid. Gaseous nitrogen was used to pressurize the LN₂ from the Dewar vessel. The nitrogen cylinder was connected to the Dewar vessel with a flexible hose through a pressure regulator. The regulator has two dials, one displaying the cylinder pressure and the other displaying the line/discharge pressure. From Dewar to bypass valve, stainless steel transfer lines were employed for establishing a connection between Dewar and bypass valve. The bypassed fluid was exhausted into the atmosphere through a flexible hose. The test section was placed subsequent to the bypass valve. The exit of the test section was connected to the heater section where coiled copper tubes were dipped in a chamber containing water. The fluid leaving the test section was made to pass through the coiled copper tubes. Two heaters, each with 2 KW capacity was employed for heating water. The test fluid is completely converted to vapour phase before expelling to the atmosphere. The exit from the heater was connected to the mass flow meter. Experiments were carried out with mass flow rates of 2.29 g/s, 2.813 g/s and 3.33 g/s, and inlet pressures of 7.5 psi, 10 psi and 12.5 psi, respectively. The test specimen was kept in a horizontal position to minimize the effect of gravity in the chill down process. Nitrile rubber was used as an insulator. Data acquisition system (KEYSIGHT 34970A) was used for monitoring the data. The test section was purged with gaseous nitrogen prior to the start of the experiment to remove water vapour and other contaminants from the transfer lines. Following this, a leak test was conducted to ensure the efficacy of joints.

The nitrogen gas from the cylinder was introduced to Dewar vessel for pressurizing the liquid nitrogen to the test section. Initially, the bypass valve was set to open and the valve to the test section was kept closed. This was to ensure the chill down of the transfer line to the test specimen prior to the experiment. The heater and data acquisition system was kept on. Then, the bypass valve was closed and the valve to the test section was made open. Dynamic response in temperature was recorded by

the data acquisition system. The flow rate was measured using a mass flow meter. The experiment was conducted until a steady state was achieved.

The Nusselt number (Nu) for the packed bed of spheres was evaluated from the correlation given below [15].

$$\text{Nu} = 2.876 \left(\frac{\text{Pr}^{\frac{1}{3}}}{\varepsilon} \right) + 0.3023 \left(\frac{\text{Pr}^{\frac{2}{3}}}{\varepsilon} \right) \text{Re}^{0.65} \quad (1)$$

where Pr denotes the Prandtl number, ε denotes the porosity of the regenerator matrix, and Re denotes the flow Reynolds number.

Porosity (ε) of regenerator was calculated from

$$\varepsilon = \frac{V - V_{\text{matrix}}}{V} \quad (2)$$

where V is the total volume of regenerator in m^3 and V_{matrix} is the volume occupied by the matrix in m^3 .

The effectiveness (e) was calculated using the equation

$$e = \frac{(mC_{\text{pa}}T_{\text{ca}}) - (mC_{\text{ph}}T_{\text{h}})}{(mC_{\text{p min}})(T_{\text{c}} - T_{\text{h}})} \quad (3)$$

where m denotes the mass flow rate in kg/s , C_{pa} denotes the mean average specific heat in kJ/kg K , C_{ph} denotes the specific heat of hot fluid in kJ/kg K , $mC_{\text{p min}}$ represents the min heat capacity of fluid in kJ/K , T_{ca} denotes the mean average temperature in K and T_{c} denotes the temperature of the cold fluid in K and T_{h} is the temperature of the hot fluid in K .

Colburn factor (j) was defined by

$$j = \frac{\text{Nu}}{\text{Re} \times \text{Pr}^{\frac{1}{3}}} \quad (4)$$

and

$$\frac{\text{NPH}}{\text{NTU}} = \frac{f \times \text{Re} \times \text{Pr}}{4\text{Nu}} \quad (5)$$

And friction factor, f was calculated using Ergun's correlation.

3 Results and Discussion

The three regimes of flow boiling namely nucleate boiling, transition boiling region and film boiling are well distinguished with their underlining characteristics. The Nucleate region was identified with a constant temperature region, and here, the flow will be bubbly or slug flow. The transition region was distinguished by a sharp temperature rise, whereas the film boiling regime was distinguished by a constant temperature gradient and a flow structure that could be annular or stratified. These regimes occurred in inverse order in the normal chill down processes. In addition to this, a sudden temperature drop was found along with the transition regime. The cold blow experiment was physically similar to the chill down process. Flow through a packed bed of spheres created eddies, and hence, a large amount of turbulence was imparted to the flow. Often these eddies could tear off the boundary layer and vapour-fluid interfaces. Therefore, film boiling and transition regimes would not be distinguishable in these cases as shown in Fig. 3.

Figure 3 depicts the chill down curves of the regenerator with a porosity of 0.6 during the cold blow process at mass flow rates of 2.29 g/s, 2.813 g/s and 3.33 g/s at various locations. From Fig. 3, it was observed that for a lower mass flow rate of 2.29 g/s and there was a difference of 149 s in chill down time between inlet and exit of the regenerator and, the chill down time decreased to 67 s with an increase in mass flow rate to 3.33 g/s.

Figure 4 shows the distribution of temperature along with the regenerator for different mass flow rates. It was discovered that there was a temperature gradient along the length of the regenerator. This temperature gradient increased with the increase in mass flow rate due to the increase in utilization factor. An increase in temperature gradient with respect to the length of the regenerator with an increase in porosity was observed due to larger void spaces in the high porosity regenerator matrix. The working fluid passing through the void spaces separates into vapour and liquid phases, and this vapour phase may hinder the liquid phase from involving in heat transfer with the solid matrix. However, in low porosity beds where the void space was less, the vapour-liquid interface may tear off resulting in better heat transfer due to higher turbulence.

Figure 5 shows the chill down curves for varying mass flow rates and at different porosities of the regenerator. It was noted that the chill down time decreased with an increase in mass flow rate at constant porosities. The thermal capacity of the working fluid increased with a considerable increase in mass flow rates, which in turn resulted in an increase in utilization factor. The increased thermal capacity of the working fluid allows heat to be removed at a faster rate, allowing for faster chill down. It was observed that there was a decrease in chill down time by 226 s with an increase in mass flow rate by 45% for regenerator with porosity 0.4 and the drop in chill down time reduced to 183 s with an increase in mass flow rate by 45% for porosity 0.6.

The effect of the porosity of the packed bed on the thermal response of the regenerator is better represented by Fig. 6. The temperature drop for the regenerator bed with porosity 0.4 is much greater than for the regenerator with higher porosities, as

Fig. 3 Temperature time graph for porosity 0.6 at different mass flow rates **a** 2.29 g/s, **b** 2.813 g/s and **c** 3.33 g/s

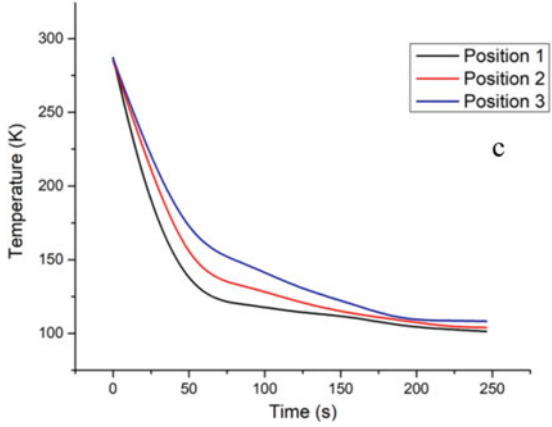
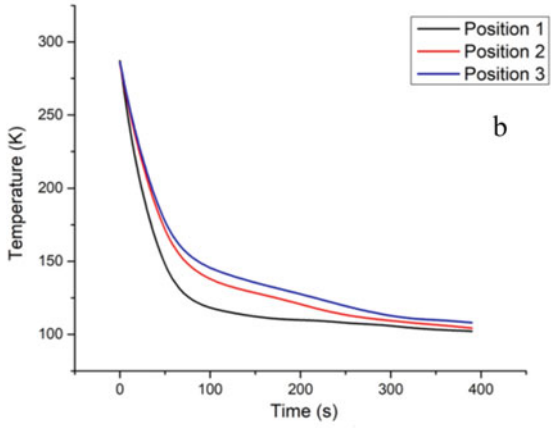
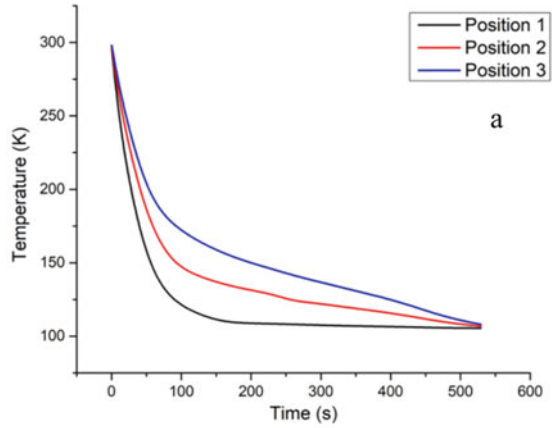


Fig. 4
Temperature-dimensionless position plot at different mass flow rates **a** 2.29 g/s, **b** 2.813 g/s and **c** 3.33 g/s

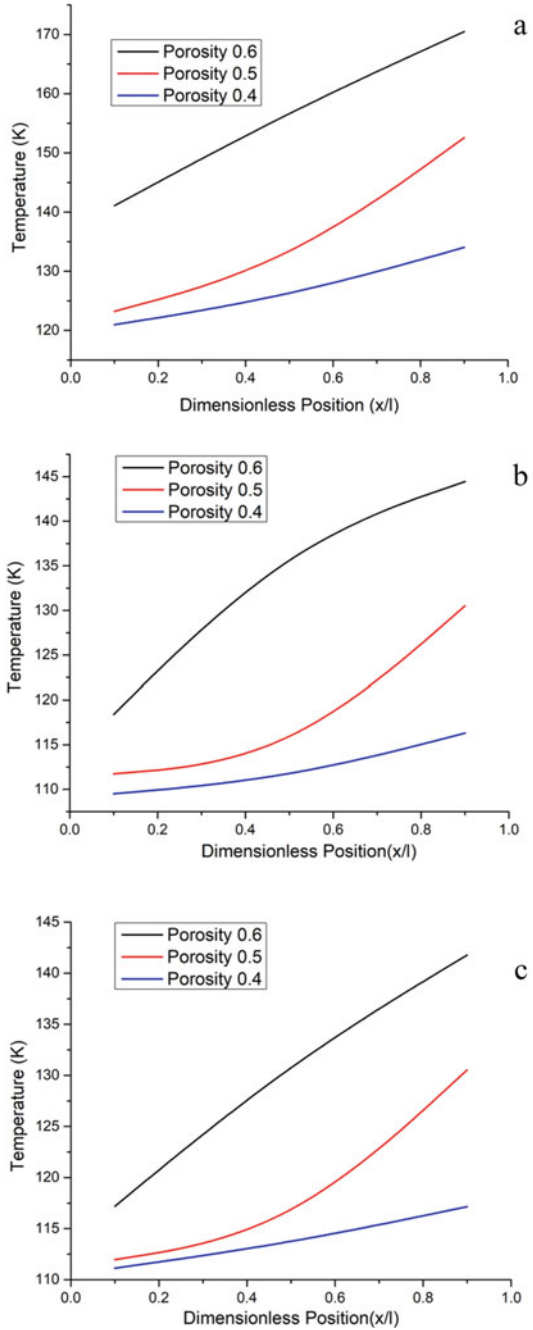
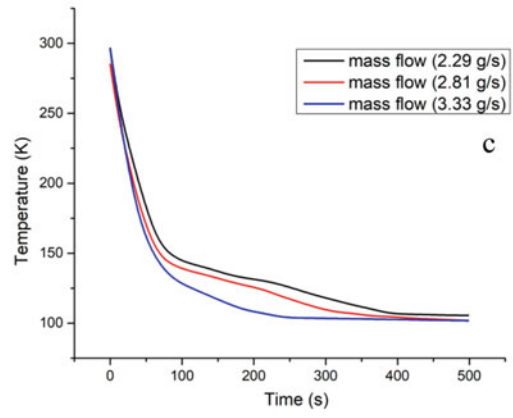
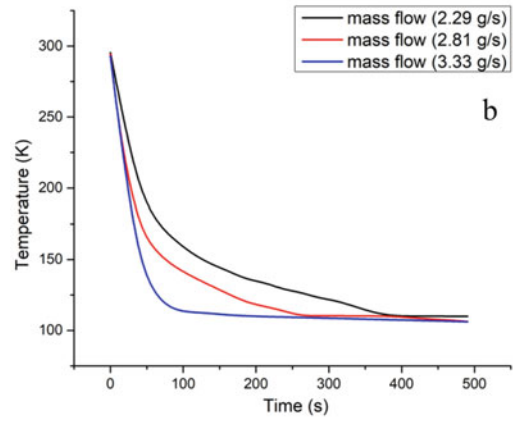
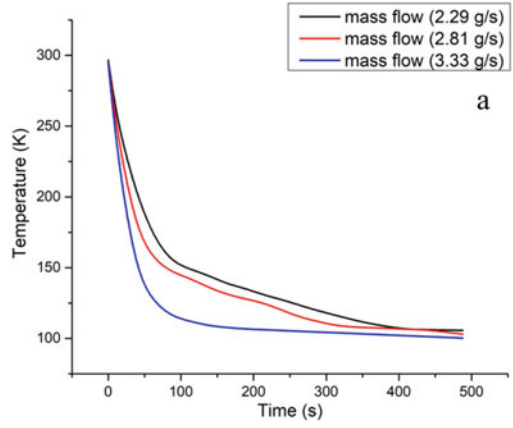


Fig. 5 Temperature time graph at different porosities **a** 0.4, **b** 0.5 and **c** 0.6



shown by the plot. A higher surface area to volume ratio is the characteristic of a lower porosity regenerator. Heat transfer between the regenerator matrix and working fluid will be increased due to increased surface area.

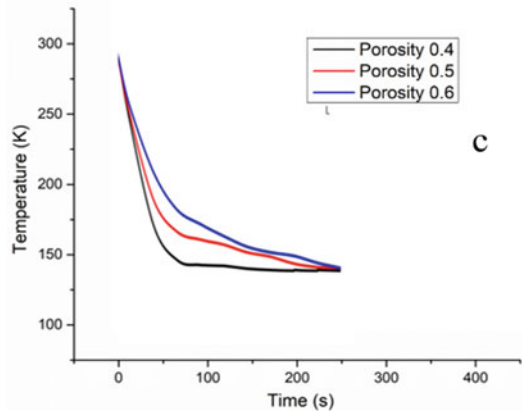
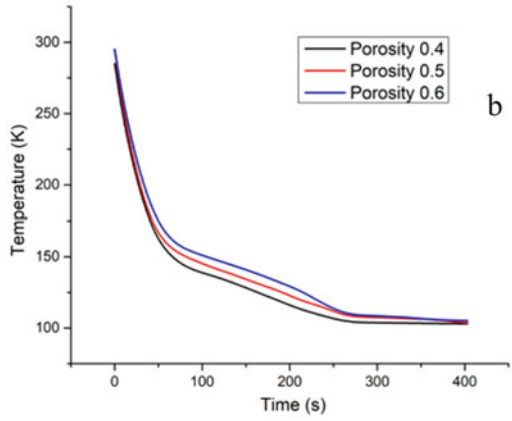
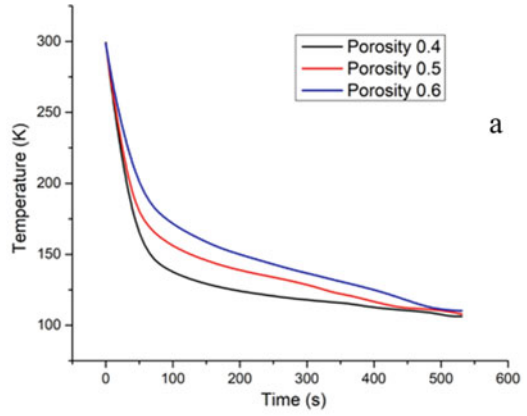
Figure 7 shows the Nusselt number–Reynolds number plot for porosities 0.4, 0.5 and 0.6. Nusselt number varied directly with Reynolds number, the heat transfer characteristics could be enhanced with the increase in Reynolds number. There was an increase in Nusselt number by 25% with an increase in mass flow rate by 45% for all the three porosities. This enhancement in heat transfer was due to the increase in the turbulence of flow with the increase in Reynolds number. Whereas the increase in Nusselt number was caused by an increase in convective heat transfer between wall and fluid as a result of a decrease in the wall and bulk temperature due to increased mass flow [16].

The particle diameter has a significant role in the pressure drop and heat transfer characteristics of a packed bed regenerator. Irrespective of operating condition and regenerator dimensions, friction factor (f) had a direct relation with pressure drop which depends on particle Reynolds number only [7]. From Fig. 8, it was observed that with the decrease in porosity of the regenerator, the friction factor increases. A linear trend was observed in regions of low particle Reynolds number values since Darcy's law remains valid over these regions. The deviation from this occurs due to inertia effects caused by increased particle Reynolds number. The Colburn factor is a direct implication of heat transfer characteristics. As shown in Fig. 9, the enhanced Colburn factor is observed with low porosity values.

Heat transfer characteristics of a packed bed regenerator could be duly enhanced with the use of a low porosity matrix. However, this could earn penalties in pressure drop of the flow through the packed bed. So, for an economical operation of the regenerator, a balance between these two factors is of greater importance. Figure 10 shows the plot between j/f and Reynolds number. The ratio j/f is of greater significance as the friction factor (f) is a direct implication of pressure drop and the Colburn factor (j) is a representation of the heat transfer characteristics of the regenerator. Regenerator geometry with higher j/f with respect to Reynolds number is better under pressure drop and heat transfer considerations [17]. Thus, regenerator bed with a low porosity value is better suited for the purpose. Similar to Fig. 10, Fig. 11 also showed the variation of the ratio of non-dimensional numbers representing pressure drop and quality of heat transfer against Reynolds number. Here, for representing pressure drop in a certain length, "number of pressure heads" (NPH) was used and the "number of transfer units" (NTU) represents the heat transfer quality. From Fig. 11, the geometry with porosity 0.4 is preferred, considering heat transfer and pressure drop. An increase in turbulence could be clearly interpreted from the elevated curves at a high Reynolds number.

The improved effectiveness is an inevitable requirement for a regenerator. Many thermophysical parameters have a direct influence on the effectiveness of a regenerator. Porosity and working mass flow rates have a better influence on it. This is better shown in Fig. 12. It indicated that with an increase in mass flow rate, the heat transfer increased in regenerator bed with lower porosities since low porosity bed provided a greater surface area for heat exchange. In addition to this, higher porosity

Fig. 6 Temperature time graph at different mass flow rates **a** 2.29 g/s, **b** 2.813 g/s and **c** 3.33 g/s



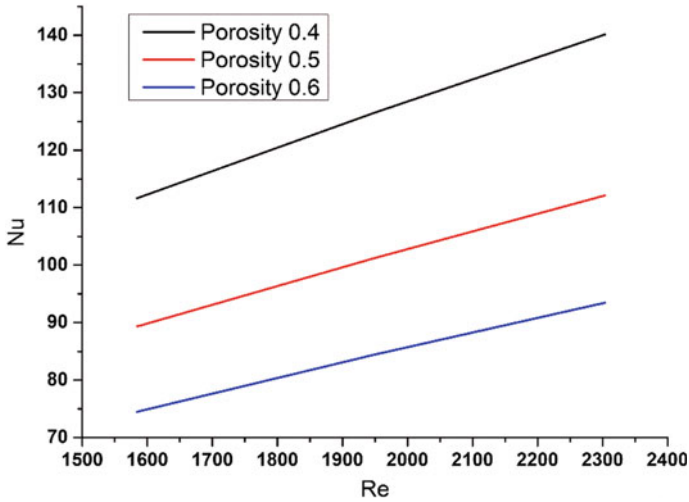


Fig. 7 Nusselt number versus Reynolds number graph

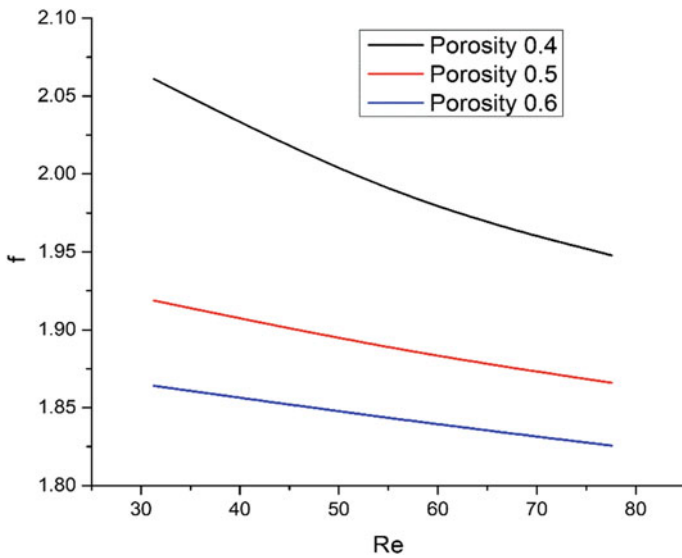


Fig. 8 Friction factor versus particle Reynolds number

regenerator bed possessed large void spaces which could facilitate the escape of a part of working fluid without proper heat exchange. An increase in mass flow rate alone will not accelerate the heat transfer rates, since a portion of the working fluid was bypassed without taking part in the heat transfer mechanism. This contributed to a significant reduction in the effectiveness of the regenerator bed. As porosity

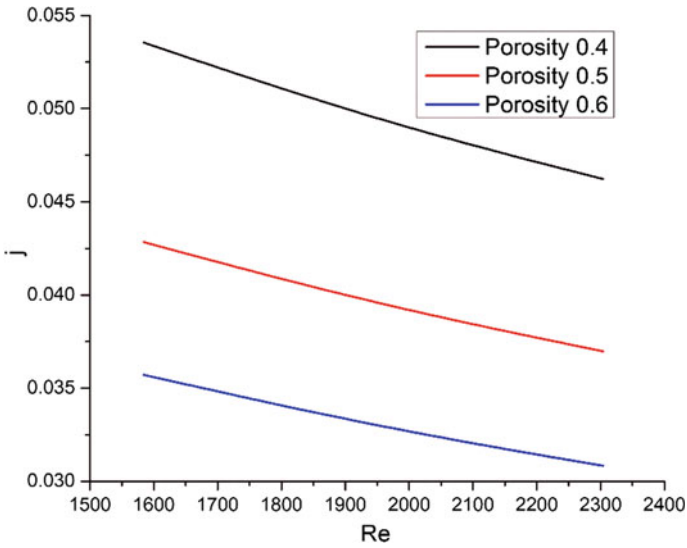


Fig. 9 Colburn factor versus Reynolds number

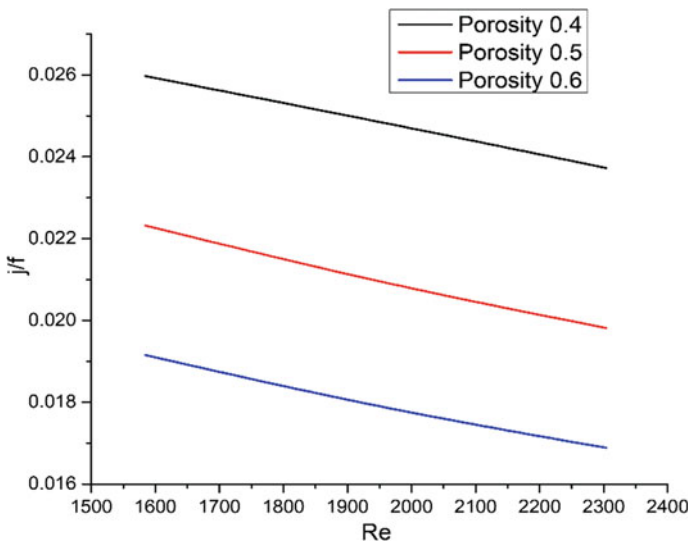


Fig. 10 j/f versus Reynolds number

decreased to 0.4, the effectiveness values were drastically increasing. This higher slope towards lower porosity values regardless of mass flow rates indicated that porosity has an inverse relation with effectiveness.

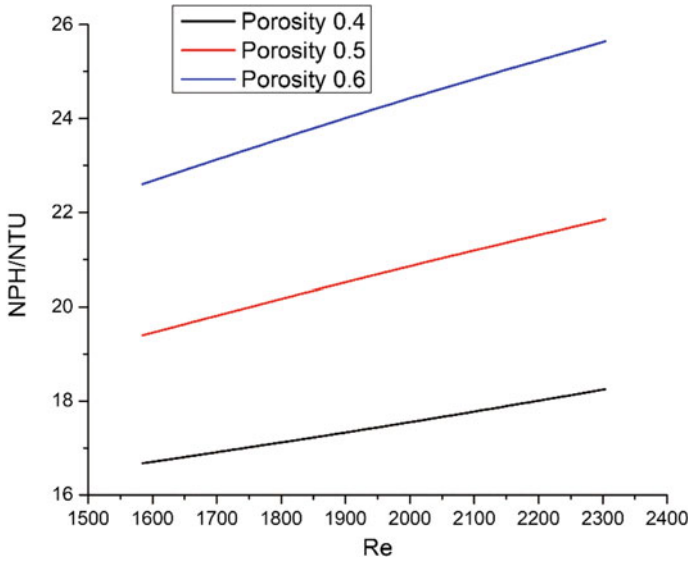


Fig. 11 NPH/NTU versus Reynolds number

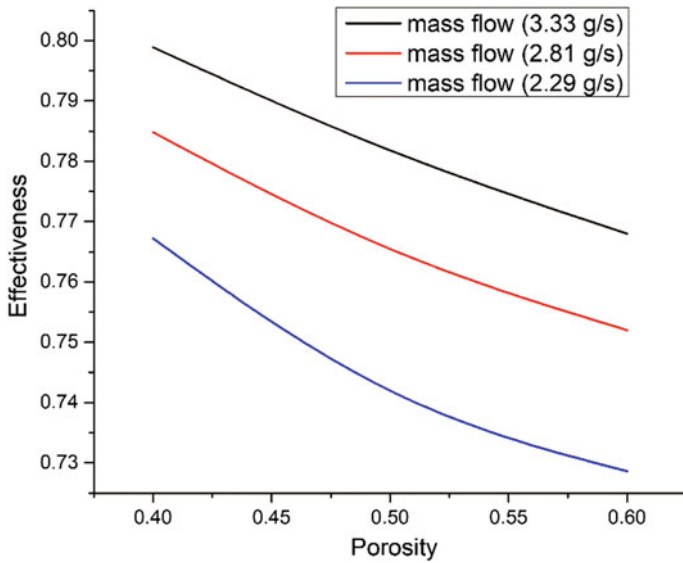


Fig. 12 Effectiveness versus porosity

4 Conclusion

An experimental investigation on stainless steel spherical bed regenerator was successfully conducted with liquid nitrogen as working fluid for three different mass flow rates (2.29, 2.813, 3.33 g/s) and porosities (0.4, 0.5, 0.6).

The following were the major findings from the study:

- The rapid chill down was achieved for the regenerator at higher mass flow rates due to a tremendous increase in utilization factor.
- The friction factor increased with an increase in mass flow rate, and this could earn penalties in the form of pressure drop.
- An increase in Nusselt number accounting to 25% was achieved with a 45% increase in mass flow rate at all three porosities.
- Maximum effectiveness of 0.798 was obtained for regenerator with porosity 0.4 at a mass flow rate of 3.33 g/s.
- An optimum porosity of 0.4 at a mass flow rate of 2.29 g/s was obtained for the regenerator in the present study, considering both pressure drop and heat transfer characteristics.

Acknowledgements The research facility provided at Space Technology Laboratory of Mechanical Engineering Department, TKM College of Engineering is duly acknowledged.

References

1. Guo D, Gao J, Yu YJ, Santhanam S, Slippey A, Fedder GK, McGaughey AJH, Yao SC (2014) Design and modeling of a fluid-based micro-scale electrocaloric refrigeration system. *Int J Heat Mass Transf* 72:559–564
2. Qian S, Geng Y, Wang Y, Ling J, Hwang Y, Radermacher R, Takeuchi I, Cui J (2016) A review of elastocaloric cooling: materials, cycles and system integrations. *Int J Refrigeration* 64:1–19
3. Gschneidner Jr KA, Pecharsky VK (2008) Thirty years of near room temperature magnetic cooling: where we are today and future prospects. *Int J Refrig* 31(6):945–961
4. Raja VB, Shanmugam V (2012) A review and new approach to minimize the cost of solar assisted absorption cooling system. *Renew Sustain Energy Rev* 16(9):6725–6731
5. Wang LW, Wang RZ, Oliveira RG (2009) A review on adsorption working pairs for refrigeration. *Renew Sustain Energy Rev* 13(3):518–534
6. Dieng AO, Wang RZ (2001) Literature review on solar adsorption technologies for ice-making and air-conditioning purposes and recent developments in solar technology. *Renew Sustain Energy Rev* 5(4):313–342
7. Trevizoli P, Liu Y, Tura A, Rowe A, Barbosa J Jr (2014) Experimental assessment of the thermal–hydraulic performance of packed-sphere oscillating-flow regenerators using water. *Exp Therm Fluid Sci* 57:324–334
8. Trevizoli PV, Peixer GF, Barbosa JR Jr (2016) Thermal–hydraulic evaluation of oscillating-flow regenerators using water: Experimental analysis of packed beds of spheres. *Int J Heat Mass Transf* 99:918–930
9. Shah RK, Sekulic DP (2003) *Fundamentals of heat exchanger design*. John Willey and Sons

10. Nielsen KK, Tusek J, Engelbrecht K, Schopfer S, Kitanovski A, Bahl CR, Smith A, Pryds N, Poredos A (2011) Review on numerical modeling of active magnetic regenerators for room temperature applications. *Int J Refrigeration* 34(3):603–616
11. Frischmann M, Engelbrecht J, Nellis G, Klein S (2008) Heat transfer coefficient in a packed sphere regenerator for use in active magnetic regenerative refrigeration
12. Schopfer S (2011) Experimental and numerical determination of thermohydraulic properties of regenerators subjected to oscillating flow. PhD dissertation
13. Zhao TS, Cheng P (1996) Oscillatory pressure drops through a woven-screen packed column subjected to a cyclic flow. *Cryogenics* 36(5):333–341
14. Abhiroop VM, Vivek RI, Roy KE (2018) Numerical investigation on the pressure drop characteristics for steady and pulse flow along a compact regenerator. *Indian J Cryogenics* 43(1):114–118
15. Gupta SN, Chaube RB, Upadhyay SN (1974) Fluid—particle heat transfer in fixed and fluidized beds. *Chem Eng Sci* 29(3):839–843
16. Pamuk MT, Özdemir M (2012) Heat transfer in porous media of steel balls under oscillating flow. *Exp Therm Fluid Sci* 42:79–92
17. Rühlich I, Quack H (2002) Investigations on regenerative heat exchangers. In: *Cryocoolers*, vol 10. Springer, Boston, MA, pp 265–274

Design, Development, and Numerical Analysis of Mist Nozzle and Its Impact on Performance Parameters of an Evaporative Cooler



Avinash M. Deshmukh, S. N. Sapali, Ajit B. Shinde, and Niyaj D. Shikalgar

Abstract The comfort cooling system is considered one of the major elements that absorbs high energy from all today's essential commodities. And, it is one of the sources for global warming. An evaporative cooling system is commonly referred to as an alternative to air-conditioning systems working on vapour compression refrigeration cycles. Comparatively, the evaporative cooling systems consume 55–75% less energy compared to the phase change refrigeration system. In this research article, the development of a mist nozzle and its CFD simulation is carried out at different inlet water temperatures and its effect on pressure drop at the outlet end of the nozzle. By measuring the reduction in temperature, cooling capacity, and saturation efficiency, the experimental analysis leads to the discovery of performance characteristics such as cooling effect. These performance parameters were measured in a variety of environments and with variable air mass flow rates. Using the experimental data, a linear regression analysis is used to construct an empirical association to forecast the decline in air temperature. The experimental cooling air temperature and the predicted cooled air temperature are validated and found with good agreement.

Keywords Mist nozzle · Evaporative cooling · Air conditioning

A. M. Deshmukh (✉)
SCTR's Pune Institute of Computer Technology, Pune, Maharashtra, India
e-mail: amdeshmukh@pict.edu

S. N. Sapali · A. B. Shinde · N. D. Shikalgar
College of Engineering Pune, Pune, Maharashtra, India
e-mail: sns.mech@coep.ac.in

A. B. Shinde
e-mail: khodashi5@gmail.com

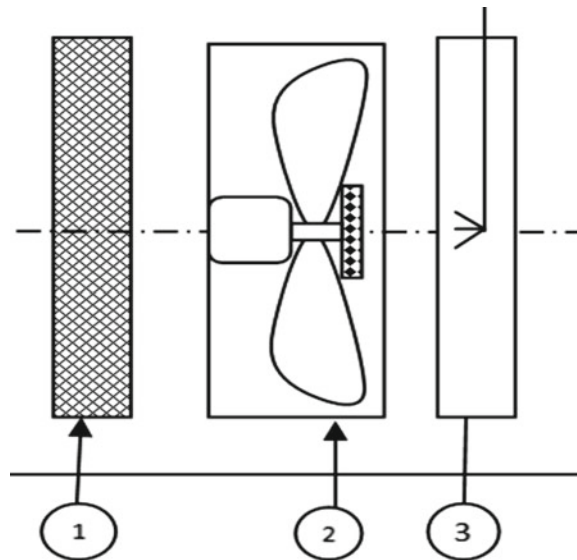
N. D. Shikalgar
e-mail: nds.mech@coep.ac.in

1 Introduction

Comfort air conditioning is an integral part of industrial and domestic applications. It helps to provide and maintain the temperature and humidity of the space/equipment/human being as per the requirement. In domestic applications, it consumes around 30% of the electricity of total electrical energy consumption, also harming the environment. The mist spray's direct evaporative cooler can be considered as an alternative system for providing and maintaining the comfort conditions as required in domestic as well as in industrial applications, of course, with certain limitations. This research article focuses on the development of design and development of an evaporative cooler without using any cooling pad and water circulation pump. A fine mist spray is generated by using a combination of mist nozzle (3) and spinning disc having projected teeth attached to the fan blade (2) as shown in Fig. 1.

The evaporation rate of swamp coolers, which are widespread in arid climates, was calculated, and it was discovered that the mist spray evaporative cooler is more efficient and effective in terms of water and energy consumption [1]. Chakrabarti et al. [2] constructed a one-dimensional energy and mass balance model that can predict the effect of various parameters on the air temperature inside the air washer heat exchanger, such as the temperature of the water used for feeding, airflow rate, and air humidity. The cooling impact of an oscillating mist fan in a large indoor space was tested, and it was discovered that a 5% increase in local humidity reduced the temperature by 0.2–2.5 K [3]. Researchers in Niamey, Niger Republic, utilized a theoretical feasibility index model to evaluate the evaporative cooler's month-by-month potential [4]. The feasibility index is used to measure whether evaporative cooling provides comfort cooling or not. It is based on the difference between wet-bulb temperature

Fig. 1 Block diagram of the test set-up



and wet-bulb depression (the difference between the DBT and WBT). To anticipate the output air temperature, Igor et al. [5] analysed a numerical model using a compact metallic air/water interface direct evaporative cooler. The experimental findings are compared to projected results, with a maximum error of 1.33%. By studying the exchange of energy and concentration between the air stream and water mist particles, Wu et al. [6] suggested a simple correlation to calculate the cooling efficiency theoretically. Sheng and Nnanna [7] established a formula to assess the performance of outlet frontal air velocity and cooling impact. According to the findings, cooling effectiveness is proportional to frontal air velocity. EI-Sayed [8] has created a mathematical model of an evaporative cooling pad's heat and mass transfer balance to optimize performance-affecting parameters and anticipate outlet air qualities under various operating parameters'. Rianguvilaikul and Kumar [9] modelled the dew point heat and mass transfer process. The testing results show that the performance of the mist spray evaporative cooler is greatly improved in terms of temperature reduction, increased cooling capacity, and saturation efficiency, as well as a significant reduction in energy input, noise level, and water usage. Because the unit does not require water storage, it is almost free of fungus and mosquitoes. Mist spray with and without cooling pads, various types of cooling pad materials, and mist generating techniques have all been the subject of extensive investigation.

2 Development of Nozzle

The nozzle body, spacer, and orifice disc are the three basic components of a low-pressure mist spray nozzle. Internally, the nozzle body has three different diameter holes. From the entrance to the outlet, the hole diameters grow. The spacer is inserted into the nozzle body and has a cylindrical pin form that freely rotates or swirls. At the nozzle body's outlet end, an orifice disc is press-fitted. A small conical hole is located in the centre of the orifice disc. Fluid enters through the inlet end, which has a smaller bore diameter than the spacer, and the spacer rotates in the nozzle body, creating a swirling effect on the fluid and forcing it onto the orifice disc, which, in turn, imparts a swirling flow to the fluid before discharging it through the spray orifice, producing very fine droplets of the fluid. In comparison to current existing mist generation systems, this unique designed mist nozzle creates swirling effect by rotation of cylindrical pin. This nozzle is easy to manufacture and having low maintenance cost along with reliable performance (Fig. 2).

2.1 CFD Analysis of Mist Nozzle

Effect of pressure drop through the nozzle by varying the inlet water temperature is analysed by keeping the water flow rate, inlet pressure constant. A nozzle is used to generate a high velocity of water by a drop in pressure. This nozzle is designed in

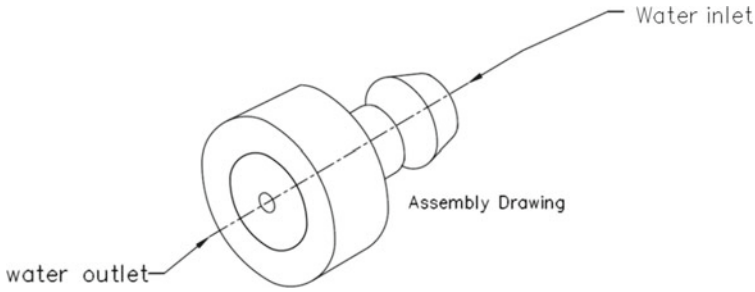


Fig. 2 Pictorial view of the developed nozzle

such a way that its internal diameters are of varying in size. A small rotating spacer is used to give the swirling action to the water particles and is used to reduce the pressure of the inlet water by increasing the velocity. When this high-velocity water is passed through a small orifice it generates the fine mist spray. In this CFD analysis, we have tried to attempt to find the effect of the inlet water temperature on the outlet pressure of water through the nozzle. The impact of incoming water temperature on pressure drop is depicted in Fig. 3. The CFD analysis is carried out by changing the water temperature from 27 to 40 °C, while the other parameters such as the rounded spacer diameter of 1.95 mm, inlet pressure 3 bar are kept constant.

The summary of variation in a drop in pressure concerning the rise in inlet water temperature is recorded as in Table 1.

According to the analysis, when the temperature of the incoming water rises, the pressure at the nozzle’s outlet drops, resulting in a rise in vacuum pressure, which causes high velocity at the exit and helps to generate the mist spray. We completed this investigation for a temperature range of 27–40 °C and observed that after 35 °C there was a maximum pressure reduction. As the temperature rises over 35 °C, the vacuum pressure begins to fall, as illustrated in Fig. 4.

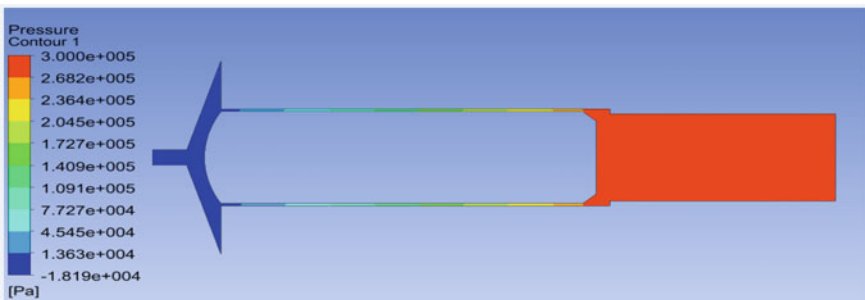


Fig. 3 Effect on a drop in pressure when the inlet water temperature is 27 °C

Table 1 Variation in a drop in pressure concerning inlet water temperature in the nozzle

Sr. No.	Inlet temperature of water (°C)	Drop in pressure (bar) (vacuum pressure)
1	27	0.09277
2	30	0.1302
3	33	0.1516
4	35	0.1819
5	36	0.1286
6	40	0.1202
7	27	0.09277

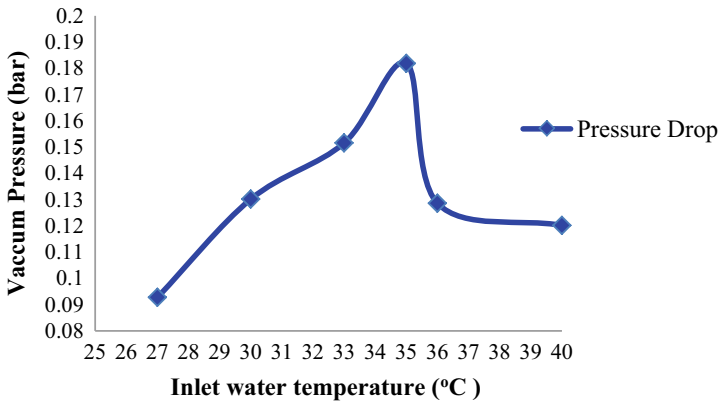


Fig. 4 Variation in vacuum pressure at the outlet of the nozzle

3 Experimentation

The rate of evaporation is determined by four key factors: the ambient temperature, relative humidity, airflow rate, and the free contact surface area between the air and the water surface. Looking at it, we do not have control over the ambient circumstances, and increasing the airflow rate increases the system’s power consumption; therefore, the only option left is the free contact surface area between the air and water surface. As a result, we used a combination of the mist nozzle and the spinning disc in the proposed experimental set-up to try to improve the free contact surface area between the air and water surface. The proposed experimental set-up is made up of five primary components: an axial fan, a low-pressure mist nozzle, a spinning disc, a fluid flow control valve, and a working duct/cabinet, as illustrated in Fig. 5. The fine mist is generated by the mist nozzle, which operates at a low pressure of 60–100 psi. This mist spray is projected on the spinning disc attached to the fan blade, and the mist water sprayed on the spinning disc is propelled outward along the disc surface due to centrifugal force and strikes the spinning disc’s projected fins, where it is sheared



Fig. 5 Experimental set-up of evaporative cooler

into small particles, increasing the surface area of open interaction between air and water particles.

4 Result Analysis

The experimental performance evaluation of the mist nozzle, effect of the orifice diameter of the nozzle on the mass flow rate, the effect of inlet water temperature of the nozzle on the mist generation or outlet pressure, and rise in velocity is performed. The role of various geometrical parameters of the spinning disc on the mist spray generation and performance of the evaporative cooler is discussed. The effect of the mass flow rate of air, the mass flow rate of water, on the performance measuring parameters of the evaporative cooler such as coefficient of performance of the cooler, saturation efficiency of the evaporative cooler, the outlet temperature of the air is discussed. Specific humidity is the mass of water contained by a unit mass of dry air. Relative humidity can be increased by introducing water in the form of numerous minute droplets into the air, using a process known as atomization by using the mist spray nozzle. The coefficient of performance is evaluated for various ambient conditions and with a varied mass flow rate of air.

The flow rate of water is varied by changing the nozzles of orifice diameter ranging from 0.3 to 1.0 mm as shown in Fig. 6, and the data recorded is as shown in Table 2.

From Fig. 7, it is observed that flow rate of water is almost linearly increasing with respect to orifice diameter. After the experimentation, as shown in Fig. 8, it is observed that the saturation efficiency increases with a rise in the mass flow rate of water, but at the same time the blow off quantity of water increases, so practically by taking care of cooling capacity and water quantity the mass flow rate of water 2.6 Lph is optimized with orifice diameter of nozzle is 0.6 mm. If you observe the saturation

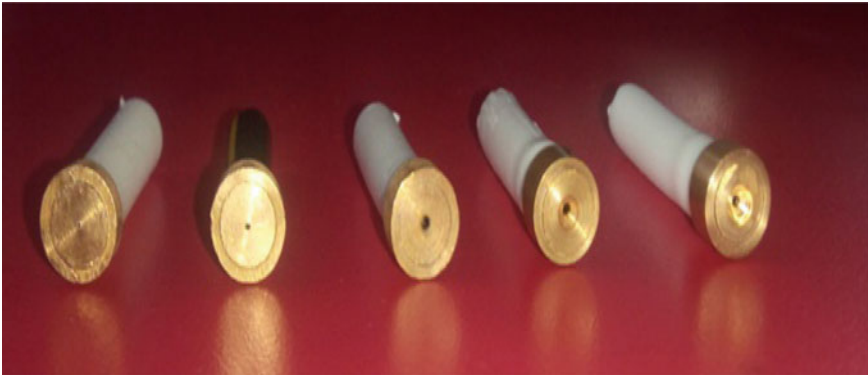


Fig. 6 Set of nozzles of varying orifice diameters

Table 2 Effect of Orifice diameter on the flow rate of water and saturation efficiency

Sr. No.	Orifice diameter (mm)	The flow rate of water (Lph)	Saturation efficiency %
1	0.3	1.2	56
2	0.5	2.3	72
3	0.6	2.6	79
4	0.7	3.1	82
5	0.8	3.96	84
6	0.9	4.8	85
7	1.0	6.2	86

efficiency at orifice diameter 0.6 mm is 79%, and at 1 mm orifice diameter, it is 86%; here, the change in saturation efficiency is only 7%; to achieve this, almost 3 times more water quantity is required. Hence, the 0.6 mm orifice diameter is optimized.

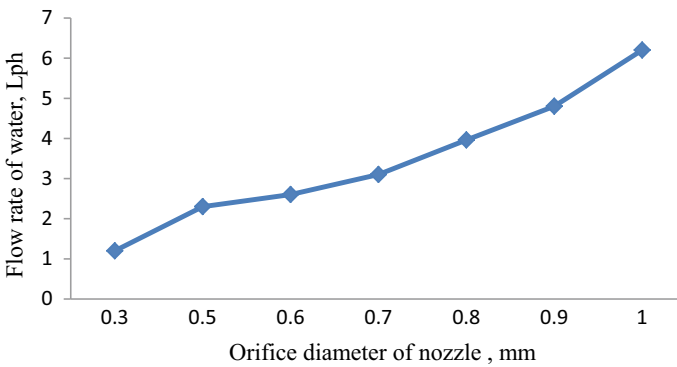


Fig. 7 Variation of flow rate of water with respect to nozzle orifice diameter

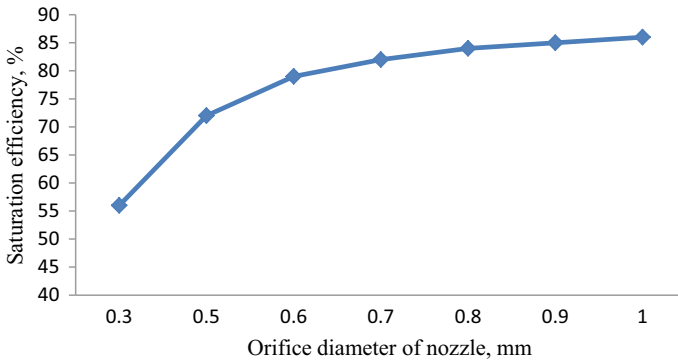


Fig. 8 Variation in saturation efficiency with respect to nozzle orifice diameter

The MSDEC’s saturation efficiency rises with an increase in air mass flow rate until it reaches a limit, at which point it begins to drop. Fine water particles are sprayed on the rotating spinning disc by the mist nozzle. Due to centrifugal action along the exterior surface of the disc, these water particles are driven forth and strike the projected fins on the spinning disc’s periphery. The disc’s projected fins shear the water particles into tiny particles once more, increasing the contact surface area between the water particles and the warm inlet air.

The mass flow rate of air was varied from 0.2 to 0.7 kg/s during the experiment. It has been noted in Fig. 9.

Minitab 17 is used to do the regression analysis. In this study, regression analysis is performed on 25 sets of experimental observations for distinct ambient conditions, and utilizing this data, the outlet air temperature T_2 of the mist spray direct evaporative cooler can be determined using empirical correlation.

$$T_{2\text{predicted}} = 5.52 + (0.394T_1) + (0.0042RH) + (439\omega) \tag{1}$$

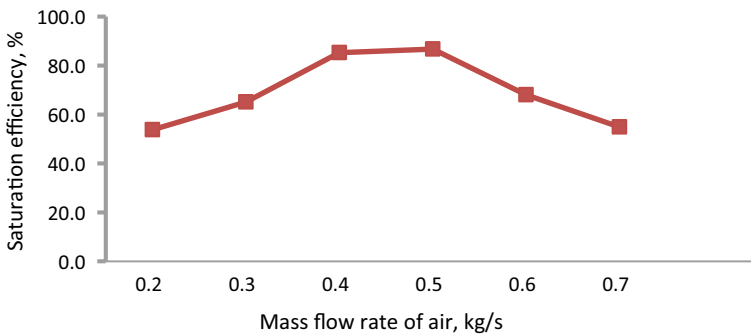


Fig. 9 Effect of mass flow rate of air on saturation efficiency

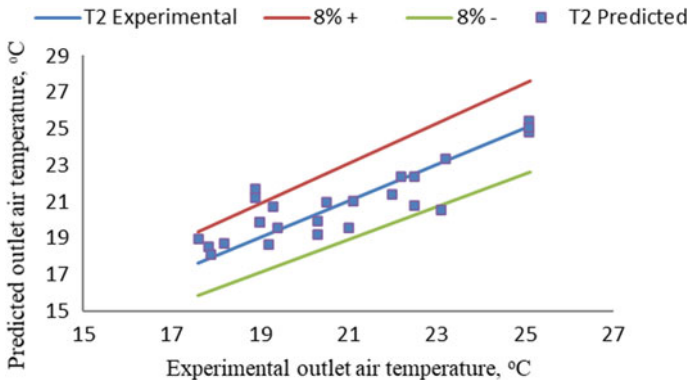


Fig. 10 Comparison of outlet air temperature

Equation 1 is specific for this experimental set-up and best suitable for the ambient air temperature range of 25–45 °C, the relative humidity in the range of 10–80% and inlet air velocity from 2 to 6 m/s. This equation predicts the outlet air temperature is in the order of $\pm 8\%$. Figure 10 shows the values of anticipated outlet air temperature estimated with the assistance of developed empirical correlation, and the values of measured outlet air temperature are in good agreement.

5 Conclusion

A low-pressure mist nozzle and its CFD simulation are carried out by varying the inlet temperature of the water. It is observed that there is an impact of variation in water temperature on the drop in pressure at the outlet end of the nozzle, resulting in a rise in vacuum pressure, which causes high velocity at the exit and helps to generate the mist spray. The experimental setup contains an axial fan with a speed regulator, spinning disc, and low-pressure mist nozzle. The temperature, cooling capacity, and saturation efficiency drop in the range of 5°–12°, cooling capacity up to 4 kW, and saturation efficiency in the range of 40% to 80%, respectively. It is also observed that these variations are an effect of ambient conditions, like ambient temperature and relative humidity, the mass flow rate of air. An empirical correlation is developed based on the experimental results by using the regression fit model. The outlet air temperature after cooling is found in good tune with the predicted value of cooling air temperature. The concept of mist generation could be applied in various industrial and agriculture industry applications, and the model can be scaled as per the applications.

References

1. Zhou K (2014) Calculation of evaporation rate of a droplets cluster and conceptual design of structure utilizing water droplets for evaporation. *Hydrol Current Res* 5(3):177
2. Chakrabarti SS, Bhandarkar LR, Vijawargiya A, Nageshwar Rao PSRK (2015) A mathematical approach in the formulation of a direct evaporative cooling device. *Int J Eng Res Technol (IJERT)* 4(2)
3. Farnham C, Zhang L, Yuan J, Emura K, Alam AM, Mizuno T (2017) Measurement of the evaporative cooling effect: oscillating misting fan. *Build Res Inf*
4. Akintunji LL, Haruna IU, Momoh BS. Theoretical evaluation of the potential of evaporative cooling for human comfort using feasibility index (Fi) model. *Int J Sci Technol Res* 3(3)
5. Kovacevic I, Sourbron M (2016) The numerical model for a direct evaporative cooler. *Appl Therm Eng*
6. Wu JM, Huang X, Zhang H (2009) Theoretical analysis on heat and mass transfer in a direct evaporative cooler. *Appl Therm Eng* 29:980–984
7. Sheng C, Nnanna AGA (2011) Empirical correlation of cooling efficiency and transport phenomena of a direct evaporative cooler. In: *Proceedings of the ASME 2011 international congress and exposition IMECE2011, Denver, Colorado, USA*
8. El-Sayed GK (2014) Performance of direct evaporative cooling system under Egyptian conditions. *J Climatol Weather Forecast* 2(2)
9. Riangvilaikul B, Kumar S (2010) An experimental study of a novel dew point evaporative cooling system. *Energy Build* 42:637–644